UNIVERSITÉ DE LORRAINE | BIBLIOTHÈQUES UNIVERSITAIRES

AVERTISSEMENT
DROIT D'AUTEUR

Ce document est le fruit d'un long travail approuvé par le jury de soutenance et mis à disposition de l'ensemble de la communauté universitaire élargie.

Il est soumis à la propriété intellectuelle de l'auteur. Ceci implique une obligation de citation et de référencement lors de l'utilisation de ce document. Toute contrefaçon, plagiat ou reproduction illicite encourt une poursuite pénale.

Contact bibliothèque : ddoc-theses-contact@univ-lorraine.fr
(Cette adresse ne permet pas de contacter les auteurs)

Code de la Propriété Intellectuelle. articles L 122. 4
Code de la Propriété Intellectuelle. articles L 335.2- L 335.10

UNIVERSITÉ DE LORRAINE
34 COURS LÉOPOLD — CS 25233
54052 NANCY CEDEX
TÉL : 03 54 50 54 00
CONTACT@UNIV-LORRAINE.FR
WWW.UNIV-LORRAINE.FR

UNIVERSITÉ DE LORRAINE

SIRENA
GeoRessources

Thèse

Présentée et soutenue publiquement pour l'obtention du titre de

DOCTEUR DE l'UNIVERSITE DE LORRAINE

Mention : Mécanique - Génie Civil

par **Baptiste FENNETEAU**

Sous la direction de Olivier DECK

Preliminary Design of Deep Tunnels in Continuous Rock Mass by Combining Numerical and Probabilistic Approaches

Soutenue publiquement le 20 novembre 2025

Membres du jury :

Directeur de thèse :	M. Olivier DECK	Professeur, École des Mines de Nancy, GeoRessources, Université de Lorraine, Nancy, France
Co-directeur de thèse :	M. Rasool MEHDIZADEH	Maitre de Conférence, École des Mines de Nancy, GeoRessources, Université de Lorraine, Nancy, France
Président de jury :	M. Jean SULEM	Professeur, École National des Ponts et Chaussées, Marne la Vallée, France
Rapporteurs :	M. Dashnor HOXHA	Professeur, Université d'Orléans, Orléans, France
	Mme Lina-Maria GUAYACAN-CARILLO	Maitre de Conférence (HDR), École National des Ponts et Chaussées, Marne la Vallée, France
Examinateurs :	Mme Nathalie CONIL	Chargée d'étude et de recherche (HDR), Ineris, Nancy, France
Membres invités :	M. François LAIGLE	Expert (Co-encadrant, PhD), Setec Terrasol, Lyon, France
	Mme Nathalie MONIN	Cheffe de Groupe (PhD), WSP France, Aix les Bains, France
	Mme Maria-Elena PARISI	Responsabile Struttura Organizzativa Geologia, TELT S.A.S, Collegno, Italie
	M. Benjamin LECOMTE	Directeur technique, Vinci Construction Grands Projets, France

Remerciements

Ce manuscrit de thèse est le résultat de trois ans de travail et je souhaite le commencer en exprimant ma profonde reconnaissance à toutes les personnes qui y ont contribué et qui m'ont assisté dans ce travail. Cette thèse est une thèse Cifre financée par WSP France (anciennement BG Ingénieurs Conseils).

J'aimerais commencer en remerciant tout particulièrement mon directeur de thèse, Olivier Deck, ainsi que mon co-directeur de thèse, Rasool Mehdizadeh, professeur et maître de conférences à l'École des Mines de Nancy, pour leur encadrement sans faille au sein du laboratoire GeoRessources. Je sais que les conditions n'ont pas toujours été optimales pour mon encadrement étant donné que je n'étais pas souvent présent à Nancy. Néanmoins, vous avez toujours été disponibles et bienveillants envers moi, tout en essayant de me challenger intellectuellement afin d'améliorer ma rigueur de travail, de m'apprendre à prendre du recul et de m'avoir poussé à me remettre en question. Un grand merci à vous deux, ce fut un vrai plaisir de travailler avec vous, et j'espère que l'occasion se représentera dans le futur.

Je souhaite aussi remercier tout particulièrement mon encadrant technique au sein de l'entreprise, François Laigle, président du comité technique de l'AFTES, expert ouvrages souterrains au sein de WSP jusque fin 2024, puis chez Setec-Terrasol. François, merci beaucoup pour ton aide et pour tout le temps que tu as consacré à me former, me transmettre tes connaissances et me faire part de ta très riche expérience professionnelle. Je pense que cela a été fondamental à la réussite de ce travail et m'a permis de remettre en question de nombreuses choses préétablies dans le domaine des ouvrages souterrains. Je n'oublierai pas nos nombreuses réunions qui ont été beaucoup plus longues que prévues, et que j'ai terminées avec beaucoup plus de questions comparées aux réponses initialement recherchées. Bonne continuation à toi chez Terrasol, j'espère que l'on aura de nouveau la possibilité de travailler ensemble.

Ce travail de thèse a été rendu possible grâce au financement de WSP France, ainsi que de l'ANR (Agence Nationale pour la Recherche), dans le cadre d'un contrat Cifre. Je souhaite donc remercier WSP France pour avoir soutenu et financé ce projet. Ce projet de thèse a été initialement développé par BG Ingénieurs Conseils, dont l'acquisition par WSP a eu lieu en 2023, et plus spécifiquement à l'initiative de François Laigle et François Martin. Un grand merci à vous deux pour avoir imaginé ce sujet de thèse passionnant et pour m'avoir fait confiance pour sa réalisation. Je souhaite aussi remercier mes responsables chez WSP, Nathalie Monin, Emmanuel Rigaud et Thibaut Métivier, qui m'ont permis de réaliser ce travail dans les meilleures conditions, en me laissant suffisamment de liberté pour pouvoir m'organiser comme je le souhaitais, ainsi qu'en me donnant l'opportunité de travailler sur d'autres projets en tant qu'ingénieur d'étude. Un grand merci à vous, je pense que cela a aussi été très important pour la réussite de ma thèse.

Dans le cadre de ma thèse, un partenariat a également été établi avec TELT (Tunnel Euroalpin du Lyon-Turin), le maitre d'ouvrage pour la construction du tunnel de base du Mont Cenis. Ce partenariat m'a permis d'accéder à de nombreuses données de ce gigantesque projet. Compte tenu de la durée limitée de ma thèse, je n'ai pas eu le temps de les exploiter autant que je l'aurais souhaité, mais je tiens tout de même à remercier profondément TELT pour m'avoir mis à disposition ces données, ainsi que pour leur réactivité et leur aide lors de nos différents échanges.

Je souhaite aussi remercier les différents membres de mon jury de thèse, M. Jean Sulem (École Nationale des Ponts et Chaussées), Mme Lina-Maria Guayacan-Carillo (École Nationale des Ponts et Chaussées), M. Dashnor Hoxha (Université d'Orléans), Mme Nathalie Conil (Ineris), M. Benjamin Lecomte (Vinci Construction Grands Projets) et Mme Maria-Elena Parisi (TELT), qui ont apporté un avis éclairé et très intéressant sur le travail effectué, ainsi que pour la richesse des échanges qui ont eu lieu au cours de la soutenance. Merci beaucoup pour votre participation et vos retours extrêmement constructifs.

Ce travail n'aurait pas non plus été possible sans l'aide scientifique et technique complémentaire que j'ai pu recevoir au cours de cette thèse. Ainsi, j'aimerais remercier les membres de mon comité de suivi de thèse, M. Abdul-Hamid Soubra (Université de Nantes), Mme Marianne Conin (École des Mines de Nancy) et M. Daniel Billaux (Itasca), pour leur suivi régulier au cours de ces trois années, ainsi que pour leurs remarques et réflexions avisées qui se sont avérées très utiles à mon travail. J'aimerais aussi remercier l'ensemble des personnes qui ont contribué à ce travail, que ce soit au sein du laboratoire, Mme Audrey Bonnelye (École des Mines de Nancy), M. Yann Gunzburger (École des Mines de Nancy), au sein de WSP, M. François Martin (WSP Canada), M. Etienne Garin (WSP Suisse), M. Robert Bewick (WSP Canada), M. Justin Roy (WSP Canada), M. Anastasios Stavrou (WSP UK), ou au sein d'autres entités, M. Michele Janutolo-Barlet (Vinci Construction Grands Projets), M. Emilio Abi Aad (Monod-Piguet), M. Mountaka Souley (Ineris) et Mme Maria-Elena Parisi (TELT), ainsi que l'ensemble de mes collègues au laboratoire et au sein de l'entreprise. Un grand merci à vous pour votre aide !

Pour finir, je souhaiterais aussi exprimer toute ma gratitude à ma famille et mes amis pour leur soutien moral sans faille au cours de ces trois années de travail, et qui m'ont permis de surmonter les périodes les compliquées pour arriver à ce résultat final.

Résumé étendu en français

Il existe actuellement plusieurs tunnels de grande profondeur (supérieur à 1500m) en cours de construction à travers les Alpes, principalement pour le développement et l'amélioration du réseau de transport transeuropéen (Trans-European Transport Network, TEN-T), financé par l'Union Européenne. L'objectif est de développer un réseau de transport (marchandises et personnes) cohérent, efficace et multimodal de bonne qualité au sein des pays de l'Union Européenne. Cela se traduit par la création ou l'amélioration de nouvelles lignes ferroviaires à travers les Alpes, et donc la construction de plusieurs grands tunnels atteignant des profondeurs très importantes (souvent supérieures à 1000 m et jusqu'à plus de 2000 m), comme les tunnels de base du Lötschberg (34.6 km de long) et du Gotthard (57.1 km) en Suisse construits au cours des deux dernières décennies. D'autres tunnels sont actuellement en cours de construction comme les tunnels de base du Mont Cenis (57.5 km) entre la France et l'Italie, du Brenner (55 km) entre l'Autriche et l'Italie ou le tunnel de Koralm (32.9 km) en Autriche. La nouvelle ligne reliant Lyon à Turin (passant par le tunnel de base du Mont Cenis) comprendra aussi trois futurs tunnels de grande profondeur (supérieurs à 1000m), le tunnel de la Chartreuse (25 km), le tunnel de Belledonne (20 km) et le tunnel du Glandon (10 km).

WSP a été impliquée dans la conception et la construction du tunnel de base du Lötschberg, et fait actuellement partie du GEIE ALLTI, en charge de la maitrise d'œuvre du creusement du tunnel de base du Mont Cenis (conception et suivi de travaux) depuis les attaques de Modane et de la maîtrise d'œuvre de la Gestion et l'Emploi des Matériaux d'Excavation (GEME) issus de l'ensemble des attaques côté français.

À partir de l'expérience acquise au cours de ces projets, il a semblé pertinent de développer ce projet de thèse traitant de la conception préliminaire des tunnels de grande profondeur. En effet, le contexte de forte profondeur rend difficile les investigations détaillées et la caractérisation fine du rocher. L'objectif de la thèse est ainsi d'essayer de mieux caractériser et quantifier les mécanismes de rupture susceptibles de se produire en fonction des incertitudes existantes à partir de données réduites, afin de pouvoir proposer une conception robuste, adaptée et adaptable dès les études préliminaires (étude de faisabilité, avant-projet ou PRO). Une mauvaise quantification de ces phénomènes conduit à une conception potentiellement non adaptée pouvant engendrer des problèmes de sécurité, des retards, et des surcoûts lors de la construction. Plus précisément, cette thèse cherche à développer de nouveaux outils ou méthodes simples permettant une meilleure quantification des potentiels mécanismes de rupture et de leur impact sur le soutènement, en prenant en compte explicitement les incertitudes sur les données géologiques et géotechniques.

La thèse se focalise sur les mécanismes de rupture se produisant dans des massifs rocheux assimilés à des milieux continus à grandes profondeurs. Ces mécanismes peuvent être regroupés en deux grandes familles : les mécanismes de grande déformation dans les massifs rocheux très fracturés (souvent connus sous le nom de roches poussantes, convergentes ou de « squeezing »), et les mécanismes de rupture fragile dans les massifs fragiles peu fracturés, pouvant être quasi-statiques (écaillage) ou violents (« rockburst »). Au cours de la thèse, les deux phénomènes ont été traités de manière indépendante.

--

Le premier phénomène étudié est le phénomène de « squeezing » (roches poussantes ou convergentes en français) qui se traduit par l'apparition d'importantes déformations des parois

des tunnels, pouvant conduire à la rupture du soutènement, au blocage de tunneliers et à la nécessité de devoir reprofiler l'ouvrage. Il se développe dans des massifs de faible résistance par rapport à l'état de contraintes et dans des massifs susceptibles d'accepter de grandes déformations (comportement post-pic parfaitement plastique ou faiblement radoucissant). Généralement, il s'agit de massifs rocheux très fracturés et les déformations peuvent être accompagnées de déformations différées dans le temps dues à du fluage au sein du massif. L'apparition de ces déformations ou à fortiori d'efforts importants appliqués sur le soutènement est due uniquement à l'état de contrainte important dans le massif par rapport à sa résistance, entrainant une plastification importante et l'apparition de déformations « mécaniques » (élastiques et plastiques, pouvant être différées). Ce phénomène ne doit pas être confondu avec un phénomène de gonflement (ou « swelling » en anglais) qui a un impact similaire sur les ouvrages (i.e. déformations et pressions importantes sur les soutènements) mais qui est dû à une réaction chimique d'absorption d'eau et donc d'une augmentation du volume du massif.

Il existe déjà de nombreuses méthodes pour quantifier le risque associé à ce phénomène, dont la plus connue est la courbe de Hoek et Marinos (2000), ainsi que pour étudier l'impact du phénomène sur le soutènement, comme la méthode convergence confinement ou les calculs numériques (2D en section plane, 2D axisymétrique, ou 3D). Chacune de ces méthodes présente des avantages et des inconvénients vis-à-vis des objectifs de la thèse, et aucune n'est forcément laplus adaptée. De nouveaux outils ont été développés afin de compenser les inconvénients des approches existantes. Les travaux de thèse concernant les phénomènes de grande déformation se focalisent sur deux points : le premier traite de la quantification du risque, et le deuxième de l'interaction du phénomène avec le soutènement.

La première étape a été d'actualiser la courbe de Hoek et Marinos (2000) pour la quantification du risque de grande déformation. Il s'agit d'un outil extrêmement simple mais très pratique qui permet de lier la résistance du massif rocheux, l'état de contrainte in-situ et la convergence radial sans soutènement. À partir de la valeur de cette convergence, les auteurs proposent de quantifier le risque à travers 5 catégories, de « pas de problème » à « problème extrême de squeezing », chacune étant associée à une présentation des problèmes géotechniques et une proposition de soutènement à mettre en place. Le gros défaut de cette approche est qu'elle se base sur la valeur de résistance du massif rocheux. Il s'agit d'un paramètre très simple à comprendre mais extrêmement difficile à estimer dans la réalité car elle ne peut pas être mesurée directement. Plusieurs formules existent dans la littérature, mais, pour une situation identique, elles conduisent à des résultats pouvant être très différents, impactant la quantification du risque et introduisant des incertitudes supplémentaires. Pour éviter l'introduction de cette incertitude supplémentaire, la courbe de Hoek et Marinos a été refaite à partir d'une simulation de Monte Carlo (10 000 réalisations). Elle a été réalisée à partir d'un modèle numérique 2D en section plane sur une gamme étendue de variation des paramètres d'entrée. Le nouvel ensemble d'abaques prend comme données d'entrée uniquement des paramètres provenant des essais de laboratoire (la résistance à la compression simple de la roche intacte ; le paramètre de résistance m_i du critère de rupture de Hoek et Brown ; le Modulus Ratio, traduisant la raideur de la roche, liant la résistance à la compression simple et le module d'Young) et des investigations géologiques (l'état de contraintes in-situ et le GSI, Geological Strength Index, traduisant l'état de fracturation du massif) pour estimer la convergence radiale sans soutènement. Les résultats de la simulation de Monte Carlo ont aussi permis de créer un métamodèle (régression linéaire multiple) permettant l'estimation du rayon plastique sans soutènement, cette information étant importante pour la suite du travail.

Afin de faciliter l'introduction et la propagation des incertitudes à l'aide de cette version améliorée de la courbe de Hoek et Marinos, une méthode a été proposée permettant de

facilement déterminer la distribution de probabilité de la convergence radiale. Elle se base sur la lecture graphique de 3 points particuliers, appelée la « méthode des 3-points ». Connaitre la distribution de probabilité de la convergence sans soutènement permet de calculer la probabilité de se trouver dans chacune des classes de risques introduites par Hoek et Marinos, en fonction des incertitudes existantes sur les données d'entrée, et donc permet une quantification explicite du risque en fonction de ces incertitudes.

Après avoir quantifié le risque de grande déformation, il est important de connaitre l'impact de ce phénomène sur les solutions de soutènement envisagées. L'une des méthodes les plus classiques est la méthode convergence confinement (au sens large, incluant les modèles numériques 2D en section plane). Elle avait été développée dans cet objectif, mais, comme cela a été montré dans la littérature (Bernaud et Rousset 1992 ; Cantieni et Anagnostou 2009b ; De La Fuente Mata *et al*. 2019) elle conduit en réalité à une sous-estimation de la pression du massif sur le soutènement, ce qui n'en fait pas un outil pertinent ici. Les calculs numériques 2D axisymétriques et 3D fournissent eux des résultats plus pertinents, mais les modèles sont longs à créer et à exploiter, faisant d'eux des outils peu adaptés pour les processus itératifs permettant d'obtenir une conception préliminaire et pour la propagation d'incertitudes. Afin de compenser les inconvénients de ces méthodes, le choix a été fait de développer des méta-modèles à partir des résultats de calculs numériques axisymétriques afin de prendre explicitement en compte l'interaction entre le soutènement et le comportement du massif rocheux. Un méta-modèle, ou modèle de substitution, est une expression mathématique explicite ou non (formule analytique, réseau de neurone, etc.) permettant d'approximer le lien entre des grandeurs d'entrée et une ou plusieurs grandeurs de sortie. Ces méta-modèles servent à estimer la pression sur le soutènement à l'infini (loin du front de taille), la déformation du massif entre le front et l'installation d'un soutènement rigide, ainsi que la valeur de déformation qui a lieu dans le massif avant le front.

Pour la création de ces méta-modèles, deux bases de données ont été développées, l'une d'entrainement et l'autre de test. Elles ont été créées grâce à des calculs numériques axisymétriques couvrant une large gamme de situations dans lesquelles de grandes déformations seraient susceptibles de se développer. La base d'entrainement comprend 1000 calculs axisymétriques et la base de test en comprend 600. Plusieurs méthodes ont été testées pour créer les méta-modèles à partir de la base d'entrainement. Le choix a été fait de conserver une approche analytique combinant une décomposition des méta-modèles principaux en sous-méta-modèles ayant moins de paramètres d'entrée et de la régression multiple non-linéaire. Les méthodes basées sur des approches d'apprentissage automatique n'ont pas été privilégiées ici car il est complexe, voir même impossible, de les transformer en représentation graphique afin d'être facilement utilisables. Il a été privilégié leur facilité d'utilisation devant leur précision, étant donné qu'ils sont destinés à être utilisés dans des phases de conception préliminaire. Les métamodèles permettent d'estimer la pression sur le soutènement, la convergence entre le front de taille et l'installation du soutènement, et la convergence au front, à partir des informations basiques suivantes : le comportement du massif sans soutènement (convergence et rayon plastique), le module de déformation du massif rocheux, la raideur du soutènement et sa distance d'installation par rapport au front de taille.

Afin d'élargir la gamme d'utilisation de ces métamodèles, trois études complémentaires ont été réalisées. La première permet de fournir des recommandations sur le choix de la contrainte in-situ équivalente à utiliser lorsque l'état de contraintes est anisotrope et qu'une plastification importante a lieu dans le massif. La seconde traite de l'impact de l'utilisation d'un soutènement flexible entre le front de taille et l'installation du soutènement rigide (celui pris en compte dans les méta-modèles). Cette étude a permis de mettre en évidence que la mise en place d'un

soutènement flexible n'avait qu'un faible impact sur la pression que le massif applique sur le soutènement rigide, et qu'il permettait de réduire la convergence entre le front et le soutènement rigide. Des coefficients de réduction ont été déduits en fonction de la pression de confinement appliquée par le soutènement souple et de la distance d'installation du soutènement rigide. La dernière étude complémentaire présente une méthode pour pouvoir prendre en compte un comportement à long terme du massif associé à une modification des propriétés de ce dernier.

Le développement de l'ensemble de ces métamodèles (amélioration de la courbe de Hoek and Marinos, estimation du rayon plastique sans soutènement, pression du massif sur le soutènement à l'infini, convergence radiale entre le front et la mise en place du soutènement) permet de créer un cadre cohérent et auto suffisant pour facilement estimer le comportement d'un massif rocheux fracturé à grande profondeur, ainsi que son interaction avec le soutènement (approche déterministe). Cela permet à l'ingénieur d'avoir rapidement un aperçu des solutions techniques envisageables et des leurs impacts sur l'ouvrage, afin de proposer une conception pertinente en phase d'étude préliminaire en ayant uniquement un nombre limité de données géologiques et géotechniques : la résistance à la compression de la roche intacte (σ_{ci}), le paramètre de résistance m_i du critère de rupture Hoek&Brown, le Modulus Ratio caractérisant la raideur de la roche intacte (lien entre le module d'Young et σ_{ci}), le GSI traduisant l'état de fracturation du massif, et l'état de contraintes in-situ (σ_0).

Comme ces métamodèles sont in-fine uniquement des expressions analytiques, il est aussi très facile et rapide de les utiliser pour faire des calculs probabilistes, en utilisant par exemple des simulations de Monte Carlo. Ces calculs probabilistes ont de nombreux avantages comparés à des approches déterministes car ils permettent de prendre directement en compte et de propager les incertitudes existantes sur les données d'entrée afin d'obtenir des lois de probabilité des grandeurs d'intérêt, comme la pression à l'infini sur le soutènement, ou la convergence radiale entre le front et la mise en place du soutènement. Ces lois de probabilité peuvent ensuite être utilisées pour faire des calculs de fiabilité, c'est-à-dire estimer des probabilités de défaillance vis-à-vis d'un ou plusieurs états limites. Les états limites sont à définir par l'ingénieur, il peut s'agir de la rupture du soutènement, d'une convergence maximale à ne pas dépasser, mais aussi d'un facteur de sécurité global à respecter, etc. Les métamodèles développés dans cette thèse sont tout à fait adaptés pour ce type de calcul. Une méthode est proposée pour pouvoir facilement faire ces calculs de probabilité de défaillance et réaliser une conception dite « fiabiliste » (RBD, « Reliability-Based Design » en anglais). Dans la méthode proposée, il est possible de prendre en compte les incertitudes sur les données géologiques et géotechniques et les incertitudes sur la résistance du soutènement. Il est aussi possible de comparer la compatibilité d'une ou plusieurs conceptions vis-à-vis de deux états limites pour lesquels des probabilités de défaillance maximales admissibles ont été définies : le premier traite de la rupture du soutènement (pression du massif rocheux supérieure à une pression maximale admissible) et le deuxième traite du dépassement du rayon minimale admissible (la convergence conduit à obtenir un rayon final plus faible que celui imposé par le porjet). Cette méthode pourrait facilement être généralisée en incluant les incertitudes sur l'épaisseur du soutènement ou sur le rayon d'excavation.

Un point fondamental permis par cette méthode est la possibilité de facilement calculer une probabilité de rupture et de pouvoir comparer plusieurs philosophies de conception : les approches déterministes basées sur l'obtention d'un facteur de sécurité global ; les approches semi-probabilistes (au sens des Eurocodes) basées sur des coefficients partiels de sécurité sur les actions et les résistances ; les approches fiabilistes basées sur des probabilités de défaillance limites à respecter. Dans le cadre des ouvrages souterrains, les approches les plus utilisées sont les approches déterministes ou semi-probabilistes comme recommandées par l'AFTES en

France (Recommandation GT29.R2F1). Les coefficients partiels fournis par les Eurocodes (Eurocode 0, 2, 3) ont été obtenus de telle sorte que les probabilités de défaillance soient globalement inférieures à des valeurs seuils fixées. Le problème est qu'ils ont été définis au regard de variabilités classiquement observées des paramètres de résistance ou sollicitation pour des structures non souterraines (bâtiments, ouvrages d'art, etc..) pour lesquelles les incertitudes sont globalement plus faibles que pour les tunnels. Il est alors possible de se questionner sur la pertinence d'utiliser ces coefficients partiels pour le dimensionnement de tunnels. Dans cette thèse l'effort a uniquement porté sur l'influence de l'incertitude sur les propriétés mécaniques du massif afin d'estimer la probabilité de défaillance lorsque les coefficients partiels de sécurité proposés par les Eurocodes sont utilisés et selon différents contextes d'incertitudes. Les métamodèles et la méthode de conception fiabiliste sont utilisés ici pour essayer de fournir quelques éléments de discussion sur ce questionnement. Plusieurs milliers de comparaison ont été faites entre les coefficients de sécurité utilisés pour le dimensionnement, la variabilité des paramètres d'entrée et la probabilité de rupture. Plus précisément, pour chaque comparaison, un dimensionnement optimisé a été réalisé en utilisant une approche déterministe incluant des coefficients partiels de sécurité. Dans le cas spécifique des métamodèles (soutènement circulaire chargé par une pression uniforme), utiliser des coefficients partiels ou viser un facteur de sécurité global est identique. Une fois l'optimisation réalisée (via l'épaisseur du soutènement), une variabilité des propriétés du massif est prise en compte, et le calcul de la probabilité de défaillance vis-à-vis de la résistance du soutènement est réalisé. Généraliser cette approche dans un grande nombre de situations, avec des propriétés du massif différentes, des types de soutènement différents et différentes hypothèses de dimensionnement (valeur des coefficients partiels, choix des propriétés déterministes du massif à prendre en compte dans les calculs, etc..), permet d'obtenir pour chacune des situations un ordre de grandeur des probabilités de défaillance en fonction de la variabilité des propriétés du massif. Dans le cadre de la thèse, un seul type de soutènement a été testé ainsi que trois hypothèses de dimensionnement. Par exemple, si un soutènement est composé d'une coque de béton projeté et est dimensionné en prenant en compte un coefficient partiel sur les actions internes de 1.35 et un coefficient de réduction de sa résistance de 1.5 (conformément à la recommandation GT29.R2F1 de l'AFTES), et que les propriétés de calcul du massif sont les valeurs moyennes, alors la probabilité de défaillance (i.e. rupture ici) de ce soutènement est compris entre 0.001% et 1% pour une variabilité des propriétés du massif de 10% (coefficient de variation, défini comme le rapport entre l'écart type et la moyenne), alors qu'elle varie entre 0.8% et 13% pour une variabilité des propriétés du massif de 30%. La durée de la thèse n'a pas été suffisante pour aller plus loin sur la question, mais met en évidence la nécessité de questionner le choix des coefficients partiels à prendre en compte lors du dimensionnement des soutènements, ou du moins de la nécessité de les rendre dépendantes de la variabilité des propriétés du massif.

Afin de valider la pertinence des résultats fournis par les métamodèles, ils ont été appliqués à deux sections du tunnel du Yacambu-Quibor au Venezuela, cas emblématique d'un tunnel ayant subi de grandes déformations. Cela a permis de comparer les résultats avec d'autres approches de dimensionnement et des observations faites lors du creusement du tunnel, afin de mettre en évidence les limites de certaines approches classiques comme la méthode convergence-confinement (CV-CF) ou les calculs numériques 2D en section plane. La première section étudiée correspond au principe de soutènement à appliquer dans le cas le plus défavorable (plus grande profondeur et pires propriétés du massif). Lorsque cette philosophie de soutènement a été installée, aucune rupture n'a été observée ni à court terme, ni à long terme. La deuxième section étudiée correspond à une section pour laquelle le soutènement a rompu deux ans après sa mise en place, il a donc résisté à court terme mais a rompu à long terme. Sur ces deux cas d'étude, les métamodèles ont permis d'obtenir des résultats pertinents en mettant en évidence

la tenue à court terme et à long terme du soutènement sur la première section, la tenue à court terme de la seconde section et sa rupture à long terme. Inversement, les méthodes classiques n'ont pas permis de mettre en évidence la rupture du soutènement à long terme de la seconde section. Ce cas concret d'application permet de donner relativement confiance dans les résultats de métamodèles développés, à minima lors d'études de conception préliminaire.

--

La deuxième famille de phénomènes étudiée au cours de cette thèse concerne les ruptures fragiles dans les massifs rocheux peu fracturés. Ces mécanismes peuvent être quasi-statiques, comme le détachement progressif d'écailles à la paroi, ou alors brutaux associés à de l'éjection de matière, connus sous le nom de rockburst en anglais (similaire au « coup de terrain » anciennement utilisé dans le jargon des mines de charbon en France). Ces deux phénomènes se développent dans des conditions similaires, lorsque les massifs rocheux sont composés de roches généralement dures, peu fracturées avec un comportement fragile, mais ont des conséquences très différentes sur les ouvrages. L'impact d'un phénomène d'écaillage (rupture quasi-statique) est relativement limité, il peut poser quelques problèmes de sécurité mineure (s'il se développe en voûte du tunnel par exemple) et potentiellement des problèmes de vitesse d'avancement pour des tunneliers à gripper. Inversement les phénomènes de rupture violente, rockburst, peuvent engendrer de gros problèmes de sécurité lors du creusement, pouvant conduire à des accidents mortels et l'endommagement voire la destruction d'équipements. La question fondamentale en phase de conception préliminaire est de savoir si la rupture fragile qui est susceptible de se produire est plutôt quasi-statique ou alors violent. Les choix de conception, le phasage, les techniques de creusement, les équipements de sécurité à mettre en place, etc…, sont grandement influencés par la réponse à cette question.

Dans un premier temps, une recherche approfondie des méthodes existantes permettant de répondre à cette question a été réalisée. La plupart des méthodes utilisables en phase de conception sont des méthodes empiriques basées soit sur des critères de résistance (comparaison entre une valeur de résistance de la roche et une valeur d'état de contrainte) soit sur des critères énergétiques (comparaison entre l'énergie élastique emmagasinée en phase de chargement par rapport à l'énergie totale fournie, ou l'énergie dissipée pendant la rupture de l'échantillon). Certaines approches (empirique, analytique, graphique) combinent ces deux critères. Il a été conclu de cette analyse que la grande majorité de ces méthodes considère l'écaillage comme une rupture fragile de faible intensité alors que les rockburst sont des ruptures fragiles d'intensité plus importante. L'une des méthodes les plus complètes pour les phases d'étude préliminaire a été proposées par Diederichs (2018). Elle comprend à la fois un critère de résistance vis-à-vis de l'état de contrainte et un critère énergétique à travers la notion de fragilité et d'énergie libérable, pour estimer un paramètre caractérisant l'intensité de la rupture, le BHP « Burst Hazard Potential ». En fonction de la valeur de ce paramètre, Diederichs (2018) y associe une classe de risque. Cette méthode a été développée spécialement pour les phases d'étude préliminaire d'analyse de risques afin d'identifier les zones potentiellement problématiques le long du tracé du tunnel. Néanmoins, elle se base uniquement sur des paramètres d'entrée déterministes, sans prendre en compte les incertitudes existantes. Dans le cadre des travaux de thèse, cette méthode a été améliorée pour pouvoir propager les incertitudes sur les données d'entrée afin d'obtenir la distribution de probabilité du BHP, et donc la probabilité de se trouver dans chacune des classes de risques. Elle a ensuite été appliquée au cas d'étude de la section la plus profonde du tunnel de base du Mont Cenis (nouvelle ligne ferroviaire entre Lyon et Turin). La section d'étude correspond à 15 km entre le site de sécurité de Modane (France) et le site de sécurité de Clarea (Italie) excavée au tunnelier à roche dure avec grippers. L'ensemble de cette section possède une profondeur supérieure à 1000m,

atteignant 2200m localement. Il existe de nombreuses incertitudes sur les paramètres géotechniques et sur l'état de contrainte, et le risque de rockburst n'est pas exclu, mais aucune étude approfondie n'avait jusqu'à présent été réalisée sur le sujet. Les résultats de l'application de la méthode à cette section du tunnel mettent en évidence deux zones potentiellement concernées par des risques de rockburst d'intensité faible à modérée. La première zone n'avait pas été identifiée dans les études précédentes mais l'étude probabiliste met en évidence que le risque de rockburst ne peut être complètement exclu, dû entre autres, aux grandes incertitudes existantes sur l'état de contrainte dans cette zone. La seconde zone avait, elle, déjà été identifiée, néanmoins les résultats permettent une interprétation plus fine du risque en fonction de la variabilité des propriétés du massif. La dernière partie de la section d'étude (1.5km) recoupe la galerie de reconnaissance de la Maddalena. Les résultats obtenus sur cette section ont pu être comparés aux phénomènes observés lors du creusement de cette galerie, confirmant ainsi la cohérence du modèle par rapport à la réalité.

L'inconvénient des méthodes empiriques précédentes est qu'elles ne prennent pas en compte un facteur essentiel conduisant à une rupture quasi-statique ou une rupture violente : la rigidité de l'encaissant. L'ensemble de ces méthodes se contente de comparer des paramètres issus d'essai de laboratoire entre eux ou avec des valeurs de contraintes in-situ. Aucune n'inclut la raideur du système encaissant, qui pourtant est un paramètre fondamental. Des travaux récents de Hou *et al.* (2022) ont mis en défaut la fameuse « Classe II » de comportement introduite par Wawersik et Fairhurst (1970), ce qui signifie qu'un échantillon de roche ne peut pas se rompre de manière violente en ayant uniquement comme source d'énergie l'énergie élastique emmagasinée en son sein. Un apport d'énergie extérieure est forcément nécessaire pour avoir une rupture violente. Cette énergie est généralement restituée à l'échantillon par le milieu encaissant sous forme de déformation élastique aux extrémités. Donc en théorie, un encaissant infiniment rigide (pas de déformation) ne peut engendrer une rupture violente d'un échantillon car aucune énergie ne lui est restituée. Pour qu'une rupture violente se produise, il faut que cet apport d'énergie extérieure soit supérieur à l'énergie nécessaire pour rompre l'échantillon. Si c'est le cas, il y a un déficit énergétique et une partie de l'énergie restituée par le massif se transforme en énergie cinétique à travers l'éjection de matière. L'énergie restituable par le massif est directement associée à sa raideur (sauf cas particulier d'énergie sismique). Pour savoir si la rupture va être violente ou non, il est donc essentiel d'arriver à estimer la raideur du massif encaissant et la raideur post-pic de la roche afin de les comparer. Si la raideur du massif encaissant est supérieure à la raideur post-pic de la roche, la rupture sera quasi-statique, et inversement si elle est inférieure, l'énergie restituée par le massif sous forme de déformation conduira à une rupture violente. L'estimation de ces deux raideurs est complexe. Des travaux récents de Hou et Cai (2022b) ont permis de développer une approche expérimentale pour estimer la raideur post-pic de la roche intacte. Inversement, les approches existantes pour l'estimation de la raideur du massif autour d'une zone susceptible de rompre sont très limitées. Plusieurs approches basées sur la théorie des raideurs sont présentées, discutées et comparées (approche unidirectionnel et multidirectionnel) a l'aide de calcul numérique 2D en section plane (comportement élastique). Elles ont ensuite été appliquées à deux cas d'étude l'un plutôt caractéristique d'un phénomène d'écaillage, le galerie expérimentale MineBy de l'AECL au Canada et l'autre de rockburst, le rockburst 11.28 qui s'est produit lors du creusement de la galerie de drainage du projet hydroélectrique Jinping II en Chine. Plusieurs géométries de la zone rompue, plusieurs processus de développement de cette zone, ainsi que la présence d'une discontinuité ont été testées afin d'étudier leur impact sur l'évolution de la raideur du massif. Ces raideurs ont ensuite été comparées avec les raideurs post-pics des roches concernées. Sur les deux cas d'étude, les résultats des comparaisons sont pertinents. Néanmoins, ils ont aussi permis de mettre en évidence un certain nombre de questionnements concernant l'applicabilité

réelle de cette comparaison entre la raideur du massif encaissant et la raideur post-pic lors d'étude prédictive, comme lors des études préliminaires, les exemples traités étant basés sur des rétro-analyses.

Pour conclure, cette thèse a l'objectif d'améliorer les outils destinés aux ingénieurs en phase de conception en prenant explicitement en compte les incertitudes existantes. Pour les phénomènes de grande déformation, un ensemble de métamodèles a été développé pour permettre de facilement caractériser le comportement du massif rocheux et son interaction avec le soutènement. Ces métamodèles permettent de facilement introduire et propager les incertitudes, ce qui laisse la possibilité d'utiliser des approches de conception fiabiliste basées sur des calculs de probabilités de défaillance. Ils permettent aussi d'interroger la pertinence des coefficients partiels utilisées classiquement vis-à-vis des incertitudes existantes et des probabilités de défaillances associées. Pour les phénomènes de rupture fragile, une méthode existante a été améliorée pour permettre d'estimer la probabilité de se trouver dans différentes classes de risque de rupture fragile en fonction des incertitudes existantes sur les données d'entrée. Néanmoins, cette méthode n'était pas en mesure de répondre explicitement à la problématique principale : est-ce que des ruptures violentes sont susceptibles de se produire ? Pour essayer de répondre à cette question, une méthode basée sur le calcul de la raideur du massif encaissant a été testée sur deux cas d'étude. Malgré des résultats encouragements, l'applicabilité réelle de cette méthode peut être encore questionnée.

List of contents

Remerciements 1

Résumé étendu en français 3

List of figures 17

List of tables 27

List of symbols: 29

Chapter 1 - Thesis Framework 38

1.1 Thesis context 39

1.2 Framework of the thesis and limitations 40

1.3 Structure of the manuscript 44

Chapter 2 - Introduction 46

2.1 Basis of rock mechanics: from laboratory to rock mass scale 47

2.1.1 Rock behavior at laboratory tests scale 47

2.1.2 Transitioning from laboratory scale to project scale 56

2.2 Presentation of the failure mechanisms studied 62

2.2.1 Large deformation, squeezing phenomenon 62

2.2.2 Brittle failures 69

2.3 Conclusions 73

Chapter 3 - Quantification of the risk of large deformation in highly fractured rock mass .. 75

3.1 Existing methods for risk quantification 76

3.1.1 Methods in the literature 76

3.1.2 Methods based on machine learning 79

3.1.3 Hoek and Marinos (2000) curve 80

3.2 Improvement of the H&M curve 83

3.2.1 Numerical model 84

3.2.2 Procedure used for the improvement 85

3.3 Results 87
3.3.1 Results of the Monte Carlo simulation: radial strain 88
3.3.2 Graphical representation 90
3.3.3 Comparison with the H&M curve 93
3.3.4 Results of the Monte Carlo simulation: Plastic radius 94
3.4 Conclusion 96
Chapter 4 - Support and rock mass interaction in highly fractured rock mass 97
4.1 Existing approaches for tunnel design in squeezing ground 98
4.1.1 Technical solutions and design approach 98
4.1.2 Calculation techniques during preliminary design 100
4.2 New approach for preliminary design 106
4.2.1 Developed numerical model 107
4.2.2 Input parameters for the database 111
4.2.3 Creation of the surrogates models 112
4.2.4 Conclusions of the surrogate models 126
4.3 Generalized framework 126
4.3.1 Anisotropic stress state 127
4.3.2 Impact of a yielding support 127
4.3.3 Consideration of a long-term behavior 128
4.4 Conclusions 129
Chapter 5 - Introduction and propagation of uncertainties for reliability calculations 131
5.1 Reliable approaches and uncertainties quantification 132
5.1.1 Preliminary consideration 132
5.1.2 Quantification of the geological and geotechnical uncertainties 133
5.1.3 Reliability calculations applied to tunnel design 135
5.2 Uncertainties propagation without support 137
5.2.1 Methodology of the “3-point method” 137

5.2.2 Comparison with other approaches 140
5.2.3 Framework for uncertainties propagation 142
5.2.4 A case study 144
5.3 Method for tunnel design based on reliable approaches 146
5.3.1 Proposed method for preliminary reliability-based design 147
5.3.2 Theoretical case studies 149
5.4 Global safety factors, partial factors and failure probabilities 154
5.4.1 Methodology 154
5.4.2 Results for three situations 155
5.5 Conclusions 158
Chapter 6 - Case study of large radial deformation: Yacambu-Quibor tunnel in Venezuela 159
6.1 Preliminary considerations 160
6.1.1 Project presentation 160
6.1.2 Back analysis for long term ground properties 162
6.1.3 Yielding support used 164
6.1.4 Field observations 165
6.2 Worst case scenario 165
6.2.1 CV-CF method and equivalent 166
6.2.2 Surrogate model 170
6.3 Failed section: PM12+750 – PM12+850 173
6.3.1 CV-CF method and equivalent 173
6.3.2 Surrogate models 176
6.4 Conclusion 177
Chapter 7 - Risk assessment of brittle failures during early tunnel design stages 179
7.1 Risk assessment of brittle failure in literature 180
7.1.1 Methodologies for rockburst prediction 180
7.1.2 “Burst hazard potential” proposed by Diederichs (2018) 188

7.2 Civil engineering projects facing brittle failures 192
7.2.1 Case histories 192
7.2.2 Rockburst risk management in civil engineering 195
7.3 Rockburst risk assessment under uncertainties: Mont-Cenis base tunnel case study 201
7.3.1 Project presentation 201
7.3.2 Methodology used 204
7.3.3 Results and interpretation, situation 3 210
7.4 Conclusion 213
Chapter 8 - Estimation of the rock mass stiffness around a notch 214
8.1 Proposed methodology 215
8.1.1 Literature review on the localization of the failed area 216
8.1.2 Calculation of the rock mass stiffness in the literature 219
8.1.3 Literature review on the estimation of the post-peak stiffness of intact rock 220
8.2 Estimation of the rock mass stiffness 224
8.2.1 Approaches used 224
8.2.2 Case study: Mine-By tunnel, AECL, Canada 231
8.2.3 Case study: 11.28 rockburst, Jinping II Hydropower project, China 235
8.3 Comparison with the post-peak stiffness 243
8.3.1 MineBy Tunnel and 11.28 rockburst 243
8.3.2 Analysis of the comparison and limitations 247
8.4 Conclusions 250
Chapter 9 - Conclusions and perspectives 251
References 253
Appendix 1 - Limitation of the convergence-confinement method and the implicit method for deep tunnel 273
A 1.1 Introduction 273
A 1.2 Methodology 274

A 1.2.1. Convergence-Confinement Method 274

A 1.2.2. Implicit method..... 276

A 1.2.3. Limits of the CV-CF method 278

A 1.3 Comparison including safety factors for the CV-CF method..... 281

A 1.3.1. Comparison methodology..... 281

A 1.3.2. CV-CF method..... 282

A 1.3.3. Implicit method..... 284

A 1.4 Conclusions 285

Appendix 2 - Graphical representations of the various surrogate models 287

Appendix 3 - Anisotropic stress state and equivalent isotropic stress 308

Appendix 4 - Application of confining pressure on the unsupported span during axisymmetric numerical calculations 311

Appendix 5 - Consideration of the long-term behavior of the rock mass..... 315

A 5.1. Limitation of the surrogate models for the long-term behavior of the rock mass ... 315

A 5.2. Method to include the long-term behavior 318

Appendix 6 - Excel file used to perform reliability calculations – Practical use of the surrogate models 321

A 6.1. “Deterministic calculations” area 323

A 6.2. “Uncertainty introduction and propagation” area..... 324

A 6.3. “Reliability calculations” area 326

A 6.4. Consideration of the long-term behavior of the rock mass 329

Appendix 7 - Results of situations 1 and 2, Mont Cenis base tunnel case study (Chapter 7).. 332

Appendix 8 - Analytical comparison of $M_{s\text{-}s}$ and $k_{f\text{-}d}$ on nonrectangular notch (Chapter 8).... 336

A 8.1. Example 1: Notch characterized by two mesh elements (depth size) with various lengths 336

A 8.2. Example 2: Notch characterized by three mesh elements (depth size) with various lengths 337

Appendix 9 - Simplified surrogate model for ground pressure on the support..... 340

A 9.1. Surrogate models of D(σ_0, ε_{us}, R_p, E_m, K) 340

A 9.2. Surrogate models of E(σ_0, ε_{us}, R_p, E_m, K) 341

A 9.3. Prediction of the ground pressure on the support 341

List of figures

Figure 1-1: Rock mass as a continuous or discontinuous medium (AFTES GT30R1A1); σ_{ci} is the uniaxial compressive strength of the intact rock; σ_{cm} is the strength of the rock mass; σ_0 is the equivalent isotropic in-situ stress state 41

Figure 1-2: Rock mass behavior based on the competence index and scale factor (AFTES GT30R1A1); more details and specific remarks can be found directly in the recommendation 42

Figure 1-3: Rock mass behavior depending on the RMR and the in-situ stress state proposed by Kaiser *et al.* (2000) 42

Figure 1-4: GDE (GeoData Engineering) multigraph developed by Russo (2014) 43

Figure 1-5: Multi-graph introduced by Majumber *et al.* (2017) to identify the rock mass behavior 43

Figure 2-1: Facture modes and equivalent from a rock mechanics and geological point of view (from Vaskou 2024) 47

Figure 2-2: Typical failure modes of intact rock sample under various confining pressure (Laigle 2004) 48

Figure 2-3: Progressive failure of intact rock under compressive loading (from Hoek and Martin 2014, modified from Martin and Christiansson 2009); AE is Acoustic Emission 49

Figure 2-4: Complete stress-strain curves and failure photographs of tested granite under uniaxial and triaxial compressions by axial-strain-controlled loading; a) differential axial stress-lateral strain relations; b) differential axial stress-axial strain relations; c) failure photographs; d) volumetric strain-axial strain relations (from Hou *et al*. 2022) 50

Figure 2-5: Complete stress-strain curves for unconfined and confined Tennessee marble (from Wawersik and Fairhurst 1970) 51

Figure 2-6: Influence of the sample size on the uniaxial compressive strength compared to that of a 50 mm diameter core sample (from Hoek and Brown 2019, based on Hoek and Brown 1980a) 52

Figure 2-7: Values of constant mi for intact rock by type of rock (from Hoek 2007); The values in parenthesis are estimates 54

Figure 2-8: Limit of applicability of the H&B criterion based on the results of triaxial tests on Indiana Limestone (from Hoek and Brown 2019) 55

Figure 2-9: Composite strength envelope with the various failure mechanisms depending on the confining pressure (adapted from Diederichs 2007) 56

Figure 2-10: Size effect in the rock mass characterization (from Hoek and Brown 2019) 57

Figure 2-11: GSI chart for jointed rock mass (Marinos and Hoek 2000) 58

Figure 2-12: Quantitative values to assess the GSI parameters based on proposition of Cai *et al*. (2004), Hoek *et al.* (2013) and Rafiei Renani *et al*. (2019a) (from Rafiei Renani and Cai 2022) 59

Figure 2-13: Guideline for the selection of Modulus Ratio (MR) values for various types of rock (from Hoek and Diederichs 2006)..... 61

Figure 2-14: Simplified post-peak behavior and associated tunnel behavior (from Lorig and Verona 2013) 62

Figure 2-15: Examples of squeezing phenomenon during tunnel construction; (a) Gotthard Base Tunnel in Switzerland (Loew *et al*. 2010); (b) Saint Martin la Porte access adit for the construction of the Mont Cenis Base Tunnel in France (Loew *et al.* 2010); (c) Yacambù-Quibor tunnel in Venezuela (Hoek and Guevara 2009)..... 64

Figure 2-16: Various types of creep (from Frenelus *et al.* 2022, referring to Qian *et al.* 2022) 65

Figure 2-17: Relationship between the rock mass strength, the intact rock parameter, the GSI and two values of disturbance factor (0 and 0.4) 67

Figure 2-18: Theorical example of the impact of the loading rate on the peak strength and post-peak behavior (Laigle 2004) 68

Figure 2-19: Comparison of the peak value and the residual value of GSI depending on the approach proposed by Cai *et al.* (2007) and Alejano *et al.* (2012) 68

Figure 2-20: Typical failure mechanism for a rockburst: (a) crack initiation; (b) crack propagation; (c) cracks coalescence; (d) failure with rock ejection (from He *et al*. 2022)..... 70

Figure 2-21: Schematic representation of rockburst potentials (from Askaripour *et al*. 2022, based on Castro *et al.* 2012)..... 71

Figure 2-22: Contributing factors for violent rock mass failure (from Keneti and Sainsbury 2018)..... 73

Figure 3-1: Chart developed by Goel (1994) to quantify the squeezing potential (from Askaripour *et al.* 2022)..... 77

Figure 3-2: Idealized stress-strain curve for a rock subjected to large radial deformation 78

Figure 3-3: Squeezing quantification proposed by Aydan *et al.* (1996); $\varepsilon_{\theta a}$ is the orthoradial strain at the tunnel boundary and $\varepsilon_{\theta e}$ is the elastic strain limit (ε_e) 78

Figure 3-4: Some matrix to quantify the squeezing potential depending on the angle between discontinuities and the tunnel wall (Mercier-Lanevin and Hadjigeorgiou 2011)..... 79

Figure 3-5: Curve to predict the radial strain for unsupported tunnels and associated recommendations proposed by Hoek and Marinos (2000) (adapted from Hoek and Marinos 2000)..... 80

Figure 3-6: Results of Monte Carlo simulation performed by Hoek and Marinos (2000)..... 81

Figure 3-7: Back analysis for the expression used by Hoek and Marinos (2000) to perform their Monte Carlo simulation using Carranza-Torres and Fairhurst (1999) expression 82

Figure 3-8: Numerical model used for the Monte Carlo simulation; R is the tunnel radius 84

Figure 3-9: Comparison of the results of 2D plane strain numerical model without support when the large strain hypothesis is used (orange points) and when the small strain hypothesis is used (blue points)..... 85

Figure 3-10: Flowchart to present the procedure used for the creation of the numerical model and Monte Carlo simulation 86

Figure 3-11: Estimated range of dilation as a function of GSI (from Lorig and Varona 2013) 86

Figure 3-12: Numerical results of the radial strain without support for different values of MR and GSI..... 89

Figure 3-13: Comparison of the fits obtained with Excel and with Python for the results associated with a modulus ratio of 400; dashed curves are obtained with Excel; continuous curves are obtained with Python 90

Figure 3-14: Interpolated curves of the radial strain without support for different values of GSI and for a Modulus Ratio (MR) of 200; the dotted lines present the 95% confidence interval for each GSI value 91

Figure 3-15: Interpolated curves of the radial strain without support for different values of GSI and for a Modulus Ratio (MR) of 400; the dotted lines present the 95% confidence interval for each GSI value 91

Figure 3-16: Interpolated curves of the radial strain without support for different values of GSI and for a Modulus Ratio (MR) of 600; the dotted lines present the 95% confidence interval for each GSI value 92

Figure 3-17: Comparison between the original H&M curve (green curve), the result of the Monte-Carlo simulation carried out with numerical calculations (points), the average fitting of this points (black curves) and the average fitting of the analytical calculations (red curves).. 93

Figure 3-18: Histogram of the values of normalized plastic radius (R_p), normalized by the tunnel radius 95

Figure 3-19: Comparison of the values of normalized plastic radius predicted with the surrogate model and the values obtained during the Monte Carlo simulation; the continuous line is the trendline and dash lines are the 95% confidence interval 96

Figure 4-1: Basic types of deformable supports: (a) compressible layer between lining and excavation boundary; (b) yielding support with steel sets, shotcrete and compressible inserts (from Cantieni and Anagnostou 2009a) 98

Figure 4-2: Example of yielding elements used in yielding supports: (a) Steel cylinder (Kovari 2009); (b) Highly compressible concrete element (Kovari 2009); (c) Wabe yielding element (Moritz 2011) 99

Figure 4-3: Pre-cast concrete segment including Meypo yielding elements in Ibbenbüren coal mine, Germany (from Moritz 2011)..... 99

Figure 4-4: Approach proposed by Jethwa *et al*. (1984) to quantify the squeezing phenomenon and to estimate the pressure on the support (from Barla 2001); σ_{cm} is the rock mass strength; γH the lithostatic stress; p_u the ground pressure on the support; the x-axis is the pre-peak friction angle 101

Figure 4-5: Theorical example of the three characteristic curves of the CV-CF method (adapted from Paraskevopoulou and Diederichs 2018); p_i / p_0 is the confining pressure normalized by the in-situ stress; x/R is the distance to the tunnel face normalized by the tunnel radius; $u_{rx}/u_{r\ maxpl}$ is the radial displacement normalized by the maximal radial displacement infinitely far from the face (i.e. no confining pressure) 102

Figure 4-6: 4 nomogram of Cantieni and Anagnostou (2009a) considering the normalized ground pressure $p(\infty)/p_0$ as a function of the normalized yield radial displacement $((u_y\ Er)/(a\ p_0)$ and the normalized uniaxial strength of the ground f_c/p_0 for friction angle ϕ= 15° and 20° and for normalized yield pressures p_y/p_0 = 0 – 0.02..... 104

Figure 4-7: Output parameters considered in the axisymmetric numerical calculation; P_i the ground pressure on the support far from the face; $\varepsilon_{f\text{-}s}$ the radial strain that develop between the face and the support; ε_{SF} the radial strain that develop before the face 107

Figure 4-8: Measurement of the 2D axisymmetric numerical calculation used; the orange values are the size of the mesh in the various sections of the model 108

Figure 4-9: Axisymmetric model including the support; the support is in red, installed at 1 R from the face; in green, it is a transiting material with a very low Young modulus 109

Figure 4-10: Histogram of the input parameters of the 100 geological situations of the training base; GSI + MR is the sum of the GSI value and the MR value..... 112

Figure 4-11: Analysis of the multilinear regression on the data of the training base and validation base..... 114

Figure 4-12: Analysis of the results of the regression using a neural network with two hidden layers, 7 neurons on the first layer and 8 neurons on the second layer..... 114

Figure 4-13: Relation between $\ln(P_i)$ and the unsupported span (e) for four examples from the training database..... 116

Figure 4-14:Evolution of the training base to create the surrogate models 117

Figure 4-15: Comparison of the real values of A and the one obtained with the surrogate model 118

Figure 4-16: Comparison of the real values of B and the one obtained with the surrogate model 119

Figure 4-17: Comparison of the real values of C and the one obtained with the surrogate model 119

Figure 4-18: Comparison between the ground pressure estimated with the surrogate model and the ones from the axisymmetric calculation of the training base and validation base. 120

Figure 4-19: Values of spans corresponding to the extremum based on the results of the training base 121

Figure 4-20: Comparison of the real values of A_{RS} and the one obtained with the surrogate model 123

Figure 4-21: Comparison of the real values of B_{RS} and the one obtained with the surrogate model 123

Figure 4-22: Comparison between the radial strain between the face and the support installation with the surrogate model and the ones from the axisymmetric calculation of the training base and validation base 124

Figure 4-23: Comparison of the real values of ε_{USF} and the one obtained with the surrogate model 125

Figure 4-24: Comparison of the real values of A_{SF} and the one obtained with the surrogate model 125

Figure 4-25: Comparison between the radial strain at the face of a supported tunnel (ε_{SF}) obtained with the surrogate model and the ones from the axisymmetric calculation of the training base and validation base 126

Figure 4-26: Method to estimate the long-term pressure on the support based on the proposed surrogate model coupled with a 2D plane strain approach 129

Figure 5-1: Relationship between acceptable risk, reliability targets and partial factors (i.e. semi-probabilistic approach) (Van den Eijnden *et al.* 2024) 133

Figure 5-2: Coefficient of variation (CoV) of various man-made and geotechnical materials (from Connor Langford and Diederichs 2015) 134

Figure 5-3: Classification of the existing reliable approach (from Tran 2020) 135

Figure 5-4: Application of the “3 points method” for the illustrative example detailed in Table 5-1 to assess the distribution of radial strain without support 140

Figure 5-5: Histogram for the MCS; the red curves are the fitted lognormal distributions; the blue curves are lognormal distributions for which the confidence interval of the “3-point method” is supposed to be a 95% confidence interval 141

Figure 5-6: Boxplot of the probability of the “3-point method” confidence interval for the different situations 1 to 7 143

Figure 5-7: Comparison of the probability density function of the radial strain without support calculated with MCS (black curve) or with the “3-point” method associated to four different assumptions about the probability associated with the confidence interval obtained. 146

Figure 5-8: Method to perform reliability-based design using the surrogate models; p(..) is a probability 148

Figure 5-9: Probability of each of Hoek and Marinos (2000) classes for the illustrative example 150

Figure 5-10: Relationship between the span, the radial strain, the ground pressure on the support far from the face and the failure probabilities for the illustrative example; t_s is the thickness of the support; pf is the failure probability; the y-axis values are the median values 151

Figure 5-11: Long term ground pressure on the support (t_s = 0.2m thick) and the lining (t_l = 0.2m thick) and the associated failure probability depending on the span of the support installation 153

Figure 5-12: Summary of the preliminary support design of the tunnel 153

Figure 5-13: Algorithm used to estimate the failure probability of an optimized random design using partial factors 155

Figure 5-14: Comparison between safety factors, probability of failures and uncertainties on the input parameters; μ is the mean; σ is the standard deviation 157

Figure 6-1: Cross-section along tunnel alignment (from Hoek and Guevara 2009) 160

Figure 6-2: Classification of Yacambu-Quibor rock unit (from Hoek and Guevara 2009) ... 161

Figure 6-3: Estimated rock mass characteristics based on the Geological Strength Index and the Hoek&Brown failure criterion (from Hoek and Guevara 2009) 161

Figure 6-4: Longitudinal Displacement Profile for the theoretical example (class D1, GSI 35) 163

Figure 6-5: Ground Reaction Curve for several values of GSI (35, 30, 25, 20, 17) and Support Characteristic Curve for the CV-CF method (red) and the long-term ground pressure on the support based on the axisymmetric calculation (green) 163

Figure 6-6: Typical yielding support used the construction of the tunnel 164

Figure 6-7 : Steel sets with sliding gaps used for the primary lining (from Connor Langford and Diederichs 2013) 165

Figure 6-8: Failed section between PM12+750 and PM12+850, with failure analyses proposed by Hoek and Guevara (2009) (from Hoek and Guevara 2009) 166

Figure 6-9: Calculated LDP of the Yacambu-Quibor tunnel associated with short-term properties and the worst-case scenario (Table 6-1) 168

Figure 6-10: CV-CF method for the worst-case scenario including short-term properties, and two values of GSI for the long-term properties 170

Figure 6-11: Estimation of the long-term ground pressure on the support based on the results of the surrogate model for the three situations 172

Figure 6-12: Geometry of the support and the lining between Chainage 12,750 and 12,850 (from Hoek and Guevara 2009)..... 173

Figure 6-13: Longitudinal Displacement Profile (LDP) for the short-term properties of the section between chainage 12+750 and 12+850..... 174

Figure 6-14: GRC and CV-CF method for the failed section between chainage 12+750 and 12+850..... 174

Figure 7-1: Graphical representation of the various parameters used in the empirical and analytical criteria (from He et al. 2022) ; S_{JKL} is the surface between point J, K and L..... 181

Figure 7-2: Chart introduce by Lee *et al.* (2004) to estimate the rockburt intensity based on a Korean waterway tunnel..... 185

Figure 7-3: Potential for spalling and rockburst failure process in intact rock (Diederichs 2018) 185

Figure 7-4: The TRC chart developed by Farhadian (2021); W_{et} is the elastic energy index; σ_θ/σ_c is the stress level index..... 186

Figure 7-5: Depth of spalling depending on the maximal orthoradial stress and the uniaxial compression strength (UCS), or the Crack Initiation stress (CI) (from Diederichs et al. 2010) 189

Figure 7-6 : Failure depth predicted as a function of maximum wall stress, Crack Initiation stress (CI) and the in-situ stress state ratio K (from Diederichs 2018) 189

Figure 7-7: Adaptation of the BHP to obtain the BHPs to include structural specificities (from Diederichs 2018) 191

Figure 7-8 : Picture of spalling that occurs during the construction of the Lötschberg base tunnel (courtesy of E. Garin)..... 193

Figure 7-9: Sudden brittle failure which could be classified as rockburst at chainage 4.200 of La Maddalena exploratory tunnel (from Fornari *et al.* 2016) 194

Figure 7-10 : Pictures of the damage associated with rockburst of May 31, 2015 (from Naji *et al*. 2019) 195

Figure 7-11: Proposed lines of defense against rockburst in deep mines (from Cai 2024).... 196

Figure 7-12 : Advantages and Disadvantages of AI techniques in rockburst prediction (from Zhang *et al*. 2024a)..... 198

Figure 7-13: Rock support function from Cai (2024), referring to Kaiser *et al.* (1996)..... 199

Figure 7-14: Pictures of the support used for some sections of La Maddalena exploratory tunnel (from Fornari *et al.* 2016)..... 200

Figure 7-15 : Presentation of the Mont Cenis base tunnel from TELT (Tunnel Euralpin Lyon Turin) website (https://www.telt.eu/en/)..... 202

Figure 7-16 : Geological map of expected geological conditions encountered during the TBM excavation of a part of the CO5 construction lot (adapted from ALLTI 2018a) 203

Figure 7-17: General methodology for a probabilistic rockburst risk assessment based on the approach developed by Diederichs (2018) ; σ_{ci} is the uniaxial compression strength of the intact rock; σ_t is the tensile strength of the intact rock; m_i is the strength of the Hoek & Brown failure criterion; γ is the specific weight of the rock expressed as kN/m^3; GSI is the Geological Strength Index; CI is the crack initiation stress; D_f is the depth of failure (Eq. 6-5); pm is the chainage of the tunnel section 205

Figure 7-18 : Histogram of m_i parameter for three geological formations obtain with a Monte Carlo situation considering a normal distribution law for σ_{ci} and a uniform distribution of σ_t 207

Figure 7-19: Results of the rockburst risk assessment for the Mont Cenis base tunnel (PM 35.000 - 50.000), situation 3 210

Figure 7-20: Results of the in-situ stress state associated with the Monte Carlo simulation for each section, situation 3; $\sigma_{\theta max}$ is maximal tangential stress at the tunnel boundary for an elastic behavior of the rock mass; σ_v is the vertical in-situ stress; σ_h is the horizontal stress perpendicular to the tunnel direction 211

Figure 7-21:Estimation of the overbreak / depth of failure based on Eq. (6-5) of the Diederichs's (2018) method, situation 3; the solid line is the median value of the overbreak for each tunnel section; the dash lines are the minimal and maximal values of overbreak 211

Figure 8-1 : Comparison between the post-peak stiffness of the rock (k_P) and two loading system (k_L), a soft one (blue) and stiff one (red) (from Wang *et al.* 2024) 215

Figure 8-2 : Example of a composite peak and residual strength envelope (adapted from Bewick et al. 2019) ; red curves are the curves of the bilinear criteria / tri-linear criteria ; green curves are the curves of the equivalent (or composite) H&B strength envelope for the peak and residual state 218

Figure 8-3 : Presentation of the notation used by Aglawe (1999) in Eq.(7-5) 220

Figure 8-4 : Study of the impact of a discontinuity on the LMS (from McDonald 2019) ; a) blue is the tunnel, green is the discontinuity, red is the notch ; b) black arrows are the forces applied on the notch, the background is the major stress before the calculation ; c) Reduction of the reaction force of 50% ; d) Final state, no reaction forces 220

Figure 8-5 : Simplified representation of the possible post-peak deformation behavior of rock (from Hou and Cai 2022b) 221

Figure 8-6 : Numerical investigation of the impact of the LESS on the post-peak behavior of the rock specimen ; a) comparison of the "real" post-peak behavior and the post-peak behavior of the rock under unstable failure, E_{in}* is the external energy provided to the system (loading system and rock specimen), E_t* is the elastic energy stored in the loading system (from Xu and Cai 2018) ; b) comparison of various LESS with the "real" post-peak stiffness under stable failure (from Xu and Cai 2017) 222

Figure 8-7 : Experimental results for post-peak deformation curves under stiff loading environment (adapted from Hou and Cai 2022b) ; a) for marble ; b) for granite ; M are the estimated post-peak stiffness of the rock specimen for each loading environment 223

Figure 8-8: Example of a notch at a tunnel boundary ; L is the height of the notch ; t is the depth of the notch ; Fi is the force applied at each grip point situated at the notch extremity before the notch removal ; Δli is the grid displacement after the removal of the notch..... 225

Figure 8-9 : Representation of the 3 possible situations to calculate the stress on a mesh element from the forces applied at grid points..... 226

Figure 8-10 : Comparison of the two methodologies to calculate the stiffness of the rock mass around several notch sizes..... 227

Figure 8-11: Relationship between $M_{s\text{-}s}$ and $k_{f\text{-}d}$ on a very simple example; t and L are the depth and the length of the notch 228

Figure 8-12 : Graphical representation of the LSS parameter 229

Figure 8-13 : Energetic consideration to determine the energy to be used for the LSS calculation; W_{modi} is the global elastic energy in the model at the ith state; W_{rmi} is the rock mass elastic energy around the notch at the ith state; W_{vol} is elastic energy include in the notch volume before removal; W_{press} is the energy associated with the work of the forces at the notch boundary for a quasi-static evolution between State 2 and State 3 230

Figure 8-14 : Final geometry of the Mine-By tunnel after excavation (Barton and Shen 2017); a) a picture of the tunnel; b) the shape and depth of the failed area..... 232

Figure 8-15 : Second method for the spalling process: progressive slab removal; red rectangles are the slab progressively removed 233

Figure 8-16 : Third method for the spalling process: progressive increase of the size and depth of the notch..... 233

Figure 8-17 : Rock mass stiffness evolution at each calculation step for the second spalling process..... 234

Figure 8-18 : Rock mass stiffness evolution at each calculation step for the third spalling process 235

Figure 8-19 : Presentation of the Jinping II Hydropower station (Zhang *et al*. 2013); the drainage tunnel is 83 m below the other tunnel 236

Figure 8-20 : Picture of buried TBM and fault localization (from Zhang *et al*. 2012) 237

Figure 8-21: Model geometry and boundary conditions for the model of the 11.28 rockburst 238

Figure 8-22 : Presentation of the "small" and "large" notch 239

Figure 8-23 : Mesh of the numerical model when the "large" notch is removed; a) is the notch considered for the stiffness calculation of $M_{s\text{-}s}$ and $k_{f\text{-}d}$; b) and c) are the forces and

displacements at the notch boundary for the sets of fault properties number 5 and an instantaneous removal of the “large” notch 239

Figure 8-24 : Maximum principal stress before the notch removal; the set “1” of discontinuity parameters is used 241

Figure 8-25 : Maximum principal stress after the “small” notch removal; the set “1” of discontinuity parameters is used 242

Figure 8-26 : Shear displacement along the discontinuity after the "small" notch removal; the set “1” of discontinuity parameters is used 242

Figure 8-27 : Shear displacement along the discontinuity after the "large" notch removal; the set “1” of discontinuity parameter is used 243

Figure 8-28: Comparison of the $M_{s\text{-}s}$ and $M_{f\text{-}d}$ (obtained with $k_{f\text{-}d}$ and Eq.(8-23)) for the two progressive notch evolutions ; process 2 is one similar to Aglawe (1999), process 3 is one considered as more realistic 245

Figure 8-29 : Comparison of the rock mass stiffness ($k_{f\text{-}d}$) and the post-peak stiffness ($k_{p\text{-}p}$) associated with the notch size; “process 2” is the progressive slab removal process; “process 3” is the progressive notch evolution process 246

Figure 8-30 : Impact of both situations on a theoretical example at a laboratory scale, engineering scale and comparison of rock mass stiffness and post-peak stiffness depending on the GSI value of the rock mass ; the red curves are associated with a situation in which the rock mass stiffness is smaller than the post-peak stiffness (ie violent failure expected) for intact rock properties ; the green curves are associated with a situation in which the rock mass stiffness is higher than the post-peak stiffness (ie quasi-static failure expected) 249

List of tables

Table 3-1 : Quantification of the squeezing potential proposed by Jethwa *et al*. (1984)..... 76

Table 3-2 : Properties and range of value used by Hoek and Marinos (2000), DeGagné et al. (2011) and in the following study; K_0 the horizontal to vertical in-situ stress ratio; USC the uniaxial compressive strength of the intact rock; m_i a parameter of the Hoek and Brown yielding criteria; α(GSI) means that α is a function of GSI 82

Table 3-3: Parameters A_i and B_i used to define the analytical formulation for the prediction of the radial strain without support ε_{usi} (equation 3-11) for different GSI and modulus ratios MR, and associated 95% confidence intervals (CI) 92

Table 4-1 : Properties and range of values used in the following study; USC the uniaxial compressive strength of the intact rock; m_i a parameter of the Hoek and Brown yielding criteria 111

Table 4-2: Values of the fitting parameters obtained for the surrogate model A..... 118

Table 4-3: Values of the fitting parameters obtained for the surrogate model B..... 118

Table 4-4: Values of the fitting parameters obtained for the surrogate model C..... 119

Table 4-5: Radial strain reduction associated with applying a confining pressure on the unsupported span (from Appendix 5)..... 128

Table 5-1: Variability of the input parameters for the illustrative example used to estimate how to propagate uncertainties of these parameters to get a valuable confidence interval of the radial strain without support..... 137

Table 5-2: Application of the PEM method on the illustrative example (Table 5-1). 138

Table 5-3: Comparison of the 3 approaches to propagate uncertainties, in order to assess the probability of each Hoek & Marinos class..... 141

Table 5-4: Variability of input parameters considered in each studied situation; μ_i is the mean of the parameter i; CoV_i is the coefficient of variation of the parameter i; the discrete probability for GSI = {GSI_{min}; GSI_{mean}; GSI_{max}} is {β; 1-2β; β} and similarly for MR with γ_{MR}..... 142

Table 5-5: Input parameters based on Connor Langford and Diedrichs (2013)..... 144

Table 5-6: Rock mass properties and support strength for the illustrative example of the RBD approach 149

Table 5-7: Constraint for the design to respect the expected failure probabilities 150

Table 6-1: Rock mass properties used by Connor Langford and Diederichs (2013), and associated variability 165

Table 6-2: Equivalent support and lining characteristics when considering composite elements; ST is for shotcrete and SS for steel sets 168

Table 6-3: Results of the surrogate models applied to the three tested situations; tunnel radius of 2.6m 172

Table 6-4: Equivalent support parameter for failed section (PM12+750 - PM12+850) 174

Table 6-5: Results of the surrogate model on the failed section, for various hypothesis on the span value and two values of long term GSI..... 176

Table 6-6: Failure probabilities for various hypotheses regarding the strength of the shotcrete, the short-term GSI value, and several long-term GSI values; sd is for standard deviation ... 177

Table 7-1: Summary of various empirical and analytical criteria based on Askaripour *et al*. (2022), He *et al.* (2022) and Zhou *et al.* (2018a) 182

Table 7-2: Classes of burst hazard potential proposed by Diederichs (2018) 188

Table 7-3: Summary of the geological data associated with the geological map (from ALLTI 2018b); for the geological formation in italic, the geotechnical values have been obtained based on laboratory test and field reconnaissance carried out on similar geological formation encountered outside the studied section 204

Table 7-4 : Geotechnical uncertainties consider for the study of the deepest section of the Mont Cenis base tunnel; CLm is the micashist of Clarea from La Maddalena exploratory tunnel. 208

Table 7-5 : Summary of the results of in-situ test (HTPF); H is the depth of test; γH is the lithostatic stress; σ_v is the measured vertical stress; $\sigma_{h\,min}$ and $\sigma_{h\,max}$ are minimal and maximal horizontal stresses 209

Table 7-6: In-situ stress state considered in the study 210

Table 8-1: Comparison of the LESS of the testing machine with the post-peak stiffness of the rock sample 223

Table 8-2 : Rock mass stiffness obtained with each methodology for the first spalling process 234

Table 8-3 : In-situ stress state of the 11.28 rockburst (Zhang *et al*. 2013); z is the vertical stress component; x and y are the horizontal stress components, perpendicular to the tunnel and in the tunnel direction..... 237

Table 8-4 : Various situations considered for the interface parameters..... 238

Table 8-5 : Results of the stiffness calculation of the 11.28 rockburst case study 240

List of symbols:

A, B, C, D, E: “Intermediate” surrogate model necessary for the estimation of the ground pressure on the support far from the face (Pi)

A_{rs}: area of the tested rock specimen

a: parameter of the generalized Hoek and Brown failure criteria

a: tunnel radius (Cantieni and Anagnostou 2009a)

AE: Acoustic Emission

AECL: Atomic Energy of Canada Limited

AFTES: French Tunnelling and Underground Space Association

ALLTI: “Alliance Lyon Turin Ingénierie”, joint venture of several engineering companies

AMF, AMA, AMD: Micaschists with quartzitic and conglomeratic facies, Bellecombe and Ambin geological unit

ANDRA: French National Radioactive Waste Management Agency

ANN: Artificial Neural Network

ANRT: National Association for Technological Research (France)

ARS, BRS: “Smaller” surrogate model necessary for the estimation of the radial strain between the face and the support ($\varepsilon_{f\text{-}s}$)

A_s: Cross-section of specified type of steel set

ASF, AMLR: “Smaller” surrogate model necessary for the estimation of the radial strain at the face of a supported tunnel (ε_{SF})

B_3: Strength Brittleness Index

B: tunnel diameter (Goel 1994)

BEM: Boundary Element Method

BG: Name of an engineering company bought by WSP

BHP: Burst Hazard Potential

BHP_m: Burst Hazard Potential adapted to include the rock mass characterization

BHP_s: Burst Hazard Potential adapted to include the effect of structural specificities

BR: Breakout Ratio

BTS: Brazilian Tensile Strength

C&M McNally: Engineering Company

Cb, tDB, tCD: Marble, Dolomite, Limestone, Bellecombe geological unit

CI: Confidence Interval

CI: Crack Initiation Stress (Diederichs 2018)

C_{ini}: Initial cohesion

CL: Micaschists and augen gneisses

CL_m: Micaschists and augen gneisses encountered during the excavation of La Maddelena exploratory galleria

CoV: Coefficient of Variation

CO: « Chantier Opérationnel », construction lot

C_p: Peak cohesion (Jethwa *et al.* 1984)

C_r: Residual cohesion (Jethwa *et al.* 1984)

C_{res}: Residual cohesion

CSFC: Cohesion Softening Frictional Constantly

CV-CF: Convergence-Confinement method

CWFH: Cohesion Weakening Frictional Hardening

CWFS: Cohesion Weakening Frictional Strengthening

D: Disturbance factor

d: Out-of-plane size of the notch

D_b: Average block size (AFTES)

d_b: Bolt diameter

DDA: Discontinuous Deformation Analysis

DDP: Damage Depth Potential

DEM: Discrete Element Method

D_f: Depth of failure

DRP: Dynamic Rupture Potential

DRP: Dynamic Rupture Potential

D_t: Excavation size (AFTES)

e: the span, the distance between the face and the rigid support installation. For Cantieni and Anagnostou (2009a), it is the distance between the face and the yielding support installation.

E_b: Young's modulus of bolt

E_g: Tangential modulus during pre-peak loading

E_i: Young's modulus of the intact rock

E_{ls}: Stiffness of the loading system during laboratory test

E_m: Young's modulus of the rock mass

E_M: Post-peak modulus of the rock (He *et al.* 2022)

E_{pp}: Post-peak stiffness of the rock mass

E_r: Young's modulus of the ground (Cantieni and Anagnostou 2009a)

Es: Young's modulus of the support element

E_{ste}: Young's modulus of steel

EU: European Union

E_u: Tangential modulus during pre-peak unloading

F_c: Competency factor (Majumber *et al.* 2017)

f_c: Uniaxial compressive strength of the ground (rock mass) (Cantieni and Anagnostou 2009a)

f_{ck}: Characteristic value of the compressive strength of the concrete or shotcrete

f_{cm}: Mean value of the compressive strength of the concrete or shotcrete

FDM: Finite Difference Method

FEM: Finite Element Method

F_i: Force applied at the ith grid point

FLAC: Finite Element software

FORM: First-Order Reliability Method

GDE: GeoData Engineering

GRC: Ground Reaction Curve

GSI: Geological Strength Index

GSI_{max}: Higher value of GSI

GSI_{med}: Median value of GSI

GSI_{min}: Lower value of GSI

GSI_{peak}: GSI value corresponding to the peak strength of the rock mass

$GSI_{residual}$: GSI value corresponding to the residual strength of the rock mass

H&B: Hoek and Brown failure criteria

H&M: Hoek and Marinos

H: Overburden of a studied section

HEA…: type of steel sets

HRSI: Hard Rock Squeezing Index

H_s: Height of the tested rock specimen

IC: Competency factor (Russo 2014)

ISRM: International Society of Rock Mechanics

jC: Joint condition

J_f: Joint Factor

Jm, cs-e: Marbles, Dolomites, Limestones, Lozes geological unit

K_0: Ratio between vertical and horizontal stress (Jain and Rao 2022)

K: In-situ stress ratio (Diederichs 2018)

K: Radial stiffness of the support

k: Stiffness of the support

$k_{f\text{-}d}$: Rock mass stiffness defined as the ratio of forces divided by displacements

K_h: Ratio between the horizontal stress and the vertical stress

k_I: Stiffness of the yielding support before reaching the yielding pressure (p_y) (Cantieni and Anagnostou 2009a)

k_{III}: Stiffness of the stiff support (Cantieni and Anagnostou 2009a)

k_L: Stiffness of a loading system (Wang *et al.* 2014)

k_{LMS}: Rock mass stiffness around the slab (Aglawe 1999)

k_P: Post-peak stiffness of the rock

k_{real}: Stiffness of the support considering the radial displacement though the span

k_{theo}: Theoretical stiffness of the support without considering the radial displacement though the span

K_v: Ratio between the vertical stress and the lithostatic stress

L: Free bolt length

LDP: Longitudinal Displacement Profile

LERR: Local Energy Release Rate

LESS: Loading Environment System Stiffness

L_i: Length of the ith removed slab

LMS: Local Mine Stiffness

LSS: Loading System Stiffness

m_b: Parameter of the generalized Hoek and Brown failure criteria

MCS: Monte Carlo Simulation

$M_{f\text{-}d}$: Transformation of $k_{f\text{-}d}$ into the unit than $M_{s\text{-}s}$

m_i: Parameter of the Hoek and Brown failure criteria

M_i: Post-peak stiffness of the rock during laboratory test

MR: Modulus Ratio

$M_{s\text{-}s}$: Rock mass stiffness defined as the ratio of stress divided by strain

$M_{s\text{-}s\ rm}$: Rock mass stiffness around a notch considering the impact of the rock mass characterization and calculated using the ratio of stresses divided by strains

N: Rock Mass number (Q value with SRF = 1)

NGI: Norvegian Geotechnical Institute

$p(\infty)$: ground pressure on the support far from the tunnel face (Cantieni and Anagnostou 2009a)

p_0: Initial in-situ stress (Cantieni and Anagnostou 2009a)

PEM: Point Estimate Method

PES: Potential energy of elastic strain

$p_{f\ adm}(P_{i\ LT\ ULS})$: Maximal admissible failure probability associated with the ULS regarding the ground pressure on the support far from the face with the long-term ground properties

$p_{f\ adm}(P_{i\ ULS})$: Maximal admissible failure probability associated with the ULS regarding the ground pressure on the support far from the face

$p_{f\ adm}(\varepsilon_{f\text{-}s\ ULS})$: Maximal admissible failure probability associated with the ULS regarding the radial strain between the face and the support installation

$p_f(P_{i\ LT})$: Failure probability regarding the ULS on the strength of the support at long-term

$p_f(P_i(e))$: Failure probability regarding the ULS on the strength of the support

$p_f(\varepsilon_{f\text{-}s}(e))$: Failure probability regarding the ULS on the radial strain between the face and the support installation

p_f: Failure probability

$P_{i\ LT\ ULS}$: Ultimate Limit State associated with the ground pressure on the support far from the face with the long-term ground properties

$P_{i\ max}$: Maximal ground pressure admissible on a support

$P_{i\ ULS}$: Ultimate Limit State associated with the ground pressure on the support far from the face

$p_i(\infty)_{LT}$: Ground pressure on the support far from the face with the long-term ground properties.

$p_i(\infty)_{ST}$: Ground pressure on the support far from the face with the short-term ground properties.

P_i: Ground pressure on the support infinitely far from the face

p_i: Weighting value (Point Estimate Method)

P_u: Ground pressure on the support (Jethwa *et al.* 1984)

p_y: Yielding pressure of yielding support (Cantieni and Anagnostou 2009a)

Q: Load-deformation constant for anchor and head (as obtained on the bolt load-extension curve of a pull-out test)

Q: Value of the Q-system

QSE: Quartzites

R(Xi): Value of the response parameters for the vector of input parameters Xi

r-t: Micaceous quartzites and Quartzitic conglomerates

R: Tunnel radius

RBD: Reliability-based Design

RBDO: Reliability-based Design Optimization

R_{ext}: External radius of the support

R_{int}: Internal radius of the support

R_{mean}: Radius associated with the middle of the support

RM_i: Rock Mass index

RMR: Rock mass rating

R_p: Plastic radius around an unsupported tunnel

RSM: Response Surface Method

R^2: Coefficient of determination

$R_{\mu,76}$: Version of the RMR published in 1976

$R_{\mu,89}$: Version of the RMR published in 1989

s: Parameter of the generalized Hoek and Brown failure criteria

S: Spacing of the steel set along the tunnel axis

S_c: circumferential bolt spacing

SCC: Support Characteristic Curve

SCM: Strength Classification Method

SF: Safety factor

S_l: Longitudinal bolt spacing

SORM: Second-Order Reliability Method

SR: Strength Ratio

SRF: Stress Reduction Factor

SS: Steel set

ST: Shotcrete

t6: Limestones and dolomites

t: Depth of the notch

T: True tensile strength (Diederichs 2018)

T_{bf}: bolt ultimate failure load

TBM: Tunnel Boring Machine

TELT: Tunnel Euralpin Lyon Turin

TEN-T: Trans-European Transport Network

tG: Anhydrite, Esseillon geological unit

TH …: Type of steel set

t_i: Mesh size of the ith element in the notch direction

tng: Anhydrite, Bellecombe and Lozes geological unit

TRC: Tunnel Rockburst Classification

t_s: Thickness of the support

u_0: Radial displacement at the support installation obtained with the CV-CF method

UCS: Uniaxial compressive strength

UDEC: Discontinuous numerical modelling software

u_e: Radial displacement at the support installation obtained with the implicit approach of the CV-CF method

ULS: Ultimate Limit State

URL: Underground Research Laboratory

u_y: Radial displacement capacity of the yielding support (Cantieni and Anagnostou 2009a)

$u_{\infty c}$: Final radial displacement estimated with the classical CV-CF method

$u_{\infty i}$: Final radial displacement after equilibrium with the implicit approach

$u_{\infty\ us}$: Maximal radial displacement without support

V_b: Rock block volume (Russo 2014)

VBA: Visual Basic

V_f: Volume of the failed area

W_{et}: Elastic Energy index (Farhadian 2021)

W_f: Energy consumed by the rock during the failure

W_k: Released kinetic energy

W_{modi}: Global elastic energy in the model at the ith state

W_{press}: Energy associated with the work of the forces at the notch boundary for a quasi-static evolution

W_{rmi}: Rock mass elastic energy around the notch at the ith state

WSP: Name of an engineering company

W_t: Total amount of energy released energy from the rock mass

W_{vol}: Elastic energy includes in the notch volume before removal

X_{est}: Value of the parameter X obtained with numerical calculation ("estimated" value)

X_{real}: Value of the parameter X obtained with numerical calculation ("real" value)

α: Dilation-to-friction ratio

β: Probability of the lower or higher value of GSI

β: Shear failure angle during laboratory test (Bésuelle *et al.* 2000)

γ: Specific weight of the rock

γ_f: Partial factor applied on the internal load of the support

γ_{MR}: Probability of the lower or higher value of MR

γ_p: Plastic shear strain

γ_s: Partial factor applied on the strength of the support element

δ: Relative gap between two values

Δl_i: Displacement of the ith grid point

Δu_θ: Change of tangential displacement after a slab removal

$\Delta W_{i\text{-}j}$: Variation of energy between the ith and the jth state

ε_0^k: Residual deformation associated with a σ_k pre-peak loading situation

ε_1: Axial strain under laboratory test

$\varepsilon_{2.5}$: Lower boundary of the 95% confidence interval of the radial strain

ε_3: Radial strain under laboratory test

$\varepsilon_{97.5}$: Higher boundary of the 95% confidence interval of the radial strain

ε_c: Pre-peak axial strain

ε_d: Axial strain at the beginning of the residual state

ε_e: Elastic strain limit (Aydan et al. 1996)

$\varepsilon_{eq\ LT}$: Radial strain with the short-term ground pressure, associated with a 2D plane strain approach leading to the same ground pressure as a 3D approach

$\varepsilon_{eq\ ST}$: Radial strain with the short-term ground pressure, associated with a 2D plane strain approach leading to the same ground pressure as a 3D approach

$\varepsilon_{f\text{-}s\ ULS}$: Ultimate Limit State associated with the radial strain between the face and the support

$\varepsilon_{f\text{-}s}$: Radial strain between the face and the rigid support installation

ε_f: Specific strain value defined by Aydan *et al.* (1996)

$\varepsilon_{fs\ mod}$: General parameters associated with the surrogate model allowing the estimation of the radial strain occurring between the face and the support installation ($\varepsilon_{f\text{-}s}$)

ε_m: Mean tangential strain after a slab removal

ε_{median}: Median value of radial strain

ε_p: Specific strain value defined by Aydan *et al.* (1996)

ε_s: Specific strain value defined by Aydan *et al.* (1996)

ε_{SF}: Radial strain at the face of a supported tunnel

ε_{tot}^{k}: Total axial strain for a σ_k pre-peak loading situation

ε_{us}: Radial strain without support

ε_{USF}: Radial strain at the face for an unsupported tunnel

ε_v: Volumetric strain under laboratory test

ε_θ^a: Orthoradial strain at the tunnel boundary (Aydan et al. 1996)

η_p: Specific parameter introduced by Aydan et al. (1996)

μ_{LN}: Parameter of a lognormal distribution (mean value of the normal distribution associated with the natural logarithm)

μ_{m_i}: Median value of m_i

μ_{rgp}: Mean value of a relative gap

$\mu_{\sigma_{ci}}$: Median value of σ_{ci}

μ_{σ_0}: Median value of σ_0

ν: Poisson's ratio of the ground (Cantieni and Anagnostou 2009a)

ν_c: Poisson's ratio of concrete or shotcrete

ν_{rm}: Poisson's ratio of the rock mass

ν_s: Poisson's coefficient of the support element

σ_0: In-situ isotropic stress state

σ_1: Major principal stress

σ_3: Minor principal stress

σ_c: Compressive strength of the concrete or shotcrete

σ_{ci}: Uniaxial compressive strength of the intact rock

σ_{cm}: Rock mass compressive strength

$\sigma_{h\,max}$: Maximal horizontal stress

$\sigma_{h\,min}$: Minimal horizontal stress

σ_h: Horizontal stress perpendicular to the tunnel axis

σ_L: Stress in the tunnel direction

σ_{LN}: Parameter of a lognormal distribution (standard deviation of the normal distribution associated with the natural logarithm)

σ_m: Mean stress

σ_{m_i}: Standard deviation of m_i

$\overline{\sigma}_m$: Average value of the mean stress in each elementary volume

σ_p: Peak strength during laboratory test (Hoek and Martin 2014)

σ_{rgp}: Standard deviation of the relative gap

σ_s: Strength of the steel

σ_t: Tensile strength of the rock

σ_v: Vertical stress

σ_x, σ_y, σ_z: Stresses in the x, y, and z direction

$\sigma_{\sigma_{ci}}$: Standard deviation of σ_{ci}

σ_{σ_0}: Standard deviation of σ_0

σ_θ: Maximal orthoradial stress at the tunnel boundary

$\sigma_{\theta\,s}$: Orthoradial stress in the support element

τ_{xz}: Shear stress between x and z direction

φ: Friction angle

φ_{res}: Residual friction angle

ψ: Dilation angle

ϕ_e: Pre-peak elastic energy

ϕ_p: Peak friction angle (Jethwa et al. 1984)

ϕ_p: Inelastic energy consumes during the pre-peak loading at the UCS

ϕ_r: Residual friction angle (Jethwa et al. 1984)

ϕ_{se}: Pre-peak elastic energy associated with an unloading at 80% or 90% of the UCS

ϕ_{sp}: Inelastic energy consumes during the pre-peak loading at 80% or 90% of the UCS

ϕ_{sf}: Complementary energy needed for the rock failure

ϕ_t: Total energy provided during the pre-peak loading

$\phi(x)$: Reduction factor of the implicit approach

Chapter 1 - Thesis Framework

Chapter Abstract: This chapter introduces the research work presented in this thesis. It clarifies the framework linking each chapter to the common objective: improving the tools available to engineers during the early design stages, in order to better anticipate the possible geological and geotechnical hazards arising from existing uncertainties. This will allow a more appropriate tunnel design and more effective risk management throughout the design and construction stages. The context, limitations, main problematic and objectives of this thesis are presented and discussed to provide a solid framework for the work.

This manuscript presents the PhD thesis of Baptiste Fenneteau titled “Preliminary Design of Deep Tunnel in Continuous Rock Mass by Combining Numerical and Probabilistic Approaches”. This thesis is an industrial thesis (Cifre thesis in France) funded by WSP France. Some funding was also provided by the ANR, National Association for Technological Research, in France. This thesis began in October 2022, and the defense occurred November 20th, 2025. It has been conducted in partnership with the GeoRessources Laboratory at the University of Lorraine in France. This work was supervised by Professor Olivier Deck and Associate Professor Rasool Mehdizadeh from Mines Nancy and researchers at GeoRessources Laboratory of the University of Lorraine in France. It was also supervised by François Laigle, underground work expert at WSP in France until the end of 2024, currently working at Setec Terrasol, and chairman of the Technical Committee of the French Tunnelling and Underground Space Association (AFTES).

1.1 Thesis context

WSP in France chose to support this PhD thesis because several of its current and potentially future projects in the French and Swiss Alps have significant depths of cover (often higher than 1000m, reaching more than 2000m). Many of those recent projects are linked to the construction and improvement of the Trans-European Transport Network (TEN-T), which is funded by the European Union (EU), and aims to develop a coherent, efficient, multimodal, and high-quality transport infrastructure across the EU. In this context, several deep railway tunnels have been constructed like the Lötschberg Base Tunnel (34.6 km long) and the Gotthard Base Tunnel (57.1 km long) in Switzerland in the past two decades. Two other base tunnels are under construction, the Brenner Base Tunnel between Austria and Italy (55 km long), and the Mont Cenis Base Tunnel between France and Italy (57.5 km long) which are expected to be operational between 2030 and 2035. The Mont Cenis Base Tunnel, which is presented in detail in Chapter 7, is part of a new railway line between Lyon in France and Turin in Italy. At least three other deep tunnels will be constructed on this new line, the Chartreuse tunnel (25 km), the Belledonne tunnel (20 km), and the Glandon tunnel (10 km), each with an overburden of more than 1000 m.

WSP has been involved in the design and construction of Lötschberg Base Tunnel (known as BG Consulting Engineers at the time, before it acquisitions by WSP) and is currently involved in the construction of the Mont Cenis Base Tunnel as a member of the joint-venture GEIE ALLTI, in charge of the design and the construction supervision of the excavation lot number 5 (CO5) as well as the management and the reuse of all the excavated materials produced on the French side of the tunnel (CO11). Based on the experience gained with these projects, it is believed that it is possible to better quantify the risk of various geological and geotechnical hazards during the preliminary design stage of a tunnel project. This could lead to a more relevant design directly at the beginning of the project, and thus a more accurate cost and duration estimations based on exciting uncertainties, as well as a better risk management approach. It is essential that the preliminary design be resilient regarding the uncertainties associated with the project, to allow adjustment later in more advanced design stages when some of these uncertainties are reduced (or not). Failing to correctly consider these uncertainties would lead to a design that can be inappropriate during a more advanced design stage of the project. This will generally result in cost overruns, delays, and limited technical solutions available, as most of the major engineering choices have already been made. Modifying these choices at an advanced stage of the project is very difficult and can have significant consequences for all parties involved.

Although identifying possible geological and geotechnical hazards is only a small part of the design of an entire project, it will have a major impact on every other engineering choice made for the tunnel construction. During a preliminary stage, engineers have limited information to identify these hazards because boreholes, field investigations, and in-situ tests, can be very expensive for deep tunnels. Nevertheless, this analysis allows engineers to make all the subsequent design choices, such as the excavation technique(s), which will impact all the logistical aspects of the project including excavation sequence, support and lining installation, management of the excavated material, additional access points, ventilation, flux of material to and from the face, the site installation at the surface, etc. The level of detail depends on the project stage. All these choices will allow an estimation of the cost and the duration, giving the client the possibility to decide whether or not to continue with the project.

For most tunnel projects, these hazards are either limited or can be correctly identified at the beginning of the project. However, there is one major exception: the deep tunnel projects, which range from several hundred to a couple of thousand meters deep. The expected hazards can be so extreme that specific technical solutions may be necessary to deal with each one, and they are highly uncertain due to the complexity and limitations of field investigations. In the most uncertain situations or in the most potentially hazardous areas, exploratory tunnels of several kilometers long can be excavated to investigate more precisely the rock mass behavior and the potential hazards in that location. Explicit consideration of the existing uncertainties is essential for these projects because the presence of these large uncertainties can lead to geological conditions that are quite different from those initially expected. The preliminary design must include these possibilities because they cannot be ruled out at the design stage. This is the main idea behind this thesis: can these uncertainties be directly considered during the early stages of a deep tunnel design, and if so, how?

1.2 Framework of the thesis and limitations

This thesis focuses on the preliminary design stage of tunnel projects. As explained above, the major engineering choices are made during these early stages based on limited information. The objective is to demonstrate the feasibility of the tunnel project and to provide an estimation of the cost and the duration. Then, based on this information, the client must decide whether or not to continue the project. Typically, if the project advances to the next stage of studies, the proposed design of the previous stages is not modified unless new and contradictory field data are obtained. It is just studied more thoroughly, leading to a more detailed design.

The thesis focuses on “deep tunnels”. This terminology can be difficult to define because its meaning can vary greatly depending on the engineering field using it. For tunneling in urban areas like subways, the meaning of “deep” is very different than for tunnels under mountain ranges or for underground mining. In the first case, 100 m can be considered as very deep, but for the other one, deep can be associated with more than 2000 m, reaching nearly 4000 m for the deepest mines in South Africa. Here, “deep” corresponds to two fundamental hypotheses. The first one is that there is no direct interaction between the tunnel and the ground surface. This means that the depth of the tunnel is high enough to prevent settlement at the ground surface. The second hypothesis is that the in-situ stress state is high enough so the variation of the vertical stress associated with the height of the underground structure can be neglected. This does not mean that gravity-driven failure mechanisms cannot happen. Regardless the depth of the tunnel, these failures can occur, they just won’t always be the predominant failure mechanism. In this thesis, the minimum depth considered is 200 m assuming a vertical stress equal to the lithostatic stress. For a 10m diameter tunnel and a specific unit weigh of 25 kN/m^3

for the ground, the variation in vertical stress between the top and the invert of the tunnel is 250 kPa, and the vertical stress is 5 MPa (250 kPa << 5 000 kPa). It is important to note that the term “deep” can also depend on the failure mechanism being studied.

From a general point of view, a rock mass is a discontinuous medium as it is composed of an intact rock matrix including more or less joints, bedding planes, or other types of discontinuities. However, depending on the size of the excavation and the density of discontinuities, the rock mass can be seen as a continuous medium in specific situations. It can be considered continuous for intact rock masses or highly fractured rock masses, as illustrated by the Figure 1-1 (AFTES, GT30R1A1, 2021).

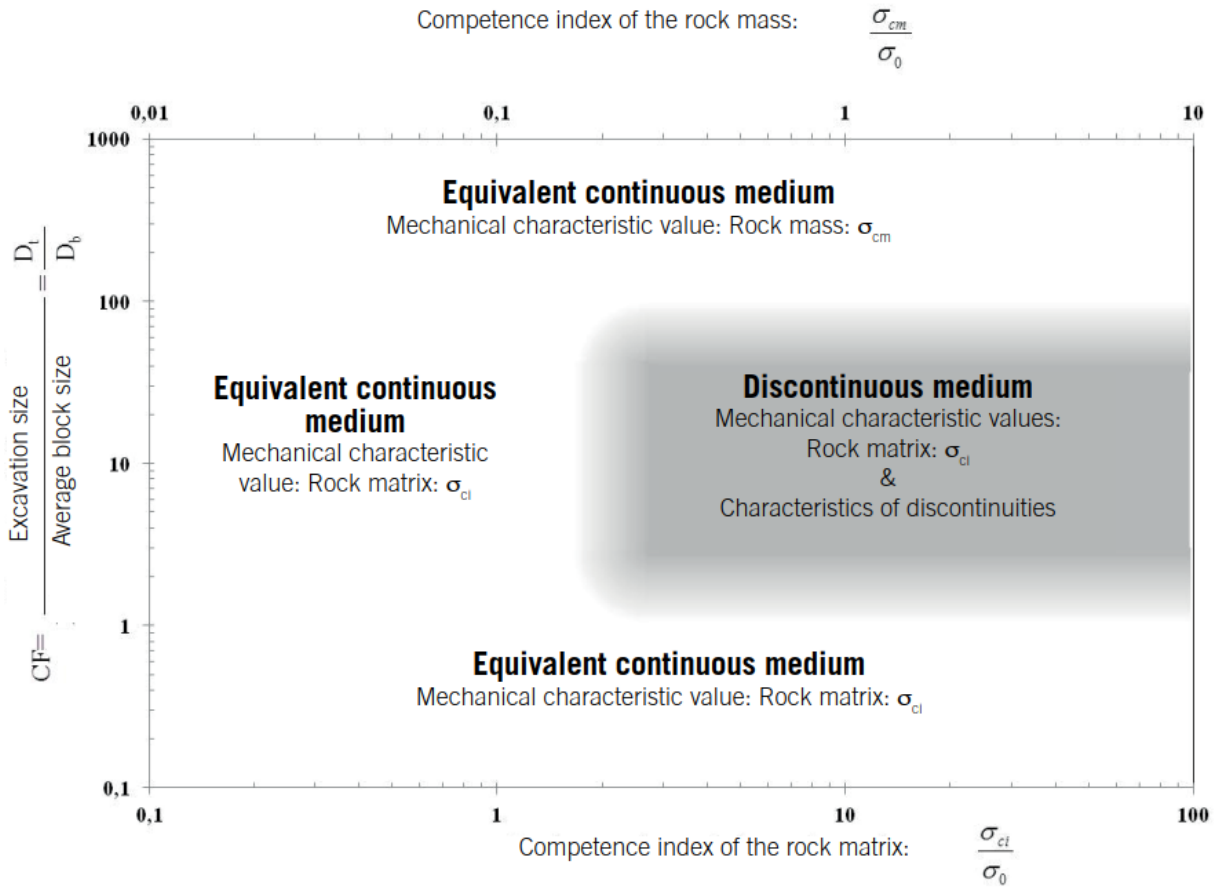

Figure 1-1: Rock mass as a continuous or discontinuous medium (AFTES GT30R1A1); σ_{ci} is the uniaxial compressive strength of the intact rock; σ_{cm} is the strength of the rock mass; σ_0 is the equivalent isotropic in-situ stress state

In a continuous medium and high in-situ stress, the two main phenomena are the large deformation phenomenon in highly fractured rock masses, often referred to as squeezing phenomenon, and brittle failures, which can be either quasi-static like spalling or violent like rockburst. The AFTES recommendation (GT30R1A1) and Kaiser *et al*. (2000) highlight this point in Figure 1-2 and Figure 1-3. These failure phenomena occurred during the construction of the deep tunnels mentioned in Section 1.1.

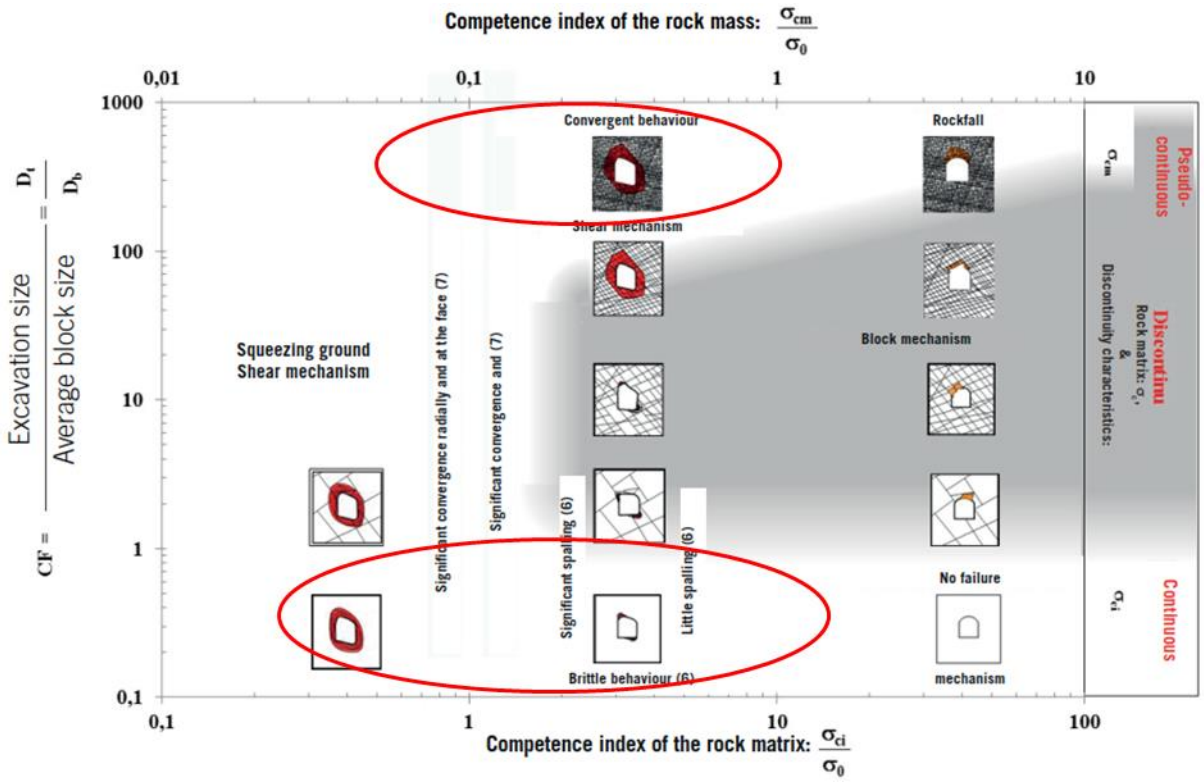

Figure 1-2: Rock mass behavior based on the competence index and scale factor (AFTES GT30R1A1); more details and specific remarks can be found directly in the recommendation

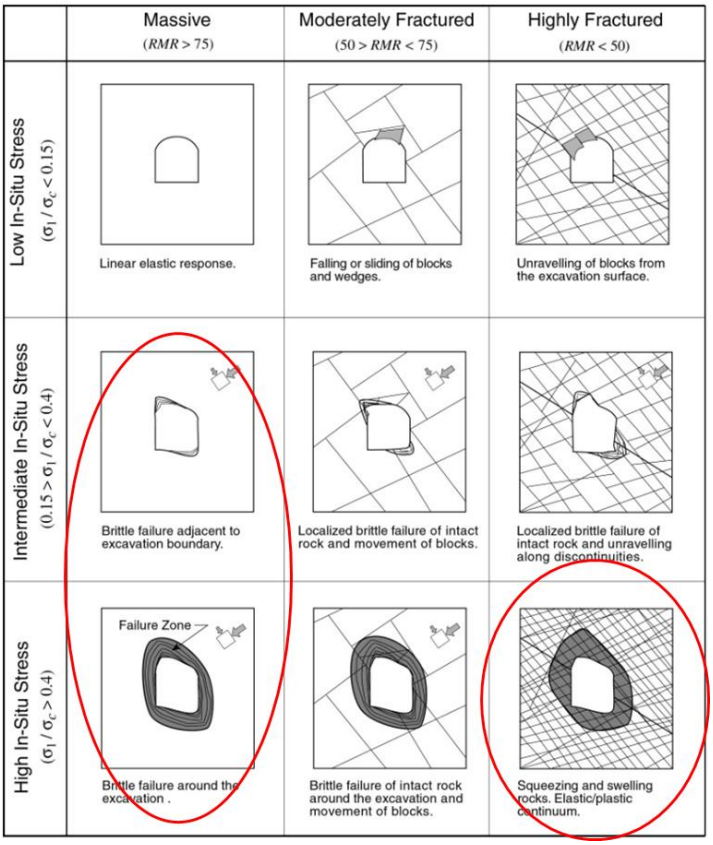

Figure 1-3: Rock mass behavior depending on the RMR and the in-situ stress state proposed by Kaiser et al. (2000)

These specific ground behaviors are also highlighted in other tools allowing an identification of the possible geological hazards that could occur, like in the GDE multi-graph developed by Russo (2014) in Figure 1-4 or a multi-graph technique introduced by Majumber *et al.* (2017) in Figure 1-5.

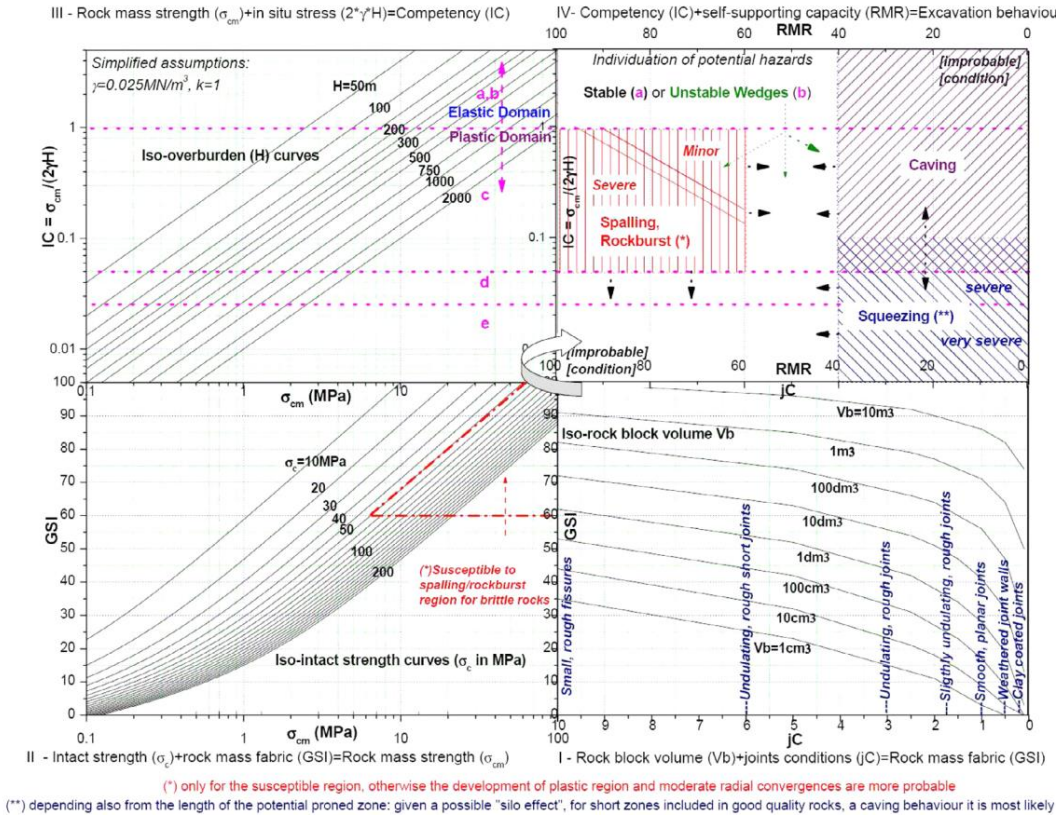

Figure 1-4: GDE (GeoData Engineering) multigraph developed by Russo (2014)

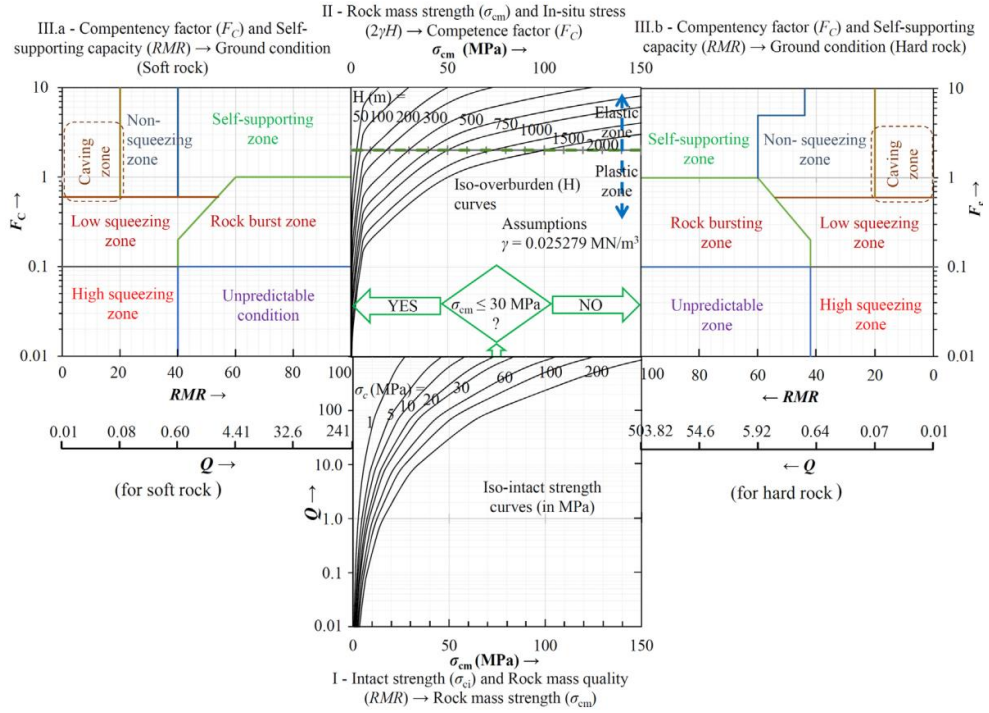

Figure 1-5: Multi-graph introduced by Majumber et al. (2017) to identify the rock mass behavior

The approaches presented above (Figure 1-2, Figure 1-3, Figure 1-4 and Figure 1-5) allow an identification of the risks during preliminary design, but do not provide a real quantification of the expected phenomenon only “severe/very severe” for Russo (2014) or “low/high” for Majumber *et al.* (2017). The information provided is not sufficient for the engineers to propose a relevant design.

A detailed description of studied phenomena is presented in the following chapter (Chapter 2.2.1 and 2.2.2). In this thesis, only mechanical failure mechanisms are studied. Other hazards could also occur based on the chemical composition of the rock itself (swelling, toxic gases, asbestos, natural radioactivity, …), on the hydrogeology or on the thermal conditions. These types of hazards are not considered in this thesis.

To study the behavior of the continuous rock masses, numerical calculations are performed with the continuum code Flac 2D 8.1, and probabilistic approaches are used. Probabilistic approaches are mathematical methods allowing the introduction and propagation of uncertainties. The main advantage of probabilistic approaches is that they allow reliable calculation in order to estimate failure probabilities. A detailed presentation can be found in Chapter 5.

As highlighted in the previous section, it is crucial for engineers to correctly assess potential geological hazards that could occur, and the impact of the existing uncertainty associated with an early stage of a tunnel project. The main objective of this thesis is to develop useful tools and methods during early design stages to better anticipate these hazards, allowing a better understanding of possible rock mass behavior and the impact of technical solutions and engineering choices. There are already many methodologies that exists for the risk identification (Figure 1-2, Figure 1-3, Figure 1-4 and Figure 1-5) and for basic quantification of the phenomenon that can be used during preliminary design. As it will be presented in several chapters of this thesis, most of these approaches or methods are either too simple to allow engineers to propose a relevant design, too complex to be used during preliminary designs (lack of specific information or too time-consuming), unsuitable for the introduction and propagation of uncertainties, or lead to incorrect results when applied to deep tunnels. Based on this analysis, the idea of this thesis is to improve or develop tools for engineers that are more appropriate than what already exists for preliminary deep tunnel design. To do so, the input parameters have to be as simple as possible and easy to determine in the early stages of a project, and the tools or methods have to easily and explicitly consider the geological and geotechnical uncertainties.

More precisely, this thesis focuses on: improving an existing method to quantify the risk of large radial deformation, while explicitly and easily introducing and propagating uncertainties; developing a new method to study the interactions between the rock mass behavior and the support in highly fractured rock mass using 2D axisymmetric calculations and surrogate models, making it appropriate for uncertainties considerations; improving an existing method for the quantification of the risk of brittle failures to explicitly consider the geological and geotechnical uncertainties; and to discuss whether or the brittle failure is expected to violent.

1.3 Structure of the manuscript

This manuscript is composed of seven main chapters, each with its own objective:

1) Chapter 2 aims to introduce the studied phenomena of large deformation and brittle failures, as well as to summarize some fundamental knowledge of rock mechanics to ensure a good understanding of the work presented.

2) Chapter 3 focuses on identifying and characterizing the risk of the large deformation. It provides a brief overview of some existing methods. Then, a new approach is presented to improve some of the shortcomings of one of the most widely used methods: the Hoek and Marinos curve (Hoek and Marinos 2000). This improvement was developed using Monte Carlo simulation carried out on a 2D plane strain numerical model.
3) Chapter 4 highlights the next step of the design. After a correct identification of the risk of large radial deformation, it is necessary to develop a specific design. This chapter presents various existing technical solutions to deal with large deformations, as well as design approaches and methods that can be used. While all these methods have advantages and limitations, none of them explicitly consider the interaction between the rock mass behavior and the support behavior while allowing them to easily introduce and propagate uncertainties. A new method has been developed that provides better results while making it easier to deal with the existing uncertainties. This method is based on surrogate models developed through axisymmetric numerical calculations performed for a wide range of tunnel situations that could be impacted by large radial deformation.
4) Chapter 5 presents how the methods and tools developed in Chapter 3 and 4 can be used for probabilistic and reliable calculations. This chapter also includes some discussions about the potential relationship between safety factors and failure probabilities for deep tunnels in highly fractured rock masses, enabled by the results presented in Chapter 4 and Monte Carlo simulations.
5) Chapter 6 applies the aforementioned tools and methods developed to the case study of the Yacambù-Quibor tunnel in Venezuela, where large radial deformations were encountered during the construction. More specifically, two sections of the tunnel are studied: one corresponding to the expected worst-case scenario and one corresponding to a failed section of the tunnel. Classical methods are also compared with the new approach proposed, to highlight its relevance.
6) Chapter 7 focuses on the prediction of brittle failures for deep tunnel within intact and massive rock mass. It summarizes most of the existing approaches for early tunnel design stages and provides examples of brittle failures in deep tunnels in civil engineering projects. It also discusses the existing monitoring techniques and the technical solutions to mitigate the risk and to guarantee the safety of the operation. Then, an existing method proposed by Diederich (2018) is improved to allow the introduction and propagation of uncertainties to assess and quantify the risk of brittle failures. This improved method is applied to the case study of the deepest section of the Mont-Cenis base tunnel between France and Italy, where major uncertainties exist on the geotechnical parameters and on the in-situ stress state.
7) As the approaches presented in the previous chapter are mostly empirical or analytical, an advanced method is studied in Chapter 8. This method uses finite element numerical calculations to determine whether a brittle failure will be quasi-static or violent. Since many studies have already been done on this topic, this chapter focuses on calculating the rock mass stiffness around a failed area at a tunnel boundary. Several methods are proposed for calculating this stiffness and are then compared using two case studies of brittle failures. Finally, the relevance and the limitations of this method based on numerical calculations are discussed.

To avoid overloading this manuscript, nine annexes are also presented at the end. Five of these are for Chapter 4, discussing and highlighting some limitations of existing approaches, and presenting some complementary studies performed to increase the method validity range.

Chapter 2 - Introduction

Chapter Abstract: In this chapter, some fundamental knowledge of rock mechanics and rock mass behavior are reminded as they are necessary for a good comprehension of the research work performed. Particular attention is given to the rock behavior during laboratory testing, and to the transition from the laboratory scale observations to the engineering scale (rock mass scale) applications. Finally, the two phenomena studied in this thesis are briefly introduced: the large deformation phenomena also known as squeezing, and brittle failures, which can be quasi-static (such as spalling), or sudden and violent (such as rockbursts).

2.1 Basis of rock mechanics: from laboratory to rock mass scale

To correctly understand the following work of this thesis, this section reminds some fundamental knowledge about the microscopic behavior of the rock, its behavior during laboratory tests, and how to switch to the project scale.

2.1.1 Rock behavior at laboratory tests scale

Laboratory tests are fundamental to understand the rock behavior and to choose appropriate behavior law and failure criterion. Most observed failure mechanisms at the tunnel scale originate from the behavior of the intact rock and so can be observed at the laboratory and at a microscopic scale.

2.1.1.1 Crack mode

The terminology used to describe cracks (microscopic scale) or fractures (macroscopic scale) that developed in an intact rock depends on the field of research (Vaskou 2024). From a geologist's perspective, there are two main types of fractures: joints and faults. From a rock engineer's perspective, they correspond to tensile fractures, or shear fractures. More precisely, four fracture deformation modes are identified (Figure 2-1).

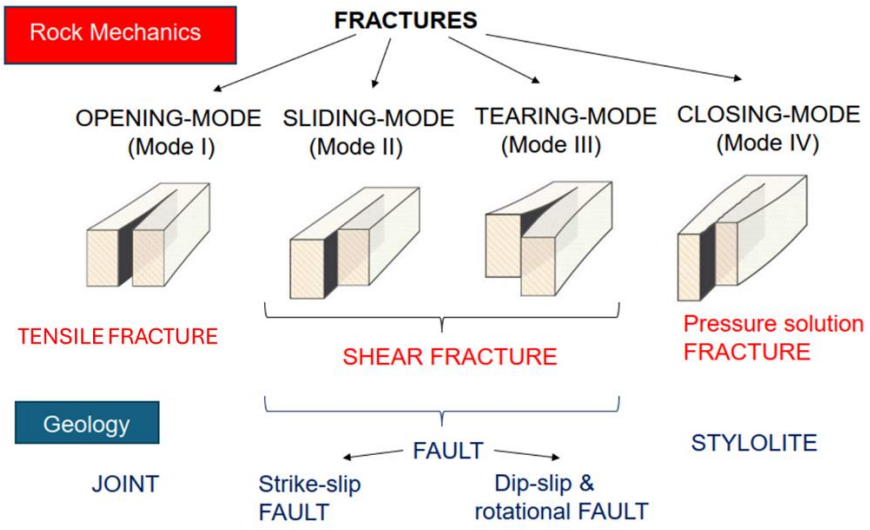

Figure 2-1: Facture modes and equivalent from a rock mechanics and geological point of view (from Vaskou 2024)

Tensile fracture and shear fracture are also fracturing modes (crack creation) while closing mode is only a mode of fracture deformation. During laboratory tests, these modes of cracking and fracture deformations lead to different failure modes of the rock. For no confining pressure or small confining pressure, the primary failure mode is tensile failure parallel to the principal stress ("splitting failure"). For intermediate confining pressure, the failure is localized through shear band. For high confining pressure, the failure mode is plastic deformation with a ductile behavior of the rock sample (Figure 2-2).



Figure 2-2: Typical failure modes of intact rock sample under various confining pressure (Laigle 2004)

2.1.1.2 Pre-peak behavior

The behavior of an intact rock sample during a compressive test can be decomposed into different phases. The number of phases used to characterize the pre-peak behavior varies among authors, but most consider four phases (Martin and Chandler 1994; Diederichs 1999; Laigle 2004; Kleine 2007; Hoek and Martin 2014; Rahimzadeh Kivi *et al*. 2018; Wang *et al.* 2020; Liu *et al*. 2022, etc). Haïed (1995) considers six phases and Paterson (1978) considers three. In general, four main phases can be distinguished, as illustrated in Figure 2-3:

1. Crack closure phase: This involves the closure of pre-existing cracks in the sample. The behavior is being guided by the microscopic behavior of the rock. This phase is therefore accompanied by contraction. Liu *et al.* (2022) argue that closing of these cracks reduces the porosity of the material.
2. Linear or quasi-elastic phase: In this phase, the material behaves elastically. Loading does not cause any microscopic degradation of the sample. This phase is also accompanied by contraction.
3. Damage phase: Cracking induced by the stress state begins to develop within the core of the sample and the cracks begin to coalesce, while remaining stable. At the microscopic scale, this cracking process leads to a macroscopic dilation of the sample, which compensates the contraction associated with the loading condition. This phase corresponds to a progressive stabilization of the volumetric strain of the sample.
4. Unstable crack growth phase: Cracking continues, and the crack coalescence is unstable. The notion of instability is highly subjective, because it depends on the loading rate and the duration of the test. There are few clear definitions of this phase in the literature. This phase begins at the point of inversion of the volumetric strain rate, when the dilation begins at the sample scale.

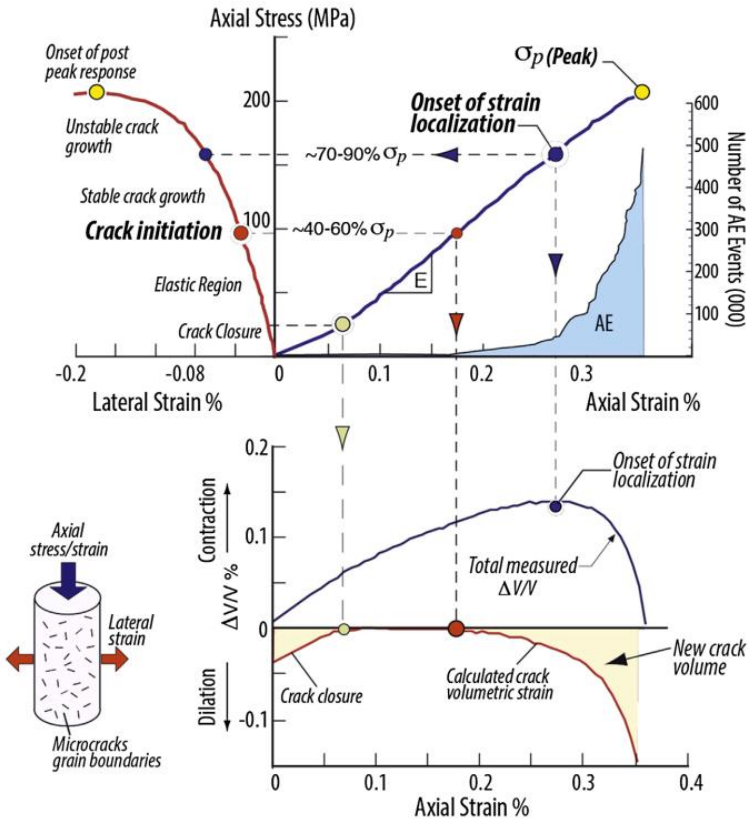

Figure 2-3 : Progressive failure of intact rock under compressive loading (from Hoek and Martin 2014, modified from Martin and Christiansson 2009); AE is Acoustic Emission

The stress associated with the transition between these different phases varies among authors:

- The transition between the crack closure phase and the linear phase: No value is given in the literature because it depends heavily on the amount of damage in the sample before the beginning of the test and the crack closure phase may not necessarily exist.
- The transition between the linear phase and the damage phase (crack initiation): Brace *et al.* (1966) consider a stress of 30% to 50% of the peak strength while Hoek and Martin (2014) consider a stress of 40% to 60% of the uniaxial compressive strength. Nicksiar and Martin (2013) conducted an extensive study on the characterization of this crack initiation threshold for crystalline and sedimentary rocks. They concluded that the threshold varies between 42% and 54% of the uniaxial compressive strength. More recently, Liu *et al.* (2022) conducted a study based on 953 laboratory tests and determined that the threshold is approximately 50% of the uniaxial compressive strength (49% for igneous rocks; 48% for metamorphic rocks; 50% for sedimentary rocks).
- The transition between the damage phase and the unstable phase: Various authors agree that the stress is around 70% to 90% of the strength of the uniaxial compressive strength obtained with a conventional test (strain rate of around 10^{-4} s^{-1} to 10^{-5} s^{-1}). Using the numerous tests collected, Liu *et al.* (2022) concluded that the stress is approximately 80% of the uniaxial compressive strength (79% for igneous rocks; 82% for metamorphic rocks; 82% for sedimentary rocks).

2.1.1.3 Post-peak behavior

One of the most important parameters influencing the post-peak behavior is the confining pressure. When the confining pressure is small or null, the failure is associated with tensile

fracture subparallel to the loading direction. This tensile cracking develops and propagates until it leads to the complete dislocation of the sample. This type of failure is associated with a sudden drop in the strength of the sample and zero residual strength. It can be associated with shape instabilities (buckling for example) at the boundary of the sample under the effect of vertical loading. It is not always possible to access the post-peak behavior of the rock during this type of failure. Figure 2-4 presents an example of recorded post-peak behavior for confining pressures (σ_3) of 0 and 10 MPa.

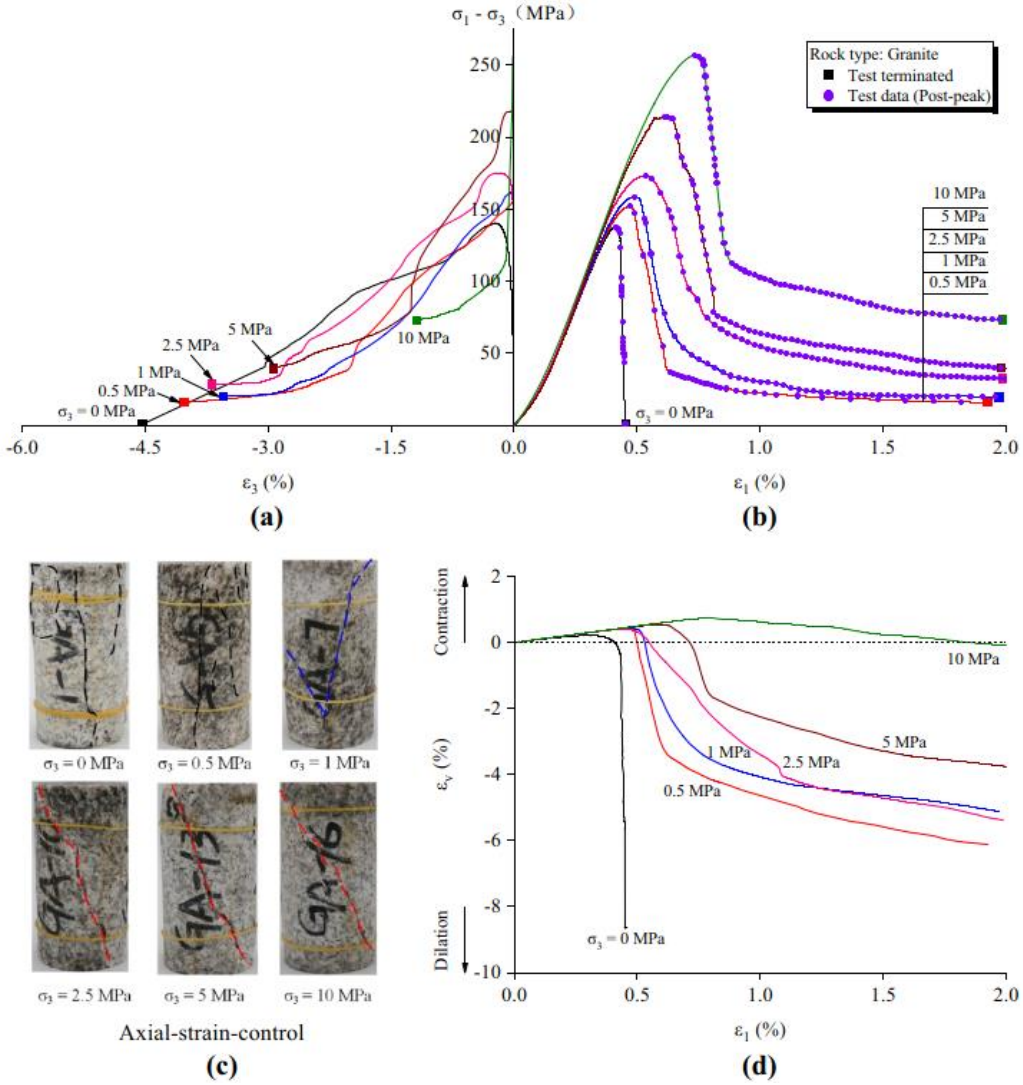

Figure 2-4: Complete stress-strain curves and failure photographs of tested granite under uniaxial and triaxial compressions by axial-strain-controlled loading; a) differential axial stress-lateral strain relations; b) differential axial stress-axial strain relations; c) failure photographs; d) volumetric strain-axial strain relations (from Hou et al. 2022)

As the confining pressure increases, the failure mechanism shifts from axial splitting to shear fracture, as illustrated in Figure 2-4, c). The microcracks are still mostly tensile fractures, but their coalescence is not vertical in the direction of major stress but makes a specific angle depending on the confining pressure. This angle (β) can be directly linked to the frictional component of the failure criteria, such as the frictional angle (φ), as demonstrated by the experimental results of Desrue (1987) on sand and Bésuelle *et al.* (2000) on sandstone:

$$\beta = \frac{\pi}{4} - \frac{\varphi}{2} \qquad (2-1)$$

It can be noted that for nonlinear failure criteria, such as the Hoek and Brown failure criterion, this "apparent" friction angle is dependent on the minor principal stress. Thus, the angle of the shear fracture depends on the confining pressure (Laigle 2004). This point can be seen by comparing the angle obtained with a σ_3 of 1 MPa and 10 MPa (Figure 2-4, c).

The post-peak behavior of shear failure mechanisms is associated with the appearance of a shear fracture within the sample. The failure process occurs in two or three phases:

- If the complete fracturing of the sample has not occurred by the time the peak is reached, crack coalescences continue until it does. The volumetric behavior of the sample remains dilatant until reaching the peak dilatancy, which corresponds to the appearance of a macroscopic shear fracture.
- Once the shear fracture occurs, the resistance of the sample depends on the friction along the newly formed discontinuity. This discontinuity has a certain roughness due to the presence of asperities on the shear surface resulting from the coalescence of tensile microcracks. These asperities will then gradually break up until the roughness disappears completely. The destruction of the asperities is associated with a decrease of dilatant behavior of the sample.
- When the roughness of the shear plane has disappeared, the behavior of the sample is solely governed by the residual friction on this plane. There is no change in the volumetric strain during this phase.

As shown in Figure 2-5, the strain-softening post peak behavior becomes increasingly ductile as the confining pressure increases. Unlike brittle fractures at small and intermediate confining pressures, ductile failures do not result in the appearance of macroscopic fractures in the sample. This indicates that the crack coalescence does not occur. At the scale of the sample, the medium remains continuous (Laigle 2004). Novello and Johnston (1995) argue that perfectly ductile behavior is not associated with dilatancy and therefore it remains with volumetric contraction, regardless of the state of deformation.

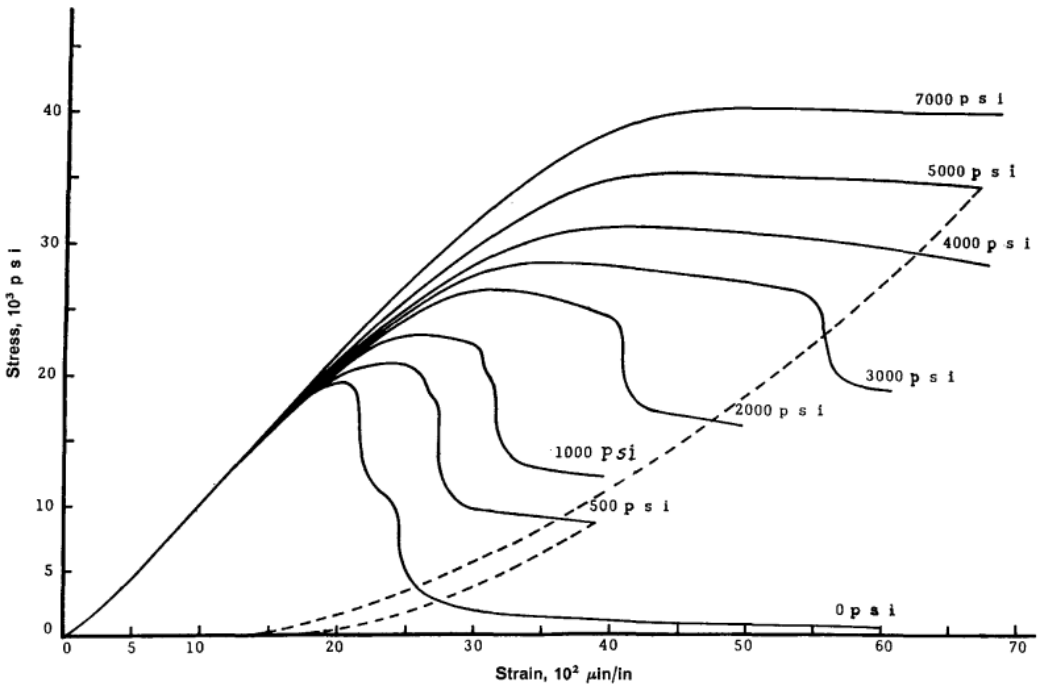

Figure 2-5: Complete stress-strain curves for unconfined and confined Tennessee marble (from Wawersik and Fairhurst 1970)

This absence of dilatancy is due to local traction being too low (e.g. confinement too high) for extensional cracks to form within the material. Most microscopic cracks are tensile cracks, expect at high confinement. Based on the work of Diederichs (1999), Kleine (2007) considers that the shear cracking mechanism can become the dominant cracking mechanism in ductile failure. Shear cracking, unlike extensional cracking, is not associated with dilatancy, which confirms the observations of Novello and Johnston (1995).

Post-peak behavior during a compression test depends on the failure mechanism as well as the loading conditions (e.g. loading rate, stiffness of the loading frame, confining pressure), the nature of the geomaterial (the chemical composition, the potential alteration, the brittleness, the water content for soil, etc.), the geometry of the tested sample, etc. (Laigle 2004). Figure 2-6 illustrates the impact of the size of the sample on the uniaxial compressive strength. A larger size of the sample (x-axis) leads to a smaller uniaxial compressive strength than a 50 mm diameter specimen.

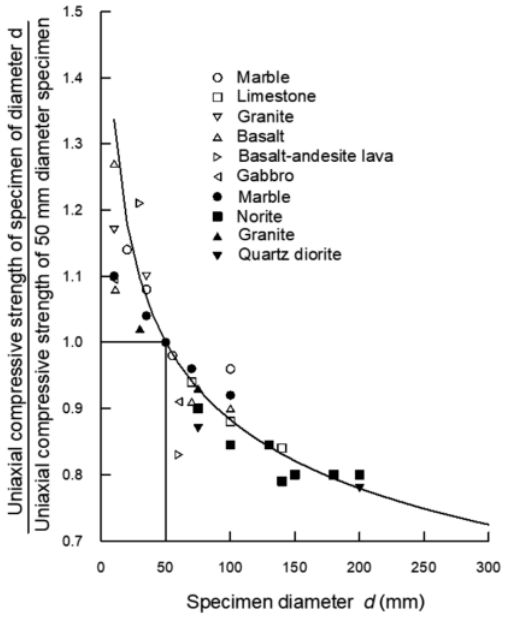

Figure 2-6: Influence of the sample size on the uniaxial compressive strength compared to that of a 50 mm diameter core sample (from Hoek and Brown 2019, based on Hoek and Brown 1980a)

Similar to the minor principal stress, the intermediate principal stress also impacts on the post-peak behavior. During a classical triaxial compression test, the intermediate principal stress is equal to the minor principal stress. A true triaxial compressive test allows the three principal stresses to be chosen separately. Xie *et al.* (2022) summarized the recent research on the behavior of rock sample:

- For a fixed minor principal stress, strains tend to decrease as the intermediate stress increases, leading to more brittle failure of the sample (Lui and Indraratna 2011).
- The major principal stress corresponding to the onset of dilatancy increases with intermediate stress. This seems logical because dilatancy is associated with the formation of extensional cracks in the sample, which become more difficult to develop as the intermediate stress increases.
- An increase in intermediate stress leads to a decrease in creep strain during a creep test (Zhao *et al.* 2018; Zhao *et al*. 2019; Xie *et al.* 2022).

- The brittle-ductile transition depends on the minor stress and the intermediate stress. With the same minor stress, the behavior changes from ductile to brittle as the intermediate stress increases.

2.1.1.4 Hoek and Brown failure criteria

In the field of rock mechanics, the Hoek and Brown criterion is the most widely used failure criterion. This criterion was developed based on the results of researches on brittle failure of intact rock performed by Hoek (1965) and on studies of jointed rock mass behavior performed by Brown (1970) (Hoek and Brown 2019). Originally published by Hoek and Brown (1980a, b), it is a nonlinear failure criterion for intact rock based on Griffith (1924) brittle fracture theory and modified by McClintock and Walsh (1962) to account for friction on sliding surfaces (Hoek and Brown 2019). Unlike other failure criteria, the Hoek and Brown failure criterion has been adapted over the years to allow a transition from the laboratory scale (intact rock) to the engineering scale (the rock mass). This point is presented in more detail in Section 2.1.2.

Hoek and Brown (1980a, b) proposed the following empirical equation to fit the results of a wide range of triaxial tests on intact rock samples (Hoek and Brown 2019):

$$\sigma_1 = \sigma_3 + \sigma_{ci}\sqrt{m_i \frac{\sigma_3}{\sigma_{ci}} + 1} \qquad (2-2)$$

Where σ_1 and σ_3 are the major and minor principal stresses respectively, σ_{ci} the unconfined compressive strength of the intact rock and m_i is a material constant. The m_i parameter can be linked to a "frictional" component of the rock (Laigle 2004, Hoek and Brown 2019), as well as the brittleness of the rock because of its direct relationship with $\sigma_{ci}/|\sigma_t|$ (Diederichs 2007, Hoek and Brown 2019).

The estimation of the σ_{ci} and m_i are obtained from triaxial test (Bewick 2021). For limited available data, it exists in the literature ranges of possible values for m_i depending on the type of rock (Hoek 2007), presented in Figure 2-7.

It is important to note that the Hoek and Brown failure criteria have some limitations:

- Based on previous studies (Bewick and Kaiser 2013a; Kaiser and Kim 2015) and personal communication with Dr. Hoek and Dr. Brown, Bewick (2021) pointed out that the results of uniaxial compressive tests should not be used to estimate σ_{ci} and m_i as the Hoek and Brown (H&B) failure criteria is associated with shear failure mechanisms. Generally, uniaxial compressive tests result in axial splitting failure mode, which is inconsistent with the H&B failure criteria. Using these results would lead to an underestimation of the actual value of σ_{ci}.
- The H&B criterion does not include tensile failure ($\sigma_3 < 0$) (Hoek and Brown 2019). Since tensile failure can be an important factor in rock engineering problems, Hoek and Martin (2014) proposed to use a tension cut-off. This tension cut-off is based on the generalized Griffith failure criterion theory proposed by Fairhurst (1964) and it can be found in Hoek and Brown (2019).
- As mentioned above, the H&B criterion is associated with a shear failure mechanism and is not suitable for large confinement pressure and ductile failure mechanisms (Hoek and Brown 2019). Mogi (1966) investigated the transition between shear failure mechanisms and ductile failure for a wide range of rock types. It was found that the

average transition is defined by $\sigma_1 = 3.4\,\sigma_3$. Figure 2-8 presents this transition for Indiana Limestone (Hoek and Brown 2019).

Rock type	Class	Group	Texture			
			Coarse	Medium	Fine	Very fine
SEDIMENTARY	Clastic		Conglomerates* (21 ± 3) Breccias (19 ± 5)	Sandstones 17 ± 4	Siltstones 7 ± 2 Greywackes (18 ± 3)	Claystones 4 ± 2 Shales (6 ± 2) Marls (7 ± 2)
	Non-Clastic	Carbonates	Crystalline Limestone (12 ± 3)	Sparitic Limestones (10 ± 2)	Micritic Limestones (9 ± 2)	Dolomites (9 ± 3)
		Evaporites		Gypsum 8 ± 2	Anhydrite 12 ± 2	
		Organic				Chalk 7 ± 2
METAMORPHIC	Non Foliated		Marble 9 ± 3	Hornfels (19 ± 4) Metasandstone (19 ± 3)	Quartzites 20 ± 3	
	Slightly foliated		Migmatite (29 ± 3)	Amphibolites 26 ± 6		
	Foliated**		Gneiss 28 ± 5	Schists 12 ± 3	Phyllites (7 ± 3)	Slates 7 ± 4
IGNEOUS	Plutonic	Light	Granite 32 ± 3 Diorite 25 ± 5 Granodiorite (29 ± 3)			
		Dark	Gabbro 27 ± 3 Norite 20 ± 5	Dolerite (16 ± 5)		
	Hypabyssal		Porphyries (20 ± 5)		Diabase (15 ± 5)	Peridotite (25 ± 5)
	Volcanic	Lava		Rhyolite (25 ± 5) Andesite 25 ± 5	Dacite (25 ± 3) Basalt (25 ± 5)	Obsidian (19 ± 3)
		Pyroclastic	Agglomerate (19 ± 3) Breccia (19 ± 5)		Tuff (13 ± 5)	

* Conglomerates and breccias may present a wide range of m_i values depending on the nature of the cementing material and the degree of cementation, so they may range from values similar to sandstone to values used for fine grained sediments.

* *These values are for intact rock specimens tested normal to bedding or foliation. The value of m_i will be significantly different if failure occurs along a weakness plane.

Figure 2-7: Values of constant mi for intact rock by type of rock (from Hoek 2007); The values in parenthesis are estimates

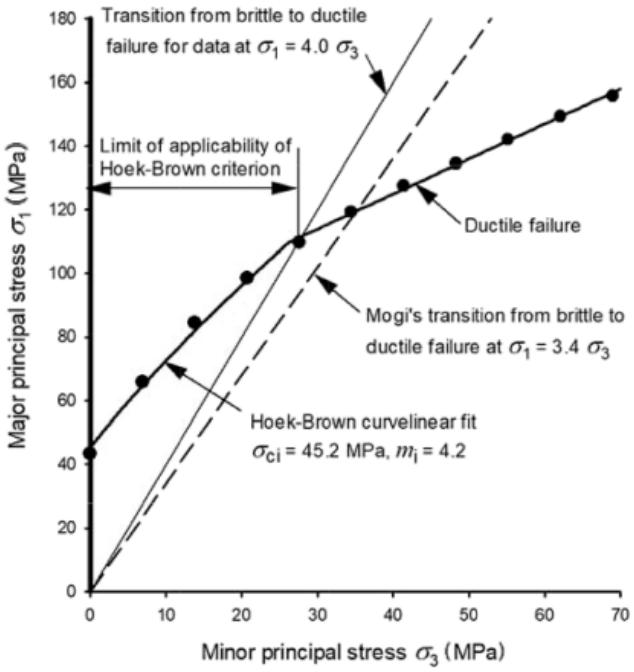

Figure 2-8: Limit of applicability of the H&B criterion based on the results of triaxial tests on Indiana Limestone (from Hoek and Brown 2019)

2.1.1.5 Composite strength envelope of intact rock

Since the H&B criterion corresponds to shear failures, it is not totally adequate for small confining pressures associated with axial splitting failure. The transition between axial splitting failure and shear failure corresponds to the spalling limit (Diederichs 2007). Various studies on this topic (Diederichs 1999, 2007; Kaiser *et al.* 2000; Cho *et al.* 2002; Diederichs *et al.* 2004) have agreed on values of σ_1/σ_3 between 10 and 20 depending on factors such as the rock type, the amount of heterogeneity, the level of preexisting damage in the rock, etc. (Diederichs *et al.* 2004).

The combination of the damage initiation thresholds (i.e. crack initiation), the spalling limit, and the H&B failure criterion forms the basis of the "composite strength envelope", shown in Figure 2-9. This envelope can be seen as the "long term" strength of the intact rock or the "in-situ strength". The long-term strength of the intact rock depends on the failure mechanism. For axial splitting, the long-term strength corresponds to the crack initiation stress (Section 2.1.1.2), while for shear failures, the long-term strength is the stress associated with the beginning of unstable crack propagation (Section 2.1.1.2).

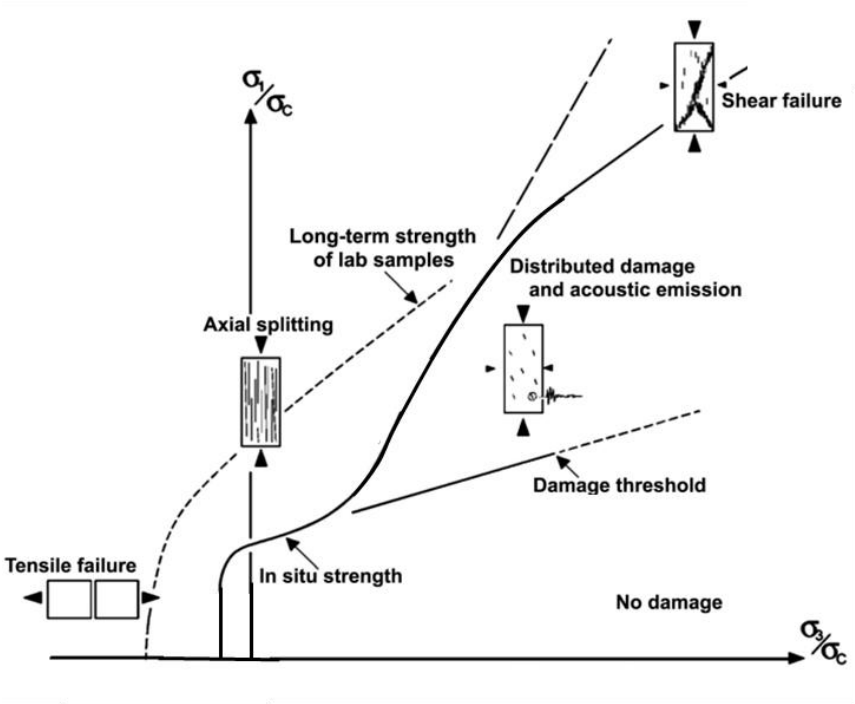

Figure 2-9: Composite strength envelope with the various failure mechanisms depending on the confining pressure (adapted from Diederichs 2007)

2.1.2 Transitioning from laboratory scale to project scale

One of the most significant differences between rock mechanics and other engineering fields such as soil mechanics or more generally continuum mechanics is the impact of the scale effects. Most of the time, the parameters obtained during laboratory tests cannot be directly used at the engineering scale. Rock masses are, by nature, discontinuous medium composed of rock matrix and discontinuities. Laboratory tests allow for characterization of rock matrix parameters (the intact parameters) or the discontinuity parameters (the joint properties) but not the complex interaction between the two. This scale effect is the cornerstone of rock engineering because it greatly impacts the behavior of the rock mass, as well as the calculation technic used. Figure 2-10 presents the impact of the scale effects and the discontinuity density on the applicability of the H&B failure criterion.

2.1.2.1 Generalized Hoek and Brown criterion

As it was briefly introduced in Section 1.2 and illustrated in Figure 1-1, the rock mass behavior can be assimilated to the one of a continuous or discontinuous medium. A rock mass can be considered as continuous if it is intact and massive or highly fractured. For intact rock mass, using the H&B criterion and the composite strength envelope is fully relevant. On the other hand, if the rock mass is highly fractured, the H&B criterion needs to be adapted to take into account the presence of discontinuities and blocks. This led to the development of the generalized Hoek and Brown criterion allowing the estimation of the rock mass strength (Hoek 1994; Hoek *et al.* 1995).

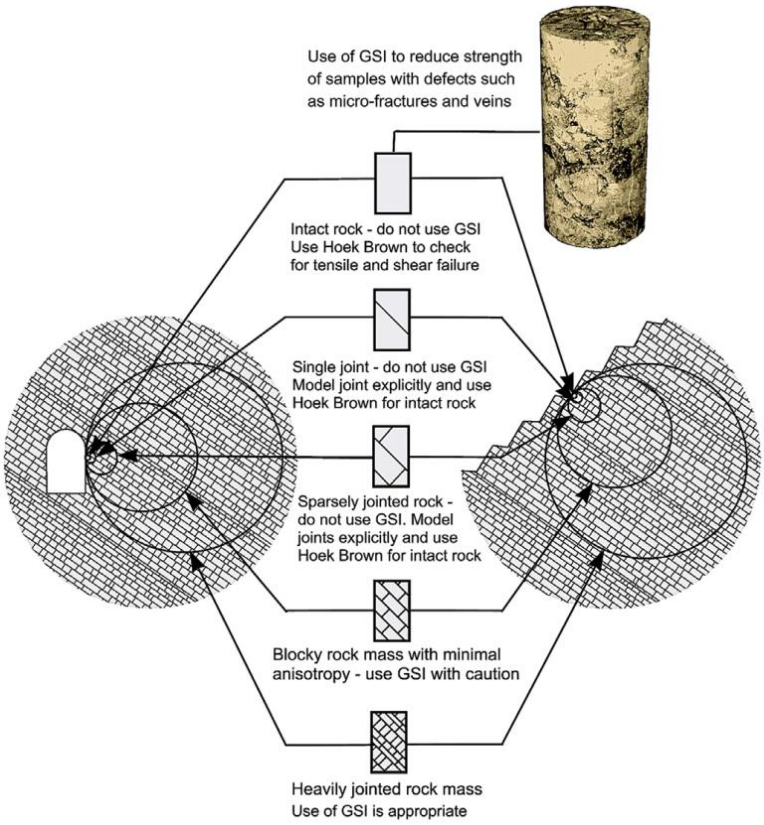

Figure 2-10: Size effect in the rock mass characterization (from Hoek and Brown 2019)

The fundamental idea behind the generalized H&B criterion is to degrade the parameters of the intact rock in function of the rock mass characterization. Rock mass characterization can be performed using various approaches like the Geological Strength Index (GSI) which was developed initially by Hoek (1994), the Rock Mass Rating (RMR) developed by Bieniawski (1973), the Q-system proposed by Barton *et al.* (1974), the Rock Mass index (RMi) from Palmstrom (1995), etc.

In this study, only the GSI is briefly presented. One of the latest versions of the Q-System can be found in NGI (2013) and Barton (2015). Similarly, detailed information regarding the RMR can be found in Bieniawski (1989) and is generally referred to as $R_{\mu,89}$ (the version of 1976 is $R_{\mu,76}$).

The Geological Strength Index aims to characterize the rock mass based on the size of the blocks delimited by joints and the quality of joints, corresponding to the surface of contact between the blocks. The initial version of the GSI has been extended through many studies: Hoek *et al*. (1998; 2005), Hoek and Marinos (2000), Marinos and Hoek (2000; 2001), Marinos *et al*. (2005), Marinos (2017), Marinos and Carter (2018). The version associated with jointed rock masses is presented in Figure 2-11. Compared to other characterization techniques, one of the major limitations of the GSI approach is that the assessment of the parameters is based mostly on qualitative parameter (Figure 2-11). Some researchers have adapted the GSI approach by providing some quantitative scales. For example, Cai *et al.* (2004) provided an estimation of the block volume and joint condition factor, while Hoek *et al.* (2013) proposed to use the value of the Joint Condition (from the RMR, version 1989) and the RQD, Rock Quality Designation, and Rafiei Renani *et al.* (2019a) used the joint persistence and joint friction angle (Figure 2-12).

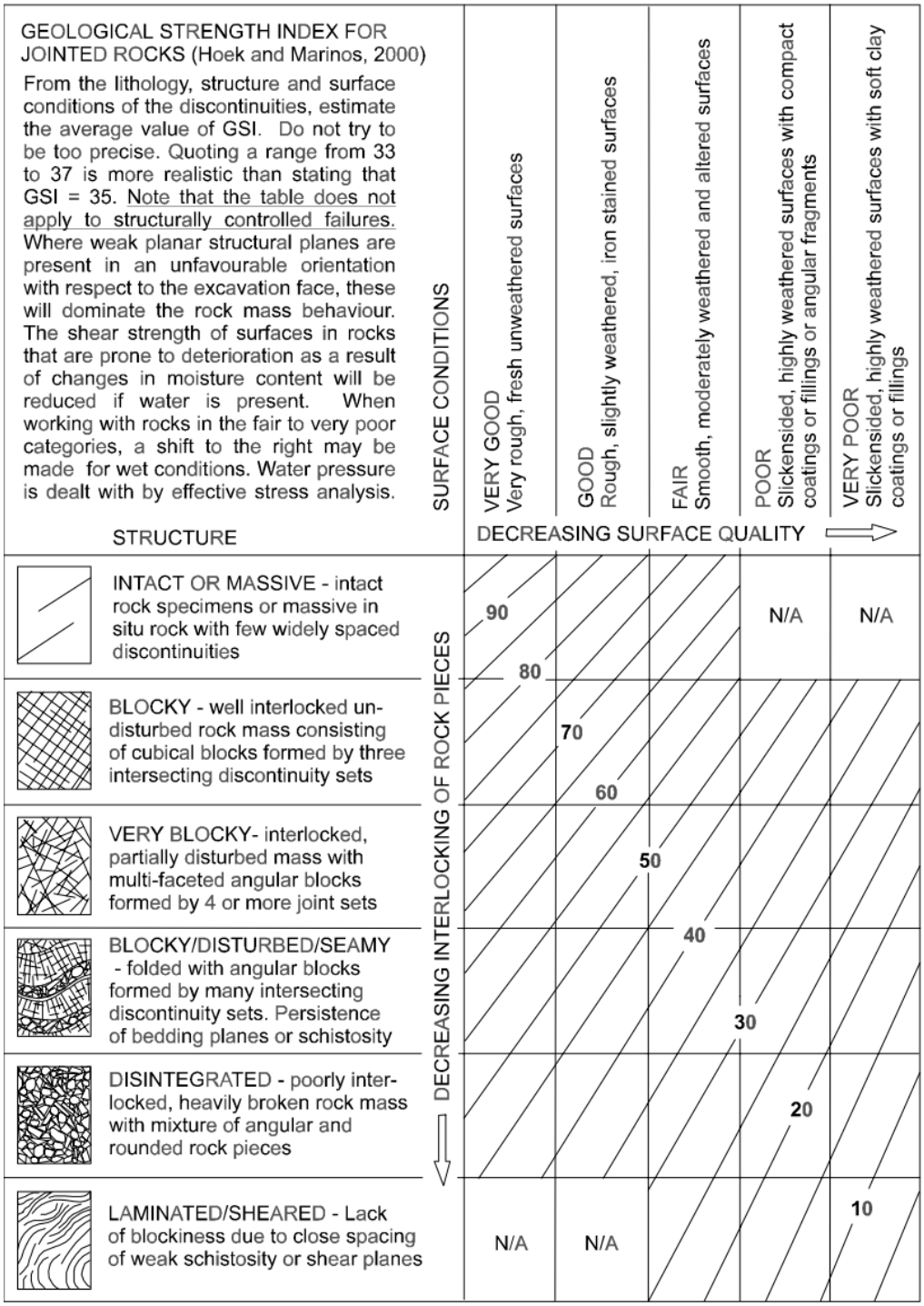

Figure 2-11: GSI chart for jointed rock mass (Marinos and Hoek 2000)

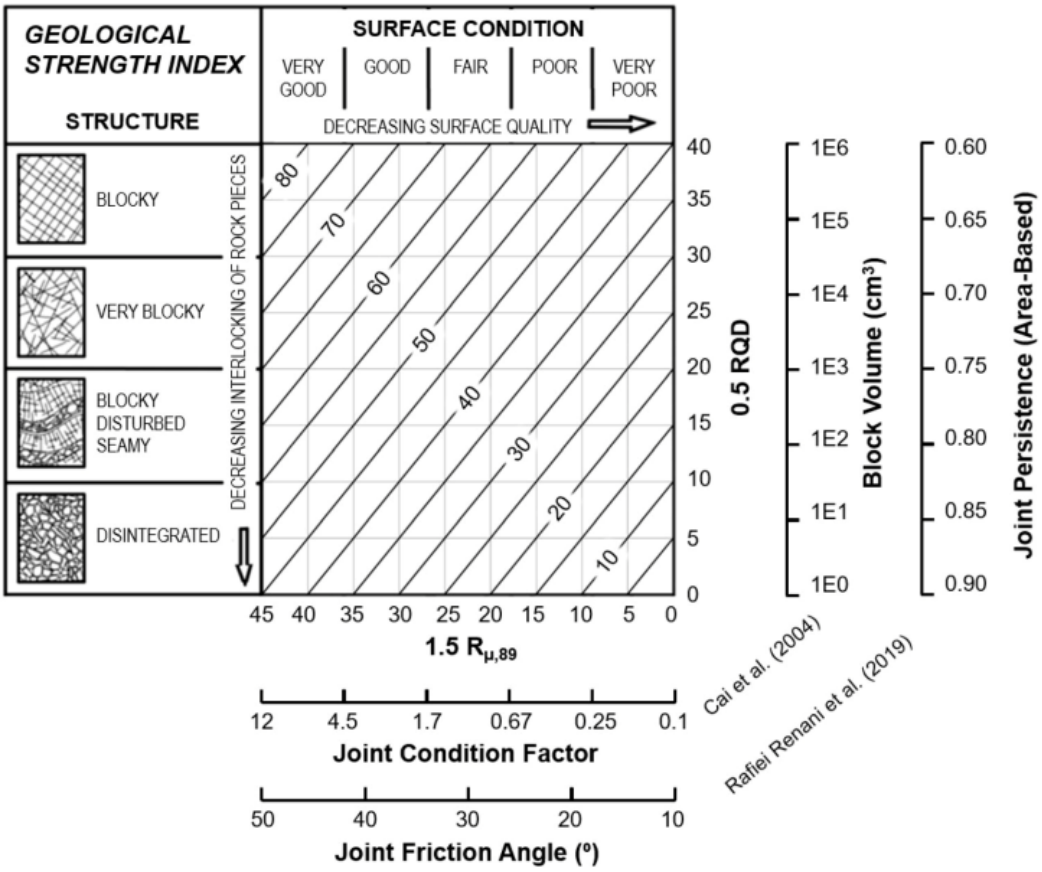

Figure 2-12: Quantitative values to assess the GSI parameters based on proposition of Cai et al. (2004), Hoek et al. (2013) and Rafiei Renani et al. (2019a) (from Rafiei Renani and Cai 2022)

The expression of the generalized H&B failure criterion is (Hoek and Brown 2019):

$$\sigma_1 = \sigma_3 + \sigma_{ci}\left(m_b\frac{\sigma_3}{\sigma_{ci}} + s\right)^a \qquad (2-3)$$

Where m_b, s and a are the rock mass material constants, given by

$$m_b = m_i \exp\left(\frac{GSI - 100}{28 - 14\,D}\right) \qquad (2-4)$$

$$s = \exp\left(\frac{GSI - 100}{9 - 3D}\right) \qquad (2-5)$$

$$a = \frac{1}{2} + \frac{1}{6}\left(e^{-\frac{GSI}{15}} - e^{-\frac{20}{3}}\right) \qquad (2-6)$$

Where s = 1, a = 0.5 and $m_b = m_i$ for intact rock, and D is the disturbance factor associated with the blast damage and stress relaxation. Guidelines for the selection of D are discussed in Hoek and Brown (2019). It can be noted that when a disturbance factor is considered, it should be considered only close to the tunnel boundary where the rock mass is disturbed by the excavation technic and not for entire rock mass.

Rafiei Renani and Cai (2022) note that, based on numerous studies, the use of the generalized H&B criterion is appropriate for GSI values between around 70 and around 30. They mention

a lower boundary of GSI around 30. As this point is relevant for high value of GSI for each a composite strength envelope is more appropriate, it can be debatable for small GSI values as no direct explanations are proposed and several studies in the literature have used the generalized H&B criterion for smaller value of GSI: Hoek and Guevara (2009), Vlachopoulos and Diederichs (2009), Langford and Diederichs (2013), etc.

The generalized Hoek and Brown failure criterion is not the only failure criteria used in rock mechanics. As in soil mechanics, the Mohr-Coulomb failure criteria can also be used in rock mechanics but present some shortcomings. Unlike soil mechanics, the strength parameters of the rock mass (i.e. its cohesion and its friction angle) cannot be directly obtained through laboratory tests and no clear method exists to estimate them. A common approach in preliminary design (when no back analysis is possible) is to transform the parameters of the generalized Hoek and Brown failure criteria into a value of cohesion and friction angle for the rock mass. The mathematical expression for the transformation can be found in Hoek *et al*. (2002). Before this transformation may have been necessary because in most of the software, the generalized Hoek and Brown failure criterion was not available, which is no longer the case. Almost all the classical engineering software allows calculations using the generalized Hoek and Brown failure criterion.

2.1.2.2 Pre-peak parameter of the rock mass

Similar to the strength parameters, the elastic parameters characterizing the pre-peak behavior of the rock mass (Young's modulus and Poisson's ratio) are also impacted by the presence of discontinuities in the rock mass. Hoek and Diederichs (2006) performed an extensive study on this topic and concluded that the Young's modulus of the intact rock (E_i) can be linked to Young's modulus of the rock mass (E_m) using the following equation:

$$E_m = E_i \left(0.02 + \frac{1 - D/2}{1 + exp\left(\frac{60 + 25D - GSI}{11}\right)} \right) \qquad (2-7)$$

Where E_i is the Young's modulus of the intact rock, that can be linked to σ_{ci} with the Modulus Ratio (MR):

$$E_i = MR\ \sigma_{ci} \qquad (2-8)$$

Figure 2-13 presents some guidelines for the selection of MR values if no laboratory tests are available.

Similarly, the Poisson's ratio of the rock mass (ν_{rm}) can be estimated based on the GSI value of the rock mass (from Lorig and Verona 2013, referring to Hoek *et al.* 1995):

$$\nu_{rm} = 0.32 - 0.0015 * GSI \qquad (2-9)$$

Rock type	Class	Group	Texture			
			Coarse	Medium	Fine	Very fine
Sedimentary	Clastic		Conglomerates 300–400 Breccias 230–350	Sandstones 200–350	Siltstones 350–400 Greywackes 350	Claystones 200–300 Shales 150–250[a] Marls 150–200
	Non-clastic	Carbonates	Crystalline limestones 400–600	Sparitic limestones 600–800	Micritic Limestones 800–1000	Dolomites 350–500
		Evaporites		Gypsum (350)[b]	Anhydrite (350)[b]	
		Organic				Chalk 1000+
Metamorphic	Non-foliated		Marble 700–1000	Hornfels 400–700 Metasandstone 200–300	Quartzites 300–450	
	Slightly foliated		Migmatite 350–400	Amphibolites 400–500	Gneiss 300–750[a]	
	Foliated[a]			Schists 250–1100[a]	Phyllites/Mica Schist 300–800[a]	Slates 400–600[a]
Igneous	Plutonic	Light	Granite[c] 300–550 Granodiorite[c] 400–450	Diorite[c] 300–350		
		Dark	Gabbro 400–500 Norite 350–400	Dolerite 300–400		
	Hypabyssal		Porphyries (400)[b]		Diabase 300–350	Peridotite 250–300
	Volcanic	Lava		Rhyolite 300–500 Andesite 300–500	Dacite 350–450 Basalt 250–450	
		Pyroclastic	Agglomerate 400–600	Volcanic breccia (500)[b]	Tuff 200–400	

[a]Highly anisotropic rocks: the value of MR will be significantly different if normal strain and/or loading occurs parallel (high MR) or perpendicular (low MR) to a weakness plane. Uniaxial test loading direction should be equivalent to field application.
[b]No data available, estimated on the basis of geological logic.
[c]Felsic Granitoids: coarse grained or altered (high MR), fined grained (low MR).

Figure 2-13: Guideline for the selection of Modulus Ratio (MR) values for various types of rock (from Hoek and Diederichs 2006)

2.1.2.3 Post-peak parameters of the rock mass

Since the post-peak behavior of the intact rock is already influenced by numerous factors, the post-peak behavior of the rock mass is even more complex because the density of discontinuities also influences this behavior. Like for intact rock, three main post-peak behaviors can be identified for rocks: Brittle behavior, Strain softening and perfectly plastic/ductile (Figure 2-14).

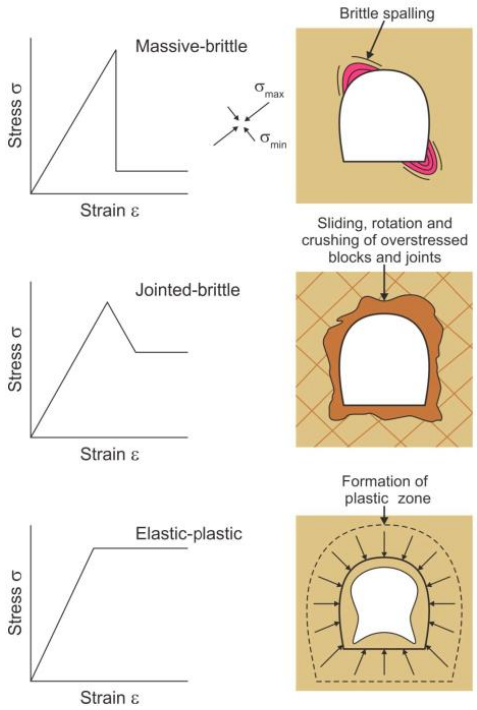

Figure 2-14: Simplified post-peak behavior and associated tunnel behavior (from Lorig and Verona 2013)

The main question is how to correctly identify the situations associated with each post-peak behavior. For brittle behavior in massive rock masses, it is mostly associated with GSI higher than 70 (Hoek and Brown 1997) or 65 (Bewick 2021). For perfectly plastic behavior, it is associated with GSI lower than 30 (Hoek and Brown 1997) or 40 (Lorig and Verona 2013). In between, the rock mass exhibits strain-softening post peak behavior.

When the rock mass exhibits strain softening behavior, Lorig and Verona (2013) proposed as first approximation, to consider the following expression to estimate the critical plastic shear strain (the plastic shear strain between the peak and the residual strength):

$$\gamma_p = \frac{12.5 - 0.125 * GSI}{100} \qquad (2-10)$$

2.2 Presentation of the failure mechanisms studied

This thesis focuses on two main phenomena: large deformations, or squeezing phenomena, in highly fractured rock masses and brittle failures in intact and massive rock masses. This section aims to summarize existing definitions and to present some examples and consequences for tunnel projects. It also defines these phenomena in the context of this thesis.

2.2.1 Large deformation, squeezing phenomenon

The definition of the squeezing phenomenon is relatively complex because it varies a lot depending on the author. There are many definitions of the squeezing phenomenon in the literature. Some authors, such as Jethwa *et al.* (1984), Sakurai (1997), Chern *et al.* (1998), Goel (1994), Aydan *et al.* (1996) or Hoek and Marinos (2000), associate squeezing solely with the apparition of significant radial deformation. A common limit is set to 1% of radial strain (Hoek and Marinos 2000). On the other hand, more recent authors such as Barla (1996; 2001), Kleine

(2007), La Fuente Mata (2018), Paraskevopoulou and Diederichs (2018), Kabwe *et al.* (2020b), consider the squeezing phenomenon to be time dependent radial deformation associated with the concept of creep and viscosity. One of the clearer definitions has been proposed by Barla (1996) for the ISRM (International Society of Rock Mechanics) as:

"Squeezing of rock is the time dependent large deformation which occurs around the tunnel and is essentially associated with creep caused by exceeding a limiting shear stress. Deformation may terminate during construction or continue over a long time period"

This definition refers to "time dependent large deformation" that "may terminate during construction or continue over a long time period". However, in reality, the Barla's (1996) definition includes two distinct phenomena (Paraskevopoulou and Diederichs 2018):

1. The first phenomenon is the elastic-plastic deformation which occurs during the excavation of the tunnel. This phenomenon is not directly time dependent. Rather, it depends on the excavation process, and the advancement rate. If the excavation stops and there is no external modification of rock mass stress state, the deformation will also stop.
2. The second phenomenon is a time dependent deformation associated with creep inside the rock mass. The excavation of the tunnel modifies the stress state inside the rock mass creating important deviatoric stress (the difference between the major and minor principal stress) close to the excavation. If the deviatoric stress is high enough, creep behavior can occur, manifesting as an increase of the radial deformation or an increase of the ground pressure on the support under a steady stress state. This creep phenomenon can decrease over time (primary creep), continue during a long period (secondary creep) or increase over time (tertiary creep). More detailed information about creep in rock masses is available in Section 2.2.1.2.

These two phenomena may occur simultaneously or one after another depending on the advancement rate of the excavation and the "viscosity" of the rock mass (creep rate and amplitude of creep deformation).

The term "squeezing" is used in various contexts such as for the description of phenomenon occurring during tunnel constructions (Terzaghi 1946; Hoek and Marinos 2000; Hoek and Guevara 2009; etc) but also to characterize a rock mass or a ground in which squeezing can be expected: "squeezing ground / squeezing rock" (Panet 1996; Barla 2001; Arora *et al.* 2021a; etc).

It is important to note that a squeezing phenomenon should not be confused with a swelling phenomenon. Although the observation in the field and the consequences on tunnels can be similar, the phenomena are completely different. Squeezing is associated with the mechanical deformation of the rock mass whereas swelling is associated with an increase in the rock mass volume due to a chemical reaction involving water absorption (Aydan *et al.* 1996; Zhao 2012). Swelling occurs in rock masses composed of large amounts of argillaceous mineral with swelling potential such as smectite (De La Fuente Mata 2018) or montmorillonite (Aydan *et al.* 1996), as well as rock masses with anhydrite (De La Fuente Mata 2018).

The squeezing phenomenon primarily occurs when the strength of the rock mass is small compared to the in-situ stress state (Malan 1997; Hoek et Marinos 2000; Damjanac and Fairhurst 2010; Paraskevopoulou and Diederichs 2018; De La Fuente Mata 2018). The smaller the ratio is, the greater the deformation will be (Aydan *et al.* 1996; Hoek and Marinos 2000).

This point is presented in more detail in Chapter 3. Weak rock masses are generally associated with the following conditions:

- Soft rock with a ductile behavior or slightly strain-softening, highly fractured rock mass, weathered rock (Zhao 2012; De La Fuente Mata 2018; Arora *et al.* 2021a). The rock mass needs to be able to accommodate large deformations.
- Generally, these types of rock mass can be associated with claystone (Jaeger *et al*. 2007; Zhao 2012; La Fuente Mata 2018; Arora et al. 2021a), as well as phyllite, flysch, mudstone, tuff, gneiss in fault zone (Zhao 2012; La Fuente Mata 2018).
- The presence of structural anisotropy like schistosity (Barla and Barla 2009) or anisotropic stress state can exacerbate the phenomenon (De La Fuente Mata 2018).

2.2.1.1 Examples and consequences on tunnel projects

Large deformation and squeezing phenomena have been encountered or are expected in numerous deep tunnel projects. Figure 2-15 illustrates squeezing that occurred during three different projects: the Gotthard Base Tunnel in Switzerland, Saint-Martin-La-Porte access adit for the Mont Cenis Base Tunnel in France, and the Yacambù-Quibor tunnel in Venezuela.

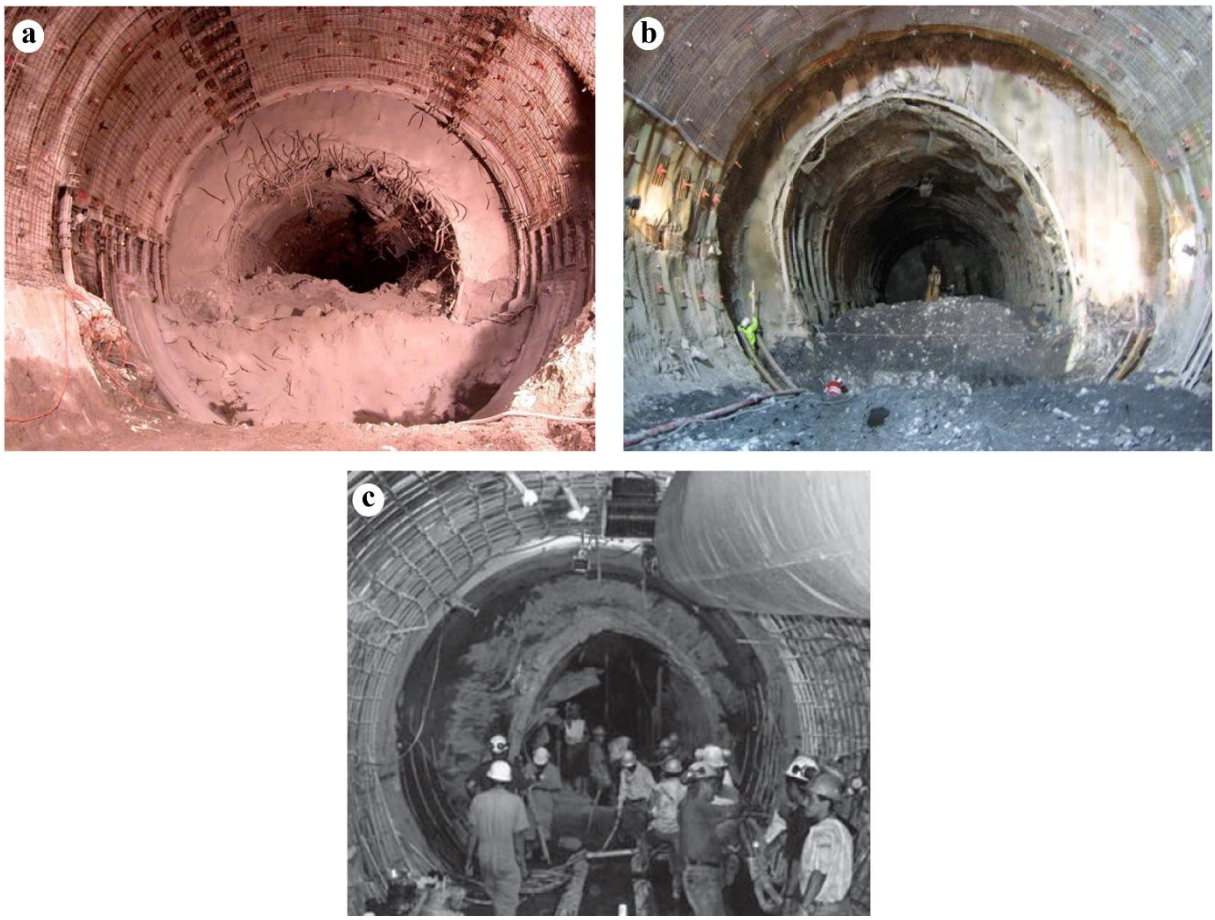

Figure 2-15: Examples of squeezing phenomenon during tunnel construction; (a) Gotthard Base Tunnel in Switzerland (Loew et al. 2010); (b) Saint Martin la Porte access adit for the construction of the Mont Cenis Base Tunnel in France (Loew et al. 2010); (c) Yacambù-Quibor tunnel in Venezuela (Hoek and Guevara 2009)

Similar behaviors have been observed during the construction of other deep tunnels under the Alps like the Lötschberg Base Tunnel in Switzerland, the Brenner Base Tunnel between Austria and Italy, the Koralm tunnel in Austria, etc (Wagner *et al*. 2009; Loew *et al.* 2010).

If the squeezing phenomenon is not properly anticipated in the early design stages of a tunnel project, it could have significant impact during the construction such as the overloading of the support, which could lead to its failure, as well as the appearance of large radial deformation. In extreme cases, repairing of the support and reprofiling may be necessary. If the excavation is performed with a TBM, it can also lead to a jamming and potentially its destruction as it happened during the construction of the Yacambù-Quibor tunnel (Hoek and Guevara 2009). Failing to properly anticipate this phenomenon leads to major increases in the project cost and duration. Detailed information on its prediction, design approaches and technical solutions to deal with squeezing phenomenon are discussed in Chapter 4.1 of this thesis.

2.2.1.2 Creep inside the rock mass

As presented above, squeezing can be associated with creep phenomena. Frenelus *et al*. (2022) conducted an extensive study on the creep behavior of rocks. In general, the behavior of rock subjected to constant loading can be decomposed into four traditional phases: instantaneous deformation, primary creep, secondary creep and tertiary creep (Figure 2-16). At great depths, some hard rocks can exhibit only two phases of creep (no secondary creep), prior to brittle failure (Wu *et al.* 2016).

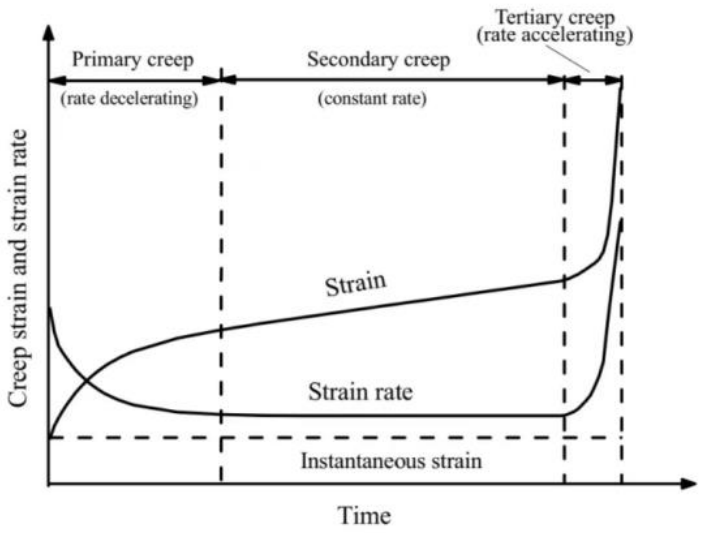

Figure 2-16: Various types of creep (from Frenelus et al. 2022, referring to Qian et al. 2022)

On a microscopic scale, creep can be seen as the propagation of existing microcracks and dislocations, and as the deformation of the constituent minerals of the rock (Zhang *et al.* 2015). This corresponds to cataclastic creep, which is a retarded degradation of the rock microstructure, or granular creep which is a friction-induced grain repositioning (Frenelus *et al.* 2022). Macroscopically, creep is a continuous anelastic deformation under constant loading (Frenelus *et al.* 2022). The creep initiation threshold corresponds to the microcracking threshold (Frenelus *et al.* 2022 referring to Aydan *et al*. 1996).

Frenelus *et al.* (2022) distinguish two types of creep in rocks, brittle creep and ductile creep. In brittle creep, the dominant mechanism is the propagation and coalescence of induced microcracking under steady loading. In the case of ductile creep, the creep is accompanied by significant deformation and the appearance of shear planes, due to sliding along dislocations and displacement of weak elements in clay matrices or displacement of interstitial atoms and atomic voids in crystalline rocks. Ductile creep occurs preferentially in soft rocks such as sandstones, mudstones, shales and other sedimentary rocks (Frenelus *et al*. 2022).

Creep affects all types of rock, but especially argillaceous, organic, low-strength or fractured rock (Frenelus *et al*. 2022). Certain external factors tend to influence creep:

- Hydraulic pressure and flow along discontinuities will facilitate crack propagation and coalescence and thereby increasing creep deformation and associated strain rates.
- The state of stress is a key factor in creep: the greater the deviatoric stresses is, the greater the creep is.
- The proportion of water significantly influences creep. In general, the presence of water reduces the mechanical properties of rocks. Dry rock deforms less than saturated rock, and creep resistance (stress state associated with the threshold of the creep deformation) decreases with increasing water content. Additionally, if the water is not neutral, chemical reactions can occur, leading to alteration of the rock (corrosion or karstification for example).
- Temperature influences creep by changing the behavior and properties of the rock.

2.2.1.3 Large deformation framework in this thesis

In this thesis, the term “squeezing” is used as little as possible in favor to “large deformation”. As it has been previously presented, squeezing is also associated with time dependent deformation and creep. In practice, it is very difficult to consider creep during the design stage, before the beginning of the tunnel excavation because, in rock mechanics, no laboratory test allows an estimation of the creep parameter of a rock mass. Although creep test exists in soil mechanics and for intact rock, these behaviors will generally not be representative of rock mass behavior. Unlike elastic-plastic parameters, there is no approach to adapt creep parameters obtained in a laboratory to the rock mass and the engineering scale. Creep parameters of a rock masses can only be obtained by performing back analyses during the construction. Considering creep behavior during the early stages of a tunnel design is very complex and would be tainted with enormous uncertainties. This does not mean that potential time dependent deformation cannot be anticipated during the design process, associated with specific technical solution (design based on observational method, excavation of a pilot tunnel, …). It just means that performing specific and complex calculations would not be realistic. An easy way to indirectly consider time dependent deformation or creep is to work with short-term rock mass properties and long-term rock mass properties.

Section 2.1.2 describes how to estimate the rock mass parameters based on laboratory tests and field investigations. These parameters correspond to a set of short-term parameters. The question is: How can the long-term parameters be determined?

In the case study of the Yacambù-Quibor tunnel in Venezuela (presented in detail in Chapter 6.1.1), Hoek and Guevara (2009) suggested dividing the GSI values in half between short-term and long-term. For the same case study, Langford and Diederichs (2013) reduced linearly the GSI inside the plastic radius from 10 at the tunnel boundary to zero at the extremity of the plastic radius. This approach is similar to one observed in some engineering practices that

consider an increase of the disturbance factor (D) within the plastic radius. Based on the rock mass strength equation proposed by Hoek *et al.* (2002) and detailed in Chapter 3.1.3.2, and in Eq.(2-4) to Eq.(2-6), it is possible to link the rock mass strength (σ_{cm}), the intact rock parameters (σ_{ci} and m_i), the GSI and the disturbance factor (D). Figure 2-17 presents an example including D=0 and D=0.4.

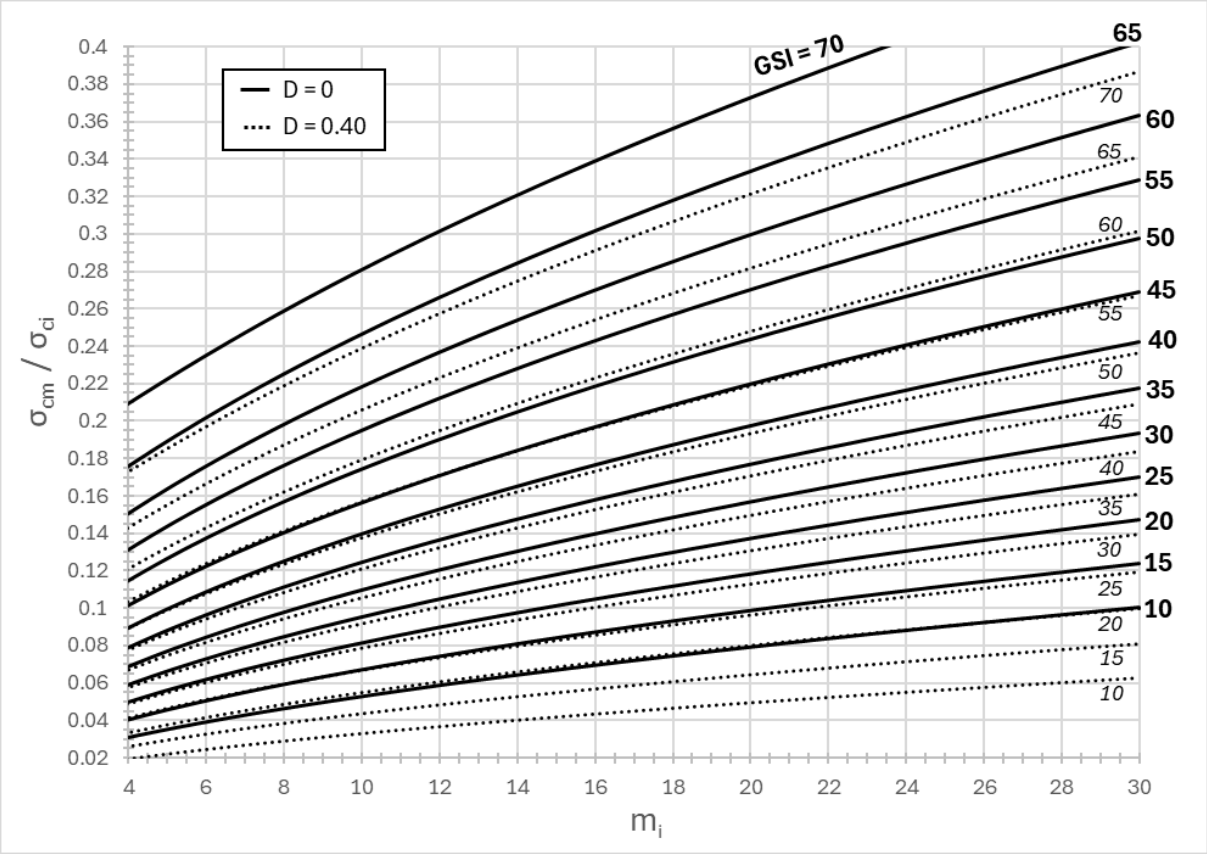

Figure 2-17: Relationship between the rock mass strength, the intact rock parameter, the GSI and two values of disturbance factor (0 and 0.4)

Laigle (2004) considers that creep is a progressive degradation of the rock matrix from its initial state to its residual state. The author highlights that the strength of a rock sample depends on the loading speed. In this case, long-term behavior corresponds to the strength associated with an infinitely slow loading rate, e.g. a residual state (Figure 2-18), while short-term behavior corresponds to relatively rapid loading.

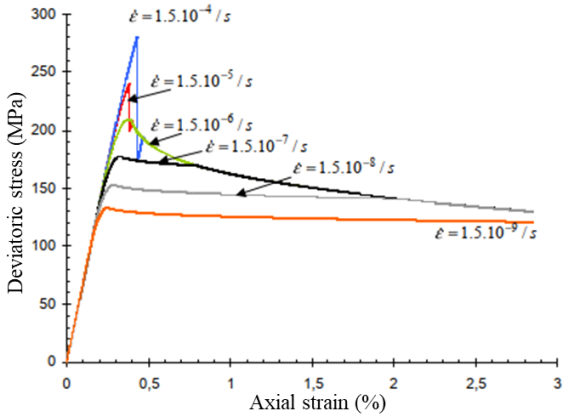

Figure 2-18: Theorical example of the impact of the loading rate on the peak strength and post-peak behavior (Laigle 2004)

A similar interpretation can be made at the scale of the rock mass. The transition from a laboratory sample to a rock mass is made using the GSI (or an equivalent characterization of the rock mass), which reflects the state of fracturing and damages of the rock mass. To account for the influence of time, it is possible to introduce the notions of initial GSI (e.g. short term) and residual GSI (e.g. long term). For perfectly plastic post-peak behavior, the residual GSI is identical to the initial GSI. Perfectly plastic behavior can be associated with GSIs of less than 30 (Hoek and Brown 1997). For higher GSIs, the behavior is softening, contrary to the above assumption, and the residual GSI is therefore lower than the initial GSI. Several authors have proposed approaches to estimate this residual GSI value: Cai *et al*. (2007); Alejano *et al.* (2012); Su *et al*. (2023). Cai *et al.* (2007) and Alejano *et al.* (2012) proposed simple approaches that depend only on the initial GSI value through Eq.(2-11) and Eq.(2-12), respectively. A graphical comparison is presented in Figure 2-19.

$$GSI_{residual} = GSI_{\ peak}\ e^{-0.0134\ GSI_{peak}} \qquad (2-11)$$

$$GSI_{residual} = 17.25\ e^{0.0107\ GSI_{peak}} \qquad (2-12)$$

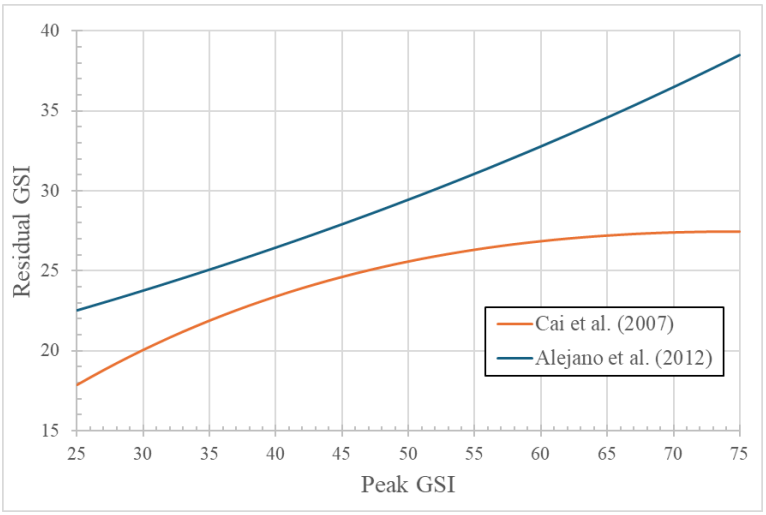

Figure 2-19: Comparison of the peak value and the residual value of GSI depending on the approach proposed by Cai et al. (2007) and Alejano et al. (2012)

The approach proposed by Su *et al* (2023) is more complex and depends on the type of rock and on the geotechnical parameters. It is not presented here.

The work presented in this thesis about squeezing phenomenon focuses on elastic-plastic large deformation in highly fractured rock masses. It does not directly consider creep. Nevertheless, it is compatible with short-term and long-term rock mass parameters. The post-peak behavior of the rock mass is considered perfectly plastic with the highest GSI value of 50. It can be noted that 50 is higher than the values proposed by Hoek and Brown (1997) and Lorig and Verona (2013) for a perfectly plastic post peak behavior. It can be argued that, for a GSI of 50, the post-peak behavior is strain softening rather than perfectly plastic. This choice was made to increase the applicability of the tools and methods presented in this thesis, and to align with common engineering practices. Engineers using this work need to be aware of this hypothesis.

2.2.2 Brittle failures

The second phenomenon studied in this thesis is brittle failures, which can be quasi-static or violent (rockburst). Rockbursts are well-known in the deep mining industry. This section aims to provide a brief overview of brittle failure phenomenon, and especially the rockburst phenomenon. This includes the failure process, the classical classifications and the contributing factors.

2.2.2.1 Quasi-static failure and violent failure (rockburst)

One of the first questions regarding brittle failure concerns the relationship between quasi-static failure and violent failure. Is quasi-static failure (spalling for example) a type of low intensity rockburst? There is no consensus on this point in the literature. Some authors such as Russenes (1974), Li *et al.* (2017a), Diederichs (2007; 2018), Askaripour *et al.* (2022), etc., consider that there are identical phenomena. On the other hand, others consider that they are different phenomena like Linkov (1992), Ortlepp and Stacey (1994), Kaiser *et al.* (1996), Singh and Goel (1999), Wang and Park (2001), Li *et al.* (2007), Cai (2016), Wang *et al.* (2020), He *et al*. (2022), etc.

It is important to note that this difference is fundamental for the conceptualization of the rockburst phenomenon. Authors who consider that static brittle failures belong to the category of rockbursts imply that the failure mechanisms at work in the case of static failures and dynamic failures (with ejection of material) are similar, and that only the intensities differ. For other authors, the notion of rockburst is not associated with a failure mechanism, but rather to a consequence, such as the release of energy or the ejection of material. Since static brittle failures do not lead to the same consequences, they cannot be considered as rockbursts. He *et al.* (2022) specify that a rockburst is always associated with a seismic event, whether natural (Kaiser *et al.* 1996b; Li *et al.* 2007) or man-made (Cai *et al.* 2016), involving a rapid and sudden release of energy and ejection of material. All 23 definitions collected by Zhou *et al.* (2018) also refer to a violent, sudden event associated with the ejection of material.

Unlike rockbursts, the consequences of the quasi-static failures are limited and not deadly. Nevertheless, they can lead to some safety issues such as small rockfalls if the spalling occurs in upper part of the tunnel. It can also lead to diminution of the advancement rate for hard rock TBM with grippers.

In this thesis, brittle failures cover both quasi-static and violent failures.

2.2.2.2 Failure mechanism

The failure mechanisms leading to rockbursts depend on the geological structures and the geometry of the excavation. They generally occur in areas of high in-situ stress in hard and brittle rock. He *et al*. (2022) consider that the failure mechanism involves several stages, the initiation of microcracking followed by crack propagation and then the cracks coalescence, which leads to the rockburst phenomenon (Figure 2-20). Similarly, Askaripour *et al.* (2022) describe the origin of rockbursts as a succession of crack creation, crack propagation and coalescence, which results in a loss of strength in the rock mass and its local failure.

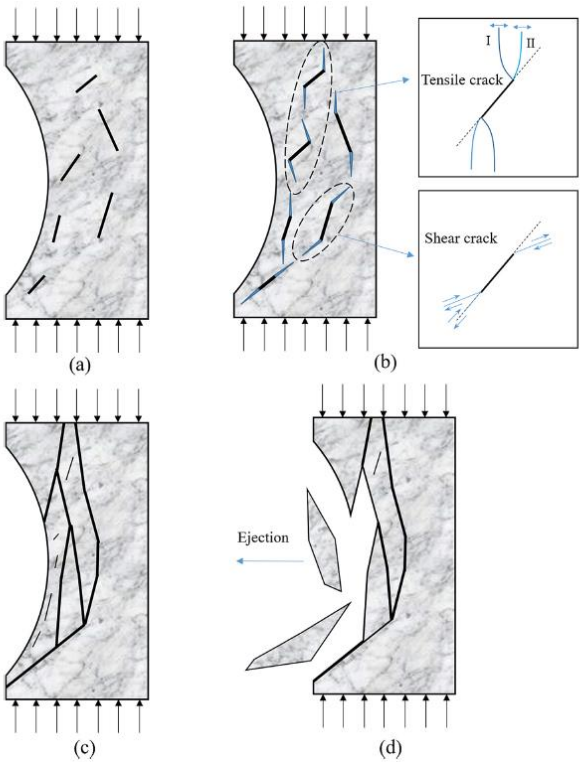

Figure 2-20: Typical failure mechanism for a rockburst: (a) crack initiation; (b) crack propagation; (c) cracks coalescence; (d) failure with rock ejection (from He et al. 2023)

Diederichs (2007) highlights the significant role of spalling in rockbursts and more specifically strainburst (presented in Section 2.2.2.3). Many authors (Meng *et al*. 2017; Zhou *et al*. 2018; Askaripour *et al*. 2022; He *et al.* 2022) pointed out that rockbursts are linked to the presence of instability, and Diederichs considers that one of the most common instabilities induced by the tunnel excavation is the development of cracks parallel to the tunnel boundary. The rock can then fail violently by buckling or progressively with the detachment of spall. Similarly, Askaripour *et al.* (2022) argue that the concept of rockburst and more specifically strainburst (type of rockburst occurring at the tunnel boundary) is strongly associated with the spalling phenomenon.

Nevertheless, He *et al.* (2022) consider that the relationship between a rockbursts and a static brittle failure is not obvious because rockbursts are unstable, violent and uncontrollable events, while static brittle failures are progressive failure mechanisms that only impacts long-term stability. Whether the failure mechanisms are similar or not, it raises the question of the possibility of another mechanism that could differentiate between quasi-static and violent failure in brittle and massive rock masses, such as the impact of the loading environment. This question is specifically studied and discussed in Chapter 8.

2.2.2.3 Classical classifications existing in the literature

There are numerous classifications of rockbursts proposed in the literature. These classifications can be grouped into broad categories based on the time before rupture, the rupture mechanism or the triggering mechanism (He *et al.* 2022). A summary of these different classifications can be found in He *et al.* (2022). This section presents only the principal classification, which considers three types of rockbursts: strainburst, pillar burst, fault slip burst (Figure 2-21). According to He *et al*. (2022), this classification was initially proposed by Hedley (1992) and has been used by many researchers including Kaiser *et al.* (1996), Kaiser (2009), Castro *et al.* (2012), Feng *et al.* (2012), Kaiser and Cai (2012), Chen *et al.* (2015), Fan *et al.* (2016), Askaripour *et al.* (2022).

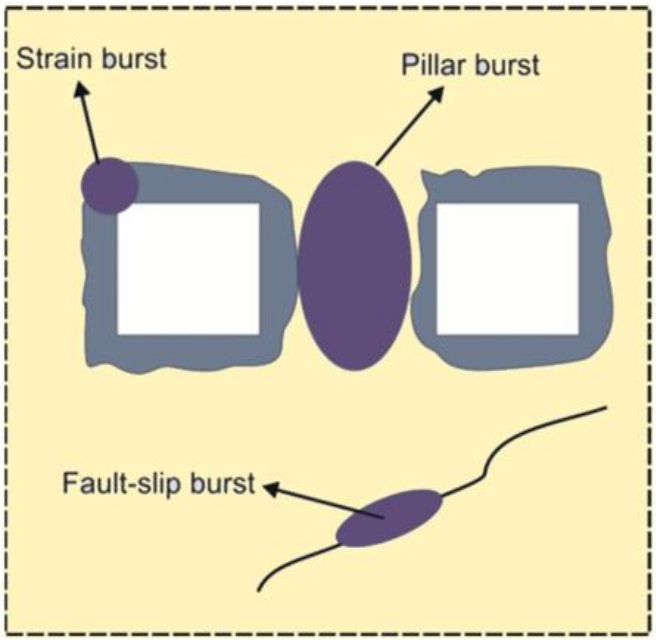

Figure 2-21: Schematic representation of rockburst potentials (from Askaripour et al. 2022, based on Castro et al. 2012)

A strainburst is a type of rockburst that occurs at the boundary of an excavation with low confinement (Askaripour *et al*. 2022) when the static or dynamic stresses exceed the rock mass strength (Kaiser *et al.* 2000). This violent failure can be stress-induced, associated with the development of sub-parallel fractures at the tunnel boundary or it can be structurally controlled (Askaripour *et al.* 2022). The energy is stored in the rock surrounding the excavation and the amount releasable energy depends on the post-peak stress-strain slope and the local stiffness of the loading system (Kaiser and Cai 2013). Kaiser and Cai (2013) also differentiate the trigger mechanism. It can be self-initiated, in which case the damage is only related to the stored energy, and the associated seismic event is co-located as it is the result of the burst. Alternatively, it can also be triggered by a remote seismic event, and the burst is a consequence of the seismic event (called a seismically triggered strainburst). Depending on the amount of radiated energy, the damage can be strongly influenced by this event compared to the damage associated with the energy stored in the surrounding rock mass.

A pillar burst is a type of rockburst that occurs in deep underground hard rock mines when mine pillar fails violently due to the high strain energy stored within it and the brittle characteristics of the rock mass (Askaripour *et al*. 2022). Pillar bursts occur under low to moderate confinement conditions. At low confinement conditions associated with a low width-to-height ratio of the pillar (Width/Height < 1), the failure process is similar to a strainburst, as surface

spalling develops due to tensile fracture. For larger confinement conditions, the small tensile cracks at the core of the pillar coalesce into a shear failure mechanism (Askaripour *et al.* 2022), similar to what is observed in laboratory tests on samples. The amount of energy released during the failure depends on the energy stored inside the pillar and the stiffness of the surrounding rock mass (Hauquin *et al*. 2018).

A fault-slip burst is a type of rockburst that occurs under high confinement and not close to the tunnel boundary. From a general point of view, a fault-slip burst can be considered as small-scale earthquake. The excavation process (stress redistribution in the rock mass, seismic wave associated with blasting, etc.) can reactivate pre-existing faults or create new seismically active structures (Askaripour *et al.* 2022). According to Askaripour *et al.* (2022), four important factors lead to fault-slip burst:

- The first factor is called “unclamping”. This involves a decrease of the normal stress applied to a discontinuity. This decrease can occur relatively close to the tunnel boundary (local unclamping) or farther away (regional unclamping). This facilitates the displacement along the discontinuity/fault creating the seismic event.
- The second factor is daylight that occurs when the excavation intersects a fault. This enables the fault to move freely into the excavation area allowing the release of large amounts of energy, which is accompanied by a large seismic event.
- The third important factor is the stress rotation associated with the excavation that modifies the orientation of the major principal stress and the discontinuity behavior.
- The last factor is the pillar shear. The pillar can inhibit the displacement of the rock mass on one side while allowing it to move freely on the other side.

Currently, the dynamic behavior of fault-slip bursts is not fully understood, because the effect of the physical characteristics of faults and the uncertainty of scale effect have not yet been completely investigated (Askaripour *et al.* 2022).

For civil engineering applications, Kaiser *et al.* (2000) specified that strainburst is the most relevant class of rockburst.

2.2.2.4 Contributing factors

Keneti and Sainsbury (2018) summarized the major contributing factors from the analysis of numerous rockburst case studies into six categories, which they divided into two groups: factors associated with the stress conditions, and factors associated with rock mass characteristics (Figure 2-22).

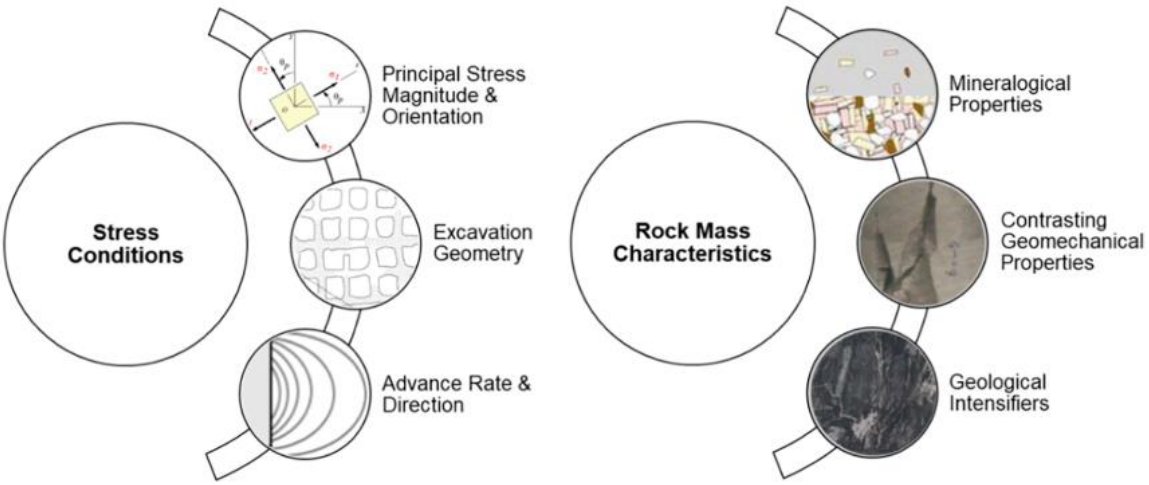

Figure 2-22: Contributing factors for violent rock mass failure (from Keneti and Sainsbury 2018)

The following contributing factors can be highlighted from this analysis (Keneti and Sainsbury 2018):

- One of the most important conditions for rockburst is to have high and anisotropic in-situ stress. This can be amplified by the presence of geological features such as dykes, contact between different geological formations or existing geological structures, which create stress concentrations.
- The likelihood of a rockburst increases with large openings or when multiple openings are created close to each other.
- A rapid excavation rate can also increase the risk of rockbursts. In highly stressed ground, fractures develop in front of the face and can progressively distress the rock mass. If the excavation rate is too rapid, the fracture zone may not have the time to stabilize, leading to a highly stressed intact rock at the tunnel wall or face. Depending on the presence of structural features, the direction of the excavation can also increase the risk of rockburst.
- Strong, brittle and stiff rocks have a high potential for bursting (Keneti and Sainsbury 2018 referring to Blake and Hedley 2009). There is no standardized definition of brittleness, but one classic definition is the ratio of compressive to tensile strength. The m_i parameter of H&B can also be seen as a brittleness parameter (Diederichs 2018).
- Contrasting properties of adjacent geological units have been identified to be a contributing factor to the occurrence of rockburst events. Under the same stress conditions, two adjacent lithological units with significant difference in their geomechanical properties (e.g. deformability, grain size, in-situ fracture density, degree of anisotropy, etc.) may present different behavior in storing strain energy, failure mode, fracture initiation and propagation (Keneti and Sainsbury 2018).
- Geological intensifiers like weaknesses such as faults or shear zones, and stress concentrators such as dykes, can create unfavorable conditions. They lead to a localized increase in the stress concentration, a diminution of the loading system stiffness (softer rock mass than without geological intensifiers), or facilitate the release of stored energy.

2.3 Conclusions

This chapter aims to remind some fundamental knowledge of rock mechanics for a better understanding of the following chapters and presents the two main geological hazards studied:

the large deformations (squeezing) in highly fractured rock mass and the brittle failures (spalling and rockbursts) in massive and intact rock mass.

The large radial deformation is studied using elastic perfectly plastic behavior of the rock mass with a generalized Hoek and Brown failure criteria. The GSI values are smaller than 50, and the potential creep behavior is not explicitly considered to stay relevant with available data during preliminary design. It could be included using the “long-term” rock mass properties.

The term “brille failures” is preferentially used compared to spalling and rockburst to stay relevant with whether or not these phenomena are similar. Spalling is associated with quasi-static failure, while rockburst is associated with violent and brutal failure.

The work presented in the next chapters focuses on providing new tools or methods for engineers to answer the main question: Can the geological and geotechnical uncertainties be considered directly during the early stages of a deep tunnel design when facing potential large deformations or brittle failures? What impact will they have on the design and on the technical solutions?

Chapter 3 - Quantification of the risk of large deformation in highly fractured rock mass

Chapter Abstract: As discussed in the first chapter, it is primordial to correctly identify and quantify the risk of large radial deformation during the early stages of a tunnel design. Several approaches have been developed to enable this quantification. The abacus introduced by Hoek and Marinos (2000) is one of the most widely used tools for estimating such deformations. Their method has some important advantages like its ease of use and the relevance of the information provided to the designer but has also some shortcomings. The principal one is the use of the rock mass strength as an input parameter, which is a very comprehensive parameter but very hard to estimate correctly and highly uncertain.

This chapter aims to clarify the assumptions of the original abacus and to update it using numerical modelling, supplemented by a Monte Carlo simulation on updated input parameters to address a broader range of geological scenarios. Unlike the original approach based on analytical expressions, the new curves incorporate a generalized Hoek and Brown failure criterion, revised parameter intervals, and enhanced practical applicability. The principal update is the use of parameters coming directly from laboratory tests and field investigations to replace the rock mass strength.

3.1 Existing methods for risk quantification

There are several methodologies to estimate the squeezing potential at an early stage of the tunnel design. They can be classified into two categories: the approaches which only highlight the probable rock mass behavior depending on the situation (Kaiser *et al.* 2000; Russo 2014; Majumber *et al.* 2017; AFTES 2021) presented in Chapter 1.2, or the approaches which try to introduce the squeezing intensity (Jethwa *et al.* 1984 ; Goel 1994 ; Aydan *et al.* 1996 ; Hoek and Marinos 2000 ; Mercier-Langevin and Hadjigeorgiou 2011 ; Arora *et al.* 2020). These approaches are briefly introduced in this section, except for the one of Hoek and Marinos (2000) for which a more detailed presentation and discussion is proposed.

3.1.1 Methods in the literature

Jethwa *et al.* (1984) proposed a method to estimate the squeezing potential and the ground pressure on the support based on the friction angle and the post-peak behavior of the rock mass. To quantify the potential of large deformation when excavating in the rock mass, they used the "stability factor" defined as the ratio between the rock mass strength divided by the in-situ stress. They proposed the following quantification (Table 3-1):

Table 3-1 : Quantification of the squeezing potential proposed by Jethwa et al. (1984)

σ_{cm} / σ_0	Type of behavior
< 0.4	Highly squeezing
0.4 – 0.8	Moderately squeezing
0.8 – 2.0	Midly squeezing
> 2.0	No Squeezing

It can be noted that the original paper has not been found, this quantification comes from Barla (2001). This intensity of the phenomenon is only qualitative; no information is provided regarding the meaning of each intensity and the corresponding consequences. Hoek and Marinos (2000) proposed also to quantify the squeezing potential based on the "stability factor" but provided quantified results and explanation for each category. More information is available in Section 3.1.1.

Goel (1994) developed a chart for squeezing quantification based on the study of 99 tunnel sections (Figure 3-1). The input parameters are the rock mass number (N), which is the value of the Q-system with a SRF parameter of 1, the depth of the section (H) and the tunnel diameter (B).

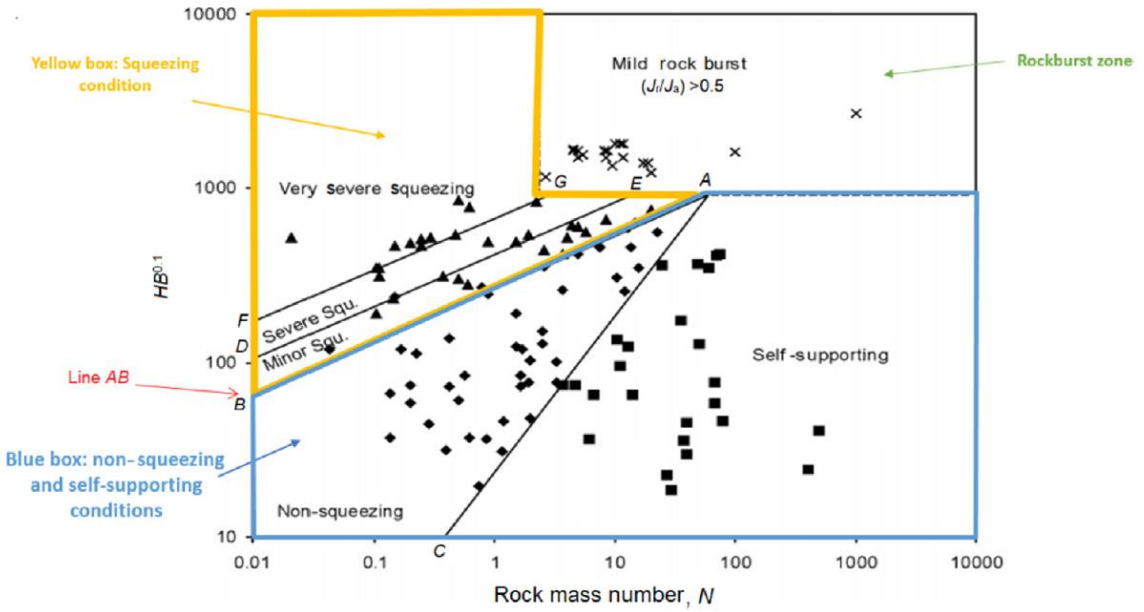

Figure 3-1: Chart developed by Goel (1994) to quantify the squeezing potential (from Askaripour et al. 2022)

The separation between "non-squeezing" ($\varepsilon < 1\%$, ε being the tunnel deformation) and "minor squeezing" ($1\% < \varepsilon < 3\%$) is (line AB):

$$H = (275\ N^{0.33})B^{-0.1} \qquad (3-1)$$

The separation between "minor squeezing" and "severe squeezing" ($3\% < \varepsilon < 5\%$) is (line DE):

$$H = (450\ N^{0.33})B^{-0.1} \qquad (3-2)$$

The separation between "severe squeezing" and "very severe squeezing" ($\varepsilon > 5\%$) is (Line FG):

$$H = (630\ N^{0.33})B^{-0.1} \qquad (3-3)$$

Aydan *et al.* (1996) introduced a classification of the squeezing problem based on the ratio between the orthoradial strain around the tunnel and the strain associated with the elastic limit in a compression test. Their approach is based on the analogy between the behavior of a rock sample during a laboratory test (stress-strain curve for limited confinement, $\sigma_3 < \sigma_{ci}$) and at the tunnel boundary (Figure 3-2). They also considered that the uniaxial compressive strength of the intact rock and the rock mass are identical (Barla 2001).

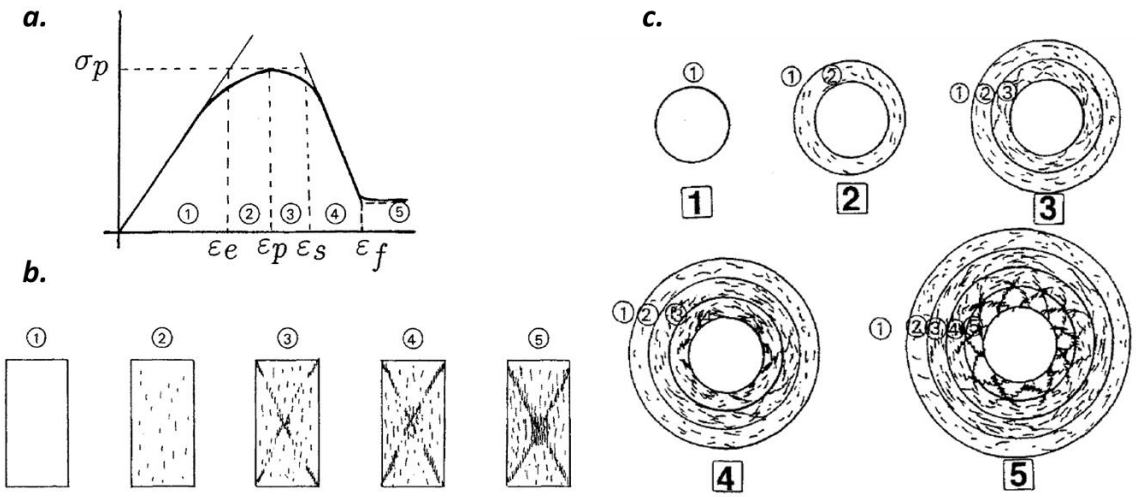

Figure 3-2: Idealized stress-strain curve for a rock subjected to large radial deformation

It allows them to define normalized state of deformation based on numerous laboratory tests:

$$\eta_p = \frac{\varepsilon_p}{\varepsilon_e} = 2\,{\sigma_{ci}}^{-0.17}\ ;\ \eta_s = \frac{\varepsilon_s}{\varepsilon_e} = 3\,{\sigma_{ci}}^{-0.25}\ ;\ \eta_f = \frac{\varepsilon_f}{\varepsilon_e} = 5\,{\sigma_{ci}}^{-0.32} \qquad (3-4)$$

Where σ_{ci} is the strength of the rock, ε_e, ε_p, ε_s and ε_f are specific strain values defined in Figure 3-2.

By making the analogy, the authors have proposed several degrees of squeezing (Figure 3-3). It can be noted that the orthoradial strain used in the classification can be deduced form the ratio between the radial displacement at the tunnel boundary divided by the tunnel radius (Aydan *et al.* 1996).

Class No.	Squeezing degree	Symbol	Theoretical expression	Comments on tunnel behaviour
1	no-squeezing	NS	$\epsilon_\theta^a/\epsilon_\theta^e \le 1$	The rock behaves elastically and the tunnel will be stable as the face effect ceases
2	light-squeezing	LS	$1 < \epsilon_\theta^a/\epsilon_\theta^e \le \eta_p$	The rock exhibits a strain-hardening behaviour. As a result, the tunnel will be stable and the displacement will converge as the face effect ceases
3	fair-squeezing	FS	$\eta_p < \epsilon_\theta^a/\epsilon_\theta^e \le \eta_s$	The rock exhibits a strain-softening behaviour, and the displacement will be large. However, it will converge as the face effect ceases
4	heavy-squeezing	HS	$\eta_s < \epsilon_\theta^a/\epsilon_\theta^e \le \eta_f$	The rock exhibits a strain-softening behaviour at much higher rate. Subsequently, displacement will be larger and it will not tend to coverge as the face effect ceases
5	heavy-squeezing	VHS	$\eta_f < \epsilon_\theta^a/\epsilon_\theta^e$	The rock flows which will result in the collapse of the medium and the displacement will be very large. And it will be necessary to re-excavate the opening and install heavy supports

Figure 3-3: Squeezing quantification proposed by Aydan et al. (1996); ε_θ^a is the orthoradial strain at the tunnel boundary and ε_θ^e is the elastic strain limit (ε_e)

Mercier-Lanevin and Hadjigeorgiou (2011) introduced the HRSI (Hard Rock Squeezing Index) based on their experience gained at LaRonde mine in Canada and in other deep mines (Figure 3-4). This approach focuses on hard rocks with highly anisotropic behavior.

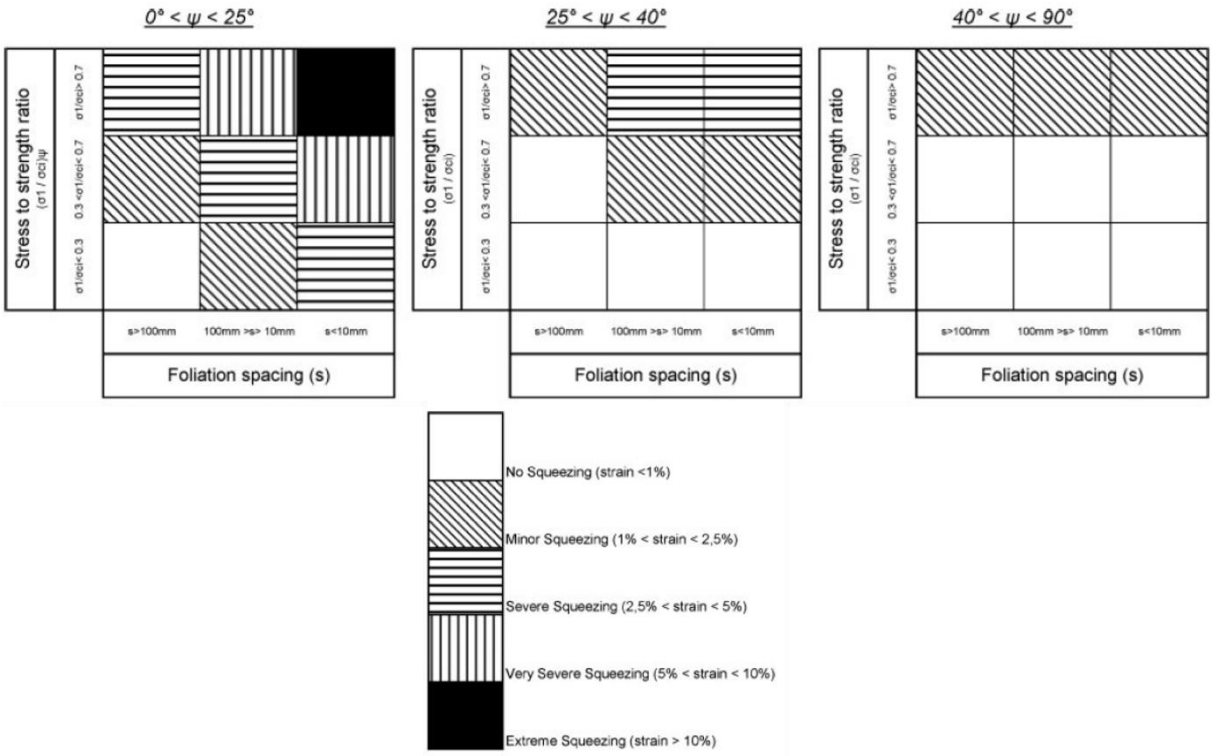

Figure 3-4: Some matrix to quantify the squeezing potential depending on the angle between discontinuities and the tunnel wall (Mercier-Lanevin and Hadjigeorgiou 2011)

There are 4 input parameters: the rock strength (σ_{ci}), the in-situ stress state (σ_0), the foliation spacing (distance between the discontinuities creating the anisotropic behavior like foliation, schistosity, etc.), and the angle between the normal to the plane of walls of interest and the normal to the foliation plan (ψ).

Arora *et al*. (2020) proposed the use of a "squeezing number" to estimate the squeezing potential for clay-based rock. This 'squeezing number" is based on the ratio between the ortho-radial stress in the rock mass after the excavation and the maximum shear strength of the rock mass.

3.1.2 Methods based on machine learning

More recently, numerous methods for predicting squeezing based on machine learning and database analysis have been developed such as Jimenez and Recio (2011), Ghasemi and Gholizadeh (2018) and Jain and Rao (2022) using logistic regression methods; Feng and Jimenez (2015) using a naive Bayes classifier; Shafiei *et al.* (2012), Sun *et al*. (2018) and Huang *et al.* (2021) using a support vector machine; Zhou *et al.* (2018) using neural networks; Chen *et al*. (2020) using a decision tree; or Zhang *et al.* (2020) using a combination of seven different machine learning methods to make predictions when input data are missing.

The vast majority of these studies only classify rock mass into two categories: those potentially impacted by squeezing or not. With the exception of Jain and Rao (2022), none of the methods quantify the range of the deformations likely to occur. Various authors consider that squeezing

occurs when radial strain exceeds 1%, based on the work of Hoek and Marinos (2000) (Ghasemi and Gholizadeh 2018; Zhang *et al*. 2020; Haung *et al*. 2021).

Ghasemi and Gholizadeh (2018) use two logistic regression methods to determine whether squeezing will occur, based solely on tunnel depth (H) and the value of the Q-system. The regression is performed on a database of 220 tunnel sections, 136 of which are subject to squeezing (as defined by Hoek and Marinos).

Jain and Rao (2022) also used logistic regressions to quantify the squeezing phenomenon. Unlike the other authors, they estimate the convergences likely to occur. Their database consists of 75 tunnel sections in the Himalayas that have undergone varying degrees of squeezing and considered the following input data using whether the Q-system (Q), the rock mass number (N corresponding to Q with a SRF of 1), or the joint factor (J_f). The other input parameters considered are the ratio between vertical and horizontal stress (K_0), the stiffness of the support (K), the vertical stress (σ_v), the radius of the tunnel (a) and the observed displacements, corresponding to the parameters to be predicted subsequently.

The studies performed by Zhang *et al*. (2020) and Huang *et al*. (2021) take as input parameters only the diameter and the depth of the tunnel, the rock mass quality (Q-system) and the stiffness of the support. Zhang *et al*. (2020) also consider the 'Strength stress ratio', (identical to the "Stability factor" presented above).

3.1.3 Hoek and Marinos (2000) curve

Hoek and Marinos (2000) developed a curve to link the "stability factor" to the radial strain of an unsupported tunnel and introduced five classes of squeezing problem to make some recommendations about the geotechnical issues that can occur and the type of support that is needed for each of those classes. The most recent methodologies generally refer to the Hoek and Marinos (2000) classification and recommendations. This makes the Hoek and Marinos (2000) curve and recommendations the most common approach to estimate the squeezing problem (Figure 3-5). The following section presents in detail this curve and some of its shortcomings.

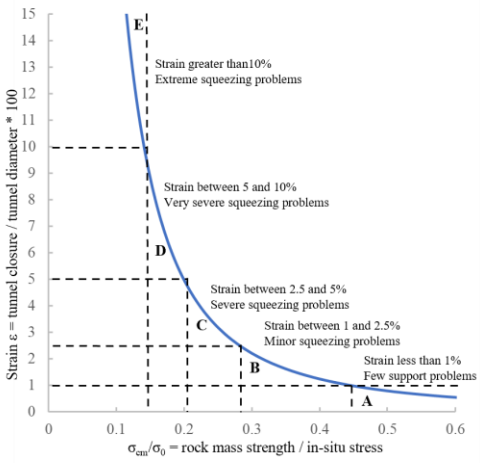

	Strain ε %	Geotechnical issues	Support types
A	Less than 1%	Few stability problems and very simple tunnel support design methods can be used. Tunnel support recommendations based upon rock mass classifications provide an adequate basis for design.	Very simple tunnelling conditions, with rockbolts and shotcrete typically used for support.
B	1 to 2.5	Convergence confinement methods are used to predict the formation of a plastic zone in the rock mass surrounding a tunnel and of the interaction between progressive development of this zone and different types of support.	Minor squeezing problems which are generally dealt with by rockbolts and shotcrete; sometimes with light steel sets or lattice girders are added for additional security.
C	2.5 to 5	Two-dimensional finite element analysis, incorporating support elements and excavation sequence are normally used for this type of problem. Face stability is generally not a major problem.	Severe squeezing problems requiring rapid installation of support and careful control of the construction quality. Heavy steel sets embedded in shotcrete are generally required.
D	5 to 10	The design of tunnel is dominated by face stability issues and, while two-dimensional finite analyses are generally carried out, some estimates of the effects of forepoling and face reinforcement are required	Very severe squeezing and face stability problems. Forepoling and face reinforcement with steel sets embedded in shotcrete are usually necessary
E	More than 10	Severe face instability as well as squeezing of the tunnel make this an extremely difficult three-dimensional problem for which no effective design methods are currently available. Most solutions are based on experience.	Extreme squeezing problems. Forepoling and face reinforcement with steel sets embedded in shotcrete are usually necessary

Figure 3-5: Curve to predict the radial strain for unsupported tunnels and associated recommendations proposed by Hoek and Marinos (2000) (adapted from Hoek and Marinos 2000)

3.1.3.1 Hypotheses of the H&M curve

The curve and recommendations provided by Hoek and Marinos (2000) (Figure 3-5) enable the estimation of tunnel radial deformation based solely on the uniaxial compressive strength of the rock mass (σ_{cm}) and the in-situ stress. This has many advantages such as its ease of use, the small number of input parameters, and the overview of the potential geotechnical problems and the type of support required. These features make it a very useful tool for engineers in the early stages of deep tunnel design in weak rock masses. It is also a reference in the literature used by many authors to characterize the onset of squeezing problem (Russo 2014, Majumber *et al.* 2017, Ghasemi and Gholizadeh 2018, Arora *et al.* 2020, Zhang *et al.* 2020, Huang *et al.* 2021).

DeGagné *et al.* (2011) proposed an adaptation of the H&M curve for an anisotropic in-situ stress state and a non-circular tunnel by using numerical calculations (FLAC software). The authors obtained an important scatter in the results of their numerical calculations. To reduce the uncertainty, they opted to use a neural network to estimate the maximum tunnel radial strain rather than relying on a graphical representation.

The Hoek and Marinos curve has been obtained by fitting the results of a Monte Carlo simulation performed over a wide range of conditions. The radial strain was calculated using the closed-form analytical solutions for a circular tunnel excavated in an elastic perfectly plastic rock mass characterized by a Mohr-Coulomb criterion (Duncan Fama 1993) and a Hoek & Brown criterion (Carranza-Torres & Fairhurst 1999). The results of these two analytical solutions are similar, and the fitting curve is presented in Figure 3-6.

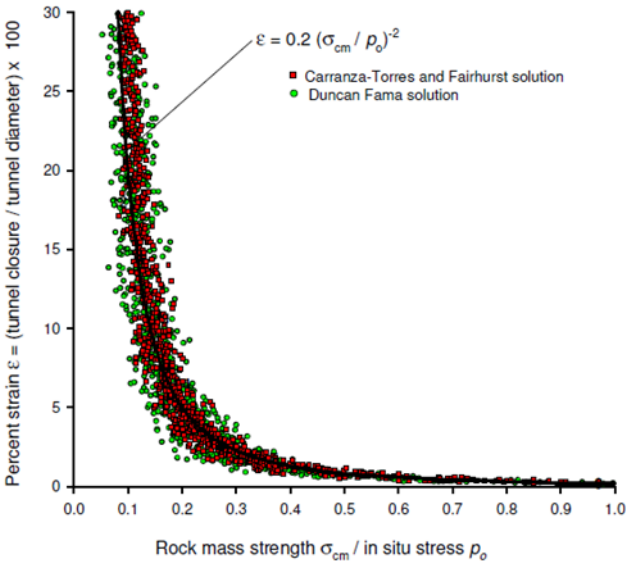

Figure 3-6: Results of Monte Carlo simulation performed by Hoek and Marinos (2000)

The hypothesis of a perfectly plastic post pic behavior is relevant for GSI (Geological Strength Index) values less than 30 according to Hoek & Brown (1997) or less than 40 according to DeGagné *et al.* (2011) and Lorig and Varona (2013). The input parameters considered as random variables are presented in Table 3-2, together with their respective range of variations. The distributions are uniform over these intervals. These random variables are then transformed into other parameters to be used in the analytical closed-form solutions of Duncan Fama (1993) and Carranza-Torres and Fairhurst (1999).

Table 3-2 : Properties and range of value used by Hoek and Marinos (2000), DeGagné et al. (2011) and in the following study; K_0 the horizontal to vertical in-situ stress ratio; USC the uniaxial compressive strength of the intact rock; m_i a parameter of the Hoek and Brown yielding criteria; α(GSI) means that α is a function of GSI

Properties	Hoek & Marinos (2000)	DeGagné *et al.* (2011)	Present study
Vertical stress (σ_0)	[2 ; 20] MPa	[5 ; 30] MPa	[5 ; 40] MPa
K_0 (σ_h/σ_v)	1	[0.5 ; 2]	1
UCS (σ_{ci})	[1 ; 30] MPa	[20 ; 100] MPa	[10 ; 110] MPa
m_i	[5 ; 12]	[10 ; 20]	[$m_{i\,min}(\sigma_{ci})$; $m_{i\,max}(\sigma_{ci})$]
Modulus Ratio (MR= σ_{ci}/E_i)	About 500	-	{200 ; 400 ; 600}
Tunnel diameter	[4 ; 16] m	5.34 m (equivalent circular diameter)	10 m
Geological Strength Index (GSI)	[10 ; 35]	[25 ; 40]	[15 ; 50]
Dilation angle (ψ)	[0° ; 10 °]	-	-
Dilation-to-friction ratio α ($\psi = \alpha\,\varphi$)	-	α(GSI)	[α_{min}(GSI) ; α_{max}(GSI)]

Hoek and Marinos (2000) do not provide any information about the hypothesis made on the elastic behavior of the rock mass. Based on a back-analysis performed with the close form analytical solution of Carranza-Torres and Fairhurst (1999), it seems that Hoek and Marinos (2000) used an expression similar to the one later proposed by Hoek and Diedrichs (2006) (Chapter 2.1.2.2), with a modulus ratio of 500. An example of the back analysis carried out with a Monte Carlo simulation of 4000 realizations is presented in Figure 3-7. DeGagné *et al*. (2011) used the "simplified version" proposed by Hoek and Diederichs (2006), which does not consider a relationship between the Young's modulus of the rock and the uniaxial compressive strength.

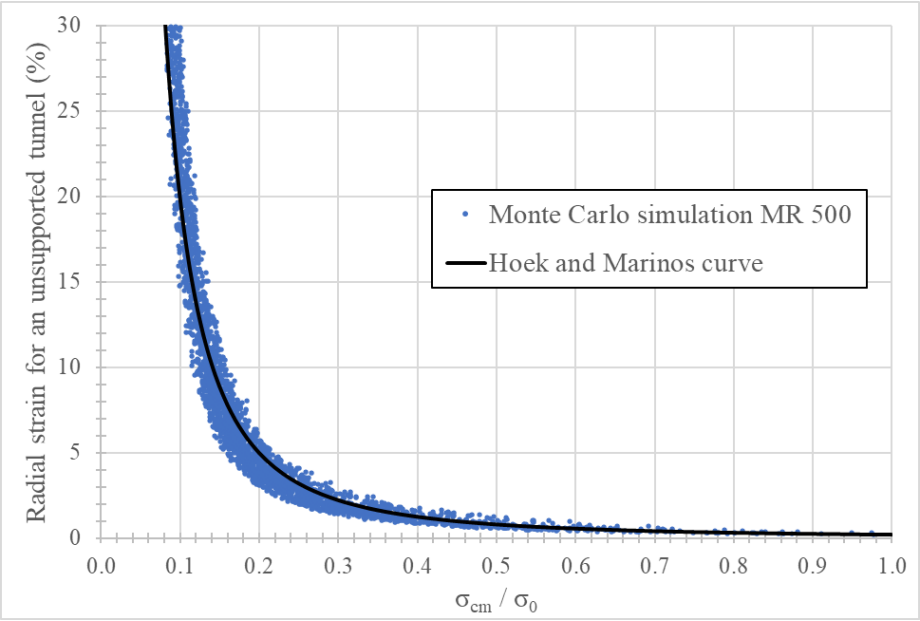

Figure 3-7: Back analysis for the expression used by Hoek and Marinos (2000) to perform their Monte Carlo simulation using Carranza-Torres and Fairhurst (1999) expression

3.1.3.2 Limitations of the H&M curve

A major problem with the H&M curve is the use of the "rock mass strength" (σ_{cm}) as an input parameter. Although easy to understand, it is very difficult to estimate in practice. Several formulations can be found in the literature which give very different values of σ_{cm}. One expression is given by Hoek and Marinos (2000), which seems to be an empirical relationship (no precise information was found on this topic):

$$\sigma_{cm} = (0.0034\, {m_i}^{0.8})\, \sigma_{ci} \left\{1.029 + 0.025\, e^{(-0.1\, m_i)}\right\}^{GSI} \qquad (3-5)$$

With m_i the Hoek and Brown parameter of intact rock, σ_{ci} the uniaxial compressive strength of intact rock, and GSI the Geological Strength Index. A more theoretical expression is also given by Hoek *et al*. (2002) which is based on an approximation of H&B criteria by the Mohr-Coulomb criteria for small confining pressures:

$$\sigma_{cm} = \sigma_{ci}\, \frac{(m_b + 4\, s - a\, (m_b - 8\, s))\, \left(\frac{m_b}{4} + s\right)^{a-1}}{2\, (1+a)\, (2+a)} \qquad (3-6)$$

With a, m_b and s the generalized Hoek & Brown parameters. The expression linking these parameters to the GSI are the classical ones, which are detailed in Chapter 2.1.2.1.

Based directly on the generalized Hoek and Brown yielding criteria, it is possible to find also the following expression (Arora *et al*. 2020):

$$\sigma_{cm} = \sigma_{ci}\, s^a \qquad (3-7)$$

To highlight the significant impact of different rock mass strength expressions on tunnel design, the following illustrative example with specified rock mass properties is considered: GSI of 25, m_i of 8 and σ_{ci} of 25 MPa. The three expressions give a rock mass strength of 1.20 MPa, 2.12 MPa and 0.3 MPa respectively. With an in-situ stress of 7 MPa, a radial strain of 6.8% for the first expression, and 2.2% for the second expression can be estimated from the H&M curve (presented in Figure 3-5). The third expression leads to a radial strain greater than 40%, which falls outside of the valid range of the curve and the first two estimated strains will lead to two very different design strategies (table in Figure 3-5). Therefore, the choice of an expression for estimating the rock mass strength significantly affects the tunnel design, even with identical rock masses and in-situ stresses.

As this example shows, the choice of a mathematical expression to calculate σ_{cm} introduces considerable uncertainties regarding the value of the rock mass strength. To avoid these 'artificial' uncertainties, the x-axis of the new curves presented in this study relies solely on parameters obtained directly from laboratory tests and field reconnaissance, such as σ_{ci}, m_i, and GSI, without the need to calculate σ_{cm}.

3.2 Improvement of the H&M curve

As the H&M curve is relevant and easy to use during preliminary design, the idea is to improve the curve regarding the limitations associated with the use of the rock mass strength and to increase its range of validity.

3.2.1 Numerical model

To create a new version of the H&M chart without the rock mass strength as an input parameter, a Monte Carlo simulation was carried out using the two-dimensional continuum code FLAC 8.1. A Monte Carlo simulation is used to cover the entire variation range of the input parameters aligning with the approach used by Hoek and Marinos. Although methods like Latin Hypercube sampling could have been used, they would have added unnecessary complexity and were deemed unnecessary for this study given the calculation time. The numerical simulation was carried out on a circular tunnel with a radius of 5 m. The rock mass is modeled by an elastic perfectly plastic behavior with a generalized Hoek & Brown yielding criteria (presented in Chapter 2.1.2.1). For symmetrical reasons, a quarter of the tunnel is modeled, and the model run time varies between 1 and 2 minutes (Figure 3-8).

The numerical calculations are carried out with the large strain hypothesis. This hypothesis means that the coordinates of each grid point are updated at each calculation step, based on the incremental deformation that occurred at the previous step. As FLAC uses an explicit approach and a Lagrangian formulation, this hypothesis has a very limited impact on the calculation time and leads to more appropriate results (FLAC 8.0 Online Manual). Figure 3-9 compares the results of the large strain hypothesis with the results of the small strain hypothesis and the Hoek and Marinos curve. The Monte Carlo simulations of 1000 realizations have been performed using the same hypothesis as Hoek and Marinos (2000). For small values of radial, the results are similar, but for large values (small x-axis values) the difference is important, and the small strain hypothesis leads to higher radial strain. This hypothesis also leads to much higher plastic radius. The maximal plastic radius is higher than 10 Radii, while for the large strain hypothesis, most of the plastic radius are smaller than 5 Radii.

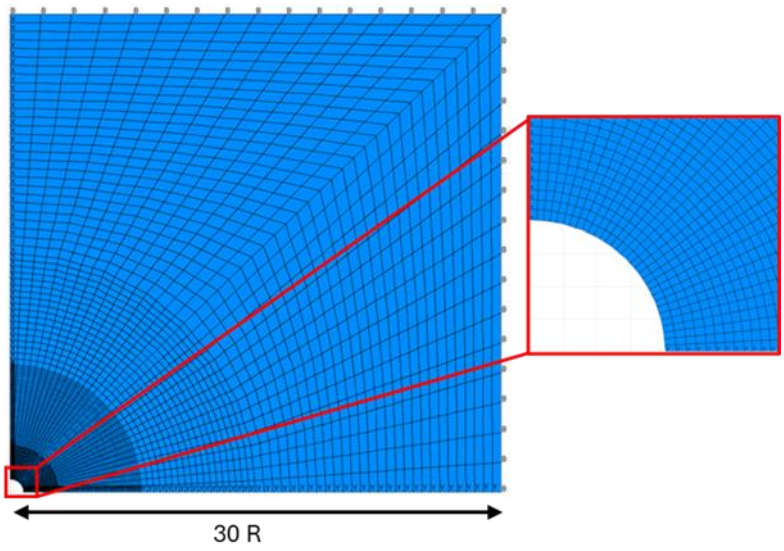

Figure 3-8: Numerical model used for the Monte Carlo simulation; R is the tunnel radius

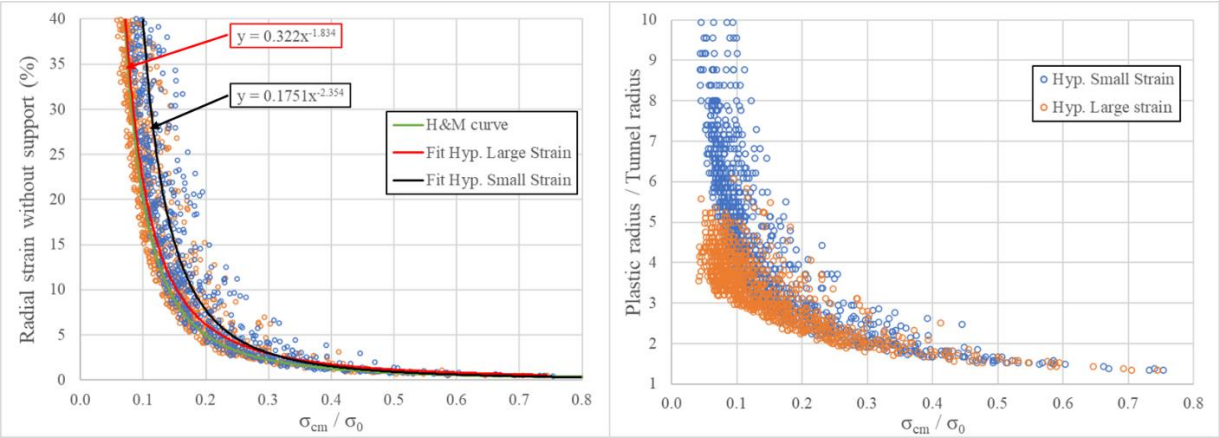

Figure 3-9: Comparison of the results of 2D plane strain numerical model without support when the large strain hypothesis is used (orange points) and when the small strain hypothesis is used (blue points)

The meshing of the model was optimized in order to minimize the computation time while ensuring results accuracy. Based on the optimization and to avoid meshing issues during the calculation (large strain hypothesis), the radial strain is limited to values smaller than 40%. Thus, for the Monte Carlo simulation, only results with radial strain below 40% are retained. This model has been validated on the example of numerical calculation provided by Carranza-Torres and Fairhurst (1999) with identical hypotheses.

3.2.2 Procedure used for the improvement

The input parameters are similar to those used by Hoek and Marinos (2000) and DeGagné *et al*. (2011), but the ranges of variation have been updated, and uniform distributions are assumed within the given intervals (Table 3-2). The variation range considered for the GSI ([15;50]) has been selected to take into account the geological conditions in which squeezing can occur. If the in-situ stress is high enough, the rock mass must be able to sustain large radial deformation, so its post-peak behavior must be perfectly plastic or slightly strain-softening (Chapter 2.1.2.3). Based on the variation range in Table 3-2, the rock mass strengths covered in this study are between 0.3 MPa and 25 MPa (according to Eq.(3-5)), and between 0.5 MPa and 33 MPa (according to Eq.(3-6)). This does not include lightly fractured or unfractured rock mass with low uniaxial compressive strength where the post-peak behavior is highly strain-softening or brittle.

The models are run in large strain mode without gravity in an isotropic stress field. The tunnel diameter is not considered as a variable since it does not affect the result (radial strain). It is defined as the tunnel wall displacement divided by the tunnel radius, which is expressed in percentage, making it independent of the tunnel radius value. For identical geological situations, a tunnel radius of 2m and 5m leads to identical radial strain. This was verified through several tests. The numerical model presented in Figure 3-8 has been optimized to reduce the calculation time while ensuring the results are not impacted when the final radial strain is up to 40%, regarding the large strain hypothesis. For radial strains bigger than 50% or 60%, meshing problems can occur, so a criterion is used to avoid these problems (Step 3 in Figure 3-10). The size of the numerical model is 30 radii, the mesh size at the tunnel boundary is radii/20 and the relaxation is carried out in 10 steps to reach 50%, then 40 steps between 50% and 90%, and 20 steps between 90% and 100%. The flowchart in Figure 3-10 presents the procedure used for the Monte Carlo simulation.

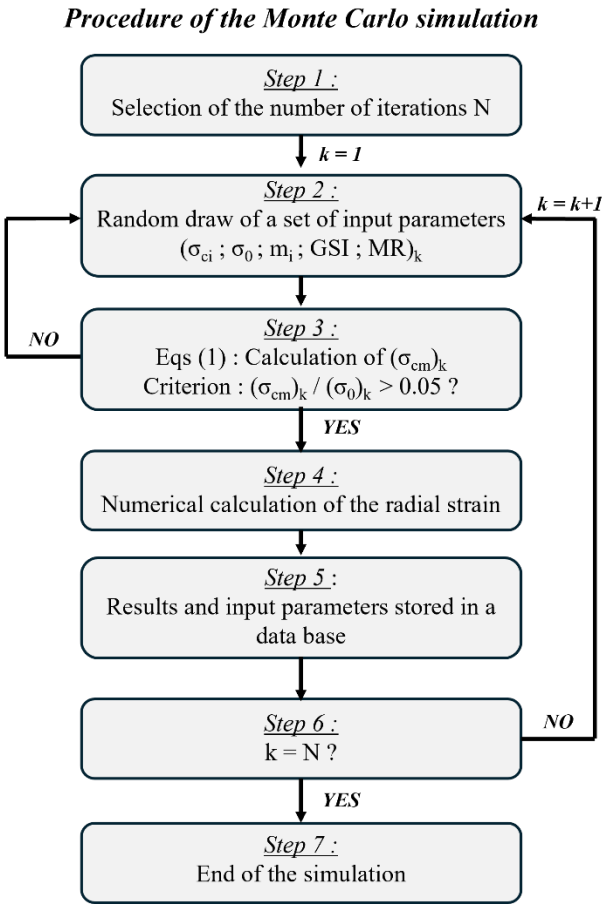

Figure 3-10: Flowchart to present the procedure used for the creation of the numerical model and Monte Carlo simulation

A dependence is considered between m_i and σ_{ci} to avoid less realistic pairs such as [σ_{ci} = 110 MPa; m_i = 5] or [σ_{ci} = 10 MPa; m_i = 30]. The interval boundaries of m_i depend linearly on σ_{ci}. For instance, when σ_{ci} = 10 MPa, m_i varies between 5 and 12 (similar to Hoek and Marinos 2000) and for $\sigma_{ci} \geq$ 70 MPa, m_i varies between 10 and 30. Another dependence is considered between α (ratio of dilation to friction angles) and the GSI, following the suggestion of Lorig and Varona (2013), who developed a chart providing starting points for α values (Figure 3-11). For a GSI ≤ 20, α is drawn between 0 and 0.33, and for GSI = 50, α is drawn between 0.2475 and 0.5775. For intermediate GSI values, the interval boundaries vary linearly with the GSI.

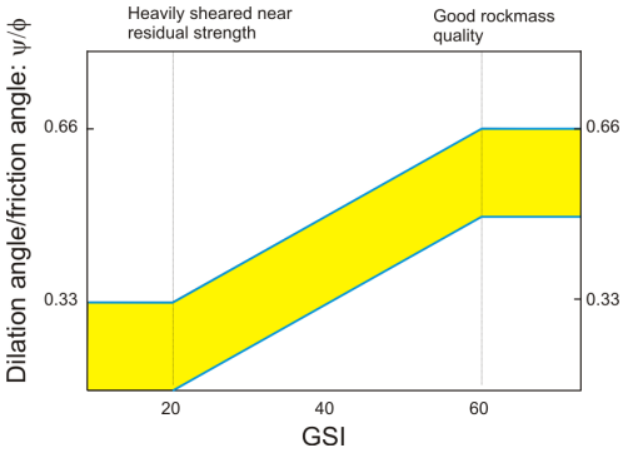

Figure 3-11: Estimated range of dilation as a function of GSI (from Lorig and Varona 2013)

The random variables of the Monte Carlo simulation (detailed in Table 3-2) are then used to calculate the parameters needed for the numerical model: Young's modulus, Poisson's ratio, the generalized Hoek & Brown parameters (σ_{ci}, a, s and m_b) and the in-situ stress σ_0. The generalized Hoek & Brown parameters can be obtained using the expression in Hoek and Brown (2019), presented in Chapter 2.1.2.1, and by considering a damage factor (D) equal to zero, which is reasonable for poor quality rock masses (DeGagné *et al.* 2011). The Young's modulus is calculated using the modulus ratio (MR), the uniaxial compressive strength (σ_{ci}) and the GSI as proposed by Hoek and Diederichs (2006). To cover a wide range of geological situations, three values of modulus ratio are considered: 200, 400 and 600. The Poisson's ratio (ν_{rm}) of the rock mass is calculated using the formula introduced by Hoek *et al*. (1995) and recommended by Lorig and Varona (2013) based on the GSI. These formulas are presented in Chapter 2.1.2.2.

An important point of the Monte Carlo simulation is the reset of the model after each realization. In the FLAC software, or at least at the knowledge of the author, it is not possible to directly reset a model. After each realization, a manual reset was performed by resetting all the deformations and velocities for each point of the model, erasing the in-situ stress state as well as the stresses in every element of the model and the applied forces at the boundaries, and by resetting the material properties through the assignation of elastic behavior to the entire model. This process has been validated on two different tests to ensure that it does not impact the results:

1) A succession of realizations with identical input parameters. At each realization, fix input parameters are considered (identical to the previous realization), the calculation is performed, and the model is reset using the above procedure.

2) A succession of realizations with randomly chosen input parameters and then compared to the results obtained from single calculations (no reset process needed). Each realization is associated with specific values of input parameters, then the calculation is performed. The result of the realization is compared with the result of 2D plane strain model without reset process (one single calculation).

It can be noted that some very small gaps, relative gaps smaller than 0.5%, have been observed during the second test. No clear pattern or tendency has been found to explain these gaps. Given the values of the gap and the objective of Monte Carlo simulation (results to be used to quantify the level of squeezing during preliminary design), the author considers the reset procedure as valid.

The results of the Monte Carlo simulation are the radial strain and the plastic radius. The radial strain is used to improve the Hoek and Marinos curve while the plastic radius without support is used mostly in Chapter 4. It can be noted that the estimation of the plastic radius is not very precise because it depends on the size of the mesh. The plastic radius is calculated as the distance between the center of the tunnel and the plasticized mesh the furthest away.

3.3 Results

This section summarizes the results of the Monte Carlo simulation, their analysis and the comparison with the Hoek and Marinos curve. An analysis of the values of plastic radius is also presented allowing the creation of a surrogate model for an easy estimation.

3.3.1 Results of the Monte Carlo simulation: radial strain

The Monte Carlo simulation was carried out with 10 000 realizations. Although using rock mass strength as an input parameter would have reduced the scattering of results, it was decided, for the reasons mentioned above, not to use it as a chart parameter. Instead, the approach relies only on information coming from laboratory tests (σ_{ci}, m_i or MR) or from the geological investigation (GSI or σ_0). In order to reduce the scattering of results without using the rock mass strength, 3 modifications were made:

- A plot is created for each value of Modulus Ratio (200, 400 and 600). These values have been selected to cover a large range of rock types based on the guideline provided by Hoek and Diederichs (2006).
- For each plot, the curves associated with the iso-value of GSI are included
- In the x-axis expression of the H&M curve, the rock mass strength (σ_{cm}) is replaced by $\sigma_{ci}\sqrt{m_i}$.

The practical significance and choice of $\sigma_{ci}\sqrt{m_i}$ can be explained through Eq.(3-6) which may be used to calculate σ_{cm}. For any GSI value between 15 and 50, s is negligible compared to m_b ($m_b > 215 * s$) and a is approximately equal to 0.5, leading to the following expressions (Eq.(3-8) and Eq.(3-9)).

$$\sigma_{cm} \sim \sigma_{ci} \frac{(m_b - a\, m_b)\left(\frac{m_b}{4}\right)^{a-1}}{2\,(1+a)\,(2+a)} \qquad (3-8)$$

$$\sigma_{cm} \propto \sigma_{ci} * \sqrt{m_b} \qquad (3-9)$$

Then, the m_b parameter can be replaced in Eq.(3-9) by its mathematical expression based on the m_i parameter and the GSI (Hoek and Brown 2019), leading to Eq.(3-10):

$$\sigma_{cm} \propto \sigma_{ci} * \sqrt{m_i} * e^{\frac{GSI-100}{28*2}} \qquad (3-10)$$

The result of the Monte Carlo simulation, presented in Figure 3-12, demonstrates that for each fixed GSI value, replacing σ_{cm} by $\sigma_{ci}\sqrt{m_i}$ is an effective solution to significantly reduce the point scatter without introducing highly uncertain parameters.

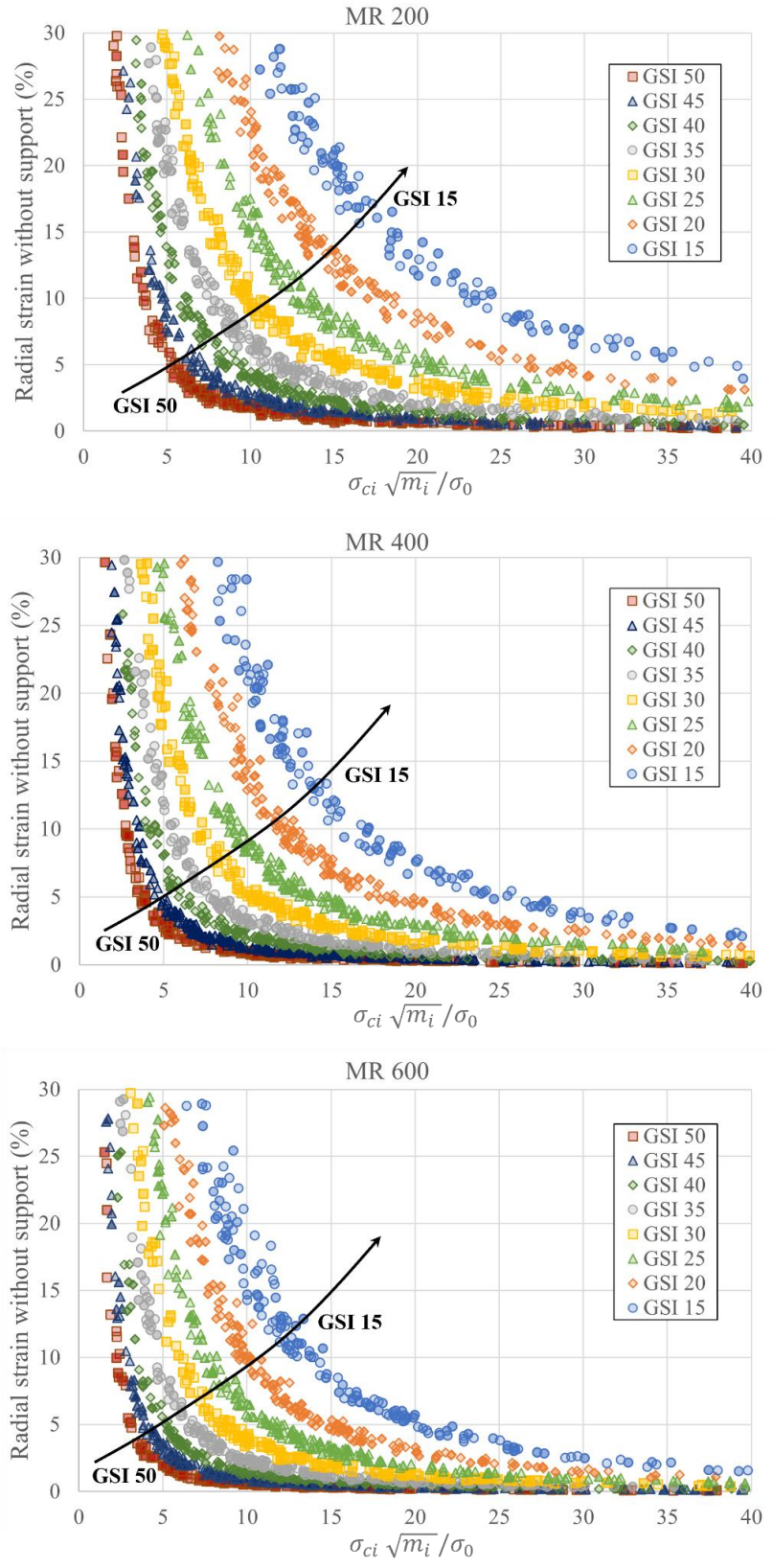

Figure 3-12: Numerical results of the radial strain without support for different values of MR and GSI

It is possible to fit a curve to each set of points based on an iso-value of GSI. Fits have been performed using the fitting module of Excel and another of Python. The fitting module of Python ("curve_fit" from "scipy.optimize") seems to lead to better results for large GSI while

the fit using Excel seems more appropriate for small value of GSI. An example is presented in Figure 3-13. There is a difference between these two fitting approaches because the method used to solve the optimization problem (calculation of the more appropriate fitting parameters) are different.

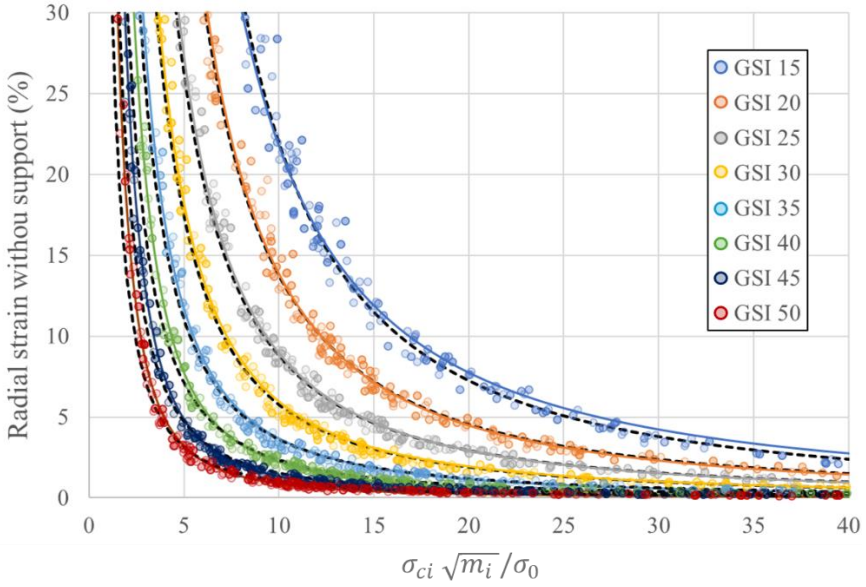

Figure 3-13: Comparison of the fits obtained with Excel and with Python for the results associated with a modulus ratio of 400; dashed curves are obtained with Excel; continuous curves are obtained with Python

The choice was made to keep the fitting curve that seems the more appropriate visually for each GSI set of points, i.e. the curve staying in the middle of the point cloud. In this situation, the fit associated with best least square value (R^2) does not always correspond to the visually more appropriate curve.

The 95% confidence interval can also be derived as twice the standard deviation of the relative gap between the fitting curve and the cloud of point. The inconvenience of this approach is that, for small values of radial strain, the relative gap can be very important even though the absolute gap is small (around a tenth of a percent). It can lead to large 95% confidence intervals. To reduce the impact of small values of radial strain, the confidence interval is calculated only by considering the radial strain higher than 1%.

3.3.2 Graphical representation

The final curves are presented in Figure 3-14, Figure 3-15and Figure 3-16. Each fitted curve is associated with the following mathematical expression:

$$\varepsilon_{usi} = A_i \left(\frac{\sigma_{ci}\sqrt{m_i}}{\sigma_0} \right)^{-B_i} \qquad (3-11)$$

where A_i and B_i are constants dependent on MR and GSI values. Table 3-3 presents the values and 95% confidence intervals.

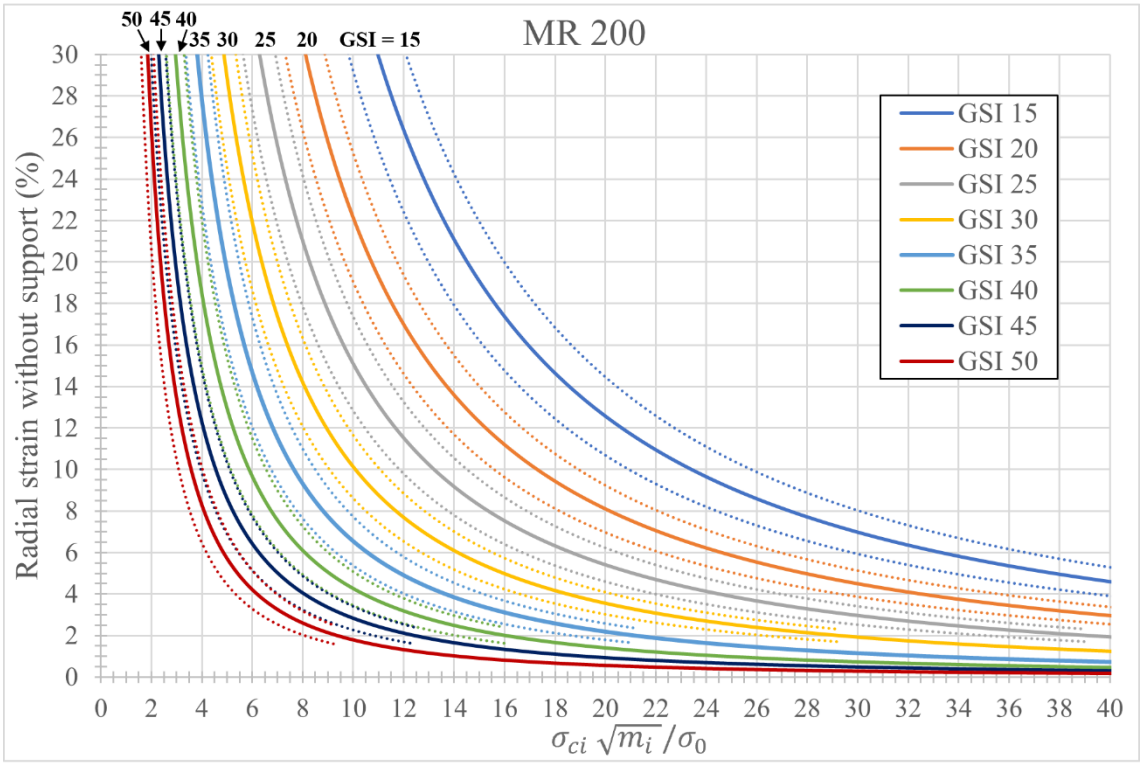

Figure 3-14: Interpolated curves of the radial strain without support for different values of GSI and for a Modulus Ratio (MR) of 200; the dotted lines present the 95% confidence interval for each GSI value

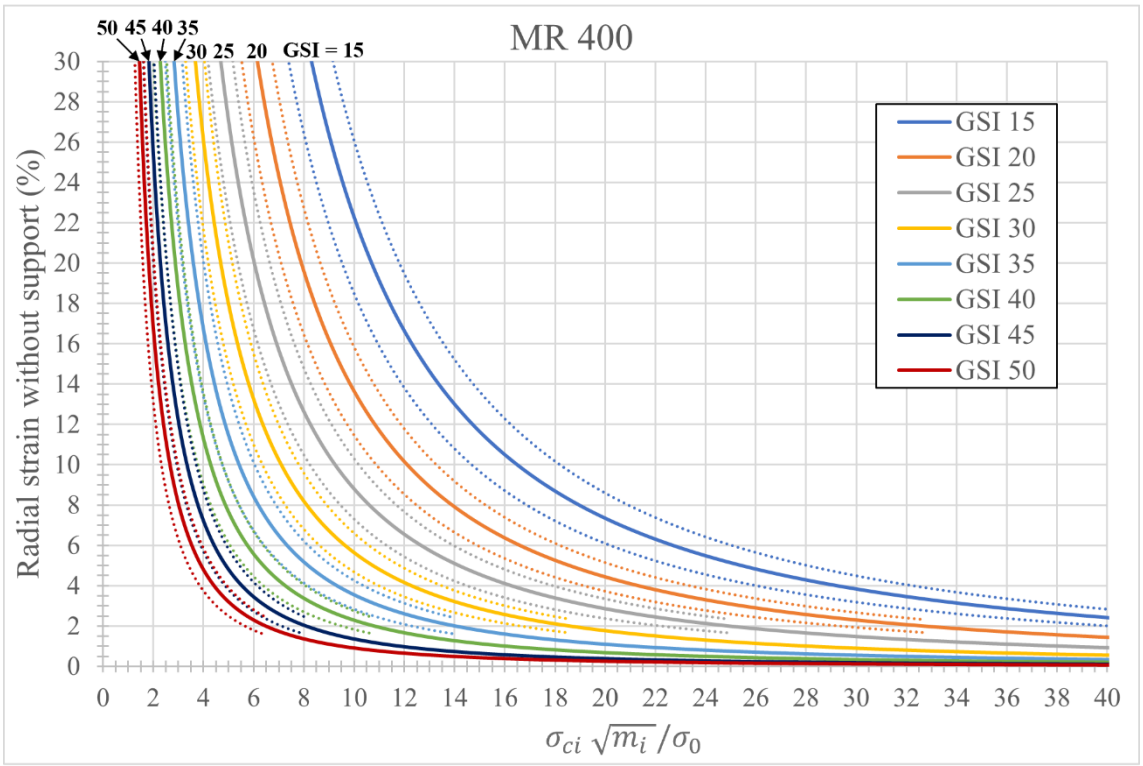

Figure 3-15: Interpolated curves of the radial strain without support for different values of GSI and for a Modulus Ratio (MR) of 400; the dotted lines present the 95% confidence interval for each GSI value

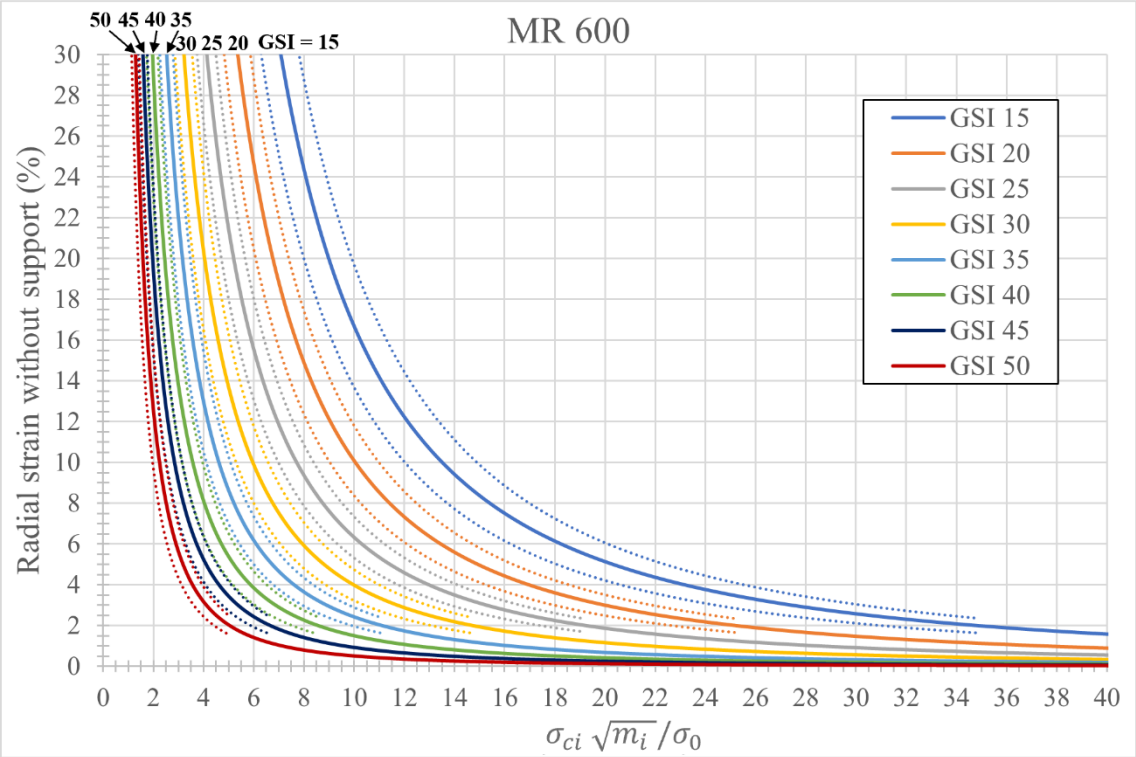

Figure 3-16: Interpolated curves of the radial strain without support for different values of GSI and for a Modulus Ratio (MR) of 600; the dotted lines present the 95% confidence interval for each GSI value

Table 3-3: Parameters A_i and B_i used to define the analytical formulation for the prediction of the radial strain without support ε_{usi} (equation 3-11) for different GSI and modulus ratios MR, and associated 95% confidence intervals (CI)

MR	GSI	A_i	B_i	CI 95%
200	15	968	1.45	+/- 0.15 ε
	20	624	1.45	+/- 0.14 ε
	25	456	1.48	+/- 0.15 ε
	30	328	1.51	+/- 0.15 ε
	35	249	1.58	+/- 0.18 ε
	40	170	1.60	+/- 0.19 ε
	45	113	1.60	+/- 0.20 ε
	50	84	1.67	+/- 0.22 ε
400	15	887	1.60	+/- 0.17 ε
	20	569	1.62	+/- 0.16 ε
	25	367	1.62	+/- 0.17 ε
	30	264	1.67	+/- 0.17 ε
	35	174	1.69	+/- 0.20 ε
	40	126	1.74	+/- 0.20 ε
	45	90	1.82	+/- 0.21 ε
	50	59	1.81	+/- 0.22 ε
600	15	836	1.70	+/- 0.18 ε
	20	567	1.75	+/- 0.17 ε
	25	364	1.76	+/- 0.16 ε
	30	240	1.78	+/- 0.19 ε
	35	164	1.83	+/- 0.19 ε
	40	104	1.84	+/- 0.21 ε
	45	72	1.89	+/- 0.21 ε
	50	50	1.99	+/- 0.23 ε

3.3.3 Comparison with the H&M curve

To compare the above results with those obtained by Hoek and Marinos (2000), it is necessary to go back to the graphical representation of Hoek and Marinos, which uses the rock mass strength as an input parameter. Eq.(3-5), as used by Hoek and Marinos, is applied to calculate this parameter. Figure 3-17 presents and compares the results of both studies, displaying four sets of information:

1. The results of the Monte Carlo simulation for each modulus ratio, presented by the points (circle, triangle and cross).

2. The fit trend curves of the above-mentioned points, for each modulus ratio, presented by the black curves ("MR … (numerical)").

3. The radial strain, for each modulus ratio, calculated using the closed-form analytical solution of Carranza-Torres and Fairhurst (1999), presented by the red curves ("MR … (analytical)"). The input data used are as identical as possible to those in the numerical calculations. The only differences lie in the yielding criteria and the hypothesis regarding the dilation angle. For the numerical calculations, the input parameter is α (ratio of dilation to friction), and the apparent friction angle is calculated automatically by the software depending on the confining stress of each element in the model. In the analytical calculations, the friction angle is determined using the expression proposed by Hoek *et al.* (2002), meaning that the dilation angle is constant for all confining stresses around the tunnel.

4. The Hoek and Marinos (2000) curve presented by the green curve ("H&M curve").

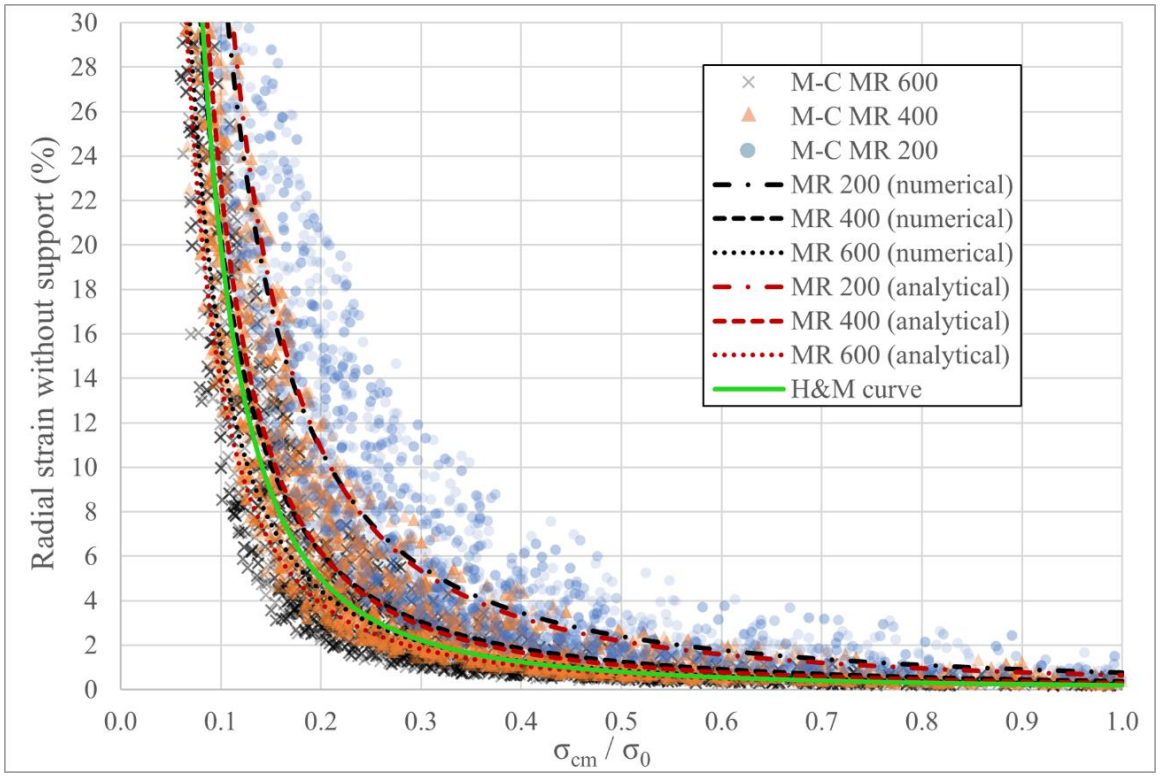

Figure 3-17: Comparison between the original H&M curve (green curve), the result of the Monte-Carlo simulation carried out with numerical calculations (points), the average fitting of this points (black curves) and the average fitting of the analytical calculations (red curves)

By comparing these curves, it is possible to draw some conclusions:

- Due to the rock mass strength as an x-axis parameter, the scattering of the Monte Carlo simulation results is quite important. The trend curves are used for the comparisons, but it is important to note that the scattering of the results of the Monte Carlo simulation around them is consequent, larger than the one obtained by Hoek and Marinos (2000) because of the modication of variation range of the input parameters.
- From a global point of view, the calculation technique (analytical or numerical) seems to have little influence on the results, as the trend curves from the numerical calculations (black curves) and analytical calculations (red curves) are closely aligned. Nevertheless, the point scattering around the trend curve is smaller for the analytical calculation than for the numerical calculation. The average coefficient of determination (R^2) obtained for the analytical calculation ($R^2 = 0.91$), based on the R^2 values of the trend curve for each modulus ratio, is higher than the one of the numerical calculations ($R^2 = 0.88$).
- The comparison of the red curves and the H&M curve (green) shows that the H&M results are similar to those given by the analytical model when the MR is taken between 400 and 600. Nevertheless, a discrepancy on the slope of the curves exists. For high x-axis value, the H&M curve is similar to the "MR 600 (analytical)" curve, but for small x-axis value, the H&M curve is close to the "MR 400 (analytical)" curve. The origin of this discrepancy lies on the modification of the hypothesis regarding the input parameters.
- The modulus ratio and consequently the Young's Modulus has a major influence on the estimation of the radial strain. For an x-axis value of 0.25, a MR of 600 leads to a radial strain of 3%, a MR of 400 leads to a radial strain of 4% and a MR of 200 leads to a radial strain of almost 8%. This impact was not considered by Hoek and Marinos (2000).

The recommendations provided by Hoek and Marinos (2000) are based on the value of the radial strain obtained and on their personal experience. These new sets of curves propose an adaptation of the methodology used to estimate the radial strain without support, meaning that the recommendations of Hoek and Marinos (2000) remain applicable in this context.

3.3.4 Results of the Monte Carlo simulation: Plastic radius

The plastic radius gives information about the size of the area around the tunnel in which the strength of the rock mass has been reached, and some plasticity has developed. From the Monte Carlo simulation, the plastic radius associated with each realization have been retrieved (Figure 3-18) and a surrogate model is created using multilinear regression considering the following input parameters: σ_{ci}, σ_0, m_i, MR, GSI, and the radial strain without support which can be estimated based on the result of section 3.3.1. It was decided to use multilinear regression model because it is the simplest method compared to nonlinear regression or neural network and the results obtained were satisfactory in regard of the framework of this study. The main focus is to provide relevant information to the engineers during an early stage of a tunnel design in which a very complex approach and very accurate results are not necessary because of the large uncertainties. The multilinear regression was performed with the software R.

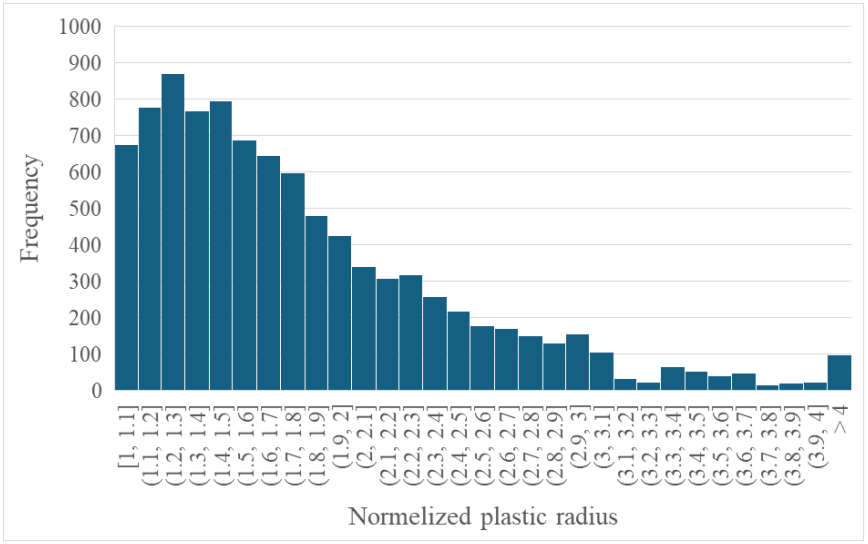

Figure 3-18: Histogram of the values of normalized plastic radius (R_p), normalized by the tunnel radius

The multilinear regression was performed on the natural logarithm of the plastic radius normalized by the tunnel radius. It is supposed that if no plasticity occurs in the model, the normalized plastic radius (Rp) is considered to be 1 and not 0 to allow a continuity in the transition between elastic behavior and elastic-plastic behavior. A Rp between 0 and 1 have no physical meaning as it corresponds to the excavated part of the tunnel. The surrogate model obtained is:

$$R_p = \begin{cases} e^{f(\sigma_{ci}\,,\sigma_0\,,m_i\,,MR,GSI\,,\varepsilon_{us}\,)} & if\ f(\sigma_{ci}\,,\sigma_0\,,m_i\,,MR,GSI\,,\varepsilon_{us}\,) > 0 \\ 1 & if\ f(\sigma_{ci}\,,\sigma_0\,,m_i\,,MR,GSI\,,\varepsilon_{us}\,) \leq 0 \end{cases} \qquad (3-12)$$

Where ε_{us} is the radial strain without support expressed in percentage (%) and f() is the function below:

$$f(\sigma_{ci}\,,\sigma_0\,,m_i\,,MR,GSI\,,\varepsilon_{us}\,) = -3.95 + 0.43\ \ln\left(\frac{\sigma_{ci}}{\sigma_0}\right) - 0.07\ \ln(m_i) + 0.48\ \ln(MR) + 0.026 * GSI + 0.46 \ln(\varepsilon_{us}) \qquad (3-13)$$

Figure 3-19 compares the results of the Monte Carlo simulation with the results of the surrogate model. The 95% confidence interval on the estimated value of the plastic radius is more or less 9% of this value: $[0.91\ R_p\ ;\ \ 1.09\ R_p]$.

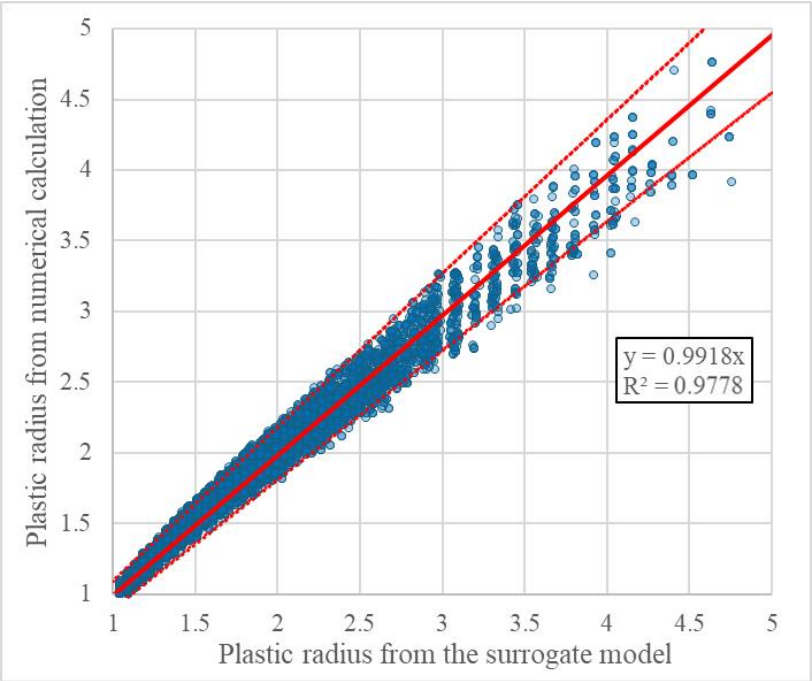

Figure 3-19: Comparison of the values of normalized plastic radius predicted with the surrogate model and the values obtained during the Monte Carlo simulation; the continuous line is the trendline and dash lines are the 95% confidence interval

To make the surrogate easier to use for engineers, it was transformed into a graphical representation allowing an estimation of the plastic radius directly from the input parameters. This chart is presented in Appendix 2.

3.4 Conclusion

This chapter provides a rapid overview of existing methods to quantify the potential of large radial deformation. One of the most widely used methods, the Hoek and Marinos (2000) curve, is precisely analyzed to highlight some of its shortcomings like the use of the rock mass strength as an input parameter which introduces unwanted uncertainty. To address this shortcoming, an improvement of this curve is proposed by performing a Monte Carlo simulation on a wide range of conditions. Compared to the Hoek and Marinos curve, this improvement covers a larger range of geological conditions and depends only on the results of laboratory tests (uniaxial compressive strength of intact rock, m_i parameter of Hoek and Brown, modulus ratio) and field investigation (in-situ stress state, geological strength index). Nevertheless, the recommendations provided by Hoek and Marinos (2000) are still valid with this improvement as they were dependent on the value of the radial strain without support.

With the performed Monte Carlo simulation, it was possible to calculate plastic radius corresponding to a variety of ground conditions. These data have been used to create a surrogate model based on multilinear regression. To make the model easier to use, a graphical representation is also proposed.

Chapter 4 - Support and rock mass interaction in highly fractured rock mass

Chapter Abstract: After identifying and quantifying the risk of large radial deformation, it is necessary to develop a relevant design regarding this risk. The technical solutions considered and thus the design is highly dependent on the amount of expected large deformation, and its impact on the support. During preliminary design, it can be difficult to correctly assess this interaction, as significant uncertainties exist regarding geological and geotechnical parameters. Moreover, the existing methods are either not well adapted or too complex to use.

This chapter aims to briefly present the technical solutions and the relevant designs to deal with large radial deformations. The classical calculation methods are also analyzed to highlight their shortcomings in the framework of this thesis. To compensate for their disadvantages, a new method is proposed. This method is based on the creation of surrogate models using the results of 2D axisymmetric numerical calculations performed on a wide range of geological conditions potentially associated with large radial deformation.

4.1 Existing approaches for tunnel design in squeezing ground

This section aims to briefly describe existing technical solutions to deal with large deformation in deep tunnels, as well as some calculation methods.

4.1.1 Technical solutions and design approach

The existing technical solutions to deal with large deformation during tunnel construction can be decomposed into two mains philosophies: the use of stiff support or yielding support.

The design philosophy behind these two approaches is very different. The first approach is associated with the installation of stiff and rigid supports close to the face to block the apparition of radial deformation. Stiff and rigid supports are necessary when the rock mass apply considerable pressure on it (no deformation allowed by this type of support). It can include thick shotcrete, rigid steel set or segmental lining depending on the excavation technique. For example, Hoek and Marinos (2000) have proposed these types of support in their recommendations.

Experience gained during the excavation of deep tunnels subjected to large radial deformation has shown that, in most cases, stiff supports are not well adapted to deal with this issue. This was evident, for example, during the construction of the Yacambu-Quibor tunnel, the Gotthard base tunnel, the Lötschberg base tunnel or Saint-Martin-La-Porte access adit. To avoid the overloading of the stiff support and its failure, yielding supports have proven to be a very effective technique as they allow the rock mass to deform while ensuring the safe working conditions during the excavation process. The yielding support can be implemented by introducing a layer of compressible materials between the excavation boundary and the extrados of stiff lining (Figure 4-1a) or through the use of yielding support elements (Figure 4-1b) (Cantieni and Anagnostou 2009a).

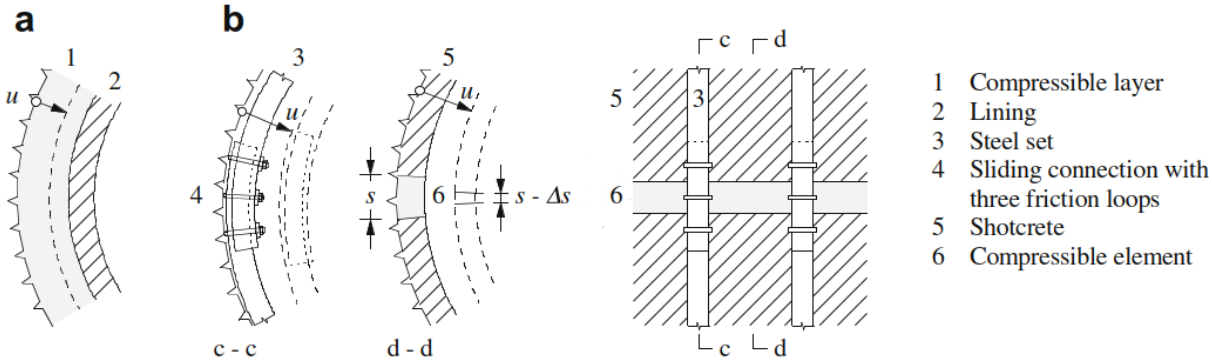

Figure 4-1: Basic types of deformable supports: (a) compressible layer between lining and excavation boundary; (b) yielding support with steel sets, shotcrete and compressible inserts (from Cantieni and Anagnostou 2009a)

A "yielding support" combines steel sets with sliding connections or deformable elements and, shotcrete in which a gap is created, or a yielding element is inserted, allowing the support to deform. Some classical yielding elements are presented in Figure 4-2. Yielding elements can also be used between pre-cast concrete segments as presented in Figure 4-3.

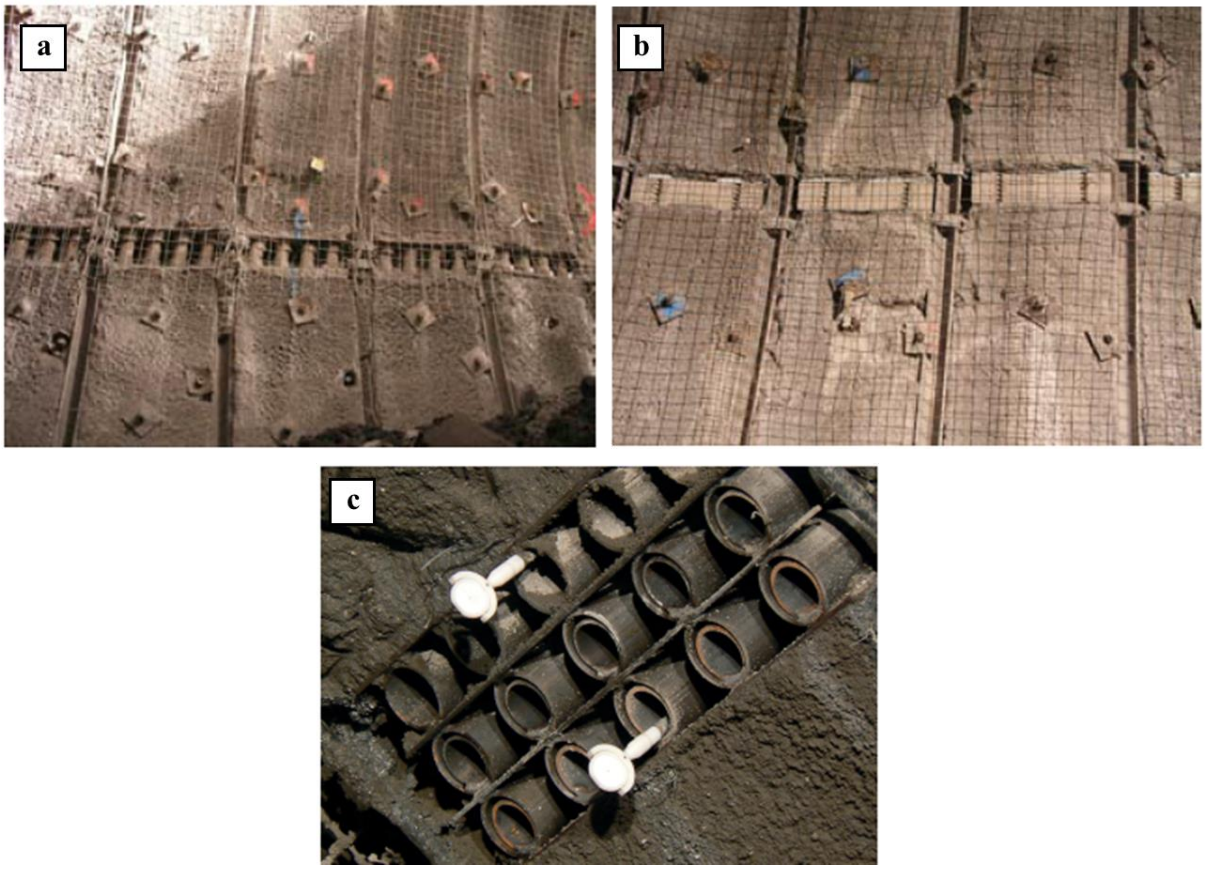

Figure 4-2: Example of yielding elements used in yielding supports: (a) Steel cylinder (Kovari 2009); (b) Highly compressible concrete element (Kovari 2009); (c) Wabe yielding element (Moritz 2011)



Figure 4-3: Pre-cast concrete segment including Meypo yielding elements in Ibbenbüren coal mine, Germany (from Moritz 2011)

For tunnelling conditions associated with large uncertainties and potentially large radial deformation, sequential excavations can be favorized combined with an observational approach. A preliminary tunnel/pilot tunnel is usually constructed with yielding support and possibly with face reinforcement. The use of yielding support combined with the observational method and extensive monitoring enables relevant back-analysis to determine the rock mass properties and to potentially fit complex behavioral laws including creep. The optimal distance to reprofile the tunnel can then be determined as well as the distance of installation of the support and the lining.

4.1.2 Calculation techniques during preliminary design

During the preliminary design phases, the objective is not to propose a definitive design with precise composition of the support, such as the type of steel sets and the precise thickness of the shotcrete or the lining. The idea is to prove the technical feasibility of the tunnel and to be able to choose the more appropriate technical solution for the tunnel construction (excavation technique, type of support, etc.) based on the available information. Most of the time, the preliminary design phase may not even require any calculations, since the existing recommendations — such as the Hoek and Marinos (2000) recommendations, or the more general recommendation of Bieniawski (1989), the Q-system (NGI 2013) or even those of the AFTES (GT7.R1.A2 – Choice of tunnel support) — may be sufficient. However, under squeezing conditions, these recommendations may not be relevant, and complementary studies can be necessary. For example, they refer only to stiff support, which, as presented above, are often unsuitable for dealing with large deformations.

The main question that engineers need to answer during preliminary design is whether or not a yielding support is necessary instead of stiff support? The answer to this question will provide essential information for selecting the excavation technique — such as whether to use TBM (which type?) or conventional excavation techniques — determining the required over-excavation, and for assessing the impact of uncertainties. All these points need to be considered to developpe an appropriate preliminary design.

In this section, four tools and methods are presented to try to answer the question above.

4.1.2.1 Method proposed by Jethwa et al. (1984)

Jethwa *et al.* (1984) linked the ground pressure on the support to various geotechnical parameters by using an analytical close form solution for a circular tunnel under lithostatic vertical stress and isotropic stress state. The mathematical expression used can be found in Barla (2001). The rock mass behavior is supposed to be elastic-brittle-plastic between the peak and the residual strength. A Mohr-Coulomb failure criterion is used, characterized by values of cohesion (C_p) and friction angle (ϕ_p) during the pre-peak and those of the post-peak phase (C_r and ϕ_r). They considered that the post-peak cohesion is equal to zero and that the post-peak friction angle is smaller than the pre-peak. The relationship between all these parameters is presented in Figure 4-4.

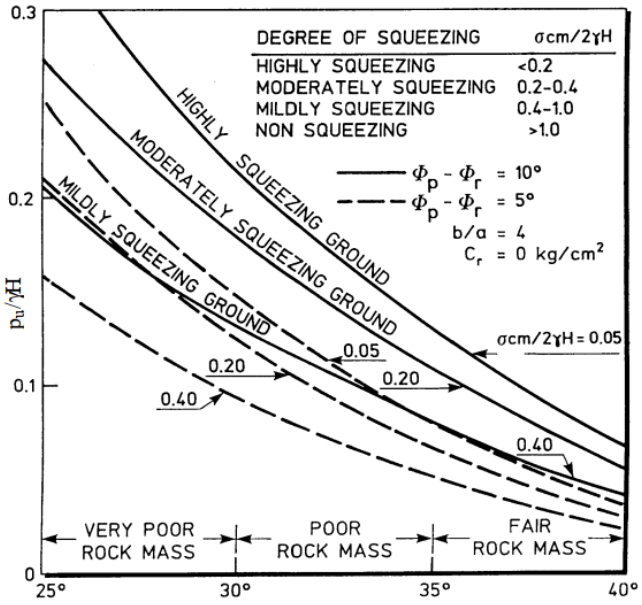

Figure 4-4: Approach proposed by Jethwa et al. (1984) to quantify the squeezing phenomenon and to estimate the pressure on the support (from Barla 2001); σ_{cm} is the rock mass strength; γH the lithostatic stress; p_u the ground pressure on the support; the x-axis is the pre-peak friction angle

Based on this approach, if the rock mass strength is equal to 10 MPa, the specific weight is 25 kN/m^3, the depth is 1000 m, the pre-peak fictional angle is equal to 30° and 20° at residual state, the degree of squeezing will be 0.2 and graphically, the ground pressure on the support would be equal to $P_u = 0.18\,\gamma\,H = 4.5\,MPa$. This approach is relevant, but it is based on highly uncertain parameters such as the rock mass strength (σ_{cm}), as discussed in Chapter 3.1.3.2, or the frictional angle of the rock mass (pre-peak and post-peak), which could make it difficult to use in practice.

4.1.2.2 The convergence-confinement method and associate

The Convergence-Confinement method (CV-CF) is an analytical approach that allows the radial strain of a tunnel and the ground pressure of the support to be estimated, based on the geological and geotechnical characteristics of the rock mass. This method is mainly used for the preliminary design of the support. However, the CV-CF has some shortcomings that lead to an underestimation of the ground pressure on the support and an overestimation of the radial strain at the support installation (Bernaud and Rousset 1992; Cantieni and Anagnostou 2009b; De La Fuente *et al*. 2019). Some improvements have been proposed in the literature to address these shortcomings, such as the "implicit" approach (Bernaud and Rousset 1992; Bernaud *et al.* 1994; Nguyen Minh and Guo 1996) or the AFTES (French Tunnelling and Underground Space Association) recommendation (AFTES – GT7 – Convergence-Confinement Method 2002).

The CV-CF method is based on three basic curves to link the confining pressure, the support behavior and the distance between the face and the support installation, henceforward referred to as span:

- GRC (Ground Reaction Curve): this curve links radial displacement to confining pressure, without any support.
- SCC (Support Characteristic Curve): this curve links the radial strain of the support to the radial pressure applied. It is only dependent on the support characteristics.
- LDP (Longitudinal Displacement Profile): this curve links radial displacement to the distance from the tunnel face.

Based on the LDP, it is possible to estimate the initial radial strain that occurs before the support installation. The final ground pressure on the support is then derived from the intersection of the GRC and the SCC, starting at the radial strain estimated with the LDP (Figure 4-5).

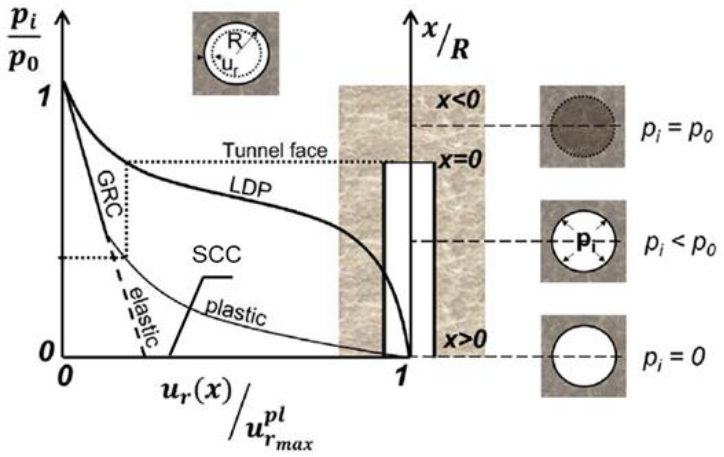

Figure 4-5: Theorical example of the three characteristic curves of the CV-CF method (adapted from Paraskevopoulou and Diederichs 2018); p_i / p_0 is the confining pressure normalized by the in-situ stress; x/R is the distance to the tunnel face normalized by the tunnel radius; $u_r(x) / u^{pl}_{r\,max}$ is the radial displacement normalized by the maximal radial displacement infinitely far from the face (i.e. no confining pressure)

A complete presentation of the CV-CF method and the "implicit" approach can be found in Appendix 1.

As highlighted in Appendix 1, the CV-CF method has two major limitations:

1) The CV-CF method is based on a simplifying hypothesis that supposes the support will not impact the rock mass behavior in front of it. It means that, no matter the type and characteristics of the support, the rock mass deformation will be identical between the face and the support, and in front of the face. This point explains why the radial strain at the support installation is overestimated, and why the ground pressure is underestimated in elastic and elastic-plastic rock mass behavior. The "implicit" approach was introduced to deal with this shortcoming. As presented in A 1.2.2, the "implicit" approach globally compensates these underestimations when the rock mass behavior is elastic.
2) When the rock mass behavior is elastic-plastic, the results of 2D axisymmetric numerical calculations (or 3D numerical calculations) do not lie on the Ground Reaction Curve (A 1.2.3). Cantieni and Anagnostou (2009b) explained the origin of this gap in their paper, a small synthesis is presented in A 1.2.3. The results of the axisymmetric calculation cannot be obtained with the CV-CF method as long as there is some plasticity occurring in the rock mass and when the support is not installed directly at the tunnel face. It is also the case for the implicit method, as its results can only be on the GRC.

During the design of a tunnel, safety factors are considered to reduce the strength of the support elements (design strength) and to increase the internal forces considered for the design of the support element. The partial safety coefficients are based on the Eurocodes and the national recommendations that allow the Eurocode to be adapted for tunnel design. The application of these safety factors increases the probability that the selected support can withstand real pressures exceeding those calculated. A 1.3 investigates the assumption that the discrepancies of the CV-CF are compensated, for classical tunnelling situations, by the use of safety factors,

which are typically applied alongside the method. When using this method, the obtained results show that the partial factors effectively compensate the discrepancies only for classical tunneling situations (small radial deformation). The "implicit" approach with safety factors compensates the discrepancies for most tunnelling situations, except stiff support install far from the face.

4.1.2.3 Nomogram of Cantieni and Anagnostou (2009a)

Cantieni and Anagnostou (2009a) developed a set of 20 nomograms to estimate the ground pressure on the support and the final radial displacement when a yielding support is considered in weak rock masses. They used 2D axisymmetric numerical calculations with a Mohr-Coulomb failure criteria on a wide range of situations. By performing dimensional analysis, Cantieni and Anagnostou (2009a) considered nine input parameters:

$$\frac{p(\infty)}{p_0} = f\left(\frac{u_y\, E_R}{a\, p_0}, \frac{f_c}{p_0}, \frac{p_y}{p_0}, \phi, \nu, \psi, \frac{e}{a}, \frac{a\, k_I}{E_R}, \frac{a\, k_{III}}{E_R}\right) \qquad (4-1)$$

Where:

- $p(\infty)$ is final ground pressure on the support far from the tunnel face
- p_0 is the initial in-situ stress (supposed isotropic)
- u_y is the radial displacement capacity of the yielding support
- p_y is the yielding pressure of yielding support (pressure at which the yielding support starts to yield and deform)
- E_R is the Young modulus of the ground
- ν is the Poisson ratio of the ground
- f_c is the uniaxial compressive strength of the ground (rock mass)
- ϕ is the frictional angle of the ground
- ψ is the dilation angle of the ground
- k_I is the stiffness of the yielding support before reaching the yielding pressure (p_y)
- k_{III} is the stiffness of the stiff support
- e is the unsupported span (between the face and the yielding support installation)
- a is the tunnel radius

To develop their nomograms (4 of them are presented in Figure 4-6), the Poisson ratio of the ground is supposed to be constant ($\nu = 0.3$), the dilation angle depends on the friction angle (ψ = max(0, ϕ-20°)), the ratio e/a is 0.25, and $a\, k_I/E_R = a\, k_{III}/E_R = 4$. The values for the friction angle (ϕ) are {15; 20; 25; 30; 35}. The values of the normalized yielding pressure (p_y/p_0) are {0; 0.02; 0.04; 0.08}. The values of the normalized uniaxial strength of the ground (f_c/p_0) are {0.05; 0.10; 0.15; 0.20; 0.30; 0.50}.

For example, if the friction angle is 20°, the depth is 1000 m (p_0 = 25 MPa), the rock mass strength is f_c = 7.5 MPa (f_c / p_0 = 0.3), the tunnel radius is a = 4m, the rock mass Young's modulus is E_r = 1 GPa, the capacity of the yielding support is u_y = 0.2m (Uy = 2) and the yielding pressure is 500 kPa (p_y/p_0 = 0.02). Figure 4-6 provides a $p(\infty)/p_0$ = 0.1, leading to a ground pressure on the support far from the face of $p(\infty)$ = 2.5 MPa.

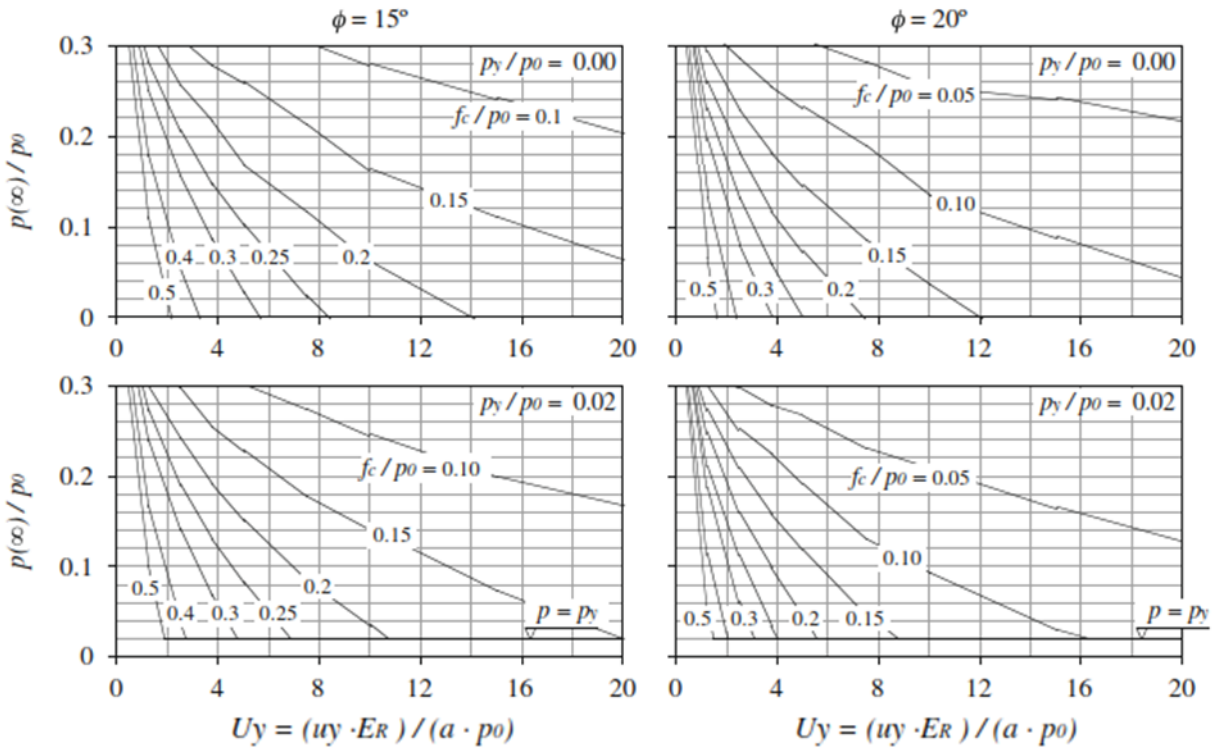

Figure 4-6: 4 nomogram of Cantieni and Anagnostou (2009a) considering the normalized ground pressure $p(\infty)/p_0$ as a function of the normalized yield radial displacement $((u_y\ E_R)/(a\ p_0)$ and the normalized uniaxial strength of the ground f_c/p_0 for friction angle ϕ= 15° and 20° and for normalized yield pressures p_y/p_0 = 0 – 0.02

4.1.2.4 Numerical calculations

The design of deep tunnel associated with potential large radial deformation can also be performed using numerical calculations. There are two main types of numerical calculations: the 2D plane strain numerical calculations (vertical cross-section of the tunnel) and the 3D numerical calculations. The 2D axisymmetric numerical modelling (longitudinal section of the tunnel) is a simplified approach of the 3D numerical modelling. The axisymmetric calculation is faster than 3D numerical approach and for the following hypothesis, the results are similar:

- The tunnel is circular.
- The initial principal stresses in the cross-section of the tunnel are isotropic. The third stress along the tunnel direction can be different.
- The rock mass is isotropic, or the geological layers are vertical (rock mass with a vertical fault zone for example).

2D plane strain numerical modelling is based on the same principles as the CV-CF method. First the radial strain at the support installation is estimated, then the associated confining pressure and finally the support loading at the equilibrium are computed. Supports are installed at a proper time in the model, depending on the deconfinement rate. The deconfinement rate is a numerical parameter allowing the diminution of the confining pressure at the boundary of the tunnel excavation. It varies between 0%, when the tunnel has not yet been excavated, and 100%, for sections of the tunnel far behind the excavation face. It allows the three-dimensional tunnel excavation process to be modelled in a 2D plane strain model. The deconfinement rate is calculated using the same curves as the CV-CF method, the GRC and the LDP, but the SCC is replaced by the numerical model. Often, the LDP is not even calculated, and the charts of Vlachopoulos & Diederichs (2009) are used instead.

The axisymmetric numerical calculation is more time-consuming than the CV-CF method, but it allows an explicit representation of the interaction between the support and the progress of tunnel excavation. It leads to a better estimation of the radial strain at the support installation and the final ground pressure on the support (Cantieni & Anagnostou 2009b, De La Fuente Mata *et al.* 2019).

3D numerical models are not restricted to the hypothesis of the 2D axisymmetric model but are even more time-consuming. They allow noncircular tunnel geometry (and tunnel intersections), anisotropic stress state and the introduction of sub horizontal geological layers.

One important advantage of numerical calculations is the possibility of using complex constitutive models for the rock mass and failure criterion. Creep can also be considered allowing more precis analysis or relevant back analysis during the tunnel excavation. Several rheological models and constitutive models have been developed or are directly included in numerical softwares. For deep tunnel in weak rock masses, it is possible to mention the CVISC rheological model (FLAC 8.0 Manual), the elastic-plastic visco-plastic L&K model (Laigle 2004; Kleine 2007), the elastic visco-plastic model VIPLA (Pellet *et al.* 2005), the elastic visco-elastic visco-plastic model of Sterpi and Gioda (2007), the elastic-plastic visco-plastic model SHELVIP (Debernardi 2008), the visco-elastic visco-plastic model FDVP (Kabwe *et al*. 2020c), and other. These models and laws are not presented in this thesis because they are not relevant for preliminary deep tunnel designs as they need many input parameters which are difficult or impossible to obtain in early stages of a tunneling project.

4.1.2.5 Limitations of existing approaches regarding the framework of this thesis

All these design approaches have some advantages and shortcomings:

- The CV-CF method is a comprehensive approach, easy to apply, for the estimation of the ground pressure on the support and radial displacements. Nevertheless, it is not adapted for deep tunnel in weak rock mass, in which significant plasticity develops around the tunnel even though its ease of use makes this method relevant for uncertainties introductions and propagations.
- The nomograms of Cantieni and Anagnostou (2009a) enable an easy estimation of the ground pressure on the support with yielding support and enable the design of the yielding support so that the rigid support is not overstressed. They cover a large range of situations. The use of these nomograms without yielding support is not straight forward. It is possible to consider no confining pressure, but it is not possible to modify the value of the unsupported span or to transform the amount of radial displacement into a specific span value (example, if 0.1m of radial displacement is allowed, it is not possible to calculate the corresponding value of span). These nomograms are also based on highly uncertain parameters like the rock mass strength or the frictional angle, and since the analytical expressions of the nomograms are not provided, it is very difficult or even impossible to use the graphical nomograms for introduction and propagation of uncertainties.
- Numerical calculations can provide all the necessary information for the tunnel design but are time-consuming and can be difficult to use during preliminary design, as it is an iterative process. They are mostly used to justify the final design or to perform back-analysis during which more data is available (geological and geotechnical conditions, field observations and monitoring). For the same reason, it is very difficult or impossible to introduce and propagate uncertainties with these methods.

Within the framework of this thesis and by the author's knowledge, there is currently no method completely adapted to preliminary design in highly fractured rock mass that directly accounts for the interaction between the support and the rock mass behavior and allowing an explicit consideration of uncertainties. The development of such a method will be the main objective of this chapter and will be presented in the following sections.

4.2 New approach for preliminary design

The main idea of this new approach is to be able to consider explicitly the interaction between the support and the rock mass during preliminary design, as well as allowing an easy introduction and propagation of the uncertainties. As discussed above, the interaction between the support and the rock mass can be performed using only numerical calculations (2D axisymmetric or 3D models). At the same time, numerical calculations are not adapted for the introduction and propagation of uncertainties because they are very time consuming.

It has been decided to simulate many situations of deep tunnel in highly fractured rock mass using 2D axisymmetric numerical calculations to collect the relevant data over a large range of input parameters. These data are then used to create surrogate models (transformation of these data into a mathematical formulation) for which the introduction and propagation of uncertainties is easy and quick, allowing also the use of reliable approaches (calculation of failure probabilities). As these mathematical formulations can be complex and so they are adapted into graphical representations to be easy-to-use during preliminary design (deterministic calculations).

During the preliminary design in highly fractured rock masses, engineers need information which allows them to propose relevant excavation methods and sequences, the tunnel radius and shape, the type of support and potentially some specific technical solutions. Three basic information have been considered in this work (Figure 4-7):

1) The ground pressure on the support far from the face (P_i) to analyze the type of support or lining to use (rigid or yielding?), and some basic characteristics like an estimation of thickness (if shotcrete or concrete) or compatibility with various type of steel sets, for example.
2) The second information is the radial strain between the face and the support ($\varepsilon_{f\text{-}s}$). This information is very important for the estimation of the tunnel excavation radius, combined with the thicknesses of the support and lining, to respect one of the major design constraints: the final internal radius of the tunnel.
3) The last information that is deemed relevant here is the radial strain at the face (ε_{SF}). This information is not directly used for the design because it does not affect the excavated radius: the radius excavated is the expected one, if some radial strain occurs in front of the face, it will not impact this radius as the deformation has already occurred. This information provides engineers with an indication of how much deformation the rock mass has already sustained at the face. The real behavior of the rock mass is not perfectly plastic (for most situations) and so the more deformation it has sustained before the face, the smaller its strength is (assuming the peak has been reached).

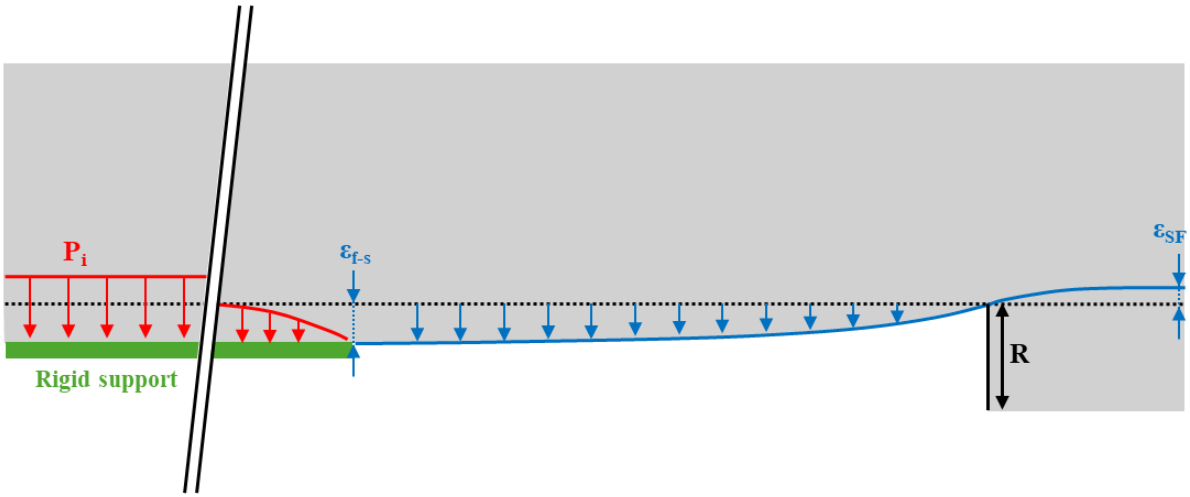

Figure 4-7: Output parameters considered in the axisymmetric numerical calculation; P_i the ground pressure on the support far from the face; $\varepsilon_{f\text{-}s}$ the radial strain that develop between the face and the support; ε_{SF} the radial strain that develop before the face

In this thesis, it was decided not to include the face deformation as a design parameter since this parameter does not directly impact the design. In highly fractured rock mass, to ensure the face stability, face reinforcements are generally considered for safety reasons during traditional excavation techniques (drill and blast or point-attack mechanical excavation), or top-bench excavation method (not full-face excavation) can be used. These face reinforcements are designed with specific approaches without using 2D or 3D continuous modelling. For TBM excavation, face extrusion impacts mostly the volume of material being excavated.

4.2.1 Developed numerical model

To perform the numerical calculations, it was preferred to use a 2D axisymmetric model compared to a 3D model. 3D models are relevant for noncircular tunnel geometry, anisotropic stress state and complex geological formation. As the work performed in this thesis focuses on preliminary design, simplifying assumptions have been made enabling the use of 2D axisymmetric model which are quicker to run.

As it is presented in Figure 4-8, the axisymmetric model used measures 35 R x 15 R (tunnel direction x perpendicular to the tunnel). The tunnel is circular, and the radius is considered to be constant with R = 5 m. This hypothesis (constant radius value), identical to the one made for the 2D plane strain model and discussed in Chapter 3.2.1, is relevant because all the results are expressed independently from this parameter: the radial deformation is expressed in radial strain (percentage), the plastic radius in a number of radii, the support is characterized by its stiffness (presented in Appendix 1, Table 1-a). Several tests have been performed on 2D axisymmetric numerical model with support to validate this independence. The tunnel is excavated over 25 R and the excavation is carried out step-by-step, and each excavation step is 0.1 R. For the calculation, the large strain hypothesis is considered. The dimensions of the model and the mesh density have been optimized so they have a limited influence on results for radial strain up to 40% without support. The model size is similar to the one used by Tristani *et al.* (2024b).

It can be noted that the mesh size far from the tunnel was optimized while avoiding the introduction of interface because in some situations, numerical problems appear at the interface during the computation when the large strain hypothesis is used.

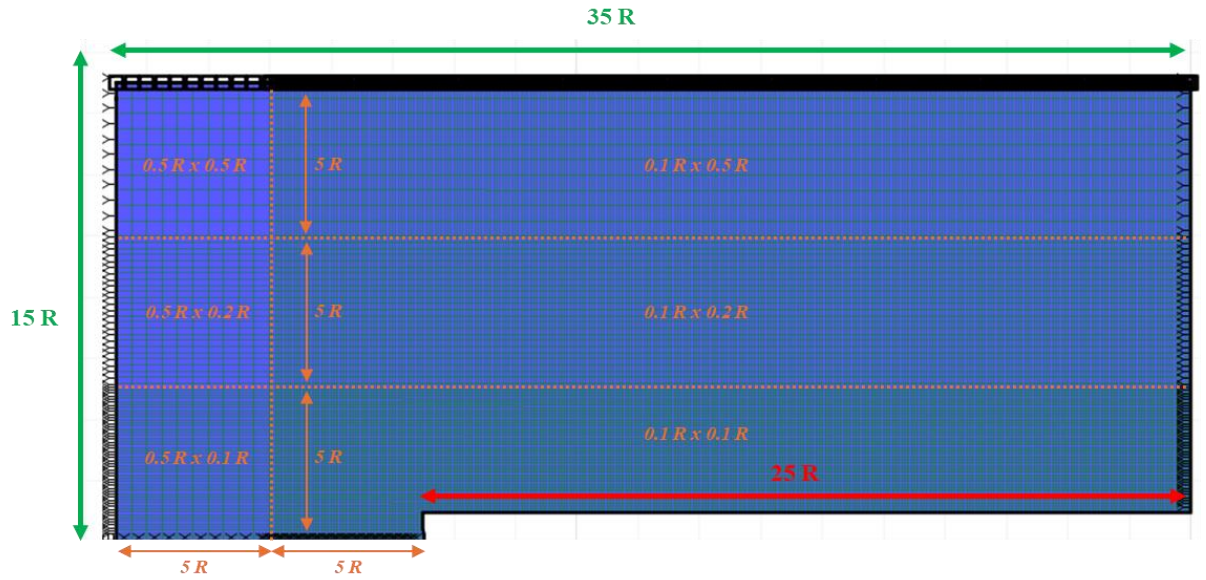

Figure 4-8: Measurement of the 2D axisymmetric numerical calculation used; the orange values are the size of the mesh in the various sections of the model

To avoid boundary effects at the extremity of the model, the results associated with infinitely far from the face are taken at a distance of 20 R from the face. In all the performed tests, no increase of the radial strain without support and ground pressure on the support has been observed between the 15R and 20R.

Two approaches have been tested to model the support. The first one uses the structural elements "shell" directly available in the Flac software while the second one uses volumetric elements with a linear elastic behavior. For similar radial stiffnesses, both methods lead to similar results. The retrieval of the results was easier using the FISH language with volumetric elements. On the Flac version used (FLAC 2D 8.0), some problems occurred when trying to retrieve results for "shell" elements using FISH language (probably because of the unavailability of the suitable packages in the version used), making it impossible to automatize the calculation. Thus, for practical reasons, it was chosen to use volumetric elements to model the support.

As explained in Section 4.2.2, the only input parameter considered for the support is its stiffness (k), From this parameter, the value of the Young modulus of the volumetric element (E_s) can be deduced using the simplified formulation for a thin ring-shaped support (Barla 2001):

$$E_s = \frac{k * (1 - \nu_s{}^2)\, R_{mean}}{t_s} \qquad (4-2)$$

Where ν_s is the Poisson's coefficient, considered to be 0.2 in the calculation, R_{mean} is radius associated with the mean of the support thickness and t_s the thickness of the support. In this model, the thickness of the support corresponds to one mesh, 0.1 R.

It can be noted that the stiffness of the support (k) corresponds to a "theoretical" value which considers the external radius of the support to be equal to radius of the excavated tunnel. This hypothesis is relevant when using small strain hypothesis as the grid points are not modified during the calculation. For a large strain hypothesis, some radial displacements occur in front of the face and between the face and the support installation, leading to a modification of the

grid point positions and a diminution of the tunnel radius when the support is installed. The "real" stiffness (k_{real}) of the support is then higher than the theoretical one (k_{theo}), but can be obtained only afterward as the stiffness influences the radial displacement at the support installation … For example, if a radial displacement of 0.1m occurs in the model presented in Figure 4-8, k_{real} is 2% higher than k_{theo} ($\frac{k_{real}}{k_{theo}} = \frac{4.75}{4.75-0.1}$), while if the radial displacement is 1m, k_{real} is 27% higher than k_{theo} ($\frac{k_{real}}{k_{theo}} = \frac{4.75}{4.75-1.0}$). To simplify the use of the approach developed here, the choice was made to keep this "theoretical" stiffness value as the support parameter.

Figure 4-9 presents the axisymmetric model including the support. It can be noted that a transitioning material is used (in green) between the face and the support. This material has a very low Young modulus, around 1 kPa, compared to the Young modulus of the rock mass and the support (higher than 100 MPa). As the Young modulus is very low, the confining pressure applied is insignificant, but it is very important for the calculation with the large strain hypothesis. When a mesh is deactivated and then reactivated, the point coordinates are the same as at its deactivation (except if the point is also associated with another mesh element which was not deactivated). It means that, if the radial displacement is consequent, the reactivated mesh can be "in" the ground, leading to a mesh superposition and potentially an impossibility to continue the calculation (calculation error). Considering this transiting material is then essential for the automatization of the calculation and to allow an update of the point coordinate of the support element through the span.

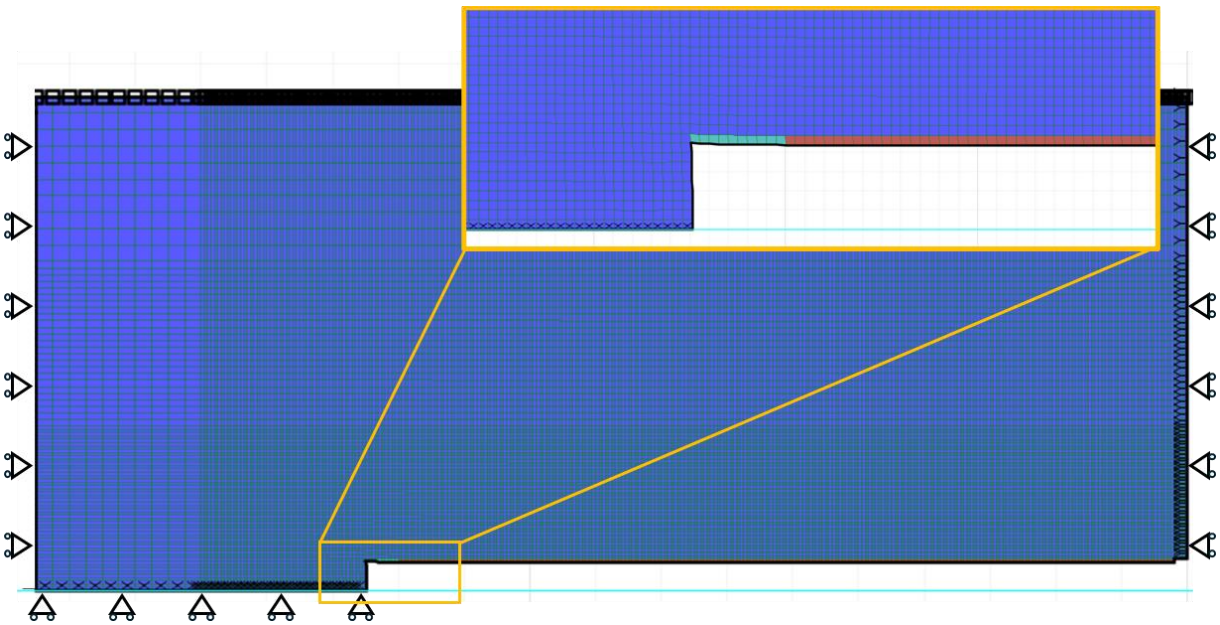

Figure 4-9: Axisymmetric model including the support; the support is in red, installed at 1 R from the face; in green, it is a transiting material with a very low Young modulus

The main result associated with this axisymmetric model is the estimation of the ground pressure on the support far from the face (at a distance of 20 R from the face). Two approaches have been tested to model the support. The first one uses the structural elements "shell" directly available in the Flac software while the second one uses volumetric elements with a linear elastic behavior. These two approaches have been compared with 2D axisymmetric calculations and lead to similar results for identical support stiffnesses. The use of a single volumetric element (though the thickness), as presented in Figure 4-9, is a simplification that is relevant to estimate the ground pressure on the support, but does not allow an estimation of the longitudinal

bending moment or a precise estimation of the radial strength in the support, which are not the targeted parameters. To perform a precise estimation of the internal forces in the support, a more accurate model needs to be used, with several volumetric elements though the thickness.

As the objective is the estimation of the ground pressure at the interface between the support and the ground. This value cannot be directly obtained with the numerical calculations as the Flac software provides only the mean stresses in a volumetric element, and not the stresses at the interface. Even if the support is modelled using several volumetric elements (though its thickness), the best estimation of the radial stress at the interface (i.e. the ground pressure) is the mean radial stress of the external volumetric element of the support, which is still an approximation. Furthermore, to model the support with enough volumetric elements (at least 5 though its thickness), leads to an important increase in the calculation time as the meshing needs to be much thinner. So, it was decided to deduce the ground pressure on the support from the mean orthoradial stress in the volumetric element. This approach has been tested and validated through several 2D axisymmetric numerical calculations. So, in this study, the ground pressure on the support is calculated based on the orthoradial stress in the support element with the following equations:

$$P_i = \frac{\sigma_{\theta\, s} * (R_{ext}^2 - R_{int}^2)}{2 * R_{ext}^2} \qquad (4-3)$$

Where R_{ext} is the external radius of the support, R_{int} is the internal radius of the support, and $\sigma_{\theta\, s}$ is the orthoradial stress in the support element.

Two other results are saved after the axisymmetric calculation with the support: the radial strain at the support installation and the radial strain at the face.

The unsupported span (e, express in radius) is the distance between the face and the support installation. Considered values of e are between 0.1 Radii and 3 Radii. The algorithm used for the excavation process is as follows (j is the iteration number of the step-by-step method, where each step corresponds to an excavation over a distance of 0.1R).

1) For the four first steps: $j \leq 4$ (excavation until 0.4R): #to avoid localized boundary effect, no support
   a) Deactivation of the ground corresponding to a step of tunnel excavation
   b) Computation of the equilibrium
2) For steps $4 \leq j \leq 4 + 10e$ (excavation until 0,4R + e): #unsupported span with transitioning material
   a) Deactivation of the ground except the last mesh in contact with the tunnel boundary
   b) Modification of the properties of the last mesh (from ground to transitioning material)
   c) Computation of the equilibrium
3) For steps $4 + 10e \leq j \leq 250$ (excavation until 25R): #classical support and tunnel excavation
   a) Deactivation of the ground except the last mesh in contact with the tunnel boundary
   b) Modification of the properties of the last mesh (from ground to transitioning material)
   c) Modification of the properties of the last transitioning mesh at e from the face (element k-10e) from transitioning to support material
   d) Computation of the equilibrium
4) Retrieval of the relevant results

The calculation time of the axisymmetric model is between 40 min and 1 hour depending on the geological conditions.

4.2.2 Input parameters for the database

The input parameters considered for the creation of the database are identical to these used for the improvement of the Hoek and Marinos curve (Chapter 3.1.3.1), reminded in Table 4-1.

The support is characterized by two parameters: its stiffness (k) and the unsupported span (e) which is the distance between the face and the support installation.

Table 4-1 : Properties and range of values used in the following study; USC the uniaxial compressive strength of the intact rock; m_i a parameter of the Hoek and Brown yielding criteria

Properties	Considered values
In-situ isotropic stress (σ_0)	[5 ; 40] MPa
UCS (σ_{ci})	[10 ; 110] MPa
m_i	[$m_{i\,min}(\sigma_{ci})$; $m_{i\,max}(\sigma_{ci})$]
Modulus Ratio (MR= σ_{ci}/E_i)	{200 ; 400 ; 600}
Geological Strength Index (GSI)	[15 ; 50]
Dilation-to-friction ratio α ($\psi = \alpha\,\varphi$)	[α_{min}(GSI) ; α_{max}(GSI)]
Radial stiffness (k)	[0.1 ; 10] GPa
Span (e)	[0.1 ; 3] Radii

Unlike the 2D plane strain numerical model performed in Chapter 3, the axisymmetric model is much more time consuming and so a direct Monte Carlo simulation is not an option. Two databases are created, one to train the surrogate model (called the "training base", 1000 axisymmetric numerical calculations with support) and one to validate the surrogate model (called the "validation base", 600 axisymmetric numerical calculations with support). To define the input parameters associated with these databases, a more advanced sampling method is used, based on the Latin Hypercube.

The training base is composed of 100 geological situations. For each situation, 11 axisymmetric calculations are performed, one without support to calculate the radial strain and the plastic radius far from the face, ten with support. Two stiffnesses were randomly chosen for the support, one between 0.1 GPa (corresponding to HEA100 steel sets every meter, in a 4m tunnel radius, Table 1-a) and 1.0 GPa (20 cm thick shotcrete in a 2m tunnel radius, or HEA300 steel sets every meter, in a 3m tunnel radius), one between 1.0 GPa and 10 GPa (60 cm thick concrete for a 2m radius tunnel). Each stiffnesses is associated with five values of span e: 0.1R, 0.5R, 1R, 2R, 3R.

The validation base is similar except for the values of span. Only three spans are considered and are randomly chosen between 0.1R et 0.4R, 0.4R and 1.5R, 1.5R and 3.0R.

Geological situations are obtained from an approach similar to a Latin Hypercube, but with one major constraint. All situations need to lead to radial strain without support smaller than 40% to stay in the validity range of the axisymmetric numerical model. To ensure the respect of this constraint, the following procedure is used:

1) Sampling of the input parameter based on the Latin Hypercube and creation of a list of 100 values of σ_{ci}, σ_0, GSI and MR. The GSI values are fixed {15, 20, 25, 30, 35, 40, 45,

50} with 12 or 13 apparitions of each. Similarly, the MR values are also fixed {200, 400, 600} with 33 or 34 apparitions of each.

2) Draw of the geological situations:
   a) Draw of a random value of σ_{ci}, σ_0, GSI and MR in the associated list. Draw of a random value of m_i and α, depending on the condition presented in Table 3-2 and Chapter 3.1.3.1.
   b) Estimation of the radial strain without support using the improvement of the Hoek and Marinos curve presented in Chapter 3.3.2
   c) If the estimated radial strain is smaller than 40%, the set of input parameters is stored as a geological situation, and the values of the input parameters are erased from the list. In this case, a new random draw is performed (back to step a). If the condition is not fulfilled the set of input parameters is not stored, and back to step a) (limited to 10 000 iterations).

As this procedure does not always lead to 100 situations with radial strain smaller than 40%, a limit is fixed at 10 000 iterations. This procedure has been launched several times to obtain various sets of geological situations respecting the constraint. The set with the best coverage of the range of radial strain was conserved. To avoid overrepresentation of small radial strain, the Latin Hypercube sampling for σ_{ci} is performed on two intervals: 67 values between 10 and 60 MPa and 33 values between 60 MPa and 110 MPa. A high value of σ_{ci} is also associated with possibly high value of m_i, and more probably to smaller value of radial strain. The set considered for the training base is presented in Figure 4-10. Its main advantage is to properly cover the range of radial strain without support. One third of the situation leads to a radial strain smaller than 5%, then the coverage of radial strain values decreases progressively.

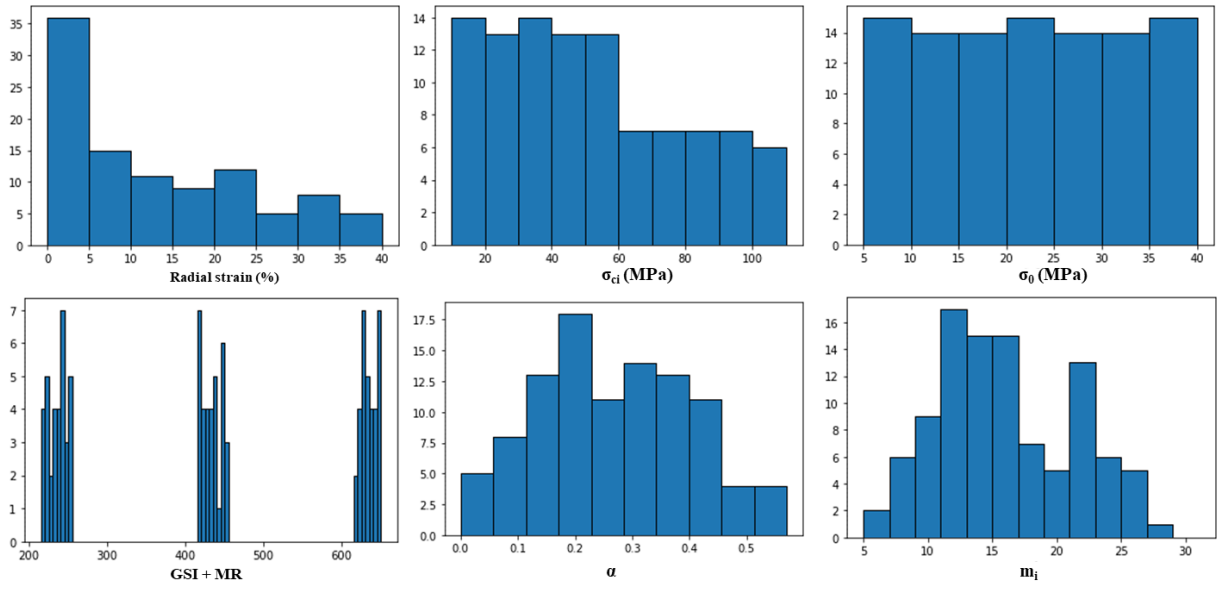

Figure 4-10: Histogram of the input parameters of the 100 geological situations of the training base; GSI + MR is the sum of the GSI value and the MR value

4.2.3 Creation of the surrogates models

After the computation of the training and validation databases, the objective is to use the results to develop surrogate models in order to estimate the ground pressure on the support far from the face (P_i), the radial strain between the face and the support installation ($\varepsilon_{f\text{-}s}$), and the radial strain at the face (ε_{SF}). The initial input parameters, as presented in Table 3-1, are the uniaxial

compressive strength of the intact rock (σ_{ci}), the isotropic in-situ stress state (σ_0), the m_i parameter of Hoek & Brown for intact rock, the geological strength index (GSI), the modulus ratio (MR), the stiffness of the support (k) and the span (e). For the surrogate models, two other parameters are also used: the radial strain without support (ε_{us}) and the plastic radius without support (R_p) far from the tunnel face. They are obtained with the first axisymmetric calculation (the one without support). They can also be estimated with the improvement of the Hoek & Marinos curve (Chapter 3.3.2) and the surrogate model presented in Chapter 3.3.4.

In this section, different surrogate models are compared using the coefficient of determination (R^2) obtained by plotting in x-axis the "real" value (obtained with the axisymmetric numerical calculation) and in y-axis the "estimated" value (obtained with the surrogate model). For a perfect surrogate model, the equation of the trend curve is y = x and $R^2 = 1$.

95% confidence intervals are also calculated for each tested surrogate model, based on the standard deviation of the relative gap between the estimated result (X_{est}) and the real results (X_{real}). The relative gap is defined as:

$$Relative\ gap\ (\%) = \frac{X_{real} - X_{est}}{X_{real}} \qquad (4-4)$$

By supposing that the distributions of these relative gaps are normal (hypothesis proven to be relatively relevant during the later analysis), the 95% confidence interval for an estimated value is defined as:

$$CI_{95\%}(X_{est}) = \left[\mu_{rgp} - 1.96\ \sigma_{rgp}\ ;\ \mu_{rgp} + 1.96\ \sigma_{rgp}\right] *\ X_{est} \qquad (4-5)$$

Where μ_{rgp} is the mean value of the relative gap and σ_{rgp} is the standard deviation of the relative gap.

It can be noted that, for specific surrogate models, the use of the absolute gap has been preferred for the 95% confidence interval.

4.2.3.1 Preliminary tests

The main issue is choosing the appropriate method to develop the surrogate model. Three methods are tested: the simplest one based on multilinear regression, basic neural networks, and nonlinear regression with genetic algorithms. These tests are performed only for the estimation of the ground pressure on the support.

The best regression obtained with a multilinear approach is:

$$\begin{aligned}\ln(P_i) = {} & 4.51 + 1.26\ \ln(\sigma_0) - 0.71\ \ln(\sigma_{ci}) + -0.15\ \ln(m_i) - 0.037\ GSI - 0.51 \ln(MR) \\ & - 1.25\ \varepsilon_{us} + 0.27\ R_p + 0.39 \ln(k) - 0.65\ e \end{aligned} \qquad (4-6)$$

Where σ_0 and σ_{ci} are expressed in MPa, R_p and e are expressed in Radii, ε_{us} is expressed in absolute value (i.e. for a radial strain of 10%, the value to consider is 0.1), and k is expressed in GPa.

The comparison of the multilinear regression and the numerical calculation is presented in Figure 4-11.

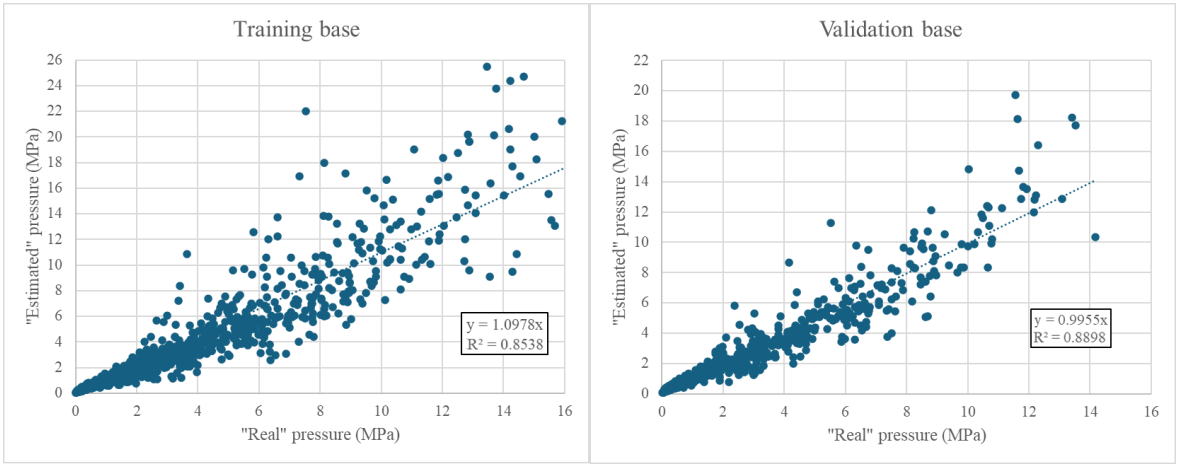

Figure 4-11: Analysis of the multilinear regression on the data of the training base and validation base

On the training base, the 95% confidence interval is [-82.7%; 71.3%] ([-84.1%; 73.9%] for the validation base). It means that, for an estimated value of 1 MPa for P_i, the real value will be between 0.173 MPa and 1.713 MPa. The uncertainty of the estimated value of P_i is too important to consider this surrogate model as relevant for preliminary design.

The second method used to develop a surrogate model is a basic neural network. Several structures for the neural network are tested, 2 or 3 hidden layers and for each layer between 4 and 10 neurons. The activation function considered is "logistic". The relevance of the neural network is tested by calculating the R^2 as explained above. These tests are done using the package "sklearn.neural_network" of Python. The results are better when using the natural logarithm of the pressure as output compared to directly the pressure.

The best neural network obtained was composed of 2 hidden layers with 7 neurons on the first layer and 8 neurons on the second layer. The results are presented in Figure 4-12.

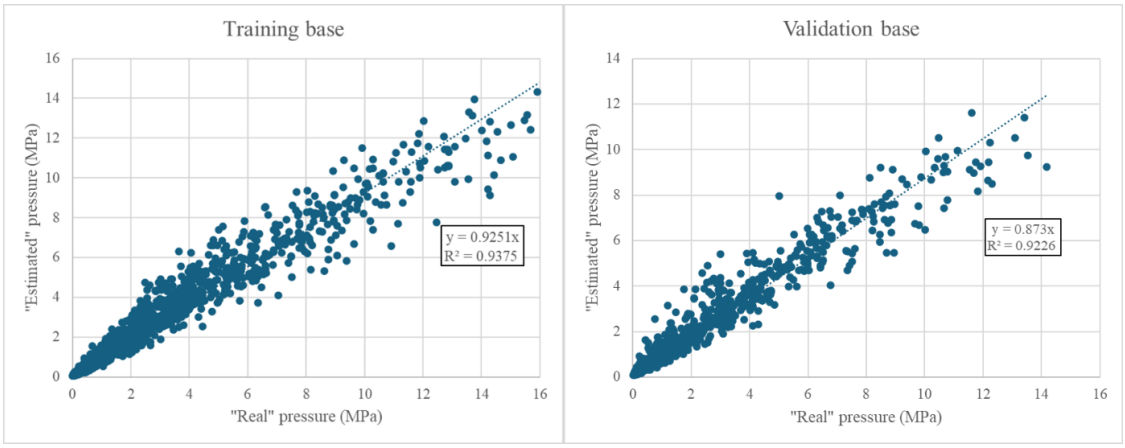

Figure 4-12: Analysis of the results of the regression using a neural network with two hidden layers, 7 neurons on the first layer and 8 neurons on the second layer

The 95% confidence intervals obtained are [-74.6%; 62.6%] for the training base and [-106.5%; 92.7%] for the validation base. It can be noted that the R^2 obtained with the neural network are much better than the one from the multilinear regression, but the 95% confidence interval are similar or worst. A high R^2 means that the points are concentrated close to the trend curve while a large confidence interval means the opposite. For the validation base, it can be contradictory

to have a better R^2 (0.923 compared to 0.890) while having larger 95% confidence intervals. This contradiction is due to the method used to estimate the 95% confidence interval based on the relative gap. For small "real" values of pressure, the relative gap can be consequent (expressed in percentage) while being not far from the trend curve (in absolute distance). The 95% confidence interval is impacted by the relative gap, while the R^2 is impacted by the absolute gap. It is one of the limits of the approach used to estimate the relevance of the surrogate model using the R^2 and the 95% confidence interval, based on the relative gap. It could have been possible to calculate the 95% confidence interval based on the absolute gap between the estimated and real pressures, but it would have made the intervals independent of the pressure value (identical for small pressures and large pressures), penalizing the small values of pressure. To estimate the ground pressure on the support, it is more relevant to focus on the "small" pressure (below 3 MPa) compared to the large pressures, as most of the classical supports cannot bear more than 3 MPa.

The approach based on neural networks was not investigated in more detail because, from the author point of view, there is one major shortcoming to neural networks (and artificial intelligence more generally) in the framework of this thesis. To the author's knowledge, it is not possible to transform a neural network into an easy-to-use graphical representation. So, it makes the surrogate model very difficult to use when there are more than two input parameters and one output parameter. The objective of this thesis is to provide tools for engineers during preliminary design which are easy and quick to use. Even if neural networks or other machine learning methods are unquestionably the best approaches to create very accurate surrogate models, they are still very complex to use unless a specific software or coding package is created. For the use of complex neural networks to create surrogate models in a similar framework, the reader can be referred to the recent work of Tristani *et al.* (2024b).

As the first two approaches are not satisfying regarding the quality of the surrogate models obtained, the choice was made to test nonlinear regression. The first approach used, which can be referred as "naïve", is based on a genetic algorithm to obtain the best expression to fit the data of the training base. The basic idea is to randomly modify the mathematical expression used to fit the data, to reach the best fitting expression. The algorithm randomly modifies the position of input parameters, the mathematical operator between input parameters, the mathematical symbol between fitting variables and input parameters as well as the parenthesis. This method was not successful as sometimes fitting errors appeared, stopping the calculations and making it impossible to reach relevant fitting expressions in time.

Thus, another approach, based on a nonlinear regression is tested. The regressions are influenced by physical considerations, and the main surrogate model is decomposed into smaller ones. The surrogate models presented in the next sections are based on this approach.

To reduce the complexity of the surrogate model and the number of input parameters, six input parameters are considered compared to nine used before:

- The radial strain without support (ε_{us}), which is obtained in the training base and validation base with the axisymmetric calculation without support. It can also be estimated with the improvement of the Hoek and Marinos curve (Chapter 3.3.2). It is expressed in **absolute value** (not in percentage)
- The plastic radius without support (R_p), which is also obtained in the training base and validation base with the axisymmetric calculation without support. It can also be estimated with the surrogate model and graphical representation presented in (Chapter 3.3.2). It is expressed in a **number of Radii**.

- The Young modulus of the rock mass (E_m), which is directly dependent on the uniaxial compressive strength of the intact rock (σ_{ci}), the modulus ratio (MR) and the geological strength index (GSI). It is calculated using the expression proposed by Hoek and Diederichs (2006), presented in Chapter 2.1.2.2. and it is expressed in **MPa**.
- The isotropic in-situ stress state (σ_0) expressed in **MPa**.
- The support stiffness (k) expressed in **GPa** and linked to the Young's modulus of support as presented in Section 4.2.1, Eq.(4-2).
- The unsupported span (e), corresponding to the distance between the face and the support installation, expressed in a **number of Radii**.

4.2.3.2 Ground pressure on the support

When analyzing the results of the axisymmetric calculations, it was noticed that for a geological situation and a value of support stiffness, the following equation fits very well the result (Eq.(4-7)):

$$ln(P_i) = A(\sigma_0, \varepsilon_{us}, R_p, E_m, k) + B(\sigma_0, \varepsilon_{us}, R_p, E_m, k) * e + C(\sigma_0, \varepsilon_{us}, R_p, E_m, k) * e^2 \qquad (4-7)$$

Where A, B and C are constant depending on the geological situation and the support stiffness. Four examples from the training database are presented in Figure 4-13. The constants A, B and C have been determined for the 200 sets of parameters (100 geological situations + 2 support stiffness for each) composing the training base. In every situation, the coefficient of determination (R^2) is higher than 0.9976. Rather than creating a unique surrogate model, smaller/intermediate surrogate models are created to estimate A, B and C, depending on ε_{us}, R_p, E_m, σ_0, and k. The initial training base for the surrogate model of P_i is transformed into three new training bases for the training of surrogate models of A, B and C (Figure 4-14).

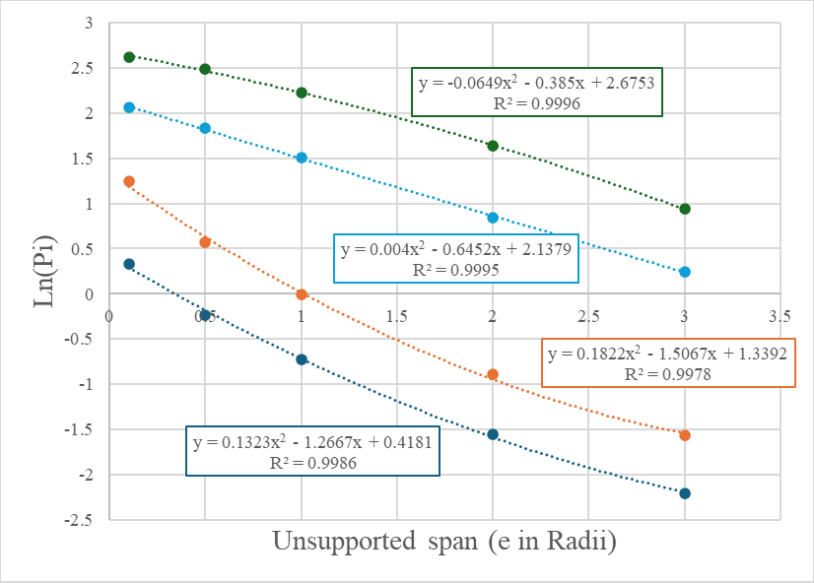

Figure 4-13: Relation between ln(P_i) and the unsupported span (e) for four examples from the training database

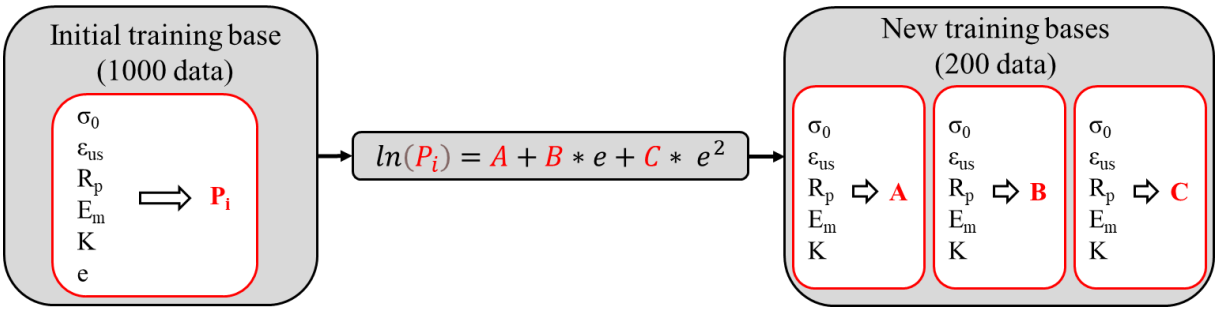

Figure 4-14:Evolution of the training base to create the surrogate models

A simplified version of Eq.(4-7) is also proposed to reduce the number of intermediate surrogate models to facilitate the graphical representation while reducing the quality of the model a little:

$$ln(P_i) = D(\sigma_0, \varepsilon_{us}, R_p, E_m, k) + E(\sigma_0, \varepsilon_{us}, R_p, E_m, k) * e \qquad (4-8)$$

Where D and E are constant depending on the geological situation and the radial stiffness. This simplified expression works well for most of the sets. For the 200 sets of parameters, the mean value of R^2 is 0.9918, while the smallest is 0.948 and 7.4% are smaller than 0.98. The approach used to obtain these results is identical as Figure 4-13, except it is performed using Python and not Excel.

It is possible to give some physical meaning of the parameters A and D to develop the associated surrogate models, based on nonlinear regression. The surrogate models used to estimate B, C and E are based on linear regression. The surrogate model of D and E are presented in Appendix 9.

4.2.3.2.1 Surrogate models of A(σ_0, ε_{us}, R_p, E_m, k)

If an unsupported span of 0 is considered (e=0) corresponding to a support installed directly at the face, the ground pressure on the support far from the face is equal to exp(A) (Eq.(4-7)). In practice, it is not feasible, but it gives the possibility here to estimate a maximal value for A. The ground pressure on the support cannot be higher than in-situ stress (σ_0). Similarly, if the support is infinitively stiff, A tends to a finite value, and if its stiffness is 0, the ground pressure on the support tends to 0, and so A tends to be minus the infinite. An appropriate expression for A can be:

$$A = \alpha \ln(\sigma_0) + \beta - \frac{\gamma}{k^{\delta}} \qquad (4-9)$$

Where α, β, γ, and δ are parameters depending on ε_{us}, R_p and E_m. δ is positive. If k tends to 0, A tends to minus the infinite. In the other hand, if k tends to plus the infinite, A tends to $\alpha \ln(\sigma_0) + \beta$.

Among the many formulations tested, the more appropriate one is kept:

$$A = a_0 \ln(\sigma_0) + {R_p}^{a_1} + a_2 E_m - \frac{a_3 \ln(\sigma_0) + a_4}{(a_7 k)^{(a_5 \varepsilon^{a_6})}} \qquad (4-10)$$

Where a_i are constants determined through nonlinear fitting and presented in Table 4-2.

Table 4-2: Values of the fitting parameters obtained for the surrogate model A

Constants	a_0	a_1	a_2	a_3	a_4	a_5	a_6	a_7
Value	1.509	-0.208	-6.85×10^{-5}	0.605	1.303	0.0458	-0.259	0.202

The comparison between the estimated value of A using Eq.(4-10) and the "real" value is presented in Figure 4-15.

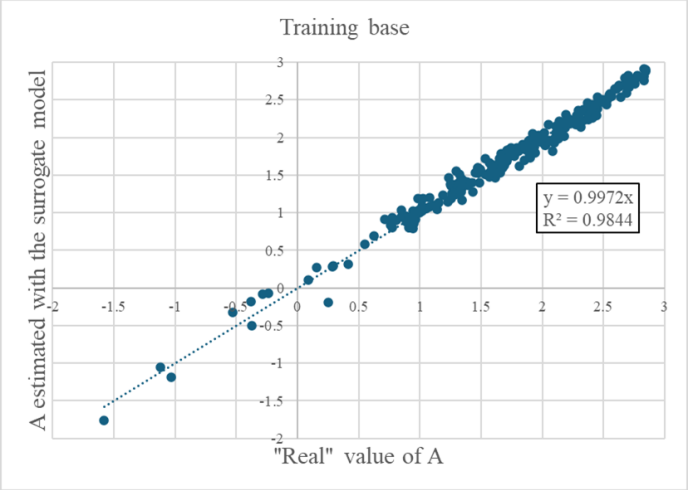

Figure 4-15: Comparison of the real values of A and the one obtained with the surrogate model

4.2.3.2.2 Surrogate model of B(σ_0, ε_{us}, R_p, E_m, k)

The surrogate model used for the estimation of B is obtained with multilinear regression:

$$B = b_0 + b_1 E_m + b_2 \ln(E_m) + b_3 \varepsilon + b_4 R_p + b_5 \ln(R_p) + b_6 k + b_7 \ln(b_8 k) \quad (3-11)$$

Where b_i are constants determined through linear fitting and presented in Table 4-3.

Table 4-3: Values of the fitting parameters obtained for the surrogate model B

Constants	b_0	b_1	b_2	b_3	b_4	b_5	b_6	b_7	b_8
Value	-0.545	6.51×10^{-6}	-0.0631	0.836	-0.357	1.47	-0.0134	0.0878	0.202

The comparison between the estimated value of B using Eq.(4-11) and the "real" value is presented in Figure 4-16.

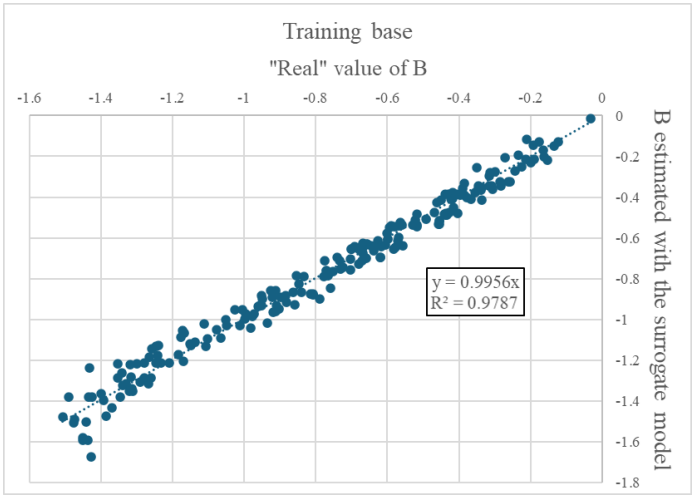

Figure 4-16: Comparison of the real values of B and the one obtained with the surrogate model

4.2.3.2.3 Surrogate model of C(σ_0, ε_{us}, R_p, E_m, K)

The surrogate model used for the estimation of C is also obtained with multilinear regression:

$$C = c_0 + c_1 \ln(E_m) + c_2\varepsilon + c_3 R_p + c_4 \ln(R_p) + c_5 k + c_6 \ln(c_7 k) \qquad (4-12)$$

Where c_i are constants determined through linear fitting and presented in Table 4-4.

Table 4-4: Values of the fitting parameters obtained for the surrogate model C

Constants	c_0	c_1	c_2	c_3	c_4	c_5	c_6	c_7
Value	-0.0195	5.71 x 10^{-3}	-0.308	0.134	-0.370	2.63 x 10^{-3}	-0.0168	0.202

The comparison between the estimated value of C using Eq.(4-12) and the "real" value is presented in Figure 4-17.

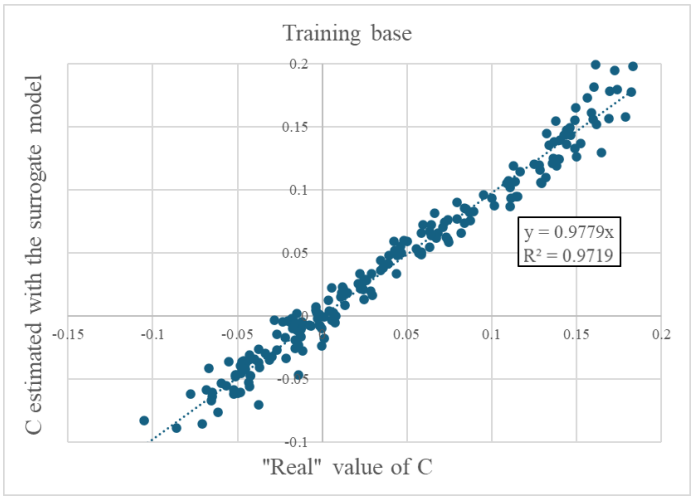

Figure 4-17: Comparison of the real values of C and the one obtained with the surrogate model

4.2.3.2.4 Surrogate model of $P_i(\sigma_0, \varepsilon_{us}, R_p, E_m, k, e)$

After defining the surrogate models of A, B, C, it is possible to define the surrogate model used for the estimation of the ground pressure on the support using Eq.(4-7). Figure 4-18 compares the results of the surrogate model with the results of the training and validations databases.

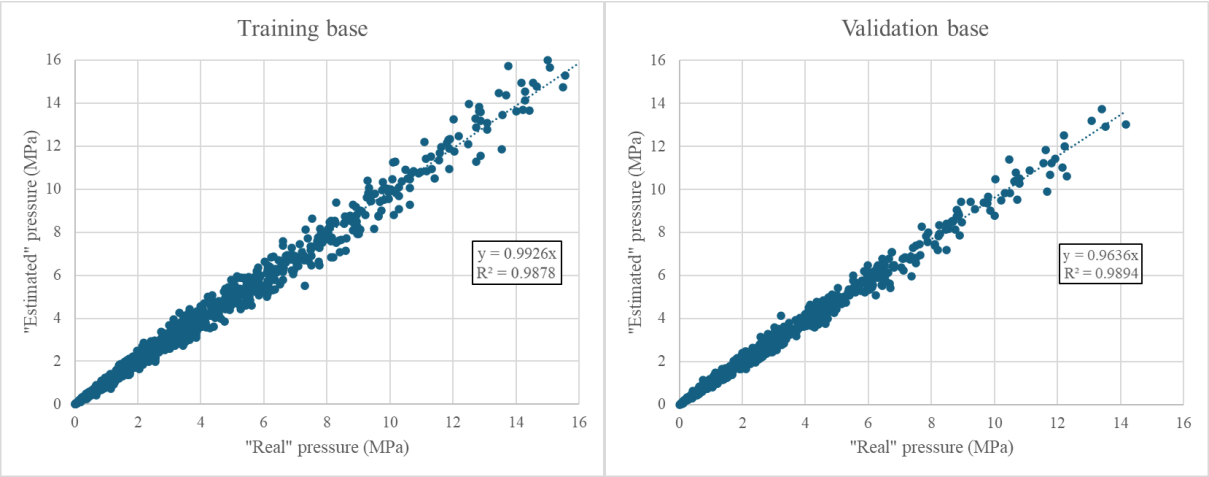

Figure 4-18: Comparison between the ground pressure estimated with the surrogate model and the ones from the axisymmetric calculation of the training base and validation base.

The 95% confidence intervals are [-23.0%; 22.0%] for the training base and [-22.2%; 23.8%] for the validation base. This surrogate model is considered satisfactory enough to be used during preliminary design for the estimation of the ground pressure on the support.

As for the simplified version, Eq.(4-8)) and detailed in Appendix 9, the graphical representation of the model can be found in Appendix 2. The simplified version is a little less precise, with a 95% confidence interval around $\pm$ 25%.

All the data used for this surrogate model are based on span values smaller than 3 Radii, and so from a theoretical point of view, the extrapolation to larger span should not be done. If the reader wishes to perform anyway this extrapolation on its own responsibility, it is recommended to use the simplified version of the surrogate model (Eq.(4-8), Appendix 9) or to carefully verify the following conditions, in order to avoid unrealistic results.

As Eq.(4-7) is a second order expression, several conditions need to be fulfilled based on the following observations:

- $C(\sigma_0, \varepsilon_{us}, R_p, E_m, k)$ can be positive or negative (Figure 4-17) and $B(\sigma_0, \varepsilon_{us}, R_p, E_m, k)$ is always negative (Figure 4-16).
- The extremum of the second order expression corresponds to the null value of its derivative, which is here:

$$e_{extremum} = -\frac{B\left(\sigma_0, \varepsilon_{us}, R_p, E_m, k\right)}{2\,C\left(\sigma_0, \varepsilon_{us}, R_p, E_m, k\right)} \qquad (4-13)$$

Two situations are possible:

- If $C(\sigma_0, \varepsilon_{us}, R_p, E_m, k)$ is negative, the span associated with the extremum ($e_{extremum}$) is negative (Eq.(4-13)). When e tends to the infinite, ln(P_i) tends to minus the infinite, and P_i tends to zero (Eq.(4-7)).
- If $C(\sigma_0, \varepsilon_{us}, R_p, E_m, k)$ is positive, the span associated with the extremum ($e_{extremum}$) is positive. Figure 4-19 shows that there is no extremum associated with spans values between 0 and 3R, corresponding to the initial validity range of the surrogate model. When e increases, ln(P_i) decreases until the extremum is reached (a minimum in this case), then starts increasing again, leading to unrealistic ground pressure.

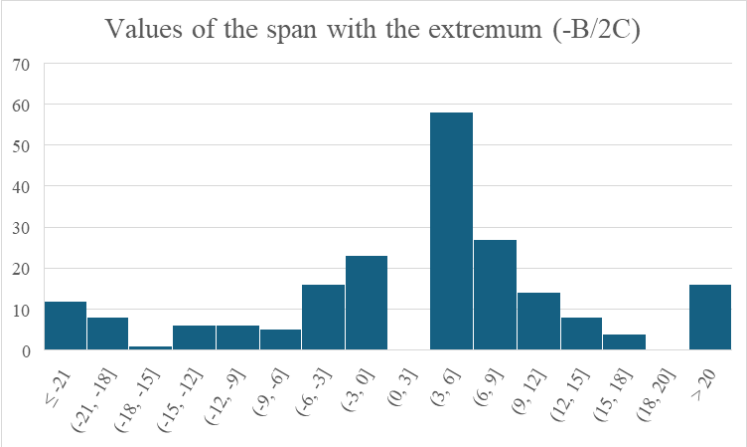

Figure 4-19: Values of spans corresponding to the extremum based on the results of the training base

If the more precise surrogate model (Eq.(4-7)) is used for span values higher than 3R, which could lead to inaccurate results, the following conditions need to be fulfilled:

$$P_i(e > 3) = \begin{cases} P_i\,(e) & if\ C < 0\ or\ e < \dfrac{-B}{2C} \\ < P_i\left(\dfrac{-B}{2C}\right) & if\ e > \dfrac{-B}{2C} \end{cases} \qquad (4-14)$$

4.2.3.3 Radial strain between the face and the support installation

As the approach used for the development of the surrogate model for the ground pressure on the support is satisfactory, a similar approach is used for the other surrogate models, such as for the estimation of the radial strain between the face and the support installation. It concerns the radial strain that occurs on the unsupported span, referred to as ($\varepsilon_{f\text{-}s}$).

Instead of considering one surrogate model for $\varepsilon_{f\text{-}s}$, it has been decomposed into two smaller ones, which are linked to $\varepsilon_{f\text{-}s}$ by the value of the unsupported span (e). There are two main constraints for the mathematical expression:

- For a span equal to 0, the radial strain between the face and the support is null.
- For a span infinitely large (i.e. far from the face), the radial strain between the face and the support is equal to the radial strain without support (far from the face) minus the radial strain at the face without support.

Several expressions fulfilling these conditions have been tested, and the following one is chosen because it provides the best results:

$$\varepsilon_{fs\,mod} = A_{RS}\left(1-\frac{1}{e+1}\right)^2 + B_{RS}\left(1-\frac{1}{e+1}\right) \qquad (4-15)$$

Where A_{RS} and B_{RS} are the "smaller"/" intermediate" surrogate models. For the 200 sets of parameters (geological situations and support stiffness) and based on the quadratic expression for ε_{fsmod} (Eq.(3-15)), the mean value of R^2 is 0.997 and minimal is 0.989. In a case a linear expression is used for ε_{fsmod}, the results are unsatisfactory (small values of R^2).

It can be noted that, in theory, A_{RS} + B_{RS} should be equal to the radial strain without support minus the radial strain at the face (the span is considered infinite). Based on the estimation of A_{RS} and B_{RS} associated with the 200 sets of parameters, A_{RS} + B_{RS} is closer to the value of the radial strain without support, including the radial strain in front of the face. This can be explained by some discrepancies between the surrogate model trained with value of e between 0.1R and 3R and the generalization to larger value of unsupported spans. **As all the data used for this surrogate model are based on span values smaller than 3 Radii, and so from a theoretical point of view, the extrapolation to larger span should not be done**. Nevertheless, if the reader wishes to perform anyway this extrapolation on its own responsibility, and to avoid unrealistic situations, such as radial strain between the face and the support higher than the radial strain without support minus the radial strain at the face, or negative values of $\varepsilon_{fs\,mod}$ (possible with the surrogate model), constraints are added to Eq.(4-15) depending on the value of e, A_{RS} and B_{RS}.

Since the mathematical expression used in Eq.(4-15) is quadratic, when considering the variable $x = 1 - 1/(e+1)$ with value between 0 (e=0) and 1 ($e = \infty$), the roots of Eq.(4-15) are $x_1 = 0$ and $x_2 = -B_{RS}/A_{RS}$. A_{RS} is positive but B_{RS} can be positive or negative. If $x_2 > 1$, the quadratic expression leads to negative value for $x \in [0;1[$ ($e \in [0;+\infty[$). x_1 and x_2 correspond to $e_1 = 0$ and $e_2 = 1/(1 + B_{RS}/A_{RS}) - 1$. To ensure positive values of $\varepsilon_{f-s}(e)$, e needs to be higher or equal to the maximal of the e_1 and e_2.

$$\varepsilon_{f-s}(e) = \begin{cases} 0 & if\ -\dfrac{B_{RS}}{A_{RS}} > 1\ or\ e < \max\left(\dfrac{1}{1+\dfrac{B_{RS}}{A_{RS}}} - 1\,;0\right) \\ \varepsilon_{US} - \varepsilon_{USF} & elif\ \varepsilon_{fs\,mod} > \varepsilon_{US} - \varepsilon_{USF} \\ \varepsilon_{fs\,mod} & else \end{cases} \qquad (4-16)$$

Where $\varepsilon_{f-s}(e)$ is the estimated value of radial strain between the face and the support, $\varepsilon_{fs\,mod}$ is the value of radial strain obtained with Eq.(4-13), ε_{US} is the radial strain far from the face for an unsupported tunnel and ε_{USF} is the radial strain at the face of an unsupported tunnel. ε_{US} can be easily obtained with the improved curve of H&M (Chapter 3.3.2) and ε_{USF} can be obtained with the surrogate model presented below, in Section 4.2.3.4.1.

The surrogate models associated with A_{RS} and B_{RS} are presented in Section 4.2.3.3.1 and 4.2.3.3.2.

4.2.3.3.1 Surrogate model of $A_{RS}(\sigma_0, \varepsilon_{us}, R_p, E_m, k)$

The surrogate model used for the estimation of A_{RS} has been obtained with multilinear regression:

$$A_{RS} = -0.075 - 0.092\ln(\sigma_0) + 0.084\ln(E_m) + 0.011\ln(0.202\,k) + 1.52\,\varepsilon_{us} + 0.061\ln(\varepsilon_{us}) - 0.058\ln(R_p) \quad (4-17)$$

The comparison between the estimated value of A_{RS} using Eq.(4-17) and the "real" value is presented in Figure 4-20. It can be noted that Eq.(4-17) can lead to negative value of A_{RS}. If it is the case $A_{RS} = 0$.

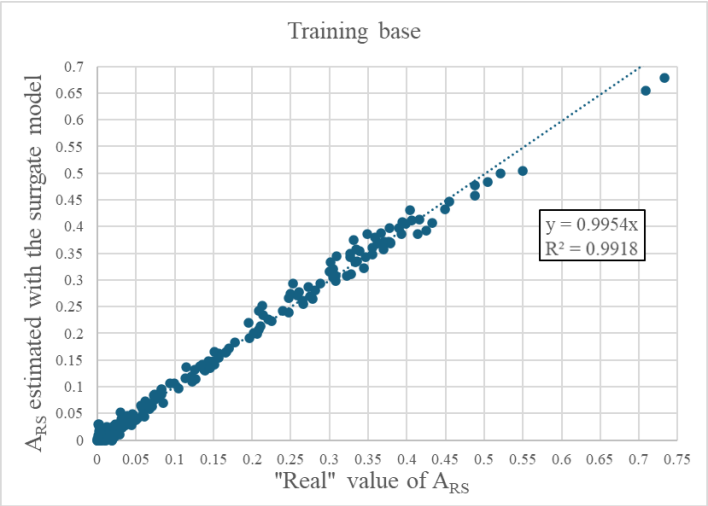

Figure 4-20: Comparison of the real values of A_{RS} and the one obtained with the surrogate model

4.2.3.3.2 Surrogate model of $B_{RS}(\sigma_0, \varepsilon_{us}, R_p, E_m, K)$

The surrogate model used for the estimation of B_{RS} has been obtained with multilinear regression:

$$B_{RS} = 0.092 + 1.92 * 10^{-3}\,k - 0.014\ln(0.202\,k) - 0.30\,\varepsilon_{us} + 0.019\ln(\varepsilon_{us}) - 0.061\ln(R_p) \quad (4-18)$$

The comparison between the estimated value of B_{RS} using Eq.(4-18) and the "real" value are presented in Figure 4-21. It can be noted that the quality of this surrogate model is not very good ($R^2 = 0.92$) but does not penalize too much the global surrogate model to estimate ε_{f-s}. It was not deemed necessary to search for a better one.

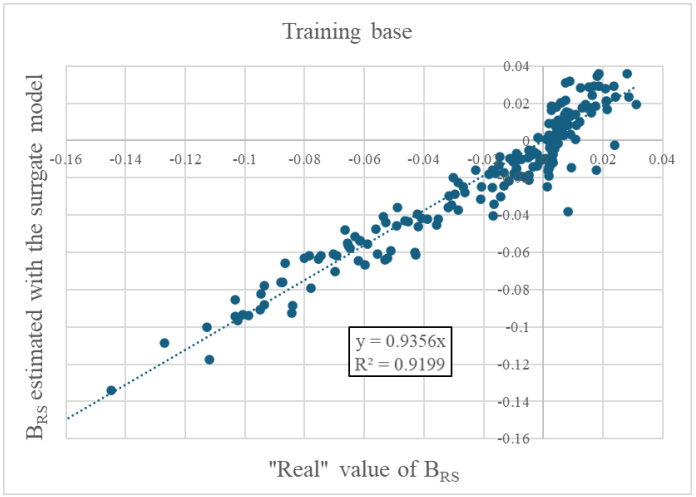

Figure 4-21: Comparison of the real values of B_{RS} and the one obtained with the surrogate model

4.2.3.3.3 Surrogate model of $\varepsilon_{f\text{-}s}(\sigma_0, \varepsilon_{us}, R_p, E_m, k, e)$

The surrogate model associated with the radial strain between the face and the support installation ($\varepsilon_{f\text{-}s}$) can be deduced from the surrogate models of A_{RS} and B_{RS}, and the Eq.(4-15) and Eq.(4-14). Figure 4-22 presents the comparison between the results of the surrogate model and the results of the numerical calculations.

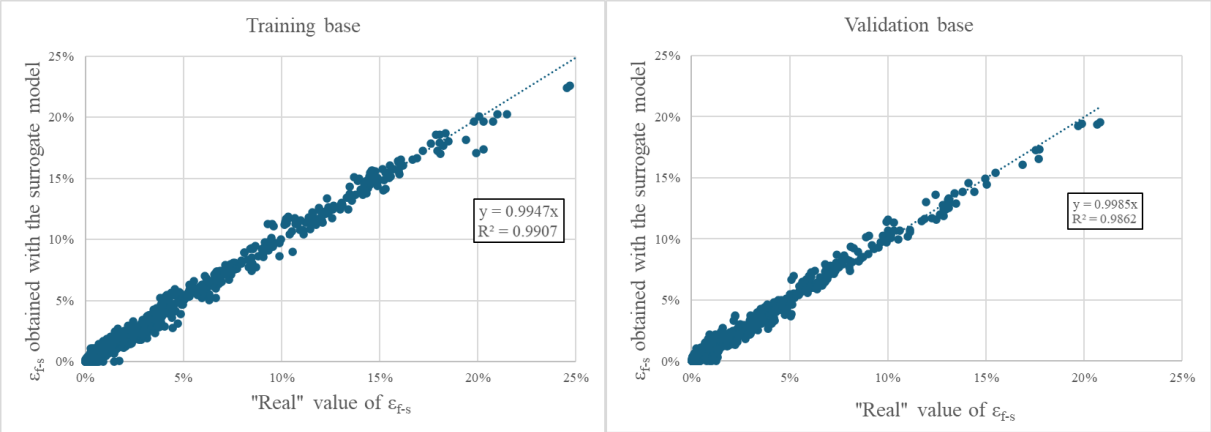

Figure 4-22: Comparison between the radial strain between the face and the support installation with the surrogate model and the ones from the axisymmetric calculation of the training base and validation base

The 95% confidence interval is ε_{f-s} (%) $\pm$ 1%. As the surrogate model is applied directly to $\varepsilon_{f\text{-}s}$, the 95% confidence interval is calculated with the absolute gap, unlike for the surrogate model for P_i calculated with the relative gap.

The graphical representations of these surrogate models are presented in Appendix 2. To reduce the impact of the constraint presented in Eq.(4-16), the graphical representation can be used only when the radial strain without support is higher than 2%.

4.2.3.4 Radial strain at the face

Similarly to the surrogate models of P_i and $\varepsilon_{f\text{-}s}$, the surrogate model used for the estimation of the radial strain at the face of a supported tunnel (ε_{SF}) is deduced from the existing constraints and some tests performed on the training base. ε_{SF} is bounded by 0 and by ε_{USF}, the radial strain at face of an unsupported tunnel (i.e. when the span (e) is infinite). The more appropriate mathematical expression found is:

$$\varepsilon_{SF} = \frac{A_{SF}}{(1+e)^2} + \varepsilon_{USF} \qquad (4-19)$$

Where ε_{USF} is the radial strain at the face of an unsupported tunnel estimated with the surrogate model presented in Section 4.2.3.4.1, and A_{SF} a "smaller" surrogate model presented in Section 4.2.3.4.2.

4.2.3.4.1 Surrogate model of $\varepsilon_{USF}(\sigma_0, \varepsilon_{us}, R_p, E_m)$

The surrogate model used for the estimation of ε_{USF} is obtained with multilinear regression:

$$\ln(\varepsilon_{USF}) = -0.402 + 0.671\ln(\sigma_0) - 0.680\ln(E_m) + 0.572\,\varepsilon_{us} + 0.341\ln(\varepsilon_{us}) - 0.0559\,R_p + 0.682\ln(R_P) \qquad (4-20)$$

The comparison between the estimated value of ε_{USF} using Eq.(4-20) and the "real" value are presented in Figure 4-23.

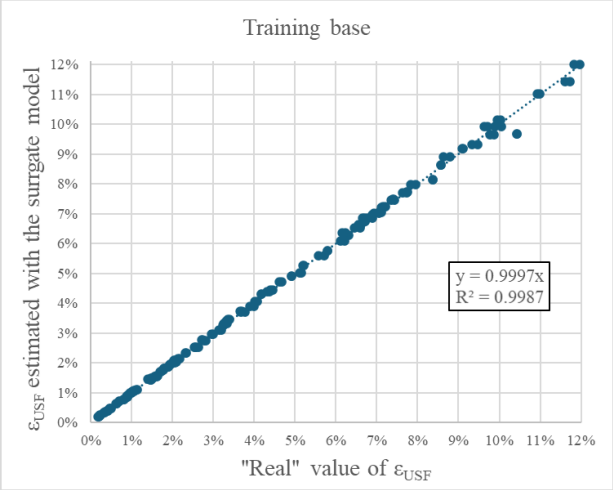

Figure 4-23: Comparison of the real values of ε_{USF} and the one obtained with the surrogate model

4.2.3.4.2 Surrogate model of $A_{SF}(\sigma_0, \varepsilon_{us}, R_p, E_m, k)$

The surrogate model used for the estimation of A_{SF} is obtained with multilinear regression:

$$A_{MLR} = -0.0583 - 0.0125\, ln(\sigma_0) - 9.67 * 10^{-7}\, E_m + 0.0163\, ln(E_m) + 7.29 * 10^{-4}\, k - 4.75 * 10^{-3}\, ln(0.202\, k) - 0.156\, \varepsilon_{us} + 9.13 * 10^{-3} ln(\varepsilon_{us}) - 7.85 * 10^{-3}\, ln(R_p) \quad (4-21)$$

To avoid unrealistic results (positive value of A_{MLR}, leading to $\varepsilon_{SF} > \varepsilon_{USF}$), a constraint has been added to the surrogate model:

$$A_{SF} = \begin{cases} A_{MLR} & if\ A_{MLR} < 0 \\ 0 & if\ A_{MLR} > 0 \end{cases} \quad (4-22)$$

The comparison between the estimated value of A_{SF} using Eq.(4-22) and the "real" value are presented in Figure 4-24.

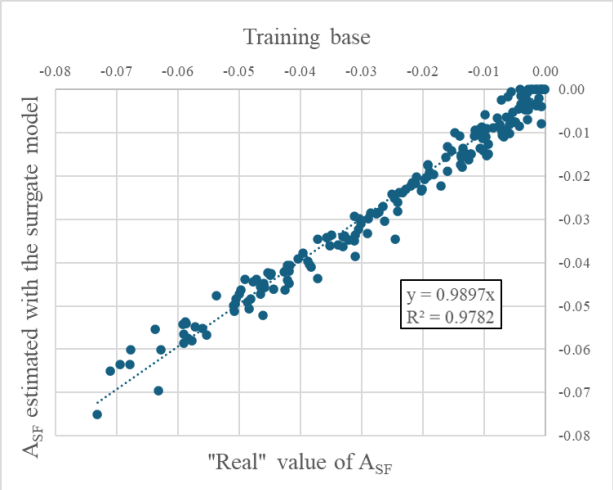

Figure 4-24: Comparison of the real values of A_{SF} and the one obtained with the surrogate model

4.2.3.4.3 Surrogate model of $\varepsilon_{SF}(\sigma_0, \varepsilon_{us}, R_p, E_m, k, e)$

Finally, the surrogate model to estimate the radial strain at the face of a supported tunnel (ε_{SF}) is deduced from the surrogate model of ε_{USF} (the radial strain at the face without support), A_{SF} and the value of the unsupported span (e). Figure 4-25 presents the comparison between the surrogate model and the results from the training and validation base.

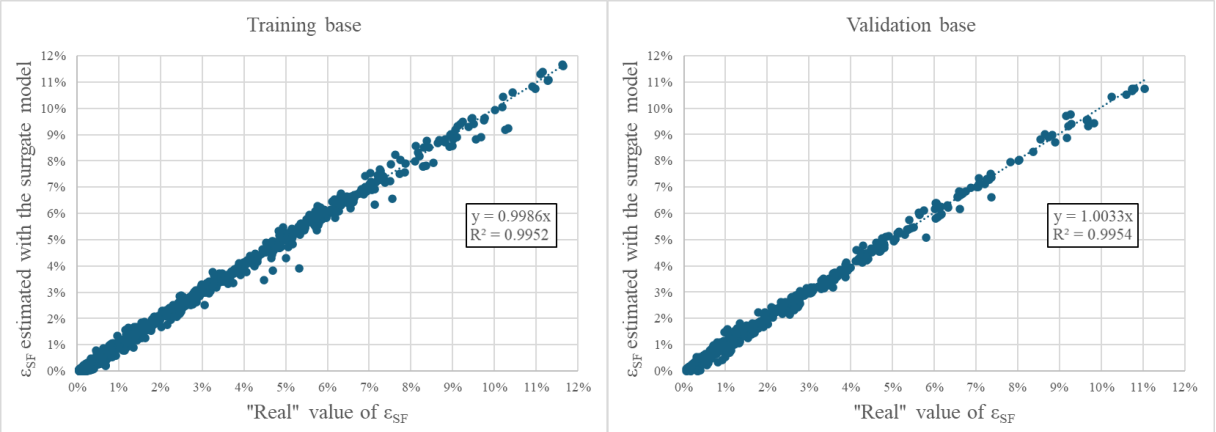

Figure 4-25: Comparison between the radial strain at the face of a supported tunnel (ε_{SF}) obtained with the surrogate model and the ones from the axisymmetric calculation of the training base and validation base

The 95% confidence interval is ε_{SF} (%) $\pm$ 0.4%. The graphical representations of the surrogate model of ε_{USF}, ε_{SF} and A_{SF} are presented in Appendix 2.

4.2.4 Conclusions of the surrogate models

To summarize, the calculations performed in Chapter 3.3 and Section 4.2 lead a set of proposed surrogate models enabling an easy estimation of the rock mass behavior without support (radial strain far from the face, at the face, and plastic radius) and providing information about the interaction between the rock mass and the support (ground pressure on the support, radial strain between the face and the support, and radial strain at the face). All of these may be obtained without performing any numerical calculation or using complex approaches, just by using graphical representation (Appendix 2) or a couple of mathematical expressions presented above. The input parameters are as simple as possible and coherent with preliminary tunnel design stages: the uniaxial compressive strength of the intact rock, the m_i parameter of Hoek&Brown, the Modulus Ratio, the Geological Strength Index, the in-situ stress state, and basic information about the support, such as the stiffness and the span. This approach is developed with the objective of providing more relevant results than other existing approaches such as the convergence-confinement method. As discussed in Chapter 5, these surrogate models can also be easily used for introducing and propagating uncertainties.

4.3 Generalized framework

The approach presented in Section 4.2 covers a large range of deep tunnel situations in highly fractured rock mass. Nevertheless, three complementary studies are performed to increase the scope of this study:

1) Unlike common hypotheses, the in-situ stress state is generally anisotropic, and not isotropic. As the calculations are performed in 2D axisymmetric, it is not possible to

directly consider anisotropic stress states (at least for a tunnel cross section). Then, some recommendations are provided in section 4.3.1 regarding the choice of the equivalent isotropic stress states to consider.

2) In highly fractured rock mass, a common technical solution not to overstress the support is to use yielding supports before installing rigid supports (Section 4.1.1). The approach presented above does not include these types of support. Some recommendations are provided in section 4.3.2 allowing an estimation of the impact of yielding support installed though the span (between the face and the rigid support installation), based on the results of a complementary study.
3) As discussed briefly in Chapter 2.2.1.3, it can be relevant to consider also the long-term behavior of the rock mass. A method is proposed in section 4.3.3 allowing the consideration of short-term and long-term behavior of the rock mass.

4.3.1 Anisotropic stress state

The surrogate models are developed with 2D axisymmetric numerical calculations considering an isotropic in-situ stress state. The classical formulation to transform an anisotropic stress state into an equivalent isotropic stress state (σ_0) is presented below (Russo 2014):

$$\sigma_0 = \frac{3\,\sigma_1 - \sigma_3}{2} \qquad (4-23)$$

Where σ_1 and σ_3 are the major and minor principal stresses perpendicular to the tunnel direction. As explained in Appendix 3, this formulation is relevant for elastic rock mass behavior, but its relevance must be argued for elastic-plastic rock mass behavior. The equivalent isotropic stress is higher than the major principal stress. Appendix 3 shows on various examples that the maximal radial strain without support obtained with this hypothesis is at least 15% higher than the one with the anisotropic stress state. Considering the maximal principal stress as the equivalent isotropic stress leads to a maximal radial strain similar or lightly higher than the one obtained with anisotropic calculations. In the other hand, no matter the equivalent isotropic stress considered, the maximal plastic radius is higher when the stress state is anisotropic. The plastic radius of the equivalent isotropic model corresponds to the mean plastic radius around the tunnel of the anisotropic model.

As the number of examples presented in Appendix 3 is limited, a general rule cannot be deduced, but it won't be illogical to consider the major principal stress as the equivalent isotropic stress. Using Eq.(4-23) increases the in-situ stress of several MPa, which may affect the design a lot.

It can be noted that an anisotropic stress state will generate bending moments and shear forces inside the support. These forces and moments cannot be estimated with the developed surrogate model (at least not directly), as the estimated pressure is supposed to be uniform at the entire tunnel boundary (2D axisymmetric model), and the tunnel to be circular.

4.3.2 Impact of a yielding support

Considering the impact of a yielding support is not directly possible using the proposed surrogate models. Since the use of yielding supports is a classical solution to deal with large deformation without overstressing the support, a complementary study is conducted in Appendix 5 to see the impact on the results.

Appendix 5 aims to study the impact of a yielding support installed on the previously unsupported span (the distance between the face and the rigid support). The yielding support is modeled as a confining pressure applied at the tunnel boundary.

It was concluded that applying a confining pressure on the span has almost no impact on the ground pressure on the support (support meaning "rigid" support here) while reducing the radial strain between the face and the support. For small plastic radius or elastic behavior, the increase of the ground pressure is at most the value of the confining pressure. For large plastic radius, it leads to no increase or even a decrease of the ground pressure on the support (in depth discussion is provided in Appendix 5). As expected, applying a confining pressure leads to a reduction of the radial strain at the support installation. Based on the various situations tested in Appendix 5, it is concluded that the following reduction factors (relative factors) can be used on the radial strain between the face and the support (Table 4-5). The value presented in Table 4-5 are minimal reduction factors that can be used. Depending on the geological situation, the reduction factors can be higher.

Table 4-5: Radial strain reduction associated with applying a confining pressure on the unsupported span (from Appendix 5)

Pressure \ Span	0.5R	1R	2R	3R
100 kPa	4%	10%	3%	15%
200 kPa	7%	7%	21%	23%
400 kPa	12%	23%	29%	34%

The surrogate models need to be used classically, and at the end the reduction factor can be applied. For example, the following geological, geotechnical and geometrical parameters (σ_{ci}=50, σ_0=25, m_i=10, GSI=30, MR=300, tunnel radius = 4m, span = 12m, 20cm thick shotcrete) leads to a ground pressure on the support of 1.13 MPa, and a radial strain between the face and the support of 7.7%. As the plastic radius is large (2.7R), applying a yielding support will not increase the ground pressure on the rigid support. For steel sets with sliding gaps spaced every 0.8m, with a sliding force of 350 kN, the confining pressure is around 100 kPa (3m tunnel radius). This yielding support will, at least, reduce the radial strain before the "rigid" support installation of 15% (Table 4-5), meaning that the expected radial strain will be around 6.5%.

4.3.3 Consideration of a long-term behavior

Appendix 6 presents a methodology to consider the long-term behavior of the rock mass. The consideration cannot be done directly with the surrogate model, except specific hypothesis such as designing directly with long-term parameters. The surrogate models enable to take into account the interactions between the rock mass behavior, the face and the support (3D problem), while the transition between the short-term and the long-term properties is a 2D plane strain problem (no perturbation associated with the face). The method proposed below uses the surrogate model for the design associated with the short-term parameters, then the problem is transformed into a 2D plane strain problem in which the transition can be made using the ground reaction curve (similarly as the convergence-confinement method).

The method can be summarized into six steps, illustrated in Figure 4-26:

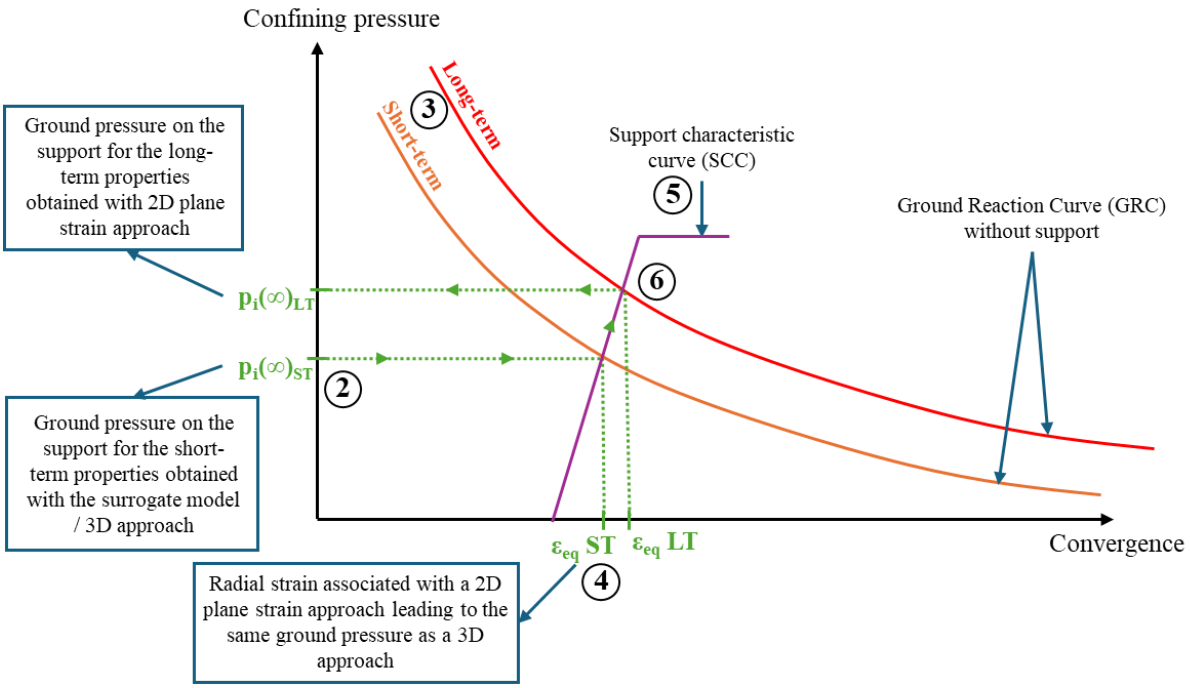

Figure 4-26: Method to estimate the long-term pressure on the support based on the proposed surrogate model coupled with a 2D plane strain approach

Step 1: definition of short-term and long-term properties of the rock mass. It can be noted that, unlike numerical modelling, it is not possible to modify the parameters only locally (in the vicinity of the tunnel). Appropriate hypotheses need to be made.

Step 2: estimation of the ground pressure $p_i(\infty)_{ST}$ on the support with the surrogate model using the short-term properties.

Step 3: calculation of the short-term and long-term ground reaction curve without support. It can be done numerically or using the close form analytical expression of Carranza-Torres and Fairhurst (1999). It can be noted that this expression is for H&B criterion and the not generalized criterion. This approximation is considered acceptable as the application concerns only preliminary design, and the GRC based on the generalized H&B criterion cannot be calculated directly (iterative calculation as specified by Carranza-Torres 2004).

Step 4: obtaining from the short-term GRC the equivalent radial strain (ε_{eq} ST) associated with a 2D plane strain approach, leading to the same ground pressure on the support $p_i(\infty)_{ST}$

Step 5: If necessary, updating the support stiffness. It is possible to install a lining far from the face to bear the increase of the ground pressure associated with the long-term properties.

Step 6: computing the intersection point between the SCC and the GRC with long-term properties. This equilibrium point is the ground pressure on the support for the long-term properties $p_i(\infty)_{LT}$. It is also possible to estimate the increase of radial strain if only a yielding support is considered.

4.4 Conclusions

This chapter aims to summarize the existing methods and approaches to deal with the large radial deformation in deep tunnels. After briefly highlighting the technical solutions and types

of support for deep tunnels in highly fractured rock masses, the existing design methodologies are presented to discuss some of their shortcomings. A new method is then developed based on surrogate models to improve some shortcomings of these methods. They have been created based on the results of 2D axisymmetric numerical calculations allowing them to explicitly consider the interactions between the rock mass behavior, the face of the tunnel, and the support. These results are combined with those of Chapter 3 (estimation of the radial strain without support and the plastic radius without support), to create a relevant framework enabling an easy estimation of fundamental parameters for design. The surrogate models allow an estimation of the ground pressure on the support far from the face, the radial strain between the face and the support installation, and the radial strain at the face in both cases of supported and unsupported tunnels. Some complementary studies have also been done to extend the framework of the surrogate models by introducing anisotropic in-situ stress state, the impact of a yielding support used between the face and the rigid support, and by proposing a method to include the long-term behavior of the rock mass.

Chapter 5 - Introduction and propagation of uncertainties for reliability calculations

Chapter Abstract: The surrogate models presented in Chapter 3 and Chapter 4 allowing the characterization of the rock mass behavior without support, and the interaction with the support, have been developed to easily allow the introduction and propagation of the geological and geotechnical uncertainties. Nevertheless, no method or approach has been really presented in these chapters. The main advantage of the introduction and propagation of uncertainty is to enable reliability calculations which focus on the estimation of a probability of failure rather than safety factors or partial factors.

This chapter starts with a brief presentation of reliability calculations used for tunnel design in the literature and discusses how the uncertainties on rock mass parameters can be quantified. Then, a simple graphical method is proposed to propagate the initial uncertainties with the improvement of the Hoek and Marinos curve (Chapter 3.3.2). It will be shown how just by estimating graphically three specific values of radial strain, it is possible to deduce its probability density and calculate the probability to be in each class of risk proposed by Hoek and Marinos (2000). As the mathematical expression of surrogate models developed in Chapter 4 are more complex but fast to use (analytical expression), the propagation of the uncertainties is performed using Monte Carlo simulations to estimate the probability density of the results and potential failure probabilities.

The propagation of uncertainties with the surrogate models creates two opportunities presented in this chapter. The first one is about performing reliability-based design which lays on maximal admissible failure probabilities including explicitly the uncertainties, compared to the use of safety factors. A method is proposed to easily perform this reliability-based design using the surrogate models during preliminary tunnel design stages. Since designing based on failure probability criteria is not always possible, the second opportunity is to use the surrogate models to link the value of safety factors to failure probabilities and to the uncertainties of the input parameters. A comparison on a wide range of situations is made at the end.

5.1 Reliable approaches and uncertainties quantification

As this chapter focuses on uncertainties propagations and reliability calculations, this section aims to present some basic considerations about uncertainties, design approaches, and their application in tunnel design.

5.1.1 Preliminary consideration

By nature, geomaterials are subject to inherent uncertainties, which may be either aleatory or epistemic. Aleatory uncertainties result from the natural variability (or intrinsic) of the geomaterial, its inherent randomness, based on its complex history of formation and its continual reworking (Tran 2020). Tran (2020) specifies that aleatoric uncertainties can be differentiated as spatial variability or as temporal variability, while Van den Eijnden *et al*. (2024) consider both as part of the inherent variability of the ground. It is impossible to reduce this uncertainty. In the other hand, epistemic uncertainties are associated with a lack of knowledge and systematic errors. Tran (2020) presents two types of epistemic uncertainties, measurement error and transformation uncertainty, while Van den Eijnden *et al*. (2024) consider three types, measurement error, model uncertainty, and statistical uncertainty. Measurement error is the uncertainty caused by imperfect measurement tools and/or sample disturbance effects (Van den Eijnden *et al*. 2024) coming from the preparation, the transport or the testing procedure (Tran 2020). Van den Eijnden *et al*. (2024) include "transformation uncertainties" into a larger category of "model uncertainty". It includes the uncertainties associated with the calculation models (approximation, close form solution, calculation error, etc.), the error in the model compared to the real behavior, and transformation uncertainties which are the uncertainties in the transformation models used to obtain a certain geotechnical parameter from measurement (Van den Eijnden *et al*. 2024). The last type of epistemic uncertainty introduced by Van den Eijnden *et al*. (2024) is statistical uncertainty. It is uncertainty due to limited information, such as a limited number of observations in a site investigation. Furthermore, there is statistical model uncertainty related to the selection of probability distributions (when limited data). Epistemic uncertainty can be reduced by collecting more data or by including systematic errors. Van den Eijnden *et al*. (2024) propose methods to quantify these various types of uncertainties.

As the consideration of the uncertainties are fundamental for the design of structural element, specific calculation approaches have been developed based on the principal of "reliability". The Eurocode 0 defines structural reliability as "*the ability of a structure to fulfil the specified requirements during the service life for which it has been designed; the notion covers safety, serviceability and durability*" (Van den Eijnden *et al*. 2024). Three main approaches exist (Van den Eijnden *et al*. 2024):

1) The risk-based approach: This approach entails economic optimization within safety constraints. It aims to minimize the direct cost of the design and the average cost due to failure (probability of failure multiplied by the cost of the failure).
2) The reliability-based approach: This approach aims to optimize the construction cost which can be linked to numerous parameters such as the volume of material, the duration, the construction sequence, etc. In this approach, immaterial constraint (like human safety), cost of repair if failure, etc., are implicitly included in the choice of targeted reliability (i.e. failure probability).
3) The semi-probabilistic or partial factor-based approach: This approach is the classical approach proposed in the Eurocodes. Design values are derived by multiplying (or dividing) the characteristic values with the respective partial and combination factors,

and aims to guarantee that the limit state function stay positive (negative values are associated with failures regarding the limit state). These partial factors are ideally calibrated in such a way that the design or assessment decision for a large class of structures fulfils the reliability target defined in Eurocode 0 (depending on the type and vulnerability of structure). Figure 5-1 illustrates the relationship between acceptable risk, reliability target and partial factors.

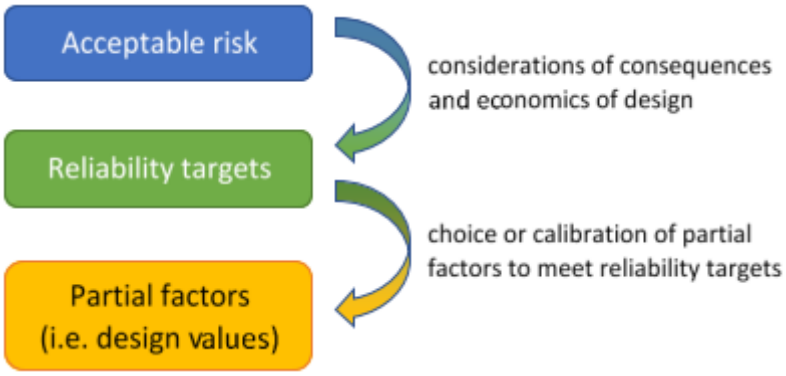

Figure 5-1: Relationship between acceptable risk, reliability targets and partial factors (i.e. semi-probabilistic approach) (Van den Eijnden et al. 2024)

It can be noted that "failure" in reliability theory is not restricted to collapse but may refer to any form of unintended behavior or incompatible results with a limit state function. It can also be noted that a design approach based on a targeted global safety factor cannot be considered as an approach based on "reliability", unlike the three presented above. It is only a deterministic approach.

In the following of this chapter, two different terminologies are used when referring to reliability calculation:

- Reliability-based design optimization (RBDO): RBDO refers to an optimization of the design based on specific characteristics and criteria to minimize (as defined above by Van den Eijnden *et al*. (2024) as "reliability-based approach")
- Reliability-based design (RBD): RBD does not refer to an optimization process, as no criteria or parameters need to be minimized. RBD refers only to a calculation technique based on failure probability calculation and compatibility to specific limit state.

5.1.2 Quantification of the geological and geotechnical uncertainties

The uncertainties characterization associated with laboratory tests is a fundamental aspect of uncertainties propagation and reliability calculations. Nevertheless, the research on this point is relatively limited when speaking about Hoek&Brown failure criterion. One of the first relevant studies was performed by Connor Langford and Diederichs (2015), in which they used a classical frequentist approach to quantify the uncertainty on the intact strength envelop through the uniaxial compressive strength of the intact rock (UCS) and the m_i parameter of Hoek&Brown. They also provided some quantification of the uncertainties for various materials (Figure 5-2). Later, this study has been discussed and adapted using a Bayesian approach with the extensive research performed by Dr. Bozorgzadeh in its PhD thesis (2018) and Prof. Harrison (Bozorgzadeh and Harrison 2016, Bozorgzadeh *et al.* 2017, Bozorgzadeh *et al*. 2018, Bozorgzadeh 2018, Bozorgzadeh et Harrison 2019). Aladejare and Wang (2017) summarized

the rock properties variability by analyzing the data found in the literature to obtain some typical ranges of variability depending on the type of rock. Contreras *et al.* (2018) highlighted the advantage of a Bayesian approach compared to a frequentist approach to deduce the parameter of a H&B failure criteria. They also discuss how outliers should be handled based on the distribution used, as well as other more specific considerations like whether to use absolute or relative residuals or to analyze the quality of the fitting results. Finally, they extended the Bayesian method to include the parameters "a" of H&B and the direct tensile strength as variable. Aladejare and Wang (2019) focuses on the estimation of the m_i parameter using a Bayesian approach on laboratory test results, while including prior information and providing a guideline chart for the method. Feng *et al.* (2020) applied the Bayesian approach to quantify the uncertainty in the in-situ stress data. Gomes *et al.* (2021) proposed a formulation of the H&B failure criterion for anisotropic rock which calculates strength anisotropy based on two scaling factors. Then, they embedded H&B formulation into a Bayesian framework to better predict the rock mass strength and to better quantify the uncertainties.

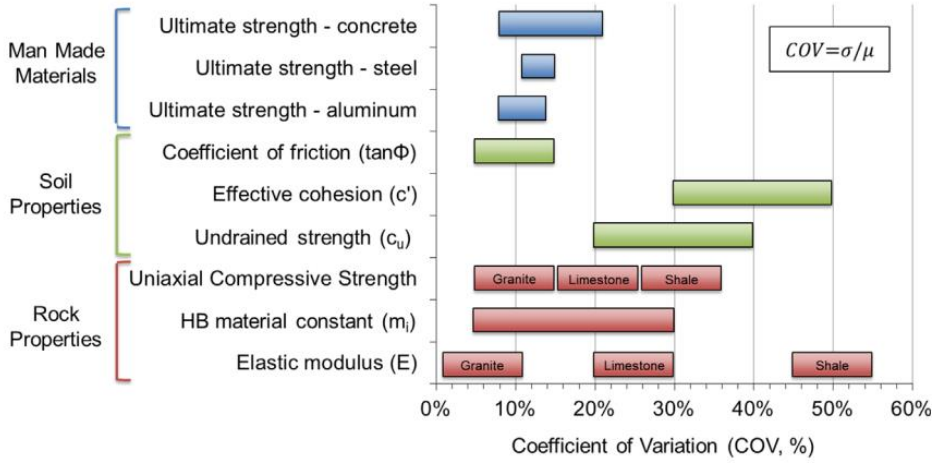

Figure 5-2: Coefficient of variation (CoV) of various man-made and geotechnical materials (from Connor Langford and Diederichs 2015)

In a frequentist approach, only experimental data (e.g. UCS results for example) are considered as random variables. Statistical parameters, such as the means and standard deviations, are considered as fixed but unknow constants. In contrast, the Bayesian approach considers all parameters - including those derived from laboratory tests or statistical analysis - as random variables characterized by their own distributions (Feng *et al.* 2020). For example, when analyzing uniaxial compression test data, the frequentist approach estimates the mean value, the standard deviation and the distribution law of the UCS. The Bayesian approach treats these statistical parameters (mean and standard deviation) themselves as uncertain, assigning them probability distributions. This allows to quantify the uncertainty associated with the mean and standard deviation of the parameter.

The main limitations for the frequentist approach in geotechnical engineering is that there is no formal framework for incorporating knowledge not represented by data, and it does not provide a proper measure of the confidence of the parameters inferred from data (Contreras *et al.* 2018), unlike the Bayesian approach. It is why the Bayesian approach is better for quantifying the uncertainties of geotechnical parameters (Contreras *et al.* 2018; Van den Eijnden *et al.* 2024).

5.1.3 Reliability calculations applied to tunnel design

It is important to note that calculating failure probabilities, performing a reliability-based design (RBD) or a reliability-based design optimization (RBDO) are different and do not have the same objective. RBD is performed to verify the compatibility of a design with specific limit states by guaranteeing the failure probability associated with each limit state to be smaller than targeted values. RBDO is a generalized version of the RBD which includes an optimization process to reach the more appropriate design parameters. This approach is based on one or several objectives to be minimized. It can be a general objective such as the global cost of the tunnel project, including for example the thickness of the support, the tunnel radius, the excavation sequence, the volume of excavated material, the excavation techniques, etc. As this type of objective can be very complex for tunnel projects, a set of several objectives can be used instead, such as minimizing the support thickness, minimizing the tunnel radius, minimizing the span, etc. At each step of the optimization process, a RBD is performed to ensure the compatibility of the design with the constraints defined by limit states. A failure probability can be calculated for a design obtained using a partial factor-based approach or a deterministic approach (targeting global safety factor) and it is not necessarily associated with a RBD or a RBDO.

Tran (2020) classified the existing methods for reliability calculations (Figure 5-3). No detailed presentation of these methods is presented in this thesis. For a mathematical aspect of these methods, the reader should refer to the following publications: Bastidas-Arteaga and Soubra (2014), Soubra and Bastidas-Arteaga (2014), Huang *et al.* (2017a; 2017b; 2017c), Tran (2020), Van den Eijnden *et al*. (2024). It can be noted that some of these methods are used to calculate failure probabilities, but also to perform reliability-based design optimizations (RBDO).

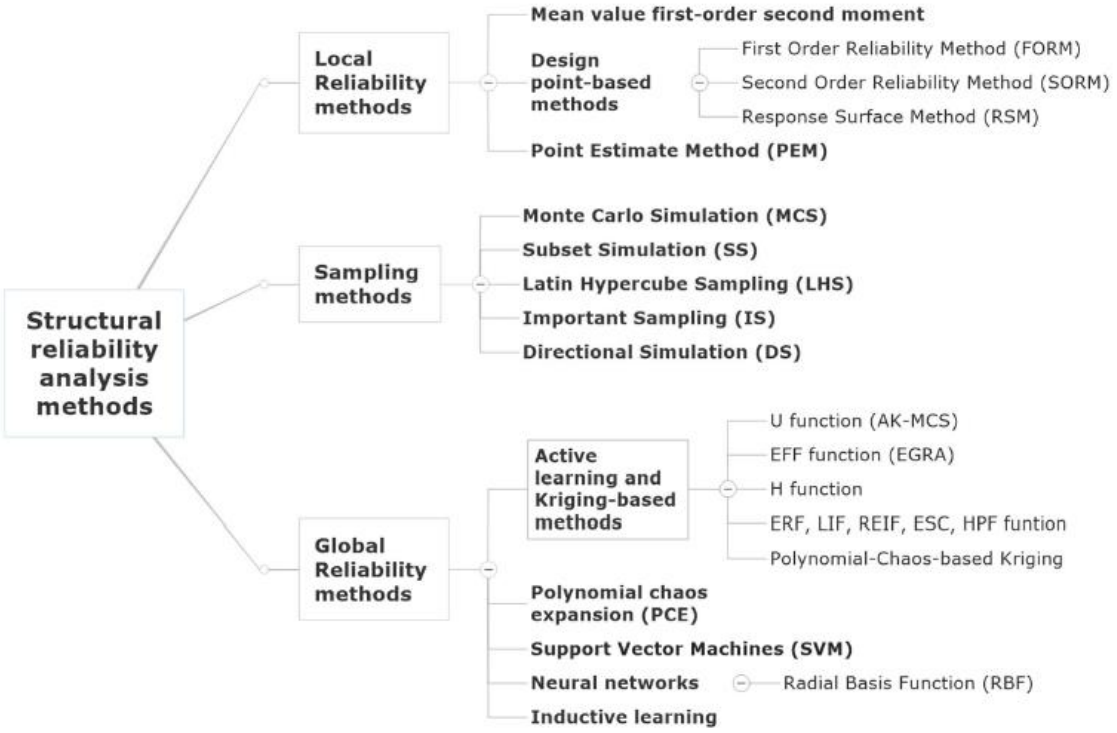

Figure 5-3: Classification of the existing reliable approach (from Tran 2020)

The use of reliability methods for underground structures is relatively limited, as many of them require analytical solutions or low computational time, which is rarely the case (except in simple situations). Reliability analyses have been studied by many researchers to make these approaches more practical, but the majority of studies deal with geotechnical issues associated with soil mechanics (Tran 2020). As highlighted by Harrison (2014), the first generation of the Eurocode 7 is very limited on rock mechanics issues, and so inappropriate partial factors are provided. Partial factors are only provided for Mohr-Coulomb failure criteria, which is rarely used in rock mechanics (Bozorgzadeh and Harrison 2019). Tran (2020) performed an extensive literature review to identify authors dealing with reliability calculation in rock mechanics. Generally, the reliability calculations are performed on closed form analytical solutions, associated with low computational time (Tran 2020).

Lü *et al.* (2011) used the First-Order Reliability Method (FORM) and Second Order Reliability Method (SORM) to evaluate failure probability of tunnel designs regarding three performance functions (limit state function) in a circular tunnel. To apply this method, the results of the CV-CF (convergence-confinement) method are approximate using the Response Surface Method (RSM). Connor Langford and Diederichs (2013) developed an approach to evaluate the performance of a composite tunnel lining (i.e. a RBD) using a modified Rosenblueth Point Estimate Method (PEM) and finite element analysis. It allows an estimation of the failure probability and the reliability index for each capacity curve of the support and lining elements, with a limited number on numerical calculations. The capacity curves (bending moment/normal stress and normal stress/shear stress) can be seen as limit state function in this case. Idris *et al.* (2016) compare five approaches for analyzing the stability of underground rock excavation: Point Estimate Method (PEM), Response Surface Method (RSM), Artificial Neural Network (ANN), Monte Carlo Simulation (MCS) and Strength Classification Method (SCM). The calculations are performed using 2D plane strain numerical model. Song *et al.* (2016) performed reliability calculations for circular tunnels in elastic-strain-softening rock mass. The ground pressure on the support is calculated using an iterative calculation process programmed in VBA (Visual Basic) coding language (Excel coding language). The failure probabilities are estimated with the FORM and SORM methods, and compared with the results of a MCS. Lü *et al.* (2017) perform a RBDO to optimize the support thickness and the span (distance between the face and the support installation). They are using FORM and RSM methods, and the results are obtained with the CV-CF method. They improved it later (Lü *et al.* 2018) to include spatial variability of the rock mass parameters, using the Random Field Theory. Tran (2020) has used a kriging-base method to consider special variability of the rock mass parameters (including creep parameters). Firstly, the results are compared with a Monte Carlo simulation on an analytical expression to validate the approach, then applied it to the results of numerical calculations. Zhao *et al.* (2021) propose a RBDO to optimize the parameters of the support. The calculations are performed with the CV-CF method while the design is optimized using the Chaotic Particle Swarm Optimization. Lu *et al*. (2022) developed a reliability assessment procedure for evaluating excavation stability using empirical approaches based on the rock mass classification Q and the FORM method. The limit state function is based on the critical strain, defined in their article as the ratio between the uniaxial compressive strength of the rock mass and the Young's modulus of the rock mass. Zhao (2022) proposes a reliability-based design approach (RBDO) to deduce more appropriate design parameters using the moment method and high-dimensional model representations for the optimization and the first-order second moment to estimate the failure probability.

As all these approaches are complex to be applied or are not convenient for deep tunnel design (like the CV-CF method), new methods should be developed to be easily used during preliminary tunnel design. In this chapter, an easy-to-use method, which is based on a simplified

version of the Point Estimate Method, is proposed to quantify the uncertainty on the radial strain without support (Section 5.2). When the interaction between the rock mass and the support is considered, the surrogate models developed in Chapter 4 are used to perform Monte Carlo simulations to calculate failure probability regarding two limit states: the ground pressure on the support and the radial strain between the face and the support.

5.2 Uncertainties propagation without support

During an early stage of tunnel design, due to limited available data and high costs of laboratory tests and field investigations, there are many uncertainties regarding the input parameters. Generally, these uncertainties are not taken directly into account in calculations; instead, they are often considered through conservative assumptions and the use of safety factors. However, this approach just hides the impact of these uncertainties on the design and prevents engineers from correctly understanding the rock mass behavior and its interaction with the support system. As a result, it can lead to inappropriate or suboptimal designs.

This section presents a method to easily quantify the effect of uncertainties on the estimation of the radial strain in an unsupported tunnel, based on results of Chapter 3.3.1 (improvement of the Hoek and Marinos curve). This method facilitates the characterization of the probability density of radial strain based on a graphical reading of three specific points. An example is provided to illustrate the method and demonstrate its efficiency. The variability of the considered input parameters is summarized in Table 5-1. The coefficients of variation considered are similar to those found in the literature (Connor Langford and Diedrichs 2013,2015; Song *et al.* 2016; Lü *et al.* 2017,2018; Lu *et al.* 2022). For this example, the modulus ratio is supposed to be constant at 400.

Table 5-1: Variability of the input parameters for the illustrative example used to estimate how to propagate uncertainties of these parameters to get a valuable confidence interval of the radial strain without support.

	σ_{ci} (MPa)	m_i	σ_0 (MPa)	GSI
Mean (μ)	50	16	25	30
Standard deviation (σ)	10	2.4	3.75	/
Coefficient of variation	20 %	15 %	15 %	/
Density function	Normal	Normal	Normal	Discrete GSI 25 (25%) GSI 30 (50%) GSI 35 (25%)

The methodology proposed here is based on several hypotheses presented below. When these hypotheses are not fulfilled, it is recommended to use directly a Monte Carlo simulation with the mathematical expression provided in Chapter 3.3.2.

5.2.1 Methodology of the “3-point method”

The improvement of Hoek and Marinos curve (Chapter 3.3.2, Figure 3-14 Figure 3-15 and Figure 3-16) cannot be used directly to quantify the uncertainty of radial strain when considering the uncertainties of the input parameters. Although a Monte Carlo simulation can be conducted using the analytical expressions of the curves, this method is not straightforward and can be time consuming.

In this section, a method called “3-point method” is presented which allows the density probability of the radial strain to be easily estimated. This method is based on the PEM method.

By knowing the density probability of the radial strain, it is possible to estimate the probability of being in each class of the Hoek and Marinos squeezing problem classification (Chapter 3.1.3), leading to a more relevant quantification of the squeezing potential. A confidence interval of the radial strain without support can also be deducted from density probability.

5.2.1.1 The Point Estimate Method (PEM)

The PEM method was introduced by Rosenblueth (1981) and adapted for tunnel design by Connor Langford and Diederich (2013) through a modification of the points to consider. The classical PEM method allows the estimation of the mean and standard deviation of an output based on the calculation of a limited number of points (2^n where n is the number of input parameters). Two values are possible for an input parameter: the mean value minus one standard deviation and the mean value plus one standard deviation. After calculating the output for each possible combination, an approximation of the mean (μ_r) and the standard deviation (σ_r) can be deduced based on the following expressions (general expression from Connor Langford and Diederichs 2013):

$$\mu_r = \sum_{i=1}^{2^n} p_i \, R(X_i) \qquad (5-1)$$

$$\sigma_r^2 = \sum_{i=1}^{2^n} p_i \, (R(X_i) - \mu_r) \qquad (5-2)$$

Where p_i is a weighting value that depends on the correlation between the variables. For uncorrelated variables, p_i is constant and equal to $1/2^n$. $R(X_i)$ is the value of the response parameters, and X_i is the vector of input parameters. The PEM method is based on the assumption that the density probability of the output is a normal distribution.

In this study, the use of the PEM method leads to the following output: $\frac{\sigma_{ci}\sqrt{m_i}}{\sigma_0}$. The GSI and the MR cannot directly be considered because their distributions are discrete based on the developed curves from the improvement of H&M curve (Chapter 3.3.2). Table 5-2 summarize the PEM method for this situation. Because 3 parameters are considered, $2^3 = 8$ calculations are required. It is important to note that, as a multiplication of normal distribution (σ_{ci}, m_i and σ_0), the output is a lognormal distribution, which can be easily verified with a simple Monte Carlo simulation. To apply the PEM method here, it is up most importance to work with the logarithm of the output, which has a normal distribution.

Table 5-2: Application of the PEM method on the illustrative example (Table 5-1).

σ_0	σ_{ci}	m_i	x-axis value	Ln(x-axis value)
28.75	60	18.4	8.952	2.192
28.75	40	18.4	5.968	1.786
28.75	60	13.6	7.696	2.041
28.75	40	13.6	5.131	1.635
21.25	60	18.4	12.112	2.494
21.25	40	18.4	8.074	2.089
21.25	60	13.6	10.413	2.343
21.25	40	13.6	6.942	1.938

By considering σ_{ci}, m_i and σ_0 uncorrelated, the application of Eq(5-1) and Eq.(5-2) on the "Ln(x-axis value)" leads to a $\mu_r = 2.065$ and $\sigma_r = 0.264$. They are the parameters of the normal distribution of the logarithm of the x-axis values, and also the parameters of the lognormal distribution of the x-axis values.

5.2.1.2 The "3-point method"

The "3-point method" is a simplification of the PEM ("Point Estimate Method") introduced by Rosenblueth (1981). As its name suggests, the "3-point method" is based on the graphical reading of 3 specific points to obtain a median value for the radial strain, as well as lower and upper bounds.

In this study, there are 3 input parameters (σ_{ci}, m_i and σ_0), and the proposed "3-point method" can also consider the variability of the GSI and MR. To apply the 3-point method, some hypotheses regarding the variability of the input parameters are required:

1. σ_{ci}, m_i and σ_0 are random variables with a normal distribution

2. The GSI is a random variable with a discrete distribution. There is a median value for GSI (GSI_{med}) with a probability 1-2β, a lower value (GSI_{med} - 5) with a probability β and a higher value (GSI_{med} + 5) with also a probability β, with $\beta \in [0; 0.33]$. The mean value of the GSI cannot be 15 or 50 because results for GSI 10 or 55 have not been investigated in the improved version presented in Chapter 3.3.1. In this example, β is set to 0.25.

3. The Modulus Ratio (MR) can be considered as a random variable similarly to the GSI, but the mean value needs to be 400. Additional information is provided in section 5.2.3.

4. As it will be shown in section 5.2.2, several Monte Carlo simulations performed on the numerical model and on the curves of Figure 3-14, Figure 3-15 and Figure 3-16, demonstrated that the radial strain has a lognormal distribution. By the same approach, the x-axis expression of graphical representations ($\frac{\sigma_{ci}\sqrt{m_i}}{\sigma_0}$) also has a lognormal distribution. In general, by knowing three points of a lognormal distribution, it is possible to deduce the distribution's parameters. For the 3-point method, the idea is to know the median value of radial strain, a lower bound and a higher bound. By knowing the median value (ε_{median}), the lower boundary of the 95% confidence interval ($\varepsilon_{2.5}$) and the higher boundary ($\varepsilon_{97.5}$), the parameters of the lognormal distribution (mean value μ_{LN} and standard deviation σ_{LN}) can be deduced using the following equations:

$$\mu_{LN} = \ln(\varepsilon_{median}) \qquad (5-3)$$

$$\sigma_{LN} = \frac{\ln(\varepsilon_{97.5}) - \ln(\varepsilon_{2.5})}{3.92} \qquad (5-4)$$

It is important to note that for expression Eq.(5-4), a hypothesis is made regarding the quantile of the lower bound and the higher bound. Sections 5.2.2 and 5.2.3 present the relevance of these hypotheses. If necessary, Eq.(5-4) can be adapted to other hypotheses on the quantiles.

The "3-point method" only considers the mean and extreme combination of the PEM method to estimate the radial strain:

- To obtain a median value of the radial strain, the mean values of parameters are considered ($\mu_{\sigma_{ci}}$; μ_{m_i} ; μ_{σ_0} ; GSI_{med}), which are for the example: (50 MPa; 16; 25 MPa; 30)
- To obtain a high value of the radial strain, the x-axis value and the GSI must be minimal. This leads to considering the following values : ($\mu_{\sigma_{ci}} - \sigma_{\sigma_{ci}}$; $\mu_{m_i} - \sigma_{m_i}$; $\mu_{\sigma_0} + \sigma_{\sigma_0}$; GSI_{min}), which are for the example : (40 MPa; 13.6; 31.5 MPa; 25)
- To obtain a low value of the radial strain, the x-axis value and the GSI must be maximal. This lead to consider the following values : ($\mu_{\sigma_{ci}} + \sigma_{\sigma_{ci}}$; $\mu_{m_i} + \sigma_{m_i}$; $\mu_{\sigma_0} - \sigma_{\sigma_0}$; GSI_{max}), which are for the example : (60 MPa; 18.4; 28.5 MPa; 35)

The graphical application for the addressed example is presented in Figure 5-4. The median value of radial strain is estimated to be 8.2% and the confidence interval is [2.6%; 26.0%]. Based on the hypothesis associated with Eq.(5-4), the probability distribution of the radial strain is LogNormal and the confidence interval is reasonably a 95% confidence interval, as discussed for this example in section 5.2.2 and generalized in the section 5.2.3.

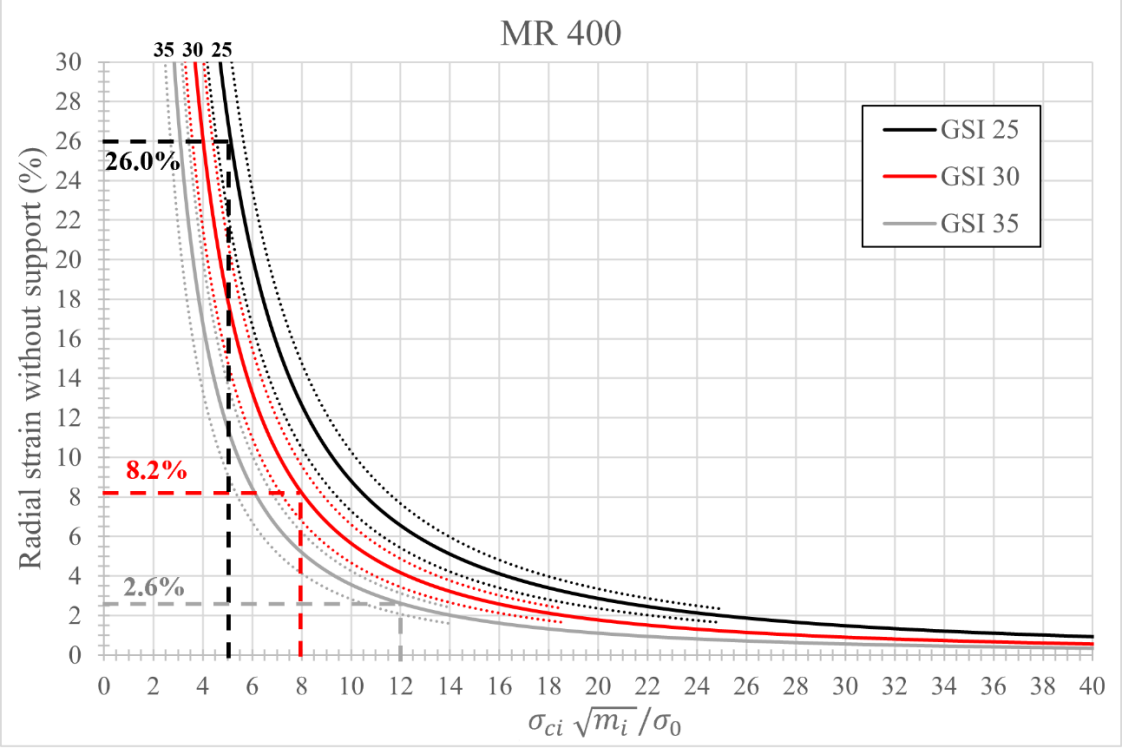

Figure 5-4: Application of the "3 points method" for the illustrative example detailed in Table 5-1 to assess the distribution of radial strain without support

5.2.2 Comparison with other approaches

The "3-point method" allows the estimation of a median value for the radial strain, and a confidence interval. However, the probability of the confidence interval is unknown, which is necessary to calculate the density probability parameters. To estimate this probability, two methods that allow the propagation of uncertainties are compared:

1. A Monte Carlo Simulation (MCS) carried out on the equation of the improved curve with a MR of 400 (Figure 3-15). 100 000 realizations are carried out, and the computation time is short (around 2 minutes).

2. A Monte Carlo Simulation (MCS) carried out with the numerical model presented in Chapter 3.2.1. 10 000 realizations are carried out, and the computation time is significant (between 1 and 2 minutes per realization, total around 250 hours).

The objective of the first MCS is to test the relevance of this approach to quantify the probability of the confidence interval. The idea is to use this first method to estimate the probability of the confidence interval obtained with the "3-point method" in section 5.2.3. The second MCS is used here as reference, in order to prove that the existing discrepancies between the surrogate model and the numerical results have no influence.

The results of these two MCS are presented in Figure 5-5.

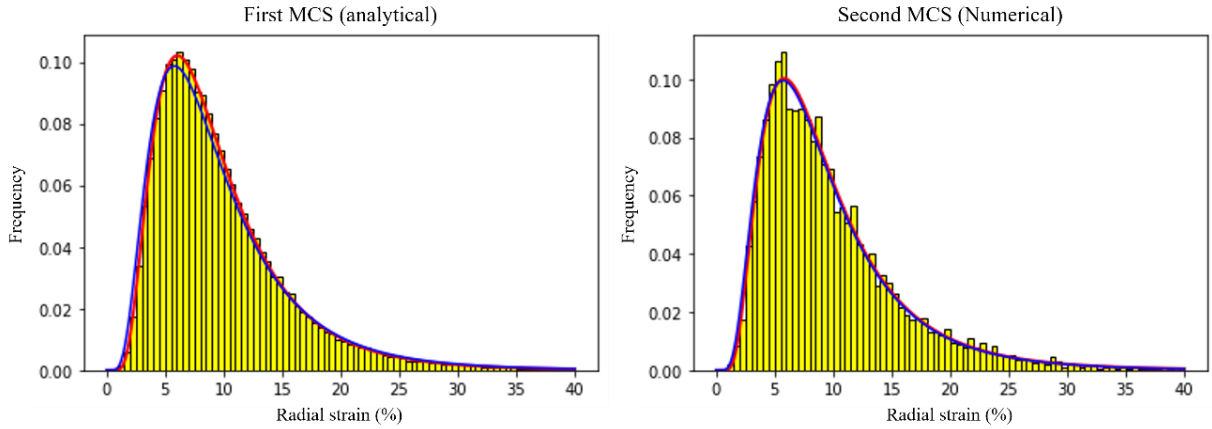

Figure 5-5: Histogram for the MCS; the red curves are the fitted lognormal distributions; the blue curves are lognormal distributions for which the confidence interval of the "3-point method" is supposed to be a 95% confidence interval

The first simulation gives a median value of radial strain of 8.3% and a 95% confidence interval of [2.9%; 25.0%]. The second simulation gives a median value of radial strain of 8.3% and a 95% confidence interval of [2.8%; 26.3%]. The confidence interval of the "3-point method" corresponds to the quantiles 1.4% and 97.8% for the first MCS and 1.9% and 97.4% for the second MCS. The probability associated with the confidence interval obtained with the "3-point method" is 96.4% for the first approach and 95.5% for the second approach. As a first step, it seems relevant to consider the confidence interval obtained with the "3-point method" as an approximation of a classical 95% confidence interval used for engineering applications. The blue curves in Figure 5-5 are the distribution obtained with this hypothesis and Eq.(5-1) and Eq.(5-2). Table 5-3 summarizes the probability of being in each of the Hoek and Marinos (2000) categories.

Table 5-3: Comparison of the 3 approaches to propagate uncertainties, in order to assess the probability of each Hoek & Marinos class.

Hoek & Marinos class	**A**	**B**	**C**	**D**	**E**
"3 points method"	0%	2.2%	17.9%	43.1%	36.8%
First MCS (analytical)	0%	1.4%	16.4%	45.5%	36.7%
Second MCS (numerical)	0%	1.8%	17.0%	44.2%	38.2%

The first MCS gives results close to those of the second MCS, which is much more time-consuming, so it is used in the following section to estimate the probability of the confidence interval in a wide range of situations, and not only for this illustrative example.

5.2.3 Framework for uncertainties propagation

The previous section highlighted that the confidence interval of the "3-point method", for the presented example, is close to a 95% confidence interval. The aim of this section is to test the validity domain of this observation in order to get general conclusions. The objective is to test the relevance of the hypothesis for a large number of geological situations, and to highlight the situations where the hypothesis is or is not relevant. For the situations in which the hypothesis is not relevant, the objective is also to estimate a variation range for the value of the confidence interval that can be used.

Many factors can impact the value of the confidence interval, like the mean value of the input parameter, their coefficient of variation, the β value of the GSI variability, the variability of the MR, etc. To test the impact of each of those factors, several situations are considered, starting with the simplest and with progressive complexification (Table 5-4). The first situation focuses on the impact of the value of the CoV, the second on the impact of the mean values of the input parameters, the third on the combined impact of the CoV and the mean values, the fourth on the impact of the MR value, the fifth on the GSI variability, the sixth on the MR variability and the seventh does not consider GSI variability.

Table 5-4: Variability of input parameters considered in each studied situation; μ_i is the mean of the parameter i; CoV_i is the coefficient of variation of the parameter i; the discrete probability for GSI = {GSI_{min}; GSI_{mean}; GSI_{max}} is {β; 1-2β; β} and similarly for MR with γ_{MR}

Input parameters	**Variability considered in each situation**						
	1	**2**	**3**	**4**	**5**	**6** [2]	**7** [3]
$\mu_{\sigma ci}$ **(MPa)**	50	[10; 110][1]	[10; 110][1]	[10; 110][1]	[10; 110][1]	[10; 110][1]	[10; 110][1]
$CoV_{\sigma ci}$ **(%)**	[0; 30]	20	[0; 30]	[0; 30]	[0; 30]	[0; 30]	[0; 30]
μ_{mi}	16	[5; 30] [1]	[5; 30] [1]	[5; 30] [1]	[5; 30] [1]	[5; 30] [1]	[5; 30] [1]
CoV_{mi} **(%)**	[0; 30]	15	[0; 30]	[0; 30]	[0; 30]	[0; 30]	[0; 30]
$\mu_{\sigma 0}$ **(MPa)**	25	[5; 40] [1]	[5; 40] [1]	[5; 40] [1]	[5; 40] [1]	[5; 40] [1]	[5; 40] [1]
$CoV_{\sigma 0}$ **(%)**	[0; 30]	15	[0; 30]	[0; 30]	[0; 30]	[0; 30]	[0; 30]
μ_{GSI}	30	[20; 45] [1]	[20; 45] [1]	[20; 45] [1]	[20; 45] [1]	[20; 45] [1]	[20; 45] [1]
β_{GSI} **(%)**	25	25	25	25	[0; 33]	[0; 33]	0
μ_{MR}	400	400	400	[200; 600]	[200; 600]	400	[200; 600]
γ_{MR} **(%)**	0	0	0	0	0	[0; 33]	0

[1] The mean values are chosen randomly under two conditions: the variation range of m_i is dependent of the value of σ_{ci}, as it is presented in Chapter 3.2.2; the median value of the radial strain (the first point of the "3-point method") must be less than 30% to avoid situations that are not relevant with the graphical representations presented in Chapter 3.

[2] The introduction of the MR variability is similar to the GSI variability, which means that the curves associated with the value 600 must be considered for the estimation of the lower value of the radial strain, the curves associated with the value 400 must be considered for the estimation of the median value of the radial strain and the curves associated with the value 200 must be considered for the estimation of the highest value of the radial strain.

[3] Since no GSI variability is considered (β=0%), the median, lower and upper values of the radial strains are estimated based on the mean GSI value.

For each situation 1, 2, 3, 4, and 7, 500 Monte Carlo simulations are computed based on the analytical expressions of Eq.(3-11) (Chapter 3.3.2) and compared with the confidence interval obtained using the "3-point method".

For the situations 5 and 6, a decomposition into smaller situations has been done:

- In situation 5, β is not completely random. Its values are {0%; 5%; 10%, 15%, 20%, 25%, 30%, 33%}. For each value of β, 500 Monte Carlo simulations are computed.
- In situation 6, γ_{MR} is not completely random. Its values are {5%; 10%, 15%, 20%, 25%, 30%, 33%}. For each value of γ_{MR}, 500 Monte Carlo simulations are computed.

The probabilities of the confidence interval obtained are presented in Figure 5-6. In this figure, the effects investigated are summarized at the bottom of each situation. "CoV" means that the coefficient of variation variability is considered in the situation; similarly, for "μ_i" the mean of the input parameter i. If the "CoV" or "μ_i" are not summarized at the bottom of the associated situation in Figure 5-6, it means that their value is fixed as presented in Table 5-4. The crosses are the median values, and the points are extreme values, values which are smaller than the first quartile minus 1.5 time the interquartile (third quartile minus first quartile).

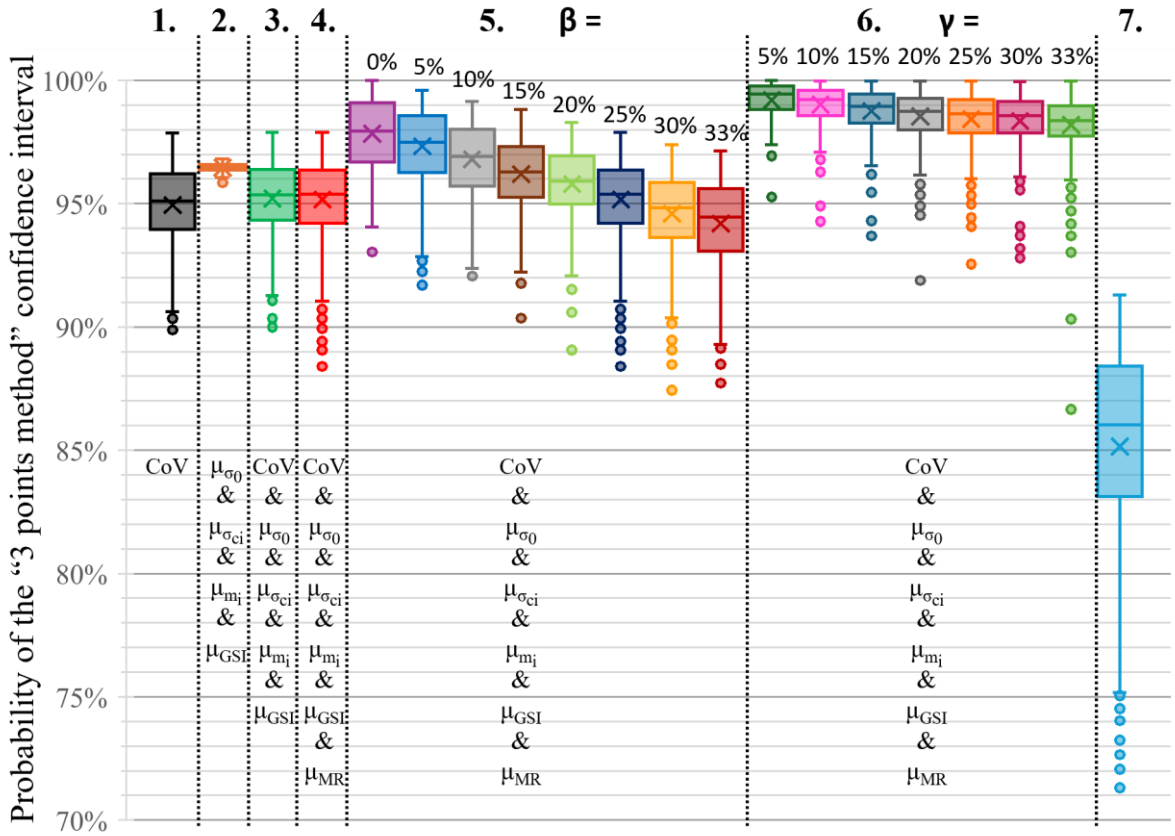

Figure 5-6: Boxplot of the probability of the "3-point method" confidence interval for the different situations 1 to 7

From Figure 5-6, the following conclusions can be drawn:

- As long as some variability is considered for the GSI (every situation except the 7th), the value of the confidence interval obtained with the "3-point method" is higher than 88%.
- In a first approximation, the previous hypothesis considering the confidence interval of "3-point method" as a 95% confidence interval is relevant when some variability exists on all the input parameters, except the modulus ratio (situation 1 to 5). Nevertheless, the real confidence interval might differ and is very likely to be between 90% and 99%.
  The coefficients of variation of the input parameters have a great influence on the probability of the confidence interval obtained by the "3-point method" (situation 1), unlike the mean values (situation 2). Most of the dispersion observed is due to the

variability of the coefficients of variation of the input parameters.A more precise study of the results in Figure 5-6 shows that when the three coefficients of variation (those of σ_{ci}, m_i, σ_0) are similar, as in the example of Table 5-1, the probability of the confidence interval is high (>95%). In the contrary, if the three coefficients of variation are very different, for example one input parameter has a high uncertainty compared to the others, the probability of the confidence interval tends to be lower.

- The modification of the MR value has no effect on the probability of the confidence interval because the results of situations 3 and 4 are very similar.
- The choice of the value of the β parameter has an effect on the mean value of the probability obtained but not really on the dispersion of the result. The height of the boxplots is similar regardless of the β value (situation 5). While the γ_{MR} parameter has little effect on the mean value of probability, it does have an effect on the dispersion of the probability of the confidence interval. The greater is γ_{MR} and the bigger the dispersion is (the height of the boxplot in situation 6).
- If no variability of the GSI is considered (β=0%), estimating the radial strain confidence interval by using only the mean value of the GSI will lead to a large uncertainty in the probability of the confidence interval (situation 7) and the value of the confidence interval is relatively small (between 75% and 91%). However, considering the lower and upper values of the GSI in the "3-point method" leads to a high probability for the confidence interval (median value around 98%) with a limited uncertainty on this value (situation 5 with β=0%).

In conclusion, in a first approach, it is possible to consider that the confidence interval on the radial strain obtained with the "3-point method" is about 95% when the following hypothesis are fulfilled:

- The coefficients of variation of the input parameters (σ_{ci}, σ_0, m_i) are less than 30% and are similar.
- The mean GSI is included in [20;45] and the β value for the GSI variability is at least 20%.
- The modulus ratio variability is not considered, but the MR value may be {200; 400; 600}.

For other situations, it is necessary to at least consider the probability of the confidence interval based on Figure 5-6 or to perform a Monte Carlo simulation based on the mathematical expression of the curves presented in Eq.(3-11) and Table 3-3 (Chapter 3.3.2).

5.2.4 A case study

As a practical example, the new curves are applied to a real case, specifically the Yacambu-Quibor tunnel in Venezuela, to verify their accuracy and validate their effectiveness. Connor Langford and Diedrichs (2013) proposed a reliability-based approach to justify the chosen support in this project. They considered the following input parameters (Table 5-5) for a section at a depth of 1150 m:

Table 5-5: Input parameters based on Connor Langford and Diedrichs (2013)

	σ_{ci} (MPa)	**m_i**	**σ_0 (MPa)**	**GSI**
Mean (μ)	50	7	30	25
Coefficient of Variation	6.0%	14.3%	5.0 %	8.0%
Standard deviation (σ)	3	1	1.5	2

In their article, Connor Langford and Diederichs (2013) do not consider the in-situ stress variability as an input parameter, but they also specify that the chosen value is an approximation. A small variability of 5.0% is then considered here. The in-situ stress state is isotropic, and the modulus ratio is 550, which is approximated at 600 for using Figure 3-16. All the random variables follow a normal distribution. For this example, the β value of the GSI is 11% to get an equivalent CoV of 8%; it is the cumulative probability of the GSI being less than 22.5 (or greater than 27.5). The tunnel radius is 2.6m.

Connor Langford and Diederichs (2013) used a modified version of the PEM method which resulted in a lognormal distribution of probability for the radial strain with a mean value of 50.7% and a standard deviation of 21.2%. The authors do not specify whether the "large strain" hypothesis was considered for the numerical calculation in their study, but a mean value for radial strain of 50.7% seems somewhat surprising. They also specified that the extremum value obtained for the radial strain are 10% and 100%. In this situation, the Hoek and Marinos curve gives a radial strain of 36.5%. The use of the "3-point method" gives a median value of radial strain of 26.7% and a confidence interval of [12.5%; 58.7%]. A numerical calculation using the Flac software, and the model presented in Chapter 3.2.1 is carried out with and without the large strain hypothesis. With the large strain hypothesis, a radial strain without support of 30.3% is obtained, and with the small strain hypothesis, the radial strain is 52.1%. It seems that the radial strains obtained in this study are more relevant.

The parameters of the lognormal distribution can be deduced based on a hypothesis regarding the probability of the confidence interval. To illustrate the effect of the choice of the probability, four values of this probability are compared:

1. 99% associated with the upper bound of situation 5, β=10%, in Figure 11.
2. 98% associated with the upper quartile of situation 5, β=10%, in Figure 11.
3. 97% associated with the median value of situation 5, β=10%, in Figure 11.
4. 95%, to highlight that for this example, this approximation is not the most precise.

A MCS was also performed with the analytical equation of the curves. The density of the probability of radial strain for each of these hypotheses is presented in Figure 5-7. The choice of the probability of the confidence interval has an effect on the density of probability of the radial strain without support. In this example, the "3-point method" used with the assumption of a 99% confidence interval gives a density probability very similar to the one got with MCS. A comparison with Figure 5-6 (situation 5, β=10%) shows that this situation corresponds to the upper limit.

This case study illustrates that the developed methodology is efficient to make a quick assessment of the possible radial strain. If additional investigations are required to make the definitive design of the tunnel, this result allows a first estimation of possible situations in order to identify both the most probable situation and the extreme situations.

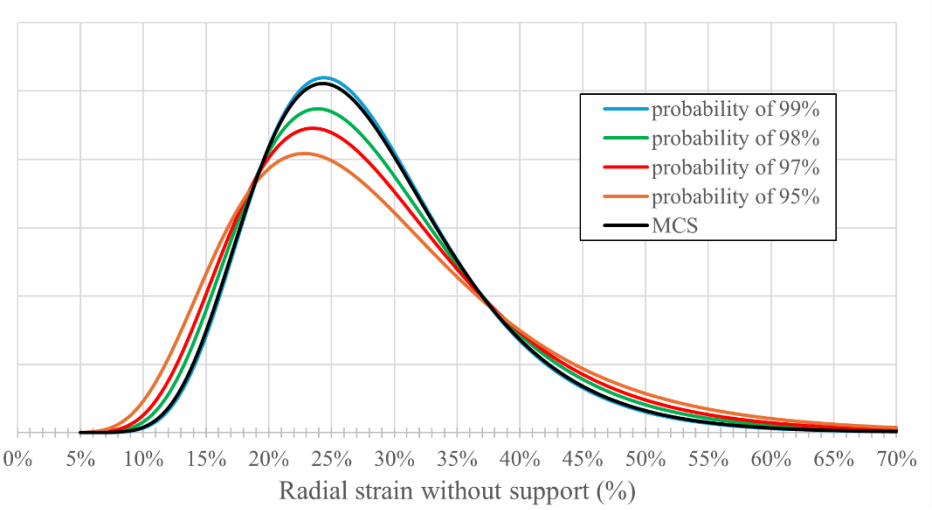

Figure 5-7: Comparison of the probability density function of the radial strain without support calculated with MCS (black curve) or with the "3-point" method associated to four different assumptions about the probability associated with the confidence interval obtained.

Generally, at the early stages of a tunnel design, uncertainties of input parameters are typically larger due to the limited number of laboratory tests and field investigations. It is not really possible to fully eliminate them in tunnel design, as they are inherently linked to the ground parameters and variability (aleatory uncertainties). Even with a lot of laboratory tests, which can be costly, uncertainties will persist. It is then necessary to take them directly into account in the design process, rather than masking them with safety factors and conservative values of input parameters. In this case study, the initial uncertainties on the input parameters are relatively limited because the tunnel was already under construction years before the Connor Langford and Diederichs (2013) article was published. The construction started in the 80's (Hoek and Guevara 2009), which likely allowed back analysis to be carried out to reduce uncertainties, but they could not be fully eliminated.

5.3 Method for tunnel design based on reliable approaches

The previous section describes how uncertainties on the input parameters can be easily propagated using the improved curve of Hoek and Marinos to determine the density of probability of the radial strain without support. It enables a probabilistic quantification of the risk of squeezing problem. The following step is to study the impact of these uncertainties on the interactions between the rock mass behavior and the support, and on the tunnel design. Mainly, the impact will appear though two parameters: the ground pressure on the support and the radial strain between the face and the support. The distribution of probability of these two parameters can easily be determined by performing Monte Carlo Simulation on the surrogate models developed in Chapter 4. These distributions are essential for an explicit consideration of the uncertainty in the design (e.g. determination of failure probability regarding a limit state) and to perform a simple reliability-based design, and design optimization (RBDO).

As briefly discussed in Section 5.1, designs in civil engineering and geotechnical engineering are performed using the limit state approach. It means that the design is deemed acceptable if it complies with criteria defined by the limit states. Most limit states are associated with deformation criteria or strength criteria. For deterministic or semi-probabilistic approaches, these criteria are fixed values not to cross (minimal value or maximal value depending on the limit state). For probabilistic approaches, these criteria are defined by maximal admissible

failure probabilities (e.g. probability of the design leading to a value incompatible with the defined limit state).

This section proposes a simple method to easily perform reliability-based design during preliminary design stages of a tunnel project. It is not really a RBDO as there is no real optimization. The approach allows several designs to be compared with external design constraint (or ultimate limit state), but strictly speaking, does not allow an optimization based on specific criteria. The approach used to calculate failure probabilities based on the surrogate models is presented in Appendix 6. A theoretical example is also provided to show how the method can be applied.

5.3.1 Proposed method for preliminary reliability-based design

The reliability-based design method presented in this section aims to reach the more appropriate design while explicitly considering the various uncertainties and guaranteeing a probability of failure regarding the limit states smaller than the imposed constraints. The surrogate models developed in Chapter 3 and Chapter 4 can be used relatively easily to apply this method. A theoretical example is provided in Section 5.3.2.

As the main focus is the preliminary design, only two ultimate limit states are considered: the ground pressure on the support and the radial strain between the face and the support installation. The objective of the RBD method is to find an appropriate thickness for the support and an appropriate distance for the installation of stiff support. As presented in Appendix 6 and Chapter 4.2.1, the surrogate model considers a continuous support. The results can also be applied to composite support using for example the approach proposed by Carranza-Torres and Diederichs (2009), or discontinuous support by using an equivalent continuous support with the same strength and stiffness.

The method for reliability-based design using the surrogate models is as follows (Figure 5-8):

1) The first step is to define a relevant geological and geotechnical model for the tunnel based on laboratory tests and field investigations. This model needs to include the existing uncertainties.
2) Then, it is necessary to identify the tunnel section potentially associated with large radial deformation or squeezing problems using the improved Hoek and Marinos curve. These sections are the ones subjected to a reliability-based design.
3) The first important step for the RBD is to determine the external design constraints, such as the internal tunnel diameter. Generally, they are imposed by the client, or by the use of the upcoming tunnel.
4) Initially, a value for the tunnel excavation diameter needs to be chosen. This value will probably evolve during the design process. It impacts the stiffness of the support and so the maximal admissible ground pressure on the support. In most cases (except extreme squeezing problems), the tunnel excavation radius will not evolve a lot, leading to a limited impact. It might not be necessary to re-perform the RBD when modifying this radius, only to verify the compatibility of the chosen design.

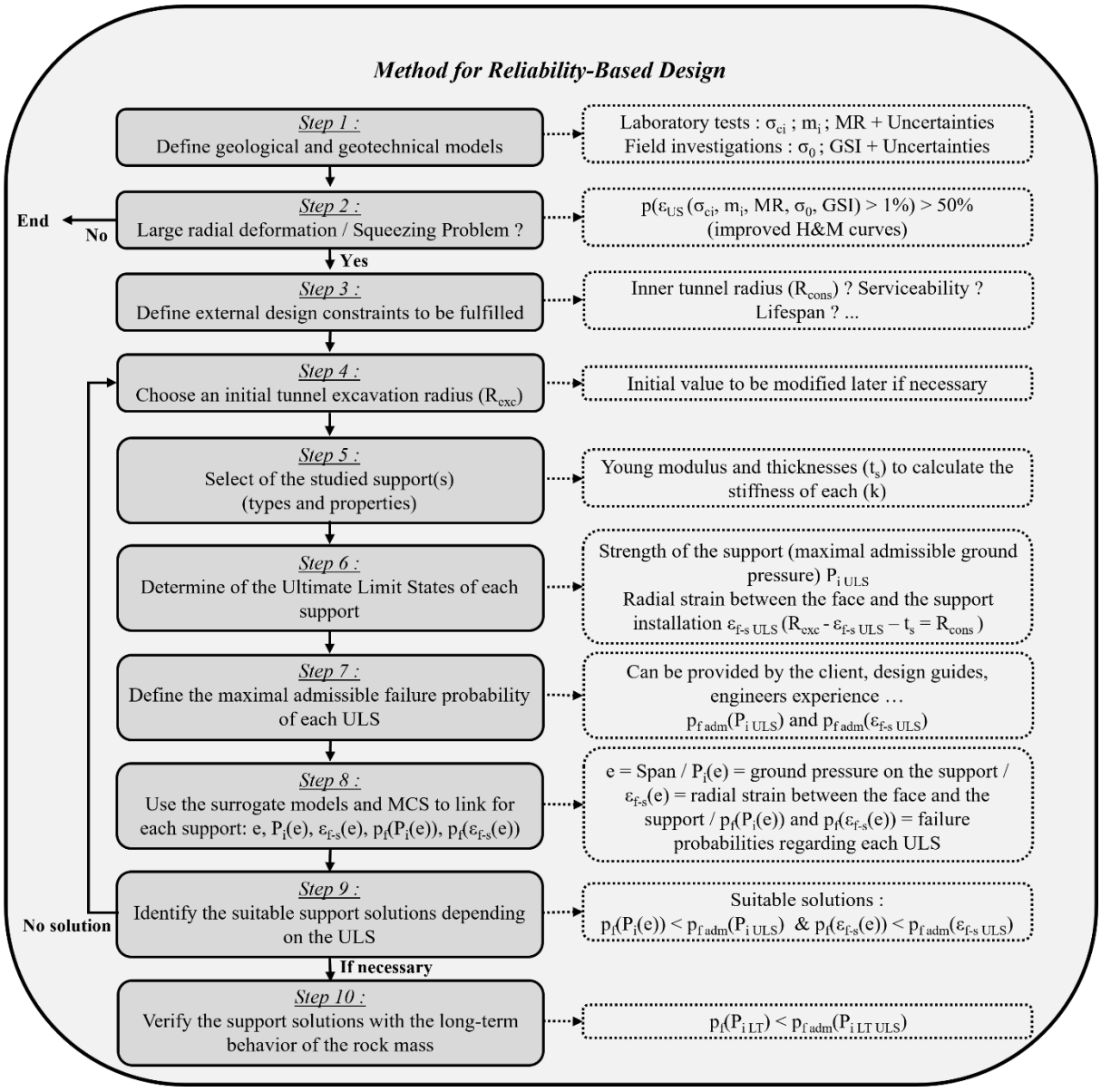

Figure 5-8: Method to perform reliability-based design using the surrogate models; p(..) is a probability

5) A specific or range of stiff support (types and properties) also needs to be selected. It is with these supports that the RBD will be performed: rigid steel set, shotcrete, classes of strength, etc. It can be necessary to determine the equivalent Young's modulus, thicknesses and strength, for discontinuous support or composite support.
6) For each support, ultimate limit states (ULS) have to be defined. The ULS are based on external constraints and do not include partial factors. They are used for the calculation of failure probabilities. They can be fixed values such as the maximal admissible ground pressure on the support or maximal radial strain, but also random variables if uncertainty is considered regarding the support (strength of the support element, thickness, tunnel radius, etc.). For example, if the internal radius needs to be at least 4m (external constraint, Step 3), the excavation radius is chosen to be 4.5m (Step 4) and the support thickness (stiff support, shotcrete, σ_c = 30 MPa) is 30 cm (Step 5). The ultimate limit state for the ground pressure on the support is 2.0 MPa (30*0.3/4.5 approximate expression). The ULS for the radial strain is 4.4%: (4.5-0.3-4)/4.5.

7) For each ULS, a maximal admissible failure probability for the design (external constraints) has to be determined. For example, the maximal admissible failure probability of the support is chosen to be 1%, e.g. it is the maximal acceptable probability of the results being higher than the ULS.
8) After defining all the external constraints and tested design, the surrogate models are used to develop curves linking the distance between the face and the support installation (span), the ground pressure on the support, and the radial strain between the face and the support. The failure probabilities of each ULS are also estimated using Monte Carlo Simulation performed on the surrogate models and considering the various uncertainties.
9) It is possible to determine the suitable support solutions respecting the maximal admissible failure probability of each limit state. If no relevant solution exists from the proposed type of support, the approach can be performed using other supports, yielding supports can be included, or the excavation diameter can be increased. This have to be repeated until satisfactory solutions are found (back to Step 4).
10) The last step is to include long term behavior, as the ground pressure on the support might also be a ULS. If necessary, a lining can be introduced to accommodate the long-term behavior of the rock. As for the support, the lining might be associated with an ultimate limit state and a maximal admissible failure probability.

An illustrative example of this reliability-based design approach is presented in the following section.

5.3.2 Theoretical case studies

To illustrate the reliability-based design method presented above, the following example is considered (step 1 and 2):

Table 5-6: Rock mass properties and support strength for the illustrative example of the RBD approach

Properties	σ_{ci}	m_i	MR	GSI	σ_0	σ_c shotcrete (C30/35)
Mean value	60 MPa	12	450	30	25 MPa	38 MPa
Coefficient of Variation	20%	15%	-	15%	15%	13%
Min - Max	40 - 80 MPa	8 - 16	400 - 500	20 - 40	20 – 30 MPa	-
Distribution law	Normal	Normal	Uniform	Normal	Normal	Normal

The long-term property corresponds to a reduction of 5 of the GSI value (arbitrary choice from the author) in the entire rock mass, and not just at the vicinity of the tunnel, as it is impossible with the methodology proposed based on the results of the surrogate models.

The final internal radius needs to be at least 4m (external constraints, Step 3). The objective is to determine whether or not a yielding support is necessary, the radius of excavation (R), the distance of installation of the stiff support (e) and its thickness (t_s), as well as the thickness of the lining (t_l). The failure probability associated with ULS on the strength of support needs to be smaller than 1%, the failure probability associated with ULS on the radial strain between the face and the support needs to be smaller than 5%, and the failure probability associated with ULS on the strength of the lining needs to be smaller than 0.1% (Step 7). The stiff support and the lining are composed of shotcrete with a Young Modulus of 10 GPa and f_{ck} of 30 MPa (characteristic value). The calculations are performed using the Excel sheet presented in

Appendix 6, and the methodology presented in Chapter 4.3.3 and Appendix 5 for the long-term behavior.

The radial strain without support is expected to be 7.2% with a 95% confidence interval of [3.1%; 16.9%] associated with the existing uncertainties (Table 5-6). The plastic radius is 2.39 Radii with a 95% confidence interval of [1.93R; 3.01R].

The risk of squeezing problem based on the Hoek and Marinos (2000) classes is:

Hoek and Marinos's (2000) classes				
A (ε<1%)	B (1%<ε<2.5%)	C (2.5%<ε<5%)	D (5%<ε<10%)	E (ε>10%)
0.00%	1.56%	21.31%	49.21%	27.93%

Figure 5-9: Probability of each of Hoek and Marinos (2000) classes for the illustrative example

The squeezing problem is expected to be severe (class C) to extreme (class E), depending on the geological and geotechnical uncertainties.

Initially based on the expected radial strain without support (Figure 5-9), the excavation radius is chosen to be 4.8 m (Step 4). It is chosen to vary the span between 2 m and 16 m, and the thickness of the support between 0.2 m and 0.4 m (Step 5). The lining is supposed to be 0.2 m thick, which could be modified afterward if necessary. The surrogate models synthetized in the Excel sheet (Appendix 6) are used to link the span, the ground pressure on the support, the radial strain between the face and the support, and the failure probabilities (both for the pressure and the radial strain), for each thickness of the support (0.2m, 0.3m, and 0.4 m) (Step 8). The results are presented in Figure 5-10. For each configuration (a span and a thickness), values of ground pressure on the support far from the face, of radial strain, failure probabilities are calculated. Then the results are connected using a continuous curve, leading to Figure 5-10.

For the failure probability associated with the ground pressure, the ultimate limit states correspond to maximal admissible pressure before failure of the support. No partial factors are considered, and the variability of the strength of the shotcrete is included, as defined in the Eurocodes (Appendix 6). The ultimate limit states for the radial strain ($\varepsilon_{f\text{-}s\ ULS}$) are obtained as follows (Step 6):

$$\varepsilon_{f-s\ ULS} = \frac{R_{exc} - t_s - t_l - R_{int}}{R_{exc}} \qquad (5-5)$$

Where R_{exc} is the excavation radius, R_{int} is the internal radius to be guaranteed (design constraint), t_s the thickness of the support and t_l the thickness of the lining.

Table 5-7 summarize the results of Figure 5-10 regarding the acceptable failure probabilities (Step 9). It can be noted that the value of the ULS of Pi (Table 5-7) is a deterministic value associated with the characteristic value of the shotcrete strength (f_{ck}). The calculation of the failure probability includes the uncertainty associated with this parameter (Table 5-6).

Table 5-7: Constraint for the design to respect the expected failure probabilities

	Pressure		**Radial Strain**	
Support thickness	**ULS (P_i MPa)**	**p_f < 1% ?**	**ULS ($\varepsilon_{f\text{-}s}$)**	**p_f < 5% ?**
t_s = 0.2 m	1.22	Span (e) > 14.5 m	8.3%	Span (e) < 16 m
t_s = 0.3 m	1.82	Span (e) > 12 m	6.3%	Span (e) < 10.5 m
t_s = 0.4 m	2.40	Span (e) > 10.5 m	4.2%	Span (e) < 6.5 m

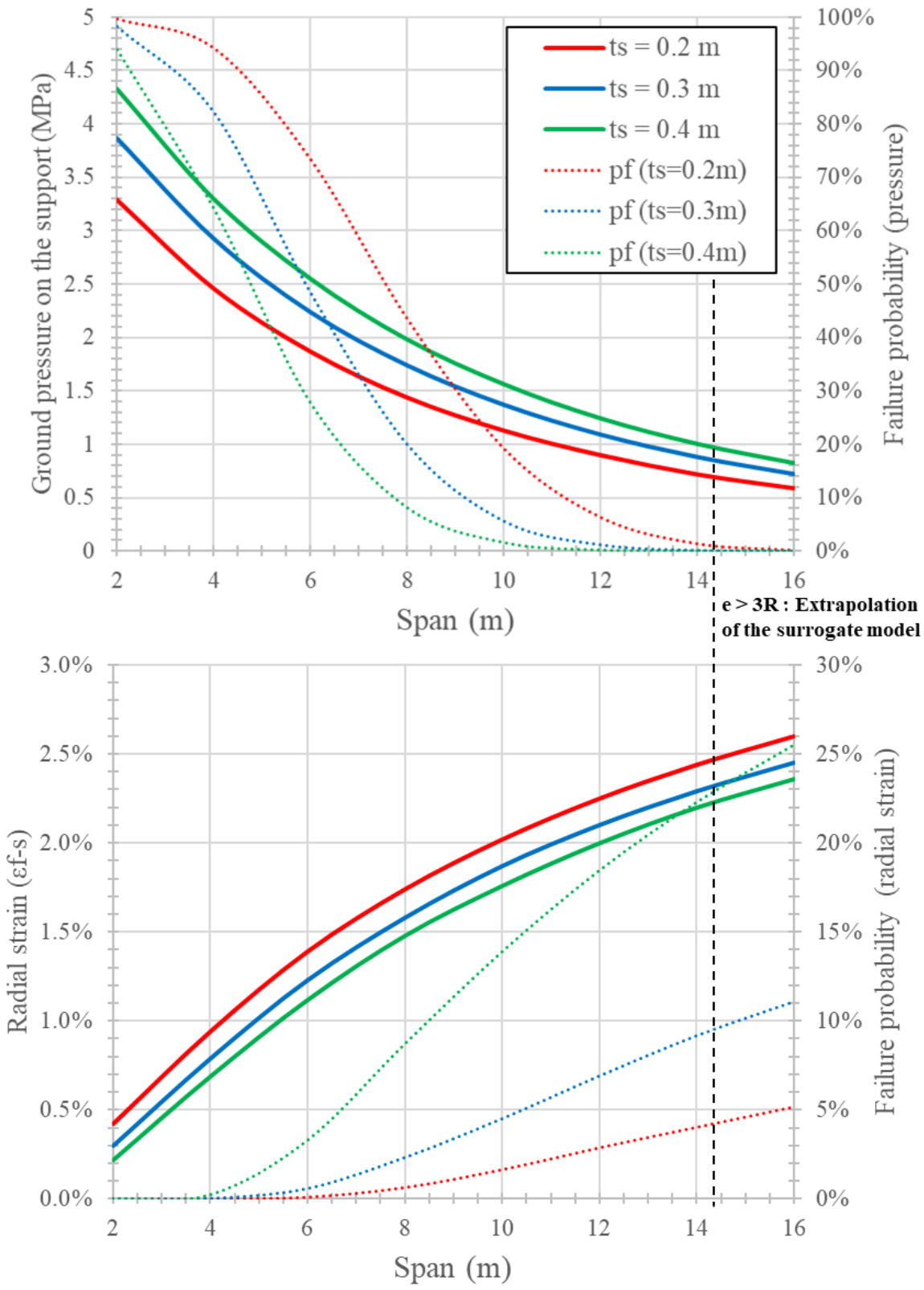

Figure 5-10: Relationship between the span, the radial strain, the ground pressure on the support far from the face and the failure probabilities for the illustrative example; t_s is the thickness of the support; pf is the failure probability; the y-axis values are the median values

The only solution here is to install a 0.2 m thick shotcrete between 14.5m and 16m from the face. For the other possibilities, it is necessary to increase the excavation radius to respect both

limit states. As the span is relatively important here, yielding support could be used to guarantee the safety of the operation between the face and the support.

5.3.2.1 Consideration of a yielding support

Steel set with sliding gaps (TH type) embedded with 20cm of shotcrete are considered as yielding support. Gaps are also created in the shotcrete ring to allow the support the converge (typical example presented in Chapter 4.1.1). Then, when the targeted radial displacement is reached or the distance to the face is large enough, the gaps in the shotcrete are filled, transforming it into a stiff support. Complementary shotcrete is also added to reach the targeted thickness. To respect the constraint on the radial strain, the yielding support can accommodate 35 cm of radial deformation (7.3% of radial strain) as the excavation radius is 4.8 m, the support is 0.2 cm thick, the lining is 0.2 cm thick, and the internal final radius is 4m. 5 cm are considered as margin of error. 35 cm of radial displacement (4.8m tunnel radius) corresponds to a reduction of the tunnel circumference of around 2.2 m. 7 sliding gaps of 30 cm are necessary to accommodate the maximum expected radial displacement.

As presented in Appendix 4, using a yielding support applies a confining pressure on the span, leading to a reduction of the radial strain. For this situation (tunnel radius and yielding support), a reduction of 15% of the radial strain between the face and the stiff support can be expected (steel set with sliding force of 500 kN, spaced every 0.8m in a 4.8m tunnel radius leads to a confining pressure of around 130 kPa, and the span is 3 Radii). The calculation associated with a thickness of 0.2 cm (Figure 5-10) is performed with the consideration of this reduction through an increase of 15% of the ultimate limit state for the radial strain. A 5% failure probability regarding this limit state is reached 20m from the face (p_f = 5.0%). The associated ground pressure on the support far from the face is 0.41 MPa (failure probability < 0.01 %). All solutions considering a span between 14m and 20m are suitable regarding the limit states.

5.3.2.2 Consideration of the long-term behavior

The choice of the span value to use (between 14 m and 20m) is made to respect the long-term failure probability. The calculation of this ground pressure is performed by transforming the problem into a 2D plane strain problem, then by reducing the GSI of the rock mass to its long-term value and then calculating the equilibrium using the close form analytical formulation of Carranza-Torres and Fairhurst (1999).

The maximal admissible ground pressure before failure for the combination of support and lining is 2.50 MPa (Eq(A6-3), Appendix 6, no partial factor, radius of 4.8 m, thickness of 0.2 m + Eq(A6-3), Appendix 6, no partial factor, radius of 4.6 m, thickness of 0.2 m). Figure 5-11 summarizes the long-term ground pressure and the failure probability for the support and the lining depending on the span value. The estimation of the failure probability has been performed using a 100 000 realizations Monte Carlo simulation, as presented in Appendix 6. To obtain this figure, the calculation of the short-term ground pressure is performed using only the support, then the lining is introduced, the rock mass properties are modified, and the long-term ground pressure is calculated, as well as the failure probability. This is done for each value of span between 14m and 20m, then the results are connected using a continuous curve, leading to Figure 5-11.

To guarantee a long-term failure probability smaller than 0.1%, the span needs to be at least 16.3 m (Figure 5-11). The choice is made to consider a span of 17m to respect all the constraints.

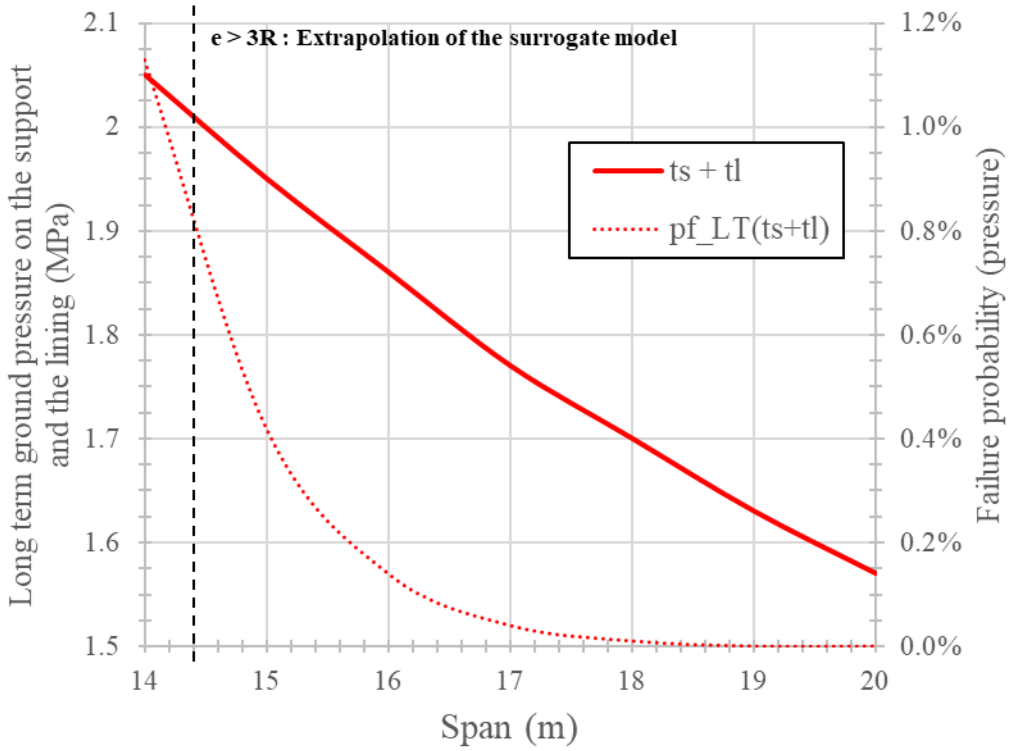

Figure 5-11: Long term ground pressure on the support (ts = 0.2m thick) and the lining (tl = 0.2m thick) and the associated failure probability depending on the span of the support installation

Figure 5-12 summarizes the preliminary support design considered here. The lining is supposed to be installed 72 m from the face (15 Radii), when the maximal ground pressure on the support is reached (i.e. far from the face).

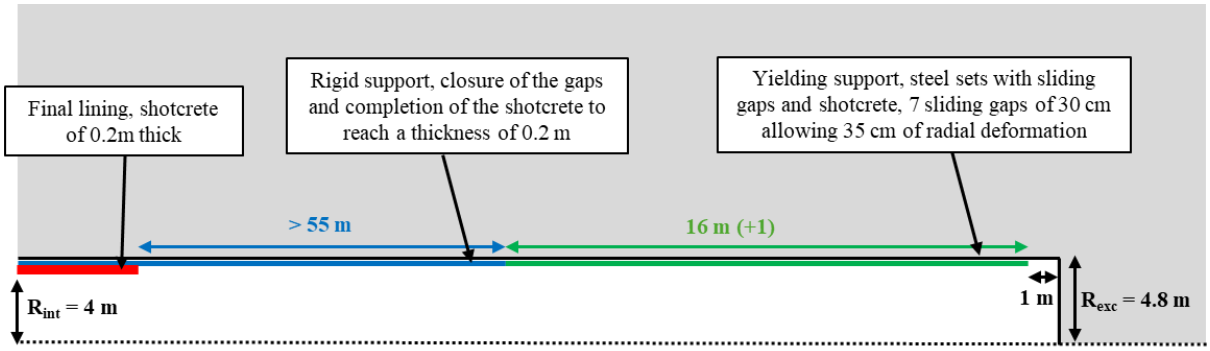

Figure 5-12: Summary of the preliminary support design of the tunnel

The rigid support is composed of 0.2 m of shotcrete installed 17 m from the face and leads to a short-term ground pressure on the support of 0.59 MPa (p_f = 0.04% < 1%). The associated radial strain between the face and the support is 2.3% (2.7%*0.85, including the confining pressure of the yielding support, p_f = 3.6% < 5%), and the long-term ground pressure on the support and the lining is 1.86 MPa (p_f = 0.03% < 0.1%). So, the support design is validated regarding all the ultimate limit states and external constraints.

5.4 Global safety factors, partial factors and failure probabilities

When speaking of tunnel support design and consideration of uncertainties, three approaches exist: deterministic approach based on targeted global safety factors, semi-probabilistic approach based on partial factors, and probabilistic approach based on failure probabilities. As Bozorgzadeh (2018) pointed out, there is no consensus about safety criteria within the rock engineering community, unlike in structural or soil engineering. An in-depth analysis and discussions regarding the limit state, development of partial factors and similarities to other engineering fields can be found in Bozorgzadeh (2018).

Unlike to other engineering fields (structural engineering or soil engineering), the global safety factor or partial factors such as in the Eurocode 7 and the French Recommendation on the adaptation of the Eurocode for tunnel designs (AFTES – GT 29R2F1) that can be used, are not directly associated with rock tunnel engineering, but rather adapted from other fields. For example, the partial factor 1.35 that needs to be applied on the internal forces of the support for the design comes directly from the Eurocode, and it corresponds to a partial factor applied on the load combination (1.35 for permanent actions, 1.5 for unfavorable variable action). It originates from reliability analysis perform in structural engineering loading conditions, and has absolutely no link with support tunnel design, or the uncertainties existing on the internal forces in a support. The external load and their variability are completely different to the one of a building. The main question that it is possible to ask is: Can safety factors, partial factors and failures probabilities be linked depending on the geological and geotechnical uncertainties for rock tunnels?

In this section, a methodology is proposed to try to give some answers using the surrogate models developed in Chapter 3 and Chapter 4, as they enable to easily perform basic reliability calculations. It means that it is possible to define a design using a deterministic approach (global safety factor) or a semi-probabilistic approach (partial factors) and then, based on the existing uncertainties, to estimate the failure probably of the support.

5.4.1 Methodology

In the specific situation associated with the surrogate models, applying partial factors on the internal load in the support (γ_f) and on the strength of the support element (γ_s) is identical to target a global safety factor ($SF = \gamma_f * \gamma_s$) because the design parameter is the orthoradial compressive stress in the support, the tunnel is circular and the ground pressure is uniform around the support.

The idea is to estimate for a large number of randomly chosen situations the failure probability associated with a design optimized through deterministic calculations (e.g. safety factors) and to introduce a specific amount of uncertainties on the input parameters (fixed Coefficient of Variation and identical for every parameter) to calculate the associated failure probabilities. The algorithm used is presented in Figure 5-13, and has been coded using Python language.

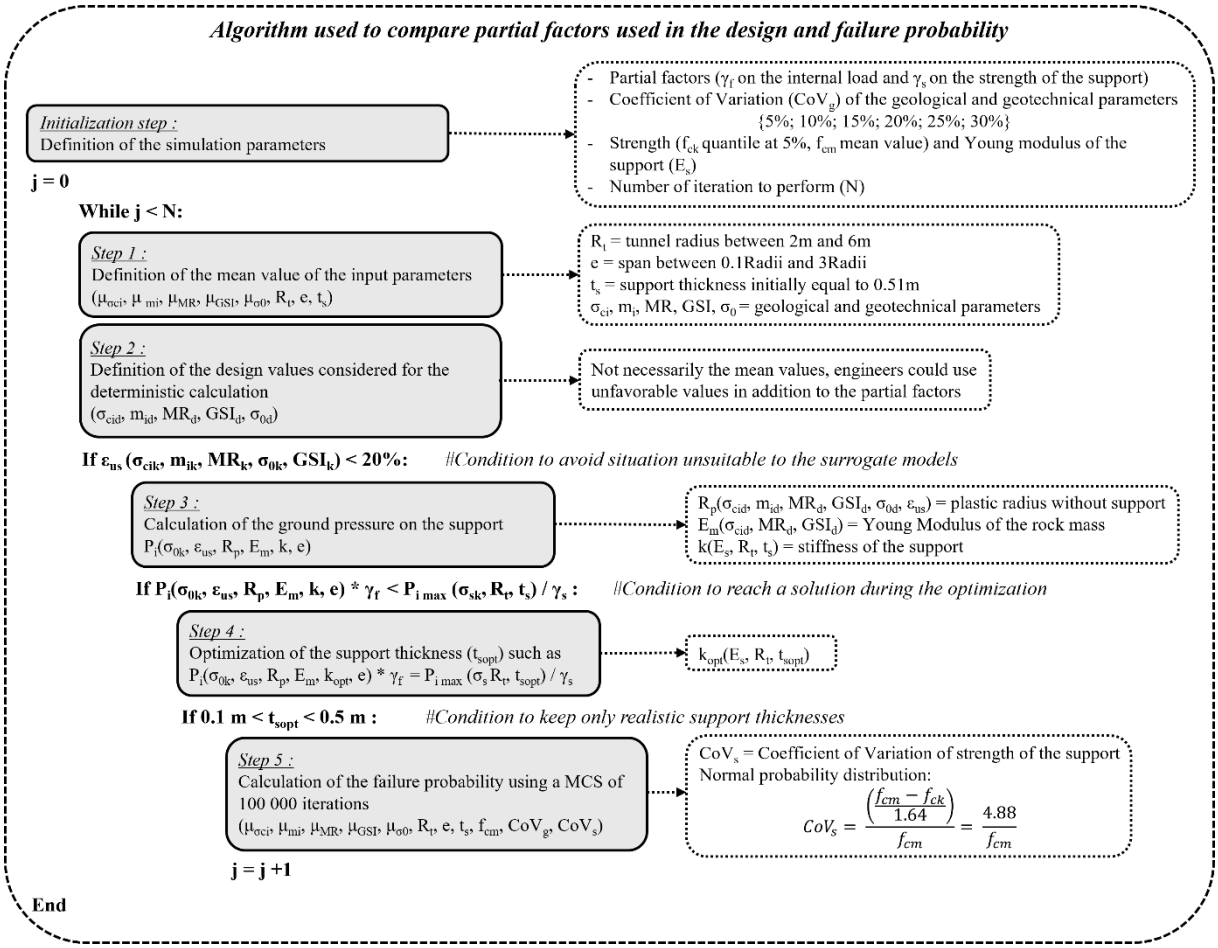

Figure 5-13: Algorithm used to estimate the failure probability of an optimized random design using partial factors

This method is applied for several values of CoV, safety factors and hypothesis regarding the geological and geotechnical parameters.

5.4.2 Results for three situations

The method presented above is applied to three situations:

1) The first situation considers a partial factor of 1.35 on the internal forces (γ_f) and a partial factor of 1.5 on the strength of the support element (γ_s). The global safety factor is 2.025 (1.35*1.5). The deterministic calculations and the optimization are performed on the mean value of input parameters (σ_{ci}, m_i, MR, GSI, σ_0). For each value of CoV, 10 000 calculations of failures probabilities are performed.
2) The second situation considers a partial factor of 1.35 on the internal forces (γ_f) and a partial factor of 1.5 on the strength of the support element (γ_s). The global safety factor is 2.025 (1.35*1.5). The deterministic calculations and the optimization are performed on the mean value minus one standard deviation for σ_{ci}, m_i, and GSI. The mean value is considered for MR and σ_0. In this situation, unfavorable hypotheses are made on the strength of the rock mass. For each value of CoV, 2 000 calculations of failures probabilities are performed.
3) The third situation considers a partial factor of 1.35 on the internal forces (γ_f) and a partial factor of 1.0 on the strength of the support element (γ_s). The global safety factor is 1.35 (1.35*1.0). The deterministic calculations and the optimization are performed on

the mean value minus one standard deviation for σ_{ci}, m_i, and GSI. The mean value is considered for MR and σ_0. In this situation, unfavorable hypotheses are made on the strength of the rock mass. For each value of CoV, 2 000 calculations of failure probabilities are performed.

It can be noted that, for situations 2 and 3, only 2 000 calculations are performed each time compared to the 10 000 for situation 1. This limitation is due to time constraints. Each failure probability calculation takes about 10s using Python. For the first situation alone, 60 000 calculations (10 000 for each CoV value) are required, amounting to approximately 170 hours of computation. The convergence of the results of the simulation is better for 10 000 realizations compared to 2 000 realizations but stay acceptable.

The results of each three situations are presented in Figure 5-14. It can be noted that it is not possible to obtain smaller probabilities than 0.001% as the Monte Carlo simulation performed in Step 6 only includes 10^5 realizations. As Monte Carlo simulation is not adapted for small probabilities, the probabilities smaller than 0.1% (10^{-3}) need to be used with extreme caution (Huang *et al.* 2017b).

As expected, the larger the uncertainty on the input parameters is, the larger the failure probability is. For the first situation with CoV of 30%, most of the failure probabilities are between 0.7% and 21%, while with a CoV of 5%, all the failure probabilities are smaller than 1%. For the CoV of 15%, the failure probabilities are between 0.002% and 13%. Some tests have also been performed in which the tunnel radius and the span are fixed. The range of failure probabilities is still important.

Unfavorable hypotheses on the rock mass strength during the deterministic calculation leads to smaller failure probabilities. In the situation 2 with a CoV of 30%, most of the failure probabilities are between 0.04% and 0.6%, compared to 0.7% and 21% in situation 1.

Smaller targeted safety factors (comparison of situation 2 and 3) are associated with larger failure probabilities, mostly for small CoV. It also leads to a smaller variability in the failure probabilities obtained. For a CoV of 30%, most of the failure probabilities of situations 3 are between 0.7% and 2%.

The uncertainty on the input parameters has a major impact on the failure probabilities of a design obtained with deterministic approach. Similarly, hypothesis regarding conservative value for the rock mass strength or the choice of targeted safety factors also have a nonnegligible impact on the failure probability. For a tunnel support composed of shotcrete designed based on the Eurocode (situation 1), more than half of the results including an uncertainty on the input parameters higher than 20% are associated with a failure probability higher than 1%. Depending on the external constraints, this failure probability could be seen as relatively high, and so for preliminary design under large uncertainties, careful reflections are necessary on the choice of the safety factor/partial factors, or the maximal admissible failure probability.

*Situation 1 : SF = 2.025 (1.35*1.5), μ for σ_{ci}, m_i, and GSI*

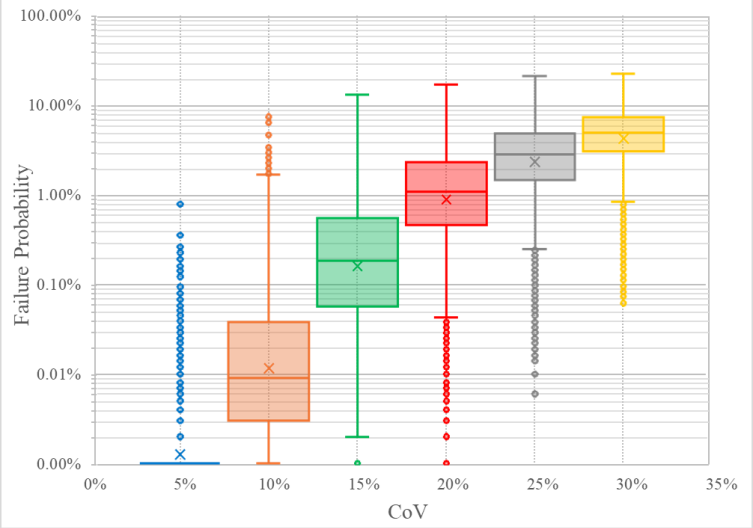

*Situation 2 : SF = 2.025 (1.35*1.5), μ-σ for σ_{ci}, m_i, and GSI*

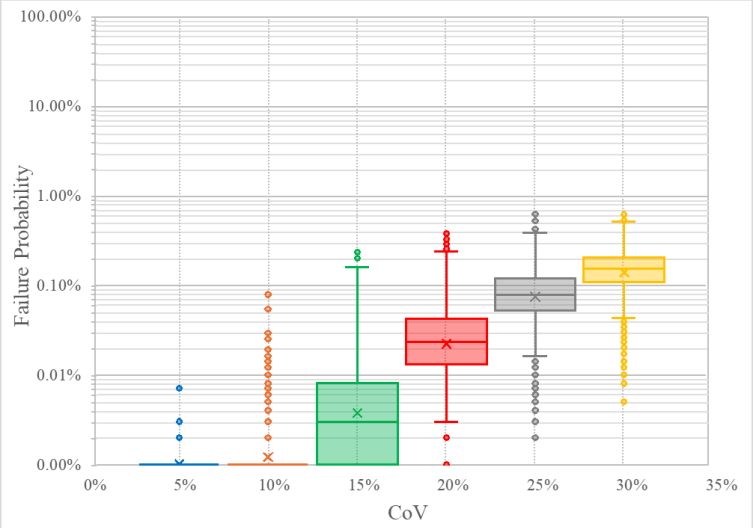

*Situation 3 : SF = 1.35 (1.35*1.0), μ-σ for σ_{ci}, m_i, and GSI*

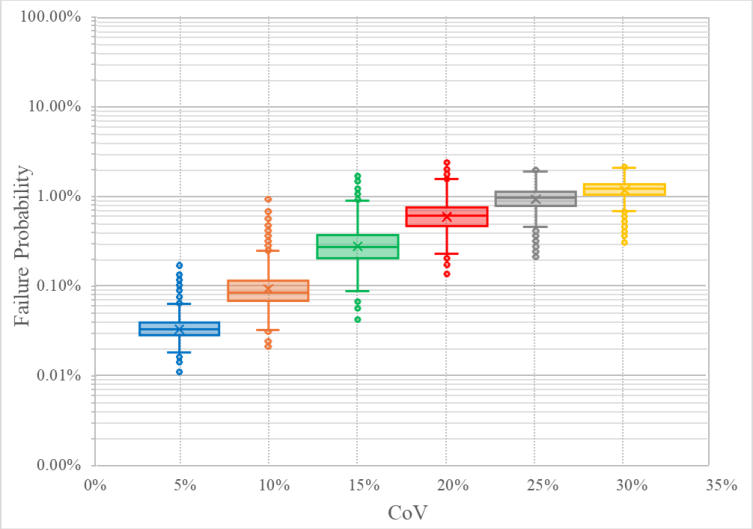

Figure 5-14: Comparison between safety factors, probability of failures and uncertainties on the input parameters; μ is the mean; σ is the standard deviation

5.5 Conclusions

This chapter presents how uncertainties can be introduced and propagated through the various surrogate models presented in Chapter 3 and Chapter 4. It starts with a brief introduction on how these geological and geotechnical uncertainties can be quantified and highlights some examples of reliability calculations used for tunnel design. Then, a method called the “3-point” method is presented to easily introduce and propagate the uncertainties based on the improved curve of Hoek and Marinos developed in Chapter 3. The probability density of the radial strain without support can be estimated by considering only three specific points, when couple of hypotheses are fulfilled. An in-depth analysis of this method is performed.

For the surrogate models considering the interaction between the rock mass behavior, the support, and the face advancement, a method is proposed to perform reliability-based design easily. A theoretical example is provided to show how easily it could be used during preliminary tunnel design. The reliability calculations performed with this method enable the creation of a link between safety factors, failure probability and uncertainties on the input parameters. To study this relationship, a large number of comparisons is made when the uncertainties of the input parameters are fixed (CoV), the tunnel design is optimized using deterministic approach based on safety factors (global safety factors are equivalent to partial factors in this situation), and the failure probability of this design is calculated. For large uncertainties, the failure probability can be high, higher than 1% or more, even when designing with large safety factors.

Since the comparison is made only for a small number of hypotheses (three), it could be generalized to a larger set of design situations including other assumptions on the partial factors and design values, and also other support types (here, only structural shotcrete is considered). This could lead to more general recommendations on which safety factors or hypotheses on the design values are to adopt, depending on the level of uncertainty during preliminary tunnel design, in order to reach a target failure probability, without explicitly calculating it (as in the Eurocode with the semi-probabilistic approach).

Chapter 6 - Case study of large radial deformation: Yacambu-Quibor tunnel in Venezuela

Chapter Abstract: The Yacambu-Quibor tunnel in Venezuela is one of the most typical case studies of large radial deformation in highly fractured rock mass. This chapter briefly presents this tunnel project, and then the surrogate models are applied to two sections of the tunnel: one corresponding to the worst-case scenario expected to be encountered, and one corresponding to a failed section (between PM12+750-PM12+850). The results of the surrogate models are compared with numerical calculations performed in the literature and the convergence-confinement method. In this chapter, the objective is not to propose a relevant design using the reliability-based design method presented in Chapter 4, but to test the relevance of the results of the surrogate models on a real case study compared to other classical approaches.

6.1 Preliminary considerations

Hoek and Guevara (2009) performed a detailed presentation of the project. Some important elements are presented below.

6.1.1 Project presentation

The Yacambu-Quibor tunnel is a Venezuelan tunnel aiming to carry more than 350 million cubic meters of water per year from the wet and tropical valley of Orinoco to the semi-arid Quibor valley (Hoek and Guevara 2009). The tunnel is 23.3 km long with an internal diameter of around 4m. The construction was completed in July 2008 after more than 32 years and eight successive contracts (Hoek and Guevara 2009).

The principal technical issues that had to be overcome were the severe squeezing problems in very weak graphitic phyllites at depths of up to 1270 m below surface (Hoek and Guevarra 2009) (Figure 6-1).

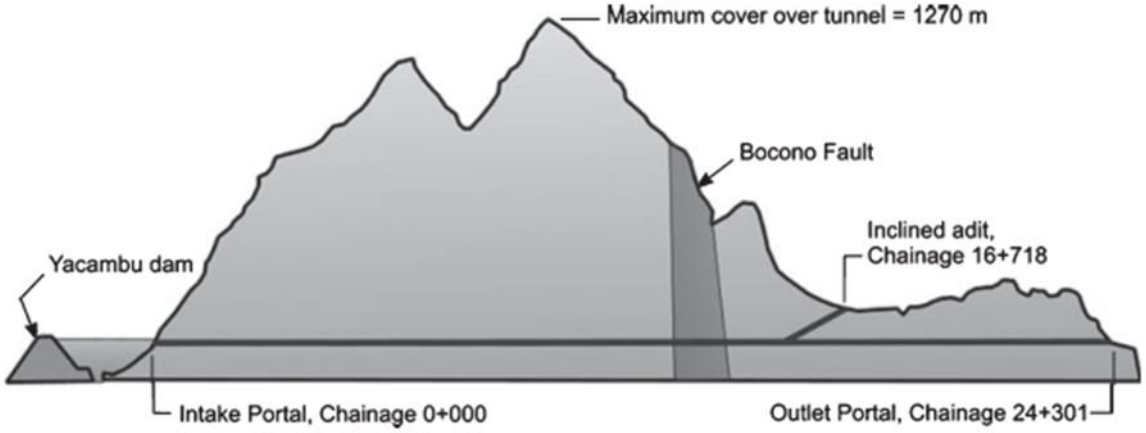

Figure 6-1: Cross-section along tunnel alignment (from Hoek and Guevara 2009)

According to Hoek and Guevara (2009): *"The phyllitic rock mass which dominates the mountain range in the Yacambu-Quibor area ranges from strong and reasonably massive silicified phyllites in the dam area to severely tectonically deformed graphitic phyllite along most of the tunnel alignment [...] but rather than the silicified phyllites anticipated on the basis of the dam site investigations, a high proportion of the rock consists of a highly tectonically deformed graphitic phyllite which behaves in a completely different way than the silicified phyllite"* Only three vertical borehole were done, and the deepest one was abandoned at 300 m because of technical difficulties.

The incorrect interpretation of the geological conditions led to inappropriate technical solutions. The excavation started with two open faces hard rock TBMs (Hoek and Guevara 2009). After two contracts (between 1976 and 1979) associated with slow advance rates of the TBM (unsuitable design for weak and foliated rock), the work was suspended (technical and contractual discussion). One TBM was removed from the tunnel while the other one was left in place which was finally completely destroyed by the squeezing ground. The work resumed in this part of the project only eight years after (Hoek and Guevara 2009). Yielding supports were introduced in 1991, but difficulties were still encountered with floor heaves in tunnel sections with horseshoes profile. Steady progress started to be made in 2004 after the owner and

contractor agreed on using only yielding support and circular geometry, and to use routine constructive procedure no matter the rock conditions encountered at the face (Hoek and Guevara 2009). A detailed summary of the advancement and difficulties of each contract can be found in Hoek and Guevara (2009).

Figure 6-2 and Figure 6-3 present the various class of rock units encountered in the project and rock mass properties for each one of them.

Class	Type of rock	Characteristics
A	Predominance of silicified phyllite with small amounts of calcareous and/or graphitic phyllite	Cemented layers from 5 to 10 cm in thickness with high strength and high deformation modulus
B	Predominance of calcareous silicified phyllite with intervals of graphitic phyllite	Cemented layers from 2 to 3 cm in thickness with average strength and average deformation modulus
C	Graphitic phyllite with some intervals of silicified phyllite	Thin lamination from 0.1 to 1 mm with low strength and highly deformable
D1	Tectonically deformed, folded and sheared in Classes A, B and C	Behaves as homogeneous rock mass with zero volume change during deformation
D2	As for D1 with clay gouge in contacts	Highly plastic deformation with zero volume change

Figure 6-2: Classification of Yacambu-Quibor rock unit (from Hoek and Guevara 2009)

Class	Condition	σ_{ci} MPa	GSI	m_i	m_b	s	a	σ_{cm} MPa	E MPa	c MPa	ϕ deg
A	Design	100	75	10	4.095	0.0622	0.501	32.49	45,000	5.76	43.2
	Long term	100	38	10	1.092	0.010	0.513	13.34	7656	2.49	33.0
B	Design	75	65	10	2.865	0.0205	0.502	18.49	26,000	3.73	38.6
	Long term	75	32	10	0.882	0.0005	0.520	8.66	3825	1.99	29.0
C	Design	65	50	7	1.174	0.0039	0.506	9.59	11,000	2.36	30.3
	Long term	65	25	7	0.481	0.0002	0.531	5.14	2140	1.40	22.9
D1	Design	50	35	7	0.687	0.0007	0.516	5.19	3119	1.59	24.1
	Long term	50	17	7	0.361	0.0001	0.553	2.99	1091	0.99	18.7
D2	Design	50	25	7	0.481	0.0002	0.531	3.95	1646	1.26	21.2
	Long term	50	13	7	0.313	0.0001	0.570	2.51	928	0.84	17.4

σ_{ci}, Uniaxial compressive strength of intact rock pieces; GSI, Geological Strength Index; m_i, Material constant m for intact rock pieces; m_b, Material constant m for rock mass; s, Material constant for rock mass; a, Material constant for rock mass; σ_{cm}, Uniaxial compressive strength of rock mass; E, Modulus of deformation; c, Equivalent cohesive strength of rock mass; ϕ, Equivalent friction angle for rock mass

Figure 6-3: Estimated rock mass characteristics based on the Geological Strength Index and the Hoek&Brown failure criterion (from Hoek and Guevara 2009)

Hoek and Guevara (2009) specified that "*the design values are based on short term observation of freshly exposed rock in the tunnel and […] have been used for the calculation of the performance of the tunnel during construction. The long-term values are based on estimates of the deterioration of the rock mass over time as a result of […] creep, progressive breakdown of individual rock pieces under high stress and groundwater percolation. Since some portions of the tunnel were constructed 20 or 30 years ago […] it has been possible to carry out crude checks on the assumed long-term parameters by means of back analyses*" The long-term properties correspond to the GSI being divided by a factor 2.

It is of the outmost importance to note that the calculation and more specially the back analyses have been performed using a convergence-confinement method with potentially 2D plane strain model. As discussed in Chapter 4.1.2.5 and Appendix 1, the CV-CF method for highly fractured rock mass (large plastic radius) is known to underestimate the ground pressure on the support compared to 2D axisymmetric and 3D numerical calculations. The back analyses for long-term behaviors are expected to be unfavorable compared to the real behavior. As the CV-CF method underestimates the real ground pressure, long-term properties need to be worse to reach the same ground pressure as the 2D axisymmetric. This point will be demonstrated in the next section.

6.1.2 Back analysis for long term ground properties

The calculation method impacts the results of back analyses and associated long-term properties. This section highlights this point with a theoretical example as no relevant data is available in the literature for this case study.

Considering a circular tunnel section in rock mass classified D1 (Figure 6-2 and Figure 6-3, design parameter) in an isotropic in-situ stress state of 30 MPa (1150 m of overburden). The radius considered is 2.6m and the support thickness is 0.6m. The support is supposed to be installed 6 m from the face. The maximal admissible ground pressure on the support before failure is 6.1 MPa (Chapter 4.3.3, shotcrete with a characteristic strength of 30MPa and a Young's modulus of 10GPa). It is supposed that this hypothetical tunnel section failed several years after the completion of the section (the face is far from the face). The support failed during the transition between the short-term properties and the long-term properties. As no creep or temporal parameter is considered, it is not possible to know whether the transition had just begun or was almost finished at the time of the failure.

The surrogate models based on axisymmetric numerical calculations lead to a short-term ground pressure on the support of 3.3 MPa. According to this approach, the global safety factor is 1.85. The uncertainty of the surrogate model leads to 95% confidence interval on the safety factor between 2.39 and 1.50. Since no uncertainties are considered here on the input parameters, the uncertainty in the strength of the support is not considered.

The short-term ground pressure obtained with convergence-confinement method (CV-CF) is much smaller, around 0.8 MPa (Figure 6-4 and Figure 6-5) leading to a safety factor of 7.7. The LDP (Longitudinal Displacement Profile) and the GRCs (Ground Reaction Curve) are obtained using numerical modelling rather than close from analytical solutions. The models used are the ones presented in Chapter 3.2.1 and Chapter 4.2.1. In Figure 6-5, several GRC are represented corresponding to various GSI value (30, 25, 20 and 17). The SCC (Support Characteristic Curve) is presented as the results of the CV-CF method (red curve). The equivalent SCC associated with the axisymmetric model used to estimate the long-term ground pressure is also represented in green (Figure 6-5). The surrogate model allows the estimation of the short-term ground pressure on the support (3.3 MPa), then GRC with a GSI of 30 is used to determine an equivalent radial strain (3.1%). Finally, the long-term ground pressure can be estimated using the equivalent SCC (in green) and the GRC of smaller GSI value. A detailed presentation of the method can be found in Chapter 4.3.3 or Appendix 5.

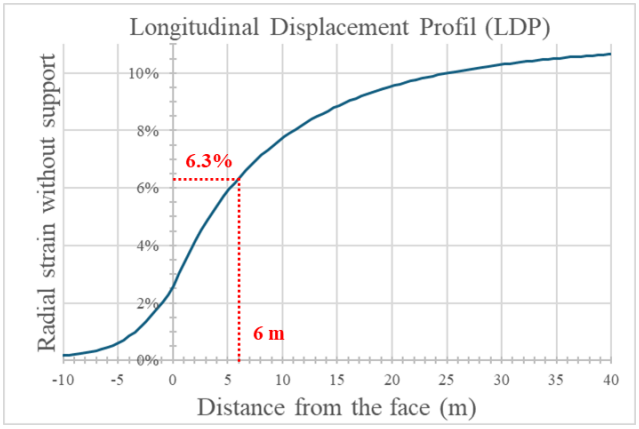

Figure 6-4: Longitudinal Displacement Profile for the theoretical example (class D1, GSI 35)

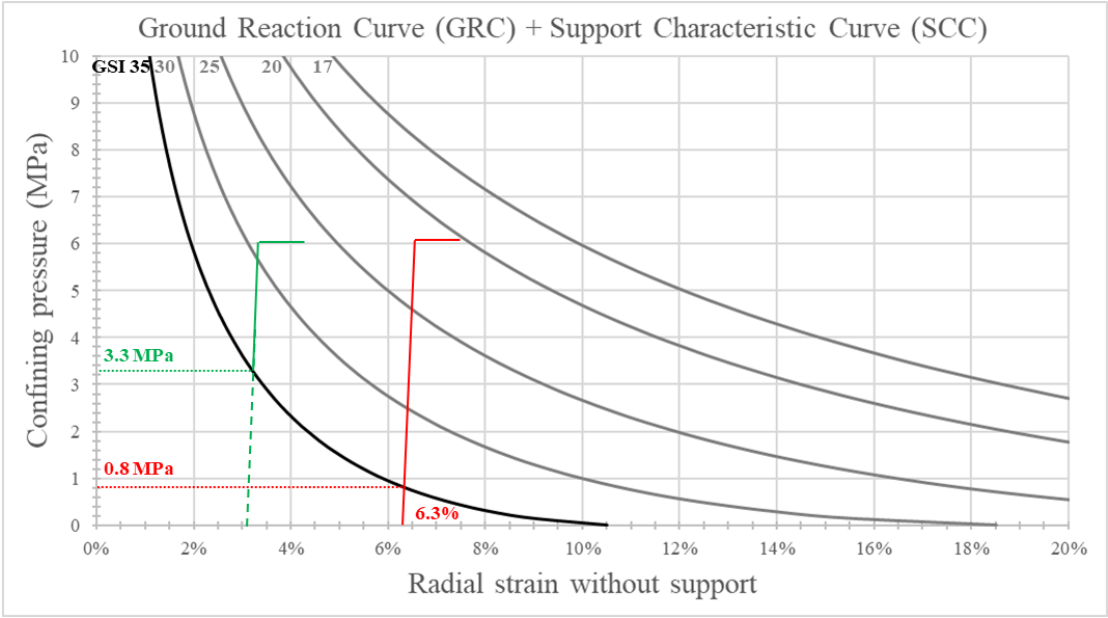

Figure 6-5: Ground Reaction Curve for several values of GSI (35, 30, 25, 20, 17) and Support Characteristic Curve for the CV-CF method (red) and the long-term ground pressure on the support based on the axisymmetric calculation (green)

In this theoretical example the support failed during the transition between short-term behavior and long-term behavior. Performing the back analysis using the axisymmetric numerical results (surrogate models), the method associated for the estimation of the long-term ground pressure (green in Figure 6-5, method presented in Chapter 4.3.3) leads to results that differ from the CV-CF method. Based on surrogate model (and associated method), the support is supposed to fail when the GSI becomes smaller than 29. In the other hand, the support failure obtained with the CV-CF method occurs for a GSI smaller than 22. Mixing both approaches can lead to unrealistic results. For example, performing the back analysis using the CV-CF method and then using axisymmetric approach for designing another section can lead to large overestimation of the ground pressure on the support. If the long-term properties is assumed to be GSI = 22 (Figure 6-5), based on a back analysis performed with the CV-CF method, and if this value of GSI is used with the axisymmetric approach for another section, it will result in long-term ground pressure on the support of 9.3 MPa (prolongation of the SCC until the intersection with the GRC of GSI 22).

The important point here is that the ground properties obtained using back analysis are highly dependent on the calculation technique used. When designs are performed using ground parameters obtained through back analysis, the calculation technique to use should be identical as the one used for back analysis.

This point is important for the following part of this chapter as the objective is to compare the results of the surrogate model with a real case study. Some of the ground parameters used were obtained in the literature through back analysis most likely performed using CV-CF method or equivalent (2D plane strain numerical model). For the long-term behavior, the ground parameters to be used are discussed for each studied section to try to stay relevant with the field observations while not using too unfavorable value due to the modification of the calculation technique (as presented above).

6.1.3 Yielding support used

During the construction several yielding supports have been tested (Hoek and Guevara 2009). Real progress started to be made when the following yielding support was used (Figure 6-6).

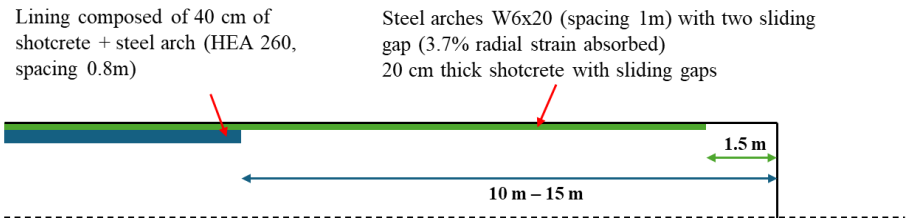

Figure 6-6: Typical yielding support used the construction of the tunnel

The first yielding support was installed at the face and completed between 1.5m to 3m from the face depending on whether the excavation was performed full face or using a top-bench method (Hoek and Guevara 2009, Connor Langford and Diederichs 2013). It is composed of W6x20 steel sets (Anglo-Saxon standard, similar to HEA160 in European standard) with two sliding gaps of 30 cm each. This yielding support accommodates 3.7% of radial strain before the gaps close and starts behaving as a rigid support (Figure 6-7). They are installed every 1m. In between the steel set, a 20 cm thick layer of shotcrete is installed, in which gaps are created not to block the deformation of the yielding support. When the sliding gaps of the steel set are closed or the distance to the face is 15 m, the gaps in the shotcrete are filled. Then a 40 cm thick shotcrete lining is installed 10 m from the face if the sliding gaps were closed before, or otherwise 15 m from the face (Connor Landford and Diederichs 2013). The lining also includes steel sets (similar to HEA260) every 0.8m.

It can be noted that this support has been adapted (distance of installation and thickness of the lining) depending on geological conditions encountered and the overburden (Hoek and Guevara 2009).

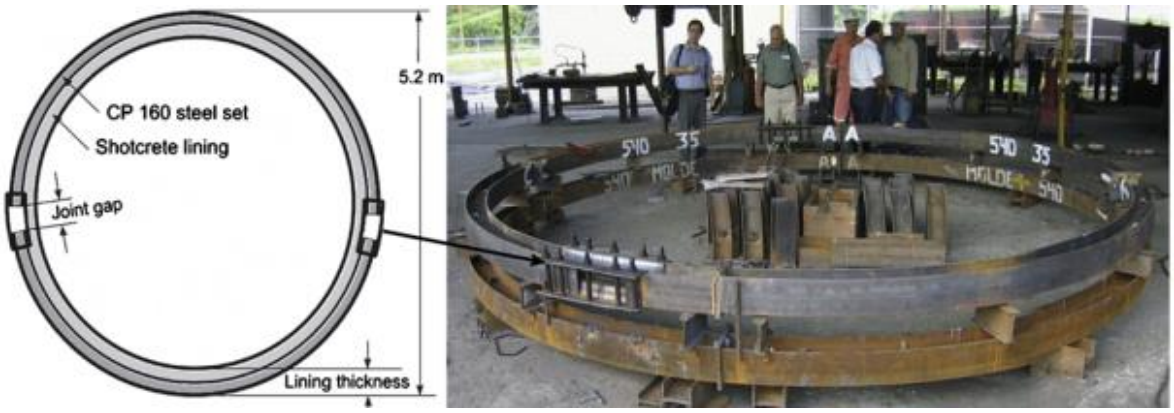

Figure 6-7 : Steel sets with sliding gaps used for the primary lining (from Connor Langford and Diederichs 2013)

6.1.4 Field observations

The design presented above has been used for all the tunnel sections situated in D1 or D2 geological units. Depending on the depth of the tunnel section, the lining was modified through a modification of the shotcrete thickness or without using steel set. The D2 unit was the worst expected geological condition, for most of the tunnel sections, rock mass properties were more favorable. Connor Langford and Diederichs (2013) specified that the shotcrete of the support was regularly damaged when the lining was installed (10 m from the face). Hoek *et al.* (2008) pointed out that the sliding gaps of the steel sets were closed between 5m from the face and 15m from the face (maximal distance for the installation of lining). Hoek and Guevara (2009) present a section of the tunnel where the support has resisted but the lining failed two years after the completion of the excavation of the tunnel section (Figure 6-8). This specific section is studied in detail in Section 6.3.

6.2 Worst case scenario

The design associated with the worst-case scenario has been studied through reliability calculations by Connor Langford and Diederichs (2013). The worst geological unit is considered (D2, Figure 6-2 and Figure 6-3) at the maximal relevant depth 1150 m. The value of the parameters and the associated variability are presented in Table 6-1.

Table 6-1: Rock mass properties used by Connor Langford and Diederichs (2013), and associated variability

	σ_{ci} (MPa)	m_i	σ_0 (MPa)	GSI	MR
Mean (μ)	50	7	30	25	550
Coefficient of Variation	6.0%	14.3%	5.0 %	8.0%	1.0%
Standard deviation (σ)	3	1	1.5	2	5.5
Min and Max values	[40, 60]	[4, 10]	[27, 33]	[19, 31]	[530, 570]

In their study, Connor Langford and Diederichs (2013) did not consider any variability for the in-situ isotropic stress and the modulus ratio. A small variability of these parameters is taken into account during the calculation of failure probabilities.

In the following sections, the methodology used by Connor Langford and Diederichs (2013) is presented, then some calculations are performed using the CV-CF method to show the similarity of the results. Finally, the surrogate model is used considering the support presented above.

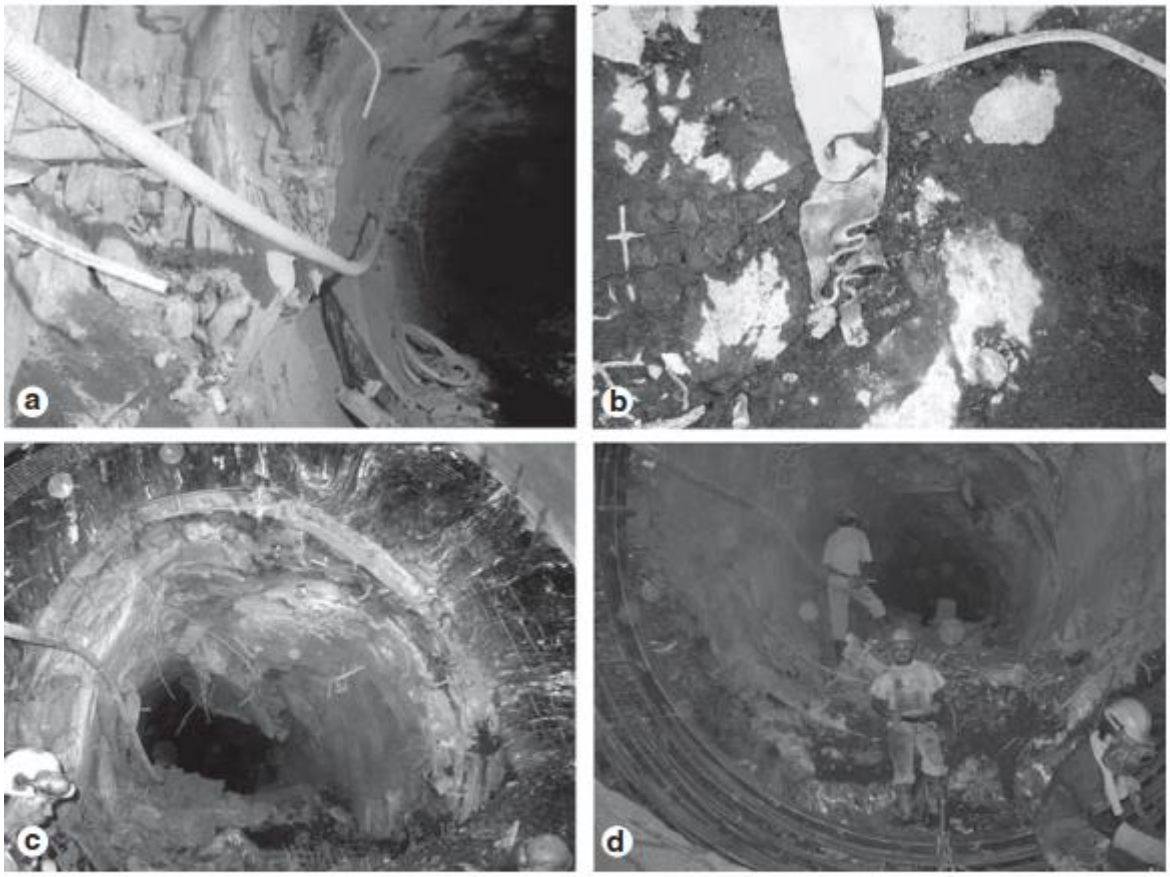

Fig. 28. Evolution of the damage between Chainage 12 + 750 and 12 + 850. (Reproduced from Guevara et al., 2004.) (a) Initial damage with cracking of the shotcrete and loss of alignment of the track. (b) After removal of the cracked shotcrete, significant deformation of the WF 6 × 20 steel ribs could be observed. (c) In spite of having placed rings of rockbolts to isolate the damaged section, failure propagated to the roof of the section after removal of the damaged shotcrete in the invert. (d) As the failure developed, with closures of up to 1 m being observed, it was decided to re-mine the tunnel and replace the lining. The photograph shows a repaired section of the tunnel in the foreground and the damaged tunnel in the background

Figure 6-8: Failed section between PM12+750 and PM12+850, with failure analyses proposed by Hoek and Guevara (2009) (from Hoek and Guevara 2009)

6.2.1 CV-CF method and equivalent

As explained in several chapters of this thesis, the CV-CF method and 2D plane strain numerical calculations are based on the same philosophy and lead to very similar results when the unconfinement rate is estimated using the LDP. The main advantage of 2D plane strain models is that they allow more complex modelling (anisotropic stress state, non-circular geometry) and a more refined result analysis (mostly for the support behavior and determination of internal forces).

6.2.1.1 Methodology of Connor Langford and Diederichs (2013)

Connor Langford and Diederichs (2013) performed reliability calculations based on the results of the 2D plane strain numerical model. The method used for the reliability calculations is not presented here (some information is provided in Chapter 5.2.1.1). Only the method used for numerical calculations is presented:

1) They start by calculating the LDP without support using a 2D axisymmetric numerical calculation. They also calculate the GRC using 2D plane strain numerical models without support.
2) They estimate the unconfinement rate corresponding to a distance of 1.5 m and 10 m from the face, which is used in the 2D plane strain numerical model with support.
3) They create the 2D plane strain model in which the yielding support and the lining are modelled using elastic support element (Phase 2 software, Rocscience). The numerical calculations include several steps: 1. Application of the field stress to the rock mass; 2. Reduction of the confining pressure until the unconfinement rate reaches the one of 1.5m from the face; 3. Activation of the yielding support which allows 3.7% of radial strain before becoming a rigid support; 4. Reduction of the confining pressure until the confinement rate reaches the one of 10 m from the face; 5. Activation of the lining; 6. Reduction of the confining pressure until reaching zero; 7. Modification of the rock mass properties to the long-term properties. They do not consider the same long-term properties as the one proposed by Hoek and Guevara (2009). The GSI is reduced at the vicinity of the tunnel, only in the plastic radius. The reduction factor is calculated as follows:

$$\Delta GSI = 10\left(\frac{R - R_t}{R_p - R_t} - 1\right) \qquad (6-1)$$

Where R_t is the tunnel radius, R_p is the plastic radius and R is the radius to the axis of the tunnel. The GSI reduction is linear through the plastic zone.
It can be noted that equivalent homogeneous support and lining were used because it is not possible to model the steel sets and the shotcrete separately. To obtain the equivalent properties, they used the equation proposed by Carranza-Torres and Diederichs (2009). These equations can also be used in reverse to estimate the internal force on each support element.
4) They extract the results (the bending moment, the axial thrust and shear force) from the numerical model and estimate the failure probabilities (several limit states are considered depending on the global safety factor targeted).

As mentioned above, this approach is very similar to a convergence-confinement method, except the SCC is not explicitly calculated, it is obtained through 2D plane strain numerical model.

It can be noted that the numerical calculations performed by Connor Langford and Diederichs (2013) are based on the small strain hypothesis (already discussed in Chapter 5.2.4). Compared to the large strain hypothesis, it leads to larger value of radial strain and larger plastic radius. For unsupported tunnel, the impact of these hypotheses is studied in Chapter 3.2.1. The impact of this hypothesis on the ground pressure on the support has not been studied here.

Since the approach used by Connor Langford and Diederichs (2013) for the long-term properties is based on a local degradation of the GSI, it cannot be directly reproduced using the basic CV-CF method or the surrogate models. One option would be to consider a GSI reduction for the entire rock mass similar to the one proposed at the vicinity of the tunnel (minus 10, Eq.(6-1)). Compared to the results of Connor Langford and Diederichs (2013), this hypothesis leads to an overestimation of the ground pressure on the support, as presented with the CV-CF method in the next section. The other solution is to consider an equivalent long-term GSI value leading to similar ground pressure as the approach of Connor Langford and Diederichs (2013). A GSI reduction of 5 for the entire rock mass is considered for the surrogate models.

6.2.1.2 CV-CF method

The CV-CF method is applied to this worst-case scenario as basis of reference and to allow discussion with the results of the surrogate model. The LDP is presented in Figure 6-9, as well as the radial strain for the support installation (1.5 m from the face) and the lining installation (10 m from the face). The LDP and GRC are obtained from 2D axisymmetric and 2D plane strain numerical calculations with the models presented in Chapter 3.3.2 and Chapter 4.2.1, and using the large strain hypothesis.

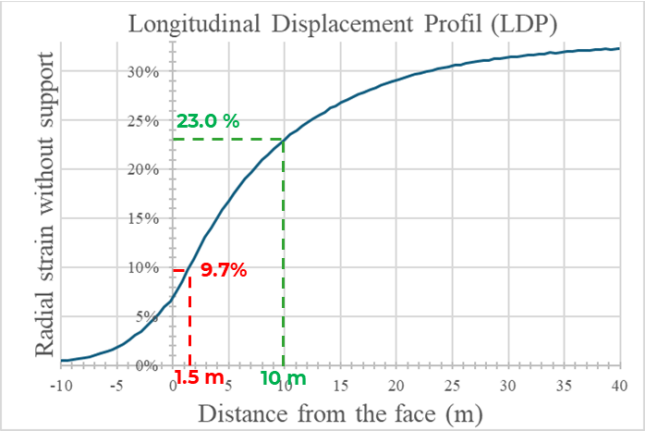

Figure 6-9: Calculated LDP of the Yacambu-Quibor tunnel associated with short-term properties and the worst-case scenario (Table 6-1)

The stiffness of the support and the lining is calculated using equivalent properties obtained with the method proposed by Carranza-Torres and Diederichs (2009) for composite support. The maximal ground pressure admissible on the equivalent elements is supposed to be the summation of the maximal pressure admissible on the shotcrete and the steel set. The properties are presented in Table 6-2.

Table 6-2: Equivalent support and lining characteristics when considering composite elements; ST is for shotcrete and SS for steel sets

Equivalent properties	**Support (0.2m shotcrete + HEA160, 1m)**	**Lining (0.4m shotcrete + HEA260, 0.8m)**
Elastic modulus	14 GPa	16.5 GPa
Thickness	0.21 m	0.39 m
Stiffness	1.28 GPa	3.18 GPa
Maximal admissible ground pressure on the support	2.92 MPa ST = 2.30 MPa SS = 0.62 MPa	6.65 MPa ST = 4.76 MPa SS = 1.89 MPa

It can be noted that an external radius of 2.5m is considered for the estimation of the support stiffness and the maximal pressure, as it can accommodate 10 cm of radial displacement (3.7% of radial strain) before loading itself. The external radius for the lining is 2.3m (the support is 0.2m thick).

Based on these radial strains, the CV-CF method is applied. According to this method, the yielding support is installed when the radial strain is 9.7% (Figure 6-9). Then, it is designed to accommodate an additional 3.7% of radial strain before the rock mass starts loading the support. Using the LDP, this radial strain should be reached at 3.4 m from the face (associated radial strain of 13.4%, 9.7%+3.7%). The equilibrium point between the GRC and the SCC is reached

at 1.65 MPa. This ground pressure corresponds to the ground pressure on the support far from the face when no lining is installed. It can be observed that the equilibrium point is reached before the installation of the lining, around 3.5m from the face (radial strain of 13.5%, Figure 6-9 and Figure 6-10). In Figure 6-10 a), at the lining installation (10m, corresponding to 23% of radial strain without support, Figure 6-9), the equilibrium point is already reached, and so the support will withstand all the short-term ground pressure. Therefore, the lining is only loaded when the long-term ground properties are considered, and so the proper way of considering it is presented in Figure 6-10 b). Because the lining is stiffer than the support, it is supposed that all the long-term ground pressure is supported by the lining, allowing the calculation of the safety factor of the lining itself.

It can be noted that in the 2D plane strain numerical approach used by Connor Langford and Diederichs (2013), the lining is installed when the confining pressure is reduced to the one corresponding at 10m from the face (around 0.40MPa, Figure 6-10 a)), and so in their calculations, the lining is supporting a part of the short term ground pressure (smaller than 0.38 MPa).

Then the safety factors are deduced for the support and the lining using the following expressions:

$$SF_{ST\ support} = \frac{P_{imax\ support}}{P_{iST\ support}} = \frac{2.92}{1.65} \qquad (6-2)$$

$$SF_{LT\ lining} = \frac{P_{imax\ lining}}{P_{iLT\ lining}} \qquad (6-3)$$

The short-term safety factor for the support is 1.8, and the long-term safety factor for the lining is 3.9 (6.65/1.70) when considering a GSI of 20, and 1.8 (6.65/3.70) when considering a GSI of 15.

In their study, Connor Langford and Diederichs (2013) do not provide an explicit value of the ground pressure on the lining with their long-term properties. Nevertheless, it is said that the failure probability for the associated limit state being “global safety factor < 3” is 0%. It means that in their calculations, the global safety factor associated with the mean ground properties is much higher than 3 to reach this failure probability. This point is coherent with the results of an equivalent global long-term GSI of 20, and incoherent with a long-term GSI of 15. A GSI of 15 leads to a safety factor of 1.8, which is smaller than 3. A safety factor of 1.8 obtained considering the means values of the input parameters is associated with a failure probability of 50% regarding the limit state “global safety factor < 1.8” when the uncertainties are considered (probability distributions of the input parameters are symmetrical). It means that, if the probability distributions of the input parameters are symmetrical and the global safety factor is 1.8 for the mean values, the probability of the safety factor being smaller than 1.8 is 50%. Connor Langford and Diederichs (2013) obtained that the probability of the safety factor being smaller than 3 is 0%. This constat is relevant with the hypothesis “long-term GSI equal 20” but not with the hypothesis “long-term GSI equal 15”.

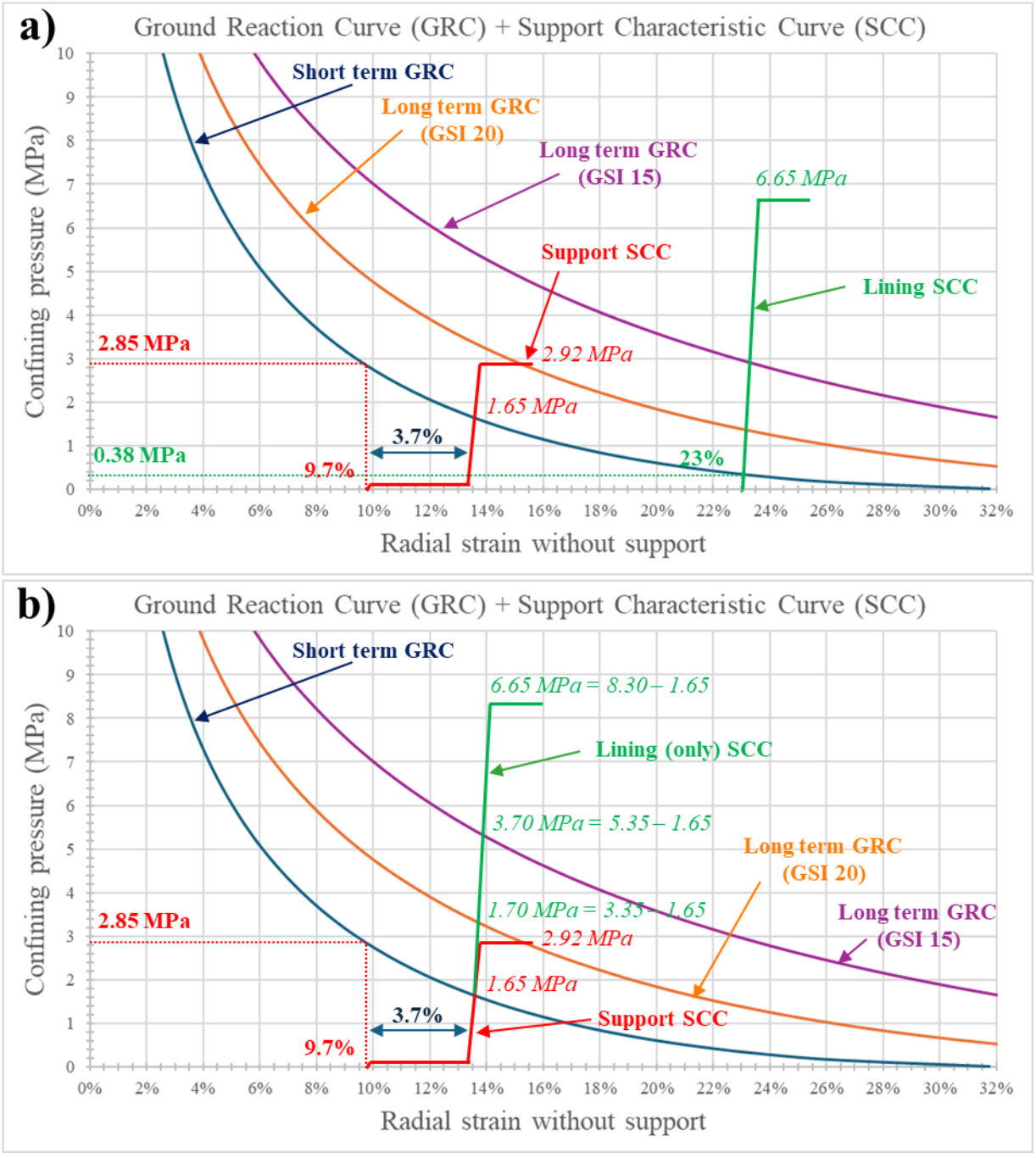

Figure 6-10: CV-CF method for the worst-case scenario including short-term properties, and two values of GSI for the long-term properties; a) wrong representation to highlight the fact that the equilibrium point is reached before the lining installation; b) relevant representation considering the lining only for the long term ground properties

6.2.2 Surrogate model

The design proposed by Connor Langford and Diederichs (2013) cannot be applied directly to the surrogate models because it is not possible to consider specific sizes of sliding gaps and the installation of a rigid support and a lining at various spans. One shortcoming of the surrogate models is that it is impossible to estimate the ground pressure on the support for a specified distance to the face. For example, the main design parameters of the support here would be the ground pressure 10 m from the face, just before the lining is installed. The only information available with the surrogate model is the ground pressure on the support far from the face.

Three different hypotheses can be made to apply the surrogate models:

1) The rigid support is installed for a span relevant with radial strain between the face and the yielding support, plus the radial strain accommodated by the yielding support. At short-term, only the support is considered, and the lining is considered only for the long-term.
2) The rigid support and the lining are installed simultaneously for a span relevant with radial strain between the face and the yielding support, plus the radial strain accommodated by the yielding support. The support considered for the surrogate model is equivalent to the support defined above plus the lining.
3) Only the lining is considered. The main objective of the support is to limit the ground deformation on the first 10 m before the installation of the lining. The support stability is not verified for these 10m. Only the ground pressures on the lining are studied in the short-term and the long-term. It is supposed to be installed 10m from the face. This hypothesis seems relevant because in reality the support objective is to guarantee the safety of the operation while avoiding large deformation by applying a confining pressure. By doing so, it could be considered that this confining pressure will increase the ground pressure on the lining later being installed. As discussed in Appendix 4, this statement is true only for elastic rock behavior or small plastic radius. In this situation, the plastic radius is large, around 4 Radii and so this confining pressure applied by the support will not increase the ground pressure on the lining and even may reduce it (Appendix 4).

The equivalent properties of the support (situation 1) and the lining (situation 3) are estimated using the approach of Carranza-Torres and Diederichs (2009), as presented in Table 6-2. For situations 2, the radial stiffness considered is the summation of the radial stiffness of support and of the lining (similar for the maximal admissible pressure).

In situations 1 and 2, it is necessary to estimate the span for which the sliding gaps of the steel sets are closed, corresponding to the beginning of the loading of the rigid support. During the construction, the yielding support was completed between 1.5 and 3m from the face depending on the excavation sequence (full face or top-bench). The radial strain between the face and the yielding support installation is at least 1.5% according to the surrogate model (value corresponding to a 0.2m thick shotcrete, 1.5m from the face). It can be noted that using the LDP results, the radial strain is at least 3%. As the yielding support will apply a small confining pressure, the results of Appendix 4 specify that a reduction of 10% (100 kPa, a span of 1R) of the radial strain can be applied to the one occurring during the yielding the support. The equivalent radial strain on the span for an unsupported ground associated with the closing of the sliding gap is 5.6% (1.5%+3.7%*1.10). Using the equivalent support properties (Table 6-2) and the surrogate models, this value of radial strain between the face and the stiff support is obtained for a span of 3.3 m.

This span is smaller than the field observation of Hoek *et al.* (2008) as the smallest span for the closure of the sliding gap is 5m. Nevertheless, these results are relevant as the geological situation studied here corresponds to a worst-case scenario and the yielding support could have been completed up to 3m from the face.

The results of the surrogate models (calculation performed with the Excel sheet presented in Appendix 6) for each situation are presented in Table 6-3 and Figure 6-11 (graphical illustration). There is the mean ground pressure on the support, the associated failure probability, and the global safety factor. As discussed in the previous section, the long-term GSI

is 20. The failure probabilities do not include the variability of the strength of the shotcrete. It is supposed to be constant equal to f_{ck} = 30 MPa. The long-term ground pressures are estimated using the methodology presented in Chapter 4.3.3 and Appendix 5. The failure probability associated with the long-term ground pressure is estimated using a Monte Carlo simulation of 100 000 realizations performed using the Excel file presented in Appendix 6.

Table 6-3: Results of the surrogate models applied to the three tested situations; tunnel radius of 2.6m

Situation	1	2	3
Stiffness	1.28 GPa	4.46 GPa	3.18 GPa
Maximal admissible ground pressure	2.92 MPa	9.57 MPa	6.65 MPa
Span	3.3 m	3.3 m	10 m
Short-term ground pressure	5.52 MPa	7.78 MPa	2.58 MPa
Short-term failure probability	100%	0.69%	< 0.005%
Short term safety factor	0.53	1.23	2.58
Long-term ground pressure	-	10.05 MPa	4.32 MPa
Long-term failure probability	-	88.26%	< 0.005%
Long-term safety factor	-	0.95	1.54

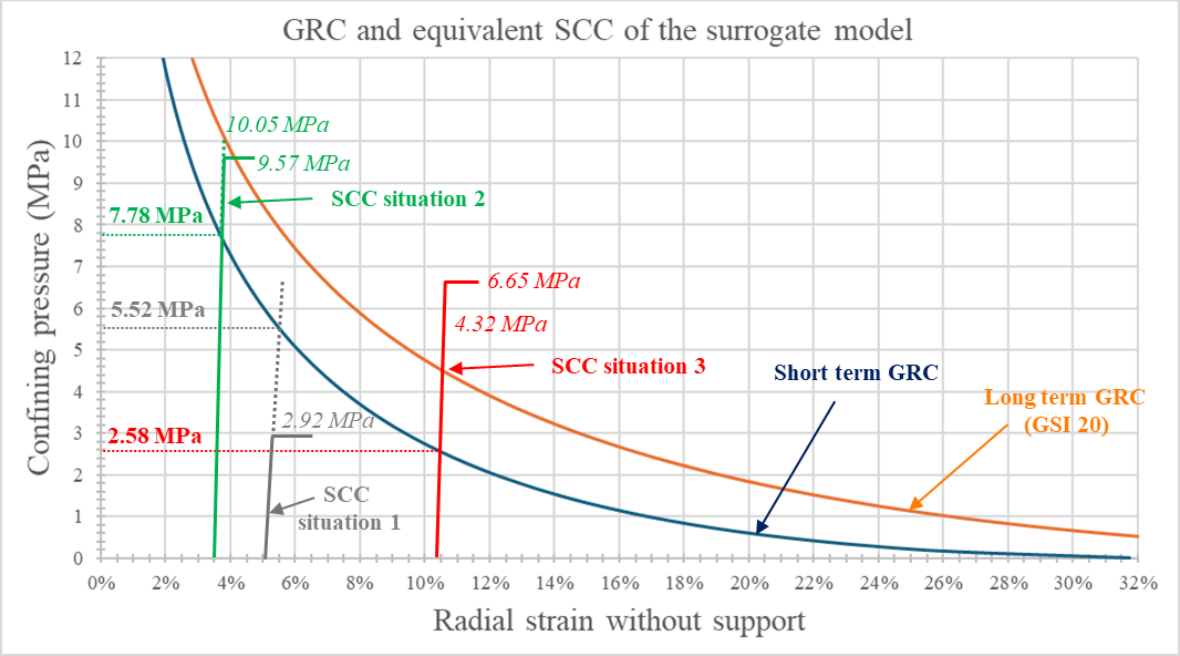

Figure 6-11: Estimation of the long-term ground pressure on the support based on the results of the surrogate model for the three situations

It can be noted that, to apply the surrogate model, the radius considered is the excavation radius (2.6m), which is different to the one used to estimate the equivalent properties (Table 6-2). As the relevant input parameters of the surrogate models is the support stiffness, the Young's modulus of the support is modified to reach the relevant radial stiffness in the Excel sheet used for the calculation (Appendix 6).

Situation 3, the more relevant one, results in a very small failure probability of the lining with the short-term properties. The long-term safety factor of the lining is relatively low, but higher than the 1.5 targeted by Connor Langford and Diederichs (2013), and the failure probability is very small (<0.01%), without considering the strength variability of the shotcrete. It is also possible to estimate the ground pressure on the support (situation 3) with a long term GSI of 15, which is an unfavorable hypothesis regarding the values proposed by Connor Langford and

Diederichs (2013). The long-term ground pressure is 6.11MPa, the associated safety factor is 1.09 and the failure probability is 9.7% (without the uncertainty on the strength of the support).

As the geological conditions considered correspond to the worst-case scenario, having a small failure probability leads to very unlikely failure of the lining in the reality. From this point of view, the results are relevant with field observations as no failure of this type of lining was presented in the various papers studied.

6.3 Failed section: PM12+750 – PM12+850

As it is presented in Section 6.1.4, the lining failed between PM12+750 and PM12+850 two years after the completion of the section. After the failure, the radial displacements have reached 1 m, corresponding to around 38% of radial strain (radial displacement divided by the initial tunnel radius).

Compared to the worst-case scenario presented in the previous section, the depth of this section is smaller (850 m, $\sigma_0 = 22$ MPa) and the lining thickness was reduced (Figure 6-12). The spacing of the steel sets is 0.8m, and the strength of the shotcrete is 40 MPa. The sequence of construction of this lining is not clear in documents available to Hoek and Guevara (2009), and they feared that the lining may have been placed directly after the closure of the sliding gaps.

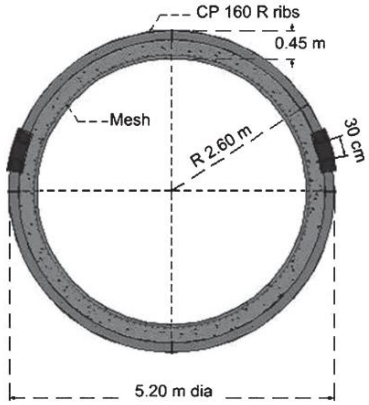

Figure 6-12: Geometry of the support and the lining between Chainage 12,750 and 12,850 (from Hoek and Guevara 2009)

For the long-term properties, Hoek and Guevara (2009) considered the same hypothesis as the one they used in Figure 6-3: the long-term GSI is divided by 2. So, they considered a long-term GSI of 10. A 2D plane strain numerical model (presented in Chapter 3.2.1) leads to a radial strain without support of 67% (1.7m of radial displacement), while a long-term GSI of 15 leads 47% of radial strain. Maybe a long-term GSI of 15 is more in accordance with the field observations. The calculations performed in the following section take into account this possibility by conspiring both values of long-term GSI.

6.3.1 CV-CF method and equivalent

The CV-CF method is performed to test if it could have been used to predict the failure, based on the assumption of the long term GSI and to highlight the proximity of its results with the results of the numerical calculation performed by Hoek and Guevara (2009). For this section, it is considered that the rigid support and the lining are installed at the same span, after the closure of the sliding gaps. The stiffness of the support including the lining is calculated using the formulation proposed by Carranza-Torres and Diederichs (2009) and presented in Table 6-4.

Table 6-4: Equivalent support parameter for failed section (PM12+750 - PM12+850)

Equivalent properties	0.45m shotcrete + HEA160, 0.8m
Elastic modulus	13.7 GPa
Thickness	0.42 m
Stiffness	2.62 GPa
Maximal admissible ground pressure on the support	7.33 MPa ST = 6.55 MPa SS = 0.78 MPa

It can be noted that an external radius of 2.5m is considered for the support as it can accommodate 10 cm of radial displacement (3.7% of radial strain). For the shotcrete, the 40 MPa provided by Hoek and Guevara (2009) is supposed to be a f_{ck} value (5% quantile). This hypothesis is also discussed in the next section.

The LDP and the GRC are obtained using numerical calculations, similarly to Section 6.2.1.2 and are presented in Figure 6-13 and Figure 6-14.

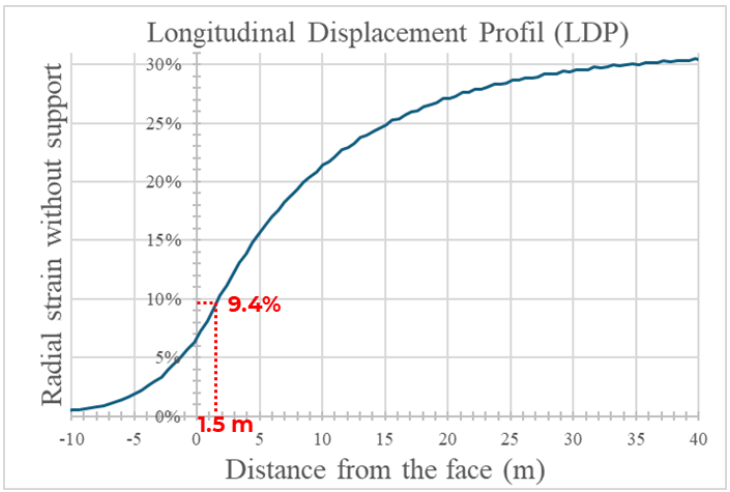

Figure 6-13: Longitudinal Displacement Profile (LDP) for the short-term properties of the section between chainage 12+750 and 12+850

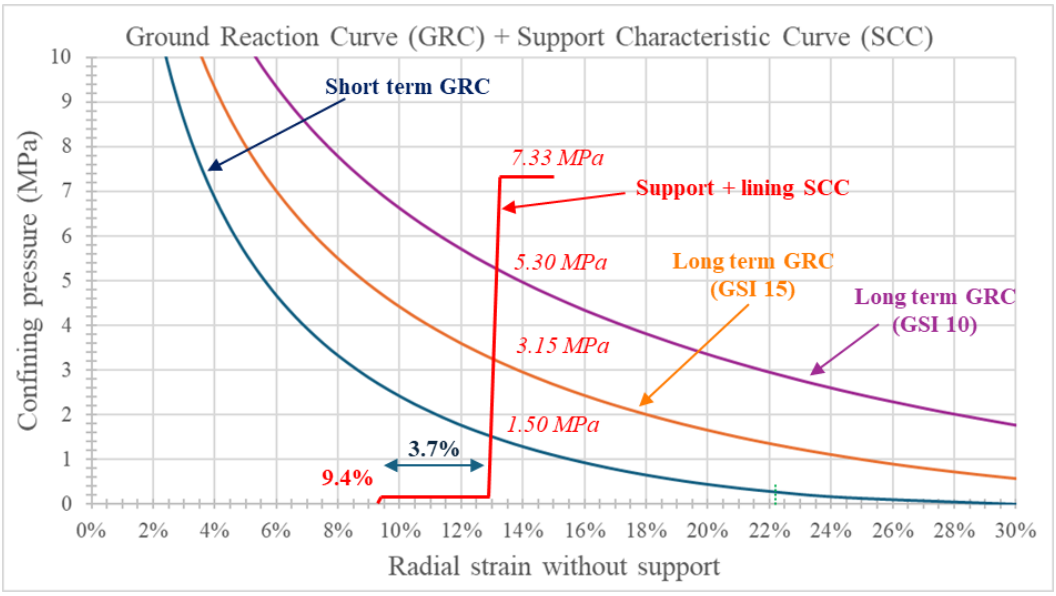

Figure 6-14: GRC and CV-CF method for the failed section between chainage 12+750 and 12+850

The CV-CF method leads to short term ground pressure on the support (including the lining) of 1.5 MPa (Figure 6-14). The associated safety factor is 4.9. The long-term safety factor is 1.4 for a GSI of 10 (same hypothesis as Hoek and Guevara 2009) and 2.3 for a GSI of 15. Based on this simple analysis, the support (including the lining) should not have failed during the transition between the long-term behavior and the short-term behavior.

Hoek and Guevara (2009) used the finite element software Phase 2 to study the behavior of the support and the lining. In their model, the yielding support is installed for a radial strain corresponding to 50% of the maximum radial displacement of an unsupported tunnel. According to Figure 6-13, it corresponds to a distance to the face of around 5m (radial strain of 15%). Two different elements are considered for the support, the steel sets with sliding gaps and the shotcrete, 0.45m thick, installed when the sliding joints are fully closed. No information is provided on how the support and lining are modelled (probably elastic behavior as safety factors smaller than 1 can be reached) and on how they interact with each other. They studied the behavior of both of the support elements independently. For the short-term conditions, they obtained a safety factor of 1.2 for the steel sets, which decreased to 0.8 for the long-term conditions. In the other hand, the shotcrete carries very little load under short term conditions, while the safety factor is approximately 2.2 for the long-term conditions. They justified their results as follows (Hoek and Guevara 2009):

"This is not surprising since the steel ribs carried practically all of the loading before the shotcrete lining was installed. However, failure of the steel ribs under long term loading conditions would result in a transfer of the load carried by the ribs onto the shotcrete lining and this would almost certainly overload the shotcrete. In addition, buckling of the steel ribs would cause local spalling of the shotcrete which would reduce its load carrying capacity."

Several remarks can be made based on their analysis, which make their interpretation debatable:

- They are considering that the steel set failed before the shotcrete. It means that when the shotcrete and the steel sets are installed, the steel sets will load preferentially compared to shotcrete ring. For that to happen, the stiffness of the steel sets needs to be higher than the stiffness of the shotcrete ring. The stiffness of the HEA160 spaced every 0.8m in 2.6 tunnel radius is 0.39 GPa (A 1.2.1, E_s = 210 GPa, A_s = 38.77 cm²) while the stiffness of the 45cm thick shotcrete ring is 2.05 GPa (A 1.2.1, E_c = 10 GPa, ν_c = 0.2). From these stiffness values, after the shotcrete is installed, it should carry most of the load. As no information is provided on the method used by Hoek and Guevara (2009) to model these elements, a more detailed analysis of the results of each support element is not possible here.
- They stated that the transfer of the load carried by the steel sets on the shotcrete ring would overload the shotcrete. This statement is surprising as the maximal admissible ground pressure on the steel sets is 0.75 MPa (A 1.2.1, σ_s = 400 MPa, A_s = 38.77 cm²), the maximal ground pressure on the shotcrete ring is 6.3 MPa and the associated safety factor is 2.2 for the long-term conditions. The results are slightly different from Table 6-4 because here the tunnel radius is supposed to be 2.6m for every calculation, as for Table 6-4, this value was adapted to include the radial displacement of the yielding support. Even if the steel set loses all load bearing capacity, the ground pressure on the shotcrete ring would be 3.80 MPa (6.3/2.2 + 0.75/0.8, including the long-term safety factors determined by Hoek and Guevara 2009). The load on the shotcrete ring would still be much smaller than the maximal admissible pressure, with a safety factor of 1.7.

- The bucking of the steel ribs would cause local spalling, but it can be difficult to imagine that the load bearing capacity of the shotcrete ring would be reduced by 40% and led to failure of the support.

This example highlights perfectly the limitations of the CV-CF method or 2D plane strain numerical model for which no failure could have been anticipated, even with the lining installed too close to the face (at the sliding gaps closure and not 10 m from the face).

6.3.2 Surrogate models

Unlike the worst-case scenario presented in Section 6.2, the section studied here is much easier to be applied to the surrogate models as the support and the lining are installed at the same time. Hoek and Guevara (2009) do not present the uncertainty associated with the input parameters, but the mean values are identical to the one used by Connor Langford and Diederichs (2013), and so, the same uncertainties are considered (CoV) to perform calculations of the failure probabilities.

Firstly, it is necessary to estimate the span at which the sliding gaps are closed, and the rigid support + lining is installed. The yielding support is supposed to be installed 1.5 m from the face, and the radial strain associated with these 1.5 m is 1.2%. As the yielding support will apply a small confining pressure, the results of Appendix 4 specify that a reduction of 10% of the radial strain can be applied for the one occurring during the yielding of the support. The equivalent radial strain between the face and closing of the sliding gaps is 5.3% (1.2%+3.7%*1.10). Using the equivalent support properties (Table 6-4) and the surrogate models, this value of radial strain between the face and the rigid support + lining is obtained for a span of 3.4 m.

As this span is slightly smaller than the one observed by Hoek and Guevara (2009), two hypotheses can be tested:

1) The rigid support and the lining have been installed at 3.4m from the face, which is an unfavorable hypothesis compared to the field observations.
2) The rigid support and the lining have been installed at 5m from the face, in accordance with the most unfavorable situation observed by Hoek and Guevara (2009) during the construction.

The results are presented in Table 6-5. The support characteristics are identical to the one used in the CV-CF method, presented in Table 6-4.

Table 6-5: Results of the surrogate model on the failed section, for various hypothesis on the span value and two values of long term GSI

Hypothesis	**1**	**2**
Span	3.4m	5m
Short term safety factor	1.41	1.75
Short-term failure probability	< 0.01%	< 0.01%
Long-term safety factor (GSI 15)	1.10	1.30
Long-term failure probability (GSI 15)	5.04%	0.01%
Long-term safety factor (GSI 10)	0.92	1.06
Long-term failure probability (GSI 10)	99.96%	14.68%

The failure is expected when the rigid support and the lining are installed at 3.4m from the face, and if the long-term GSI is 10. If it is installed at 5m, the safety factor is really close to 1.0 and the probability of failure is high (around 15%) also when considering a GSI of 10. It can be concluded that for this section, failure can be expected based on the uncertainties on the span values and the long-term GSI, unlike with the CV-CF method. Another parameter could impact the probability of failure: the uncertainty on the strength of the shotcrete. For the results in Table 6-5, no uncertainty is considered, and the characteristic strength of the shotcrete is supposed to be 40 MPa.

Hoek and Guevara (2009) do not mention if the 40 MPa for the shotcrete strength is the mean strength (f_{cm}) or the characteristic value (f_{ck}, 5% quantile as in the Eurocode). Table 6-6 presents the failure probabilities for both hypotheses on the shotcrete strength value and on the span (3.4m and 5m). It can be noted that the uncertainty about the strength of the shotcrete has a major impact on the failure probability in this situation. If the 40 MPa is the mean strength, and not the characteristic strength, the failure probabilities are much higher. For the long-term behavior, the higher failure probability can be obtained without considering the variability on the strength of the shotcrete or considering that 40MPa is the mean value.

Table 6-6: Failure probabilities for various hypotheses regarding the strength of the shotcrete, the short-term GSI value, and several long-term GSI values; sd is for standard deviation

Hypothesis on the strength of the shotcrete	**Short-term GSI**		**Long-term GSI**			
	20		**15**		**10**	
	3.4m	**5m**	**3.4m**	**5m**	**3.4m**	**5m**
Without uncertainty (40 MPa considered)	<0.01%	<0.01%	5.04%	0.01%	99.96%	14.68%
With uncertainty (f_{ck} = 40 MPa; f_{cm} = 48 MPa; sd = 4.9)	<0.01%	<0.01%	1.51%	0.05%	25.50%	2.99%
With uncertainty (f_{ck} = 32 MPa; f_{cm} = 40 MPa; sd = 4.9)	0.85%	0.03%	24.50%	2.92%	81.15%	35.18%

Unlike the other methods presented in Section 6.3.1, in this situation the use of the surrogate models highlights the potential failure of the rigid support and lining when they are both installed at the same time, when the sliding gaps are closed. Depending on the hypotheses on the strength of the shotcrete, the long-time behavior of the support, and the span, the failure probability is between 0% and 100%.

6.4 Conclusion

This chapter aims to apply the surrogate models developed in Chapter 4 to the case study of the Yacambu-Quibor tunnel in Venezuela and to compare the results with classical approaches such as the CV-CF method and 2D plane strain numerical model. Two tunnel sections have been studied, one associated with the worst-case scenario, and another associated with the failed section between chainages 12+750 and 12+850.

The results show that the surrogate models lead to relevant interpretations for both tunnel sections as the first one is expected to be stable during short-term and long-term loading, while a failure can be expected in the second tunnel section. Classical approaches lead to both sections being stable for short-term and long-term loading which is not appropriate compared to field observations. As expected, the global safety factors and failure probabilities are less optimistic compared to those of the classical approaches. This is explained because these approaches are based on the same hypothesis as the CV-CF method, which has already been proven to

underestimate the ground pressure on the support (Appendix 1). This case study also highlights one of the limitations of the surrogate models when considering complex support such as a combination of yielding support, rigid support and lining. For these situations, simplifying hypotheses are needed.

On this case study, the surrogate models provide relevant results compared to the field observations and the shortcomings of other approaches, making it appropriate and an easy-to-use tool during preliminary design of deep tunnel in highly fractured rock mass.

Chapter 7 - Risk assessment of brittle failures during early tunnel design stages

Chapter abstract: As explained in the first chapter, brittle failure is another type of failure mechanism that can occur during the construction of deep tunnels. It is crucial to correctly identify and assess the risk associated with these phenomena, in particular whether the brittle failure will be quasi-static (spalling) or violent (rockburst). A correct risk assessment will allow the selection of an appropriate risk mitigation strategy and technical solution to overcome these potential phenomena.

This chapter aims to summarize the different methods available in the literature to assess the risk of brittle failure at an early stage of tunnel design, as well as the methods to mitigate the associated risk — such as the use of short-term prediction based on tunnel auscultation during the excavation process or the classical support techniques in rock mass prone to rockburst. Finally, one of the most advanced methods for an early risk assessment, proposed by Diederichs (2018), is applied to a case study of an early stage of tunnel design: the deepest section of the Mont Cenis base tunnel (France). Diederichs' approach is further generalized to incorporate the geological and geotechnical uncertainties of the input parameters by using Monte Carlo simulations, allowing the identification of the most hazardous tunnel sections depending on the existing uncertainties and discussions about the relevance of the approach.

7.1 Risk assessment of brittle failure in literature

Since rockburst is a major problem in deep mining and, increasingly, in deep tunnels associated with civil engineering projects, many approaches have been developed to try to predict the maximum intensity of the expected rockburst. All these methods can be grouped into two categories:

1) The "general approaches", which are easily applicable (mostly analytical and empirical criteria) aiming to reach a quick and qualitative assessment of the intensity of the maximum possible rockburst in a given situation. Most of them are relevant for a risk assessment at an early stage of tunnel design, and are presented in Section 7.1.1.1 (analytical formulation) and in Section 7.1.1.2 (graphical presentation).
2) The "specific approaches", which allow an in-depth study of the rockburst phenomenon in a specific case study. These approaches are mostly based on numerical modelling to study specific tunnel configuration or to perform back-analysis. They can be difficult to apply for a risk assessment in the early design stages because of limited information on the input data but may be necessary in the final stages of the design. They provide quantitative results on the situation studied. They are briefly presented in section 7.1.1.3.

Manouchehrian (2016), Zhou *et al.* (2018a), Wang *et al.* (2021), Askaripour *et al*. (2022) and He *et al*. (2022) have synthetized most of these approaches to study and predict rockburst. In the following sections, only the approaches relevant to risk assessment during preliminary tunnel design will be presented.

7.1.1 Methodologies for rockburst prediction

In this section, a synthesis of all the empirical and analytical criteria found in the literature is presented, followed by methodologies based on graphical representations, and then a brief presentation of the methodologies based on numerical calculations and machine learning.

7.1.1.1 Analytical expression

Table 7-1 summarizes many existing empirical and analytical criteria that allow a qualitative rockburst risk assessment. In these criteria, the quasi-static phenomena are considered as low intensity rockbursts. Since the risk assessment is only qualitative, it is difficult to define a precise scale for the rockburst phenomenon as it is highly dependent on the authors. In this section, the rockburst intensity levels considered are those proposed by Askaripour *et al.* (2022):

- None: No rockburst corresponds to the condition where no sounds of rockburst and no rockburst activity are expected.
- Light: Light rockburst is considered when the surrounding rock mass is deformed, cracked, or rib-spalled, and there is a weak sound with no ejection phenomenon.
- Moderate: Medium rockburst defines the conditions where the surrounding rock mass is deformed and fractured, and a significant number of rock fragments are ejected. In these cases, light and sudden destruction occurs, accompanied by crisp crackling often in surrounding rock.
- Severe: Severe rockburst is considered in situations where the surrounding rock mass bursts severely and is ejected suddenly into the opening void, accompanied by a continuous strong burst, roaring sound, air spray, and storm phenomena.

It is noteworthy that in some classifications, “severe” is replaced by 2 categories: “heavy” and “serious” (Zhou *et al.* 2018a, He *et al.* 2022). In order to facilitate the comparison of the different criteria, a homogenization of the symbols used is done, which are presented below and in Figure 7-1.

List of symbols:

σ_{ci} = Uniaxial compression strength of the intact rock E_u = Tangential modulus during pre-peak unloading E_G = Tangential modulus during pre-peak loading E_M = Post-peak modulus of the rock ε_c = Pre-peak axial strain ε_d = Axial strain at the beginning of the residual state ε_{tot}^k = Total axial strain for a σ_k pre-peak loading situation ε_0^k = Residual deformation associated with a σ_k pre-peak loading situation σ_θ = Maximal orthoradial stress at the tunnel boundary σ_L = Stress in the tunnel direction	ϕ_e = Pre-peak elastic energy ϕ_{se} = Pre-peak elastic energy associated with an unloading at 80% or 90% of the UCS ϕ_p = Inelastic energy consumes during the pre-peak loading at the UCS ϕ_{sp} = Inelastic energy consumes during the pre-peak loading at 80% or 90% of the UCS ϕ_{sf} = complementary energy needed for the rock failure ϕ_t = total energy provided during the pre-peak loading

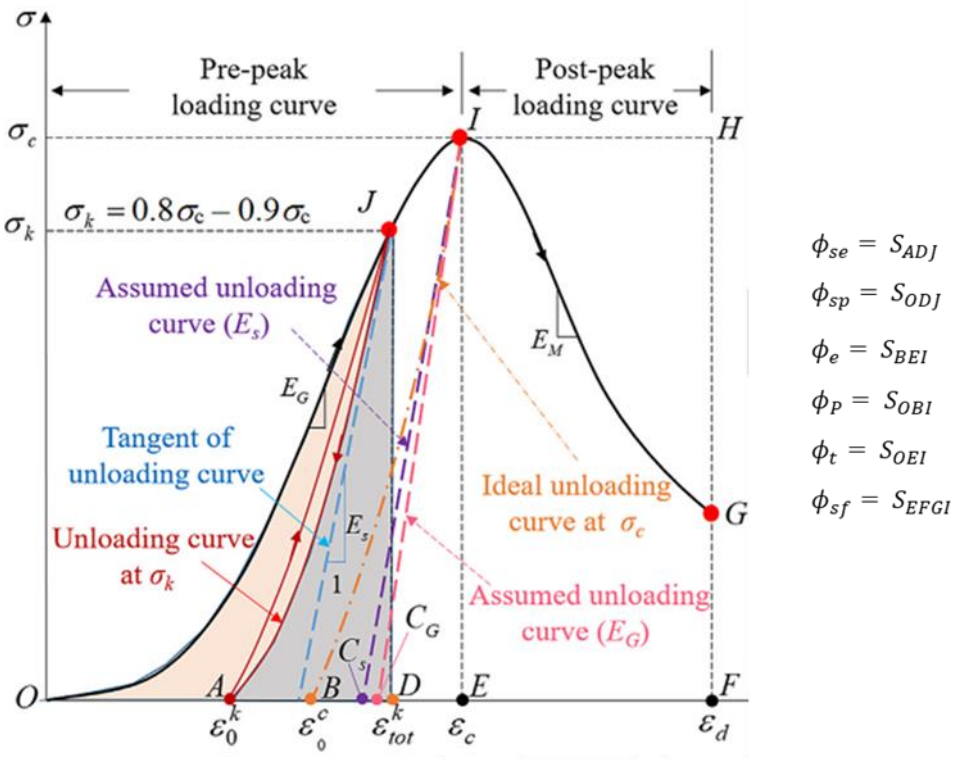

Figure 7-1: Graphical representation of the various parameters used in the empirical and analytical criteria (from He et al. 2022) ; S_{JKL} is the surface between point J, K and L

Table 7-1: Summary of various empirical and analytical criteria based on Askaripour et al. (2022), He et al. (2022) and Zhou et al. (2018a)

Type	Reference	Criteria	Expression	Rockburst intensity				
				None	**Light**	**Medium**	**Heavy**	**Serious**
Energy approach	Neyman *et al.* (1972) Kidybinski (1981) Zhang and Fu (2008) Zhou *et al.* (2017)	Strain energy storage index / Elastic energy index	$W_{et} = \frac{\phi_{se}}{\phi_{sp}}$	≤ 2 ≤ 2 < 2 ≤ 2	2 – 3.5 2 – 4.99 2 – 3.5 2 - 5	3.5 – 5 - 3.5 - 5 5 - 10	≥ 5 ≥ 5 ≥ 5 > 10	-
	Aubertin *et al.* (1994)	Brittleness index modified (BIM)	$BIM = \frac{\phi_t}{\phi_e}$	-	> 1.5	1.5 – 1.2	1.2 – 1	-
	Wang and Park (2001) Miao *et al.* (2016)	Potential energy of elastic strain (PES / SED) (kJ/m3)	$PES = \frac{{\sigma_c}^2}{2\,E_u}$	< 50 -	50 – 100 < 40	100 – 150 40 -100	150 – 200 100 - 200	> 200 > 200
	Gong *et al.* (2018; 2021)	Residual elastic energy index (kJ/m3)	$A_{EF} = \phi_e - \phi_{sf}$	< 50 < 15	50 – 150 15 - 30	150 – 200 -	> 200 > 30 (coal)	-
	Gong *et al.* (2019a)	Peak-strength strain energy storage index	$W_{et}^{p} = \frac{\phi_e}{\phi_p}$	< 2	2 - 5	-	>5	-
Strength approach	Turchaninov *et al.* (1972)		$\frac{\sigma_\theta + \sigma_L}{\sigma_{ci}}$	≤ 0.3	0.3 – 0.5	0.5 – 0.8	> 0.8	-
	Barton *et al.* (1974) Tao (1988) Zhao *et al.* (2017)		$\frac{\sigma_{ci}}{\sigma_1}$	> 10 > 14.5 > 5	10 – 5 14.5 – 5.5 5 - 4	5 – 2.5 5.5 – 2.5 4 – 2.5	< 2.5 < 2.5 2.5 – 1.5	- - < 1.5
	Barton *et al.* (1974)		$\frac{\sigma_t}{\sigma_1}$	> 0.66	0.66 – 0.33	0.33 – 0.16	> 0.16	-
	Russenes *et al.* (1974) Hoek and Brown (1980) Grimstad and Barton (1993) Wang *et al.* (1999) Zhang and Fu (2008) Zhao *et al.* (2017)	Stress coefficient / Stress level index	$\frac{\sigma_\theta}{\sigma_{ci}}$	≤ 0.2 - - < 0.3 ≤ 0.2 ≤ 0.2	0.2 – 0.3 0.34 0.3 – 0.4 0.3 – 0.5 0.2 – 0.3 0.2 – 0.5	0.3 – 0.55 0.42 0.5 – 0.65 0.5 – 0.7 0.3 – 0.55 0.5 – 0.7	> 0.55 0.56 0.65 - 1 0.7 – 0.9 > 0.55 0.7 – 0.9	- ≥ 0.7 > 1 > 0.9 - > 0.9
	Singh (1989)	Decrease modulus index	$DMI = \frac{E_G}{\lvert E_M \rvert}$	≥ 1	< 1	-	-	-
	Palmström (1995)	Competency factor	$C_g = \frac{RMi}{\sigma_\theta}$	> 2.5	1.0 – 2.5	0.5 – 1.0	< 0.5	-
	Feng *et al.* (2000) Tang and Wang (2002)	Brittleness index	$B = 0.1\,\frac{\sigma_{ci}}{\sigma_t}\,\frac{\varepsilon_c}{\varepsilon_d}$	< 3 < 2	3 – 5 2 – 7.5	- 7.5 - 13	> 5 > 13	-

	Li *et al.* (2001) Lee *et al.* (2004) Zhang & Fu (2008)	Strength brittleness index (*)	$B_2 = \frac{\sigma_c}{\sigma_t}$	< 10 < 5.75 < 15	- ≈ 7.85 15 -18	10 – 18 ≈ 9.87 18 -22	> 18 ≈ 12.18 > 22	-
	Li *et al*. (2001)	Deformation brittleness index	$K_u = \frac{\varepsilon_{tot}^k}{\varepsilon_0^k}$	< 2	2 - 6	6 - 9	≥ 9	-
	Tang (2000) Li *et al.* (2008)	RQD index		> 25 > 25	25 – 50 25 - 50	50 – 75 50 - 70	75 - 90 > 70	90 – 100
	Hosseini *et al* (2010) Castro *et al.* (2012)	Normalized deviatoric stress (NDS) Brittle shear ration (BSR)	$\frac{\sigma_1 - \sigma_3}{\sigma_{ci}}$	≤ 0.35 < 0.45	0.35 – 0.5 0.45 – 0.6	0.5 – 0.8 0.6 – 0.7	0.8 – 1 > 0.7	> 1 -
Combined approach	Zhang *et al*. (2013)	Stress index	**	< 0.25	0.25 – 0.5	0.50 – 0.75	> 0.75	-
	Zhang *et al*. (2016)	Potential rockburst index	***	< 0.4	0.4 – 1.05	1.05 – 2.5	> 2.5	-

* Remark: several authors have proposed contradictory values (None: $B_2 > 40$; …; Massive: $B_2 < 14.5$) (Chunsheng and Zhiyou 1998; Qiao and Tian 1998; Sepeheri *et al.* 2020 referring to Caï 2015 referring to Peng and Wang 1996). The original papers were not found as they are in Chinese, so these contradictory values were not considered.

** $S = tanh\left\{\left[0.1648\ (\frac{\sigma_\theta}{\sigma_{ci}})^{3.064}\ (\frac{\sigma_{ci}}{\sigma_t})^{-0.4625}\ (\frac{\phi_e}{\phi_p})^{2.672}\right]^{\frac{1}{3.6}}\right\}$

*** $\Omega = (3 - \lambda_0)\frac{\phi_e}{\phi_p}\frac{\sigma_\theta}{\sigma_{ci}}$

Some remarks can be made about these criteria:

- Several criteria are based on parameters (E_M, ε_d, ϕ_{sf}) associated with the post-peak behavior of the rock sample, making them highly dependent on the loading system stiffness, and thus difficult to use in practice. This point is discussed in Chapter 8.
- Many of these criteria focus only on the rock itself (all the brittleness index) without including the stress state in which the rockburst is expected to occur. These criteria cannot be used alone because important information may be missing.
- Some authors combine several of these criteria to increase the relevance of the result. Xue *et al.* (2020a) used five different empirical criteria with specific weight coefficients and applied them to twenty rockburst case studies. Similarly, Li *et al*. (2022) used 3 indexes and also determined the weight coefficients.
- The energetic criteria focus mainly on a comparison of the elastic energy accumulated during the pre-peak loading with the total amount of energy provided or the inelastic energy dissipated during the failure.
- Similarly, most of the strength criteria consist of a comparison between the strength of the intact rock (uniaxial compressive strength or tensile strength) and the stress state in the rock mass (the maximal stress at the tunnel boundary, the major principal stress, etc.). Others also include the strain of the sample at various loading stages and the pre-peak and post-peak modulus. Only the competency factor of Palmström (1995) takes into account information about the rock mass and not only parameters from laboratory tests.
- The “combined criteria” consider energetic parameters and strength parameters.

7.1.1.2 Graphical representation

Several graphical representations (charts) have been developed to facilitate the assessment of the potential rockburst risk:

- Lee *et al.* (2004): they proposed a chart (Figure 7-2) that combines three criteria to estimate the maximum intensity of the rockburst: the PES criterion presented in Table 7-1, the B_3 criterion corresponding to the “strength brittleness index” in Table 7-1, and the uniaxial compressive strength of the rock. Four categories of intensity (NR: No Rockburts; LR: Low Rockburst; MR: Moderate Rockburt; HR: High Rockburst) are defined based on the ones that occurred during the construction of a waterway tunnel in Korea.

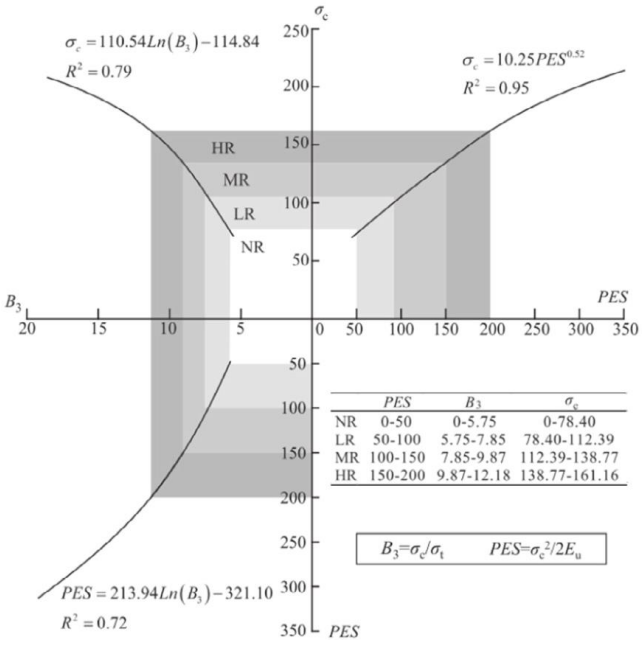

Figure 7-2: Chart introduce by Lee et al. (2004) to estimate the rockburt intensity based on a Korean waterway tunnel

- Diederichs (2007, 2018): Diederichs (2007) developed the following chart (Figure 7-3) to predict spalling potential in intact rock. This chart is based only on the USC and the tensile strength of the rock, and allows the estimation of the strainburst (Chapter 2.2.2.3) potential (high energy and spalling process). Later, Diederichs (2018) improved the chart by introducing the Dynamic Rupture Potential (DRP), which is related to the average ejection velocity potential of the intact rock. It should be noted that this chart does not contain any information about the stress state and can only be used to estimate the maximum intensity of the brittle failure that could occur for a given rock type as a general point of view.

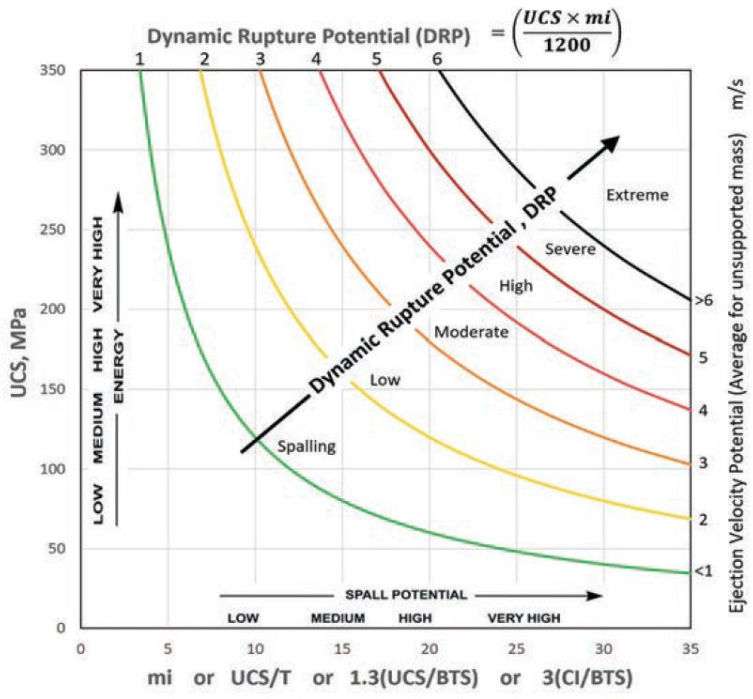

Figure 7-3: Potential for spalling and rockburst failure process in intact rock (Diederichs 2018)

- Farhadian (2021): The TRC (Tunnel Rockburst Classification) chart (Figure 7-4) was developed with a geostatistical method (kriging method) applied to a database of 220 rockbursts of various intensity. This chart has also been tested on 28 rockbursts with good results (only one error). It includes 2 indexes: the elastic energy index (W_{et}) and the stress level index ($\sigma_\theta/\sigma_{ci}$) presented in Table 7-1.

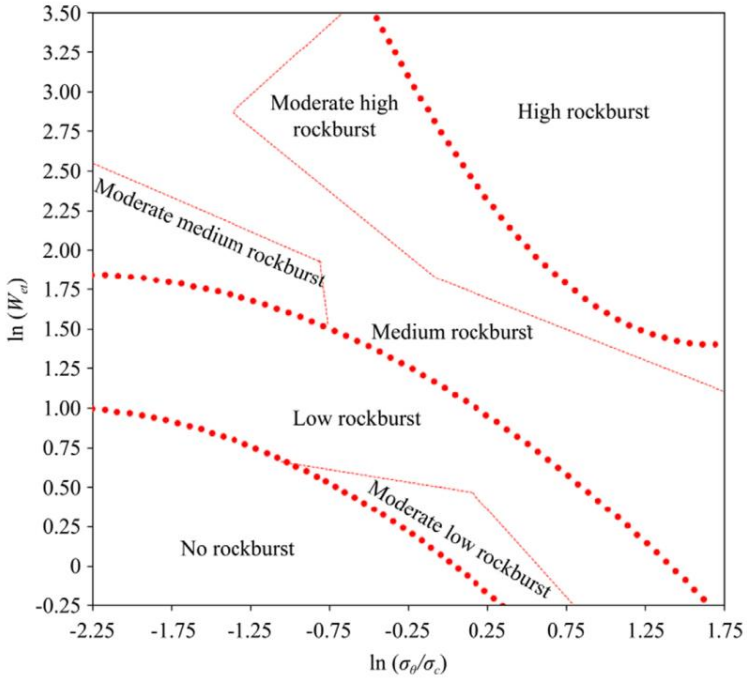

Figure 7-4: The TRC chart developed by Farhadian (2021); W_{et} is the elastic energy index; σ_θ/σ_c is the stress level index

Zhou *et al.* (2018a) presented other graphical representations which were complex, difficult to understand and to use, so it was decided not to present them here.

7.1.1.3 Other approaches

Empirical criteria are not the only technique to quantify the rockburst risk. Machine learning approaches or numerical modelling can also be used.

7.1.1.3.1 Machine learning

Pu *et al.* (2019), Askaripour *et al.* (2022) and Baset *et al.* (2023) summarize the different machine learning methods used in the literature for rockburst prediction: Su *et al.* (2008) use a k-nearest neighbor algorithm; Zhou *et al*. (2012) use a support vector machine; Cai *et al*. (2016a) perform a principal component analysis (data analysis technique); Zhou *et al*. (2016b) use a stochastic gradient algorithm; Li *et al*. (2017b) use a Bayesian classifier; Xu *et al*. (2018) use 'ideal point theory'; Li and Jimenez (2018) use logistic regression; Zhou *et al*. (2020) use neural networks; Faradonbeh *et al*. (2021) a hybrid algorithm between a genetic algorithm and a logistic regression algorithm ; Ahmad *et al.* (2022) an adaptative boosting classifier.

Pu *et al.* (2019) pointed out that prediction methods based on machine learning are used to make either short-term or long-term predictions. Long-term methods use the mechanical and energetic properties of the massif to predict whether the area is likely to have a rockburst (see the different methods cited in Section 7.1.1.1). Short-term methods monitor changes in various parameters obtained through monitoring to determine whether a rockburst is likely to occur.

The main parameter monitored is the evolution of the intensity and frequency of induced microseismic events to determine whether a rockburst is imminent. These short-term prediction methods are presented in more detail in Section 7.2.2.1.

For long-term methods, majority of the databases used to train these different algorithms contain input parameters similar to those of empirical methods: tensile strength, uniaxial compressive strength, maximum orthoradial stress, brittleness index, elastic strain energy, depth, ratio between uniaxial compressive strength and initial major principal stress, stress coefficient, excavation size, Young's modulus, Poisson's ratio.

The study carried out by Zhou *et al.* (2016a) concluded that the most influential parameters on rockbursts are the stress coefficient, the maximum orthoradial stress and the elastic strain energy (Askaripour *et al*. 2022). Conversely, the study by Afraei *et al.* (2018) concludes that the overburden, tensile strength and brittleness index have a very limited influence on the rockburst phenomenon (Askaripour *et al*. 2022).

Currently, the main problem associated with the use of machine learning algorithms for rockbursts prediction is the size of the databases used. These databases generally lack enough training data. For a simple model that makes the following prediction: “rockburst” / “no rockburst”, a training database consisting of 50% of each would be required, but in reality, the proportion of “no rockburst” events are higher, creating a problem of balancing the database (Pu *et al.* 2019). The problem of unbalanced classes is not really an issue when classification is performed; the least represented class needs to be large enough to train the model and some of the data needs to be used to develop a test or validation database.

7.1.1.3.2 Numerical modeling

For more specific rockburst studies, numerical calculations can be used. Wang *et al.* (2021) and He *et al*. (2022) have synthetized the approaches used in the literature. 3 different types of numerical calculations can be performed:

- Continuous modelling: These models are based on continuum mechanics. There are several methods: Finite Element Methods (FEM), Boundary Element Methods (BEM) and Finite Difference Methods (FDM). These techniques use continuum mechanics to calculate stress-strain relationships, based on the principles of conservation of energy, momentum and mass. These approaches have difficulties in simulating rockburst failure mechanisms, because they are dynamic phenomena with discontinuities. Typically, these models are coupled with empirical energy or resistance criteria but will still suffer from these limitations.
  According to He *et al.* (2022), the FDM method is more suitable than the FEM for modelling rockbursts because it is able to take into account local dynamic processes without a complete failure in the model (Muller 1991). This is due to the use of methods based on an explicit solving approach (implicit for FEM), as explicit numerical calculations can be stable when the physical system is not (Keneti and Sainsbury 2018).
- Discontinuous/discrete models: The rock mass is divided into distinct blocks separated by joint surfaces. There are two modelling methods: the Discrete Element Method (DEM) and Discontinuous Deformation Analysis (DDA), which can be seen as a generalized version of the DEM, despite some differences in the resolution techniques (He *et al.* 2022). These discrete approaches generally do not take into account the deformation of the constituent elements and therefore ignore the elastic energy stored in them, except by using some specific packages as in UDEC for example. The only

energy considered would be the one stored into the joints between the model elements. These models have the advantage of being able to generate/reproduce fractures while their shape is not imposed by the mesh. The computational cost of these methods is high, which limits their use in engineering projects (He *et al.* 2022).

- Hybrid models: Hybrid approaches have been proposed to take advantage of both the continuum and discrete approaches. In general, the hybrid approach model uses the finite element and the contact surface to describe the continuous deformation and discontinuous fracture, respectively. The rockburst failure process is characterized by a transition from a continuum to a discontinuous state, and from a static state to dynamic damage (He *et al.* 2022). The hybrid approaches can describe the transition from continuous deformation to discontinuous fracture better than continuum and discrete approaches, revealing their advantage in simulating the rockburst. However, the computational cost of hybrid approaches is extremely high, which limits their applications (He *et al*. 2022).

7.1.2 "Burst hazard potential" proposed by Diederichs (2018)

One of the most advanced and complete approaches for rockburst risk assessment in the early stages of tunnel design is the methodology proposed by Diederichs (2018). A detailed presentation of this method is carried out in this section as it will be improved and applied to the Mont Cenis Base Tunnel in Section 7.3. This method is based on the estimation of the value of the Burst Hazard Potential (BHP), which is associated with a class of hazard levels allowing a risk assessment (Table 7-2).

Table 7-2: Classes of burst hazard potential proposed by Diederichs (2018)

Class	**Hazard level**	**Issues**
0 – 0.1	Low stress	No indications
0.1 – 0.5	Local stress concentration	Minor local and intermittent stress noise
0.5 – 1	Consistent stress	Consistent stress 'popping' for several hours after blast
1 – 2	Spalling	Visible slab formation <5 cm thick, with rock noise but minimal kinetic energy (or velocity) developing after blasting and scaling – stops after 1–3 diameters of advance
2 – 3	Minor dynamic rupture (burst)	Slabbing with significant noise, minor ejection (5–20 cm thick) at or near the face. Less than 2 kJ/m^2 kinetic energy of release (per unit wall area). Less than 5 cm closure potential
3 – 4	Moderate dynamic rupture (burst)	Constant or strong noise with high frequency of ejection 15–65 cm thick at >3–4 m/s initial surface velocity for hours after blasting, near or away from face. Kinetic energy 2–14 kJ/m^2 or 5–15 cm closure potential
4 – 5	Major or severe dynamic rupture (burst)	Large volumes of ejection or dynamic heave (floor) with constant and large noise events, occurring after blast, near face or well after blast and back into tunnel away from face or with long delay. 30–85 cm average thickness at >4 m/s surface velocity or 14–35 kJ/m^2 ejection or 15–30 cm closure potential
5 +	Extreme bursting	Very large events >85 cm average thickness, >6 m/s velocity, kinetic energy >35 kJ/m2, >30 cm closure potential. Can occur any time

Unlike other empirical criteria presented in Table 7-1, this approach includes the depth of failure, the dynamic rupture potential, and some rock mass specificities (the GSI and specific geological conditions).

The Diederichs' approach is based on two steps: 1) to estimate the potential depth of the failure; 2) to estimate the potential of dynamic rupture.

The depth of the failure can be estimated based on numerical calculations using peak and residual strength (presented in Chapter 8.1.1) or using an empirical method (Martin *et al*. 1999; Diederichs 2007; Diederichs *et al*. 2010) which is presented in Figure 7-5 and based on several case histories. This empirical method has been improved by Diederichs (2018) with numerical calculations for various horizontal to vertical stress ratios (K), as presented in Figure 7-6.

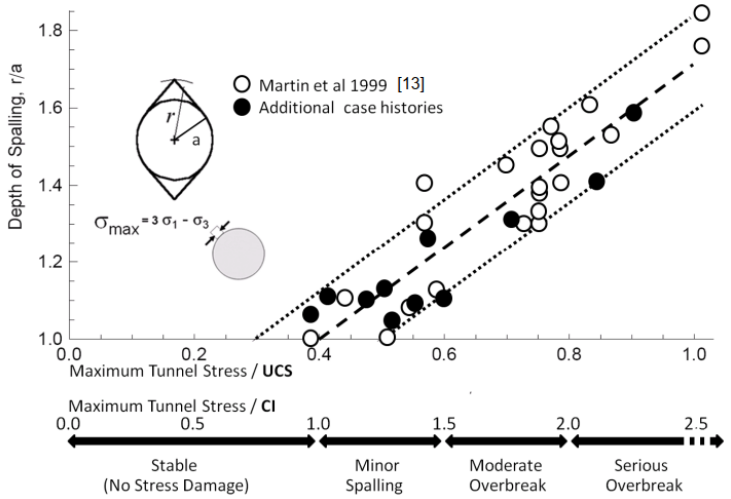

Figure 7-5: Depth of spalling depending on the maximal orthoradial stress and the uniaxial compression strength (UCS), or the Crack Initiation stress (CI) (from Diederichs et al. 2010)

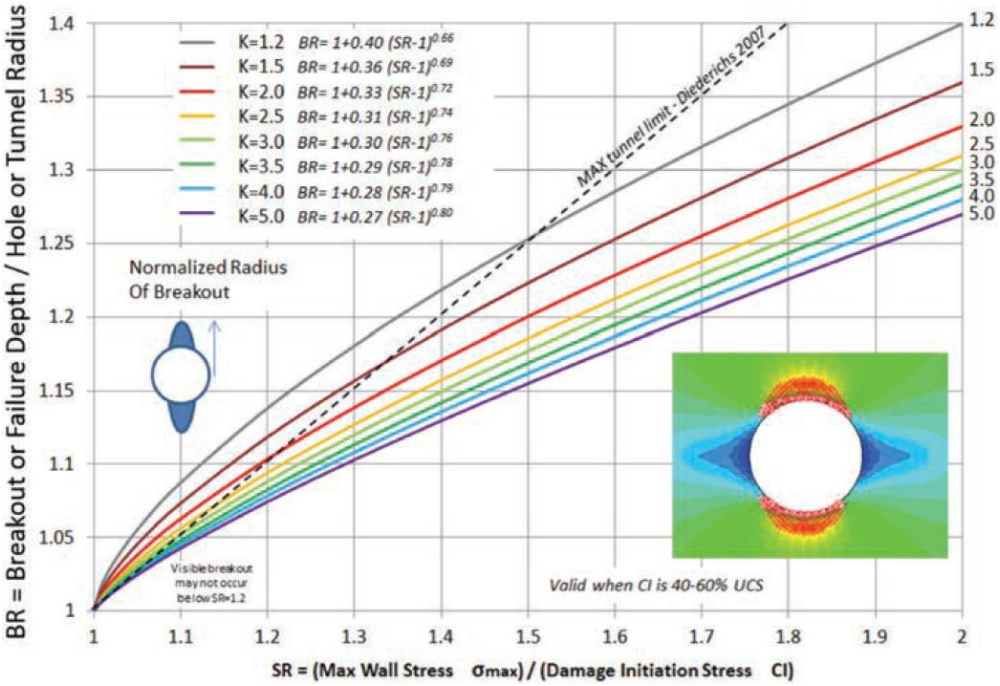

Figure 7-6 : Failure depth predicted as a function of maximum wall stress, Crack Initiation stress (CI) and the in-situ stress state ratio K (from Diederichs 2018)

The estimation of the potential depth of the failure can be done by using the following procedure (Diederichs 2018):

1) Get an estimate of the principal stresses σ_1 and σ_3 in a 2D plane perpendicular to the tunnel.

2) Get an estimation of the damage threshold, the Crack Initiation stress (CI), for a rock types along the tunnel (use 0.5*UCS if no data exists).
3) Calculate the strength ratio:

$$SR = \frac{3\,\sigma_1 - \sigma_3}{CI} \qquad (7-1)$$

4) Calculate the in-plane in-situ stress ratio:

$$K = \frac{\sigma_1}{\sigma_3} \qquad (7-2)$$

5) Calculate the calibration factors:

$$M = 0.4\,K^{-0.27} \qquad (7-3)$$

$$N = 0.65\,K^{0.14} \qquad (7-4)$$

6) Calculate the breakout ratio:

$$BR = 1 + M(SR-1)^N \qquad (7-4)$$

7) Predict the depth of failure (D_f):

$$D_f = (BR-1) * R \qquad (7-5)$$

Where R is the tunnel radius or half of the tunnel span when the tunnel is not circular. It can be noted that in the original paper of Diederichs (2018): $D_f = BR * R$. Using this expression compared to Eq.(7-5) leads to very high values of BHP and is not coherent with the meaning of D_f: the depth of failure, e.g. the depth of the failure from the tunnel boundary and not from the center of the tunnel. Since the tunnel radius does not appear in the expression below used for the calculation of the BHP, if the breakout ratio is null (e.g. no failure expected), the depth of failure according to the expression provided by Diederichs (2018) would be equal to the tunnel radius, while the real depth of failure (Eq.(7-5)) would be 0m.

This first step has a similar objective to some of the strength empirical criteria presented in Table 7-1: to compare the strength of the rock and the maximal stress at the tunnel boundary. Unlike the other empirical criteria, the approach here is more complex because it will take into account several other factors such as the in-situ stress state (σ_1, σ_3, K), the strength of rock which corresponds here to the long-term strength at the tunnel boundary (Crack Initiation threshold), and the size of the tunnel. All of this allows an estimation the depth of failure corresponding to the volume of rock impacted by the brittle failure.

The second step aims to introduce the Dynamic Rupture Potential (DRP, presented in Figure 7-3) and to combine it with the depth of failure (D_f) to obtain the Burst Hazard Potential (BHP). The DRP is not directly an energetic criterion, as it depends only on the UCS and m_i parameters, and it is not associated with an energetic parameter. It is closer to a brittleness index characterizing the ability of the rock to fail in a dynamic manner.

8) Calculate the Damage Depth Potential (DDP) and Dynamic Rupture Potential (DRP):

$$DDP = \alpha\, {D_f}^{0.5} \qquad (7-6)$$

$$DRP = \beta \left(\frac{UCS * m_i}{1200}\right) \qquad (7-7)$$

Where α=4.5 and β=1 are empirical constants that can be calibrated for local conditions (the one used are suggested by Diederichs 2018), m_i is the Hoek and Brown parameter, which here, is estimated as $m_i \approx \frac{UCS}{T}$ *or* $1.3\frac{UCS}{BTS}$ *or* $3\,\frac{CI}{BTS}$, UCS is the uniaxial compression strength, T is the true tensile strength, BTS is the Brazilian tensile strength and CI the crack initiation stress.

9) Calculate the Burst Hazard Potential (BHP) for intact rock:

$$BHP = (DDP * DRP)^{0.5} \qquad (7-8)$$

Some adjustments of BHP can be made to integrate the effect of structural specificities on the bursting process (BHPs) as shown in Figure 7-7. The consideration of the impact of the rock mass characterization is possible though the GSI value (BHPm). The BHPs and BHPm are calculated using the following equations:

$$BHPs = BHP + \sum_1^n SH_i \qquad (7-9)$$

$$BHPm = \frac{BHPs}{1 + exp\left(\frac{40 - GSI}{10}\right)} \qquad (7-10)$$

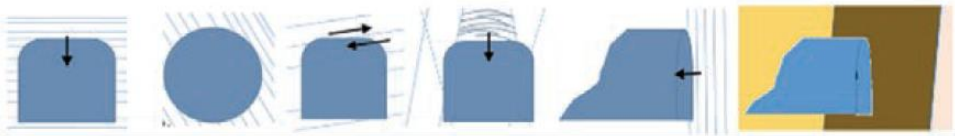

BHP These numbers are based on existing hazard index INITIAL INTACT ROCK RESPONSE	ROCKBURST HAZARD INCREASE DUE TO STRUCTURE (sum all that apply and add to BHP to get BHPs)									
	LAMINATIONS << 20 cm thick			BEDDING (>> 20cm wide) or SPACED PERSISTANT JOINTS			STRUCTURE PARALLEL to FACE spacing:		STIFFNESS CHANGE Aproaching <15m or next to tunnel wall <6m	
	Horizontal	Vertical Parallel to Tunnel	Inclined 20-45 degrees	Horizontal	Dip > 60 Parallel to Tunnel	Inclined Dip 10-45 degrees	<10 cm	> 10 cm	Soft to Stiff	Stiff to Soft
0	0	0	0.1	0.1	0	0	0	0	0	0
0.1	0.2	0	0.2	0.2	0	0	0.1	0	0	0.2
0.5	0.5	0.1	0.5	0.5	0	0.1	0.3	0.1	0.1	0.5
1	0.7	0.2	0.5	0.5	0.2	0.2	0.5	0.2	0.2	0.7
2	0.7	0.5	0.5	0.5	0.5	0.5	0.5	0.5	0.5	0.7
3	0.2	0.5	0.2	0.5	0.5	0.5	0.2	0.5	0.5	0.7
4	0	0	0	0.2	0.2	0.2	0	0.2	0	0.5

Cubic Function Fit Parameters $SHI_i = A(BHP^3) + B(BHP^2) + C(BHP) + D$ Sum for each condition: $BHP_S = BHP + \sum_1^n SHI_i$

A	0.0847	-0.0485	0.0504	0.0219	-0.044	-0.0339	0.046	-0.0339	-0.0485	0.0554
B	-0.6716	0.1693	-0.4085	-0.2301	0.1746	0.1115	-0.396	0.1115	0.1693	-0.4659
C	1.3291	0.0978	0.7962	0.5872	0.053	0.1453	0.8467	0.1453	0.0978	1.107
D	0	0	0.1	0.1	0	0	0	0	0	0

Figure 7-7: Adaptation of the BHP to obtain the BHPs to include structural specificities (from Diederichs 2018)

For example, if the BHP obtained is supposed to be 2, and the studied section presents structure parallel to the face spaced of around 20 cm and is closed (10 m) to a soft geological formation, the BHP needs to be adapted as follows: $BHP_s = 2 + 0.5 + 0.7 = 3.2$. The structural specificities increase the burst hazard potential.

7.2 Civil engineering projects facing brittle failures

Spalling and rockbursts occur mostly in deep mining operations, and in some civil engineering projects. This section briefly presents case histories of spalling and rockburst in civil engineering projects and the methods used to manage the associated risk. Case histories related to mining operations are not highlighted here but can be found in the literature (Cai 2016; Leveille *et al*. 2017; Keneti and Sainsbury 2018; Konicek and Schreiber 2018; …).

7.2.1 Case histories

Quasi-static phenomenon, such as spalling, is a classic situation encountered when tunnelling in intact or moderately fractured rock mass at significant depths. It does not represent a direct safety issue (if appropriate support is used) or concern during the tunnel construction, expect perhaps for the excavation rate or the larger volume of filling material (shotcrete or concrete) associated with the depth of failure. This phenomenon has been encountered in many projects, and it has not always been mentioned in comparison to violent failure. Unlike rockburst, spalling occurs not only in brittle and hard rock masses, but also in softer rock as encountered in several underground research laboratories, such as the one developed by the French National Radioactive Waste Management Agency (ANDRA) in Bure, France (Armand *et al.* 2017) or the Mont Terri Rock Laboratory in Switzerland (Yong *et al*. 2013; Amann *et al.* 2017). In contrast, violent and dynamic failures such as rockburst can lead to major safety issues. Many deep tunnels have been constructed or are under construction in the Alps, and some of them have endured rockburst phenomenon:

- One of the first civil engineering tunnels to experience violent brittle failure was the Mont Blanc tunnel in France, which reaches almost 2500 m of overburden. During its construction, which started in 1957, sudden rockbursts were reported (Loew *et al.* 2010). Panet (1969) gives more detailed description of violent failures, spalling associated with the tunnel excavation and the technical solutions used. He reported many violent failures, which can be classified as moderate rockbursts and intense spalling, even several hours after blasting.
- The Lötschberg base tunnel is 34.6 km long tunnel (Rojat *et al.* 2008). During construction, large spalling events occurred in several tunnel sections, such as in the Steg lateral adit (Rojat *et al.* 2008), with a depth of failure up to 1 m. Some other spalling phenomena have also been observed during the TBM excavation (Figure 7-8) as well as locally some minor rockburst events (personal communication with E. Garin, 2025). The spalling and rockbursts encountered during the construction were not as intense as expected (Loew *et al*. 2010; personal communication with E. Garin, 2025), with some violent events at the face, affecting the advancement rate and damaging the TBM cutterhead.

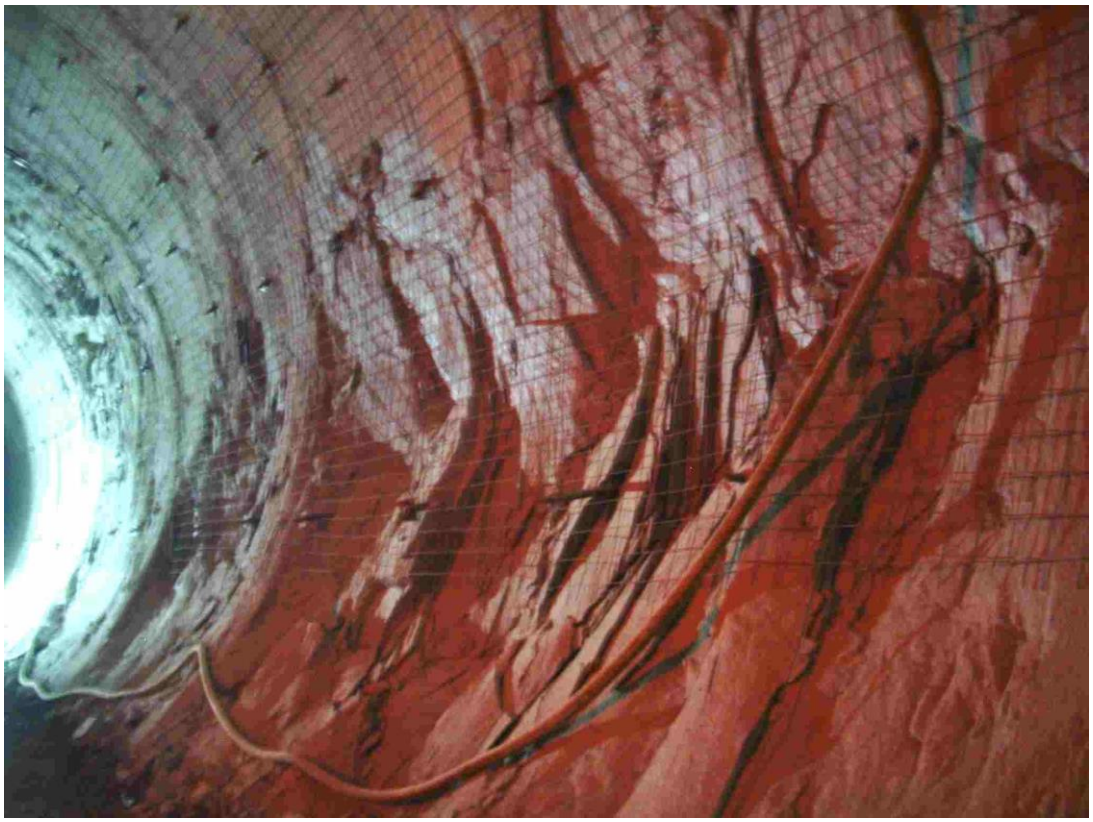

Figure 7-8 : Picture of spalling that occurs during the construction of the Lötschberg base tunnel (courtesy of E. Garin)

- The Gotthard Base Tunnel is a 57 km long tunnel in Switzerland. During construction, several rockbursts of various intensity (from spalling to major rockbursts) have occurred. The strongest rockbursts occurred in a location where the rockburst risk was not initially identified (Röthlisberger *et al.* 2016b). Between May 2004 and March 2006, several strong rockbursts occurred at the MFS Faido section severely damaging the support (shotcrete) and the utility lines. The biggest event occurs in March 2006 and was classified as a 2.4 magnitude event (Richter scale), damaging the tunnel over a distance of 100 m. No casualties were reported during this rockburst as the area was temporarily closed for safety reasons (Röthlisberger *et al.* 2016b). Spalling and minor to moderate rockbursts (based on Diederichs' classification, Table 7-2) also occur during the Faido-Sedrun TBM drives (Röthlisberger *et al.* 2016a), as well as rockbursts at the tunnel face.
- La Maddalena exploratory tunnel is one of the four exploratory tunnels excavated as part of the Mont-Cenis Base Tunnel associated with the Lyon-Turin high-speed rail project (Parisi *et al*. 2017). During the excavation, rockbursts were expected, but mostly spalling occurs reaching a depth of failure of 1 to 1.5 m (Parisi *et al*. 2017). One event referred as "sudden brittle failure" occurred in December 2015 at chainage 4.200, causing significant deformation of the support and bending of the steel ribs (Fornari *et al*. 2016; Parisi *et al*. 2017), and shown in Figure 7-9.



Figure 7-9: Sudden brittle failure which could be classified as rockburst at chainage 4.200 of La Maddalena exploratory tunnel (from Fornari et al. 2016)

- According to Voza *et al.* (2022), during the construction of the 55 km long Brenner Base Tunnel, some spalling also occurred when crossing the Brixner granite unit with over 1000 m of overburden.

Rockbursts also have occurred in other mountain ranges around the world such as in the Andes and in the Himalayas:

- The Olmos Transandean Tunnel in Perou is a 19.3 km long water tunnel with a maximum overburden of almost 2000 m. 13.9 km were excavated using a TBM. During the construction of the first 8.4 km, mostly spalling occurs. Then after crossing a major fault, which was associated with a change in the principal stress orientation and magnitude, severe rockbursts, including at the tunnel face, occurred, as well as extreme overbreak forming massive caverns above the TBM (Diederichs *et al*. 2013). The biggest event occurs on April 29th, 2010, which severely damaged the TBM and leads to a stop of the operation for more than 3 months (Diederichs *et al.* 2013).
- The excavation of the various tunnels for the Jinping II Hydropower Project has been associated with numerous severe and extreme rockbursts, resulting in the complete destruction of a TBM, the damage of many pieces of equipment and several casualties (Shan and Yan 2010; Zhang *et al*. 2012; Zhang *et al*. 2013). One of those rockbursts is studied in Chapter 8.2.3.
- According to Mcfeat-Smith (2008), the first Parbati Hydroelectric Project in India was abandoned due to several rockbursts during the construction and the associated contractual constraints.
- The Neelum-Jhelum Hydroelectric Project includes a 28.5 km long headrace tunnel to convey the water to the hydropower station. During the construction, several strainburst occurred as well as one major fault-slip burst (Naji *et al.* 2019) and spalling. This fault-slip burst which happened on May 31, 2015, killed three workers and partially destroyed a TBM. Some of the damage is presented in Figure 7-10.



Figure 7-10 : Pictures of the damage associated with rockburst of May 31, 2015 (from Naji et al. 2019)

- Another iconic case study of brittle failure in deep tunnels is the Underground Research Laboratory (URL) of the AECL in Canada, where spalling has occurred leading to extensive research, and also some violent brittle failures (Martin *et al.* 1997). This case study is presented in more detail in Chapter 8.2.2.
- Many other case studies of rockbursts during civil engineering projects in China can be found in the literature: Zhou *et al*. (2018b); Xue *et al.* (2020b); Lui *et al.* (2021); Li *et al.* (2022); Zhang *et al*. (2023); Hu *et al.* (2024).

7.2.2 Rockburst risk management in civil engineering

As presented in the first section of this chapter, there are several approaches to assess the risk associated with rockburst phenomenon at an early stage of a tunnel design. Depending on the level of risk identified, the design will include a specific risk management approach based on the geological conditions encountered during the excavation, monitoring data and technical solutions. The aim of this section is to provide some information on relevant monitoring that could be used for short-term rockburst prediction allowing better rockburst risk management and to present some technical solutions for rockburst prone rock masses.

Cai (2024) proposes a complete framework for dealing with rockburst problems in deep mines, which is summarized in Figure 7-11. Many of the considerations are similar or can be adapted to civil engineering projects:

1) It starts with a good understanding of the rockburst mechanism (“Outpost”) which is important for developing and choosing engineering tools to manage rockburst risk (Caï 2024).
2) The first line of defense is the reduction of the risk, which for civil engineering projects is the selection of an appropriate tunnel geometry, excavation sequence, and tunnel layout to avoid potentially problematic geological and geotechnical conditions. Most of these choices are made during the early design stage of the tunnel project.
3) The second line of defense is the use of appropriate monitoring systems (mostly micro-seismicity monitoring) and risk management frameworks, such as the stop of the operation for safety reasons (TBM excavation) or re-entry protocols for drill and blast method, to mitigate the consequences of the rockburst and to provide short-term prediction.

4) The last line of defense is the use of rockburst resistant support to reduce the vulnerability of the tunnel to rockburst and to ensure the safest possible working environment.

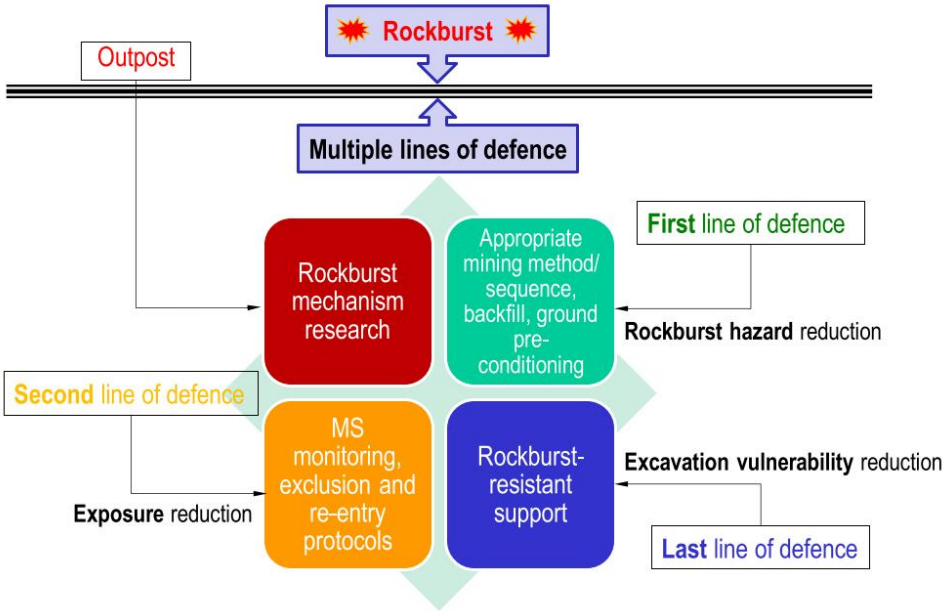

Figure 7-11: Proposed lines of defense against rockburst in deep mines (from Cai 2024)

7.2.2.1 Monitoring during tunnel excavation

During the construction of a tunnel, the choice of an appropriate monitoring system is primordial to perform short-term predictions of the rockburst risk and to guarantee the safety of the operation. For effective risk management and a better short-term rockburst prediction, the monitoring of specific data might be associated with other parameters and treated with complex mathematical approach based on artificial intelligence, allowing a real time rockburst risk assessment. Usually, there are three main monitoring techniques that focus on microseismicity, acoustic emission and electromagnetic radiation (Voza *et al.* 2022).

This section presents only examples of civil engineering projects where microseismics or acoustic emissions have been monitored, or where artificial intelligence has been used to process these data. Relevant mining case studies can be found in Glazer (2016), Feng *et al.* (2017), Wesseloo (2018), Wang *et al.* (2021), Wang *et al.* (2022), Di *et al.* (2023a,b), Faradonbeh *et al.* (2023), Lhoumaud (2023) or Roy *et al.* (2023). It can be noted that the "prediction" of rockburst based on early indicators obtained from the monitoring of micro-seismicity have not yet been fully successful at a mine scale (Personal communication with J. Roy, 2025). It would be surprising that civil engineering projects have more advanced methodologies and techniques than mining on this subject. Therefore, the application found in the literature and presented below needs to be considered with caution regarding their large-scale applicability.

Rockbursts are accompanied by microseismic precursors (Zhang *et al*. 2024a referred to Zhao *et al*. 2016). Microseismic monitoring consists of the deployment of seismometers strategically placed, which after processing, allow the localization of the microseismic events (rock fracturing or failure), the magnitude and the frequency (Cai 2024). It has been used in several deep tunnel projects as real-time monitoring associated with early warning systems. Ma *et al.*

(2015) and Lui *et al*. (2018) analyzed the microseismic data from the construction of the Jinping II Hydropower Project (China) to propose early warning and to identify seismic precursors to improve accuracy. Similarly, Xue *et al.* (2020b) used the data from the construction of the Shuangjiangkou Hydropower station (China), Lui *et al*. (2020a) and Zhang *et al*. (2023) from a 42 km long headrace tunnel in northwestern China, Lui *et al.* (2021) from the Qinling water conveyance tunnel (China), Feng *et al*. (2022) and Li *et al.* (2023) from the Neelum-Jhelum hydropower project (Pakistan), Zhang *et al*. (2024b) have monitored the microseismic event for a tunnel excavated by drilling and blasting to understand the evolution process of rockbursts. Glazer (2016) specified that the monitoring frequencies associated with microseismicity for rockbursts prediction are generally between 10^{-1} to 10^{3} Hz.

Acoustic emission monitoring is a technique that has been widely used in laboratory experiments (Kao *et al.* 2011; Liu *et al.* 2020b, c) and has been adapted to larger scale problems, such as rockburst forecasting for example (Voza *et al.* 2022). Cheng *et al.* (2013) analyzed and compared the characteristic acoustic emission of rockbursts for different excavation techniques (drill and blast or TBM) during the construction of the Jinping II Hydropower Project (China). Zhou *et al.* (2018b) used acoustic emissions to predict the magnitude and location of the area with high-risk of rockburst. They also proposed an AE-based rockburst criterion which was developed using statistical analysis performed on the data from The Gaoligongshan tunnel (China). Based on experiments during the construction of the Brenner Base Tunnel (Austria/Italy), Voza *et al.* (2022) proposed the "Mule method" to determine the rockburst alarm threshold based on in-situ stress measurement and acoustic emissions during the excavation process. They also mentioned that acoustic emission monitoring was used during the excavation of La Maddalena exploratory tunnel (Italy). Ma *et al.* (2024) proposed a rockburst early warning framework based on time series prediction of acoustic emissions, obtained with true triaxial unloading test that the authors considered to be a "rockburst experiment". Some acoustic emission monitoring (mostly based on the sound heard during the TBM excavation) has also been used during the construction of the Lötschberg Base Tunnel (Switzerland) for the selection of the support (several classes of risk associated with the level of acoustic emissions, for which specific support should be used) (personal communication with E. Garin 2025).

As briefly presented in section 7.1.1.3.1 for the long-term prediction, Machine Learning and Artificial Intelligence can also be used for short-term prediction and forecast. To process these real-time monitoring data obtained and to make rockburst predictions, several authors have used artificial intelligence and machine learning. Zhang *et al.* (2024a) and Baset *et al.* (2023) summarized, analyzed and compared various methods based on artificial intelligence for rockburst prediction. Zhang *et al.* (2024a) highlighted three main methods: data mining, traditional machine learning methods and deep learning methods. Data mining integrates various disciplines to rapidly analyze large datasets and extract implicit information (Zhang *et al.* 2024a). Some examples of data mining used for rockburst prediction can be found in He *et al.* (2015b), Ribeiro e Sousa *et al.* (2017), Shirani and Taheri (2019) or Ahmad *et al.* (2022). Traditional machine learning methods include support vector machine, k-nearest neighbor, bayesian network, logistic regression, random forest, and decision tree (Zhang *et al.* 2024a). Deep learning methods include artificial neural network, self-organizing map, back propagation neural network, ant colony clustering algorithm and genetic algorithm (Zhang *et al* 2024a). Figure 7-12 briefly presents the advantages and disadvantages of each method (Zhang *et al.* 2024a). Baset *et al.* (2023) realized a more detailed comparison of the strengths and weaknesses of each model. Cai (2024) pointed out that the limitation of all the AI methods for rockburst prediction is the "randomness" of rockburst and the availability of high-quality data to train these models.

Methodology	Advantages	Disadvantages
Data mining methods	Rapidly analyzing big data on rockburst and extracting implicit information	Strong dependence on data, mainly for high-quality data samples. Rockburst data are mixed and prone to anomalies and loss
Traditional machine learning methods	Better handling of non-linear problems	Feature extraction heavily depends on manual efforts, suitable for straightforward tasks with limited rockburst data, but falters in generalizability when faced with unclear rockburst features
Deep learning methods	Automatic feature extraction is better suited to situations where rockburst features are not obvious and does not require prior knowledge of the input-output relationship	A large amount of rockburst data is required, the prediction results are affected by the model parameters, and the training time is long

Figure 7-12 : Advantages and Disadvantages of AI techniques in rockburst prediction (from Zhang et al. 2024a)

Liang *et al*. (2020) used several machine learning methods to predict short-term rockburst risk using microseismic data from Jinging II Hydropower project (China). Liang *et al*. (2021) performed an estimation of the probability of short-term rockburst risk based on various ensemble classifiers also for Jinping II Hydropower project (China). Zhang *et al.* (2021) analyzed microseismic data from various deep underground construction in China with convolutional neural network. Yin *et al.* (2024) developed probabilistic assessment models of rockburst risk that include several types of input data, such as microseismic monitoring, TBM excavation parameters and surrounding rock mass parameters. They used probabilistic ensemble learning (aggregation of several individual machine learning models) and quantum particle swarm optimization to develop their model and applied it to a case study of a water transfer tunnel in Xinjiang (China). The maximum predicted rockburst intensity for each day (test period of 20 days) was fully relevant with the field observation.

Monitoring for short-term rockburst prediction is essential for early warning and to guarantee safe working conditions. The two main parameters monitored are microseismicity and acoustic emissions. To perform accurate real-time rockburst prediction, these large amounts of data need to be processed rapidly with detection of specific patterns associated with rockburst precursors. The development of artificial intelligence methods has some major advantages, such as the identification of complex patterns and the inclusion of other input data like the one coming from the TBM or the rock mass characteristics, which greatly improves the relevance of the rockburst risk prediction.

7.2.2.2 Technical solutions, rockburst support

As pointed out by Cai (2024) (Figure 7-11), the last line of defense against rockburst is the choice of appropriate supports which will be the more efficient method to reduce the vulnerability of the excavation. The fundamental approach for rockburst support has been developed and presented in the Canadian Rockburst Support Handbook (Kaiser *et al.* 1996). The fourth primary support functions are to reinforce, to retain, to hold and to connect (Kaiser *et al.* 1996, Cai 2024). The objective is to mix several support techniques to reinforce the rock mass (rebar for example), while others aim to retain the rock mass (aerial or surface component such as mesh or shotcrete), and also to be able to absorb energy and to hold during the violent

failure (yielding bolt). The last function is to connect all these supports together to make the support more resilient (Cai 2024). These different functions are summarized in Figure 7-13.

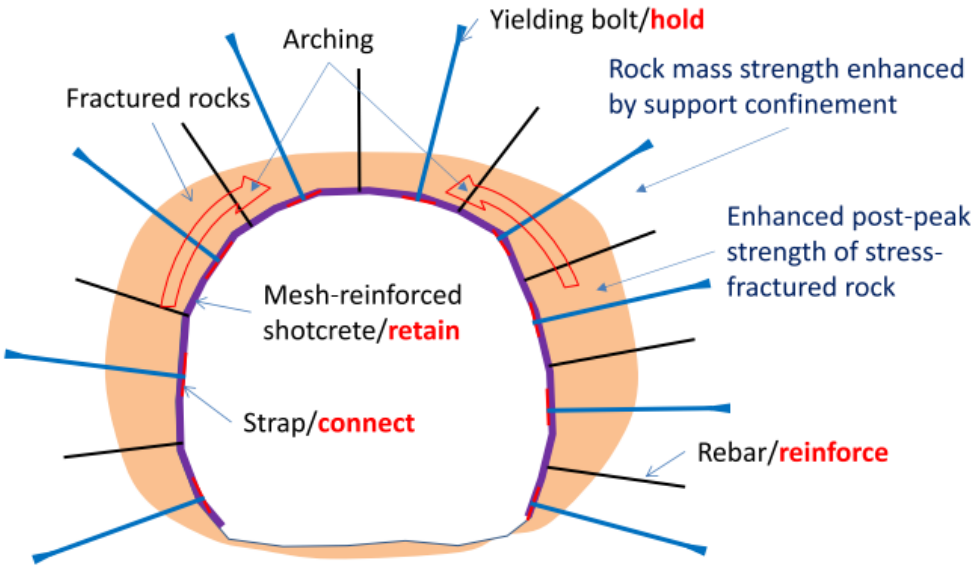

Figure 7-13: Rock support function from Cai (2024), referring to Kaiser et al. (1996)

Cai (2024) explained that a classical approach for the support installation in mining is based on a two-pass system, which could also be true for civil engineering tunnels excavated using drill and blast or TBM. First, rebars with mesh are installed to reinforce the rock mass, and second, dynamic rockbolt and mesh straps or high-strength mesh are installed later. This approach puts workers at great risk because a rockburst may occur before the rockburst resistant support (yielding bolts and mesh straps) is installed (Cai 2024). It is recommended to use one-pass approach for rock support systems in potential rockburst conditions or to use hybrid bolts that combine reinforcement and yielding support functions (Cai 2024). Cai (2024) presents many types of yielding bolts which have been compared (strength and yielding capacity) by Cai and Kaiser (2022).

This method, based mostly on yielding bolts and high-strength mesh, has been used during the construction of the Lötschberg Base Tunnel (personal communication with E. Garin 2025) and the Gotthard Base Tunnel (Röthlisberger *et al*. 2016a, b) in Switzerland. Where necessary, some steel arches were also installed to reinforce the support (Röthlisberger *et al*. 2016a, b) as well as a modification of the excavation sequence when using the drill and blast excavation method. The full-face excavation approach was modified to reduce the excavation area by first excavating the top heading of the tunnel and then excavating the bench and the invert. According to Röthlisberger *et al*. (2016b), this results to a substantial reduction of the rockburst risk. It is noteworthy that in both projects, bypass between the two tubes were also excavated, but no mention of rockbursts during their excavation was found.

For tunnel excavated with TBM, there is another support technique: the McNally Support System which has been designed and patented by C&M McNally for exclusive use on the Robbins TBMs. This system has been successfully used during the excavation of the Olmos Transandean Tunnel in Peru (Diederichs *et al.* 2013) and possibly for some section of La Maddalena exploratory tunnel in Italy (Fornari *et al*. 2016, Figure 7-14). This system can be defined as "*an umbrella support system consisting of rebar straps fed from cartridges above*

the shield [...] providing a continuous roof retention system" (Diederichs *et al.* 2013). Figure 7-14 presents pictures of this system.



Figure 7-14: Pictures of the support used for some sections of La Maddalena exploratory tunnel (from Fornari et al. 2016)

When the excavation is done by drilling and blasting, another method can be used: the pre-conditioning technique. The idea is to intentionally damage the rock mass during the blasting (creating fractures inside the rock mass) to change the stress concentration inside the rock at the tunnel boundary (wall or face), or to change the rock properties (injection of water or chemicals) to reduce the risk of rockburst (Cai 2024). It can be done by destress blasting, hydrofracturing, water injection, … (Cai 2024).

Hu *et al.* (2024) present the "Excavation Compensation Method" which was applied during the construction of the Qinling Water Conveyance Tunnel in China, where there were very high horizontal stresses, believed to be up to 100 MPa. Unlike the previously presented methods, which are based on passive support, the support method proposed by Hu *et al.* (2024) uses an active support concept. The idea is to apply a pretensioning force of 200 kN to each bolt very close to the face (using a specially adapted TBM), immediately after the bolt installation (max 30 min). This method was applied on a test section of the tunnel and proven to be very effective since the burst pit was divided by 2 (Hu *et al.* 2024).

In conclusion, there are several support techniques for rockburst prone rock masses depending on the excavation method used. The most widely used approach is based on using mixed support elements to retain, reinforce and hold the rock mass. Some more detailed information can be found in Kaiser *et al.* (1996), Potvin and Wesseloo (2013), Cai (2013), Villauescusa *et al.* (2014), Kaiser (2014), Cai and Kaiser (2018), Morissette and Hadjigeorgu (2019), Cai and Kaiser (2022) or Kaiser and Moss (2022).

7.3 Rockburst risk assessment under uncertainties: Mont-Cenis base tunnel case study

The assessment of the rockburst risk at an early stage of the tunnel design is fundamental to propose adapted tunnel design, excavation sequence, monitoring system and support techniques. It allows engineers to select the appropriate technical solution and to better estimate the cost and duration of the tunnel construction.

The risk assessment depends on the methodology used as well as on the geological and geotechnical uncertainties. Since the Diederichs' (2018) method (Section 7.1.2) is a deterministic approach, this section aims to improve the method for a direct consideration of the existing uncertainties and to apply it on the case study of the deepest part of the Mont Cenis base tunnel between France and Italy. The objective is to quantify the risk of rockburst depending on the existing uncertainties by calculating the probability of being in each class of hazard levels. To simplify the study, only the uncertainties related to the geotechnical parameters and the in-situ stress state are considered.

7.3.1 Project presentation

The Mont Cenis Base Tunnel is 57.5 km long twin tube tunnel in the Alps between France and Italy. It is part of the construction of the new railway line between Lyon (France) and Turin (Italy) for the Trans-European Transport Network. The tunnel construction started with the construction of three access galleries in France, and one exploratory tunnel in Italy (La Maddalena) between 2001 and 2017. Then the major part of excavation of the base tunnel started in 2022, using drilling and blasting, and seven TBMs (Figure 7-15). The project is managed by TELT SAS (Tunnel Euralpin Lyon Turin) which is a public binational promoter owned 50% by the French State (Ministry of the Ecological Transition) and 50% by the Italian State (Ferrovie Dello Stato Italiane group). The maximum depth of the tunnel is more than 2000 m.

The deepest section of the tunnel will be excavated by two hard rock TBM which will perform an 18.5 km drive between the Modane safety site (France) and the Clarea safety site (Italy) (Figure 7-15). On this section, almost 16 km of tunnel has an overburden of more than 1000 m and preliminary studies highlighted the possible risk of rockbursts. Nevertheless, there are major uncertainties regarding the geological conditions, the geotechnical parameters and the in-situ stress state since the field investigations are limited. They are very expensive and complex or near impossible to carry out for some sections (in the middle of a mountain range with very limited ground access).

Since the TBM work will begin in the next two years, the objective of this section is to perform a more precise and detailed study to assess the rockburst risk by taking into account these substantial uncertainties. The studied section is 15 km long associated with an overburden of more than 1000 m (right part of the CO5 construction lot, Figure 7-15) with an overlap of 1.5 km of La Maddalena exploratory tunnel. This is a 7 km long tunnel constructed to improve the understanding of the behavior of the Ambin massif at depth and to complete a mechanized excavation test (Parisi *et al.* 2017).

The expected geological conditions are presented in Figure 7-16, as well as other relevant information. The geotechnical properties associated with the geological map and the tunnel section studied are summarized in Table 7-3.

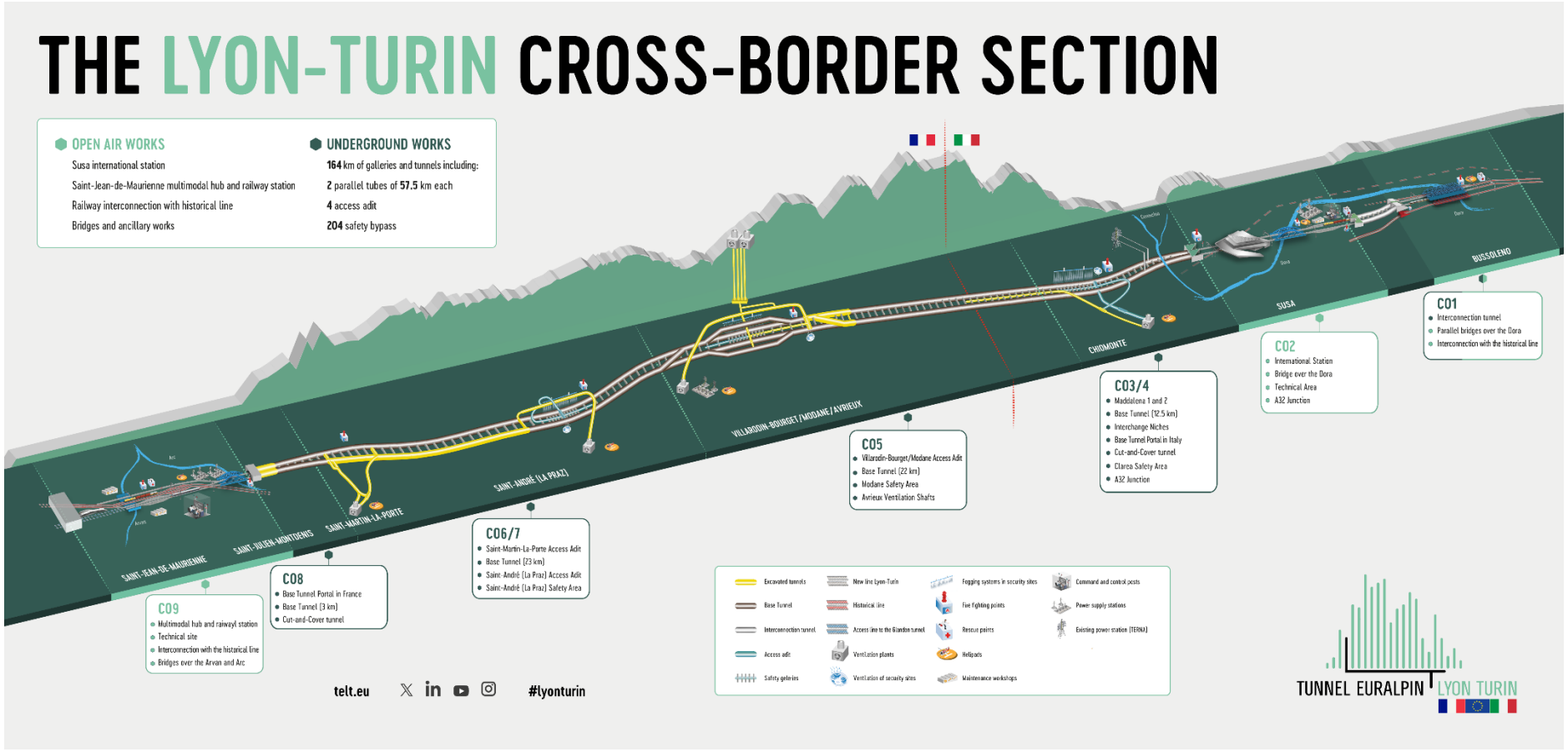

Figure 7-15 : Presentation of the Mont Cenis base tunnel from TELT (Tunnel Euralpin Lyon Turin) website (https://www.telt.eu/en/)

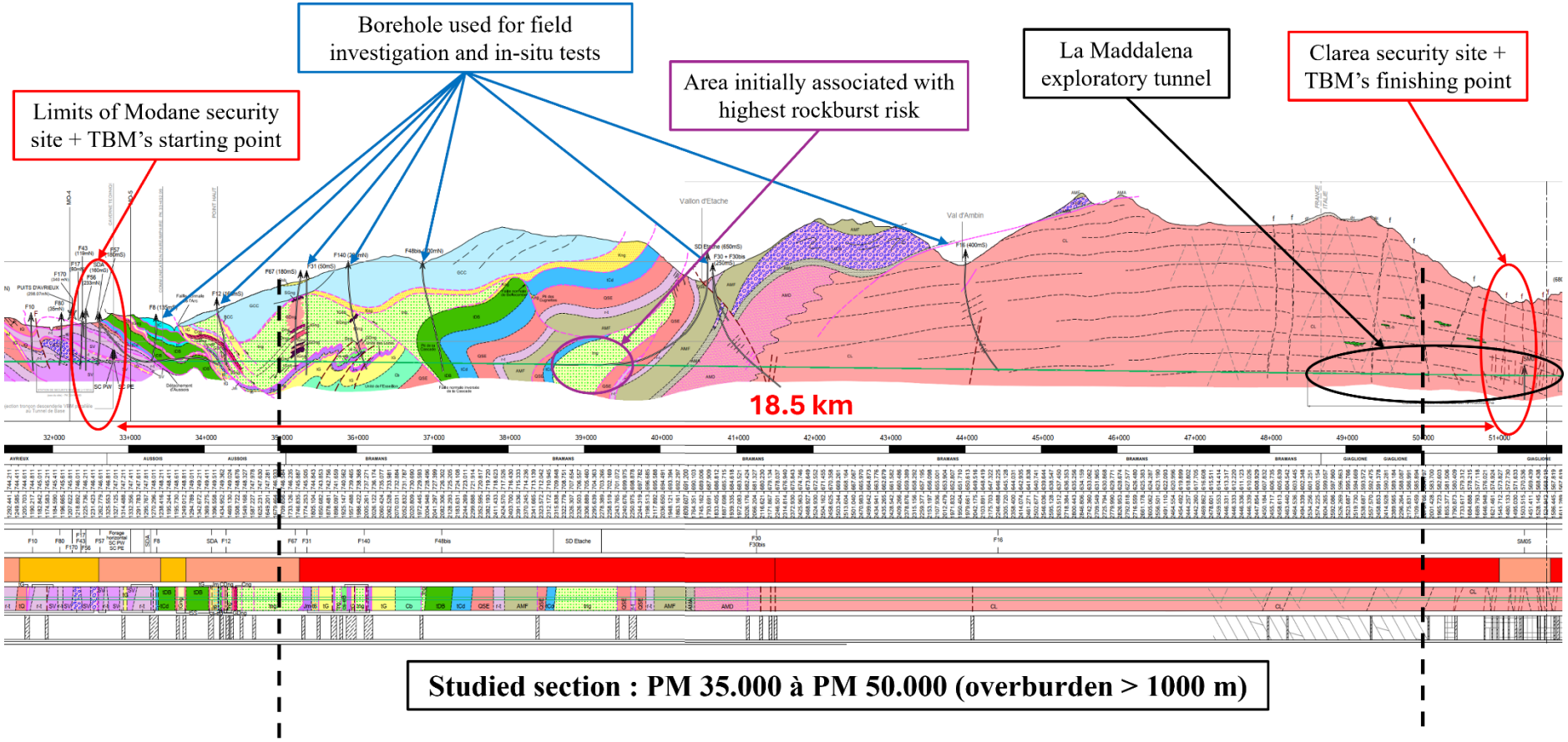

Figure 7-16 : Geological map of expected geological conditions encountered during the TBM excavation of a part of the CO5 construction lot (adapted from ALLTI 2018a)

Table 7-3: Summary of the geological data associated with the geological map (from ALLTI 2018b); for the geological formation in italic, the geotechnical values have been obtained based on laboratory test and field reconnaissance carried out on similar geological formation encountered outside the studied section

Geological formation		**γ (kN/m³)**			**σ_c (MPa)**			**σ_t (MPa)**			**GSI**		
		Min	Means	Max	Min	Means	Max	Min	Means	Max	Min	Means	Max
Limestone	Jm	26.5	27.6	29.1	34.5	91	155.2	4.1	6	9.3	58	63	67
Dolomite	t6	27.2	27.8	28.2	104	133.6	163	3.3	7	10.7	55	59	63
Anhydrite	tG	28.2	28.9	29.6	39.6	92	168.6	3.1	4.8	6.6	65	69	72
Marble	cs-e	26.5	27.6	29.1	34.5	91	155.2	4.1	6	9.3	58	63	67
Dolomite	Cb	28.2	28.4	28.6	67.2	152	224.3	7	9	11	73	77	80
Anhydrite	*tng*	*28.2*	*28.9*	*29.6*	*39.6*	*92*	*168.6*	*3.1*	*4.8*	*6.6*	*70*	*74*	*77*
Dolomite	tDB	28.2	28.4	28.6	67.2	152	224.3	7	9	11	73	77	80
Dolomite	tCD	28.2	28.4	28.6	67.2	152	224.3	7	9	11	73	77	80
Quartzite	*QSE*	*25.5*	*26.9*	*28*	*86.9*	*142*	*223*	*7.6*	*8.9*	*10.9*	*59*	*65*	*75*
Micaschist quartzitic	*r-t*	*25.9*	*26.6*	*27.6*	*22*	*60*	*97.7*	*3.1*	*4.7*	*8.6*	*59*	*64*	*68*
Quartzitic micaschist	*AMF*	*27.5*	*27.8*	*28*	*37.2*	*77*	*136.2*	*8.3*	*8.5*	*8.7*	*43*	*53*	*70*
Quartzitic micashist	*AMA*	*27.5*	*27.8*	*28*	*37.2*	*77*	*136.2*	*8.3*	*8.5*	*8.7*	*43*	*53*	*70*
Quartzitic micaschist	*AMD*	*27.5*	*27.8*	*28*	*37.2*	*77*	*136.2*	*8.3*	*8.5*	*8.7*	*43*	*53*	*70*
Micaschist	CL	26.5	27.7	29	37.6	101.5	232.1	7.2	13.9	22.8	30	64	85

All the geological and geotechnical information used comes from the geological and geotechnical synthesis associated with the design studies performed by ALLTI (Alliance Lyon Turin Ingénierie) composed of the following engineering companies: Arcadis, WSP (formerly BG Ingénieurs Conseils), Lombardi Engineering, Amberg Engineering and TTS.

7.3.2 Methodology used

To quantify the rockburst risk associated with the deepest section of the Mont Cenis base tunnel, it is decided to use the method proposed by Diederichs (2018) and presented in Section 7.1.2, and to include uncertainty propagation.

7.3.2.1 Adaptation of Diederichs's method for uncertainties propagation

The method proposed by Diederichs (2018), presented in Section 7.1.2, allows only deterministic calculations. The objective is to incorporate this method into a larger framework that allows the propagation of uncertainties by using Monte Carlo simulations and to estimate, for each section, the probability of being in each class of hazard levels proposed by Diederichs (2018), presented in Table 7-2. The general proposed methodology is presented in Figure 7-17.

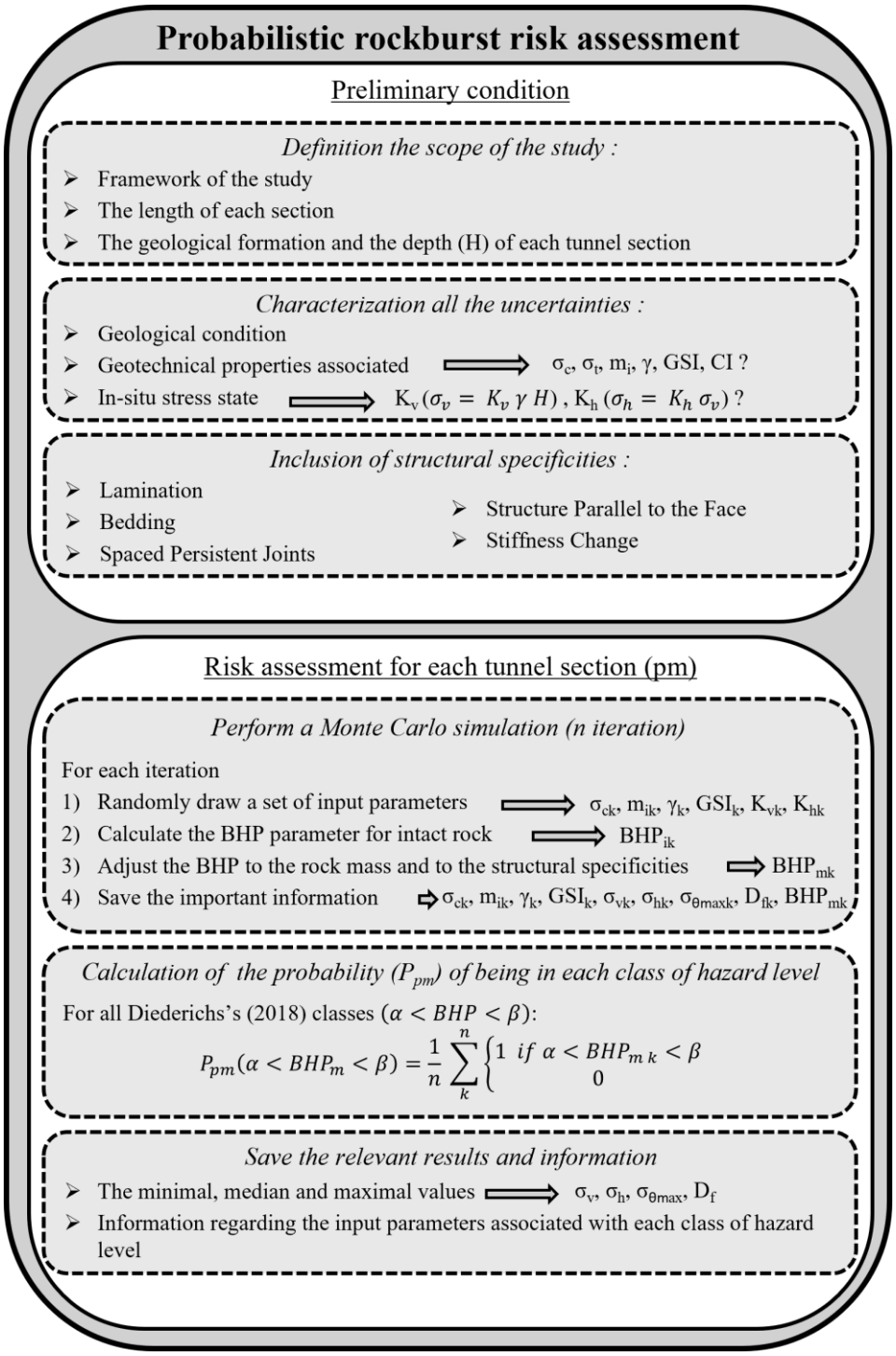

Figure 7-17: General methodology for a probabilistic rockburst risk assessment based on the approach developed by Diederichs (2018) ; σ_{ci} is the uniaxial compression strength of the intact rock; σ_t is the tensile strength of the intact rock; m_i is the strength of the Hoek & Brown failure criterion; γ is the specific weight of the rock expressed as kN/m³; GSI is the Geological Strength Index; CI is the crack initiation stress; D_f is the depth of failure (Eq. 6-5); pm is the chainage of the tunnel section

For the application of this methodology (Figure 7-17) to the deepest section of the Mont Cenis Base Tunnel, some hypotheses are made:

- The methodology is applied to the tunnel section between PM35.000 and PM50.000 (Figure 7-16). Each section is considered to be 100 m long, the geological conditions

and the depth are considered constant for all sections, equal to the middle of the section. 150 sections are studied.
- The characterization of the uncertainties of the geotechnical parameters and the in-situ stress state is presented in the following section (7.3.2.2). In this study, the uncertainty of the geological formation associated with each section is not considered.
- Since the field investigations are limited and the structural specificities are poorly known, they are not included in the study. Only the GSI is considered to affect the BHP.
- For moderately fractured rock mass (GSI below 60), the risk of large rockbursts is relatively low. In this approach, this consideration is not directly taken into account. The GSI will only lead to a reduction of the BHP as proposed by Diederichs (2018) (Eq. 6-10). Therefore, the approach used can be described as "naïve".
- For each section, a Monte Carlo of 1,000,000 realizations is performed, and the computation time is between 10 and 20 s per section. It is noteworthy that a smaller number of realizations (100,000 for example) leads to very similar results.
- The classes of hazard levels are simplified. The first three classes are combined in a single class corresponding to BHP < 1. This simplification is performed as no failures are observed for BHP < 1 (Table 7-2).
- After the Monte Carlo simulation of each section, some information about the input parameters associated with the various class of hazard levels are retrieved. The idea is to access the range of values of the input parameters associated with a class. Each input parameter (σ_{ci}, m_i, γ, K_v, K_h, GSI) is divided into three groups of values with the same initial probability (33.3%). For example, if it is supposed that the studied section is located in the Jm geological formation (Table 7-3) and σ_{ci} has a uniform distribution law between [34.5 MPa; 155.2 MPa]. The first group corresponds to "σ_{ci} < 74.7 MPa", the second group to "74.7 MPa < σ_{ci} < 115.0 MPa" and the last group to "σ_{ci} > 115.0 MPa". Then, for a class of hazard level of a specific tunnel section, the proportion of values associated with these three groups can be estimated. In the previous example, it is assumed that the probability of being in the spalling class (BHP between 1 and 2, Table 7-2) is 40%. It is possible to know that, for example, 80% of the situations leading to a BHP ∈ [1; 2] are associated with the first group ("σ_{ci} < 74.7 MPa"), 15% with the second group and 5% with the last group. The same approach is used for the other input parameters, for all classes of all the tunnel sections studied. It allows a more refined interpretation of the results.
- The calculations are carried out using the Python programming language and the Spyder environment.

7.3.2.2 Quantification of the input parameters uncertainties

The uncertainties considered are about the geotechnical parameters and the in-situ stress state.

7.3.2.2.1 Geotechnical uncertainties

As presented in Table 7-3, there are large uncertainties on the input parameters. To properly take them into account, there are several points of discussion about the distribution law to use and the standard deviation to consider. This section does not intend to start a general discussion on these points.

Three distributions laws are generally used for the uncertainties of geotechnical parameters, a uniform distribution, a normal distribution, or a lognormal distribution. In this situation for the uniaxial compressive strength (σ_{ci}), choosing a uniform distribution for this parameter seems unlikely because the minimum and maximum values are extreme. Since the number of

laboratory tests performed is limited for each geological formation, it was decided to use a normal distribution. A comparison has been made which shows the very limited influence of the distribution law on the results (between normal and lognormal).

For the specific weight (γ) and the GSI, a uniform distribution was chosen because of the limited information available (test or field observations) and their small variation ranges, except for the CL geological formation. For this formation, the minimum GSI is 30 which corresponds to the crossing of faults or highly fractured area. For this range of GSI, brittle failures are not expected (Kaiser *et al.* 2000) and the impacted sections are very localized. The choice is made not to consider it. The minimum GSI value considered for the CL geological formation in the Monte Carlo simulations is 50.

Table 7-3 highlights the uncertainty on the tensile strength of the intact rock (σ_t). The estimation was obtained with a very limited number of tests (between 1 and 10, depending on the geological formation). This parameter is not directly used to calculate the BHP. It is rather the m_i parameter of the Hoek and Brown failure criterion. The m_i can be calculated as the ratio of σ_{ci} and σ_t in the Diederichs' (2018) method, or using the following expression (Hoek and Brown 2019):

$$m_i = \frac{1}{0.81}\left(\frac{\sigma_{ci}}{|\sigma_t|} - 7\right) \qquad (7-11)$$

Direct consideration of the uncertainty on the tensile strength leads to unrealistic values of m_i, regardless of the expression used as presented in Figure 7-18, for three geological formations (tng, Cb/tDB/tCD and CL). The values of m_i are generally between 5 and 30 (Hoek 2007), depending on the type of rock. The range of values for one geological formation presented in Figure 7-18 covers the entire possible range of m_i values and also leads to unrealistic values. Figure 7-18 is obtained with a Monte Carlo simulation considering a normal distribution law for σ_{ci} and a uniform distribution for σ_t.

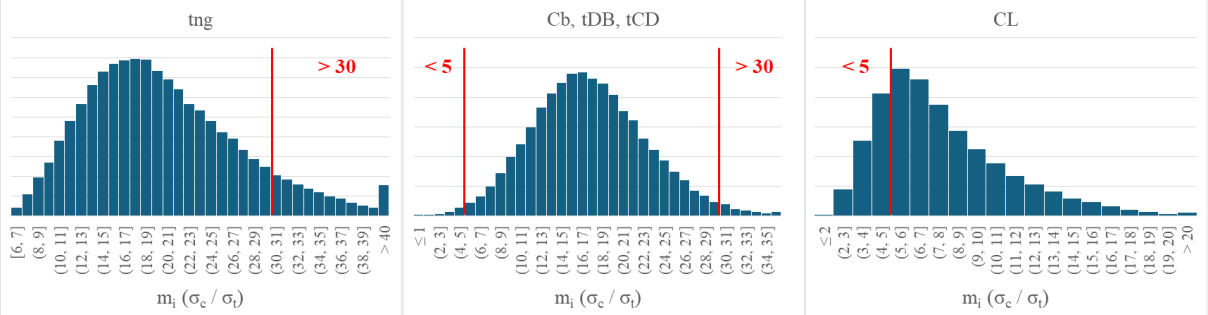

Figure 7-18 : Histogram of m_i parameter for three geological formations obtain with a Monte Carlo situation considering a normal distribution law for σ_{ci} and a uniform distribution of σ_t

Based on this consideration, the choice is made to include the uncertainty of m_i and not the uncertainty of σ_t in the BHP calculation in order to avoid unrealistic values and to include some dependence between σ_{ci} and σ_t. The m_i parameter is characterized by a bounded normal distribution law, with the mean value calculated as $\sigma_{ci\ mean} / \sigma_{t\ mean}$ for each geological formation. A coefficient of variation of 20% is used to highlight the large uncertainty existing on this parameter. In order to avoid unrealistic values during the Monte Carlo simulation, limits are introduced associated with a 95% confidence interval ($\mu_{m_i} \pm 2\,\sigma_{m_i}$).

It is noteworthy that in the geological and geotechnical synthesis (ALLTI 2018b), small values of m_i were considered, which can be seen as a "safe hypothesis" regarding the strength of the rock mass and finite element numerical calculations (overestimation of the potential plastic radius and radial deformation), but also as an "unsafe hypothesis" regarding the rockburst risk assessment. A small value of m_i leads to a lower failure intensity (calculation of the Dynamic Rupture Potential, Eq. 7-7) and thus to a potential underestimation of the rockburst risk.

Since a part of the studied section overlaps 1.5 km of La Maddalena exploratory tunnel, the GSI values used for this section are those observed during the construction of the exploratory tunnel: between 60 and 68 (ALLTI 2018b). Similarly, the σ_{ci} for the geological formation "micaschist of Clarea" associated to these 1.5 km are those from Armetti *et al*. (2018). They performed laboratory tests on rock sample collected during the excavation.

Table 7-4 summarizes the uncertainties considered in this study for each geological formation.

Table 7-4 : Geotechnical uncertainties consider for the study of the deepest section of the Mont Cenis base tunnel; CLm is the micaschist of Clarea from La Maddalena exploratory tunnel

Geological formation	**γ (kN/m³) (Uniform)**		**σ_{ci} (MPa) (Normal)**				**m_i (Normal)**				**GSI (Uniform)**	
	Min	Max	Means	St Dev	Min	Max	Means	St Dev	Min	Max	Min	Max
Jm	26.5	29.1	91	27.3	34.5	155.2	15.2	3	9.2	21.2	58	67
t6	27.2	28.2	133.6	39.9	104	163	19.1	3.8	11.5	26.7	55	63
tG	28.2	29.6	92	27.6	39.6	168.6	19.2	3.8	11.6	26.8	65	72
cs-e	26.5	29.1	91	27.3	34.5	155.2	15.2	3	9.2	21.2	58	67
Cb	28.2	28.6	152	45.6	67.2	224.3	16.9	3.4	10.1	23.7	73	80
tng	28.2	29.6	92	27.6	39.6	168.6	19.2	3.8	11.6	26.8	70	77
tDB	28.2	28.6	152	45.6	67.2	224.3	16.9	3.4	10.1	23.7	73	80
tCD	28.2	28.6	152	45.6	67.2	224.3	16.9	3.4	10.1	23.7	73	80
QSE	25.5	28	142	14.6	86.9	223	16.0	3.2	9.6	22.4	59	75
r-t	25.9	27.6	60	20	22	97.7	12.8	2.6	7.6	18	59	68
AMF	27.5	28	77	23.1	37.2	136.2	9.1	1.8	5.5	12.7	43	70
AMA	27.5	28	77	23.1	37.2	136.2	9.1	1.8	5.5	12.7	43	70
AMD	27.5	28	77	23.1	37.2	136.2	9.1	1.8	5.5	12.7	43	70
CL	26.5	29	101.5	30.5	37.6	232.1	7.3	1.5	4.3	10.3	50	85
CLm	26.5	29	112.7	28.3	74	224	8.1	1.6	4.9	11.3	60	68

It can be noted that the m_i values obtained for some of the rocks (Table 7-4) are much higher than the range of value recommended by Hoek (2007). Hoek (2007) recommended between 7 and 15 for limestone (Jm), between 6 and 12 for Dolomite (t6, Cb, tDB, tCD), between 10 and 14 for the anhydrite (tG, tng). The choice has been made to keep the m_i value obtained from the laboratory test and the geological synthesis (ALLTI 2018b) in regard to the recommendation of Hoek (2007). This choice can have an impact on the results, leading to a higher risk of rockburst.

7.3.2.2.2 In-situ stress state

Data on the in-situ stress state is limited for this tunnel section (between PM 35.000 and 50.000). Several in-situ Hydraulic Test on Preexisting Fracture (HTPF) tests were performed during the early field investigation of the project (Figure 7-16). The results of those associated with the sections studied are summarized in Table 7-5 :

Table 7-5 : Summary of the results of in-situ test (HTPF); H is the depth of test; γH is the lithostatic stress; σ_v is the measured vertical stress; $\sigma_{h\,min}$ and $\sigma_{h\,max}$ are minimal and maximal horizontal stresses

Borehole	H (m)	γH (MPa)	σ_v (MPa)	$\sigma_{h\,min}$ (MPa) and direction	$\sigma_{h\,max}$ (MPa) and direction	Kv (σ_v / γH)	Kh (σ_h / σ_v) (σ_H / σ_v)
F67	1027	27.7	27.5	15.0 (N057)	22.5 (N158)	0.99	0.55 0.82
F31	864	24.6	37.4	8.1 (N043)	22.8 (N133)	1.52	0.22 0.61
F16	920	29	23	28 (N036)	36 (N126)	0.79	1.22 1.57
S4	777	21	17	20 (N143)	30 (N053)	0.81	1.18 1.76
SM05	1163	31.4	32.8	25 (N142)	45.4 (N102)	1.04	0.76 1.38

It can be noted that the vertical stress is not necessarily equal to the lithostatic stress and there is large difference between the minimum and maximum horizontal stress. The direction of the tunnel is N077 between PM35.000 and PM42.000, then it turns progressively to N061 between PM42.000 and PM45.000, and then the direction is N061.

K_v and K_h are defined based on the following expressions:

$$\sigma_v = K_v\, \gamma\, H \qquad (7-12)$$

$$\sigma_h = K_h\, \sigma_v \qquad (7-13)$$

Where σ_v is the vertical stress, γ is the specific weight, H is the depth and σ_h is horizontal stress perpendicular to the tunnel direction.

Since the number of in-situ tests are very limited and it is difficult to make assumptions about the in-situ stress state, three situations are considered:

1) The in-situ stress state is considered isotropic and equal to the lithostatic stress.
2) Minimal and maximal values of K_v and K_h are chosen based on the results of the in-situ test and are used on the entire section studied. The distribution laws are uniform between 0.8 and 1.4 for K_v and 0.6 and 1.3 for K_h.
3) The variation range of K_v and K_h are dependent on the geological units. ALLTI (2018a,b) considered 4 different geological units between PM35.000 and PM50.000: "Unité des Lozes" (PM35.000 to PM36.900); "Unité de Bellecombe" (PM36.900 to PM39.900); "Complexe d'Ambin" (PM39.900 to PM41.300); and "Complexe de Clarea" (PM41.300 to PM50.000). No HTPF tests have been performed in "Unité de Bellecombe" and "Complexe d'Ambin" geological units. F67 and F31 took place in the "Unité des Lozes" geological unit and F16, S4 and SM05 took place in the "Complexe de Clarea" geological unit. The variation range of K_v and K_h are presented in Table 7-6. Since no data are available, the variation range associated to "Unité de Bellecombe" and "Complexe d'Ambin" geological units are considered identical with minimal and maximal values in between the two other geological units. The distribution law for these two parameters is uniform.

Table 7-6: In-situ stress state considered in the study

Tunnel section	K_v		K_h	
	Min	Max	Min	Max
PM 35.000 – 36.900	1	1.4	0.6	0.8
PM 36.900 – 41.300	0.9	1.2	0.7	1
PM 41.300 – 50.000	0.8	1	0.8	1.3

K_v smaller than 1 means that the vertical stress is smaller than the lithostatic stress. K_h smaller than 1 means the horizontal stress is smaller than the vertical stress. It can be noted that the extreme values of K_v and K_h such as 0.22 or 1.76 are not covered by the range of variation presented in Table 7-6 because they are not considered to be totally realistic in this project, as it is very complex to perform these types of test at such depth.

Only the results of the situation 3 are presented below. The results of the other situations can be found in Appendix 7.

7.3.3 Results and interpretation, situation 3

The rockburst risk assessment is carried out on the deepest section of the Mont Cenis Base Tunnel by applying the methodology presented in Section 7.3.2.1 and by taking into account the uncertainties presented in Section 7.3.2.2. The main result is the probability of being in each of the hazard level classes defined by Diederichs (2018) (Table 7-2), for each tunnel section. Figure 7-19 presents the cumulative probability of every class for each tunnel section studied. Figure 7-20 presents the mean, minimum and maximum values of the in-situ stress state for each tunnel section, as well as the maximal tangential stress at the tunnel boundary assuming an elastic behavior for the rock mass. Figure 7-21 shows the variation range of the value of overbreak / depth of failure obtained from Eq.(7-5) for each tunnel section.

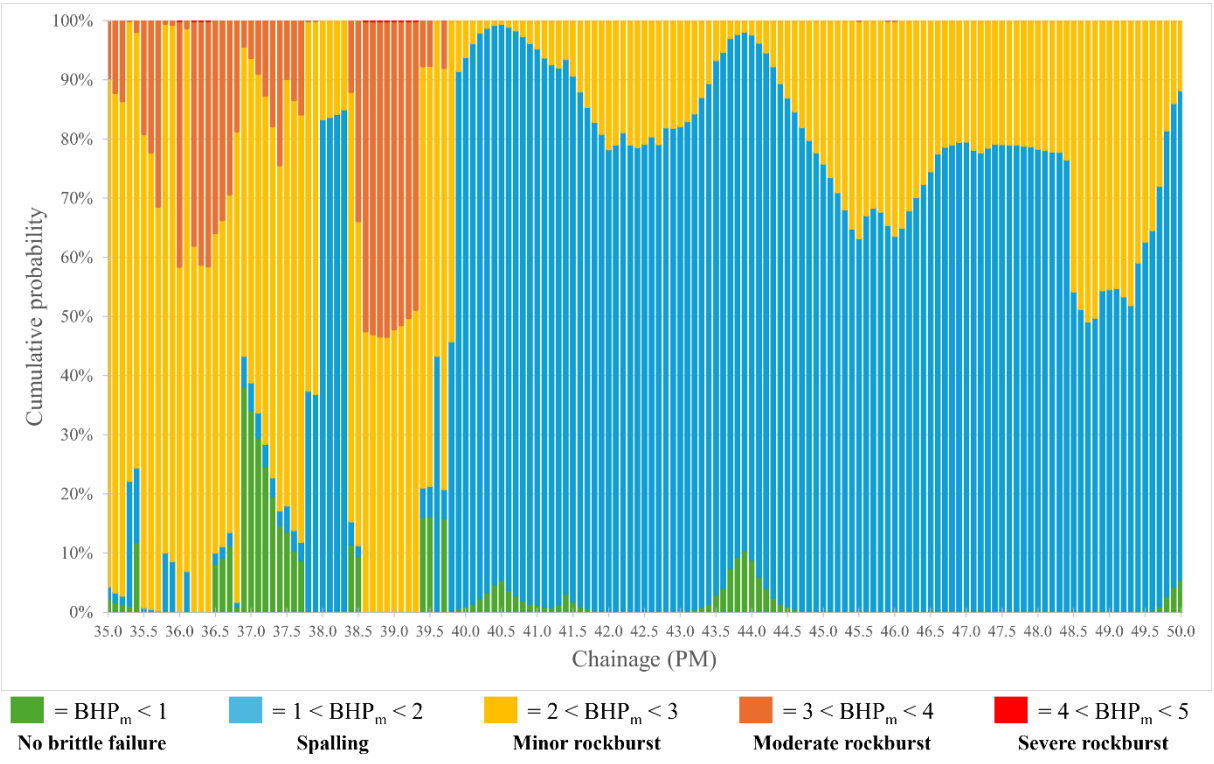

Figure 7-19: Results of the rockburst risk assessment for the Mont Cenis base tunnel (PM 35.000 - 50.000), situation 3

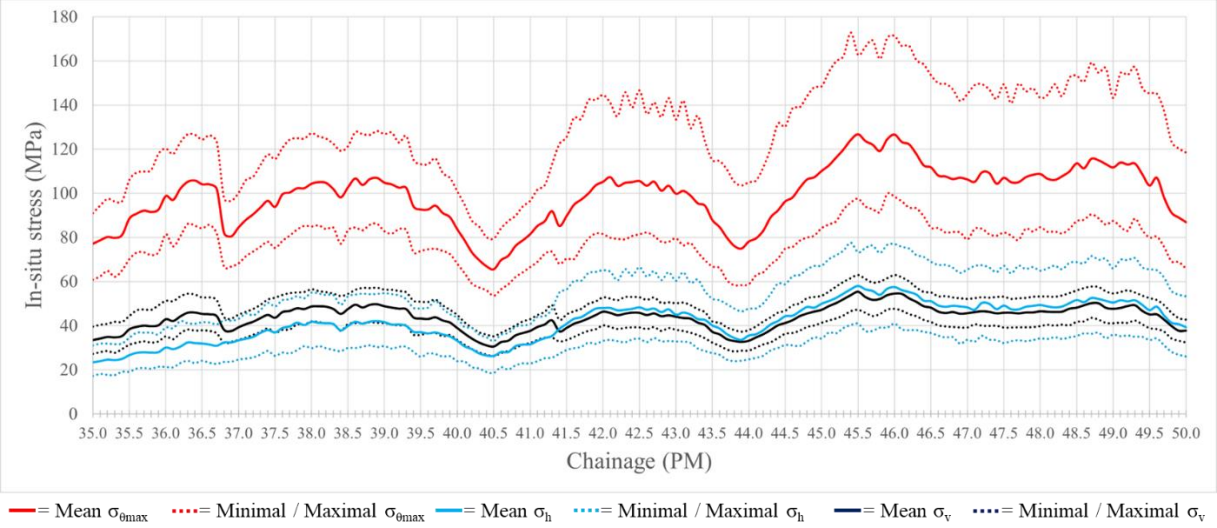

Figure 7-20: Results of the in-situ stress state associated with the Monte Carlo simulation for each section, situation 3; $\sigma_{\theta max}$ is maximal tangential stress at the tunnel boundary for an elastic behavior of the rock mass; σ_v is the vertical in-situ stress; σ_h is the horizontal stress perpendicular to the tunnel direction

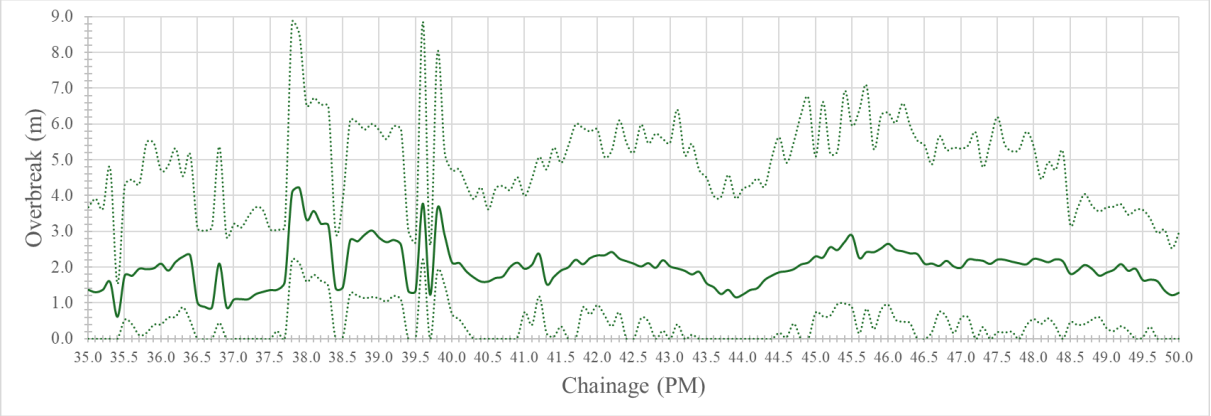

Figure 7-21:Estimation of the overbreak / depth of failure based on Eq. (6-5) of the Diederichs's (2018) method, situation 3; the solid line is the median value of the overbreak for each tunnel section; the dash lines are the minimal and maximal values of overbreak

The following comments can be made on the results presented above:

- Two tunnel sections are associated with a risk of minor to moderate rockburst intensity: PM35.000 to PM37.700 and PM38.400 to PM39.700.
  The first section was not initially identified as rockburst prone area because it is an area with complex geotechnical structures and limited depth (Figure 7-16). There is a succession of different geological formations which some are expected to be highly tectonized and to present fault zones (up to PM 36.100). No GSI reduction is considered in this zone, based on the limited field investigation and the presence of localized massive and stiff rock conditions cannot be excluded, which could lead to stress concentrations enhancing the risk of rockburst (soft loading environment in hard brittle rock, Chapter 8). The risk of moderate rockburst increases when the m_i and the K_v parameters are high (values associated with the upper third of the variation range). Between section PM36.200 and 37.700, the rock mass is expected to be massive, hard and relatively brittle (geological formation: tG, Cb, tDB, tCd, QSE), except for the

crossing of a fault around PM36.900. There are also large uncertainties on the in-situ stress state in all the area, with possibly high values of vertical stress (compared to the lithostatic stress) and relatively low horizontal stress, leading to high tangential maximum stress at the tunnel boundary. The mean value increases progressively from 80 MPa to 110 MPa (assuming an elastic behavior of the rock mass). It is important to note that, in reality, there are also some uncertainties regarding the exact location of the tunnel crossing of each geological formation. As explained in Section 7.3.2, this uncertainty is not considered in this study.

The second section associated with a high rockburst risk is located between PM38.400 and PM39.800. This section, composed of hard brittle anhydrite (tng) and quartzite (QSE), has already been identified as hazardous for rockbursts. There is nearly 50% of probability that the maximum intensity event that could occur be classified as "moderate rockburst" (Table 7-2). However, this section is not the deepest (around 1600 m), the maximum tangential stress at the tunnel boundary is very high (about 110 MPa, assuming elastic rock mass behavior) and the in-situ stress state is very uncertain because no in-situ tests are available in this section. The combination of massive and brittle rock mass with high and uncertain in-situ stress state leads to major risk of rockburst events. Based on laboratory tests, this geological formation seems to be the more brittle one (m_i values in Table 7-4). It can be noted that the "brittle" characteristic of the anhydrite is based on the estimated value of m_i from its low tensile strength. As discussed in section 7.3.2.2.1, this value may be overestimated, in which case, the associated rockburst risk would be lower.

- In the Clarea formation (PM 41.300 to PM 48.500), the risk of rockburst is limited, and mostly spalling is expected. For the deepest section of the tunnel (PM 45.500) which reaches 2200 m of overburden, the probability of the maximum event to be classified as minor rockburst is about 35%. It is associated with higher-than-average values of σ_{ci}, m_i and GSI. This result is not very surprising since the Clarea formation has a small m_i value, the mean considered is around 7. The rock of this formation is not very brittle and leads to a small value of Dynamic Rupture Potential (Diederichs 2018). So, the ability of the rock to fail violently is very limited.
- The last 1.5 km (PM48.500 – PM50.000) overlaps La Maddalena exploratory tunnel. The rock properties (CLm) considered for this section are slightly different from those of ALLTI (2018b), corresponding to the CL geological formation. The mean value of σ_{ci} is 10 MPa higher, the lower bound is twice higher, the standard deviation is slightly lower and the GSI has a limited variation range. These modifications lead to an increase of about 20% in the risk of having a maximum intensity event classified as "minor rockburst". During the construction of La Maddalena, mostly spalling occurred and the maximum depth of the overbreak was between 1 and 1.5 m for the worst events (Parisi *et al*. 2017). It can be noted that the excavation diameter La Maddalena exploratory tunnel is 6.3m. The median value of overbreak obtained by Diederichs' (2018) method (Figure 7-21) is between 1 and 2 m for a tunnel diameter of 10.4m. The maximum overbreak ratio for La Maddalena tunnel is about 1.24, and the median value obtained in this study is around 1.2. The median value obtained with Diederichs' method seems to correspond to the worst situation encountered during excavation.
- As presented above, the estimation of the overbreak using the median value obtained seems to provide an estimation of the maximum depth of failure that could be faced during the construction. Nevertheless, these results regarding the expected overbreak should be used very cautiously as the approach is only relevant for brittle rock mass behavior which corresponds only to massive and moderately fractured rock mass (GSI > 65). For strain softening or plastic post-peak behavior, referring to a depth of failure

or an overbreak seems less relevant, and the plastic radius should be used instead. Another important remark is that the overbreak is not always easy to measure in the field, as it depends on the support used.

This approach provides relevant results but there are still some limitations. A limitation is the uncertainties associated with the quantification of uncertainties. Even though some data were provided to quantify these uncertainties, several hypotheses are necessary such as the minimal and maximal values, the distribution laws used, the geological formation of a specific tunnel section, etc, which create also some uncertainties not considered in the work presented above. Another limitation, which is associated with the first one, is the reliability of the results of laboratory and in-situ tests used to quantify these uncertainties. The Mont-Cenis base tunnel is one of the largest tunnel projects in the world, for which extensive field investigations were conducted (several exploratory tunnels, several very deep boreholes, geophysics analyses, etc.) but for this section (between PM35.000 and PM50.000) the uncertainties remain very important for intermediate to advance design stages. For some parameters, the number of tests is very small, and the reliability of the results can be questioned. Is the result of tests performed on a rock sample collected 1000 m deep very reliable because of all the perturbations, change of loading conditions, induced damage, etc ?

7.4 Conclusion

The aim of this chapter is to present existing methods for rockburst risk assessment during early stages of tunnel design, with a particular focus on the approach of Diederichs (2018). These methods highlight the potential risk of brittle failure that cannot be ignored for deep tunnels in civil engineering projects, since many case histories have been subjected to it. After identifying the risk, it is necessary to mitigate it and to reduce the vulnerability of the tunnel by using appropriate tunnel designs, monitoring and supports techniques. Based on a literature review, the main methods for monitoring and support in rockburst prone rock mass are presented. The Diederichs' method is then applied to the case study of the deepest section of the Mont Cenis Base Tunnel in France. The objective is to perform a probabilistic assessment of the rockburst risk on a 15 km long tunnel section. This required some improvements of the Diederichs' method to allow for uncertainty propagation. This new method proved to be quite relevant to assess the risk of rockburst based on the existing uncertainties and led to the identification of two areas with high probabilities of the maximum possible event of brittle failure to be classified as "moderate rockburst". The results obtained with this method are also relevant compared to the field observations from the excavation of La Maddalena exploratory tunnel.

Chapter 8 - Estimation of the rock mass stiffness around a notch

Chapter abstract: As presented in the previous chapter, the empirical criteria available during design stages of deep tunnels allows a rough estimation of the possibility to experience brittle failures with spalling or rockburst. This point is fundamental to determine the worst-case scenario, but it is not sufficient to choose an appropriate design for a civil engineering project as these approaches are mostly empirical and so partly insufficient. The type and the localization of the brittle failure are also important information that needs to be obtained. The main objective of this chapter is to propose a methodology to obtain more information about the type of failure to answer the following question: Is it possible to determine the location of the probable failures and whether there are static (such as spalling) or violent (such as rockburst)?

To investigate this question, a methodology based on a literature review is tested. The main idea of the methodology is to compare the stiffness of the rock mass around a failed area and the post-peak stiffness of the rock to estimate the type of the brittle failure (quasi-static, spalling, or violent, rockburst). While this approach is not fundamentally new, complementary studies and thorough analysis of its relevance are necessary. The main focus is on the estimation of the rock mass stiffness around a failed area. For pillar burst, this question has been studied by many authors, but for strainburst, the studies are limited. Several approaches are tested in the following chapter to calculate this stiffness and then applied to two case studies followed by a comparison with the post-peak stiffness for each type of rock. This comparison raises numerous questions and leads to debatable conclusions, leading to the conclusion that the proposed methodology is not fully suitable to answer the main question during preliminary tunnel design.

8.1 Proposed methodology

As the empirical criteria provide the maximum intensity of the brittle failure that can be expected, they do not provide any information on the types and localizations of these events, which are influenced by the excavation techniques, the tunnel geometry, local heterogeneities in the encountered geology or external disturbances. Most empirical criteria classify spalling as a low-intensity rockburst but is it really the case? As empirical criteria aim to quantify the risk of brittle failure, spalling may be considered as a low-intensity rockburst because it is a progressive and mostly quasi-static phenomenon. Nevertheless, the transition between spalling and small rockburst is not really straightforward as some progressive spalling can result in local violent failure because of slab or spall buckling, as well as when intense rockbursts are expected, spalling also occur. It means that the transition between one or another type of failure is more complex, and it is dependent on external considerations, such as the loading environment. The difference between spalling and rockburst is the temporality of the failure. The former is a "stable" failure while the latter is a violent and "instable" failure. This difference is similar to the rock failure under uniaxial compression tests. The rock samples can fail progressively or violently. The rock type influences the susceptibility to violent and instable failure, as well as the stiffness of the loading system (the press for uniaxial compression test, the rock mass for an underground structure), and the loading rate of the sample. For identical samples, a stiffer loading system environment (LESS) results in a more stable failure while softer LESS results in a more violent failure. It can be interpreted as an excess of energy being transmitted to the sample compared to the one that can be absorbed (Figure 8-1). The excess energy is then converted into surface energy (multifracturing of the sample), kinetic energy (ejection of blocks) and seismic and acoustic emissions.

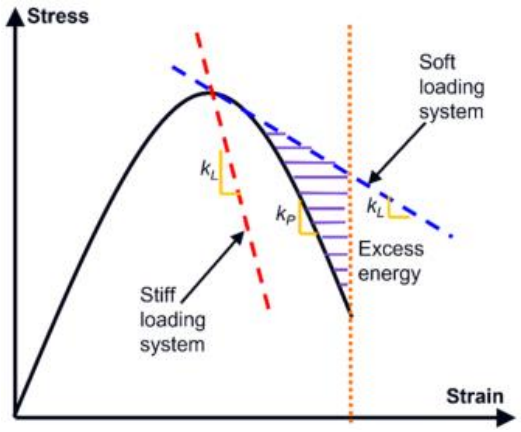

Figure 8-1 : Comparison between the post-peak stiffness of the rock (k_P) and two loading system (k_L), a soft one (blue) and stiff one (red) (from Wang et al. 2024)

An analogy can be made with the loading of a volume of rock at a tunnel boundary. As the stiffness of the press influences whether the rock failure is stable or unstable, the stiffness of the rock mass will also influence the intensity of the failure. If the rock mass is stiffer than the post-peak behavior of the investigated volume of rock, the failure will be stable (spalling), and if the rock mass is softer, the failure will be unstable, leading to energy being released. To make this comparison, three main steps are required:

1) The first step is to determine the geometry and the location of the investigated volume of rock. It is assumed to be the most probable failed area.
2) The second step is to estimate the rock mass stiffness around this area.

3) The third step is to compare this stiffness with the post-peak stiffness of the rock.

This methodology was first introduced at the end of the 60's (Cook 1965; Salomon 1970). Most of the focus has been on pillar burst (Salomon 1970; Pen 1994; Kias and Ozbay 2013; Hauquin 2016; Hou and Cai 2022a) because the localization of the failed area is easy (the whole pillar), the estimation of the rock mass stiffness is relatively simple, and it is a direct analogy to a uniaxial compression test. For strainburst in tunnels, researches are more limited. While several authors proposed methodology to estimate the rock mass stiffness (Aglawe 1999; Wiles 2002; Wang *et al.* 2024), only Wang *et al*. (2024) attempted a direct comparison with the post-peak stiffness. However, their methodology focuses on the stiffness of the rock mass at the whole tunnel scale, without considering the localization and the geometry of the failed area. Their approach is not directly comparable to the proposed methodology.

8.1.1 Literature review on the localization of the failed area

The first step is to identify the location of the brittle failure and the geometry of this failure.

Many studies and methodologies have been developed to identify the location and the depth of the rock failure around tunnels in massive rock mass. There are analytical approaches such as those of Martin *et al.* (1999) or Diederichs (2018) presented in Chapter 7.1.1 or numerical modeling which has proven to be very effective (Bewick 2021). All the methods currently used are based on the concept of "peak" and "residual" strength. When the "peak" strength is reached, the "peak" strength envelope evolves towards the "residual" strength envelope. The most common approach is based on the Mohr-Coulomb strength envelope, referred to as the bilinear or trilinear criteria (Bewick 2021). This approach includes the CWFS (Cohesion Weakening Frictional Strengthening) model introduced by Hajiabdolmajid *et al*. (2002), the CWFH (Cohesion Weakening Frictional Hardening) model proposed by Edelbro (2009) or the CSFC (Cohesion Softening Frictional Constantly) model of Pourhosseini and Shabanimashcool (2014). The difference between these approaches is the evolution of the cohesion and the frictional angle with respect to the value of the plastic shear strain between the peak state and the residual state.

This method is generally referred as "the bilinear criteria" and is based on the estimation of the peak value, the residual value and the choice of an evolution law for the strength parameters (cohesion, friction angle, dilatancy angle). There is no consensus in the literature on this subject:

- *Cohesion:* For every author, the cohesion decreases during the post-peak deformation of the rock. The initial cohesion is estimated from the value of the crack initiation stress (detailed in Chapter 2.1.1.2) obtained during laboratory tests (Walton 2019). Renani and Martin (2018) propose the following formulation for the initial cohesion which incorporates the characterization of the rock mass by introducing the GSI parameter.

$$C_{ini} = \frac{CI}{2}\left(0.3 + \frac{0.2}{1 + \exp(26 - 0.3\,GSI)}\right) \qquad (8-1)$$

  Where C_{ini} is the initial cohesion and CI is the crack initiation stress under uniaxial compressive tests. The value of the residual cohesion is more controversial. Several authors consider the residual cohesion to be zero (Diederichs 2007; Lv *et al.* 2018; Walton 2019) but others consider a non-zero residual cohesion such as Hajiabdolmajid *et al*. (2002), Edelbro (2009; 2010), Zhang *et al.* (2012), Pourhosseini and Shabanimashcool (2014), and Renani and Martin (2018). Renani and Martin (2018)

suggest using 10% of the initial cohesion as residual cohesion, which is similar to the value proposed by Pourhosseini and Shabanimashcool (2014). Walton (2019) considers that the residual cohesion should theoretically be equal to zero for an infinite plastic shear strain. However, in real applications the author considers the following empirical expression when the initial cohesion is higher than 6.1 MPa:

$$C_{res} = -0.46\ MPa + 0.73 * C_{ini} \quad (8-2)$$

Where C_{res} is the residual cohesion.
The evolution of the cohesion between the initial and residual values differs among authors, but all consider that the strain-softening of the cohesion depends only on the plastic shear strain (Pourhosseini and Shabanimashcool 2014; Renani and Martin 2018). Hajiabdolmajid *et al*. (2002) consider a linear evolution while Pourhosseini and Shabanimashcool (2014), Renani and Martin (2018) and Lv *et al.* (2018) consider a non-linear evolution, and Eldelbro (2009; 2010) considers an instantaneous transition between the initial and residual cohesion.

- *Friction angle*: There is less consensus regarding the evolution of the friction angle. Some authors consider a constant friction angle during the rock failure (Pourhosseini and Shabanimashcool 2014; Lv *et al*. 2018; Alidaryan *et al.* 2023) while others consider an increase of the mobilized friction angle during the failure (Hajiabdolmajid *et al*. 2002; Diederichs 2007; Edelbro 2009, 2010; Renani and Martin 2018; Walton 2019). Expect Diederichs (2007) and Edelbro (2010), the initial friction angle is 0° for all the authors who consider an increase of the friction angle. Walton (2019) suggests that residual friction angle to be equal to the spalling limit:

$$\varphi_{res} = 20° + 1.33 * m_i \quad (8-3)$$

Where m_i is the Hoek and Brown strength parameter. Renani and Martin (2018) suggest, based on the work of Barton and Choubey (1977), that the residual friction angle should be 34° for igneous rocks, 33° for sedimentary rocks and 29° for metamorphic rocks in the absence of specific tests.

- *Plastic shear strain between the initial and residual values*: Recent studies (Renani and Martin 2018; Walton 2019; Alidaryan *et al.* 2023) highlighted the need for an identical value of plastic shear strain for the cohesion and the friction angle to avoid unrealistic rock behavior. Walton (2019) advises a plastic strain between 0.1 and 0.3%, while Renani and Martin (2018) advise in a first approximation to use a plastic strain of 0.5%. Lorig and Verona (2013) proposed to adjust this plastic shear strain (γ_p) to the GSI value of the rock mass as follows:

$$\gamma_p = \frac{12.5 - 0.125\ GSI}{100} \quad (8-4)$$

They also stated that in case of evident localization (i.e. shear band) in the numerical model, the critical strain needs to be scaled to zone size to avoid this numerical phenomenon to occur.

A second and similar approach is based on an equivalent Hoek & Brown strength envelope. The peak strength envelope is a fit of the bilinear criteria (damage threshold and spalling limit). The Figure 8-2 presents an example of the peak strength envelope compared to the bilinear criteria (Damage threshold and Spalling limit).

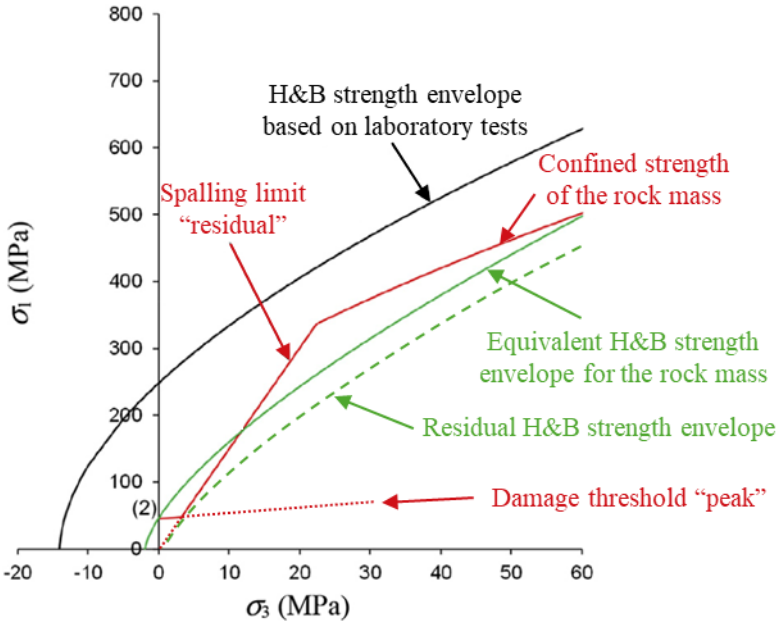

Figure 8-2 : Example of a composite peak and residual strength envelope (adapted from Bewick et al. 2019) ; red curves are the curves of the bilinear criteria / tri-linear criteria ; green curves are the curves of the equivalent (or composite) H&B strength envelope for the peak and residual state

Several authors have proposed methodologies to determine the H&B parameters of each curve. For instance, Bewick (2021) and Bewick *et al*. (2019) presented a methodology to estimate the peak strength envelope for massive, veined or moderately jointed rock mass. In an initial approach, the evolution between the peak strength and the residual strength is conducted by reducing the "s" parameter from 1 to 0 or (0.0001 to avoid numerical problems), which enables a complete loss of strength at low confining stress and a minor loss of strength at high confining stress. Based on their laboratory tests, Cai *et al.* (2021) proposed a residual parameter of 0 for "s" and to modify the value of the "m" parameter based on the uniaxial compressive strength of the intact rock. This "m" value can be obtained using the cohesion loss model from Peng and Cai (2019). Furthermore, Hou and Cai (2022) have provided evolution laws for the "m" and "s" parameters as a function of the plastic strain between the peak strength and the residual strength, based on laboratory tests. It is noteworthy that the use of an equivalent H&B strength envelope with strain-softening is really similar to what has been proposed by Laigle (2004). Laigle (2004) suggested an evolution law for the H&B strength envelope function of the plastic shear strain, and it is achieved by varying the "a", "m" and "s" parameters. The initial version of Laigle's evolution law includes only an elastic-plastic failure criteria, which have been improved to include creep (viscous-plasticity) by making the H&B parameter time-dependent (Laigle 2004; Klein 2007).

As with the strength parameters used for the bilinear/trilinear approach or the equivalent H&B strength envelope, the selection of the dilatancy parameter and its evolution law have an impact on the shape and the size of the failed rock area. Most researchers agreed about the dilatancy angle to be dependent on the rock type, the plastic shear strain and the confining pressure (Alejano and Alonso 2005; Zhao and Caï 2010; Pourhosseini and Shabanimashcool 2014; Walton and Diederichs 2015b; Rahjoo and Eberhardt 2016, 2021; Cai *et al.* 2023) but have proposed various mathematical formulations for the evolution law of the dilatancy angle. Since these evolution laws are quite complex, some suggestions have been made to use constant value for the dilatancy angle. Alejano *et al.* (2010) proposed an estimation of the constant dilation angle based on the GSI and on the frictional angle, while Lorig and Verona (2013) proposed a

fixed value for the ratio of the dilation angle to the apparent friction angle (between 0 and 0.66) depending on the GSI. The apparent friction angle is defined as the friction angle for a Mohr-Coulomb strength envelope, while it is confining pressure dependent for a Hoek and Brown strength envelope (nonlinear strength envelope).

Hence the parameters of the numerical model are determined, and the calculation are performed, the failure area can be considered as the yield zone in the model, the area for which the peak strength has been reached, and plasticity has developed (i.e. non-zero plastic shear strain) (Hajiabdolmajid *et al*. 2002; Diederichs 2007, 2018).

8.1.2 Calculation of the rock mass stiffness in the literature

The second step of the mentioned methodology is to calculate the rock mass stiffness around a failed area. In the literature, several terminologies exist to refer to the stiffness of a loading system, which can be a laboratory test machine or the rock mass.

The stiffness of a testing machine in laboratory can be referred as the LSS (Loading System Stiffness) according to Hou and Cai (2022b) and Wang *et al.* (2024) or as the LESS (Loading Environment System Stiffness) according to Hou and Cai (2022b). In the other hand, the rock mass stiffness can be referred as the LMS (Local Mine Stiffness) by Wang *et al.* (2024) or LSS by Wiles (2002). It is noteworthy that, for Wiles (2002), the LSS is also a mathematical parameter characterizing the rock mass stiffness.

To avoid any misunderstanding in this chapter, the LESS is the stiffness of the laboratory test machine while the LMS is the stiffness of the rock mass. Both stiffnesses can be calculated in various ways, which will be presented in section 8.2.1.

As Wang *et al.* (2024) pointed out, the majority of researches about the estimation of the rock mass stiffness (LMS) has been conducted for pillar burst. A classical approach to estimate the LMS around a pillar is to calculate the ratio between the force applied on the pillar before removal or failure and the displacement after the removal or failure (Jaiswal and Shrivastva 2012; Hauquin *et al*. 2018; Gao *et al*. 2019; Wang *et al.* 2024). Rather than using the forces, Khademian and Ozbay (2019) and Khademian and Ugur (2018) employed the stresses applied on the pillar to calculate the LMS. Wiles (2002) and Bewick (2013) estimated the LMS around a pillar and studied the change of stiffnesses along failed zones based on the calculation of the LSS parameter.

The studies on the estimation of the LMS around tunnels are more limited. Wang *et al.* (2024) point out the lack of research on this topic and propose to calculate the LMS as the ratio of the in-situ stress divided by the radial strain when the internal pressure is reduced to zero and when a perfectly plastic rock mass behavior is supposed. The method of Wang *et al.* (2024) leads to an estimation of the stiffness of all the rock mass in which the tunnel is excavated, but brittle failures (spalling or strainburst) are generally a localized phenomenon. This method does not allow the estimation of the LMS around a localized failed area. Aglawe (1999) presents a formulation to estimate the LMS around a slab:

$$k_{LMS} = \frac{Tangential\ force}{Tangential\ displacement} = \frac{t\ \sigma_\theta}{\Delta u_\theta} \qquad (8-5)$$

Where k_{LMS} is the rock mass stiffness around the slab, t is the thickness of the slab, σ_θ is the tangential stress acting on the slab before removal and Δu_θ is the change of tangential

displacement after the slab removal (Figure 8-3). This formulation is very similar to the ones used for mine pillars.

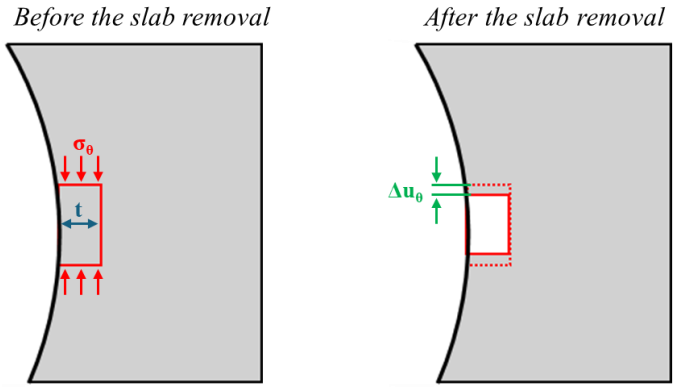

Figure 8-3 : Presentation of the notation used by Aglawe (1999) in Eq.(7-5)

McDonald (2019) also used a similar approach to investigate the impact of discontinuities near the tunnel boundary on the LMS. The LMS is not directly calculated, but the evolution of the forces and the displacements at a notch boundary gives an in-sight of the LMS evolution (Figure 8-4) depending on the discontinuity and rock mass characteristics. It is possible to deduce the LMS around the notch based on the Eq.(8-5).

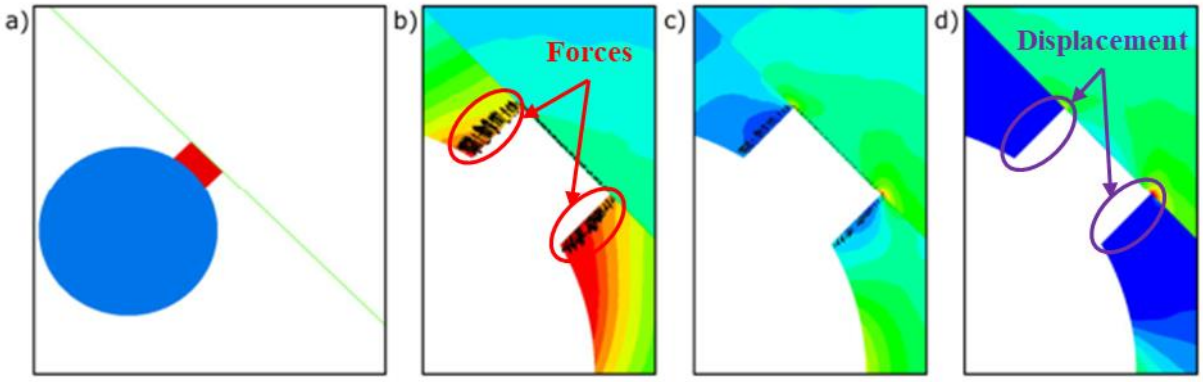

Figure 8-4 : Study of the impact of a discontinuity on the LMS (from McDonald 2019) ; a) blue is the tunnel, green is the discontinuity, red is the notch ; b) black arrows are the forces applied on the notch, the background is the major stress before the calculation ; c) Reduction of the reaction force of 50% ; d) Final state, no reaction forces

To estimate the rock mass stiffness around a notch at a tunnel boundary, two methodologies seem available in the literature: the first method is the one proposed by Aglawe (1999), based on the Eq.(8-5) ; the second method is the LSS, based on an energetic calculation (Wiles 2002) and presented in detail in section 8.2.1.2.

8.1.3 Literature review on the estimation of the post-peak stiffness of intact rock

The third step of the proposed methodology is to estimate the post-peak stiffness of the rock which is difficult to be obtained through laboratory testing (Hou and Cai 2022b). It is influenced by numerous external parameters, including the stiffness of the testing machine (LESS), the strain rate, the choice of the parameter used for the servo-control of the testing machine, etc. This makes it a challenging parameter to measure.

Based on laboratory tests, two types of post-peak stress-strain curves are generally obtained (Figure 8-5). Class I and Class II (Wawersik and Fairhurst 1970) present fundamentally different post-peak behavior. The Class II post-peak stress-strain curve (red curve) has a positive slope while the Class I post-peak stress-strain curve (black curve) has a negative slope. Hou *et al.* (2022) highlighted that the post-peak stress–strain curves of brittle hard rocks, classified as Class I and Class II, are predominantly dependent on the loading-controlled mode. Specifically, Class I is obtained under axial-strain-controlled loading while Class II is obtained under lateral-strain-controlled loading for the same rock type.

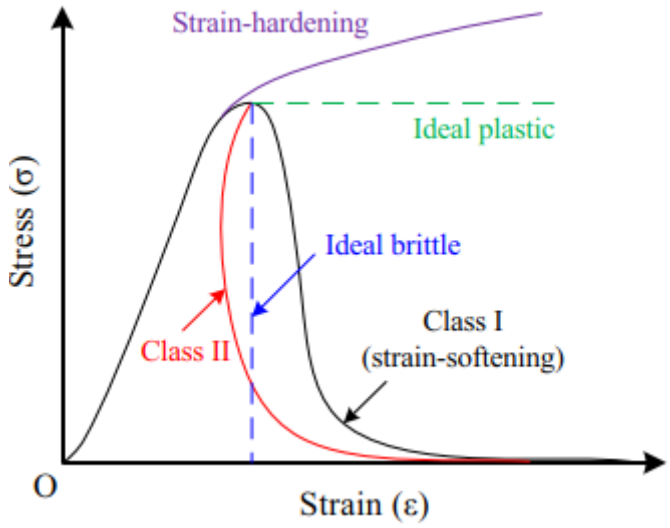

Figure 8-5 : Simplified representation of the possible post-peak deformation behavior of rock (from Hou and Cai 2022b)

The physical interpretation of the Class II post-peak deformation is that the rock failure is unstable no matter the LESS value. This indicates that the elastic energy stored in the rock sample during the pre-peak deformation stage exceeds the energy required for the failure of the rock sample. Consequently, an excess of energy is available, which is associated with an unstable failure under axial-strain controlled loading, or with some energy restitution to the loading system under lateral-strain-controlled loading (positive post-peak slope). In contrast, for a Class I failure process, complementary energy is necessary to complete the failure of the rock specimen. Hou *et al.* (2021) used a very stiff testing machine to compare the axial-strain-controlled loading and lateral-strain-controlled loading of four types of brittle rocks and concluded that the Class II post-peak stress-strain curve "*is not a true property of brittle rock but an illusion caused by actuator unloading driven by the servo-control system*". Consequently, the researchers concluded that only Class I should be considered as a post-peak stress-strain curve of a brittle rock (Hou *et al.* 2021).

In order to access the post-peak deformation of a rock under axial-strain-controlled loading, it is imperative that the LESS of the testing machine is sufficiently high, as it dictates the rock failure process. If it is too soft, the failure will be unstable and the post-peak deformation curve will not be available, while a stiffer LESS will result in stable failures, thereby making the post-peak deformation curve available (Hou and Cai 2022b). On this point, several studies have been carried out to demonstrate the impact of the LESS on the failure process. Bieniawski *et al.* (1969) conducted experiments using three different LESS values, resulting in different post-peak slopes for identical rocks specimens. However, these tests covered only a small portion of the post-peak stress strain curve. The LESS were too soft and the failure evolves from stable to unstable (Hou and Cai 2022b). Sinha and Frederking (1979) conducted tests on ice specimens and found that LESS had a large influence on the complete stress-strain curves. Rist *et al.*

(1991) pointed out that the strain rate might also impact the stress-strain behavior. Laigle (2004) also considered that the strain rate has a massive impact on the stress-strain curve.

In addressing the challenge of experimentally demonstrating the impact of the LESS, several researchers have employed numerical calculations (Hemami and Fakhimi 2014; Manoucherian and Cai 2016; Xu and Cai 2017, 2018) to simulate the interaction between the testing machine and the post-peak behavior of the rock sample. In these studies, the "real" slope of the post-peak stress-strain curve is determined by the selection of the post-peak parameter (numerical model) of the tested rock specimen. Xu and Cai (2017, 2018) demonstrated that if the LESS is softer than the "real" post-peak stiffness of the rock specimen, the obtained slope of the post-peak curve is similar to the LESS. This results in an unstable failure, as illustrated in Figure 8-6 a). The "real" post-peak behavior of the rock is the dash line, while the obtained post-peak behavior during the numerical experiment is the solid line which is identical the LESS. In the other hand, if the LESS is stiffer than the "real" post-peak slope, then as LESS increases, the slopes of the post-peak stress–strain curves firstly increase and then decrease to reach the "real" post-peak slope for an infinitely stiff LESS (Figure 8-6 b)). However, the authors do not provide an explanation for this unexpected behavior.

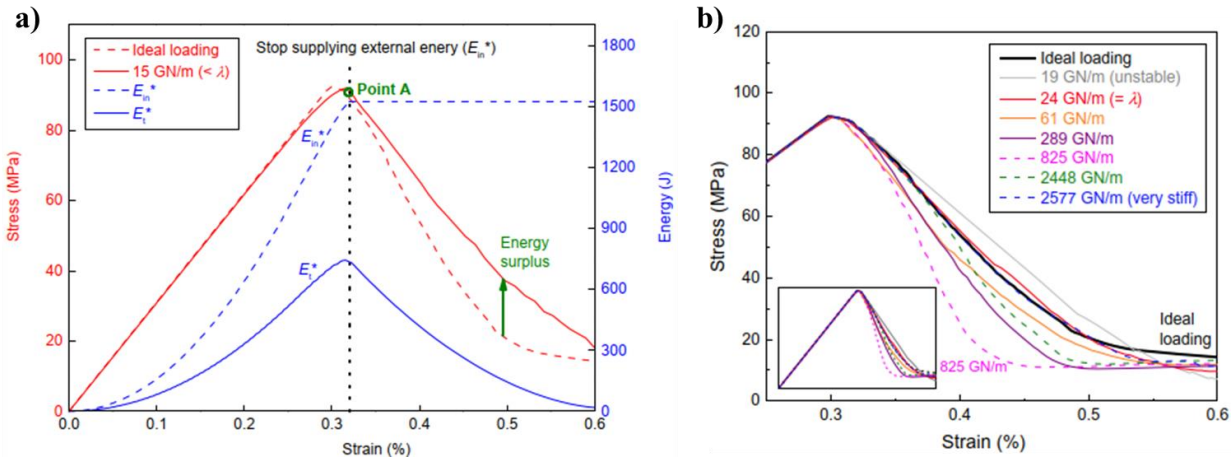

Figure 8-6 : Numerical investigation of the impact of the LESS on the post-peak behavior of the rock specimen ; a) comparison of the "real" post-peak behavior and the post-peak behavior of the rock under unstable failure, E_{in} is the external energy provided to the system (loading system and rock specimen), E_t* is the elastic energy stored in the loading system (from Xu and Cai 2018) ; b) comparison of various LESS with the "real" post-peak stiffness under stable failure (from Xu and Cai 2017)*

Hou and Cai (2022b) corroborated a portion of these numerical results through experimental testing on two types of rock: marble and granite. To conduct these tests, four LESS between 4.7 GN/m and 7.4 GN/m are used. It is noteworthy that these LESS are relatively small compared to the one used by Xu and Cai (2017) but, in reality, they cannot be compared with each other because the LESS is expressed as Newton per meter and is dependent on the size of the rock sample. Xu and Cai (2017) used a 2D numerical model, assuming an out on plane length of 1m. The post-peak curves obtained by Hou and Cai (2022b) are presented in Figure 8-7:

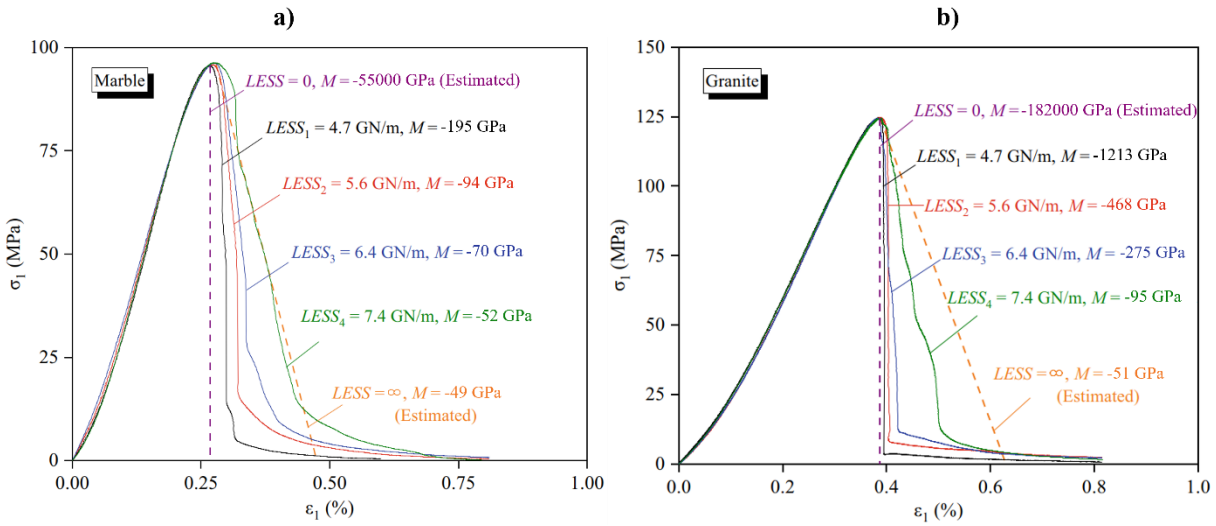

Figure 8-7 : Experimental results for post-peak deformation curves under stiff loading environment (adapted from Hou and Cai 2022b) ; a) for marble ; b) for granite ; M are the estimated post-peak stiffness of the rock specimen for each loading environment

Figure 8-7 has been modified in comparison to the original results of Hou and Cai (2022b), because a minor miscalculation of the post-peak stiffness (M parameter) was identified. To obtain the M value presented in their paper, they used the values of the strains expressed in percentage instead of the actual values of the strains. This resulted in an underestimation of the M values by a factor of 100. Based on the results given in their paper, the values of the M parameter presented in Figure 8-7 have been recalculated.

Hou and Cai (2022b) estimated the value of the post-peak stiffness associated with an infinite value of LESS to be -49 GPa for the marble and -51 GPa for the granite. It is imperative to note that the stiffness values presented in Figure 8-7 cannot be directly compared with the LESS, they must be adapted into similar units. This can be achieved using the following expression:

$$LESS_i = \frac{A_{rs}\, E_{ls}}{H_S} \qquad (7-6)$$

Where $LESS_i$ is the LESS associated with the ith test expressed in Newton per meter, E_{ls} is the value of the associated loading system stiffness expressed in Pascal, A_{rs} and H_s are the area and the height of the tested rock specimen. The rock specimen used by Hou and Cai (2022b) are cylindrical with 50 mm of diameter and 100 mm of height. Table 8-1 compares the stiffness of the loading system (E_{ls}) with the post-peak stiffness of the rock (M_i):

Table 8-1: Comparison of the LESS of the testing machine with the post-peak stiffness of the rock sample

LESS expressed as E_{ls} in GPa		0	239	285	326	377	∞
Marble	Post-peak stiffness (M_i) in GPa	55000	195	94	70	52	49
	$E_{ls} > M_i$?	No	Yes	Yes	Yes	Yes	Yes
Granite	Post-peak stiffness (M_i) in GPa	182000	1213	468	275	95	51
	$E_{ls} > M_i$?	No	No	No	Yes	Yes	Yes

For the comparison of the LESS and the post-peak stiffness leading to unstable failures, if the LESS is smaller than the post-peak stiffness the failure is unstable (Hou and Cai 2022b refer to Cook 1965; Bieniawski *et al.* 1969; Salamon 1970; Hudson *et al.* 1972). Hou and Cai (2022b) argued that the value considered for the post-peak stiffness to be used in engineering applications (pillar burst in their paper) should be estimated based on the results of laboratory tests carried out with a similar value of LESS than the value of the LMS associated with the application. If this statement is true, it means that unstable failure occurs during a laboratory test when the LESS is smaller than the post-peak stiffness obtained during the same test. In other words, the post-peak stiffness is dependent on the testing machine stiffness and can be obtained only when the LESS is higher than this post-peak stiffness.

All marble samples tested exhibit a post-peak stiffness smaller than the LESS (see Table 8-1). It means that all the failure processes in marble samples were stable, which contrasts with the results of granite samples. For LESS values of 4.7 GN/m and 5.6 GN/m (corresponding to E_{ls} of 239 GPa and 285 GPa respectively), the post-peak stiffness is higher than the stiffness of the testing machine. This means that these failures should have been unstable according to the statement of Hou and Cai (2022b). Nevertheless, Hou and Cai (2022b) do not point out any unstable failure during their laboratory tests and the pictures of the failed granitic rock samples for these LESS values do not show any sign of unstable failures. This suggests that the interpretation of Hou and Cai (2022b) regarding the comparison of the LESS and the post-peak stiffness might be questionable. It might be because of their miscalculation of the post-peak stiffnesses (underestimation by a factor of 100). A more appropriate comparison would be between the LESS and the post-peak stiffness associated with an infinitely stiff loading environment to determine whether the failure will be stable or unstable. This approach is not incompatible with the results and discussions proposed by Hou and Cai (2022b) on the impact of the various LESS on the failing process of the rock sample when the failure is stable.

Recent improvements on testing machines and methodologies have enabled a better understanding of the post-peak behavior of intact brittle rocks, as well as an estimation of the post-peak stiffness. From the results of the study of Hou and Cai (2022b) and the aforementioned discussion, it can be concluded that the relevant post-peak stiffness to compare with the LESS is the one corresponding to an infinitively stiff loading environment. This comparison could be generalized to the LMS. Now that the experimental apparatus and the methodology has been tested and validated (Cai *et al.* 2021; Hou *et al*. 2021; Hou and Cai 2022a; Hou and Cai 2022b), it can be assumed that upcoming study similar to the one proposed by Hou and Cai (2022b) may provide estimations of post-peak stiffness for a large range of rock types, to be used directly by engineers when available data are limited.

8.2 Estimation of the rock mass stiffness

This section focuses on the estimation of the rock mass stiffness around a notch. Three different calculations techniques are presented, two based on unidirectional loading (analogy with a uniaxial compression test) and one based on the multidirectional loading (LSS parameter of Wiles 2002). These calculations techniques are compared to two case studies, one typical of a spalling phenomenon and a rockburst case study.

8.2.1 Approaches used

The literature review (section 8.1.2) reveals two approaches that have been used to estimate the rock mass stiffness around a failed area. The first approach is an analogy with uniaxial

compression tests (Aglawe 1999; Jaiswal and Shrivastva 2012; Hauquin *et al*. 2018) and the second approach is more complex and based on energetic calculations (Wiles 2002; Bewick 2013). A comparison and analysis of these two approaches is conducted on two case studies: one for which mostly spalling occurs and another associated with a rockburst.

8.2.1.1 Analogy with a uniaxial compression test

The approach proposed by Aglawe (1999) to estimate the rock mass stiffness around a slab (presented in Eq. 7-5) is based on the ratio of forces divided by displacements, which is the usual approach to estimate the stiffness of a loading system like a testing machine or a spring. Another possible way to define a stiffness is based on the ratio of stress divided by strain like for an elastic modulus or a post-peak stiffness. As it will be demonstrated subsequently, the choice of a methodology to calculate the rock mass stiffness around a notch at a tunnel boundary has a considerable impact on it. The formula proposed by Aglawe (1999) in Eq.(8-5) necessitates to be generalized for a random notch geometry.

All the numerical modelling performed in this chapter are based on the finite element software Flac 8.1. The Figure 8-8 presents the various parameters used for stiffness calculation in both cases.

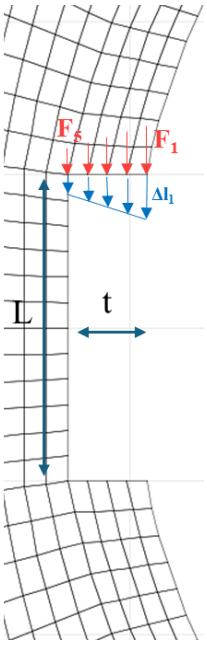

Figure 8-8: Example of a notch at a tunnel boundary ; L is the height of the notch ; t is the depth of the notch ; Fi is the force applied at each grip point situated at the notch extremity before the notch removal ; Δli is the grid displacement after the removal of the notch

The rock mass stiffness is defined as the ratio of stress divided by strain. It is called $M_{s\text{-}s}$ and expresses in Pascal:

$$M_{s-s} = \frac{\sigma_{\theta\, mean}}{\varepsilon_m} \qquad (8-7)$$

Where the $\sigma_{\theta\, mean}$ is the mean tangential stress applied on the notch before removal and ε_m is the mean tangential strain after removal. These means are weighted by the mesh size when there are not uniform:

$$X_{mean} = \frac{\sum X_i \, t_i}{t} \qquad (8-8)$$

Where X is a parameter for which the mean is calculated, t_i the mesh size of the ith element in the notch direction, t the notch depth (i.e. the sum of t_i). The tangential stress and the strain of the ith mesh element are deduced from the forces and the displacements of the grid points at the extremity of the mesh element. 3 possible situations can be encountered for the stress calculation (Figure 8-9):

- Case 1: The forces at both grid points are associated with a unique mesh zone on which the stress is calculated.
- Case 2: The forces at one grid point are associated with two mesh zones on which the stress is calculated, and the second grid point is associated with a unique mesh zone.
- Case 3: The forces at both grid points are associated with two mesh zones on which the stress is calculated.

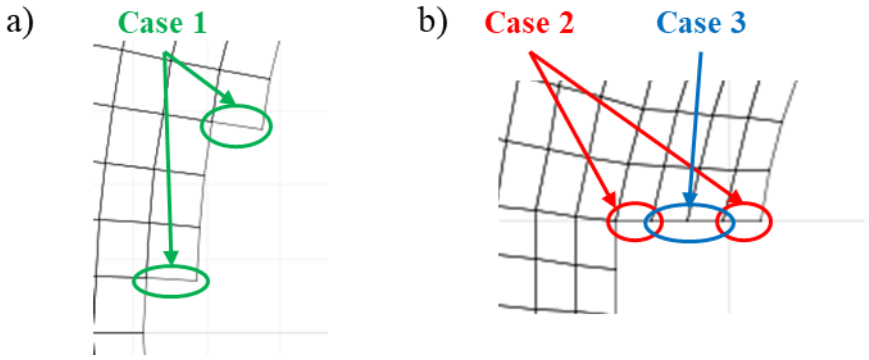

Figure 8-9 : Representation of the 3 possible situations to calculate the stress on a mesh element from the forces applied at grid points.

Eq.(8-9) and Eq.(8-10) allow the estimation of the stress, and the strain of a mesh element based on the three cases:

$$\sigma_{\theta i} = \begin{cases} \dfrac{F_{i+1} + F_i}{t_i * 1} & if\ case\ (1) \\ \dfrac{F_{i+1}/_2 + F_i}{t_i * 1} \ or \ \dfrac{F_{i+1} + F_i/_2}{t_i * 1} & if\ case\ (2) \\ \dfrac{F_{i+1}/_2 + F_i/_2}{t_i * 1} & if\ case\ (3) \end{cases} \qquad (8-9)$$

$$\varepsilon_i = \frac{\frac{\Delta l_{i+1} + \Delta l_i}{2}}{\frac{L_i}{2}} = \frac{\Delta l_{i+1} + \Delta l_i}{L_i} \qquad (8-10)$$

Where F_i and F_{i+1} are the forces applied at the ith and $(i+1)^{th}$ grid points, Δl_i and Δl_{i+1} are the displacement of the ith and $(i+1)^{th}$ grid points, L_i is the length of the ith removed slab. For Figure 8-8, all the L_i are equal to L, but it might not generally be the case. Eq.(8-10) supposes that the displacement at each point at the top and bottom of the notch are equal (symmetrical compared

to the middle of notch, at L/2). If the displacements are not symmetrical, it is also necessary to include the strain associated to the bottom of the notch, when calculating the mean strain.

It is important to note that all the numerical calculation are carried out in 2D, which mean that the size of the model in the out of plane direction is implicitly considered to be 1 m, hence the "1" at the denominator of Eq.(8-9). In the case of 3D numerical model, Eq.(8-9) and (8-10) need to be generalized.

Through a similar approach, the formula proposed by Aglawe (1999), Eq. (8-5), can be generalized as:

$$k_{f-d} = \frac{\sum F_{i\,s1} + \sum F_{i\,s2}}{\Delta l_{mean\,s1} + \Delta l_{mean\,s2}} \qquad (8-11)$$

Where s1 and s2 referred to one side of the notch and the opposite side of the notch. For symmetrical situations, the forces and displacements are equal at both sides of the notch. The general unit of k_{f-d} is Newton per meter. For 2D numerical model, the forces are expressed in Newton per meter of model in the out on plane direction, which means that the k_{f-d} unit is Newton per meter per meter of out plane model.

Rigorously, the direction of the forces and the displacements should be the same during a stiffness calculation. While this condition is generally met in most case studies, there are situations where this may not be strictly fulfilled. To simplify in this study, the calculations are done by considering the absolute values of the forces and displacements, disregarding the potential slight difference between the force and displacement orientations.

The choice of the mathematical expression to estimate the stiffness of the rock mass results in opposite stiffness evolutions when the notch size is modified. Based on the notch geometry presented in Figure 8-8, both stiffnesses $M_{s\text{-}s}$ and $k_{f\text{-}d}$ have been calculated for multiple values of notch length (L) and notch depth (t). The numerical model inputs are as follows: Young's modulus of 20 GPa, Poisson's coefficient of 0.2, vertical stress of 15 MPa, ratio horizontal stress to vertical stress of 0.5, and a circular tunnel with a radius of 5m. The results are presented in Figure 8-10.

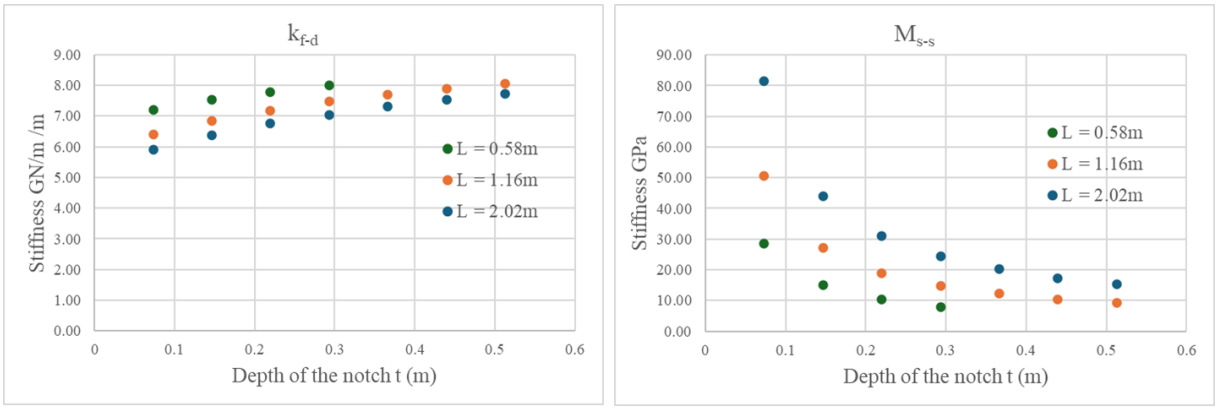

Figure 8-10 : Comparison of the two methodologies to calculate the stiffness of the rock mass around several notch sizes

Figure 8-10 shows that, for a fix length value (L), if the depth of the notch (t) increases, $k_{f\text{-}d}$ increases while $M_{s\text{-}s}$ decreases. On the other hand, for a fixed depth value (t), if the length of

the notch increases, $k_{f\text{-}d}$ decreases while $M_{s\text{-}s}$ increases. Other numerical calculations have been performed for an isotropic in-situ stress state which led to similar tendency for both stiffnesses.

From a physical perspective, it is challenging to predict the tendency of the rock mass stiffness. For an increase of the notch depth (fix length), the stiffness of the rock mass can be anticipated to decrease (the higher the depth is, the higher the displacement will be, and so the softer the rock mass is), similarly to the $M_{s\text{-}s}$ evolution. For an increase of the notch length (fix depth), it is difficult to predict the evolution of the rock mass stiffness.

As no methodology to estimate the rock mass stiffness can be proven more relevant than the other, both will be used on the two case studies presented in sections 8.2.2 and 8.2.3.

It is noteworthy that these methods to calculate the rock mass stiffness are not independent. From a general point of view, for a specific notch geometry and a specific geological situation, the LMS is unique as there is only one deformation shape of the notch. In addition, $M_{s\text{-}s}$ and $k_{f\text{-}d}$ are based on the same hypothesis which is an analogy with a uniaxial compression test. Thus, $M_{s\text{-}s}$ and $k_{f\text{-}d}$ can be mathematically linked as presented on Figure 8-11. This relationship is relevant for simple notch geometry like for the results of the Figure 8-10, but is more complex for none rectangular notch geometry (Appendix 8), as it will be discussed in section 8.3.1.

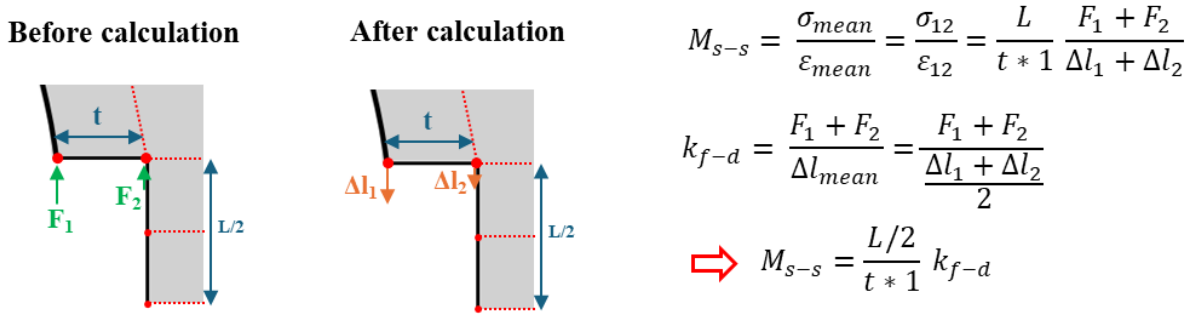

Figure 8-11: Relationship between $M_{s\text{-}s}$ and $k_{f\text{-}d}$ on a very simple example; t and L are the depth and the length of the notch

8.2.1.2 Loading System Stiffness (LSS) presentation and calculation

The two methodologies presented previously are based on the simplifying hypothesis that the loading at the tunnel's boundary is analogous to a uniaxial compression test. However, the actual loading state of the rock at the tunnel's boundary is more complex. To compare with the aforementioned methodologies, a more complex approach is used, which aims to incorporate the multidirectional loading state of the rock at a tunnel boundary.

The definition of the Loading System Stiffness (LSS) parameter is not straightforward. It can be seen as the stiffness of a loading system around a failed area. Wiles (2002) proposed to express this parameter in terms of mean stress (σ_m) and volumetric strain (ε_v) of a fictitious material whose post-peak stiffness exactly matches the loading system response (Figure 8-12):

$$\sigma_m = LSS\ \varepsilon_v \qquad (8-12)$$

Where:

$$\sigma_m = {}^1/_3\ (\sigma_1 + \sigma_2 + \sigma_3) \qquad (8-13)$$

$$\varepsilon_v = \varepsilon_1 + \varepsilon_2 + \varepsilon_3 \qquad (8-14)$$

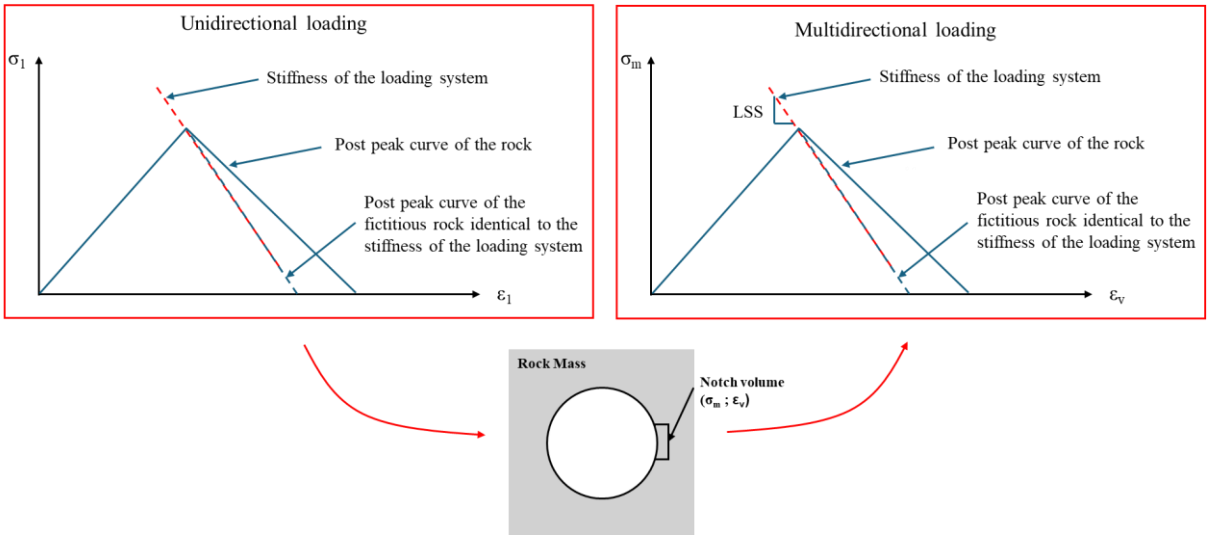

Figure 8-12 : Graphical representation of the LSS parameter

Based on energetic consideration, Wiles (2002) demonstrated that the LSS is equivalent to normalizing the LERR (Local Energy Release Rate) by the square of the mean stress in the volume material (failed area):

$$LSS = \frac{\bar{\sigma}_m^2}{2 * LERR} \qquad (8-15)$$

Where $\bar{\sigma}_m$ is the average value of the mean stress in each elementary volume of the failed area. The LERR quantifies the total amount of energy (W_t) released from the rock mass during the failure process of a certain volume of material (V_f). This energy can be expressed as:

$$W_t = W_k + W_f \qquad (8-16)$$

Where W_k is the release kinetic energy and W_f is the energy consumed by the rock during the failure. The LERR is defined as (Wiles 2002):

$$LERR = \frac{W_t}{V_f} \qquad (8-17)$$

This mathematical expression cannot be used directly to calculate the LERR and to deduce the LSS in a numerical model. Bewick (2013) used the three-dimensional elastic numerical stress modeling tool MAP3D to calculate the LSS. The total energy transfer is calculated "*as the integral of the stresses through their deformations overall all elements*", assuming that the failed volume loses all load-bearing capacity. Jiang *et al.* (2010) proposed to calculate the LERR as the change of elastic energy before and after the failure in failed area, utilizing a CWFS model. Their approach focuses on presenting the contour map of the LERR around a tunnel, obtained by calculating the variation of elastic energy in each mesh volume. However, it does not include the energy released by the rock mass. As the LSS represents the stiffness of the loading system, the energy to be considered is solely the energy released by the loading environment, no matter the amount of elastic energy already stored in the failed volume of material.

The choice of the LERR to be used to estimate the LSS can be clarified through energetic considerations in elastic numerical model. Figure 8-13 presents the three progressive states in

the numerical model and the associated energy for a quasi-static evolution between State 2 and State 3. This consideration assumes an elastic behavior of the rock mass, which at an equilibrium state, allows an easy estimation of the global model energy.

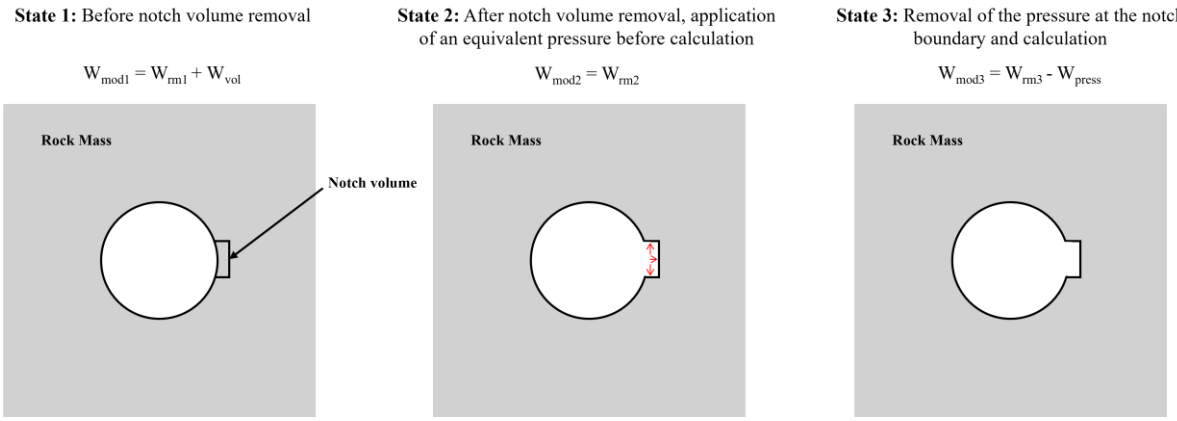

Figure 8-13 : Energetic consideration to determine the energy to be used for the LSS calculation; W_{modi} is the global elastic energy in the model at the ith state; W_{rmi} is the rock mass elastic energy around the notch at the ith state; W_{vol} is elastic energy include in the notch volume before removal; W_{press} is the energy associated with the work of the forces at the notch boundary for a quasi-static evolution between State 2 and State 3

The first approach is to consider for the calculation of the LERR the energy released from the rock mass between State 1 and State 3. This energy released can be directly calculated as the difference between W_{rm1} and W_{rm3}, without considering the elastic energy on the notch volume. This calculation of the elastic energy in the rock mass can be performed by adding the elastic energy included in each mesh element of the model (adapted from Jiang *et al.* 2010):

$$W_{rm} = \sum V_i \left([\sigma_{1i}^2 + \sigma_{2i}^2 + \sigma_{3i}^2 - 2\nu(\sigma_1\sigma_2 + \sigma_2\sigma_3 + \sigma_1\sigma_3)]/2E\right) \qquad (8-18)$$

Where V_i is the volume of the ith mesh element, σ_{1i}, σ_{2i} and σ_{3i} are the principal stress in the ith element and ν and E are the Poisson's ratio and Young's modulus of the rock. Bewick (2013) used a similar approach to calculate LSS values, but it is not clear whether the elastic energy of notch volume was included or not ($W_{rm3} - W_{rm1} + W_{vol}$ or only $W_{rm3} - W_{rm1}$).

As only external modifications will impact the global energy in the model, the energy released can also be calculated based on the following consideration. Between State 1 and State 2, two external modifications are made: the notch volume is deactivated, and a pressure is applied at the notch boundary to guarantee the equilibrium. The variation of energy between State 1 and State 2 can be expressed as follows:

$$\Delta W_{2-1} = W_{mod2} - W_{mod1} = W_{rm2} - W_{rm1} - W_{vol} \qquad (8-19)$$

As no modification of the equilibrium is made in the numerical model (no calculation) between State 1 and State 2, there is no modification of the elastic energy stored in the rock mass ($W_{mod2} = W_{mod1}$). The Eq.(8-19) can be rewritten as:

$$|\Delta W_{2-1}| = W_{vol} \qquad (8-20)$$

Between State 2 and State 3, no external modifications are made, which means that there is no evolution of the global energy in the model:

$$\Delta W_{3-2} = W_{mod3} - W_{mod2} = W_{rm3} - W_{press} - W_{rm2} = 0 \quad (8-21)$$

Yet, as there is no modification of the elastic energy in the rock mass between State 1 (W_{rm1}) and State 2 (W_{rm2}), Eq.(8-21) can be rewritten as follows:

$$W_{rm3} - W_{rm1} = W_{press} \quad (8-22)$$

Where W_{press} is the work of the applied forces between State 2 and State 3 for a quasi-static evolution. At Stage 2, the forces applied at the notch boundary guarantee the equilibrium state, so they do not work (i.e. no displacement at the notch boundary), and so are not associated with energies. During a quasi-static evolution between State 2 and 3, the forces are progressively reduced leading to displacement at the notch boundary and so strain energy (W_{press} at the final equilibrium). Thus, Eq.(8-22) highlights that $W_{rm3} - W_{rm1}$ is also equivalent to the strain energy at the notch boundary. Wiles (2002) used this approach to calculate LSS values.

The second approach for the calculation of the LERR is the calculation of the strain energy at the notch boundary (W_{press}). It can be done by considering that each point of the notch boundary acts like a spring (one in x-direction and one y-direction) and to sum the strain energy of all the springs between Stage 2 and Stage 3 (the forces are considered in Stage 2 while the displacement is considered in Stage 3).

The two approaches and the associated equation (from Eq.(8-19) to (8-22)) have been validated through an example on a numerical model, and as expected, leads to identical results. For the two case studies below, the energy used for the LERR calculation is W_{press}.

8.2.2 Case study: Mine-By tunnel, AECL, Canada

The objective of this section is to estimate the rock mass stiffness using the three calculation methods presented in the previous section (M_{s-s}, k_{f-d}, LSS) on a typical spalling case study. The process of the notch development and the evolution of the rock mass stiffness during this development are also investigated.

8.2.2.1 Context of the Mine-By tunnel

The AECL (Atomic Energy of Canada Limited) has constructed an Underground Research Laboratory (URL) in order to study the feasibility of an underground nuclear waste disposal. The AECL conducted several experiments at the URL, including the Mine-By Experiment. The objective was to investigate the formation and characteristics of the excavation disturbed zone (EDZ) (Martin *et al*. 1997). The laboratory is situated at a depth of 420 m within in the Lac du Bonnet granite of the Canadian Shield. A non-explosive excavation technique was employed to eliminate the transfer of energy from the excavation process to the formation of the excavation disturbed zone (Martin *et al*. 1997).

The Mine-By tunnel has been intensively studied in the literature (Read and Martin 1996; Martin *et al.* 1997; Aglawe 1999; Hajiabdolmajid *et al*. 2002; Laigle 2004; Diederichs 2007; and others) and is regarded as a typical spalling case study, given the observed failure, geological conditions (hard brittle massive rock mass) and experimental conditions (circular geometry, extensive monitoring, excavation technique). It is the reason why this case study has been considered in this section. However, it has been brought to the author's attention that some violent failure also occurred during the tunnel excavation, which was partly due to the buckling of slabs and spalls (Martin *et al*. 1997). Additionally, there were also some instantaneous violent

failures which could be characterized as little to medium intensity rockburst (personal conversation with R. Bewick in 2025).

Figure 8-14 shows a picture of the Mine-By tunnel after excavation and the shape and depth of the failed area. The stress state is highly anisotropic, with a principal major stress of 60 MPa, an intermediate stress of 45 MPa (tunnel axis), and a minor stress of 11 MPa (Martin *et al.* 1997). The uniaxial compressive stress of the granite is 213 MPa, the Young's modulus is 65 GPa and the Poisson's ratio is 0.25.

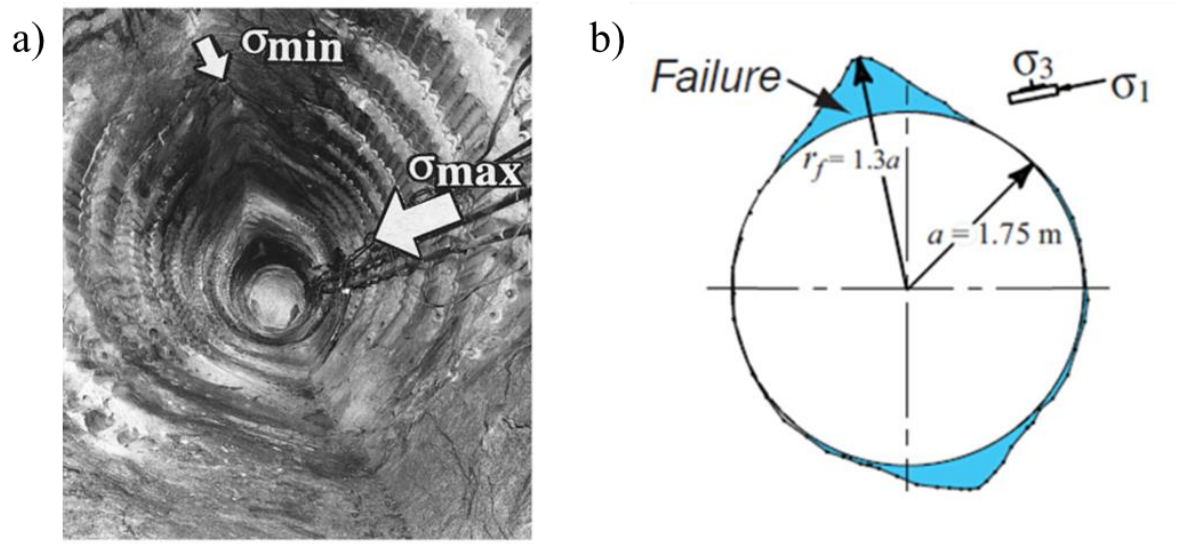

Figure 8-14 : Final geometry of the Mine-By tunnel after excavation (Barton and Shen 2017); a) a picture of the tunnel; b) the shape and depth of the failed area

8.2.2.2 Model and spalling process used

In order to estimate the rock mass stiffness, a 2D numerical model is developed. The calculations are carried out considering an elastic behavior of the rock mass. The first calculation step corresponds to the initialization of the numerical model (definition of the geometry, rock mass properties and in-situ stress state). The second step corresponds to the excavation of the tunnel. The rock material inside the tunnel is suppressed and forces are applied at every point of the tunnel boundary to maintain equilibrium. These forces are progressively decreased to zero and a new equilibrium is calculated at each reduction step, until the final equilibrium is reached. The third step, and subsequent steps, correspond to the notch creation, which is the suppression of the associated model elements, the application of forces at the notch boundary, and their progressive decreased to zero, reaching another equilibrium state. To simplify, the major principal stress is supposed to be horizontal, and the minor principal stress is vertical, resulting in the notch being at the top of the tunnel. It is noteworthy that the notch at the tunnel invert is not modeled. Numerical tests have shown that the results are nearly identical whether the notch at the invert is modeled or not.

As the spalling process is a progressive phenomenon, the hypothesis regarding the development of the failure mechanism will impact the calculation of the rock mass stiffness and its evolution during the spalling process. Three different spalling processes are modelled:

1) Instantaneous removal of all elements in the notch representing the final failed area. This can be seen as a situation when a violent failure occurs, and all the failed material is ejected simultaneously.

2) A progressive development of the notch was proposed by Aglawe (1999). The first slab (the one closest to the tunnel boundary) is removed, followed by the second slab, and so on. Each slab has a length that corresponds to the final size of the notch. To reach the top of the notch, 10 steps are necessary (Figure 8-15).
3) A progressive notch formation which seems more coherent with the field observations (Martin *et al.* 1997) and numerical calculations performed using a CWFS model (section 8.1.1) and the input parameters of Diederichs (2007). The evolution of the notch starts with the formation of a small notch, localized at the point of maximum tangential stress. Thereafter, the depth and length of the notch undergo a progressive increase to reach the final notch size in 10 steps (Figure 8-16).

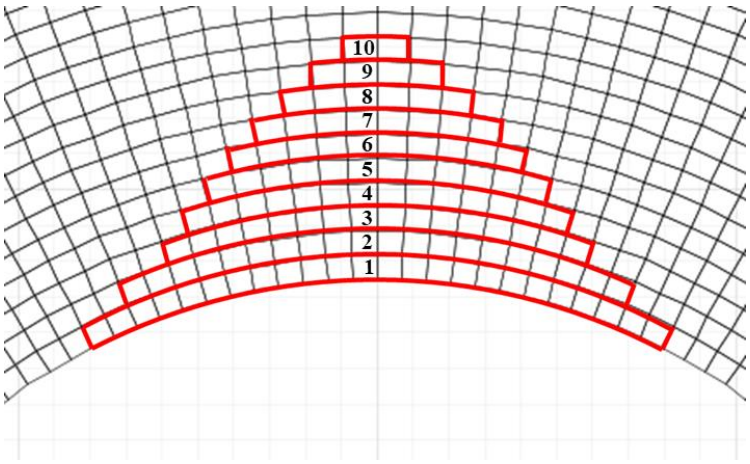

Figure 8-15 : Second method for the spalling process: progressive slab removal; red rectangles are the slab progressively removed

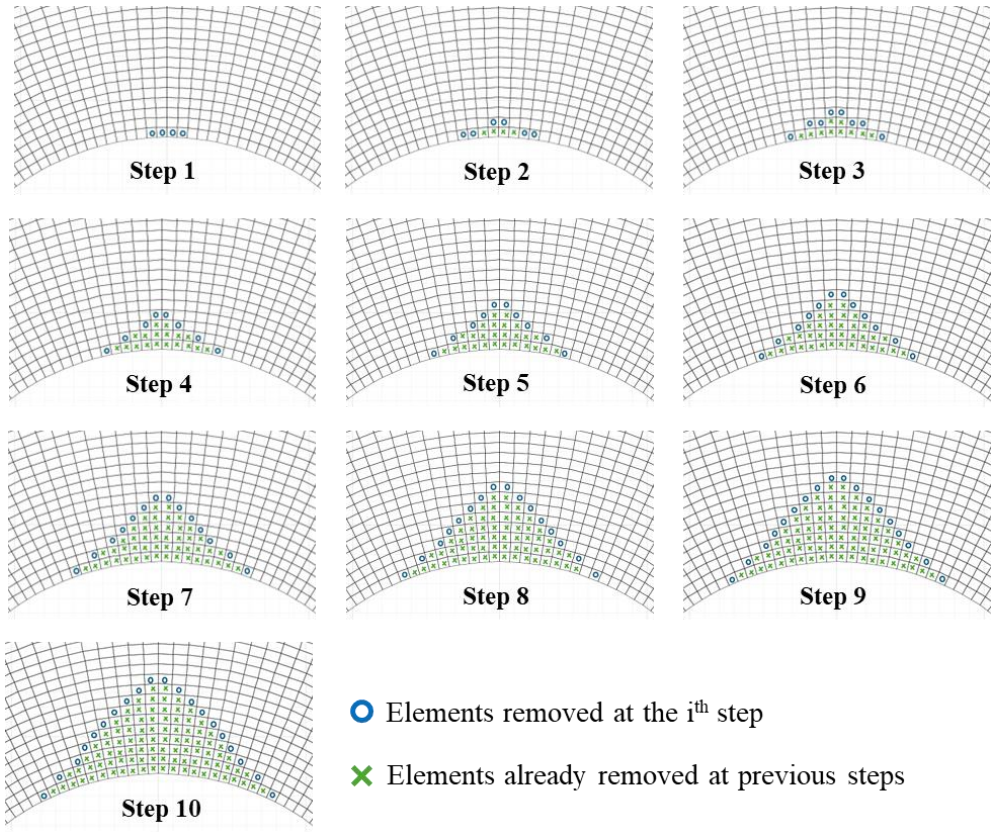

Figure 8-16 : Third method for the spalling process: progressive increase of the size and depth of the notch

The calculation of the rock mass stiffness is carried out for the three different methodologies presented in section 8.2.1 (M_{s-s}, k_{f-d}, LSS) and for each spalling process at each step of the process. The data used for these calculations are retrieved from the forces applied at each point of the notch boundary (before a calculation step), the displacement of each point (after the calculation step), and the coordinate of each point. These data allow the deduction of all the value of the necessary parameters.

8.2.2.3 Results

The rock mass stiffness depends on the calculation methodology. For the first spalling process (instantaneous removal of all the slabs), the stiffnesses are presented in Table 8-2. When the stiffness is considered as the ratio of forces divided by displacements, it reaches the highest value. On the other hand, the LSS parameter results in the smallest stiffness value.

Table 8-2 : Rock mass stiffness obtained with each methodology for the first spalling process

Methodology	M_{s-s}	k_{f-d}	LSS
Value	23.6 GPa	46.9 GN/m/m	9.6 GPa

Figure 8-17 and Figure 8-18 present the evolution of the rock mass stiffness calculated with the various methodologies for the second and third spalling process. M_{s-s} and k_{f-d} results in opposite tendencies, no matter the spalling process. M_{s-s} tends to decrease while the depth of the notch increases while k_{f-d} increases. It is similar to the first observation made in section 8.2.1.1. Unlike M_{s-s} and k_{f-d}, the tendency of the LSS depends on the spalling process. The second spalling process leads to a decrease of the LSS from 82.1 GPa to 10.3 GPa, while remaining consistently higher than the value obtained through the first spalling process (Table 8-2). The third spalling process, on the other hand, results in an increase of the LSS from 8.4 GPa to 23.4 GPa.

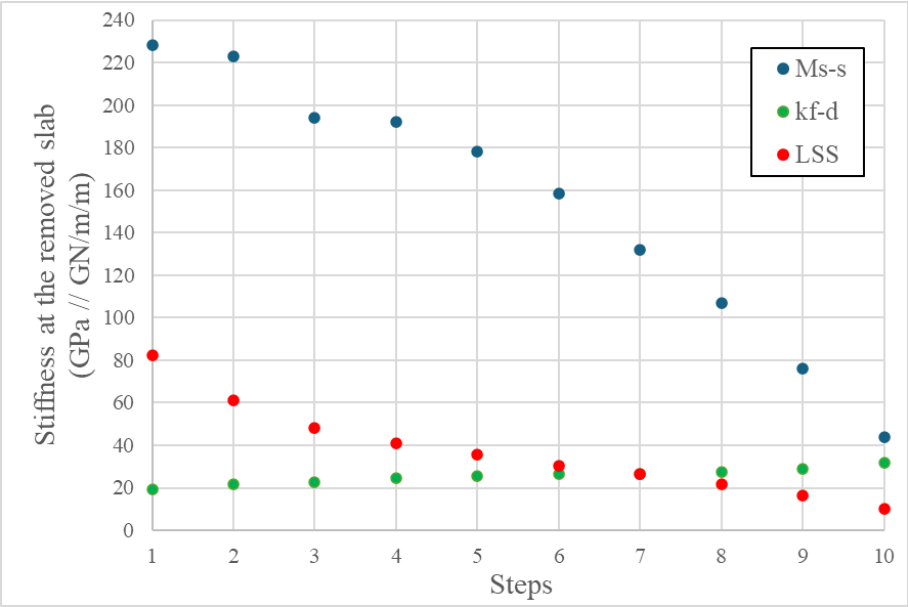

Figure 8-17 : Rock mass stiffness evolution at each calculation step for the second spalling process

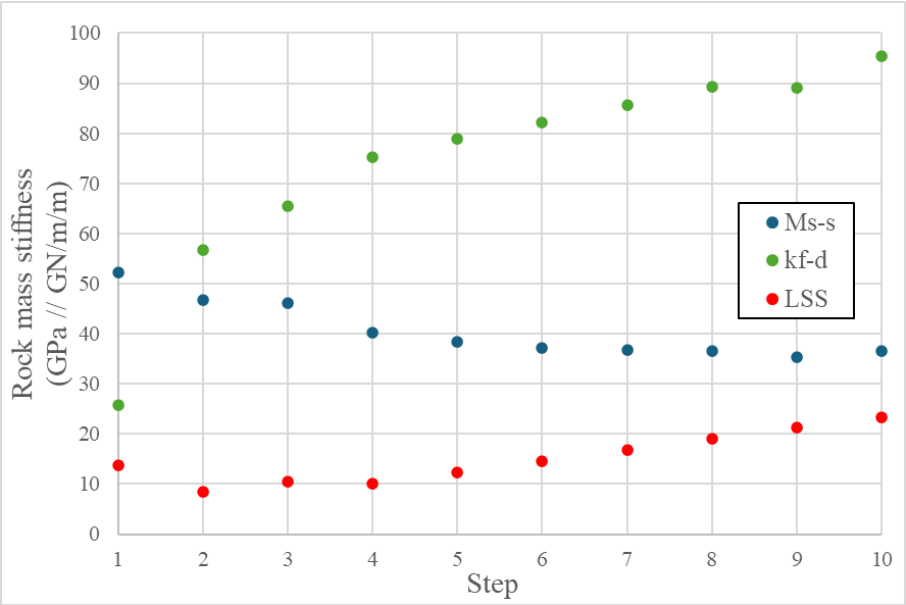

Figure 8-18 : Rock mass stiffness evolution at each calculation step for the third spalling process

The spalling process also impacts the values of $M_{s\text{-}s}$ and $k_{f\text{-}d}$. The $M_{s\text{-}s}$ stiffness is higher for the second process than for the first process, while $k_{f\text{-}d}$ is smaller. On the other hand, the third process results in higher $M_{s\text{-}s}$ and $k_{f\text{-}d}$ values than the first process.

Based on the results related to $k_{f\text{-}d}$ and the second spalling process, Aglawe (1999) concluded that an increase in the rock mass stiffness coupled with a decrease in spall length leads to the stop of the failure process. This statement is debatable because it is not necessarily true depending on the methodology used for the stiffness calculation and the spalling process. No matter what the spall length is, the rock mass stiffness does not always increase as the depth of the notch increases. In addition, explaining the stop of the failure mechanism based on the evolution of the stiffness may seem surprising. The purpose of the stiffness calculation is to provide information about whether the failure is progressive or violent, or to localize a softer spot in the rock mass. The depth and size of the failure zone are determined with the first step of the tested methodology (section 8.1). No matter the stiffness of the rock mass, no failure will occur if the stress state is not high enough to reach the damage threshold envelope.

8.2.3 Case study: 11.28 rockburst, Jinping II Hydropower project, China

The objective of this case study is to estimate the rock mass stiffness using the three methodologies on a rockburst case. The impact of a discontinuity near the tunnel on the rock mass stiffness is also studied, as well as the discontinuity characteristics and the succession of localized rockburst.

8.2.3.1 Context of the 11.28 rockburst

The 11.28 rockburst occurred on the 28th of November 2009 in the drainage tunnel of the Jingping II Hydropower station in southwest China (Zhang *et al.* 2013). The tunnelling work associated with the Jingping II Hydropower Project consists of seven parallel 17 km long tunnels with a maximum depth of 2525 m, mostly in marble rock. It includes two auxiliary tunnels, four headrace tunnels and one drainage tunnel (Figure 8-19). The drainage tunnel was

constructed using a TBM measuring 7.2 m diameter, two headrace tunnels were constructed using two TBMs measuring 12.4 m diameter and the other two headrace tunnels (13 m diameter) as well as the two auxiliary tunnels were constructed using the drill and blast method.

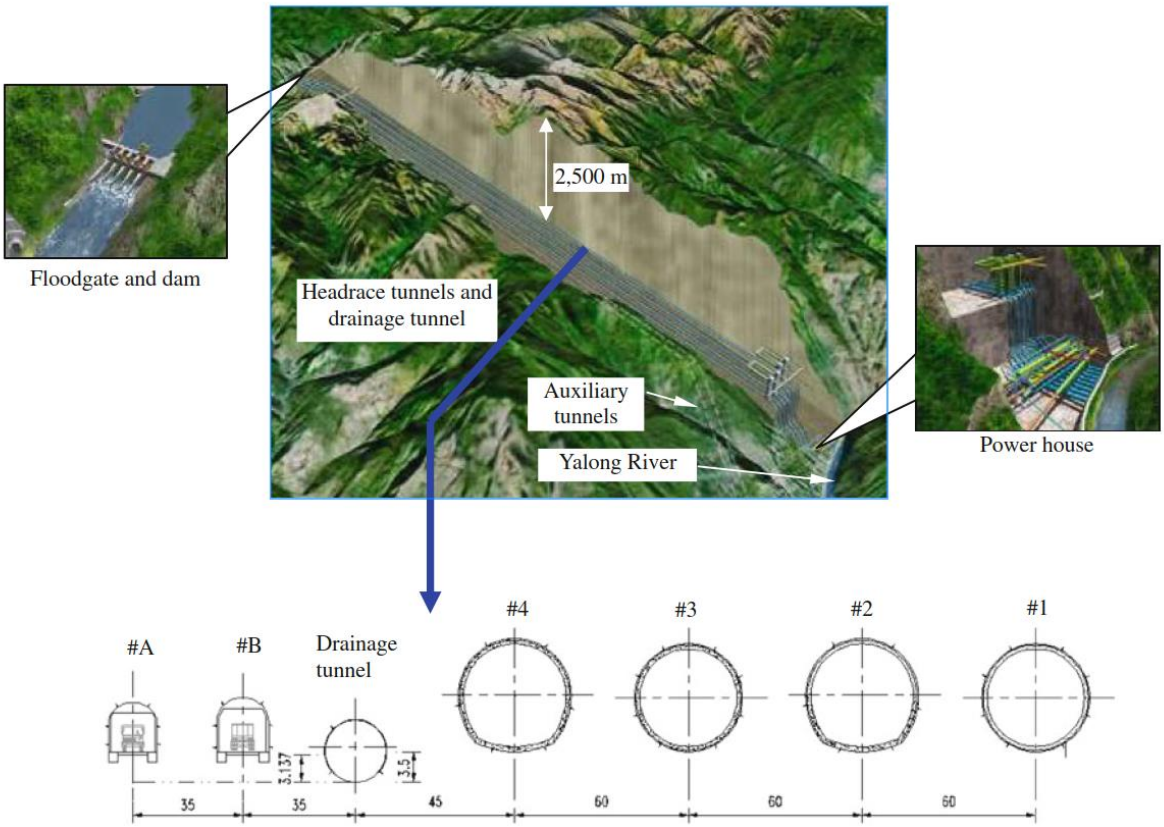

Figure 8-19 : Presentation of the Jinping II Hydropower station (Zhang et al. 2013); the drainage tunnel is 83 m below the other tunnel

During the construction of the drainage tunnel and the headrace tunnels, several extremely intense rockburst occurred, including the 11.28 rockburst which killed 7 workers and damaged many pieces of equipment (Zhang *et al.* 2013). In the drainage tunnel, the TBM has been buried under 400 m^3 of rock. It can be noted that at the same location (35 m long area), 9 rockbursts of lower intensity occurred in the previous month and half before the 11.28 rockburst occurred.

Zhang *et al.* (2012; 2013) provide an overview of some of these rockburst. The 11.28 rockburst was chosen because several studies have already been done on it. At the rockburst site, a discontinuity subparallel to the tunnel direction with a dip angle of 50° was detected near the tunnel boundary after the events (Figure 8-20). The discontinuity affected the rock mass stiffness and increased the rockburst intensity (Zhang *et al.* 2013; Manouchehrian 2016; McDonald 2019). The depth of the section where the rockburst occurred is 2330m.

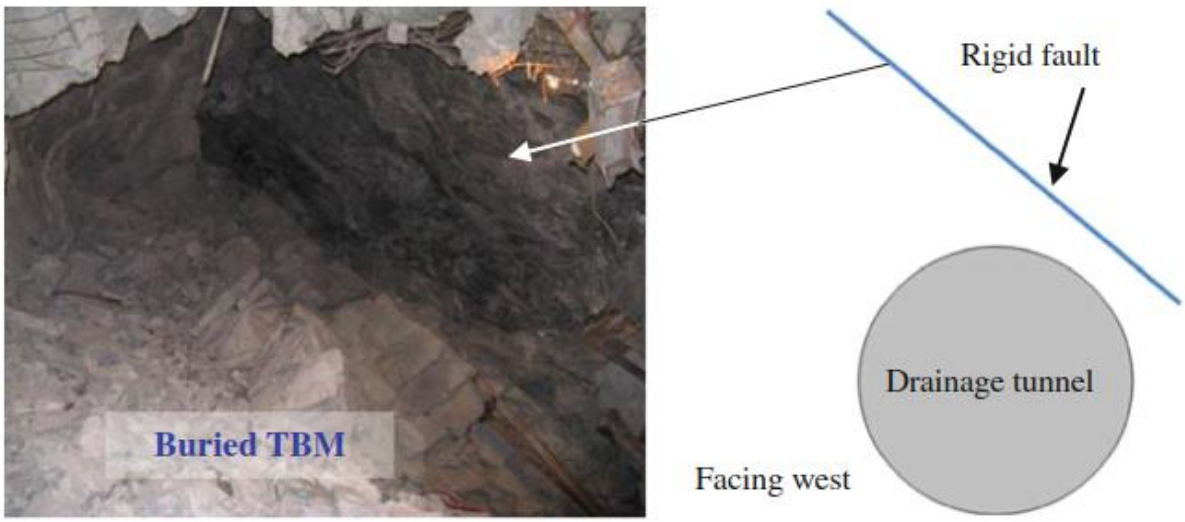

Figure 8-20 : Picture of buried TBM and fault localization (from Zhang et al. 2012)

Zhang *et al*. (2013) used the CWFS method and the LERR approach to estimate the released energy between the peak and the residual state of the rock around the tunnel. Manouchehrian (2016) simulated this rockburst using Abacus, a CWFS approach (residual parameters different from Zhou *et al.* 2013) and heterogeneous rock mass properties. Each property is defined with a probability density (coefficient of variation of 15% for the Young's modulus and the cohesion, and 5% for the friction angle). The authors were able to obtain a failure zone close to the one observed during the rockburst. McDonald (2019) used an elastic model to study the effect of the discontinuity properties on the rock mass stiffness by following the evolution of the rock mass deformation when a volume of rock is removed from the model. McDonald (2019) did not perform a direct calculation of the rock mass stiffness.

No information was found on the laboratory properties of T_{2b} marble. The authors (Zhang *et al.* 2012, 2013; Manouchehrian 2016) only refer to the rock mass properties directly, expressed as elastic and Mohr-Coulomb parameters. Table 8-3 presents the in-situ stress state. The major principal stress makes an angle of 25° with the vertical axis. The Young's modulus of the rock mass is 18.9 GPa and the Poisson's coefficient is 0.23.

Table 8-3 : In-situ stress state of the 11.28 rockburst (Zhang et al. 2013); z is the vertical stress component; x and y are the horizontal stress components, perpendicular to the tunnel and in the tunnel direction

Stress	σ_x (MPa)	σ_y (MPa)	σ_z (MPa)	τ_{xy} (MPa)	τ_{yz} (MPa)	τ_{xz} (MPa)
Value	-46.4	-51.7	-61.5	-2.37	-0.64	3.45

8.2.3.2 Numerical model

The numerical model used is similar to the one used by McDonald (2019) and Manouchehrian (2016). The discontinuity/fault is assumed to be long compared to the tunnel size (90 m long for Manouchehrian (2016), not specified by McDonald (2019) but it seems relatively long based on the figures available in the study), straight and smooth without infilling (Zhou *et al.* 2015). The distance between the fault and the tunnel boundary is between 1.2 and 1.5m according to the field observations (Zhang *et al.* 2013). Manouchehrian (2016) considered 0.72 m and McDonald (2019) considered around 0.8 m (not directly specified in his study). In order to

remain relevant with the works of Manouchehrian (2016) and McDonald (2019), 0.72m is used in this study. This choice leads to a possible underestimation of the rock mass stiffness, which could be associated with a worst-case scenario.

Zhang *et al.* (2013) did not provide the parameters used to model the fault in their study. Manoucherian (2016) suggested a friction coefficient between 0.4 and 0.8, corresponding to a friction angle between 22° and 39°. McDonald (2019) used three types of discontinuities, a "weak, a "moderate" and a "strong". The friction angles are between 30° and 50°, the dilation angles are between 5° and 20°, the shear stiffnesses are between 5 and 50 GPa/m and the normal stiffness is fixed at 100 GPa/m. The characteristics of the discontinuity considered in this study correspond to a weak discontinuity with a linear elastic perfectly plastic behavior. Several sets of parameters are used as a small-scale sensitivity analysis, as well as a version without discontinuity (attached interface). Table 8-4 presents the different parameter sets.

Table 8-4 : Various situations considered for the interface parameters

Sets	Friction angle	Dilation angle	Shear stiffness	Normal stiffness
Attached	-	-	189 GPa/m	189 GPa/m
1	25°	0°	18.9 GPa/m	18.9 GPa/m
2	40°	0°	18.9 GPa/m	18.9 GPa/m
3	25°	0°	2 GPa/m	2 GPa/m
4	25°	0°	50 GPa/m	50 GPa/m
5	25°	15°	18.9 GPa/m	18.9 GPa/m

Figure 8-21 presents the geometry and the boundary conditions of the model used. The first two steps of the numerical calculations are the initialization steps and the excavation step of the tunnel. Then, similarly to the MineBy model, the notch is removed from the model, initially replaced by forces at each mesh point to ensure the equilibrium, then these forces are progressively reduced to zero.

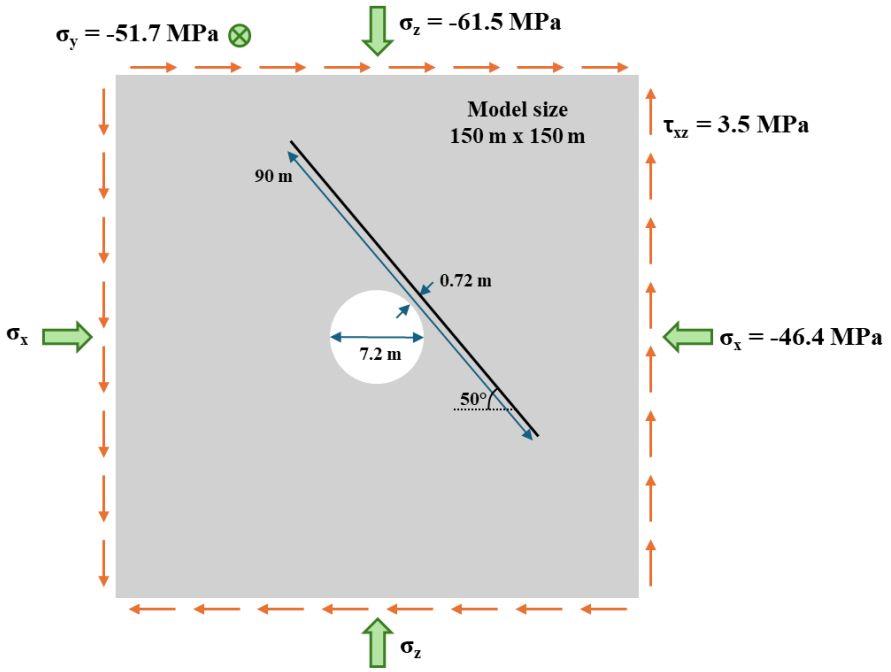

Figure 8-21: Model geometry and boundary conditions for the model of the 11.28 rockburst

The rock mass stiffness is calculated for different notch situations:

1) A “small” notch is removed instantaneously where the stresses are the highest, similar to McDonald (2019) (Figure 8-22 a)).
2) A “large” notch is removed instantaneously similar to the plastic zone obtained by Manouchehrian (2016) and to the field observation (Zhang *et al.* 2012; 2013) (Figure 8-22 b)).
3) The “small” notch is removed before the “large” notch, to introduce some progression in the 11.28 rockburst model.

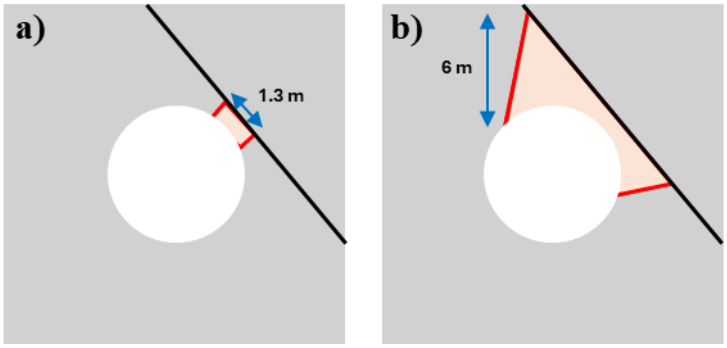

Figure 8-22 : Presentation of the "small" and "large" notch

8.2.3.3 Results

Based on the mathematical formulation of section 8.2.1 for unsymmetrical forces and displacements at the notch boundary, the stiffness of the rock mass is calculated with the $M_{s\text{-}s}$, $k_{f\text{-}d}$ and LSS approaches. Since the geometry of the “large” notch is complex, the $M_{s\text{-}s}$ and $k_{f\text{-}d}$ calculations are also complex. To simplify, it was decided to calculate these stiffnesses based only on the forces and displacements of the points at the notch boundary shown in Figure 8-23 a). Figure 8-23 b) and c) present an example of the forces and displacements at the notch boundary used to calculate the rock mass stiffness. The forces and displacements at the notch boundary are not totally colinear, but as mentioned previously (section 8.2.1.1), only the absolute values are considered for the calculation of the rockmass stiffness ($M_{s\text{-}s}$ and $k_{f\text{-}d}$). It is noteworthy that, based on the geometry and the size of the notch, the analogy with a uniaxial compression test reaches its limit.

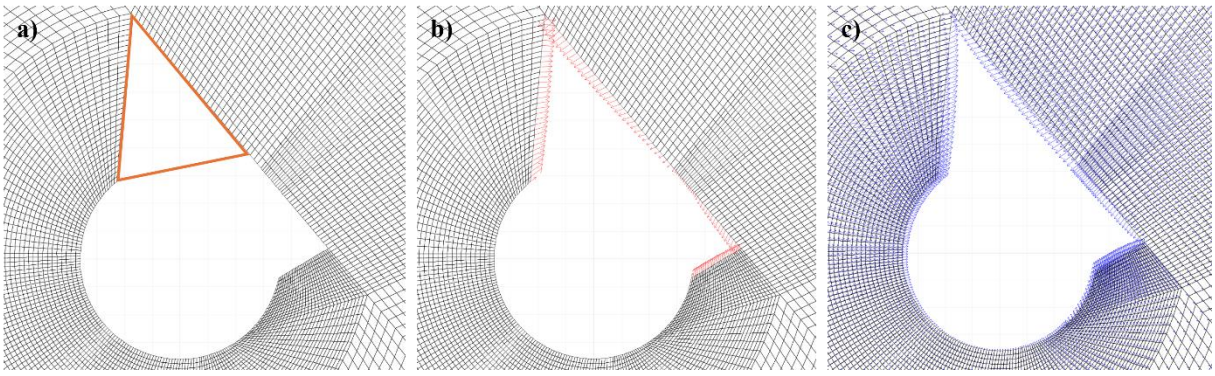

Figure 8-23 : Mesh of the numerical model when the "large" notch is removed; a) is the notch considered for the stiffness calculation of $M_{s\text{-}s}$ and $k_{f\text{-}d}$; b) and c) are the forces and displacements at the notch boundary for the sets of fault properties number 5 and an instantaneous removal of the “large” notch

The stiffness calculations were performed for the six sets of parameters used for the discontinuity (presented in Table 8-4) and for the three notch situations (described in section 8.2.3.2). Table 8-5 summarizes the values of M_{s-s}, k_{f-d} and LSS obtained:

Table 8-5 : Results of the stiffness calculation of the 11.28 rockburst case study

Sets	"Small" notch			"Large" notch			"Small" then "large"		
	M_{s-s} GPa	k_{f-d} GN/m/m	LSS GPa	M_{s-s} GPa	k_{f-d} GN/m/m	LSS GPa	M_{s-s} GPa	k_{f-d} GN/m/m	LSS GPa
Attached	6.80	8.20	1.92	1.96	14.83	2.66	1.91	14.66	2.62
1	2.73	3.29	0.76	1.76	13.95	2.62	1.62	13.37	1.07
2	4.04	4.86	1.09	1.76	13.82	2.50	1.69	13.63	1.30
3	2.74	3.29	0.76	1.33	11.11	2.24	1.25	10.71	0.88
4	2.74	3.29	0.76	1.88	14.43	2.71	1.71	13.92	1.11
5	2.49	2.99	0.75	1.77	13.87	2.63	1.62	13.24	1.07

The following conclusions can be drawn from the results presented in Table 8-5:

- *Impact of a discontinuity:* The introduction of a discontinuity (comparison of the "Attached" and "1" sets) leads to a decrease in the stiffness of the rock mass. For a "small" notch, the stiffness is reduced by a factor 2.5, regardless of the calculation method. For a "large" notch the decrease is much smaller and depends on the calculation method. M_{s-s} gives the largest decrease, while the LSS remains almost identical. The succession of the "small" notch followed by the "large" notch leads to similar rock mass stiffnesses as the "large" notch directly, except for the LSS with a discontinuity. The introduction of an intermediate state (the "small" notch) leads to a LSS value of 1.07 GPa, while without discontinuity, the LSS value is 2.62 GPa. This variation can be explained by the evolution of the mean stress inside the notch and the energy released by the rock mass, the two parameters needed to calculate the LSS (Eq.(8-15)). The energy released by the rock mass are relatively similar in the two situations (942 kJ for "large" notch, 701 kJ for "small" then "large"), while the mean stress in the notch volume is almost twice smaller for the "small" then "large" situation (52.2 MPa for "large" notch, 29.3 MPa for "small" then "large"). Removing the "small" notch before the "large" notch results in displacements along the discontinuity and to a reduction of the stresses in the vicinity of the notch, as presented in Figure 8-24 and Figure 8-25.
- *Stiffness calculation methods:* In this case study, regardless of the sets of parameters considered and the size of the notch, the stiffness obtained with the LSS is always the lowest, and the stiffness obtained with the k_{f-d} is always the highest. The tendencies are similar, when a discontinuity parameter leads to an increase or a decrease of one stiffness value, the other two have the same evolution.
- *Discontinuity properties:* The impact of the discontinuity parameters on the stiffness value is dependent on the size of the notch. For example, an increase in the friction angle (comparison of sets "1" and "2") leads to an increase of the rock mass stiffness for a "small" notch while having no effect on the "large" notch, and a small effect on the "small" then "large" evolution. The plastic properties of the discontinuity (friction angle, dilation angle, cohesion if considered) modify the rock mass stiffness for a "small" notch, while the elastic properties (normal and shear stiffness) modify the stiffness for a "large" notch. These conclusions are not surprising because, for the "small" notch, the shear forces are sufficient to reach the plastic state of the discontinuity, large shear displacements occur (Figure 8-26) and the amount of forces transmittable through the discontinuity depends on these plastic parameters. On the

other hand, for the “large” notch, the shear forces are not sufficient to reach the plastic state, the amount of forces that can be transmitted through the discontinuity depends on the elastic parameters, and the shear displacement are limited (Figure 8-27).

- *Progressive notch removal:* Progressive removal of the “small” notch then the “large” notch has a limited impact on the rock mass stiffness calculated with $M_{s\text{-}s}$ and $k_{f\text{-}d}$. On the other hand, the impact on the stiffness calculated with LSS is massive. The stiffness is reduced by more than a factor 2. Another calculation has been performed with two intermediate notches (the “small” notch and an “intermediate” notch before removing the “large” notch) with the set “1” of discontinuity parameters. The final LSS is slightly slower than that obtained with one intermediate notch (0.99 GPa compared to 1.07 GPa).

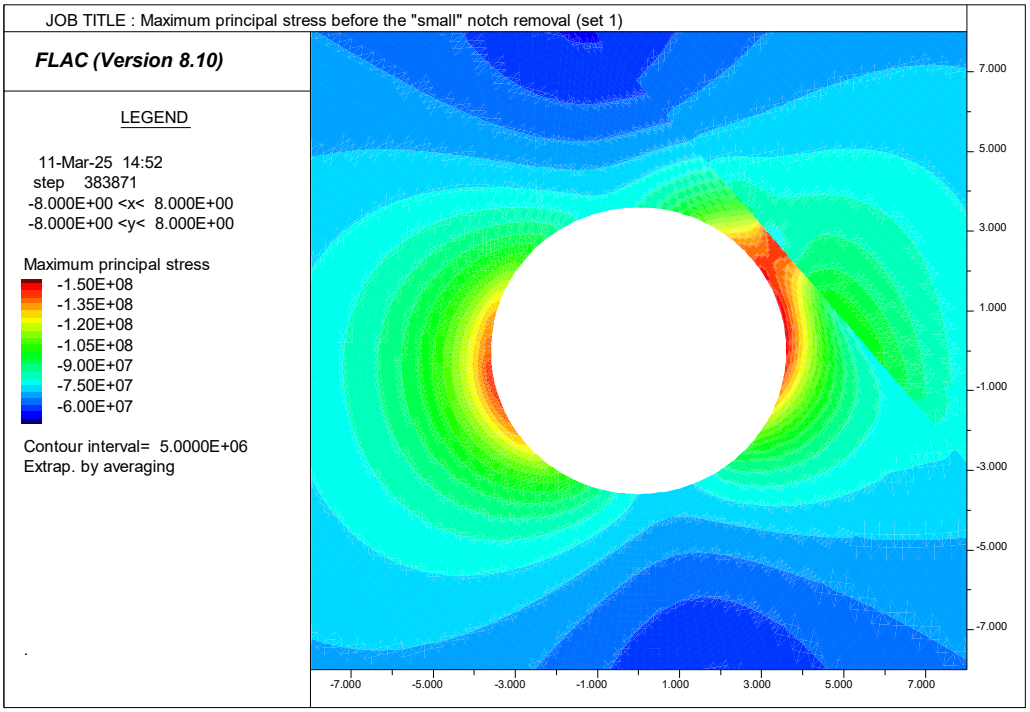

Figure 8-24 : Maximum principal stress before the notch removal; the set “1” of discontinuity parameters is used

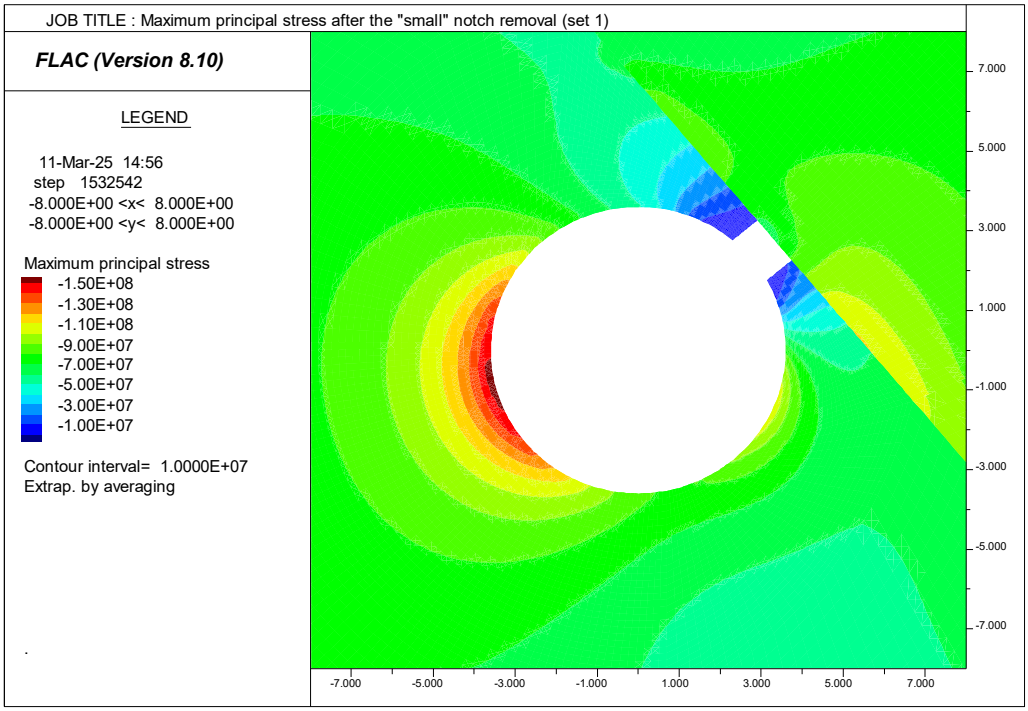

Figure 8-25 : Maximum principal stress after the "small" notch removal; the set "1" of discontinuity parameters is used

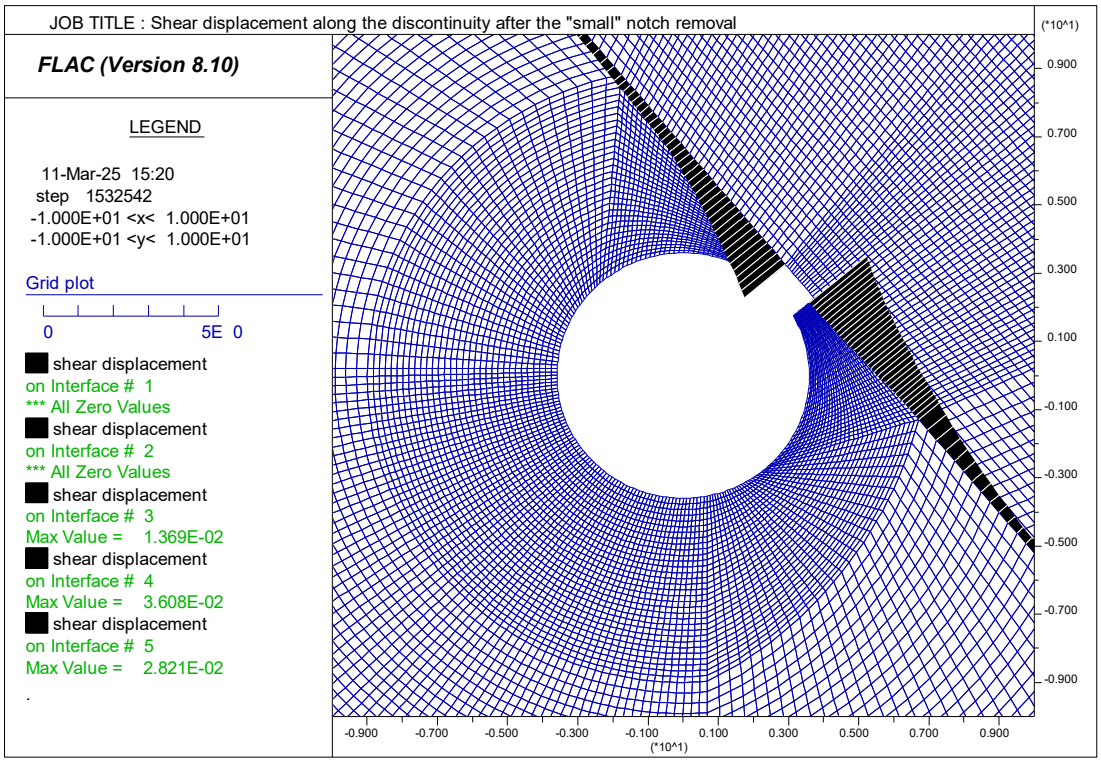

Figure 8-26 : Shear displacement along the discontinuity after the "small" notch removal; the set "1" of discontinuity parameters is used

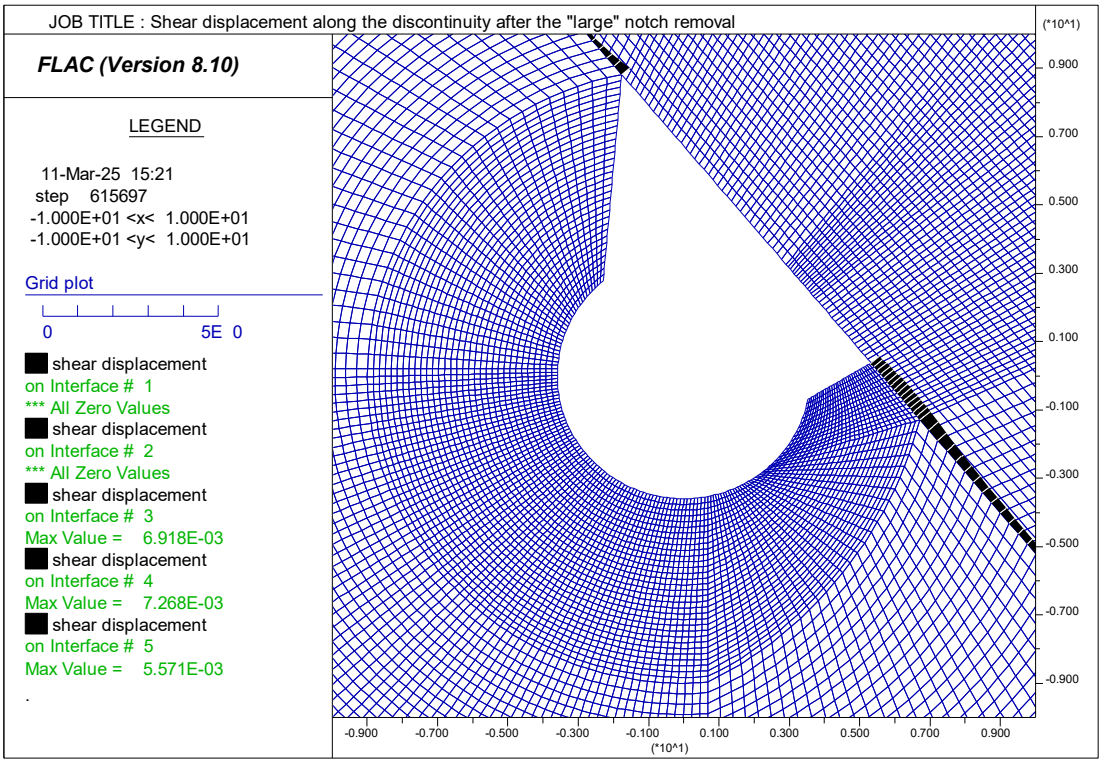

Figure 8-27 : Shear displacement along the discontinuity after the "large" notch removal; the set "1" of discontinuity parameter is used

8.3 Comparison with the post-peak stiffness

Now that approaches for estimating the rock mass stiffness around a notch have been presented and applied to two case studies, the final step in the proposed methodology is to compare these stiffnesses with the post-peak stiffness of the rock mass. When the rock mass stiffness is less than the post-peak stiffness, violent failure should occur. First, this comparison is made on the two case studies, then the discussion is generalized about whether this comparison is relevant or not, and how it can be done properly depending on the methodology used to estimate the rock mass stiffness.

8.3.1 MineBy Tunnel and 11.28 rockburst

No direct information is provided regarding the post-peak stiffness of the granite from the Lac du Bonnet geological formation and the marble from the Baishan formation. Hou and Cai (2022b) estimate the post-peak stiffness of intact granite and marble for an infinitely stiff loading system environment.

The granite tested by Hou and Cai (2022b) had a UCS of 125 MPa which was obtained with a low strain rate (10^{-6} /s). The Lac du Bonnet granite has the UCS estimated at 213 MPa (Martin *et al*. 1997) and a strength around 100 MPa was used in the back analysis (Hajiabdolmajid *et al.* 2002; Diederichs 2007), which could be associated with the long-term strength of the rock. The Young's modulus of Hou and Cai (2022b) is around 50 GPa while the Young's modulus of Lac du Bonnet granite is around 65 MPa (Martin *et al*. 1997). The rock mass around the MineBy tunnel is considered intact and the excavation technique is chosen so not to damage the surrounding rock mass. As a first approximation, the use of the post-peak stiffness obtained by Hou and Cai (2022b) may be relevant.

For the marble of the Baishan formation, using the result from Hou and Cai (2022b) is more delicate because the UCS is around 95 MPa and the Young modulus is around 45 GPa, while for marble of Baishan formation, the strength is 50 MPa and a Young's modulus is 18.9 GPa which are twice smaller but correspond to the rock mass properties, and not the intact rock. In the absence of laboratory tests information, the post-peak stiffness of Hou and Cai (2022b) is used but this may be an overestimation. It can be noted that Wang *et al*. (2024) estimated the post-peak stiffness of the rock based on the numerical simulation of a uniaxial compression test using the CWFS model. In their paper, they said they used the CWFS parameters of Zhang *et al.* (2013), but after comparison, they do not match. The residual cohesion used by Zhang *et al*. (2013) is 7.4 MPa and it is reached at 0.45% of plastic strain, while the one used by Wang *et al*. (2024) is 0.01 MPa and it is reached at 0.1% of plastic strain. Thus, the value obtained by Wang *et al.* (2024) does not seem to be relevant in this study. More importantly, the use of the CWFS model to estimate the post-peak stiffness of rock does not seem to be the most appropriate solution because these parameters are estimated based on back analysis, which highly depend on the hypothesis taken by the engineers and the calculation techniques used (analytical, numerical in 2D, axisymmetric, 3D, etc.). Nevertheless, it raises on fundamental questions that will be discussed later: Is the post-peak stiffness of the intact rock or of the rock mass to be used?

As presented in Section 8.1.3, the post-peak stiffness of a granite rock and a marble rock for an infinitively stiff loading environment are estimated to be 51 GPa and 49 GPa respectively (Hou and Cai 2022b). This value can be directly compared with $M_{s\text{-}s}$ and LSS because they are expressed in the same unit. The comparison with $k_{f\text{-}d}$ is more complex because it is not expressed in GPa but in N/m (general form). Since 2D numerical models are used, the unit of $k_{f\text{-}d}$ is N/m per meter of model, which ultimately leads to a Pascal unit, but does not have the same meaning as $M_{s\text{-}s}$ or LSS. The post-peak stiffness of the rock expressed as a modulus (stresses divided by strains) can be considered as an intrinsic parameter of the rock, it is independent of the size of the rock sample. On the other hand, a post-peak stiffness expressed as a "spring stiffness" (forces divided by displacements) is dependent on the size of the rock sample. Since $k_{f\text{-}d}$ is determined as forces divided by displacements, the post-peak stiffness of the rock must also be adjusted to the size of the notch to be compared, or $k_{f\text{-}d}$ must be transformed into a Pascal parameter. As presented in Figure 8-11, the transformation of $k_{f\text{-}d}$ in $M_{s\text{-}s}$ is possible for simple notch geometries. The relationship is the following:

$$M_{s-s} = \frac{\frac{L}{2}}{t * d} k_{f-d} \qquad (8-23)$$

Where t, d and L are the notch size, the depth, the out of plane size and the length of the notch respectively. For more complex notch geometry (i.e. nonrectangular), this formulation is not valid anymore, as it will be highlighted in section 8.3.1.1. In addition, Appendix 8 presents an analytical comparison of $M_{s\text{-}s}$ and $k_{f\text{-}d}$ on several examples on nonrectangular notch.

It is noteworthy that choosing an adaptation of the post-peak stiffness to the notch size to compare it with $k_{f\text{-}d}$ leads to the same interrogations (the choice of t and L) for more complex notch geometry.

8.3.1.1 MineBy comparison

From the results presented in section 8.2.2.3, it was concluded that the $M_{s\text{-}s}$ depends on the spalling process used in the numerical model. For an instantaneous removal of the entire notch,

the value was 24 GPa. For a progressive removal of the slab, as proposed by Aglawe (1999), the values are between 228 GPa for the first slab and 44 GPa for the last slab (Figure 8-17). For a progressive process of the notch formation, which is more relevant with the field observation, the values are between 52 GPa and 36 GPa (Figure 8-18). From the comparison with the post-peak stiffness (51 GPa), it can be concluded that most of the situations lead to a rock mass stiffness slightly lower than the post-peak stiffness, which means that a violent failure would occur. On the other hand, the rock mass stiffness associated with a progressive slab removal is higher than the post-peak stiffness, corresponding to a quasi-static failure.

The LSS value varies between 8 GPa and 80 GPa depending on the spalling process considered. Only two calculations lead to a LSS value higher than the post-peak stiffness, corresponding to the first two slabs of the process used by Aglawe (1999) (quasi-static failures). This process is not fully consistent with field observations (Martin *et al.* 1997). The use of the LSS leads to the conclusion that almost only violent failure would occur because the rockmass stiffness is almost always smaller than the post-pic stiffness.

As discussed in the previous section, $k_{f\text{-}d}$ cannot be directly compared to the post-peak stiffness. Either $k_{f\text{-}d}$ needs to be transformed into a Pascal parameter, or the post-peak stiffness needs to be transformed to include the size of the notch. For an instantaneous removal of the entire notch (depth of 0.65 m and length of 1.6 m), the Eq.(7-23) gives an equivalent stiffness value for $k_{f\text{-}d}$ (called $M_{f\text{-}d}$) of 58 GPa, which is different from the $M_{s\text{-}s}$ (24 GPa). Figure 8-28 presents a comparison of the $M_{s\text{-}s}$ and the $M_{f\text{-}d}$ (recalculate based on Eq.(8-23)) for the two processes of the notch formation. For the notch formation corresponding to a progressive removal of the slab (Aglawe's approach), $M_{s\text{-}s}$ and $M_{f\text{-}d}$ are very similar, meaning that Eq.(8-23) is relevant in this situation. This result was expected because the slab removed at each step is pseudo-rectangular. In the over hand, the second process (progressive notch evolution) leads $M_{s\text{-}s}$ and $M_{f\text{-}d}$ to be different starting from the step 2. For these steps, the notch geometries are not rectangular (Figure 8-16).

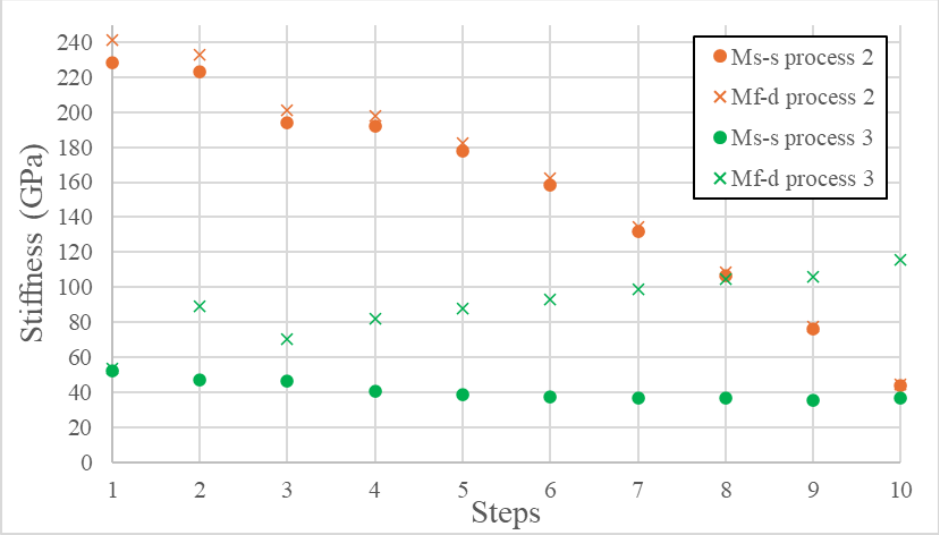

Figure 8-28: Comparison of the $M_{s\text{-}s}$ and $M_{f\text{-}d}$ (obtained with $k_{f\text{-}d}$ and Eq.(8-23)) for the two progressive notch evolutions ; process 2 is one similar to Aglawe (1999), process 3 is one considered as more realistic

As $k_{f\text{-}d}$ cannot be transformed into a Pascal parameter, the post-peak stiffness needs to be adapted to the notch size (i.e. transformed into Newton per meter) to be compared with $k_{f\text{-}d}$. During this transformation, the same interrogation occurs regarding the value to use for the size of the notch when it is not rectangular. The formulation is identical to Eq.(8-23) expects $M_{f\text{-}d}$ is

replaced by $E_{p\text{-}p}$ (post-peak stiffness of the rock expressed in Pascal) and $k_{f\text{-}d}$ by $k_{p\text{-}p}$ (post-peak stiffness of the rock adapted to the notch size expressed in Newton per meter). Figure 8-29 presents a comparison of $k_{f\text{-}d}$ and $k_{p\text{-}p}$ calculated this way. For process 2, the interpretation of the results is identical as $M_{s\text{-}s}$, unlike for process 3. Based on the uncertainty of the calculation of $k_{p\text{-}p}$, it is not possible to draw relevant conclusions from this comparison on process 3.

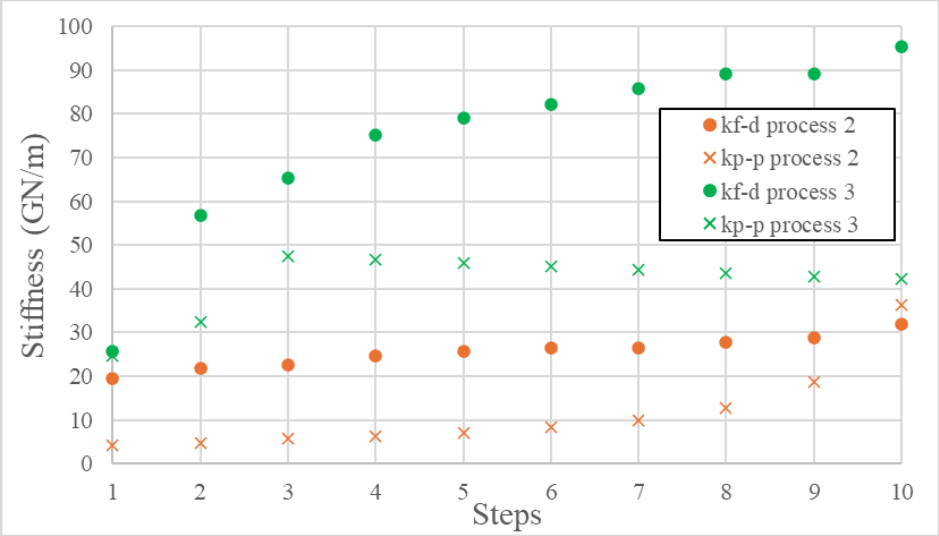

Figure 8-29 : Comparison of the rock mass stiffness ($k_{f\text{-}d}$) and the post-peak stiffness ($k_{p\text{-}p}$) associated with the notch size; "process 2" is the progressive slab removal process; "process 3" is the progressive notch evolution process

During the tunnel construction, both quasi-static and violent failures occurred, mostly small rockburst close to the tunnel face, and buckling failure of spall further away from the face. Regardless of the intensity of the local failure, the notch developed progressively. The comparison of the post-peak stiffness and $M_{s\text{-}s}$ is coherent in this example because the post-peak stiffness and the rock mass stiffnesses are of the same order of magnitude, resulting in either quasi-static or violent failure, depending on the local rock mass stiffness variations. The comparison with LSS leads only to violent failures while the comparison with $k_{f\text{-}d}$ is not possible for nonrectangular notch geometry.

8.3.1.2 11.28 rockburst comparison

For the small notch, Eq.(8-23) leads to $M_{f\text{-}d}$ values identical to $M_{s\text{-}s}$, but for the large notch, $M_{f\text{-}d}$ and $M_{s\text{-}s}$ are not the same, as in AECL case study. Thus, the comparison between the post-peak stiffness and $k_{f\text{-}d}$ is not possible.

No matter which stiffness calculation method is used ($M_{s\text{-}s}$ or LSS), the post-peak stiffness of the rock (49 GPa) is always higher than the stiffness of the rock mass (Table 8-5). Thus, the failure is expected to be violent, as it happened in the reality. Nevertheless, the discontinuity impacts the rock mass stiffness but even without it, violent failures were expected. The shape of the notch is highly dependent on the presence of the discontinuity, as highlighted by Manouchehrian (2016). The discontinuity creates a stress concentration in the rock between the discontinuities and the tunnel boundary (Figure 8-24), which will fail first. Without the discontinuity, the failed area will be a "v-shape" similar to the MineBy tunnel. It can be noted that the post-peak stiffness is probably overestimated, and perhaps without the discontinuity, the failure may be quasi-static and progressive.

8.3.2 Analysis of the comparison and limitations

The comparison of the rock mass stiffness and the post-peak stiffness on the two case studies has proven to be relevant with respect to the field observations. Nevertheless, several important questions remain regarding the method to be used to estimate the rock mass stiffness, the use of the correct process to model the notch evolution or the characterization of the post-peak stiffness for intact rock and the adaptation for moderately jointed rock mass.

Among the three different methods tested to estimate the stiffness of the rock mass, M_{s-s} shows relevant results for both case studies and is easy to compare with the post-peak stiffness of the rock. The results with k_{f-d} are slightly less relevant because it does not highlight possible violent failures that have been observed in the MineBy tunnel and the post-peak stiffness to be compared with the rock mass stiffness depends on the size of the failed area, which complicates the comparison. On the other hand, the conclusions with the LSS were that violent failures occur at the MineBy tunnel, which is also not entirely consistent with the field observations. Nonetheless, a direct comparison of the LSS and the post-peak stiffness obtained by a uniaxial compression test may not be as relevant as originally thought.

As presented in section 8.2.1.2, the LSS can be considered as the post-peak stiffness of a fictious rock with a post-peak behavior identical to the rock mass behavior around the failed area. This parameter is defined by Eq.(8-12) as the mean of the average stress of each fictious rock volume in the model, divided by the volumetric strain of this same fictious rock volume. The LSS is an equivalent stiffness of a multidirectionally loaded rock volume, unlike the post-peak stiffness obtained from a uniaxial compression test, which corresponds to a unidirectional stiffness. The post-peak stiffness to be compared with a LSS should be a stiffness calculated with the Eq.(8-12) for an infinitively stiff loading environment. Hou and Cai (2022b) provided the volumetric strain obtained with various LESS values, but no estimation of the volumetric strain associated with an infinite LESS. For the marble, the post-peak stiffness obtained with the $LESS_4$ (Figure 8-7 a)) is really close to their estimation of the post-peak stiffness with an infinite LESS. The volumetric strain obtained between the peak and the beginning of the residual state is about 2%, and by applying the Eq.(8-12), the post-peak stiffness of the marble comparable with the LSS would be 1.6 GPa, which is quite different from the 49 GPa obtained for an uniaxial compression test. As also pointed out by Hou and Cai (2022b), the LESS has an influence on the failure mechanism of the rock sample and the associated volumetric strain. For the granite, no post-peak stiffnesses obtained are close to those associated with an infinite LESS (Figure 8-7 b)), and so it is impossible to estimate the volumetric strain to be used to calculate the post-peak stiffness to be compared with the LSS.

Another important point is the process of the notch creation. It can be an instantaneous removal of the entire notch, or progressive development of the notch before reaching its final size. The choice associated with whether the notch is entirely removed or progressively formed has a massive impact on the rock mass stiffness. These choices are highly dependent on the results of the first steps of the tested methodology, which aims to identify the probable failed area around the tunnel, but also the evolution process of the failure.

The last major limitation of this approach is to correctly estimate the post-peak stiffness of the rock mass. The available information on the post-peak stiffness of the rock comes from laboratory tests. As discussed above, this value depends on the stiffness of the loading system. Directly at the laboratory scale, other parameters can also modify the post-peak stiffness such as the strain rate used (time dependency of the peak strength), the confinement stress, and the parameters used to control the loading frame (axial strain, lateral strain, acoustic emission, etc.),

etc. For an unfractured rock mass such as the MineBy experiment, as a first approach, it could be reasonable to use directly the value obtained from a uniaxial compression test but, in reality, it will also be influenced by external factors such as the excavation technique, the advance rate, the local heterogeneity, etc. Unfractured rock masses are an exception, most rock masses encountered in deep underground works are massive to moderately jointed and brittle failure can be expected starting from GSI of 65 (Bewick 2021), as for the 11.28 rockburst (no information is provided about the rock mass characterization). In these situations, the strength parameters of the rock mass are adjusted compared to those obtained in the laboratory, so why should the post-peak stiffness not also be adjusted as well? It may seem reasonable to think that the post-peak behavior of the rock mass will be different from the one obtained during laboratory tests. The main question is how to estimate the post-peak behavior of the rock mass. Actually, there is no real answer to this question.

If it was possible to answer this question and to estimate the post-peak stiffness of a rock mass, what would be the implications for the interpretation of the previous results? Some theoretical discussions are proposed below.

As presented in Chapter 2.1.1.3, the post-peak behavior of geomaterials varies from perfectly plastic (soil) to an almost brittle behavior (hard rock) under uniaxial loading conditions. The results of Hou and Cai (2022b) show that the post-peak stiffness of the granite and the marble under infinitely stiff loading conditions is similar to the pre-peak Young's Modulus (in absolute value). For the sake of the discussion, let's assume that this is the case for most brittle rocks (very strong hypothesis). Then, the transition between the intact rock and the rock mass can lead to two situations:

- Situation 1: The transition from the laboratory scale (intact rock) to the engineering scale (rock mass) does not change the relationship between the post-peak stiffness and the Young's modulus, i.e. the post-peak stiffness of the rock mass is equal (in absolute value) to the Young's modulus of the rock mass.
- Situation 2: The transition from the laboratory scale (intact rock) to the engineering scale (rock mass) affects the post-peak stiffness of the rock mass, i.e. the post-peak stiffness of the rock mass is smaller than the Young's modulus of the rock mass. This situation may be more realistic because, for the same rock type, the post-peak behavior of the rock mass evolves from brittle to perfectly plastic as the GSI value decreases (Hoek and Brown 1997).

Let's also assume that for identical stress states and notches, under elastic conditions, the stiffness of the rock mass around the notch depends only on the Young's modulus of the rock mass. This means that, if the Young's modulus of the rock mass is divided by 2, then the rock mass stiffness is also divided by 2. This hypothesis seems to be relevant for some simple tests carried out on numerical models. Figure 8-30 summarizes both situations in a theoretical example. For each situation, two different Young's moduli are considered, one hypothetically leading to a violent failure (rock mass stiffness around the notch smaller than the post-peak stiffness of the rock, red curves) and another one leading to a quasi-static failure (green curves). The evolution of the stiffnesses based on the GSI is derived from the previous hypothesis of each situation and the evolution of the rock mass stiffness around the notch with the Young's modulus. The shape of the evolution is theoretical and inspired by the formulation of Hoek and Diederichs (2006) for the Young's modulus of a rock mass.

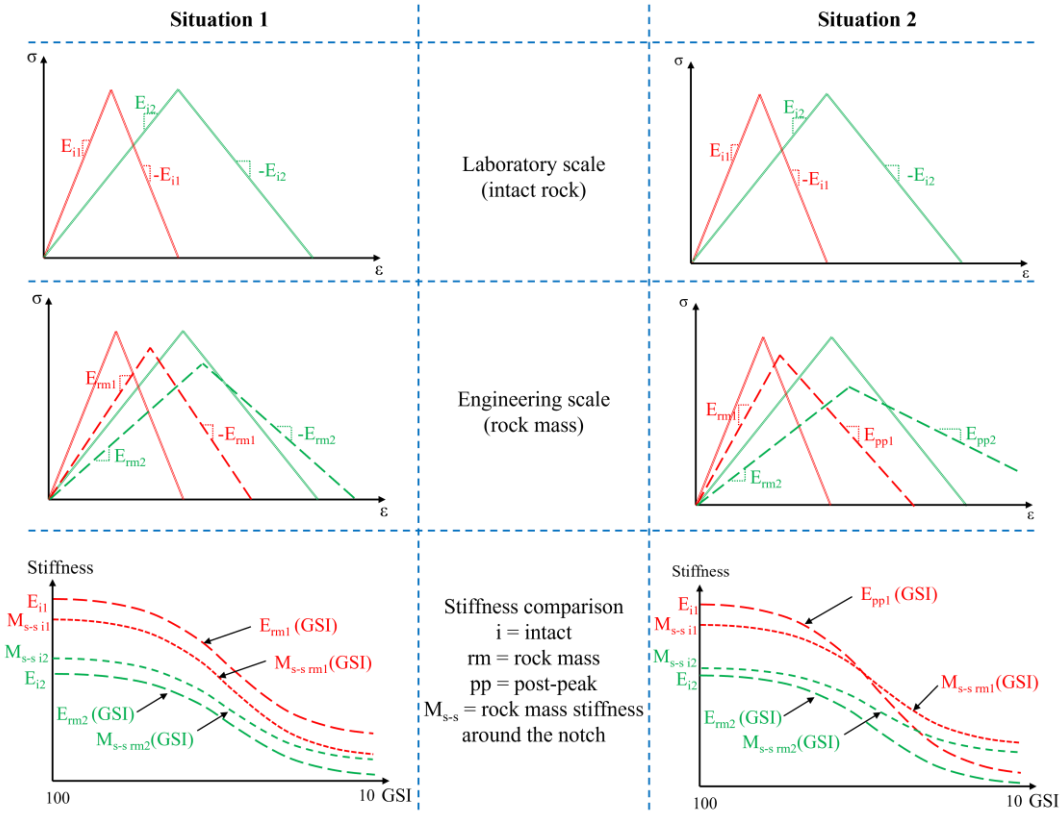

Figure 8-30 : Impact of both situations on a theoretical example at a laboratory scale, engineering scale and comparison of rock mass stiffness and post-peak stiffness depending on the GSI value of the rock mass ; the red curves are associated with a situation in which the rock mass stiffness is smaller than the post-peak stiffness (ie violent failure expected) for intact rock properties ; the green curves are associated with a situation in which the rock mass stiffness is higher than the post-peak stiffness (ie quasi-static failure expected)

From Figure 8-30, the following comments can be made:

- In situation 1, it is assumed that the transition between the intact rock to the rock mass does not impact the post-peak stiffness (always equal to the Young's modulus of the rock mass). In this situation, when a failure is expected to be violent ($M_{s\text{-}s1}$ less than E_{i1}, red curves) or if the failure is expected to be quasi-static ($M_{s\text{-}s2}$ greater than E_{i2}, green curves), the transition at the rock mass scale does not change the expected type of failure. Even if energy plays a role in the intensity of violent failure, this result seems unrealistic for moderately to highly fractured rock mass (relatively low GSI).
- In situation 2, it is assumed that the transition from the intact rock to the rock mass does affect the post-peak stiffness. The post-peak stiffness of the rock mass becomes smaller than the Young's modulus of the rock mass. If the expected failure is violent, the transition at the rock mass scale can transform it into a quasi-static failure when the GSI becomes smaller (the $M_{s\text{-}s\ rm1}(GSI)$ curve crosses and goes over the $E_{pp1}(GSI)$ curve). On the other hand, if the failure is already expected to be quasi-static for the intact rock, the transition to the rock mass scale will only increase the gap between the stiffness of the rock mass around the notch and the post-peak stiffness of the rock mass.

This theoretical example shows the importance of the hypothesis regarding the post-peak behavior of the rock mass. The consideration of the post-peak behavior of the intact rock leads to an overestimation of the risk of brittle violent failure, which is mitigated by the presence of damage in the rock mass (associated with the excavation technics, joints family, etc.). It can also be noted that the introduction of rock mass characteristics leads generally to a decrease in

the rock mass strength and Young's modulus. The shape of the failed area also depends on this modification and will impact the stiffness of the rock mass, as well as the ability of the rock mass to store elastic energy.

8.4 Conclusions

Attempting to use the stiffness theory to determine whether a brittle failure around a tunnel will be quasi-static or violent is more complex than originally anticipated. In this chapter, a methodology has been proposed and tested to rigorously estimate the rock mass stiffness and to compare it with the post-peak stiffness of the rock. This methodology has been applied to two case studies, the MineBy tunnel of the AECL and the 11.28 rockburst of the Jingping II Hydropower project. For these case studies, the rock mass stiffness has been estimated using three different calculation techniques and different failure processes and notch developments. Then this was compared with an estimation of the post-peak stiffness of the rock in each case study. Both the calculation technique and the failure process have proven to influence the rock mass stiffness obtained, as well as the presence of discontinuities near the tunnel. The comparison with the post-peak stiffness is more complex than expected because it has to be adapted to the mathematical expression used to characterize the rock mass stiffness. Since the proposed method is relatively simple, relevant results have been obtained on the two case studies, but important questions remain regarding the applicability of the comparison of a post-peak stiffness with a rock mass stiffness.

Chapter 9 - Conclusions and perspectives

The objective of this PhD thesis entitled “Preliminary Design of Deep Tunnel in Continuous Rock Mass by Combining Numerical and Probabilistic Approaches” was to develop tools and methods useful for engineers during early design stages of deep tunnels to better assess the risk of geological and geotechnical hazards, depending on the existing uncertainties. Two phenomena have been considered: large radial deformations (often referred to as squeezing) in highly fractured rock masses and brittle failures (quasi-static failures such as spalling and dynamic failures such as rockburst) in intact and brittle rock masses. A special focus was made on the introduction and propagation of the geological and geotechnical uncertainties to explicitly consider their potential impacts on these phenomena. The two phenomena have been studied separately.

For the part of the work focusing on the large radial deformation, the idea was to improve or to create new tools to be used during preliminary design allowing to quantify the potential of large radial deformations and to provide information about the interaction between the support behavior and the rock mass behavior, while considering directly the geological and geotechnical uncertainties.

The quantification of the risk of large radial deformation has been performed through the improvement of the Hoek and Marinos curve, using a Monte Carlo simulation performed on a 2D plane strain numerical model. The initial curve has been replaced by a set of several curves developed on a larger range of input parameter values, and the variability of the Young’s modulus of the intact rock has been included. The major advantage of the improvement is the modification of the x-axis expression. The initial version (Hoek and Marinos 2000) was based on the rock mass strength, which is a very comprehensive parameter but very hard to obtain in practice and tainted with large uncertainties. The improved version is based only on parameters coming from laboratory tests or field investigations. The introduction and propagation of uncertainties can be done with Monte Carlo simulations, but to make it even easier to use, a method (called the “3 points method”) has been proposed for the uncertainty propagation, based on couple of hypotheses. Then, the quantification of the risk can be done by estimating the probability of being in each class of risk proposed by Hoek and Marinos (2000), depending on the geological and geotechnical uncertainties.

The study of the interaction between the support and the rock mass behavior is performed using 2D axisymmetric numerical calculations. These numerical calculations have been used to create surrogate models allowing the estimation of the ground pressure on the support far from the face, the radial strain between the face and the support installation and the radial strain at the face. The combination of the various surrogate models developed (with and without support) creates a framework allowing to easily study the rock mass behavior and its interaction with the support, based only on simple input parameters: the strength of the intact rock, the m_i parameter of Hoek and Brown, the modulus ratio, the geological strength index, the in-situ stress state, the support stiffness, and the span (the distance between the face and the support). To enhance the use of these models, graphical representations have been created. These surrogate models also allow an easy introduction and propagation of uncertainties through Monte Carlo simulations.

One of the advantages of these surrogate models is to allow reliability calculations based on failure probabilities and an explicit consideration of the uncertainties. It enables discussions

about the relationship between safety factors and failure probabilities, depending on the amount of uncertainties on the input parameters. In the thesis, this comparison has been made for three design hypotheses, leading to very interesting results. A perspective of the work performed in this thesis would be to generalize this comparison to develop a more precis relationship between the safety factors, the failure probabilities and the variability of the input parameters. The final idea could be to introduce safety factors to use during the design based on the uncertainties on the input parameters, while respecting targeted values of failure probability.

Finally, these developed tools have been applied to the famous case study of the Yacambu-Quibor tunnel in Venezuela to validate the relevance of the approach compared to other design methods. As the validation has been done only on one case study (i.e. two tunnel sections of the same project), another perspective would be to validate the result of the surrogate models on other case studies when enough relevant data is available.

For the part of the work on brittle failures, the main focus was about the risk assessment of brittle failures during early design stages of a tunnel project subjected to large uncertainties, and in particular whether the brittle failure is going to be quasi-static or violent. An existing analytical method for early risk assessment, proposed by Diederichs (2018), has been improved to allow the introduction and propagation of uncertainties. This method has been applied to the case study of the deepest section of the Mont Cenis Base Tunnel providing a more relevant assessment of the risk of rockburst. For each tunnel section (every 100 m), a Monte Carlo simulation has been performed to quantify the risk of brittle failure by calculating the probability of being in each class of risk provided by Diederichs (2018), depending on the existing geological and geotechnical uncertainties. This new method proved to be quite relevant to assess the risk of rockburst based on the existing uncertainties and led to the identification of two areas with high probabilities of the maximum possible event of brittle failure to be classified as “moderate rockburst”. The results obtained with this method are also relevant compared to the field observations from the excavation of La Maddalena exploratory tunnel. Nevertheless, some suspicion remained on the reliability of the data used to quantify the uncertainties of the input parameters, which could impact the risk quantification and the results. The next step would be to compare this risk analysis with the event effectively observed during the upcoming construction of the tunnel, and to update the study when new input data will be available.

One key element, on whether the brittle failure is going to be quasi-static or violent, is the stiffness of the rock mass around the potential failed area. To discuss this specific point, a complementary study has been performed about the calculation of this stiffness using simple 2D elastic numerical calculation. In this study, a method is proposed, based on the literature, to determine whether the brittle failure is going to be quasi-static or violent, and then has been applied to two typical case studies of brittle failures: the Mine-By tunnel of the AECL in Canada and the 11.28 rockburst at Jinping II Hydropower project in China. For these case studies, the rock mass stiffness has been estimated using several calculation techniques, different failure processes and notch developments. Then these stiffnesses have been compared with an estimation of the post-peak stiffness of the rock for each case study. The comparison with the post-peak stiffness is more complex than initially expected because it has to be adapted to the mathematical expression used to characterize the rock mass stiffness. Since the proposed method is relatively simple, relevant results have been obtained on the two case studies, but important questions remain regarding the applicability of this comparison of a post-peak stiffness with a rock mass stiffness. The main perspective here would be to be able to properly characterize the post-peak stiffness of the rock mass. If it is possible to clarify this issue, then the method could be more relevant and easier to apply.

References

AFTES, 1993, GT7R1A2: Choice of tunnel support

AFTES, 2001, GT7R6A1: The convergence-confinement method

AFTES, 2007, GT29R2F1 : Compatibilité des recommandations AFTES relatives aux revêtements des tunnels en béton avec les Eurocodes

AFTES, 2021, GT30R1A1: Radial rock bolting in tunnels: Design and sizing guide

Aglawe, J.P., 1999. Unstable and Violent Failure around Underground Openings In Highly Stressed Ground. Queen's University at Kingston, Kingston, Ontario.

Ahmad, M., Katman, H.Y., Al-Mansob, R.A., Ahmad, F., Safdar, M., Alguno, A.C., 2022. Prediction of Rockburst Intensity Grade in Deep Underground Excavation Using Adaptive Boosting Classifier. Complexity 2022, 6156210. https://doi.org/10.1155/2022/6156210

Aladejare, A.E., Wang, Y., 2019. Probabilistic Characterization of Hoek–Brown Constant mi of Rock Using Hoek's Guideline Chart, Regression Model and Uniaxial Compression Test. Geotech Geol Eng 37, 5045–5060. https://doi.org/10.1007/s10706-019-00961-7

Aladejare, A.E., Wang, Y., 2017. Evaluation of rock property variability. Georisk: Assessment and Management of Risk for Engineered Systems and Geohazards 11, 22–41. https://doi.org/10.1080/17499518.2016.1207784

Alejano, L.R., Alonso, E., 2005. Considerations of the dilatancy angle in rocks and rock masses. International Journal of Rock Mechanics and Mining Sciences 42, 481–507. https://doi.org/10.1016/j.ijrmms.2005.01.003

Alejano, L.R., Alonso, E., Rodríguez-Dono, A., Fernández-Manín, G., 2010. Application of the convergence-confinement method to tunnels in rock masses exhibiting Hoek–Brown strain-softening behaviour. International Journal of Rock Mechanics and Mining Sciences 47, 150–160. https://doi.org/10.1016/j.ijrmms.2009.07.008

Alejano, L.R., Rodríguez-Dono, A., Veiga, M., 2012. Plastic radii and longitudinal deformation profiles of tunnels excavated in strain-softening rock masses. Tunnelling and Underground Space Technology 30, 169–182. https://doi.org/10.1016/j.tust.2012.02.017

Alidaryan, M., Khosravi, M.H., Bahaaddini, M., Moosavi, M., Roshan, H., 2023. Mobilization of Cohesion and Friction Angle of Intact Rocks in the Shearing Process. Rock Mech Rock Eng 56, 8221–8233. https://doi.org/10.1007/s00603-023-03484-z

ALLTI, 2018a. Profil en long géotechnique/géomécanique avec application des profils types et risques géologiques (Cahier de plan No. 105- C18007OO30GZGPLGE0052A).

ALLTI, 2018b. Mémoire de Synthese Geotechnique et Geomecanique (Cahier B - Partie 2 No. 105-C18007OO91BZGREGE27510).

Amann, F., Wild, K.M., Loew, S., Yong, S., Thoeny, R., Frank, E., 2017. Geomechanical behaviour of Opalinus Clay at multiple scales: results from Mont Terri rock laboratory (Switzerland). Swiss J Geosci 110, 151–171. https://doi.org/10.1007/s00015-016-0245-0

Armand, G., Leveau, F., Nussbaum, C., De La Vaissiere, R., Noiret, A., Jaeggi, D., Landrein, P., Righini, C., 2014. Geometry and Properties of the Excavation-Induced Fractures at the Meuse/Haute-Marne URL Drifts. Rock Mech Rock Eng 47, 21–41. https://doi.org/10.1007/s00603-012-0339-6

Armetti, G., Migliazza, M.R., Ferrari, F., Berti, A., Padovese, P., 2018. Geological and mechanical rock mass conditions for TBM performance prediction. The case of "La Maddalena" exploratory tunnel, Chiomonte (Italy). Tunnelling and Underground Space Technology 77, 115–126. https://doi.org/10.1016/j.tust.2018.02.012

Arora, K., Gutierrez, M., 2021. Viscous-elastic-plastic response of tunnels in squeezing ground conditions: Analytical modeling and experimental validation. International Journal of Rock Mechanics and Mining Sciences 146, 104888. https://doi.org/10.1016/j.ijrmms.2021.104888

Arora, K., Gutierrez, M., Hedayat, A., Xia, C., 2021. Tunnels in squeezing clay-rich rocks. Underground Space 6, 432–445.
Askaripour, M., Saeidi, A., Rouleau, A., Mercier-Langevin, P., 2022a. Rockburst in underground excavations: A review of mechanism, classification, and prediction methods. Underground Space 7, 577–607. https://doi.org/10.1016/j.undsp.2021.11.008
Askaripour, M., Saeidi, A., Rouleau, A., Mercier-Langevin, P., 2022b. Rockburst in underground excavations: A review of mechanism, classification, and prediction methods. Underground Space 7, 577–607. https://doi.org/10.1016/j.undsp.2021.11.008
Askaripour, M., Saeidi, A., Rouleau, A., Mercier-Langevin, P., 2022c. Rockburst in underground excavations: A review of mechanism, classification, and prediction methods. Underground Space 7, 577–607. https://doi.org/10.1016/j.undsp.2021.11.008
Aubertin, M., Gill, D., E., Simon, R., 1994. On the use of the brittleness index modified (BIM) to estimate the post-peak behavior or rocks. Presented at the First North American Rock Mech. Symposium, Balkema, pp. 945–952.
Aydan, Ö., Akagi, T., Kawamoto, T., 1996. The Squeezing Potential of Rocks Around Tunnels ; Théory and Prediction with Examples Taken from Japan. Rock Mech. Rock Engng. 29, 125–43.
Barla, G., 2001. Tunnelling under squeezing conditions. Presented at the International Conference on Rock Engineering Techniques for Site Charactersation, Bangalore, India.
Barla, G., 1996. Squeezing rocks in tunnels. ISRM news Journal 44–49.
Barla, G., Barla, M., 2009. Innovative tunneling construction methods in squeezing rocks. Presented at the Proceedings of Tunnelbau in druckhaftem gebirge Kolloquium, Zurich, Switzerland.
Barton, N., Choubey, V., 1977. The shear strength of rock joints in theory and practice. Rock Mech. 1977;10:1–54. Rock Mech 1–54.
Barton, N., Lien, R., Lunde, J., 1974. Engineering classification of rock masses for the design of tunnel support. Rock Mech. 6, 189–236.
Barton, N., Shen, B., 2018. Extension Strain and Rock Strength Limits for Deep Tunnels, Cliffs, Mountain Walls and the Highest Mountains. Rock Mech Rock Eng 51, 3945–3962. https://doi.org/10.1007/s00603-018-1558-2
Barton, N.R., 2015. Forty Years with the Q-system – Lessons and Developments.
Barton, N.R., Lien, R., Lunde, J., 1974. Engineering classification of rock masses for the design of tunnel support. Rock Mech. 6, 189–239.
Basnet, P.M.S., Mahtab, S., Jin, A., 2023. A comprehensive review of intelligent machine learning based predicting methods in long-term and short-term rock burst prediction. Tunnelling and Underground Space Technology 142, 105434. https://doi.org/10.1016/j.tust.2023.105434
Bastidas-Arteaga, E., Soubra, A.H., 2014. Reliability Analysis Methods. Presented at the ALERT Doctoral School 2014 Stochastic Analysis and Inverse Modelling.
Bernaud, D., Benamar, I., Rousset, G., 1994. La “nouvelle méthode implicite” pour le calcul des tunnels dans les milieux élastoplastiques et viscoplastiques. Rev. Franç. Géotech.
Bernaud, D., Rousset, G., 1992. La “nouvelle méthode implicite” pour l’étude du dimensionnement des tunnels. Rev. Franç. Géotech. 60, 5–26.
Bésuelle, P., Desrues, J., Raynaud, S., 2000. Experimental characterisation of the localisation phenomenon inside a Vosges sandstone in a triaxial cell. International Journal of Rock Mechanics and Mining Sciences 37, 1223–1237. https://doi.org/10.1016/s1365-1609(00)00057-5
Bewick, R. P., 2021. The Strength of Massive to Moderately Jointed Rock and its Application to Cave Mining. Rock Mech Rock Eng 54, 3629–3661. https://doi.org/10.1007/s00603-021-02466-3
Bewick, R.P., 2013. Shear Rupture of Massive Brittle Rock under Constant Normal Stress and Stiffness Boundary Conditions. University of Toronto.

Bewick, R.P., Kaiser, P.K., 2014. Discussion on "An Empirical Failure Criterion for Intact Rocks" by Peng et al. (2013). Rock Mech Rock Eng 47, 817–823. https://doi.org/10.1007/s00603-013-0514-4

Bewick, R.P., Kaiser, P.K., Amann, F., 2019. Strength of massive to moderately jointed hard rock masses. Journal of Rock Mechanics and Geotechnical Engineering 11, 562–575. https://doi.org/10.1016/j.jrmge.2018.10.003

Bieniawski, Z., Denkhaus, H., Vogler, U., 1969. Failure of fractured rock 323–341.

Bieniawski, Z.T., 1989. Engineering Rock Mass Classifications, Wiley-Interscience. ed. John Wiley & Sons.

Bieniawski, Z.T., 1976. Rock mass classification in rock engineering. Presented at the Exploration for rock engineering, Balkema, Cape Town.

Bieniawski, Z.T., 1973. Engineering Classification of Jointed Rock Masses. Trans. S. Afr. Inst. Civ. Eng. 335–344.

Bozorgzadeh, N., Escobar, M.D., Harrison, J.P., 2018. Comprehensive statistical analysis of intact rock strength for reliability-based design. International Journal of Rock Mechanics and Mining Sciences 106, 374–387. https://doi.org/10.1016/j.ijrmms.2018.03.005

Bozorgzadeh, N., Harrison, J.P., 2019. Reliability-based design in rock engineering: Application of Bayesian regression methods to rock strength data. Journal of Rock Mechanics and Geotechnical Engineering 11, 612–627. https://doi.org/10.1016/j.jrmge.2019.02.002

Bozorgzadeh, N., Harrison, J.P., 2016. Characteristic triaxial strength of intact rock for LSD. Presented at the Proceedings of the Institution of Civil Engineers e Geotechnical Engineering, pp. 291–8.

Bozorgzadeh, N., Yanagimura, Y., Harrison, J.P., 2017. Effect of Small Numbers of Test Results on Accuracy of Hoek–Brown Strength Parameter Estimations: A Statistical Simulation Study. Rock Mech Rock Eng 50, 3293–3305. https://doi.org/10.1007/s00603-017-1352-6

Bozorgzadeh, S., 2018. Contributions in Uncertainty Quantification Towards Reliability-based Rock Engineering Design (PhD Thesis). Department of Civil Engineering University of Toronto, Canada.

Brace, W.F., Paulding, B.W., Scholz, C., 1966. Dilatancy in the fracture of crystalline rocks. J. Geophys. Res. 71, 3939–3953. https://doi.org/10.1029/jz071i016p03939

Brady, B., Brown, E., 1993. Rock Mechanics for underground mining. Springer, Netherlands.

Brown, E.T., 1970. Strength of models of rock with intermittent joints. Journal of the Soil Mechanics and Foundations Division 1935–49.

Cai, M., 2024. Rockburst risk control and mitigation in deep mining. Deep Resources Engineering 1, 100019. https://doi.org/10.1016/j.deepre.2024.100019

Cai, M., 2016a. Prediction and prevention of rockburst in metal mines – A case study of Sanshandao gold mine. Journal of Rock Mechanics and Geotechnical Engineering 8, 204–211. https://doi.org/10.1016/j.jrmge.2015.11.002

Cai, M., 2016b. Prediction and prevention of rockburst in metal mines – A case study of Sanshandao gold mine. Journal of Rock Mechanics and Geotechnical Engineering 8, 204–211. https://doi.org/10.1016/j.jrmge.2015.11.002

Cai, M., 2015. Prediction and prevention of rockburst in metal mines – a case study of Sanshandao gold mine. J. Rock Mech. Geotech. Eng. 1–8.

Cai, M., 2013. Principles of rock support in burst-prone ground. Tunnelling and Underground Space Technology 36, 46–56. https://doi.org/10.1016/j.tust.2013.02.003

Cai, M., Hou, P.Y., Zhang, X.W., Feng, X.T., 2021. Post-peak Stress–Strain curves of brittle hard rocks under axial-strain-controlled loading. International Journal of Rock Mechanics and Mining Sciences 147, 104921. https://doi.org/10.1016/j.ijrmms.2021.104921

Cai, M, Kaiser, P., 2018. Rockburst support reference book–Volume I: rockburst phenomenon and support characteristics. Laurentian University, Sudbury.

Cai, M., Kaiser, P.K., 2022. Selecting the 'Right' Rockbolts for Burst-Prone Drifts. Laurentian University, Sudbury, Ontario, Canada P3E 2C6

Cai, M., Kaiser, P.K., Tasaka, Y., Minami, M., 2007. Determination of residual strength parameters of jointed rock masses using the GSI system. International Journal of Rock Mechanics and Mining Sciences 44, 247–265. https://doi.org/10.1016/j.ijrmms.2006.07.005

Cai, M., Kaiser, P.K., Uno, H., Tasaka, Y., Minami, M., 2004. Estimation of rock mass deformation modulus and strength of jointed hard rock masses using the GSI system. International Journal of Rock Mechanics and Mining Sciences 41, 3–19. https://doi.org/10.1016/S1365-1609(03)00025-X

Cai, W., Dou, L., Si, G., Cao, A., He, J., Liu, S., 2016. A principal component analysis/fuzzy comprehensive evaluation model for coal burst liability assessment. Int J Rock Mech Min Sci 62–9.

Cai, W., Zhu, H., Liang, W., Wang, X., Su, C., Wei, X., 2023. A post-peak dilatancy model for soft rock and its application in deep tunnel excavation. Journal of Rock Mechanics and Geotechnical Engineering 15, 683–701. https://doi.org/10.1016/j.jrmge.2022.05.014

Cantieni, L., Anagnostou, G., 2009a. The interaction between yielding supports and squeezing ground. Tunnelling and Underground Space Technology 24, 309–322. https://doi.org/10.1016/j.tust.2008.10.001

Cantieni, L., Anagnostou, G., 2009b. The Effect of the Stress Path on Squeezing Behavior in Tunneling. Rock Mech Rock Eng 42, 289–318. https://doi.org/10.1007/s00603-008-0018-9

Carranza-Torres, C., 2004. Elasto-plastic solution of tunnel problems using the generalized form of the Hoek-Brown failure criterion. International Journal of Rock Mechanics and Mining Sciences 41, 629–639.

Carranza-Torres, C., Diederichs, M., 2009. Mechanical analysis of circular liners with particular reference to composite supports. For example, liners consisting of shotcrete and steel sets. Tunnelling and Underground Space Technology 24, 506–532. https://doi.org/10.1016/j.tust.2009.02.001

Carranza-Torres, C., Fairhurst, C., 1999a. The elasto-plastic response of underground excavations in rock masses that satisfy the Hoek–Brown failure criterion. International Journal of Rock Mechanics and Mining Sciences 36, 777–809. https://doi.org/10.1016/s0148-9062(99)00047-9

Castro, L A M, Bewick, R.P., Carter, T.G., 2012. An overview of numerical modelling applied to deep mining. Taylor & Francis Group, Chapter 21.

Chen, B.-R., Feng, X.-T., Li, Q.-P., Luo, R.-Z., Li, S., 2015. Rock Burst Intensity Classification Based on the Radiated Energy with Damage Intensity at Jinping II Hydropower Station, China. Rock Mech Rock Eng 48, 289–303. https://doi.org/10.1007/s00603-013-0524-2

Chen, Y., Li, T., Zeng, P., Ma, J., Patelli, E., Edwards, B., 2020. Dynamic and Probabilistic Multi-class Prediction of Tunnel Squeezing Intensity. Rock Mech Rock Eng 53, 3521–3542. https://doi.org/10.1007/s00603-020-02138-8

Cheng, W., Wang, W., Huang, S., Ma, P., 2013. Acoustic emission monitoring of rockbursts during TBM-excavated headrace tunneling at Jinping II hydropower station. Journal of Rock Mechanics and Geotechnical Engineering 5, 486–494. https://doi.org/10.1016/j.jrmge.2011.09.001

Chern, J., Yu, C., Shiao, F., 1998. Tunnelling in squeezing ground and support estimation. Presented at the Proceedings of Regional Symposium on Sedimentary Rock Engineering, Taipei, Taiwan, China, pp. 192–202.

Cho, N., Martin, C.D., Christiansson, R., 2002. Suppressing fracture growth around underground openings., in: Hammah R, Bawden WF, Curran J, Telsnicki M. Presented at the Proceedings of NARMS 2002, University of Toronto Press, Toronto, pp. 1151–58.

Chunsheng, Q., Zhiyou, T., 1998. Possibility of rockburst occurrence in Dongguashan copper deposit. Chinese J. Rock Mech. Eng. 17, 917–921.

Connor Langford, J., Diederichs, M.S., 2015. Quantifying uncertainty in Hoek–Brown intact strength envelopes. International Journal of Rock Mechanics and Mining Sciences 74, 91–102. https://doi.org/10.1016/j.ijrmms.2014.12.008

Connor Langford, J., Diederichs, M.S., 2013. Reliability based approach to tunnel lining design using a modified point estimate method. International Journal of Rock Mechanics and Mining Sciences 60, 263–276. https://doi.org/10.1016/j.ijrmms.2012.12.034

Contreras, L.F., Brown, E.T., Ruest, M., 2018. Bayesian data analysis to quantify the uncertainty of intact rock strength. Journal of Rock Mechanics and Geotechnical Engineering 10, 11–31. https://doi.org/10.1016/j.jrmge.2017.07.008

Cook, N.G.W., 1965. A note on rockbursts considered as a problem of stability. Journal of the South African Institute of Mining and Metallurgy 437–446.

Corbetta, F., Bernaud, D., Nguyen Minh, D., 1991. Contribution à la méthode convergence-confinement par le principe de la similitude. Rev. Fr. Geotech. 5–11. https://doi.org/10.1051/geotech/1991054005

Damjanac, B., Fairhurst, C., 2010. Evidence for a Long-Term Strength Threshold in Crystalline Rock. Rock Mech Rock Eng 43, 513–531. https://doi.org/10.1007/s00603-010-0090-9

De La Fuente, M., Taherzadeh, R., Sulem, J., Nguyen, X.-S., Subrin, D., 2019. Applicability of the Convergence-Confinement Method to Full-Face Excavation of Circular Tunnels with Stiff Support System. Rock Mech Rock Eng 52, 2361–2376. https://doi.org/10.1007/s00603-018-1694-8

De La Fuente Mata, M., 2018. Tunneling under squeezing conditions : Effect of the excavation method (Civil Engineering PhD Thesis). Université Paris-Est, Farnce.

Debernardi, D., 2008. Viscoplastic behaviour and design of tunnels (PhD Thesis). Politecnico di Torino, Department of Structural and Geotechnical Engineering, Italy.

DeGagné, D.O., Corkum, A.G., Lorig, L.J., 2011. Estimation of tunnel squeezing in anisotropic stress fields using a FLAC-based neural network. Presented at the 2nd International FLAC/DEM Symposium, D. Sainsbury, R. Hart, C. Detournay and M. Nelson (eds), Melbourne, Australia, pp. 141–151.

Desrue, J., 1987. Naissance des bandes de cisaillement dans les milieux granulaires : expérience et théorie, Manuel de Rhéologie des Géomatériaux. Presses de l'Ecole Nationale des Ponts et Chaussées.

Di, Y., Wang, E., Huang, T., 2023a. Identification method for microseismic, acoustic emission and electromagnetic radiation interference signals of rock burst based on deep neural networks. International Journal of Rock Mechanics and Mining Sciences 170, 105541. https://doi.org/10.1016/j.ijrmms.2023.105541

Di, Y., Wang, E., Li, Z., Liu, X., Huang, T., Yao, J., 2023b. Comprehensive early warning method of microseismic, acoustic emission, and electromagnetic radiation signals of rock burst based on deep learning. International Journal of Rock Mechanics and Mining Sciences 170, 105519. https://doi.org/10.1016/j.ijrmms.2023.105519

Diederichs, M., Carter, T., Martin, D., 2010. Practical Rock Spall Prediction in Tunnels. Presented at the TAC Conference.

Diederichs M.S., Eberhardt, Fisher B., 2013, Consideration of stress and structural influence on high stress response in deep tunnelling – the Olmos Tunnel, Peru, WTC 2013.in: Underground. The Way to the Future. CRC Press, pp. 1998–2005. https://doi.org/10.1201/b14769-274

Diederichs, M.S., 2018. Early assessment of dynamic rupture hazard for rockburst risk management in deep tunnel projects. J. S. Afr. Inst. Min. Metall. 118, 193–204. https://doi.org/10.17159/2411-9717/2018/v118n3a1

Diederichs, M.S., 2007. The 2003 Canadian Geotechnical Colloquium: Mechanistic interpretation and practical application of damage and spalling prediction criteria for deep tunnelling. Can. Geotech. J. 44, 1082–1116. https://doi.org/10.1139/T07-033

Diederichs, M.S., 1999. Instability of hard rockmasses the role of tensile damage and relaxation (PhD Thesis). University of Waterloo, Waterloo, Ontario, Canada.

Diederichs, M.S., Kaiser, P.K., Eberhardt, E., 2004. Damage initiation and propagation in hard rock during tunnelling and the influence of near-face stress rotation. International Journal of Rock Mechanics and Mining Sciences 41, 785–812. https://doi.org/10.1016/j.ijrmms.2004.02.003

Dong, L., Wesseloo, J., Potvin, Y., Li, X., 2016. Discrimination of Mine Seismic Events and Blasts Using the Fisher Classifier, Naive Bayesian Classifier and Logistic Regression. Rock Mech Rock Eng 49, 183–211. https://doi.org/10.1007/s00603-015-0733-y

Edelbro, C., 2010. Different Approaches for Simulating Brittle Failure in Two Hard Rock Mass Cases: A Parametric Study. Rock Mech Rock Eng 43, 151–165. https://doi.org/10.1007/s00603-008-0025-x

Edelbro, C., 2009. Numerical modelling of observed fallouts in hard rock masses using an instantaneous cohesion-softening friction-hardening model. Tunnelling and Underground Space Technology 24, 398–409. https://doi.org/10.1016/j.tust.2008.11.004

European Commission, Joint Research Centre, van Den Eijnden, B., Knuuti, M., Lesny, K., Löfman, M., Mavritsakis, A., Roubos, A., Schweckendiek, T., Sciarretta, F., Ebener, A., Escher, K., Spross, J., Commend, S., Hehenkamp, M., Arnold, P., Wilhelm, S., Ene, A., Rimoldi, P. and Pereira, R., Reliability-based verification of limit states for geotechnical structures, Schweckendiek, T. editor, Publications Office of the European Union, Luxembourg, 2024, https://doi.org/10.2760/0991189

Fairhurst, C., 1964. On the validity of the "Brazilian" test for brittle materials. International Journal of Rock Mechanics and Mining Sciences 1, 535–46.

Fan, Y., Lu, W., Zhou, Y., Yan, P., Leng, Z., Chen, M., 2016. Influence of tunneling methods on the strainburst characteristics during the excavation of deep rock masses. Engineering Geology 201, 85–95. https://doi.org/10.1016/j.enggeo.2015.12.015

Farhadian, H., 2021. A new empirical chart for rockburst analysis in tunnelling: Tunnel rockburst classification (TRC). International Journal of Mining Science and Technology 31, 603–610. https://doi.org/10.1016/j.ijmst.2021.03.010

Feng, G.-L., Chen, B.-R., Xiao, Y.-X., Jiang, Q., Li, P.-X., Zheng, H., Zhang, W., 2022. Microseismic characteristics of rockburst development in deep TBM tunnels with alternating soft–hard strata and application to rockburst warning: A case study of the Neelum–Jhelum hydropower project. Tunnelling and Underground Space Technology 122, 104398. https://doi.org/10.1016/j.tust.2022.104398

Feng, T., Xie, X.B., Wang, W.X., Pan, C.L., 2000. Brittleness of rocks and brittleness indexes for describing rockburst proneness. Min. Metall. Eng. 20, 18–19.

Feng, X., 2017. Rockburst: mechanisms, monitoring, warning, and miti- gation. Butterworth-Heinemann, Oxford.

Feng, X., Chen, B., Li, S., Zhang, C., Xiao, Y., Feng, G., Zhou, H., Qiu, S., Zhao, Z., Yu, Y., Chen, D., Ming, H., 2012. Studies on the evolution process of rockbursts in deep tunnels. Journal of Rock Mechanics and Geotechnical Engineering 4, 289–295. https://doi.org/10.3724/sp.j.1235.2012.00289

Feng, X., Jimenez, R., 2015. Predicting tunnel squeezing with incomplete data using Bayesian networks. Engineering Geology 195, 214–224. https://doi.org/10.1016/j.enggeo.2015.06.017

Feng, X.-T., Liu, J., Chen, B., Xiao, Y., Feng, G., Zhang, F., 2017. Monitoring, Warning, and Control of Rockburst in Deep Metal Mines. Engineering 3, 538–545. https://doi.org/10.1016/J.ENG.2017.04.013

Feng, Y., Bozorgzadeh, N., Harrison, J.P., 2020. Bayesian analysis for uncertainty quantification of in situ stress data. International Journal of Rock Mechanics and Mining Sciences 134, 104381. https://doi.org/10.1016/j.ijrmms.2020.104381

Fornari, E., Russo, G., Ferrero, L., 2016. La Maddalena exploratory adit for the Turin - Lyon high speed railway base tunnel.

Frenelus, W., Peng, H., Zhang, J., 2022. Creep Behavior of Rocks and Its Application to the Long-Term Stability of Deep Rock Tunnels. Applied Sciences 12, 8451. https://doi.org/10.3390/app12178451

Gao, F., Kang, H., Lou, J., Li, J., Wang, X., 2019. Evolution of Local Mine Stiffness with Mining Process: Insight from Physical and Numerical Modeling. Rock Mech Rock Eng 52, 3947–3958. https://doi.org/10.1007/s00603-019-01798-5

Ghasemi, E., Gholizadeh, H., 2019. Development of Two Empirical Correlations for Tunnel Squeezing Prediction Using Binary Logistic Regression and Linear Discriminant Analysis. Geotech Geol Eng 37, 3435–3446. https://doi.org/10.1007/s10706-018-00758-0

Glazer, S.N., 2016. Mine seismology: data analysis and interpretation, Springer International Publishing. Switzerland.

Goel, R.K., 1994. Correlations for predicting support pressures and closures in tunnels (PhD Thesis). University of Nagpur, India.

Gomes, G.J.C., Forero, J.H., Vargas, E.A., Vrugt, J.A., 2021. Bayesian inference of rock strength anisotropy: Uncertainty analysis of the Hoek–Brown failure criterion. International Journal of Rock Mechanics and Mining Sciences 148, 104952. https://doi.org/10.1016/j.ijrmms.2021.104952

Gong, F., Wang, Y., Wang, Z., Pan, J., Luo, S., 2021. A new criterion of coal burst proneness based on the residual elastic energy index. International Journal of Mining Science and Technology 31, 553–563. https://doi.org/10.1016/j.ijmst.2021.04.001

Gong, F., Yan, J., Li, X., Luo, S., 2019. A peak-strength strain energy storage index for rock burst proneness of rock materials. International Journal of Rock Mechanics and Mining Sciences 117, 76–89. https://doi.org/10.1016/j.ijrmms.2019.03.020

Gong, F.Q., Yan, J.Y., Li, X.B., 2018. A new criterion of rock burst proneness based on the linear energy storage law and the residual elastic energy index. Chin. J. Rock Mech. Eng. 37, 1993–2014.

Griffith, A.A., 1924. Theory of rupture. Presented at the Proceedings of the 1st international congress on applied mechanics, Delft, The Netherlands, pp. 55–63.

Grimstad, E., Barton, N., 1993. Updating of the Q-System for NMT. Presented at the International Symposium on Sprayed Concrete, 22-26 October 1993, Fagernes, pp. 46–66.

Haïed, A., 1995. Etude expérimentale de la rupture en mode de déformations localisé dans un grès. (PhD Thesis). University of Lille I, Lille, France.

Hajiabdolmajid, V., Kaiser, P.K., Martin, C.D., 2002. Modelling brittle failure of rock. International Journal of Rock Mechanics and Mining Sciences 39, 731–741. https://doi.org/10.1016/S1365-1609(02)00051-5

Harrison, J.P., 2014. Eurocode 7 and rock engineering: current problems and future opportunities. Presented at the ISRM Regional Symposium-EUROCK 2014.

Hauquin, T., 2016. La rupture brutale des piliers conditionne-t-elle les effondrements miniers ? PhD Thesis, Université de Lorraine, France.

Hauquin, T., Gunzburger, Y., Deck, O., 2018. Predicting pillar burst by an explicit modelling of kinetic energy. International Journal of Rock Mechanics and Mining Sciences 107, 159–171. https://doi.org/10.1016/j.ijrmms.2018.05.004

He, M., Cheng, T., Qiao, Y., Li, H., 2022. A review of rockburst: Experiments, theories, and simulations. Journal of Rock Mechanics and Geotechnical Engineering 15, 1312–1353. https://doi.org/10.1016/j.jrmge.2022.07.014

He, M., E Sousa, L.R., Miranda, T., Zhu, G., 2015. Rockburst laboratory tests database — Application of data mining techniques. Engineering Geology 185, 116–130. https://doi.org/10.1016/j.enggeo.2014.12.008

Hedley, D.G.F., 1992. Rockburst Handbook for Ontario Hardrock Mines, Energy, Mine and Resources. ed. Ottawa, Canada.
Hemami, B., Fakhimi, A., 2014. Numerical simulation of rock-loading machine interaction. Presented at the 48th US Rock Mechanics/Geomechanics Symposium, OnePetro, San Francisco, California, USA, pp. 111–123.
Hoek, E., 2007. Practical Rock Engineering.
Hoek, E., 1994. Strength of rock and rock masses. ISRM News Journal 2, 4–16.
Hoek, E., 1965. Rock fracture under static stress conditions (CSIR report MEG). Pretoria, South Africa.
Hoek, E., Brown, E.T., 2019. The Hoek–Brown failure criterion and GSI – 2018 edition. Journal of Rock Mechanics and Geotechnical Engineering 11, 445–463. https://doi.org/10.1016/j.jrmge.2018.08.001
Hoek, E., Brown, E.T., 1997. Practical estimates of rock mass strength. Int J Rock Mech Min Sci 34, 1165–86.
Hoek, E., Brown, E.T., 1980a. Underground Excavation in Rock, CRC Press. ed. London, UK.
Hoek, E., Brown, E.T., 1980b. Empirical strength criterion for rock masses. Journal of the Geotechnical Engineering Division 1013–35.
Hoek, E., Carranza-Torres, C., Corkum, B., 2002. Hoek-Brown Failure Criterion - 2002 Edition, in: Mining and Tunnelling Innovation and Opportunity. Presented at the 5th North American rock mechanics symposium and 17th tunnelling association of Canada conference, Hammah R, Bawden W, Curran J, Telesnicki M, editors, Toronto, Canada, pp. 267–73.
Hoek, E., Carter, T.G., Diederichs, M.S., 2013. Quantification of the Geological Strength Index chart. Presented at the 47th US Rock Mechanics / Geomechanics Symposium, ARMA, American Rock Mechanics Association, San Francisco, CA, USA.
Hoek, E., Diederichs, M.S., 2006. Empirical estimation of rock mass modulus. International Journal of Rock Mechanics and Mining Sciences 43, 203–215. https://doi.org/10.1016/j.ijrmms.2005.06.005
Hoek, E., Guevara, R., 2009. Overcoming Squeezing in the Yacambú-Quibor Tunnel, Venezuela. Rock Mech Rock Eng 42, 389–418. https://doi.org/10.1007/s00603-009-0175-5
Hoek, E., Kaiser, P.K., Bawden, W.F., 1995. Support of underground excavations in hard rock. A.A. Balkema, Rotterdam.
Hoek, E., Marinos, P., 2000. Predicting tunnel squeezing problems in weak heterogeneous rock masses. Tunnels and Tunnelling International.
Hoek, E., Marinos, P., Benissi, M., 1998. Applicability of the geological strength index (GSI) classification for weak and sheared rock-masses – the case of the Athens schist formation. Bull. Eng. Geol. Environ. 57, 151–160.
Hoek, E., Marinos, P.G., Marinos, V.P., 2005. Characterisation and engineering properties of tectonically undisturbed but lithologically varied sedimentary rock masses. International Journal of Rock Mechanics and Mining Sciences 42, 277–285. https://doi.org/10.1016/j.ijrmms.2004.09.015
Hoek, E., Martin, C.D., 2014. Fracture initiation and propagation in intact rock – A review. Journal of Rock Mechanics and Geotechnical Engineering 6, 287–300. https://doi.org/10.1016/j.jrmge.2014.06.001
Hosseini, Z., Beruar, B., Sampson-Forsythe, A., Yao, M., 2010. Mining strategies of multisill pillars in burst prone ground conditions at Vale Inco's coleman mine. Presented at the 44th U.S. Rock Mechanics Symposium and 5th U.S.-Canada Rock Mechanics Symposium, Curran Associates, Inc., Red Hook, USA, pp. 1163–1170.
Hou, P.Y., Cai, M., 2023. A Modified Hoek–Brown Model for Determining Plastic-Strain-Dependent Post-peak Strength of Brittle Rock. Rock Mech Rock Eng 56, 2375–2393. https://doi.org/10.1007/s00603-022-03182-2

Hou, P.Y., Cai, M., Zhang, X.W., Feng, X.T., 2022a. Post-peak Stress–Strain Curves of Brittle Rocks Under Axial- and Lateral-Strain-Controlled Loadings. Rock Mech Rock Eng 55, 855–884. https://doi.org/10.1007/s00603-021-02684-9

Hou, P.Y., Cai, M., 2022b. Post-Peak Stress–Strain Curves of Brittle Hard Rocks Under Different Loading Environment System Stiffness. Rock Mech Rock Eng 55, 3837–3857. https://doi.org/10.1007/s00603-022-02839-2

Hu, J., He, M., Li, H., Tao, Z., Liu, D., Cheng, T., Peng, D., 2024. Rockburst Hazard Control Using the Excavation Compensation Method (ECM): A Case Study in the Qinling Water Conveyance Tunnel. Engineering 34, 154–163. https://doi.org/10.1016/j.eng.2023.11.013

Huang, C., El Hami, A., Radi, B., 02/2017a. Overview of Structural Reliability Analysis Methods — Part I : Local Reliability Methods. IncertFia 17. https://doi.org/10.21494/iste.op.2017.0115

Huang, C., El Hami, A., Radi, B., 02/2017b. Overview of Structural Reliability Analysis Methods — Part II : Sampling Methods. IncertFia 17. https://doi.org/10.21494/iste.op.2017.0116

Huang, C., El Hami, A., Radi, B., 02/2017c. Overview of Structural Reliability Analysis Methods — Part III : Global Reliability Methods. IncertFia 17. https://doi.org/10.21494/iste.op.2017.0117

Huang, Z., Liao, M., Zhang, H., Zhang, J., Ma, S., Zhu, Q., 2022. Predicting Tunnel Squeezing Using the SVM-BP Combination Model. Geotech Geol Eng 40, 1387–1405. https://doi.org/10.1007/s10706-021-01970-1

Hudson, J., Crouch, S., Fairhurst, C., 1972. Soft, stiff and servo-controlled testing machines: a review with reference to rock failure 155–189.

Hudson, J., Harrison, J., 2000. Engineering rock mechanics: part 1: an introduction to the principles. Elsevier, Pergamon.

Idris, M.A., Nordlund, E., Saiang, D., 2016. Comparison of Different Probabilistic Methods for Analyzing Stability of Underground Rock Excavations. Electronic Journal of Geotechnical Engineering, (21.21), pp 6555-6585

Jaeger, J., Cook, N.G., Zimmerman, R., 2007. Fundamentals of Rock Mechanics. John Wiley & Sons.

Jain, A., Rao, K.S., 2022. Empirical correlations for prediction of tunnel deformation in squeezing ground condition. Tunnelling and Underground Space Technology 125 https://doi.org/10.1016/j.tust.2022.104501

Jaiswal, A., Shrivastva, B.K., 2012. Stability analysis of the proposed hybrid method of partial extraction for underground coal mining. International Journal of Rock Mechanics and Mining Sciences 52, 103–111. https://doi.org/10.1016/j.ijrmms.2012.03.002

Jethwa, J.L., Singh, B., Singh, B., 1984. Estimation of ultimate rock pressure for tunnel linings under squeezing rock conditions - a new approach, in: Proceedings of Design and Performance of Underground Excavations. Presented at the ISRM Symposium, E.T. Brown and J.A.Hudson eds, Cambridge, UK, pp. 231–238.

Jiang, Q., Feng, X.-T., Xiang, T.-B., Su, G.-S., 2010. Rockburst characteristics and numerical simulation based on a new energy index: a case study of a tunnel at 2,500 m depth. Bull Eng Geol Environ 69, 381–388. https://doi.org/10.1007/s10064-010-0275-1

Jimenez, R., Recio, D., 2011. A linear classifier for probabilistic prediction of squeezing conditions in Himalayan tunnels. Engineering Geology 121, 101–109. https://doi.org/10.1016/j.enggeo.2011.05.006

Kabwe, E., Karakus, M., Chanda, E.K., 2020. Isotropic damage constitutive model for time-dependent behaviour of tunnels in squeezing ground. Computers and Geotechnics 127, 103738. https://doi.org/10.1016/j.compgeo.2020.103738

Kabwe, E., Karakus, M., Chanda, E.K., 2020c. Creep constitutive model considering the overstress theory with an associative viscoplastic flow rule. Computers and Geotechnics 124, 103629. https://doi.org/10.1016/j.compgeo.2020.103629

Kaiser, P., 2014. Deformation-based support selection for tunnels in strainburst-prone ground. Presented at the Seventh International Conference on Deep and High Stress Mining, pp. 227–240. https://doi.org/10.36487/ACG_rep/1410_13_Kaiser

Kaiser, P., Cai, M., 2013. Critical review of design principles for rock support in burst-prone ground – time to rethink!, in: Proceedings of the Seventh International Symposium on Ground Support in Mining and Underground Construction. Presented at the Seventh International Symposium on Ground Support in Mining and Underground Construction, Australian Centre for Geomechanics, Perth, pp. 3–37. https://doi.org/10.36487/acg_rep/1304_01_kaiser

Kaiser, P.K., 2009. Failure mechanisms and rock support aspects, Consultation Report for the Key Technology of Safe and Rapid Construction for Jinping II Hydropower Station High Overburden and Long Tunnels, Jinping II.

Kaiser, P.K., Cai, M., 2012. Design of rock support system under rockburst condition. Journal of Rock Mechanics and Geotechnical Engineering 4, 215–227. https://doi.org/10.3724/sp.j.1235.2012.00215

Kaiser, P.K., Diederichs, M.S., Martin, C.D., Sharp, J., Steiner, W., 2000. Underground Works In Hard Rock Tunneling And Mining.

Kaiser, P.K., Kim, B.-H., 2015. Characterization of Strength of Intact Brittle Rock Considering Confinement-Dependent Failure Processes. Rock Mech Rock Eng 48, 107–119. https://doi.org/10.1007/s00603-014-0545-5

Kaiser, P.K., McCreath, D.R., Tannant, D.D., 1996. Canadian Rockburst Support Handbook, MIRARCO Parter For Innovative Solution. ed, GRC Geomechanics Research Center.

Kaiser, P.K., Moss, A., 2022. Deformation-based support design for highly stressed ground with a focus on rockburst damage mitigation. Journal of Rock Mechanics and Geotechnical Engineering 14, 50–66. https://doi.org/10.1016/j.jrmge.2021.05.007

Kao, C.-S., Carvalho, F.C.S., Labuz, J.F., 2011. Micromechanisms of fracture from acoustic emission. International Journal of Rock Mechanics and Mining Sciences 48, 666–673. https://doi.org/10.1016/j.ijrmms.2011.04.001

Keneti, A., Sainsbury, B.-A., 2020. Development of a comparative index for the assessment of the severity of violent brittle failures around underground excavations. Engineering Geology 270, 105596. https://doi.org/10.1016/j.enggeo.2020.105596

Keneti, A., Sainsbury, B.-A., 2018a. Review of published rockburst events and their contributing factors. Engineering Geology 246, 361–373. https://doi.org/10.1016/j.enggeo.2018.10.005

Khademian, Z., Ozbay, U., 2019. Modeling violent rock failures in tunneling and shaft boring based on energy balance calculations. Tunnelling and Underground Space Technology 90, 62–75. https://doi.org/10.1016/j.tust.2019.04.018

Khademian, Z., Ugur, O., 2018. Computational framework for simulating rock burst in shear and compression. International Journal of Rock Mechanics and Mining Sciences 110, 279–290. https://doi.org/10.1016/j.ijrmms.2018.06.022

Kias, E., Ozbay, U., 2013. Modeling unstable failure of coal pillars in underground mining using the discrete element method. 47th US Rock Mechanics/Geomechanics Symposium.

Kidybiński, A., 1981. Bursting liability indices of coal. International Journal of Rock Mechanics and Mining Sciences & Geomechanics Abstracts 18, 295–304. https://doi.org/10.1016/0148-9062(81)91194-3

Kleine, A., 2007. Modelisation Numerique Du Comportement Des Ouvrages Souterrains Par Une Approche Viscoplastique. Université de Lorraine.

Konicek, P., Schreiber, J., 2018. Heavy rockbursts due to longwall mining near protective pillars: A case study. International Journal of Mining Science and Technology 28, 799–805. https://doi.org/10.1016/j.ijmst.2018.08.010

Kovári, K., 2009. Design Methods With Yielding Support In Squeezing And Swelling Rocks. Presented at the WTC.

Laigle, F., 2004. Modèle Conceptuel pour le Développement de Lois de Comportement adaptées à la Conception des Ouvrages Souterrains. École Centrale de Lyon.
Lee, S.M., Park, B.S., Lee, S.W., 2004. Analysis of rockbursts that have occurred in a waterway tunnel in Korea, 41.
Leveille, P., Sepehri, M., Apel, D.B., 2017. Rockbursting Potential of Kimberlite: A Case Study of Diavik Diamond Mine. Rock Mech Rock Eng 50, 3223–3231. https://doi.org/10.1007/s00603-017-1294-z
Lhoumaud, E., 2023. Seismic and aseismic deformations in deep mines – Case of the Garpenberg mine, Sweden (PhD Thesis). Université de Lorraine, Nancy, France.
Li, N., Jimenez, R., 2018. A logistic regression classifier for long-term probabilistic prediction of rock burst hazard. Nat Hazards 90, 197–215. https://doi.org/10.1007/s11069-017-3044-7
Li, P.-X., Chen, B.-R., Xiao, Y.-X., Feng, G.-L., Zhou, Y.-Y., Zhao, J.-S., 2023. Rockburst and microseismic activity in a lagging tunnel as the spacing between twin TBM excavated tunnels changes: A case from the Neelum-Jhelum hydropower project. Tunnelling and Underground Space Technology 132, 104884. https://doi.org/10.1016/j.tust.2022.104884
Li, S., Kuang, Z., Xiao, Y., Qiao, Z., Yang, W., 2022. Rockburst tendency prediction based on an integrating method of combination weighting and matter-element extension theory: A case study in the Bayu Tunnel of the Sichuan-Tibet Railway. Engineering Geology 308, 106796. https://doi.org/10.1016/j.enggeo.2022.106796
Li, S.L., Feng, X.T., Wang, Y.J., Yang, N.G., 2001. Evaluation of rockburst proneness in a deep hard rock mine. J. Northeast. Univ. 22, 60–63.
Li, T., Cai, M.F., Cai, M., 2007. A review of mining-induced seismicity in China. International Journal of Rock Mechanics and Mining Sciences 44, 1149–1171. https://doi.org/10.1016/j.ijrmms.2007.06.002
Li, T., Ma, C., Zhu, M., Meng, L., Chen, G., 2017. Geomechanical types and mechanical analyses of rockbursts. Engineering Geology 222, 72–83. https://doi.org/10.1016/j.enggeo.2017.03.011
Li, X.B., Zhou, Z.L., Lok, T.S., Hong, L., Yin, T.B., 2008. Innovative testing technique of rock subjected to coupled static and dynamic loads. Int. J. Rock Mech. Min. Sci. 45, 739–748.
Liang, W., Sari, A., Zhao, G., McKinnon, S.D., Wu, H., 2020. Short-term rockburst risk prediction using ensemble learning methods. Nat Hazards 104, 1923–1946. https://doi.org/10.1007/s11069-020-04255-7
Liang, W., Sari, Y.A., Zhao, G., McKinnon, S.D., Wu, H., 2021. Probability Estimates of Short-Term Rockburst Risk with Ensemble Classifiers. Rock Mech Rock Eng 54, 1799–1814. https://doi.org/10.1007/s00603-021-02369-3
Linkov, A.M., 1992. Dynamic Phenomena in Mines and the Problem of Stability, Systems Corporation. ed. Minneapolis, Minnesota, USA.
Liu, F., Ma, T., Tang, C., Chen, F., 2018. Prediction of rockburst in tunnels at the Jinping II hydropower station using microseismic monitoring technique. Tunnelling and Underground Space Technology 81, 480–493. https://doi.org/10.1016/j.tust.2018.08.010
Liu, F., Tang, C., Zhang, Y., Ma, T., 2021. Rockburst and microseismicity characteristics in the Qinling water conveyance tunnel of the Hanjiang-to-Weihe River Diversion Project. International Journal of Rock Mechanics and Mining Sciences 148, 104973. https://doi.org/10.1016/j.ijrmms.2021.104973
Liu, J., Wang, R., Lei, G., Si, Y., Xu, S., Li, Y., 2020b. Studies of stress and displacement distribution and the evolution law during rock failure process based on acoustic emission and microseismic monitoring. International Journal of Rock Mechanics and Mining Sciences 132, 104384. https://doi.org/10.1016/j.ijrmms.2020.104384
Liu, L., Li, H., Li, X., 2022. A state-of-the-art review of mechanical characteristics and cracking processes of pre-cracked rocks under quasi-static compression. Journal of Rock Mechanics and Geotechnical Engineering 14, 2034–2057. https://doi.org/10.1016/j.jrmge.2022.03.013

Liu, M.D., Indraratna, B., 2011. General strength criterion for geomaterials including anisotropic effect. Int. J. Geomech. 11, 251–62.

Liu, Q.-S., Wu, J., Zhang, X.-P., Tang, L.-X., Bi, C., Li, W.-W., Xu, J.-L., 2020a. Microseismic Monitoring to Characterize Structure-Type Rockbursts: A Case Study of a TBM-Excavated Tunnel. Rock Mech Rock Eng 53, 2995–3013. https://doi.org/10.1007/s00603-020-02111-5

Liu, X., Liu, Z., Li, X., Gong, F., Du, K., 2020c. Experimental study on the effect of strain rate on rock acoustic emission characteristics. International Journal of Rock Mechanics and Mining Sciences 133, 104420. https://doi.org/10.1016/j.ijrmms.2020.104420

Loew, S., Barla, G., Diederichs, M., 2010. Engineering Geology of Alpine Tunnels: Past, Present and Future.

Lorig, L., Varona, P., 2013. Guidelines for numerical modelling of rock support for mines, in: Proceedings of the Seventh International Symposium on Ground Support in Mining and Underground Construction. Presented at the Seventh International Symposium on Ground Support in Mining and Underground Construction, Australian Centre for Geomechanics, Perth, pp. 81–105. https://doi.org/10.36487/ACG_rep/1304_04_Lorig

Lu, H., Gutierrez, M., Kim, E., 2022. Empirical approach for reliability evaluation of tunnel excavation stability using the Q rock mass classification system. Underground Space 7, 862–881. https://doi.org/10.1016/j.undsp.2022.01.001

Lü, Q., Sun, H.-Y., Low, B.K., 2011. Reliability analysis of ground–support interaction in circular tunnels using the response surface method. International Journal of Rock Mechanics and Mining Sciences 48, 1329–1343. https://doi.org/10.1016/j.ijrmms.2011.09.020

Lü, Q., Xiao, Z., Zheng, J., Shang, Y., 2018. Probabilistic assessment of tunnel convergence considering spatial variability in rock mass properties using interpolated autocorrelation and response surface method. Geoscience Frontiers 9, 1619–1629. https://doi.org/10.1016/j.gsf.2017.08.007

Lü, Q., Xiao, Z.-P., Ji, J., Zheng, J., 2017. Reliability based design optimization for a rock tunnel support system with multiple failure modes using response surface method. Tunnelling and Underground Space Technology 70, 1–10. https://doi.org/10.1016/j.tust.2017.06.017

Lv, A., Masoumi, H., Walsh, S.D.C., Roshan, H., 2019. Elastic-Softening-Plasticity Around a Borehole: An Analytical and Experimental Study. Rock Mech Rock Eng 52, 1149–1164. https://doi.org/10.1007/s00603-018-1650-7

Ma, K., Xie, H., Ren, F., Chang, Y., 2024. Rockburst early-warning method based on time series prediction of multiple acoustic emission parameters. Tunnelling and Underground Space Technology 153, 106060. https://doi.org/10.1016/j.tust.2024.106060

Ma, T.H., Tang, C.A., Tang, L.X., Zhang, W.D., Wang, L., 2015. Rockburst characteristics and microseismic monitoring of deep-buried tunnels for Jinping II Hydropower Station. Tunnelling and Underground Space Technology 49, 345–368. https://doi.org/10.1016/j.tust.2015.04.016

Majumder, D., Viladkar, M.N., Singh, M., 2017. A multiple-graph technique for preliminary assessment of ground conditions for tunneling. International Journal of Rock Mechanics and Mining Sciences 100, 278–286. https://doi.org/10.1016/j.ijrmms.2017.10.010

Malan, D.F., Vogler, U.W., Drescher, K., 1997. Time-dependent behaviour of hard rock in deep level gold mines. J. S. Afr. Inst. Min. Metall. 135–147.

Manouchehrian, A., 2016. Numerical Modeling of Unstable Rock Failure. Laurentian University, Sudbury, Ontario, Canada.

Manouchehrian, A., Cai, M., 2016. Simulation of unstable rock failure under unloading conditions. Can. Geotech. J. 53, 22–34. https://doi.org/10.1139/cgj-2015-0126

Marchioni, A., Di Carlo, N., Miliziano, S., 2024. Validation of a simple and effective numerical approach for modelling the ground-supports interac-tion in shield TBM. Presented at the EUROCK 2024: New Challenges in Rock Mechanics and Rock Engineering, Alicante, Spain, pp. 759–765.

Marinos, P., Hoek, E., 2001. Estimating the geotechnical properties of heterogeneous rock masses such as flysch. Bulletin of Engineering Geology and the Environment 60, 85–92. https://doi.org/10.1007/s100640000090

Marinos, P., Hoek, E., 2000. GSI: A geologically friendly tool for rock-mass strength estimation. Presented at the Proc. Geo. Eng. 2000 at the Int. Conf. on Geotechnical and Geological Engineering, echnomic Publishers, Lancaster, Pennsylvania, Melbourne, pp. 1422–1446.

Marinos, V., 2019. A revised, geotechnical classification GSI system for tectonically disturbed heterogeneous rock masses, such as flysch. Bull Eng Geol Environ 78, 899–912. https://doi.org/10.1007/s10064-017-1151-z

Marinos, V., Marinos, P., Hoek, E., 2005. The geological strength index: applications and limitations. Bull Eng Geol Environ 64, 55–65. https://doi.org/10.1007/s10064-004-0270-5

Marinos, Vassilis., Carter, Trevor.G., 2018. Maintaining geological reality in application of GSI for design of engineering structures in rock. Engineering Geology 239, 282–297. https://doi.org/10.1016/j.enggeo.2018.03.022

Martin, C.D., Chandler, N.A., 1994. The Progressive Fracture of Lac du Bonnet Granite. Int. J. Rock Mech. Min. Sci. & Geomech. Abstr. 643–59.

Martin, C.D., Christiansson, R., 2009. Estimating the potential for spalling around a deep nuclear waste repository in crystalline rock. International Journal of Rock Mechanics and Mining Sciences 46, 219–228. https://doi.org/10.1016/j.ijrmms.2008.03.001

Martin, C.D., Kaiser, P.K., McCreath, D.R., 1999. Hoek-Brown parameters for predicting the depth of brittle failure around tunnels. Can. Geotech. J. 136–151.

Martin, C.D., Read, R.S., Martino, J.B., 1997. Obersavtions of Brittle Failure Around a Circular Test Tunnel. Int. J. Rock Mech. Min. Sci. Vol. 34, 1065–1073.

McClintock, F.A., Walsh, J.B., 1962. Friction on Griffith cracks in rocks under pressure, in: American Society of Mechanical Engineers. Presented at the Proceedings of the 4th US National congress of applied mechanics, Berkeley, USA, pp. 1015–21.

McDonald, A.C., 2019. Geological Controls on Strainbursting in Deep Mining Drifts. Queen's University, Kingston, Ontario, Canada.

Mcfeat-Smith, I., 2008. Tunnelling in the Himalayas: Risk assessment and management for tunnelling in extreme geological conditions. World Tunnel Congress 2008 - Underground Facilities for Better Environment and Safety - India

Meng, F., Zhou, H., Wang, Z., Zhang, L., Kong, L., Li, S., Zhang, C., Hu, S., 2017. Experimental study of factors affecting fault slip rockbursts in deeply buried hard rock tunnels. Bull Eng Geol Environ 76, 1167–1182. https://doi.org/10.1007/s10064-016-0926-y

Mercier-Langevin, F., Hadjigeorgiou, J., 2011. Towards a better understanding of squeezing potential in hard rock mines. Mining Technology 120, 36–44. https://doi.org/10.1179/037178411X12942393517372

Miao, S.-J., Cai, M.-F., Guo, Q.-F., Huang, Z.-J., 2016. Rock burst prediction based on in-situ stress and energy accumulation theory. International Journal of Rock Mechanics and Mining Sciences 83, 86–94. https://doi.org/10.1016/j.ijrmms.2016.01.001

Minh, D.N., Guo, C., 1996. Recent progress in convergence confinement method. Presented at the ISRM International Symposium - EUROCK 96, Turin, Italy, pp. 855–860.

Mogi, K., 1966. Pressure dependence of Rock Strength and Transition from Brittle Fracture to Ductile Flow. Bulletin of the Earthquake Research Institute 44, 215–232.

Morissette, P., Hadjigeorgiou, J., 2019. Ground support design for dynamic loading conditions: A quantitative data-driven approach based on rockburst case studies. Journal of Rock Mechanics and Geotechnical Engineering 11, 909–919. https://doi.org/10.1016/j.jrmge.2019.03.002

Moritz, B., 2011. Yielding elements – requirements, overview and comparison / Stauchelemente – Anforderungen, Überblick und Vergleich. Geomechanics and Tunnelling 4, 221–236. https://doi.org/10.1002/geot.201100014

Muller, W., 1991. Numerical simulation of rock bursts. Min. Sci. Technol. 12, 27–42.

Naji, A.M., Emad, M.Z., Rehman, H., Yoo, H., 2019. Geological and geomechanical heterogeneity in deep hydropower tunnels: A rock burst failure case study. Tunnelling and Underground Space Technology 84, 507–521. https://doi.org/10.1016/j.tust.2018.11.009

Neyman, B., Szecowka, Z., Zuberek, W., 1972. Effective methods for fighting rock burst in Polish collieries, in: Proc. 5th. Presented at the Strata Control Conf. 23, pp. 1–9.

NGI, 2013. Using the Q-system. Allkopi AS, Olso, Norway.

Nicksiar, M., Martin, C.D., 2013. Crack initiation stress in low porosity crystalline and sedimentary rocks. Engineering Geology 154, 64–76. https://doi.org/10.1016/j.enggeo.2012.12.007

Novello, E.A., Johnston, L.W., 1995. Geotechnical materials and the critical state. Géotechnique 45, 223–235.

Duncan Fama, M. E., 1993. Numerical Modeling of Yield Zones in Weak Rock, in: Analysis and Design Methods. Elsevier, Chap 3 pp. 49–75. https://doi.org/10.1016/b978-0-08-040615-2.50009-5

Ortlepp, W.D., Stacey, T.R., 1994. Rockburst Mechanisms in Tunnels and Shafts. Tunnelling and Underground Space Technology 9, 59–65.

Palmstrom, A., 1995. Rmi - a rock mass characterization system for rock engineering purposes (PhD thesis). Oslo University, Norway.

Panet, M., 1969. Quelques problèmes de mécanique des roches posés par le Tunnel du Mont-Blanc. Annales de l'Institut Technique du bâtiment et des travaux publiques, n°264, Série : Essais et mesures (120), p1952-1987

Panet, M., 1995. Calcul des Tunnels par la Methode de Convergence-Confinement. Presses de l'Ecole Nationale des Ponts et Chaussées, Paris, France.

Panet, M., 1996. Two case histories of tunnels through squeezing rocks. Rock Mechanics and Rock Engineering 29, 155–164.

Panet, M., 1993. Understanding deformations in tunnels. Presented at the Proc. of the Comprehensive Rock Engineering, Hudson, J.A., Brown, E.T., Fairhurst, C., Hoek, E. (Eds.), Pergamon, London, pp. 663–690.

Panet, M., Guenot, A., 1982. Analysis of convergence behind the face of a tunnel. Presented at the Proc. of the International Symposium Tunnelling, London, pp. 197–204.

Paraskevopoulou, C., Diederichs, M., 2018. Analysis of time-dependent deformation in tunnels using the Convergence-Confinement Method. Tunnelling and Underground Space Technology 71, 62–80. https://doi.org/10.1016/j.tust.2017.07.001

Parisi, M.E., Brino, L., Gilli, P., Fornari, E., Martinotti, G., Lo Russo, S., 2017. La Maddalena exploratory tunnel. Geomechanics and Tunnelling 10, 265–274. https://doi.org/10.1002/geot.201700011

Paterson, M.S., 1978. Experimental Rock Deformation : The Brittle Field, Springer-Verlag. ed. Berlin.

Pellet, F., Hajdu, A., Deleruyelle, F., Besnus, F., 2005. A viscoplastic model including anisotropic damage for the time dependent behaviour of rock. Num Anal Meth Geomechanics 29, 941–970. https://doi.org/10.1002/nag.450

Pen, Y., 1994. Chain Pillar Design in Longwall Mining for Bump-Prone Seams. University of Alberta, Edmonton, Canada.

Peng, J., Cai, M., 2019. A cohesion loss model for determining residual strength of intact rocks. International Journal of Rock Mechanics and Mining Sciences 119, 131–139. https://doi.org/10.1016/j.ijrmms.2019.03.032

Peng, Z., Wang, Y., 1996. Griffith theory and the criteria of rockburst. Chinese Journal of Rock Mechanics and Engineering 15, 491–495.

Potvin, Y., Wesseloo, J., 2013. Towards an understanding of dynamic demand on ground support, in: Proceedings of the Seventh International Symposium on Ground Support in Mining and Underground Construction. Presented at the Seventh International Symposium on Ground Support in Mining and Underground Construction, Australian Centre for Geomechanics, Perth, pp. 287–304. https://doi.org/10.36487/ACG_rep/1304_18_Potvin

Pourhosseini, O., Shabanimashcool, M., 2014. Development of an elasto-plastic constitutive model for intact rocks. International Journal of Rock Mechanics and Mining Sciences 66, 1–12. https://doi.org/10.1016/j.ijrmms.2013.11.010

Pu, Y., Apel, D.B., Liu, V., Mitri, H., 2019. Machine learning methods for rockburst prediction-state-of-the-art review. International Journal of Mining Science and Technology 29, 565–570. https://doi.org/10.1016/j.ijmst.2019.06.009

Qiao, C.S., Tian, Z.Y., 1998. Possibility of rockburst occurrence in dongguashan copper deposit. Chin. J. Rock Mech. Eng. 17, 917–921.

Rafiei Renani, H., Cai, M., 2022. Forty-Year Review of the Hoek–Brown Failure Criterion for Jointed Rock Masses. Rock Mech Rock Eng 55, 439–461. https://doi.org/10.1007/s00603-021-02661-2

Rafiei Renani, H., Martin, C.D., 2018. Cohesion degradation and friction mobilization in brittle failure of rocks. International Journal of Rock Mechanics and Mining Sciences 106, 1–13. https://doi.org/10.1016/j.ijrmms.2018.04.003

Rafiei Renani, H., Martin, C.D., Cai, M., 2019. An analytical model for strength of jointed rock masses. Tunnelling and Underground Space Technology 94, 103159. https://doi.org/10.1016/j.tust.2019.103159

Rahimzadeh Kivi, I., Ameri, M., Molladavoodi, H., 2018. Shale brittleness evaluation based on energy balance analysis of stress-strain curves. Journal of Petroleum Science and Engineering 167, 1–19. https://doi.org/10.1016/j.petrol.2018.03.061

Rahjoo, M., Eberhardt, E., 2021. Development of a 3-D confinement-dependent dilation model for brittle rocks; Part 1, derivation of a Cartesian plastic strain increments ratios approach for non-potential flow rules. International Journal of Rock Mechanics and Mining Sciences 145, 104668. https://doi.org/10.1016/j.ijrmms.2021.104668

Rahjoo, M., Eberhardt, E., 2016. A Simplified Dilation Model for Modeling the Inelastic Behavior of Rock. Presented at the 50th U.S. Rock Mechanics/Geomechanics Symposium, Houston, Texas.

Ramoni, M., Anagnostou, G., 2011. The Interaction Between Shield, Ground and Tunnel Support in TBM Tunnelling Through Squeezing Ground. Rock Mech Rock Eng 44, 37–61. https://doi.org/10.1007/s00603-010-0103-8

Ribeiro E Sousa, L., Miranda, T., Leal E Sousa, R., Tinoco, J., 2017. The Use of Data Mining Techniques in Rockburst Risk Assessment. Engineering 3, 552–558. https://doi.org/10.1016/J.ENG.2017.04.002

Rist, M.A., Sammonds, P.R., Murrell, S.A.F., 1991. Strain rate control during deformation of ice: An assessment of the performance of a new servo-controlled triaxial testing system. Cold Regions Science and Technology 19, 189–200. https://doi.org/10.1016/0165-232X(91)90008-5

Rojat, F., Labiouse, V., Kaiser, P.K., Descoeudres, F., 2009. Brittle Rock Failure in the Steg Lateral Adit of the Lötschberg Base Tunnel. Rock Mech Rock Eng 42, 341–359. https://doi.org/10.1007/s00603-008-0015-z

Rosenblueth, E., 1981. Two-point estimates in probabilities. Appl Math Modelling 5, 329–35.

Röthlisberger, B., Spörri, D., Rehbock-Sander, M., 2016a. Unexpected Difficult Ground Conditions at MFS Faido, in: Tunneling the Gotthard. STS Swiss Tunnelling Society, pp. 384–91.

Röthlisberger, B., Spörri, D., Jesel, T., 2016b. Unexpected Difficult Ground Conditions in the Faido-Sedrun TBM Drives, in: Tunneling the Gotthard. STS Swiss Tunnelling Society, pp. 368–75.
Roy, J.M., Eberhardt, E., Bewick, R.P., Campbell, R., 2023. Application of Data Analysis Techniques to Identify Rockburst Mechanisms, Triggers, and Contributing Factors in Cave Mining. Rock Mech Rock Eng 56, 2967–3002. https://doi.org/10.1007/s00603-022-03206-x
Russenes, B. F., 1974. Analysis of Rock Spalling for Tunnels in Steep Valley Sides (MSc Thesis). Department of Geology, Norwegian Institute of Technology, Trondheim, Norway.
Russo, G., 2014. An update of the "multiple graph" approach for the preliminary assessment of the excavation behaviour in rock tunnelling. Tunnelling and Underground Space Technology 41, 74–81. https://doi.org/10.1016/j.tust.2013.11.006
Sakurai, S., 1997. Lessons learned from field measurements in tunnelling. Tunnelling and Underground Space Technology 12, 453–460.
Salamon, M.D.G., 1970. Stability, Instability and Design of Pillar Workings. Int. J. Rock. Mech. Min. Sci. 7, 613–631.
Sepehri, M., 2020. Evaluation of mining-induced energy and rockburst prediction at a diamond mine in Canada using a full 3D elastoplastic finite element model.
Shafiei, A., Parsaei, H., Dusseault, M.B., 2012. Rock squeezing prediction by a support vector machine classifier. Presented at the 46th US Rock Mechanics/Geomechanics Symposium, Chicago, USA.
Shan, Z., Yan, P., 2010. Management of rock bursts during excavation of the deep tunnels in Jinping II Hydropower Station. Bull Eng Geol Environ 69, 353–363. https://doi.org/10.1007/s10064-010-0266-2
Shirani Faradonbeh, R., Taheri, A., 2019. Long-term prediction of rockburst hazard in deep underground openings using three robust data mining techniques. Engineering with Computers 35, 659–675. https://doi.org/10.1007/s00366-018-0624-4
Shirani Faradonbeh, R., Vaisey, W., Sharifzadeh, M., Zhou, J., 2024. Hybridized intelligent multi-class classifiers for rockburst risk assessment in deep underground mines. Neural Comput & Applic 36, 1681–1698. https://doi.org/10.1007/s00521-023-09189-2
Singh, B., Goel, R.K., 1999. Rock mass classification: A practical approach in civil engineerinG. Elsevier, Amsterdam.
Singh, S.P., 1989. Classification of mine workings according to their rockburst proneness. Min. Sci. Technol. 8, 253–262.
Sinha, N., Frederking, R., 1979. Effect of test system stiffness on strength of ice.
Song, L., Li, H.-Z., Chan, C.L., Low, B.K., 2016. Reliability analysis of underground excavation in elastic-strain-softening rock mass. Tunnelling and Underground Space Technology 60, 66–79. https://doi.org/10.1016/j.tust.2016.06.015
Soubra, A.H., Bastidas-Arteaga, E., 2014. Advanced reliability analysis methods. Presented at the ALERT Doctoral School 2014 Stochastic Analysis and Inverse Modelling.
Sterpi, D., Gioda, G., 2009. Visco-Plastic Behaviour around Advancing Tunnels in Squeezing Rock. Rock Mech Rock Eng 42, 319–339. https://doi.org/10.1007/s00603-007-0137-8
Su, C., Zhu, H., Cai, W., Wu, W., Zhang, Q., 2023. Elastic perfect plastic rock mass analysis and equivalent GSI determination considering strain-softening behavior and three-dimensional strength. Tunnelling and Underground Space Technology 142, 105422. https://doi.org/10.1016/j.tust.2023.105422
Su, G.S., Zhang, X.F., Yan, L.B., 2008. Rockburst prediction method based on case reasoning pattern recognition. J Min Saf Eng 1–15.
Sun, Y., Feng, X., Yang, L., 2018. Predicting Tunnel Squeezing Using Multiclass Support Vector Machines. Advances in Civil Engineering 2018. https://doi.org/10.1155/2018/4543984
Tang, B.Y., 2000. Rock Burst Control Using Distress Blasting (PhD Thesis). McGill University, Montreal, Canada.

Tang, L., Wang, W., 2002. New rock burst proneness index. Chinese Journal of Rock Mechanics and Engineering 21, 874–878.

Tao, Z.Y., 1988. Support design of tunnels subjected to rockbursting. Presented at the Rock Mechanics and Power Plants, A.A. Balkema, Rotterdam, Netherlands, pp. 407–411.

Terzaghi, K., 1946. Rock defects and loads in tunnel supports. Rock tunneling with steel supports, R.V. Proctor and T.L. White eds. ed. The Commercial Shearing and Stamping Co., Youngstown, Ohio.

Tran, N.T., 2020. Long-term stability evaluation of underground constructions by considering uncertainties and variability of rock masses (PhD Thesis). Université d'Orléans, France.

Tristani, A., Guayacán-Carrillo, L., Sulem, J., 2025. Data-Driven Tools to Evaluate Support Pressure, Radial Displacements, and Face Extrusion for Tunnels Excavated in Elastoplastic Grounds. Num Anal Meth Geomechanics 49, 654–664. https://doi.org/10.1002/nag.3889

Tristani, A., Sulem, J., Guayacán-Carrillo, L.-M., 2024. Analytical solutions considering face advance and time-dependent behavior for back-analysis of convergence measurements in deep circular tunnels under isotropic initial stress state. International Journal of Rock Mechanics and Mining Sciences 182. https://doi.org/10.1016/j.ijrmms.2024.105866

Turchaninov, I.A., Markov, G.A., Gzovsky, M.V., Kazikayev, D.M., Frenze, U.K., Batugin, S.A., Chabdarova, U.I., 1972. State of stress in the upper part of the Earth's crust based on direct measurements in mines and on tectonophysical and seismological studies. Physics of the Earth and Planetary Interiors 6, 229–234. https://doi.org/10.1016/0031-9201(72)90005-2

Vaskou, P., 2024. Practical use of structural geology in rock tunnels, Workshop EUROCK 2024, Alicante, Spain.

Villaescusa, E., Player, J.R., Thompson, A.G., 2014. A reinforcement design methodology for highly stressed rock masses. Presented at the 8th Asian Rock Mechanics Symposium, American Rock Mechanics Association, Sapporo, Japan, pp. 87–94.

Vlachopoulos, N., Diederichs, M.S., 2009. Improved Longitudinal Displacement Profiles for Convergence Confinement Analysis of Deep Tunnels. Rock Mech Rock Eng 42, 131–146. https://doi.org/10.1007/s00603-009-0176-4

Voza, A., Valguarnera, L., Marrazzo, R., Ascari, G., Boldini, D., 2023. A New In Situ Test for the Assessment of the Rock-Burst Alarm Threshold During Tunnelling. Rock Mech Rock Eng 56, 1645–1661. https://doi.org/10.1007/s00603-022-03152-8

Wagner, H., Handke, D., Matter, J., Fabbri, D., Keiper, K., 2009. Concepts to overcome squeezing geological conditions at the Koralm tunnel. Geomechanics and Tunnelling 2, 601–611. https://doi.org/10.1002/geot.200900050

Walton, G., 2019. Initial guidelines for the selection of input parameters for cohesion-weakening-friction-strengthening (CWFS) analysis of excavations in brittle rock. Tunnelling and Underground Space Technology 84, 189–200. https://doi.org/10.1016/j.tust.2018.11.019

Walton, G., Diederichs, M.S., 2015. A New Model for the Dilation of Brittle Rocks Based on Laboratory Compression Test Data with Separate Treatment of Dilatancy Mobilization and Decay. Geotech Geol Eng 33, 661–679. https://doi.org/10.1007/s10706-015-9849-9

Wang, J., Apel, D.B., Pu, Y., Hall, R., Wei, C., Sepehri, M., 2021. Numerical modeling for rockbursts: A state-of-the-art review. Journal of Rock Mechanics and Geotechnical Engineering 13, 457–478. https://doi.org/10.1016/j.jrmge.2020.09.011

Wang, J., Apel, D.B., Wei, C., Xu, H., 2024. Prediction of strainburst risks based on the stiffness theory: Development and verification of a new rockburst indicator. International Journal of Rock Mechanics and Mining Sciences 175, 105667. https://doi.org/10.1016/j.ijrmms.2024.105667

Wang, J., Wang, E., Yang, W., Li, B., Li, Z., Liu, X., 2022. Rock burst monitoring and early warning under uncertainty based on multi-information fusion approach. Measurement 205, 112188. https://doi.org/10.1016/j.measurement.2022.112188

Wang, J.-A., Park, H.D., 2001. Comprehensive prediction of rockburst based on analysis of strain energy in rocks. Tunnelling and Underground Space Technology 16, 49–57. https://doi.org/10.1016/S0886-7798(01)00030-X

Wang, L.S., Li, T.B., Xu, J., Xu, L.S., Qi, X.G., Li, Y.L., Jiang, Y., Mou, L., 1999. Rockburst and rockburst intensity classification of Erlangshan highway tunnel. Highway 41–45.

Wang, R., Chen, S., Li, X., Tian, G., Zhao, T., 2023. AdaBoost-driven multi-parameter real-time warning of rock burst risk in coal mines. Engineering Applications of Artificial Intelligence 125, 106591. https://doi.org/10.1016/j.engappai.2023.106591

Wang, T., Zhang, T., Ranjith, P.G., Li, Y., Song, Z., Wang, S., Zhao, W., 2020. A new approach to the evaluation of rock mass rupture and brittleness under triaxial stress condition. Journal of Petroleum Science and Engineering 184, 106482. https://doi.org/10.1016/j.petrol.2019.106482

Wawersik, W.R., Fairhurst, C., 1970. A study of brittle rock fracture in laboratory compression experiments. International Journal of Rock Mechanics and Mining Sciences & Geomechanics Abstracts 7, 561–575. https://doi.org/10.1016/0148-9062(70)90007-0

Wesseloo, J., 2018. The Spatial Assessment of the Current Seismic Hazard State for Hard Rock Underground Mines. Rock Mech Rock Eng 51, 1839–1862. https://doi.org/10.1007/s00603-018-1430-4

Wiles, T., 2002. Loading System Stiffness A Parameter to Evaluate Rockburst Potential. First International Seminar on Deep and High Stress Mining, Perth Australia.

Wu, C., Chen, Q., Basack, S., Xu, R., Shi, Z., 2016. Biaxial Creep Test Study on the Influence of Structural Anisotropy on Rheological Behavior of Hard Rock. J. Mater. Civ. Eng.

Xie, H., Lu, J., Li, C., Li, M., Gao, M., 2022. Experimental study on the mechanical and failure behaviors of deep rock subjected to true triaxial stress: A review. International Journal of Mining Science and Technology 32, 915–950. https://doi.org/10.1016/j.ijmst.2022.05.006

Xu, C., Liu, X., Wang, E., Zheng, Y., Wang, S., 2018. Rockburst prediction and classification based on the ideal-point method of information theory. Tunnelling and Underground Space Technology 81, 382–390. https://doi.org/10.1016/j.tust.2018.07.014

Xu, Y.H., Cai, M., 2018. Influence of strain energy released from a test machine on rock failure process. Can. Geotech. J. 55, 777–791. https://doi.org/10.1139/cgj-2017-0256

Xu, Y.H., Cai, M., 2017. Influence of Loading System Stiffness on Post-peak Stress–Strain Curve of Stable Rock Failures. Rock Mech Rock Eng 50, 2255–2275. https://doi.org/10.1007/s00603-017-1231-1

Xue, R., Liang, Z., Xu, N., Dong, L., 2020b. Rockburst prediction and stability analysis of the access tunnel in the main powerhouse of a hydropower station based on microseismic monitoring. International Journal of Rock Mechanics and Mining Sciences 126, 104174. https://doi.org/10.1016/j.ijrmms.2019.104174

Xue, Y., Bai, C., Kong, F., Qiu, D., Li, L., Su, M., Zhao, Y., 2020a. A two-step comprehensive evaluation model for rockburst prediction based on multiple empirical criteria. Engineering Geology 268, 105515. https://doi.org/10.1016/j.enggeo.2020.105515

Yin, X., Cheng, S., Yu, H., Pan, Y., Liu, Q., Huang, X., Gao, F., Jing, G., 2024. Probabilistic assessment of rockburst risk in TBM-excavated tunnels with multi-source data fusion. Tunnelling and Underground Space Technology 152, 105915. https://doi.org/10.1016/j.tust.2024.105915

Yong, S., Kaiser, P.K., Loew, S., 2013. Rock mass response ahead of an advancing face in faulted shale. International Journal of Rock Mechanics and Mining Sciences 60, 301–311. https://doi.org/10.1016/j.ijrmms.2013.01.002

Zhang, C., Feng, X.-T., Zhou, H., Qiu, S., Wu, W., 2013. Rockmass damage development following two extremely intense rockbursts in deep tunnels at Jinping II hydropower station, southwestern China. Bull Eng Geol Environ 72, 237–247. https://doi.org/10.1007/s10064-013-0470-y

Zhang, C., Feng, X.-T., Zhou, H., Qiu, S., Wu, W., 2012. Case Histories of Four Extremely Intense Rockbursts in Deep Tunnels. Rock Mech Rock Eng 45, 275–288. https://doi.org/10.1007/s00603-011-0218-6

Zhang, D., Ranjith, P.G., Perera, M.S.A., 2016. The brittleness indices used in rock mechanics and their application in shale hydraulic fracturing: a review. J. Pet. Sci. Eng. 143, 158–170.

Zhang, G.C., Gao, Q., Du, J.Q., LI, K.K., 2013. Rockburst criterion based on artificial neural networks and nonlinear regression. J. Central South Univ. (Science and Technology) 44, 2977–2981.

Zhang, H., Zeng, J., Ma, J., Fang, Y., Ma, C., Yao, Z., Chen, Z., 2021. Time Series Prediction of Microseismic Multi-parameter Related to Rockburst Based on Deep Learning. Rock Mech Rock Eng 54, 6299–6321. https://doi.org/10.1007/s00603-021-02614-9

Zhang, J., Li, D., Wang, Y., 2020. Predicting tunnel squeezing using a hybrid classifier ensemble with incomplete data. Bull Eng Geol Environ 79, 3245–3256. https://doi.org/10.1007/s10064-020-01747-5

Zhang, J.J., Fu, B.J., 2008. Rockburst and its criteria and control. Chin. J. Rock Mech. Eng. 27, 2034–2042.

Zhang, Q., Zhang, X.-P., Liu, Q., Pan, Y., Chi, J., Qiu, J., Yin, X., 2024b. Microseismic Monitoring and Rockburst Characteristics in a Deep-Buried Tunnel Excavated by TBM. Rock Mech Rock Eng 57, 1565–1578. https://doi.org/10.1007/s00603-023-03643-2

Zhang, Y., Fang, K., He, M., Liu, D., Wang, J., Guo, Z., 2024a. Rockburst prediction using artificial intelligence techniques: A review. Rock Mechanics Bulletin 3, 100129. https://doi.org/10.1016/j.rockmb.2024.100129

Zhang, Y., Xu, W.Y., Shao, J.F., Zhao, H.B., Wang, W., 2015. Experimental investigation of creep behavior of clastic rock in Xiangjiaba Hydropower Project. Water Sci. Eng., 55–62.

Zhao, G., Wang, D., Gao, B., Wang, S., 2017. Modifying rock burst criteria based on observations in a division tunnel. Engineering Geology 216, 153–160. https://doi.org/10.1016/j.enggeo.2016.11.014

Zhao, H., 2022. A practical and efficient reliability-based design optimization method for rock tunnel support. Tunnelling and Underground Space Technology 127, 104587. https://doi.org/10.1016/j.tust.2022.104587

Zhao, H., Li, S., Chen, B., 2021. The Reliability-Based Design Optimization of considering Rock-Support Interaction for Rock Tunnels. Advances in Civil Engineering 2021. https://doi.org/10.1155/2021/9921881

Zhao, J., Feng, X.-T., Zhang, X., Yang, C., 2019. Brittle and ductile creep behavior of Jinping marble under true triaxial stress. Engineering Geology 258, 105157. https://doi.org/10.1016/j.enggeo.2019.105157

Zhao, J., Feng, X.-T., Zhang, X.-W., Zhang, Y., Zhou, Y.-Y., Yang, C.-X., 2018. Brittle-ductile transition and failure mechanism of Jinping marble under true triaxial compression. Engineering Geology 232, 160–170. https://doi.org/10.1016/j.enggeo.2017.11.008

Zhao, K., 2012. 3D numerical modelling of squeezing behaviour in mechanized excavation of deep tunnels (Tesi di Dottorato). Politecnico di Torino, Italy.

Zhao, X.G., Cai, M., 2010. A mobilized dilation angle model for rocks. International Journal of Rock Mechanics and Mining Sciences 47, 368–384. https://doi.org/10.1016/j.ijrmms.2009.12.007

Zhao, Z., Feng, X., Chen, B., 2016. Microseismic characteristics and rockburst risk of deep tunnel constructed by different excavation methods. Chin. J. Geotech. Eng. 38, 867–876.

Zhao, Z., Gross, L., 2017. Using supervised machine learning to distinguish microseismic from noise events. Presented at the 2017 SEG international exposition and annual meeting.

Zhou, G., Sun, Y., Peng, J., 2018. Application of genetic algorithm based BP neural network to parameter inversion of surrounding rock and deformation prediction. Modern Tunn Technol 55, 107–113.

Zhou, J., Guo, H., Koopialipoor, M., Jahed Armaghani, D., Tahir, M.M., 2020. Investigating the effective parameters on the risk levels of rockburst phenomena by developing a hybrid heuristic algorithm. Engineering with Computers. https://doi.org/10.1007/s00366-019-00908-9

Zhou, J., Li, X., Mitri, H.S., 2018a. Evaluation method of rockburst: State-of-the-art literature review. Tunnelling and Underground Space Technology 81, 632–659. https://doi.org/10.1016/j.tust.2018.08.029

Zhou, J., Li, X., Shi, X., 2012. Long-term prediction model of rockburst in underground openings using heuristic algorithms and support vector machines. Saf Sci 50, 629–644.

Zhou, J., Li, X.B., Mitri, H.S., 2017. A critical survey of empirical methods for evaluating rockburst potential. Presented at the 15th IACMAG, Wuhan, China.

Zhou, J., Shi, X.Z., Huang, R.D., Qiu, X.Y., Chen, C., 2016b. Feasibility of stochastic gradient boosting approach for predicting rockburst damage in burst-prone mines. Transactions of Nonferrous Metals Society of China 26, 1938–1945.

Zhou, K.P., Lin, Y., Deng, H.W., Li, J.L., Liu, C.J., 2016a. Prediction of rock burst classification using cloud model with entropy weight. Transactions of Nonferrous Metals Society of China 7, 1995–2002.

Zhou, X.-P., Peng, S.-L., Zhang, J.-Z., Qian, Q.-H., Lu, R.-C., 2018b. Predictive acoustical behavior of rockburst phenomena in Gaoligongshan tunnel, Dulong river highway, China. Engineering Geology 247, 117–128. https://doi.org/10.1016/j.enggeo.2018.10.023

Appendix 1 - Limitation of the convergence-confinement method and the implicit method for deep tunnel

This appendix investigates the shortcomings of the convergence-confinement method, when used for deep tunnels in weak rock masses. Axisymmetric numerical calculations are performed to evaluate the ground pressure on supports as a function of the distance to the face, the stiffness of the support and the mechanical properties of the ground. A comparison with the traditional convergence-confinement method (CV-CF) is provided to demonstrate the underestimation of the ground pressure on the support calculated. The comparison is also performed for implicit approach of the CV-CF method.

However, this shortcoming is not clearly identified when the CV-CF method is used at the preliminary design stages of projects. This appendix investigates the assumption that these discrepancies for classical tunnelling situations are compensated by the use of safety factors, which are typically applied alongside the CV-CF method. The results obtained show that the safety factors compensate the discrepancies only for classical tunneling situations with small radial deformation. The "implicit" approach with safety factors compensates the discrepancies for most tunnelling situations, except stiff support install far from the face.

A 1.1 Introduction

The Convergence-Confinement method (CV-CF) is an analytical approach that allows the radial strain of a tunnel and the ground pressure of the support to be estimated, based on the geological and geotechnical characteristics of the rock mass. This method is mainly used for the preliminary design of the support. However, the CV-CF method has some shortcomings that lead to an underestimation of the ground pressure on the support and an overestimation of the radial strain at the support installation (Bernaud and Rousset 1992; Cantieni and Anagnostou 2009b; De La Fuente *et al*. 2019). Some improvements have been proposed in the literature to address these shortcomings, such as the "implicit" approach (Bernaud and Rousset 1992; Bernaud *et al.* 1994; Nguyen Minh and Guo 1996) or the AFTES (French Tunnelling and Underground Space Association) recommendation (AFTES – GT7 – Convergence-Confinement Method 2002).

During the design of a tunnel, safety factors are considered to reduce the strength of the support elements (design strength) and to increase the stresses considered for the design of the support element. The partial safety coefficients are based on the Eurocodes and the national recommendations that allow the Eurocode to be adapted for tunnel design. The application of these safety factors increases the probability that the selected support can withstand pressures exceeding those calculated. The question is whether these safety factors are sufficient enough to compensate for the shortcomings of the CV-CF method.

A 1.2 Methodology

In this section, the convergence-confinement (CV-CF) method and the implicit approach are presented and are compared with 2D axisymmetric numerical calculation on an example of a deep tunnel in highly fractured rock mass.

A 1.2.1. Convergence-Confinement Method

The CV-CF method is based on three basic curves that link the confining pressure, the support behavior and the distance between the face and the support installation henceforward referred to as span:

- GRC (Ground Reaction Curve): this curve links radial displacement to the confining pressure, without any support.
- SCC (Support Characteristic Curve): this curve links the radial displacement of the support to the radial pressure applied. It is only dependent on the support characteristics.
- LDP (Longitudinal Displacement Profile): this curve links radial displacement to the distance from the tunnel face.

Based on the LDP, it is possible to estimate the initial radial strain that occurs before the support installation. The final ground pressure on the support is then derived from the intersection of the GRC and the SCC, starting at the radial strain estimated with the LDP (Figure 1-a).

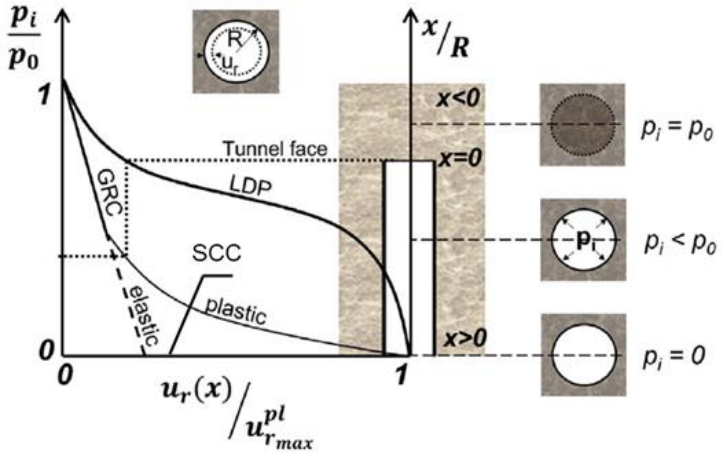

Figure 1-a:Theorical example of the three characteristic curves of the CV-CF method (adapted from Paraskevopoulou and Diederichs 2018); p_i / p_0 is confining pressure normalized by the in-situ stress; x/R is the distance to the tunnel face normalized by the tunnel radius; $u_r(x)/\ u_{r\,max}^{pl}$ is the radial displacement normalized by the maximal radial displacement infinitely far from the face (ie no confining pressure)

The main challenge of the CV-CF method is to obtain the GRC and the LDP. They can be obtained whether with analytical expression or with 2D numerical calculations (2D plane strain for the GRC and 2D axisymmetric for the LDP). In the literature, many analytical expressions have been proposed:

- For the GRC, there are two main analytical expressions: the one from Duncun-Fama (1993) for Mohr-Coulomb failure criterion and the one from Carranza-Torres and Fairhurst (1999) for a Hoek and Brown failure criterion, which was updated for a generalized Hoek and Brown failure criterion by Carranza-Torres (2004). It can be noted that a close form analytical solution is possible only for H&B failure criterion. For the generalized H&B criterion (including strain-softening), numerical resolution of

differential equations is necessary (Carranza-Torres 2004), making it more complex to use.

- For the LDP, several expressions have been proposed depending on the rock mass behavior: Corbetta *et al.* (1991) and Panet (1993; 1995) for elastic behavior of the rock mass; Panet and Guenot (1982), Chern *et al.* (1998) and Vlachopoulos and Diederichs (2009) for elastic-plastic rock mass behavior; Paraskevopoulou and Diederichs (2018) for visco-elastic rock mass behavior; Tristani *et al.* (2024a) for visco-elastic plastic rock mass behavior; Kabwe *et al.* (2020) for elastic visco-plastic rock mass behavior. More expressions can be found in Paraskevopoulou and Diederichs (2018). It can be noted that in practice, engineers use generally the abacus developed by Vlachopoulos and Diederichs (2009) to avoid explicitly calculating the LDP.

The support characteristic curve depends on the stiffness of the support and maximal pressure that can be applied to it. Table 1-a presents some expressions to estimate the support stiffness (k) and the maximal admissible pressure ($P_{i\ max}$).

Table 1-a: Stiffness of various types of support based on Barla (2001)

Type of support	Support stiffness	Maximal support pressure
Concrete or shotcrete lining ($R_{ext} < 10\ t_c$)	$k = \frac{E_s\,(R_{ext}^2 - (R_{ext} - t_c)^2)}{(1+\nu_c)\left((1-2\nu_c)R_{ext}^2 + (R_{ext} - t_c)^2\right)}$	$P_{i\,max} = \frac{1}{2}\sigma_c\left[1 - \frac{(R_{ext} - t_c)^2}{R_{ext}^2}\right]$
Concrete or shotcrete lining ($R_{ext} > 10\ t_c$)	$k = \frac{E_s\,t_c}{(1-\nu_c^2)\,R_{mean}}$	$P_{i\,max} = \frac{\sigma_c t_s}{R_{mean}}$
Steel set (perfect contact with the ground)	$k = \frac{E_{ste}\,A_s}{S\,R_{ext}}$	$P_{i\,max} = \frac{\sigma_s\,A_s}{R_{ext}\,S}$
Steel set embedded in shotcrete	$(k)^{-1} = \frac{S\,R_{ext}}{E_{ste}\,A_s} + \frac{R_{ext}}{E_s\,t_c}$	$P_{i\,max} = \frac{\sigma_s\,A_s}{R_{ext}\,S}$
Ungrouted mechanically or chemically anchored rock bolts	$(k)^{-1} = \frac{S_c\,S_l}{R_{ext}}\left[\frac{4\,l}{\pi\,d_b^2\,E_b} + Q\right]$	$P_{i\,max} = \frac{T_{bf}}{S_c\,S_l}$

Where:

- E_s = Young's modulus of concrete or shotcrete
- ν_c = Poisson's ratio of concrete or shotcrete
- t_c = concrete/shotcrete thickness
- R_{ext} = tunnel radius (external radius of the support)
- R_{mean} = Mean radius of the support / lining
- σ_c = uniaxial compressive strength of concrete or shotcrete
- E_{ste} = Young's modulus of steel
- A_s = cross sectional area of steel set
- S = steel set spacing along tunnel axis
- σ_s = yield strength of steel
- S_c = circumferential bolt spacing
- S_l = longitudinal bolt spacing
- l = free bolt length
- E_b = Young's modulus of bolt
- d_b = bolt diameter

- Q = load-deformation constant for anchor and head (as obtained on the bolt load-extension curve of a pull-out test)
- T_{bf} = bolt ultimate failure load

Several remarks can be made:

- When using the CV-CF method, special focus is necessary regarding the unit to be used for the stiffness of the SCC (slope of the curve). In Table 1-a, the stiffness is expressed in Pascal. It might be adapted depending on the unit used for the GRC (meter and pascal; normalized pressure and normalized displacement (no unit); or a mix in between).
- The expression proposed for "steel set embedded in shotcrete" include the stiffness of both, while only the strength of the steel sets is considered in the calculation of the maximal pressure. It means that the author considered that the shotcrete modifies the stiffness of the steel set, but not its strength (nonstructural shotcrete). This expression should be used carefully as it leads to a stiffness smaller than the stiffness of the steel sets alone, and so its relevance can be questioned.
- Carranza-Torres and Diederichs (2009) proposed a method to estimate the equivalent support properties of a composite support (steel set and shotcrete). It also allows to deduce the normal forces and bending moments of each element of the support. The equivalent properties lead to a different stiffness value compared to the expression proposed in Table 1-a. For example, HEA120 spaced every 1m embedded in 0.2m of shotcrete, in a 3m tunnel radius leads to a stiffness of 0.91GPa with the approach of Carranza-Torres and Diederichs (2009), and to a stiffness of 0.14GPa with the expression of Barla (2001), which is based on the theory of "two springs in series".
- In first approximation, Cantieni and Anagnostou (2009b) proposed to use the radial stiffness (K expressed in Pascal per meter), define as the ratio between the radial pressure (p) on the support and its radial displacement (u). For a thin ring-shaped lining of shotcrete or concrete, the radial stiffness is (Cantieni and Anagnostou 2009b):

$$K = \frac{dp}{du} = \frac{E_s\, d}{R^2} \qquad (A1-1)$$

  where E_s the Young's modulus, d the thickness and R the radius.

A 1.2.2. Implicit method

The classical CV-CF method is based on the hypothesis that the rock mass behavior in front of the support is not impacted by the support itself, meaning that, no matter the support (very stiff or very soft) the rock mass behavior will always be the same in front of the face and between the face and the support installation. This simplifying hypothesis is fundamental for the CV-CF method, but not totally realistic. In the 90's, research has been done to try to improve the CV-CF method by considering the interaction between the support and the rock mass behavior (Bernaud and Rousset 1992, Bernaud *et al.* 1994, Nguyen and Guo 1996). They concluded that the CV-CF method leads to an underestimation of ground pressure on the support, mostly due to this hypothesis. They improved the CV-CF method by trying to include this interaction. It is called the "implicit" approach.

The idea of the implicit method is to deduce the ground pressure on the support and the radial displacement based on the result of the CV-CF method which are then adapted to include the rock mass/support interaction (Figure 1-b). After the classical CV-CF method is performed, the radial displacement at the support installation is obtained (u_0). This value of u_0 is then reduce

using the reduction factor ϕ leading to a new value u_e. Based on the support stiffness, this new radial displacement at the support installation, and the ground reaction curve, the ground pressure on the support can be estimated. Unlike the CV-CF method, it is not possible to directly estimate u_e. It is necessary to solve a system of non-linear equations with three unknowns: the radial displacement at the support installation (u_e), the ground pressure on the support (P_i), the final radial displacement after equilibrium ($u_{\infty i}$). The system of equations is composed of three equations:

1) The equation linking u_0 and u_e through the reduction factor ϕ:

$$u_e = \phi\left(\frac{u_{\infty i}}{u_{\infty\, us}}\right)u_0 \qquad (A1-2)$$

$$\phi(x) = 0.55 + 0.45\,x - 0.42\,(1-x)^3 \qquad (A1-3)$$

Where $u_{\infty\, us}$ the maximal radial displacement without support

2) The characteristic equation of the support behavior, linking u_e, $u_{\infty i}$, and P_i:

$$P_i = K\,(u_{\infty i} - u_e) \qquad (A1-4)$$

Where K is the support stiffness expressed here as pressure per meter

3) The equation associated with the ground reaction curve which can be obtained with analytical expression or numerical fitting.

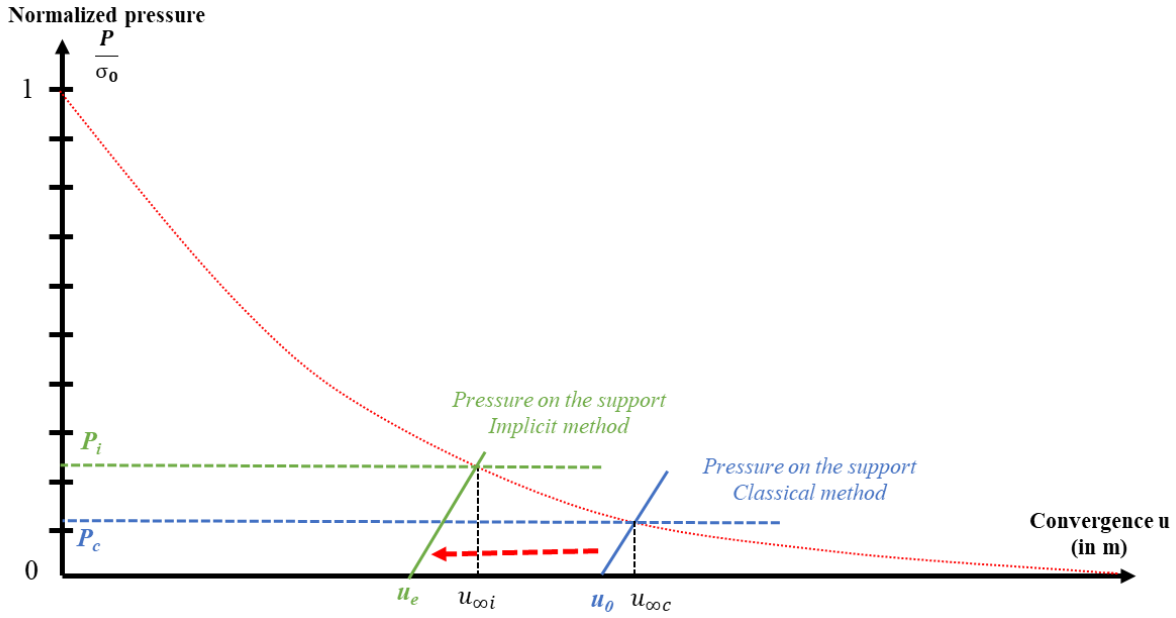

Figure 1-b:Theoretical example of the implicit approach for the CV-CF method; P is the confining pressure; σ_0 is the in-situ stress state; $u_{\infty c}$ is the final radial displacement estimated with the classical CV-CF method; $u_{\infty i}$ is the final radial displacement estimated with the implicit method; u_0 is the radial displacement associated with the support installation based on the classical method; u_e is the radial displacement associated with the support installation based on the implicit method

This system of nonlinear equation can be solved using numerical solver, such as the one available in Excel (used in this thesis) or specific algorithm like Newton iterative method (used by Cantieni and Anagnostou 2009b).

A 1.2.3. Limits of the CV-CF method

The shortcomings of the CV-CF method are highlighted through a theoretical example where a comparison is made between the CV-CF method, the implicit approach and the axisymmetric numerical calculations. It is a theoretical example of a deep tunnel in a weak rock mass. The in-situ stress is assumed to be isotropic with a value of 15 MPa. The rock mass is assumed to be elastic perfectly plastic characterized with a generalized Hoek and Brown yielding criteria, the uniaxial compressive strength of the intact rock is 45 MPa, the strength parameter of Hoek and Brown (m_i) is 15, the Geological Strength Index (GSI) is 20 and the modulus ratio (MR) is 600. The parameters used in the numerical model are derived from the classical equations that can be found in Hoek and Brown (2019). It is typical of a medium strong intact rock in a highly fractured rock mass, such as in a fault zone.

For the CV-CF method, the GRC is calculated numerically using a 2D plane strain model, while the LDP is calculated using a 2D axisymmetric model, both without considering any support. This approach reduces errors that typically arise from closed-form analytical solutions or mathematical approximations. Both types of numerical calculations are computed with the large strain hypothesis.

Without support, a 2D plane strain numerical model in this geological situation leads to a radial strain of 7.8% (Figure 1-c), classified as “very severe squeezing problems” by Hoek & Marinos (2000) and to a plastic radius of 2.4 Radii. Then, three values of radial stiffness for the support are considered in this example: 100 MPa/m, 500 MPa/m and 1000 MPa/m. A radial stiffness of 100 MPa/m can be associated with a 20 cm thick shotcrete (Young’s modulus of 10 GPa) in a tunnel radius of 5 m. A radial stiffness of 1000 MPa/m can be associated with 40 cm thick segmental lining (Young’s modulus of 30 GPa) in a tunnel radius of 3.5 m. The simplified Eq.(A2-2) proposed by Cantieni and Anagnostou (2009b) is used.

The following values are considered for the span: 0.1R, 0.5R, 1R and 2R. In weak rock masses, the support is typically installed close to the face, at a distance of around 0.5m to 1.5m, which corresponds to 0.1 to 0.3 times the tunnel radius. In this example, the maximum span was limited to 2.0R because, for greater spans, the CV-CF method results in almost no ground pressure on the support.

Figure 1-c presents the results of the CV-CF method, the implicit approach and the axisymmetric calculations. The axisymmetric numerical model used is identical to the one presented in Chapter 4.2.1. To avoid boundary effect, the results of the axisymmetric calculations are taken 20 Radii from the face (5 Radii from the model boundary). The following conclusions can be drawn from Figure 1-c and Figure 1-d:

- The CV-CF method leads to an underestimation of the ground pressure on the support and an overestimation of the radial strain, similar to what that can be found in the literature (Cantieni and Anagnostou 2009b).

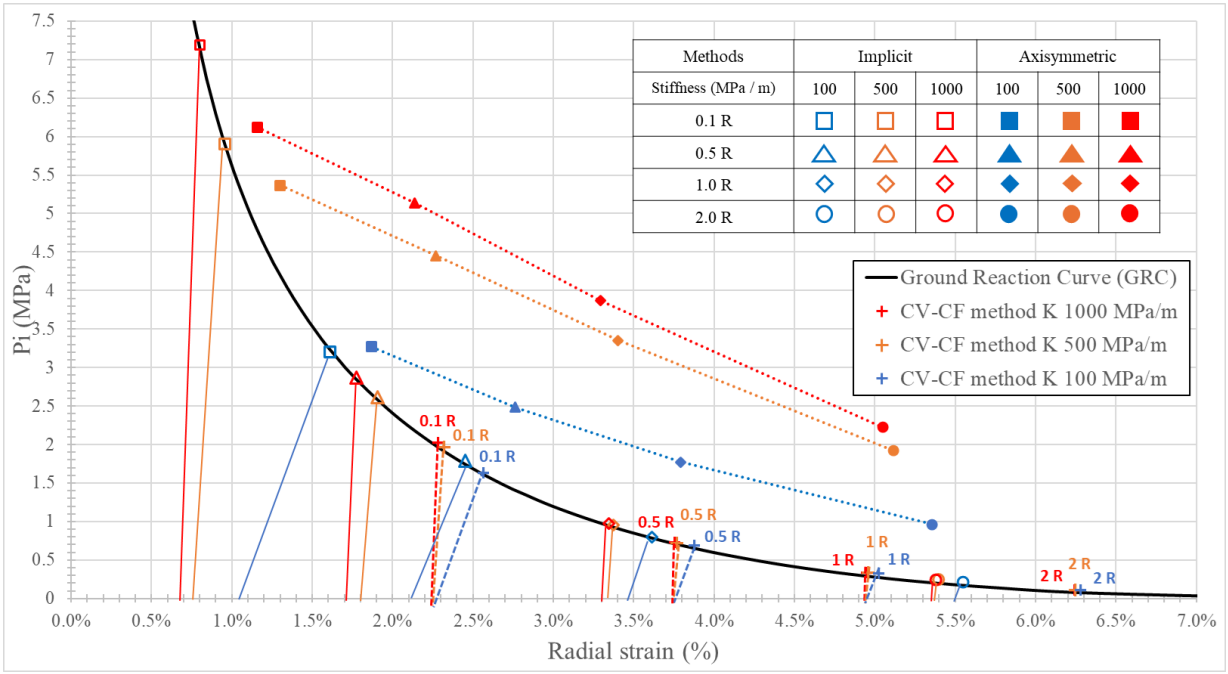

Figure 1-c: Comparison of the CV-CF method and the axisymmetric numerical calculation for an elastic-plastic rock mass behavior when the GRC being previously calculated with 2D plane strain numerical model; continuous color lines correspond to the result of the implicit method; dash lines correspond to the result of CV-CF method

- The results of the axisymmetric calculations (dotted curves in Figure 1-c) do not lie on the Ground Reaction Curve (GRC). For small spans, the results are closer to the GRC compared to large spans. This is due to the plasticity within the rock mass and to the stress path (Cantieni and Anagnostou 2009b). For elastic rock mass (Figure 1-d) where the results are independent of the stress path, the results of the axisymmetric calculation are on the GRC (Figure 1-d) but still different from those of the CV-CF method. Cantieni and Anagnostou (2009b) proposed two explanations for the gap between the GRC and the axisymmetric calculations: the first one is the development of plastic shear strains in the longitudinal section of the tunnel associated with a rotation of the principal stresses, the second is the succession of unloading and reloading at the excavation boundary. Far from the face (direction of the tunnel advance), the radial stress is equal to in-situ stress. At the tunnel face and on the unsupported span, the radial stress is zero, and when the support is installed, the radial stress starts to re-increase with the loading of the support.
- The results of the axisymmetric calculations show that, in this example, the real impact of the radial stiffness of the support is larger than what could be assessed by using the CV-CF method. For a span of 0.1 R, the variation of ground pressure on the support ranges from 1.6 MPa to 2 MPa when calculated with the CV-CF method and from 3.3 MPa to 6.2 MPa when calculated with the axisymmetric numerical model. It is important to note that the support is considered to be elastic, which may lead to ground pressure far exceeding the strength of the support.

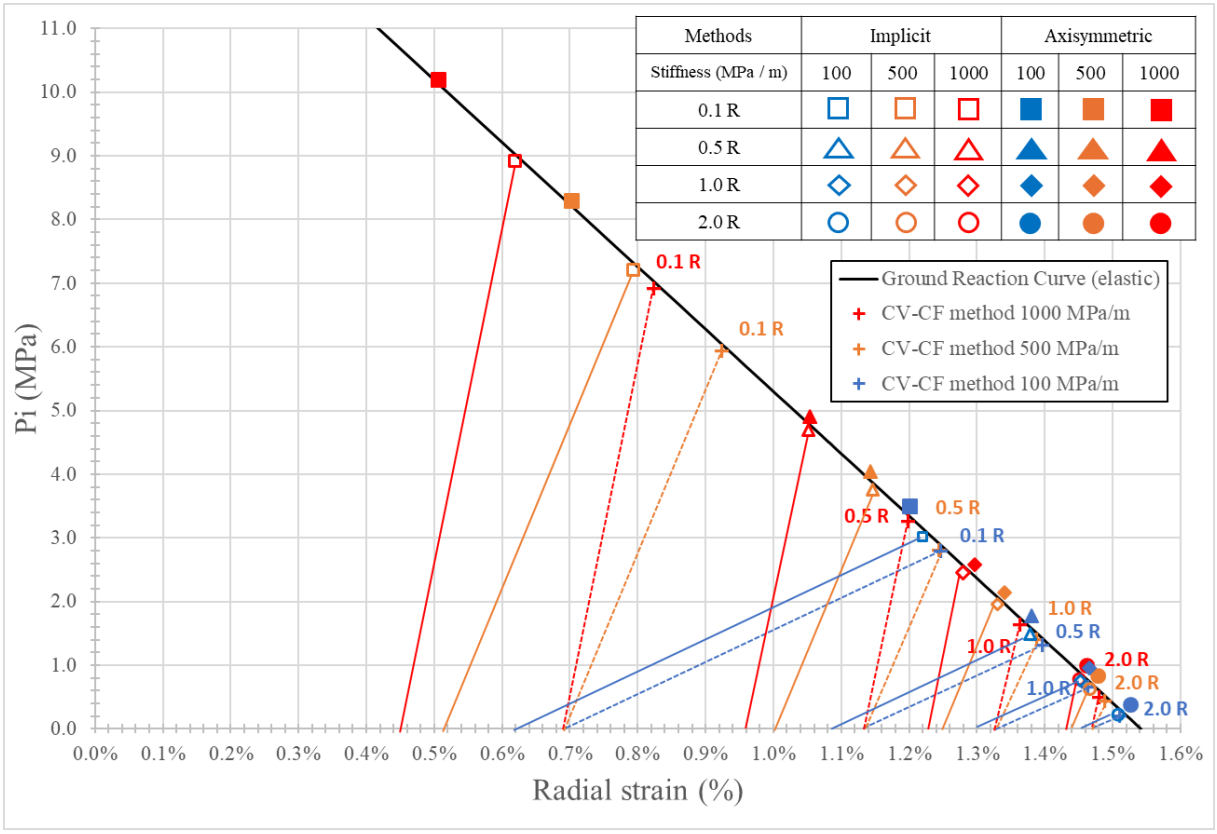

Figure 1-d: Comparison between the axisymmetric calculation and the CV-CF method for an elastic behavior of the rock mass; continuous color lines correspond to the result of the implicit method; dash lines correspond to the result of CV-CF method

- The results of the axisymmetric calculation cannot be obtained with the CV-CF method as long as there is some plasticity occurring in the rock mass and the support is not installed directly at the tunnel face. It is also the case for the implicit method, as the result can only be on the GRC.
- When significant plasticity develops in the rock mass, the implicit approach leads to results similar to CV-CF method (span of 0.5R, 1R and 2R in Figure 1-c). In the other hand, when there is no or very limited plasticity (span 0.1R in Figure 1-c or Figure 1-d), the implicit method leads to result similar the axisymmetric numerical calculations.

As it is mentioned, Figure 1-d presents the comparison between the CV-CF method and the axisymmetric numerical calculations when the rock mass behavior is supposed to be elastic. Even if the results of the axisymmetric calculations are aligned with the GRC, the CV-CF method underestimates the ground pressure on the support. For a span (e) of 0.1 R and a radial stiffness of 1000 MPa/m, the ground pressure obtained with the numerical model is 10.2 MPa whereas for the CV-CF method, the pressure is 6.9 MPa. This discrepancy can be explained by one of the fundamental hypotheses of the CV-CF method: no interaction is considered between the rock mass behavior and the support behavior. This means that, regardless of the presence of the support or its radial stiffness, the rock mass behaves in a similar manner. At a fix distance from the face before the installation of the support, for example 0.5 R, the CV-CF method considers that the radial strain is always the same (1.13% in Figure 1-d), regardless of the applied support stiffness that acts behind the unsupported span. The axisymmetric calculation gives a radial strain at the support installation of 0.95% for a radial stiffness of 500 MPa/m and 1.09% for a radial stiffness of 100 MPa/m. In reality, there is a stress redistribution leading to a

higher ground pressure on the support (arching effect, in the tunnel direction), and a smaller radial strain at the support installation.

Similar to the CV-CF method, the 2D plane strain numerical models do not consider any interaction between the rock mass behavior in front of the support and the support itself. On the over hand, 2D axisymmetric and 3D numerical calculations explicitly consider those interactions. As the CV-CF method underestimates the ground pressure on the support, the 2D plane strain model leads to the same results since it uses the same hypothesis to calculate the deconfinement rate.

To correct this discrepancy, the deconfinement rate should be estimated based on a 2D axisymmetric or 3D numerical calculations with a similar support (same stiffness), and then it can be used in a 2D plane strain model in which the support is modelled precisely enough to be designed, as required. It is important to note that, when some plasticity occurs, the 2D axisymmetric and 3D numerical calculation lead to results that are not aligned with the GRC (black curve in Figure 1-c). Thus, when plasticity occurs, it is impossible with a 2D plane strain numerical model to reach the same result as a 2D axisymmetric, or 3D model for the radial deformation and the ground pressure on the support. The deconfinement rate could be adapted to adjust the result of the 2D plane strain at the same radial strain as the 3D model, or at the same ground pressure on the support, but not both. Most of the time, the design parameter is the ground pressure, and so the radial strain with a 2D plane strain is underestimated.

A 1.3 Comparison including safety factors for the CV-CF method

A 1.3.1. Comparison methodology

The previous example illustrates the significant discrepancy between the CV-CF method and the axisymmetric numerical calculations. It leads to think that supports designed with the CV-CF method in weak rock masses are underestimated and so might fail. In reality, safety factors are taken into account during the design which may explain why the failure of the support is not common, or the preliminary design obtained with the CV-CF method might evolve during more advanced design stages.

In order to highlight the impact of the safety factors when the CV-CF method is used, 12 geological situations representing deep tunnels (>200m) in weak rock mass are considered (Table 1-b). These theoretical situations have been chosen to cover a large range of values for the radial strain and the plastic radius, by considering a small variation of the input parameters (3 values for the ratio between σ_{ci} and σ_0 ; 2 values for m_i ; 2 values for GSI). For the comparison purpose, a thirteenth situation is considered for a rock mass with an elastic behavior identical to the one of the examples presented in Section A 1.2.3. It is important to note that for the elastic behavior (the last case presented in Table 1-b), the plastic radius is considered to be 1R and not 0R. This choice was made to keep a continuity for the plastic radius between elastic behavior and elastic-plastic behavior. In situations 1 to 12, the rock mass is characterized by elastic perfectly plastic behavior with a generalized Hoek and Brown yielding criteria. The formula to calculate the input parameters of the axisymmetric numerical model based on the one presented in Table 1-b are the classical ones, that can be found in Hoek and Brown (2019).

Table 1-b: Summary of 13 geological situations used for the comparison; ε_{us} is the radial strain without support; Rp is the plastic radius without support; MR is the Modulus Ratio; "Elastic" is the situation with an elastic behavior for the rock mass

Situation	σ_0	σ_{ci}	m_i	GSI	MR	ε_{us}	Rp
1	20	30	8	25	400	39.6%	3.8 R
2	20	30	8	40	400	13.4%	2.8 R
3	20	30	13	40	400	7.8%	2.1 R
4	20	30	13	25	400	24.5%	2.7 R
5	10	35	8	25	400	9.5%	2.6 R
6	10	35	8	40	400	2.3%	1.8 R
7	10	35	13	40	400	1.6%	1.5 R
8	10	35	13	25	400	5.7%	2.0 R
9	5	40	8	25	400	2.0%	1.7 R
10	5	40	8	40	400	0.5%	1.3 R
11	5	40	13	40	400	0.4%	1.1 R
12	5	40	13	25	400	1.4%	1.4 R
Elastic	15	45	15	20	600	1.5%	1.0 R

The CV-CF method with safety factors is compared to the axisymmetric numerical calculation without safety factors. For each situation, three spans are considered (0.1R; 0.5R; 1R) and for each of them, four values of the radial stiffness of the support are also considered (50 MPa/m; 100 MPa/m; 500 MPa/m; 1000 MPa/m). The safety factors used in the CV-CF method are based on the Eurocodes and the French Recommendation on the adaptation of the Eurocode for tunnel designs (AFTES – GT 29R2F1). The first safety factor is a multiplication coefficient of 1.35 applied to the internal forces of the support (normal forces; bending moment; shear forces). In this comparison, the in-situ stress state is isotropic, the rock mass is isotropic, and the tunnel is circular, so the design constraint is the normal force (orthoradial force) in the support, which, in this situation, is directly proportional to the ground pressure on the support. The second safety factor is a reduction factor applied to the strength of the support. For temporary support in shotcrete or concrete, the reduction factor is 1.5. This means that the ground pressure used in the design is increased by a coefficient of 1.35 and the strength of the support is decreased by a factor of 1.5. In this example, the use of these two safety factors is equivalent to increasing the ground pressure obtained with the CV-CF method by a factor of 2.025 (1.35x1.5) because the support is circular and loaded by an uniform ground pressure (2D axisymmetric numerical calculations).

When the support installation is delayed (large span), yielding support might be used to ensure the safety of the excavation operation between the face and the "rigid" support, like steel ribs with sliding gap or the use of shotcrete with compressible element. Those yielding supports have an impact on the rock mass behavior (Cantieni and Anagnostou 2009a), but in this comparison, no yielding support is considered between the face and the "rigid" support.

A 1.3.2. CV-CF method

156 axisymmetric calculations are performed, and the results are compared with those from the CV-CF method with safety factors in Figure 1-e. The x-axis value in Figure 1-e is the relative gap between the two methods. The relative gap (δ) is calculated using the following equation:

$$\delta(\%) = \frac{\Delta P_i}{P_{i\,(axi)}} = \frac{P_{i\,(CV-CF\ \&\ SF)} - P_{i\,(axi)}}{P_{i\,(axi)}} \qquad (A1-5)$$

Where $Pi_{(CV\text{-}CF\ \&\ SF)}$ is the ground pressure on the support obtained using the CV-CF method including safety factors and $Pi_{(axi)}$ is the ground pressure on the support obtained with the axisymmetric calculations without safety factors. If the relative gap is negative, it means that the ground pressure obtained with the CV-CF method including safety factors is lower than the one obtained with the axisymmetric calculation. For example, considering situation 1 (Table 1-b) with a span of 0.5 Radius and a radial stiffness of 100 MPa/m. The relative gap is -54% (red square for a plastic radius of 3.8R, Figure 1-e and Table 1-b), which means the ground pressure calculated with the CV-CF method including safety factors is 54% smaller than the ground pressure obtained with the axisymmetric numerical calculations. Now, if a span of 0.1 R and a radial stiffness of 500 MPa/m are considered for the situation 10 (green circle with a plastic radius of 1.3R in Figure 1-e), the relative gap is 21%. It means that the ground pressure calculated with the CV-CF method including the safety factor is 21% higher than the ground pressure obtained with the axisymmetric numerical calculations.

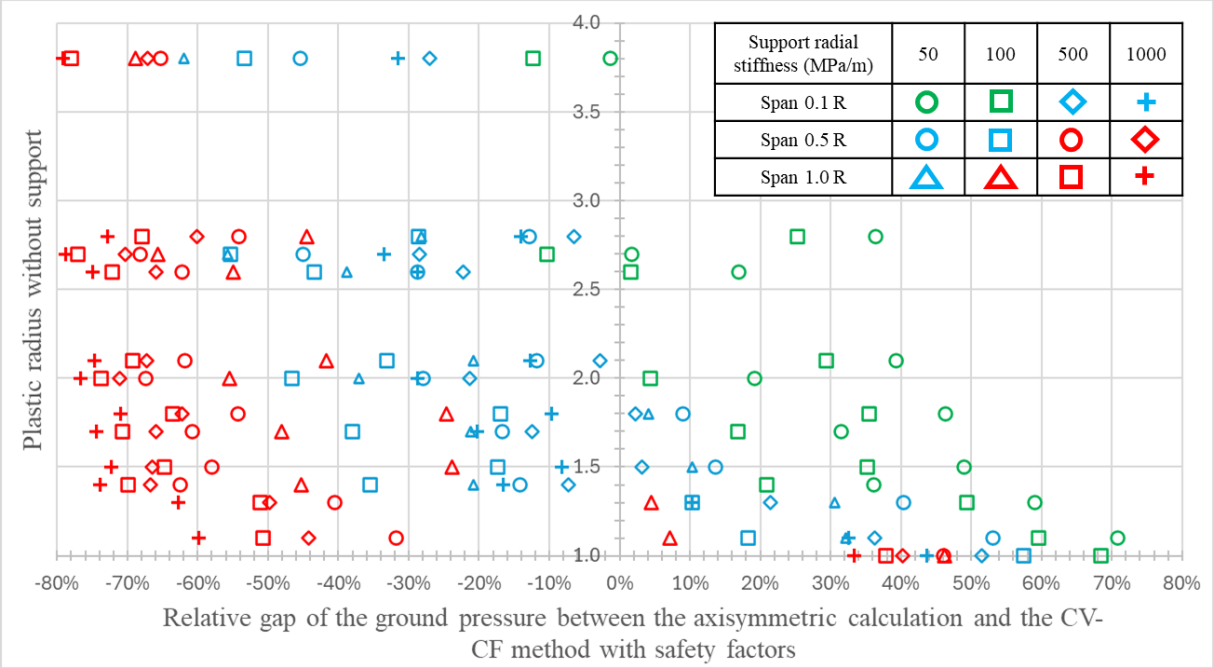

Figure 1-e: Comparison between the results of the axisymmetric numerical calculations and the CV-CF method with safety factors; the x-axis is the relative gap between the two results for a same geological situation, with the same span and the same stiffness of support; the pressure considered as reference is the one from the axisymmetric calculation; the y-axis is the plastic radius without support for each geological situation (Table 1-b)

In 30% of the situations, the CV-CF method with safety factors gives a higher pressure value than the one obtained with the axisymmetric calculations. Figure 1-e shows that these higher values of δ occur when the rock mass behavior is only elastic (points on the x-axis, plastic radius of 1.0R), or when the plastic radius is limited, the support is relatively soft (around 100 MPa/m or less) and the support is installed close to the tunnel face (around 0.1R). It is the green circles and squares for every situation, except situation 1. On the contrary, for high value of radial stiffness and for supports installed not directly at the face (span of 0.5R and 1.0R), the red circles, squares, crosses and diamonds (Figure 1-e), δ is negative and the CV-CF method with safety factors is not conservative. There is one exception: the situation for which the rock mass behavior is elastic (plastic radius of 1.0R) in which, δ is always positive.

The situations presented in Table 1-b represent theorical situations of deep tunnels in weak rock mass. In these situations, the first support is generally installed close to the face, about 1m, mostly for safety reasons and to control and reduce the radial deformation of the tunnel wall.

The span corresponds to one excavation step, and the support is generally shotcrete and/or steal ribs. This type of support has a stiffness around 100 MPa/m (example: Young's modulus of the shotcrete of 10 GPa, thickness of 0.2m and tunnel radius of 4m). This is coherent with the result of Figure 1-e (green points) for which the ground pressure calculated with the CV-CF method plus safety factors is higher than the one from axisymmetric calculation. Installation of stiff support (500 MPa/m or 1000 MPa/m) close to the face is technically challenging for traditional excavation technics. The exception would be the use of segmental lining put in place with a TBM (Tunnel Boring Machine) but it is not included in the framework of this study. The interaction between the rock mass and the TBM is more complex because it applies a confining pressure at the face, and along the shield before the segmental lining installation (Ramoni and Anagnostou 2011; Marchioni *et al.* 2024).

Figure 1-e highlights that for situations with large plastic radius and for which large radial strains are expected, the CV-CF method with safety factors underestimates the ground pressure. Those geological situations exist and lead to very high ground pressure on the support, regardless of the calculation method, which will overstress the support and probably result in failure. The point of this study is to compare the two methodologies without focusing on the strength and failure of supports. For these tunnelling situations, yielding supports are used to allow the rock mass to deform and are designed with more precise studies. The CV-CF method might be used primarily to highlight the potential problems that necessitate more complex studies.

The tunnel design is an iterative process in order to optimize the duration, the cost and the compliance with the project constraints. The CV-CF method is generally used in an early stage of the design to help the engineer design a support. Based on the hazard that can occur during the excavation, the support might need to be studied more precisely and to be justified regarding mandatory regulation. For most of the tunnelling situations, the in-situ stress state is anisotropic, and the tunnel geometry is not circular, which makes the CV-CF method difficult or even impossible to use. For precise study, numerical modelling is more adequate, but time consuming.

A 1.3.3. Implicit method

The same comparison is performed between the ground pressure on the support obtained with the implicit method and the axisymmetric numerical calculations. The relative gap is calculated as follows:

$$\delta(\%) = \frac{\Delta P_i}{P_{i\,(axi)}} = \frac{P_{i\,(impl\,\&\,SF)} - P_{i\,(axi)}}{P_{i\,(axi)}} \qquad (A1-6)$$

Where $P_{i\,(impl\,\&\,SF)}$ is the ground pressure from the implicit approach, including the safety factors.

The results are presented in Figure 1-f. When the relative gap is higher than 100%, it means that the result of the implicit approach without safety factors is already higher than the result of axisymmetric calculation.

It can be noted that, except for stiff support installation far from the face, the consideration of safety factors with the implicit approach leads to an overestimation of the ground pressure compared to axisymmetric calculations. For stiff support (500 MPa/m or 1000 MPa/m) installed close to face (blue diamonds and crosses), the implicit approach overestimates the ground

pressure on the support even without considering safety factors. In practice, it is very difficult to obtain stiff support close to the face as they are complex to install, and materials like concrete or shotcrete (except segmental lining) need drying time and will become stiffer progressively in time.

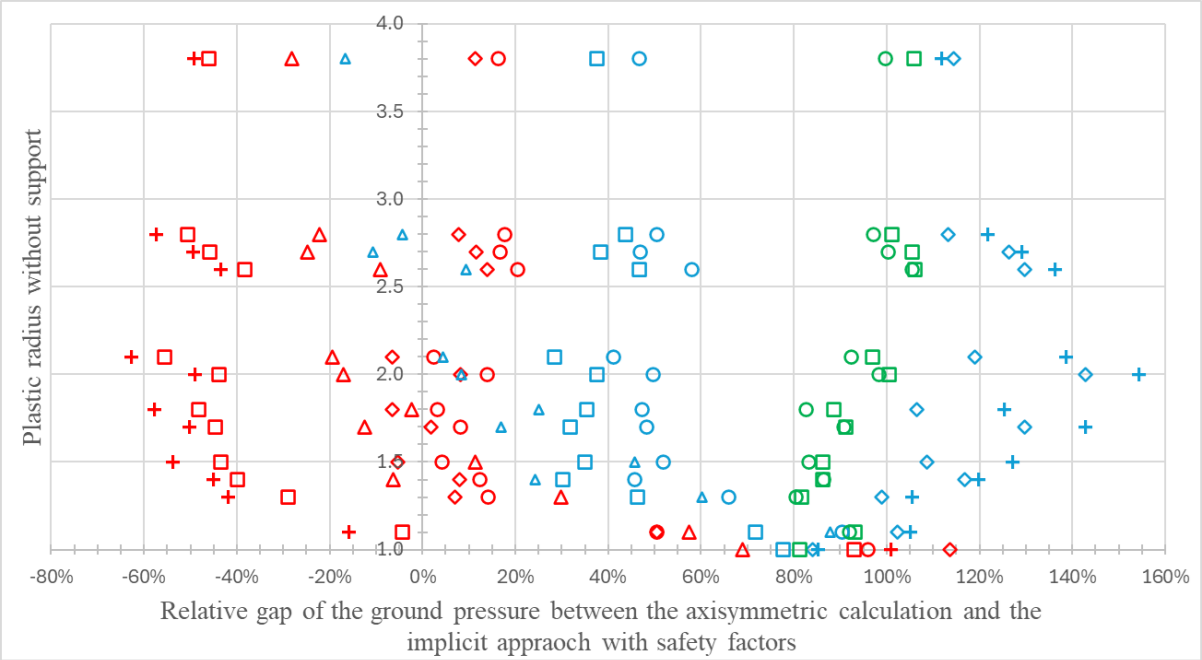

Support radial stiffness (MPa/m)	50	100	500	1000
Span 0.1 R	○	□	◇	+
Span 0.5 R	○	□	○	◇
Span 1.0 R	△	△	□	+

Figure 1-f: Comparison between the results of the axisymmetric numerical calculations and the implicit approach with safety factors; the x-axis is the relative gap between the two results for a same geological situation, with the same span and the same stiffness of support; the pressure considered as reference is the one from the axisymmetric calculation; the y-axis is the plastic radius without support for each geological situation (Table 1-b)

A 1.4 Conclusions

This appendix highlights the discrepancies between the classical Convergence-Confinement Method (CV-CF method) and axisymmetric numerical calculations for weak rock mass. The CV-CF method is based on a fundamental hypothesis considering that the rock mass behavior in front of a support is not influenced by the support characteristics. This means that the rock mass behavior on the span length, i.e. the distance between the face and the support, and in front of the face, is similar regardless of the support stiffness. On the contrary, the axisymmetric numerical calculation explicitly considered the interaction between the rock mass behavior and the support. The hypothesis used in the classical CV-CF method leads to an underestimation of the ground pressure on the support.

When some plasticity develops in the rock mass around the tunnel, another discrepancy appears between the result of the CV-CF method and the axisymmetric calculation. The results of the axisymmetric calculations differ from the Ground Reaction Curve of the CV-CF method. It is impossible to obtain the results of the axisymmetric numerical calculation with the CV-CF method. This discrepancy combined with CV-CF method hypothesis leads to a major

underestimation of the ground pressure on the support. The use of safety factors during the design of classical tunnelling situations in weak rock mass (support installed close to the face, and not too stiff) generally compensate for those underestimations. However, the overall level of safety is lower than the one targeted with the use of these safety factors.

Appendix 2 - Graphical representations of the various surrogate models

This Appendix presents the graphical representations of surrogate models allowing an estimation of the plastic radius without support (Chapter 3.3.4), the ground pressure on the support (Chapter 4.2.3.2), the radial strain between the face and the support installation (Chapter 4.2.3.3) and the radial strain at the face, with and without support (Chapter 4.2.3.4).

All the graphical representations are presented twice. The first one includes an example of how they should be used. At the end, the versions without example are presented. They have been deduced from the associated mathematical equation presented in Chapter 3 and Chapter 4. For more information, the reader should refer itself to the corresponding chapters.

The order of the graphical representation is:

1) Plastic radius without support
2) Surrogate model D, associated with the estimation of the ground pressure on the support.
3) Surrogate model E, associated with the estimation of the ground pressure on the support.
4) Combination of D and E to estimate the ground pressure on the support (P_i)
5) Surrogate model A_{RS}, associated with the radial strain between the face and the support
6) Surrogate model B_{RS}, associated with the radial strain between the face and the support
7) Combination of A_{RS} and B_{RS} to estimate the radial strain between the face and the support ($\varepsilon_{f\text{-}s}$)
8) Surrogate model associated with the radial strain at the face without support (ε_{USF})
9) Surrogate model A_{SF}, associated with the radial strain at the face with support
10) Combination of ε_{USF} and A_{SF} to estimate the radial strain at the face with support (ε_{SF})

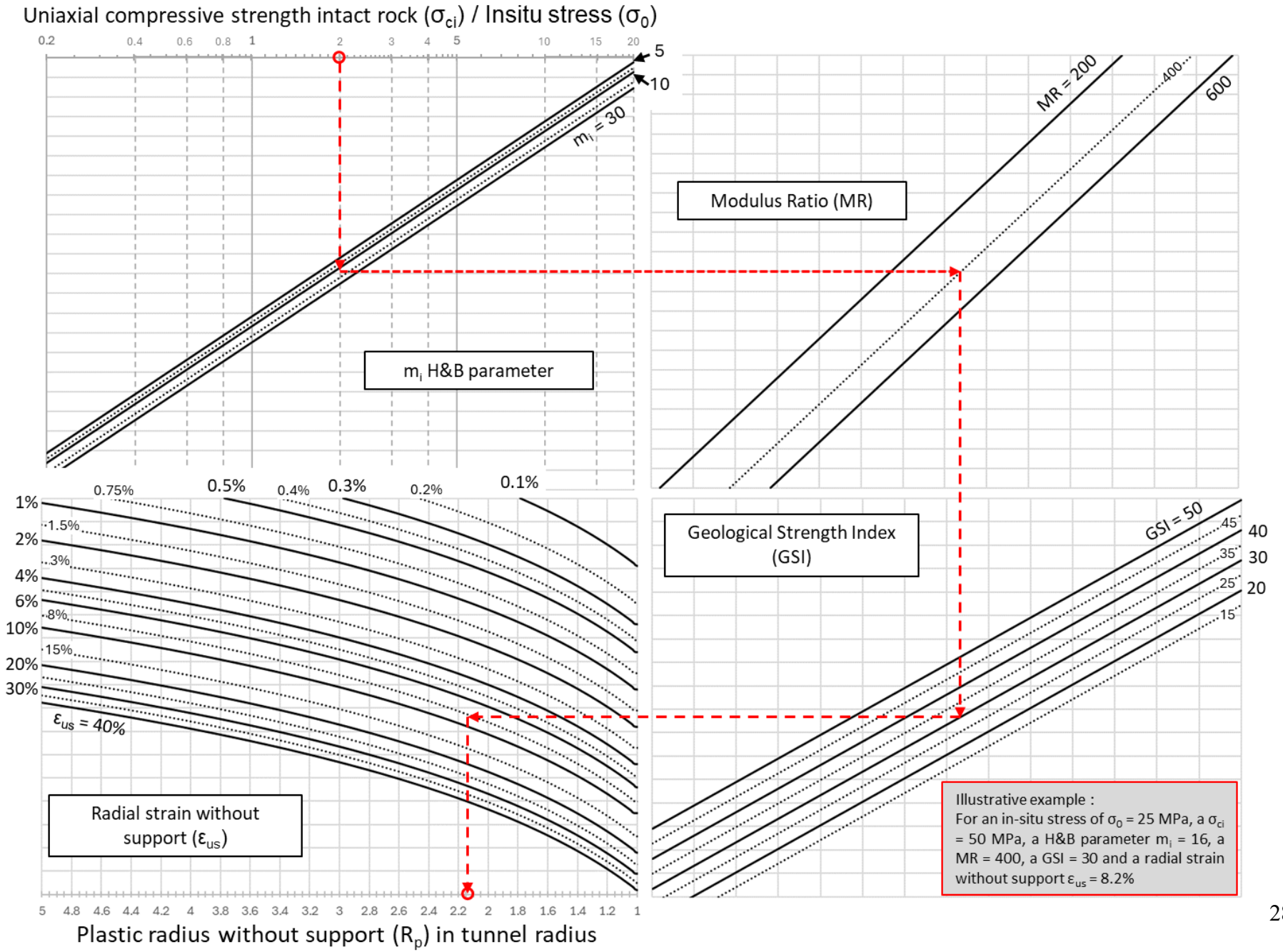
Uniaxial compressive strength intact rock (σ_{ci}) / Insitu stress (σ_0)
0.2
0.4
0.6
0.8
1
2
3
4
5
10
15
20
5
10
m_i = 30
m_i H&B parameter
MR = 200
400
600
Modulus Ratio (MR)
0.75%
0.5%
0.4%
0.3%
0.2%
0.1%
1%
1.5%
2%
3%
4%
6%
8%
10%
15%
20%
30%
ε_{us} = 40%
Radial strain without support (ε_{us})
GSI = 50
45
40
35
30
25
20
15
Geological Strength Index (GSI)
Illustrative example :
For an in-situ stress of σ_0 = 25 MPa, a σ_{ci} = 50 MPa, a H&B parameter m_i = 16, a MR = 400, a GSI = 30 and a radial strain without support ε_{us} = 8.2%
5
4.8
4.6
4.4
4.2
4
3.8
3.6
3.4
3.2
3
2.8
2.6
2.4
2.2
2
1.8
1.6
1.4
1.2
1
Plastic radius without support (R_p) in tunnel radius

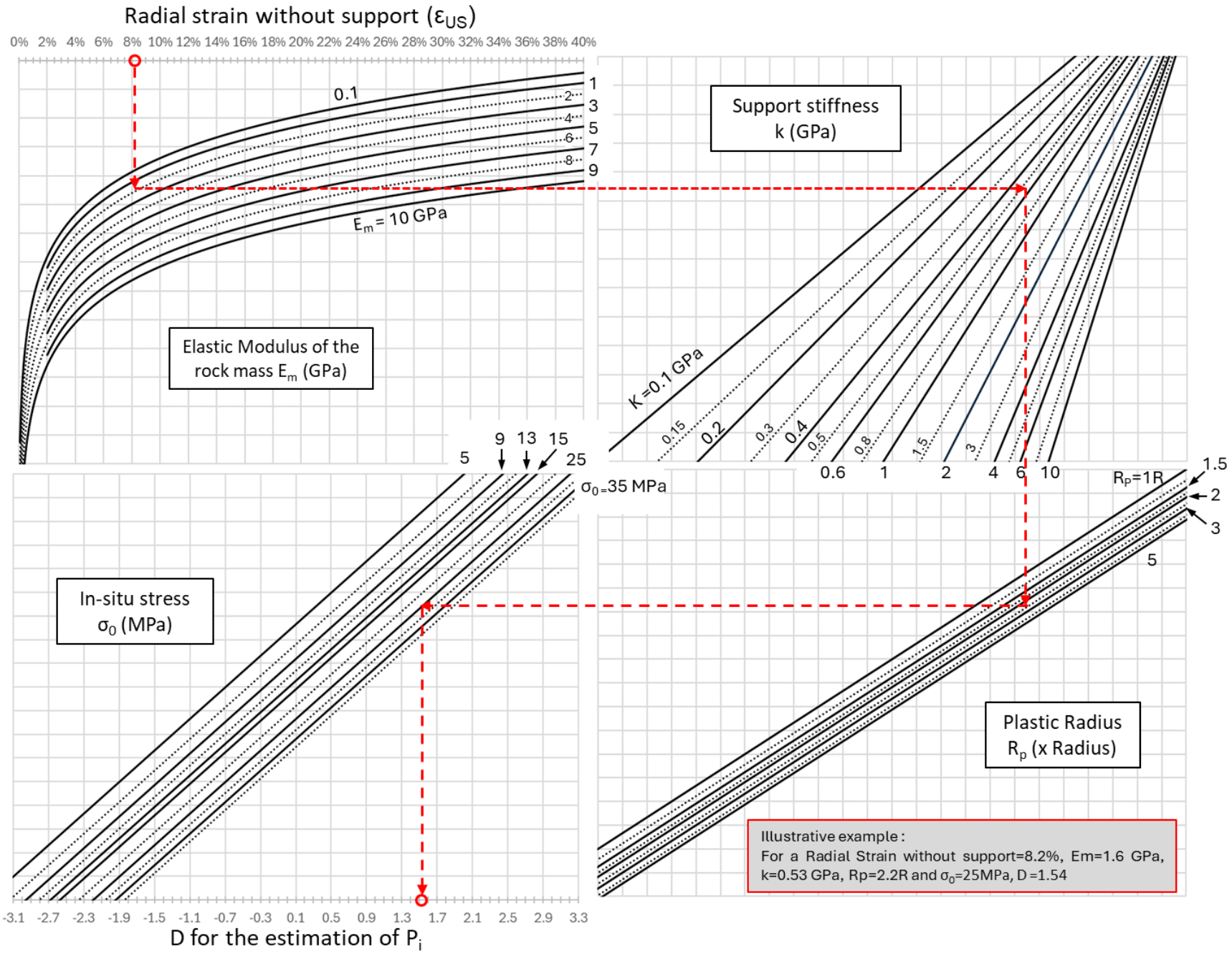
Radial strain without support (ε_{US})
0% 2% 4% 6% 8% 10% 12% 14% 16% 18% 20% 22% 24% 26% 28% 30% 32% 34% 36% 38% 40%
0.1
1
2
3
4
5
6
7
8
9
E_m = 10 GPa
Elastic Modulus of the rock mass E_m (GPa)
Support stiffness k (GPa)
K =0.1 GPa
0.15
0.2
0.3
0.4
0.5
0.6
0.8
1
1.5
2
3
4
6
10
5
9
13
15
25
σ_0=35 MPa
In-situ stress σ_0 (MPa)
R_P=1R
1.5
2
3
5
Plastic Radius R_p (x Radius)
-3.1 -2.7 -2.3 -1.9 -1.5 -1.1 -0.7 -0.3 0.1 0.5 0.9 1.3 1.7 2.1 2.5 2.9 3.3
D for the estimation of P_i
Illustrative example :
For a Radial Strain without support=8.2%, Em=1.6 GPa, k=0.53 GPa, Rp=2.2R and σ_0=25MPa, D =1.54

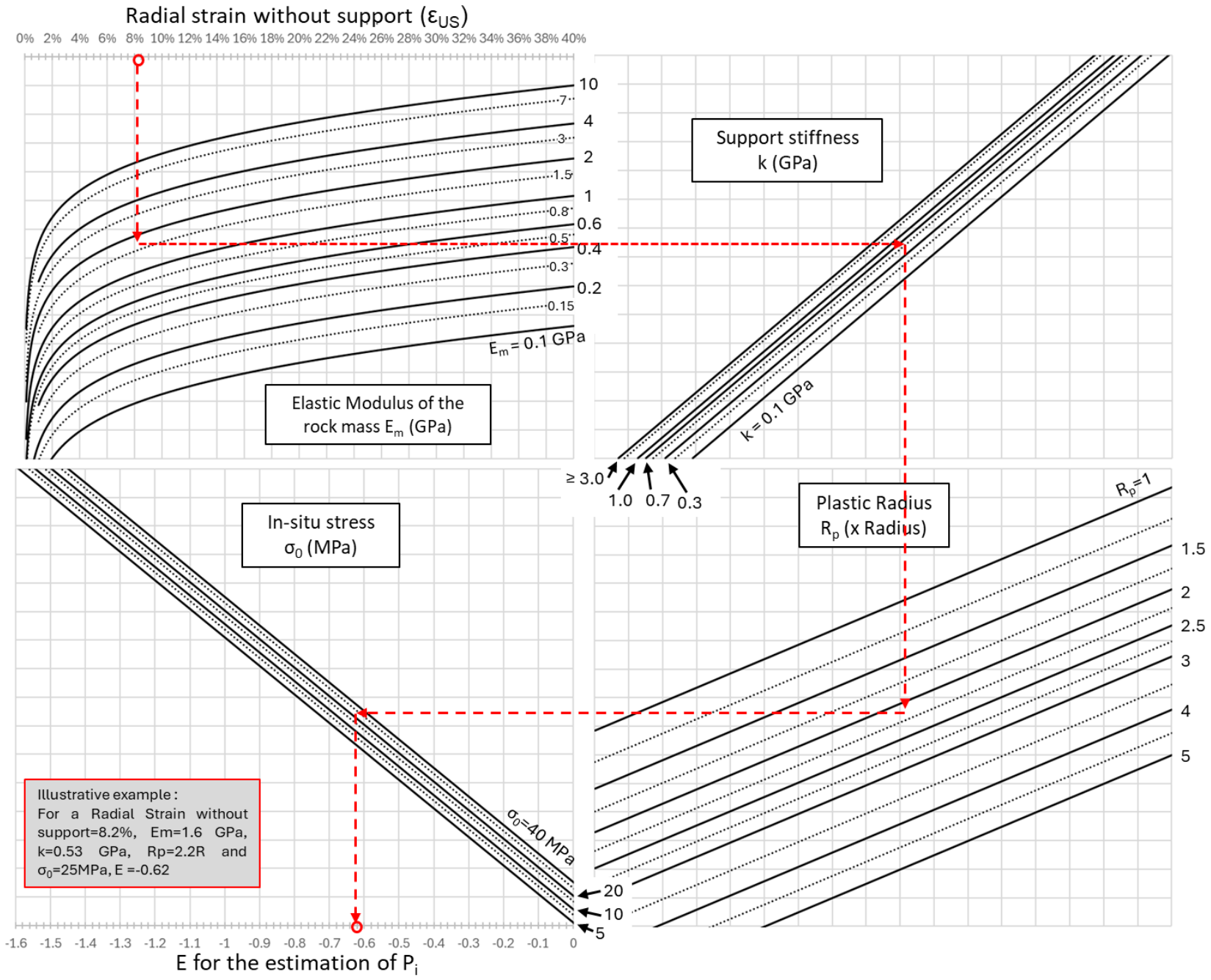
Radial strain without support (ε_{US})
0% 2% 4% 6% 8% 10% 12% 14% 16% 18% 20% 22% 24% 26% 28% 30% 32% 34% 36% 38% 40%
10
7
4
3
2
1.5
1
0.8
0.6
0.5
0.4
0.3
0.2
0.15
E_m = 0.1 GPa
Elastic Modulus of the rock mass E_m (GPa)
Support stiffness k (GPa)
k = 0.1 GPa
≥ 3.0
1.0
0.7
0.3
In-situ stress σ_0 (MPa)
σ_0=40 MPa
20
10
5
Plastic Radius R_p (x Radius)
R_p=1
1.5
2
2.5
3
4
5
Illustrative example :
For a Radial Strain without support=8.2%, Em=1.6 GPa, k=0.53 GPa, Rp=2.2R and σ_0=25MPa, E =-0.62
-1.6 -1.5 -1.4 -1.3 -1.2 -1.1 -1 -0.9 -0.8 -0.7 -0.6 -0.5 -0.4 -0.3 -0.2 -0.1 0
E for the estimation of P_i

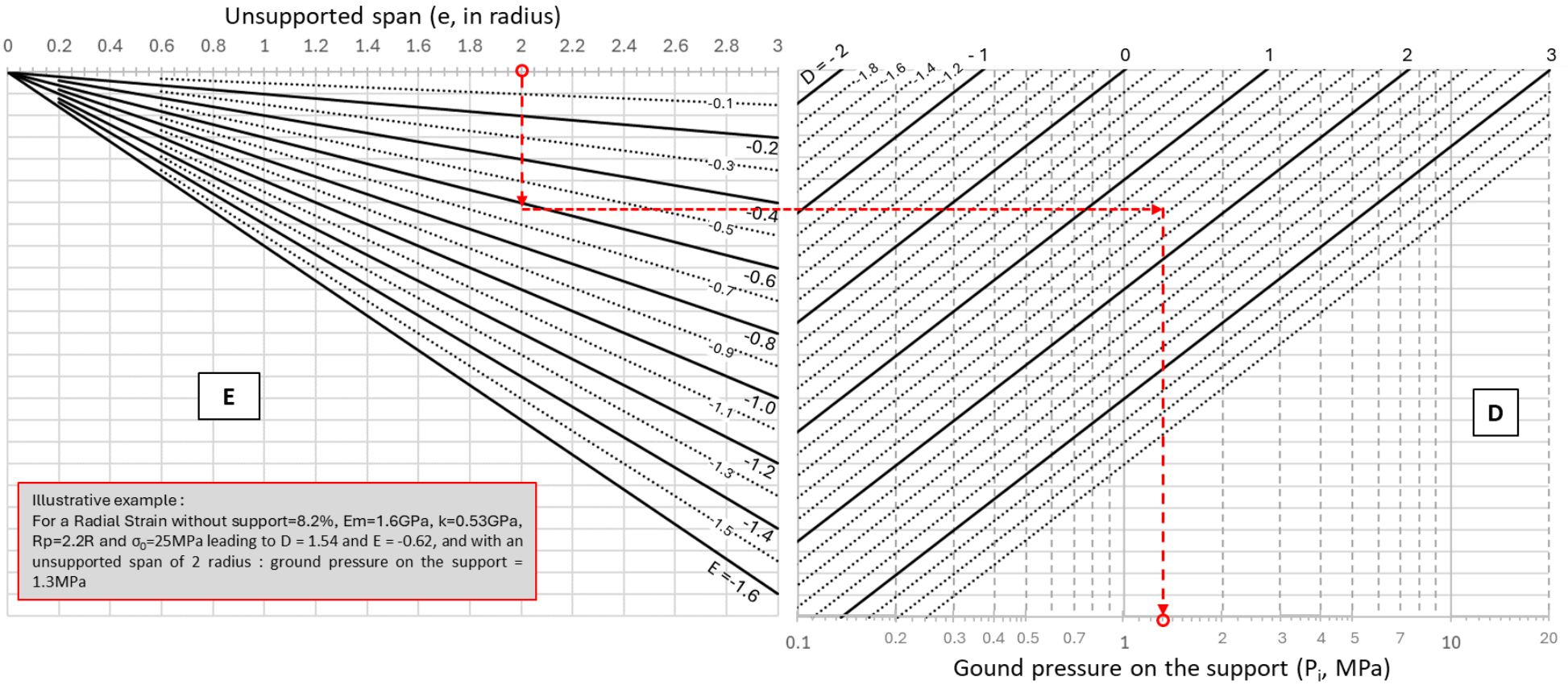
Unsupported span (e, in radius)
0 0.2 0.4 0.6 0.8 1 1.2 1.4 1.6 1.8 2 2.2 2.4 2.6 2.8 3
-0.1
-0.2
-0.3
-0.4
-0.5
-0.6
-0.7
-0.8
-0.9
-1.0
-1.1
-1.2
-1.3
-1.4
-1.5
E=-1.6
E
Illustrative example :
For a Radial Strain without support=8.2%, Em=1.6GPa, k=0.53GPa, Rp=2.2R and σ0=25MPa leading to D = 1.54 and E = -0.62, and with an unsupported span of 2 radius : ground pressure on the support = 1.3MPa
D= -2
-1.8
-1.6
-1.4
-1.2
- 1
0
1
2
3
D
0.1 0.2 0.3 0.4 0.5 0.7 1 2 3 4 5 7 10 20
Gound pressure on the support (Pi, MPa)

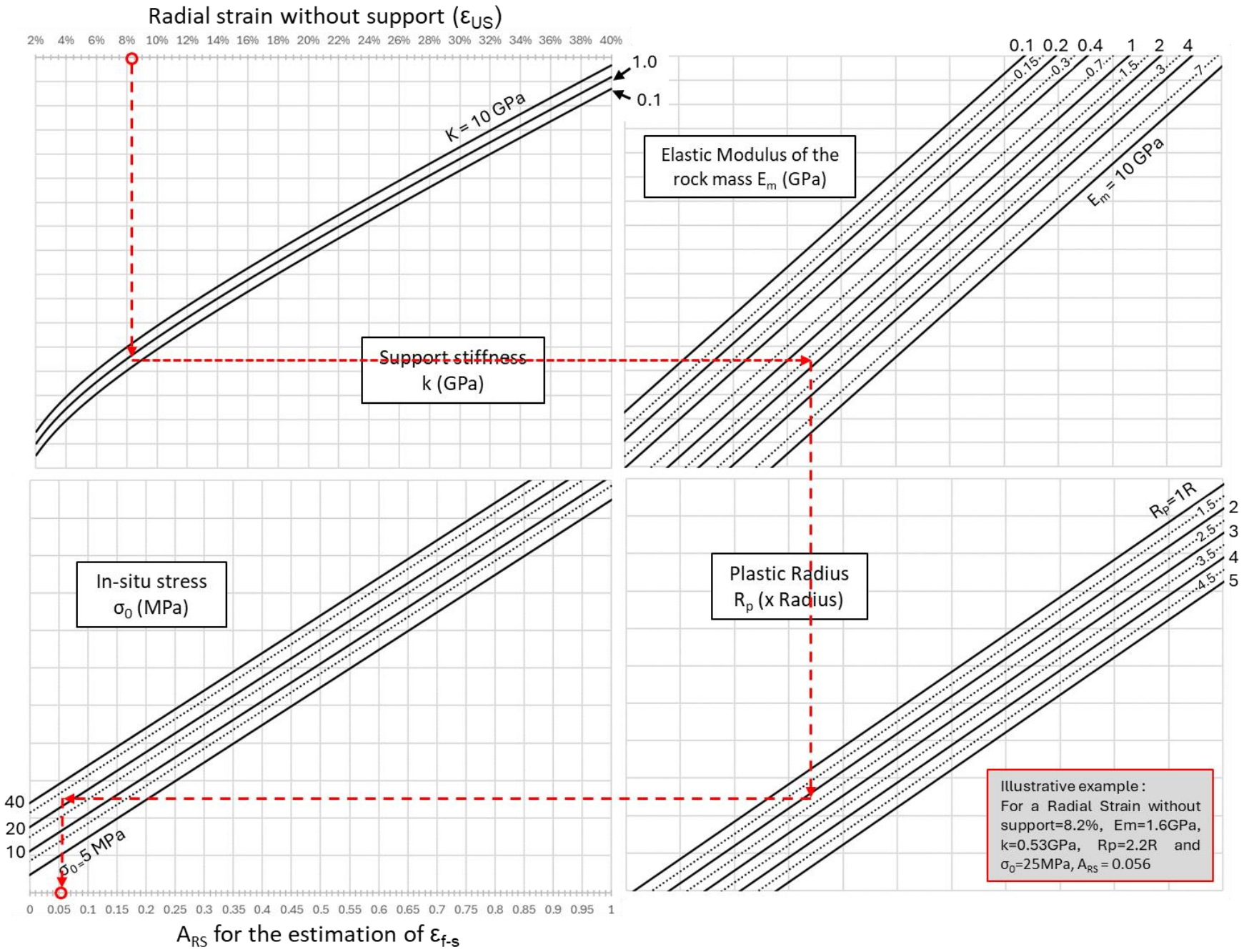
Radial strain without support (ε_{US})
2% 4% 6% 8% 10% 12% 14% 16% 18% 20% 22% 24% 26% 28% 30% 32% 34% 36% 38% 40%
1.0
0.1
K = 10 GPa
Support stiffness
k (GPa)
0.1 0.2 0.4 1 2 4
0.15 0.3 0.7 1.5 3 7
E_m = 10 GPa
Elastic Modulus of the
rock mass E_m (GPa)
In-situ stress
σ_0 (MPa)
40
20
10
σ_0=5 MPa
0 0.05 0.1 0.15 0.2 0.25 0.3 0.35 0.4 0.45 0.5 0.55 0.6 0.65 0.7 0.75 0.8 0.85 0.9 0.95 1
A_{RS} for the estimation of ε_{f-s}
R_p=1R
1.5
2.5
3.5
4.5
2
3
4
5
Plastic Radius
R_p (x Radius)
Illustrative example :
For a Radial Strain without support=8.2%, Em=1.6GPa, k=0.53GPa, Rp=2.2R and σ_0=25MPa, A_{RS} = 0.056

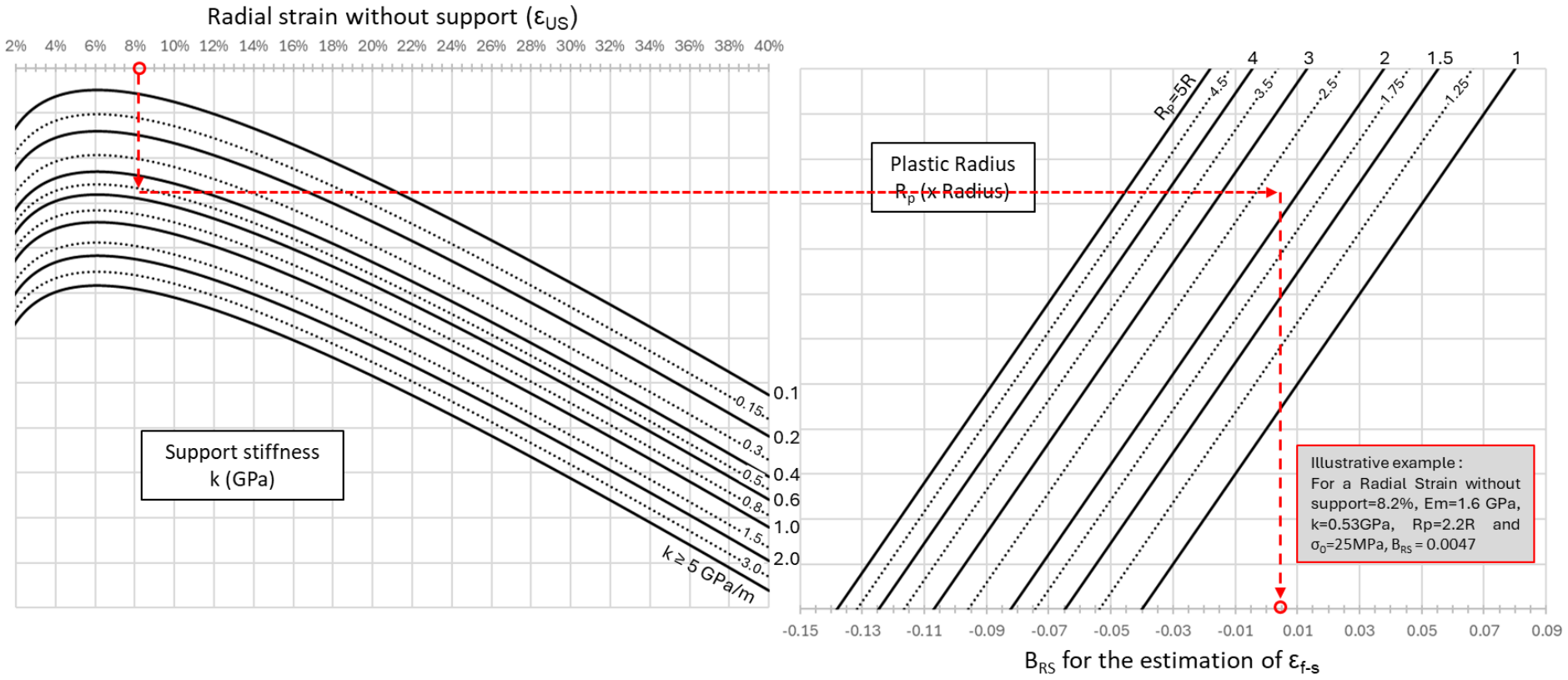
Radial strain without support (ε_{US})
2% 4% 6% 8% 10% 12% 14% 16% 18% 20% 22% 24% 26% 28% 30% 32% 34% 36% 38% 40%
Support stiffness k (GPa)
0.1
0.2
0.4
0.6
1.0
2.0
k ≥ 5 GPa/m
Plastic Radius R_p (x Radius)
R_p=5R
4.5
4
3.5
3
2.5
2
1.75
1.5
1.25
1
Illustrative example :
For a Radial Strain without support=8.2%, Em=1.6 GPa, k=0.53GPa, Rp=2.2R and σ_0=25MPa, B_{RS} = 0.0047
-0.15 -0.13 -0.11 -0.09 -0.07 -0.05 -0.03 -0.01 0.01 0.03 0.05 0.07 0.09
B_{RS} for the estimation of ε_{f-s}

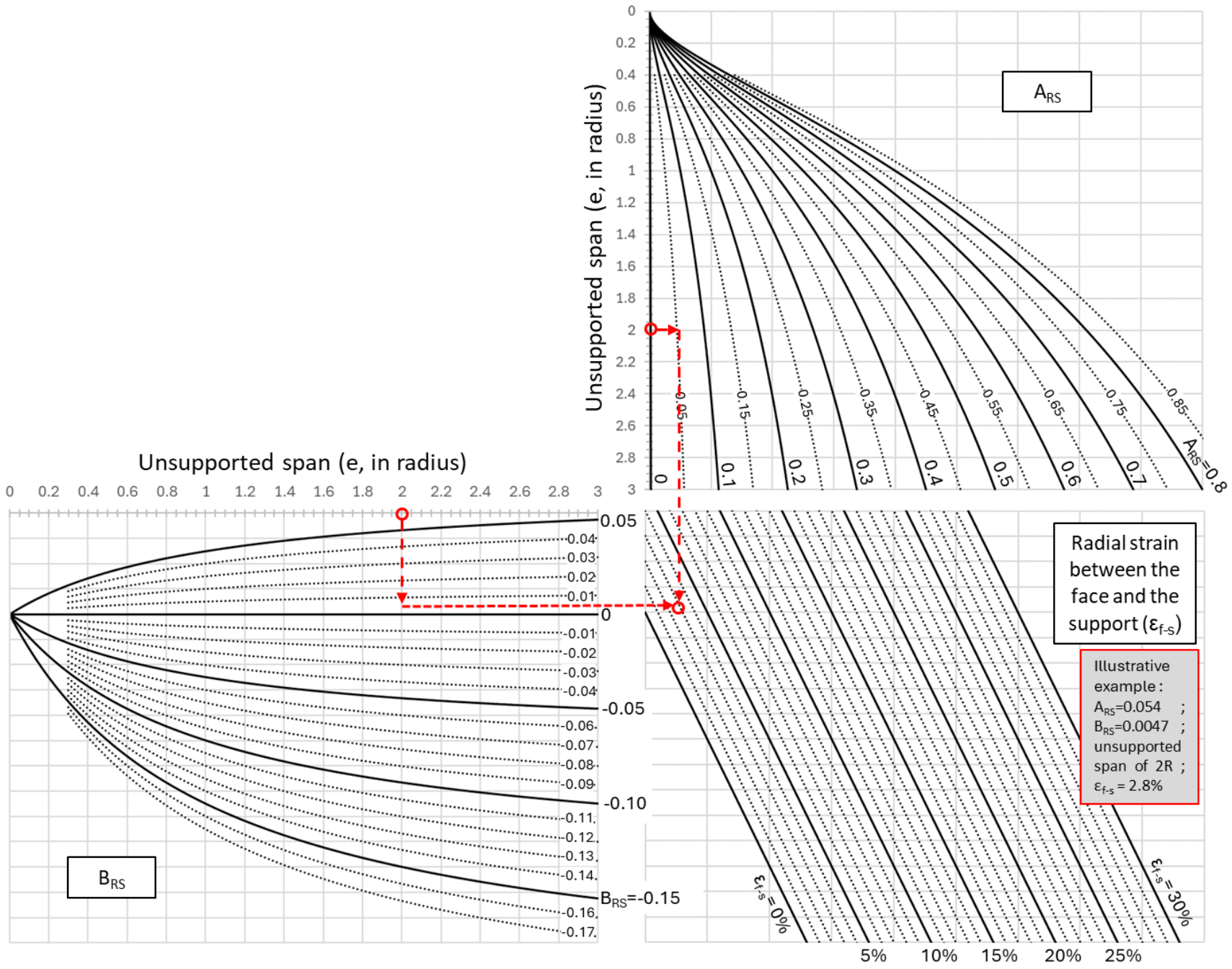
Unsupported span (e, in radius)
0 0.2 0.4 0.6 0.8 1 1.2 1.4 1.6 1.8 2 2.2 2.4 2.6 2.8 3
A_{RS}
0 0.05 0.1 0.15 0.2 0.25 0.3 0.35 0.4 0.45 0.5 0.55 0.6 0.65 0.7 0.75 0.8 0.85 A_{RS}=0.8
Unsupported span (e, in radius)
0 0.2 0.4 0.6 0.8 1 1.2 1.4 1.6 1.8 2 2.2 2.4 2.6 2.8 3
B_{RS}
0.05 0.04 0.03 0.02 0.01 0 -0.01 -0.02 -0.03 -0.04 -0.05 -0.06 -0.07 -0.08 -0.09 -0.10 -0.11 -0.12 -0.13 -0.14 B_{RS}=-0.15 -0.16 -0.17
Radial strain between the face and the support ($\varepsilon_{f\text{-}s}$)
Illustrative example : A_{RS}=0.054 ; B_{RS}=0.0047 ; unsupported span of 2R ; $\varepsilon_{f\text{-}s}$ = 2.8%
$\varepsilon_{f\text{-}s}$ = 0%
$\varepsilon_{f\text{-}s}$ = 30%
5% 10% 15% 20% 25%

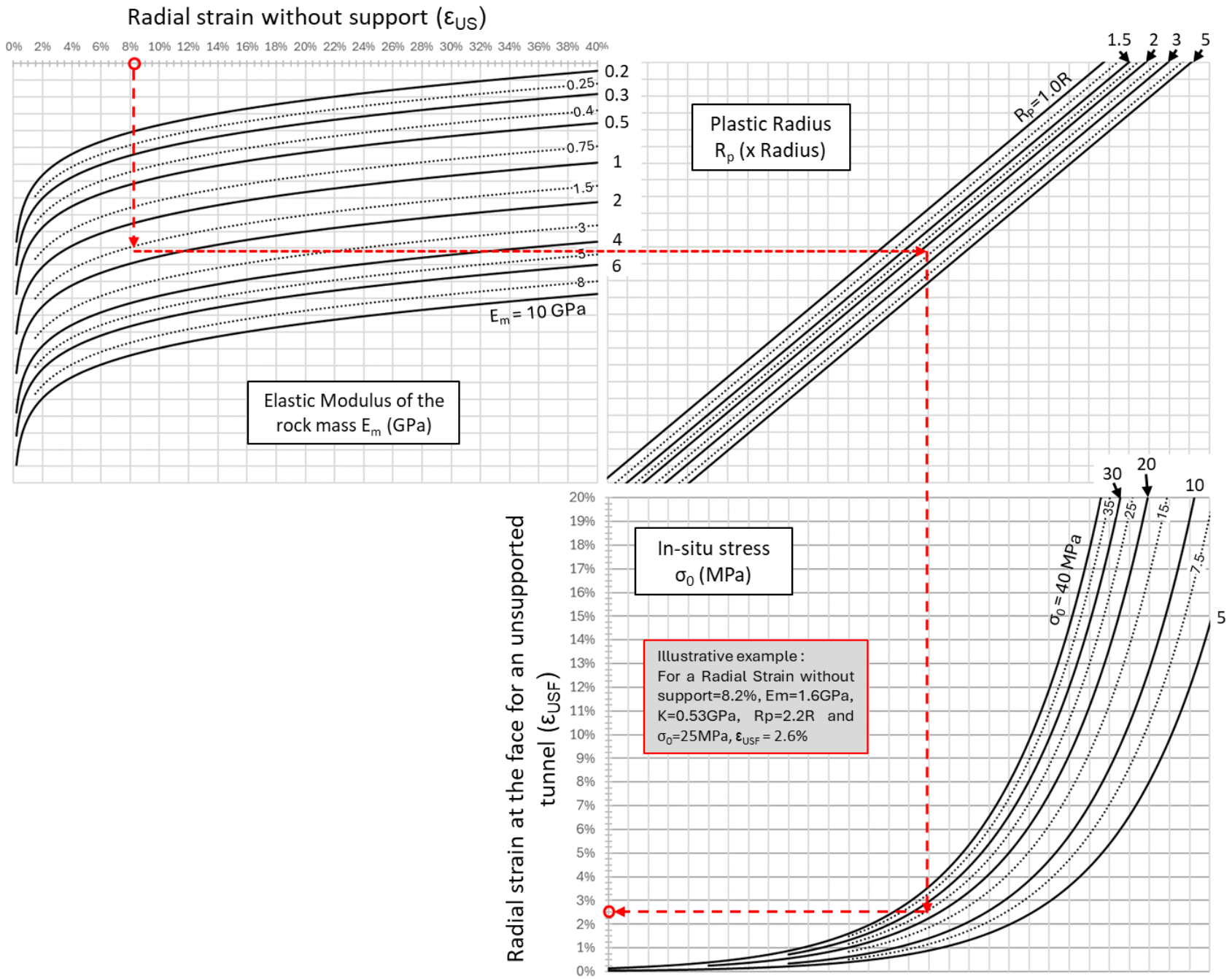
Radial strain without support (ε_{US})
0% 2% 4% 6% 8% 10% 12% 14% 16% 18% 20% 22% 24% 26% 28% 30% 32% 34% 36% 38% 40%
0.2
0.25
0.3
0.4
0.5
0.75
1
1.5
2
3
4
5
6
8
E_m = 10 GPa
Elastic Modulus of the rock mass E_m (GPa)
Plastic Radius R_p (x Radius)
1.5 2 3 5
R_p=1.0R
Radial strain at the face for an unsupported tunnel (ε_{USF})
20% 19% 18% 17% 16% 15% 14% 13% 12% 11% 10% 9% 8% 7% 6% 5% 4% 3% 2% 1% 0%
In-situ stress σ_0 (MPa)
30 20 10
35
25
15
7.5
5
σ_0 = 40 MPa
Illustrative example :
For a Radial Strain without support=8.2%, Em=1.6GPa, K=0.53GPa, Rp=2.2R and σ_0=25MPa, ε_{USF} = 2.6%

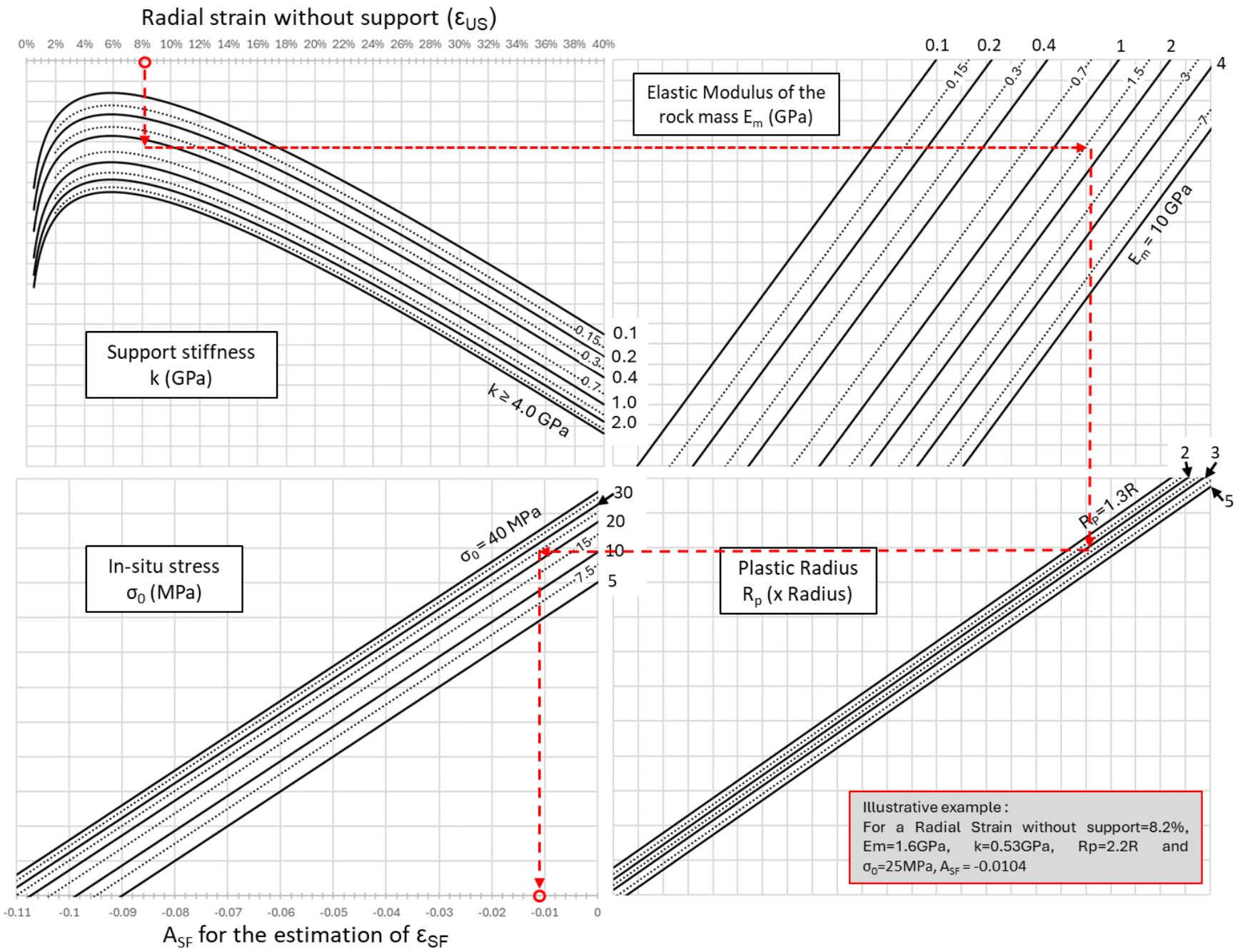
Radial strain without support (ε_{US})
0% 2% 4% 6% 8% 10% 12% 14% 16% 18% 20% 22% 24% 26% 28% 30% 32% 34% 36% 38% 40%
Support stiffness k (GPa)
0.1
0.2
0.4
1.0
2.0
k ≥ 4.0 GPa
Elastic Modulus of the rock mass E_m (GPa)
0.1 0.2 0.4 1 2 4
E_m = 10 GPa
In-situ stress σ_0 (MPa)
30
20
10
5
σ_0 = 40 MPa
Plastic Radius R_p (x Radius)
2 3 5
R_p=1.3R
-0.11 -0.1 -0.09 -0.08 -0.07 -0.06 -0.05 -0.04 -0.03 -0.02 -0.01 0
A_{SF} for the estimation of ε_{SF}
Illustrative example :
For a Radial Strain without support=8.2%, Em=1.6GPa, k=0.53GPa, Rp=2.2R and σ_0=25MPa, A_{SF} = -0.0104

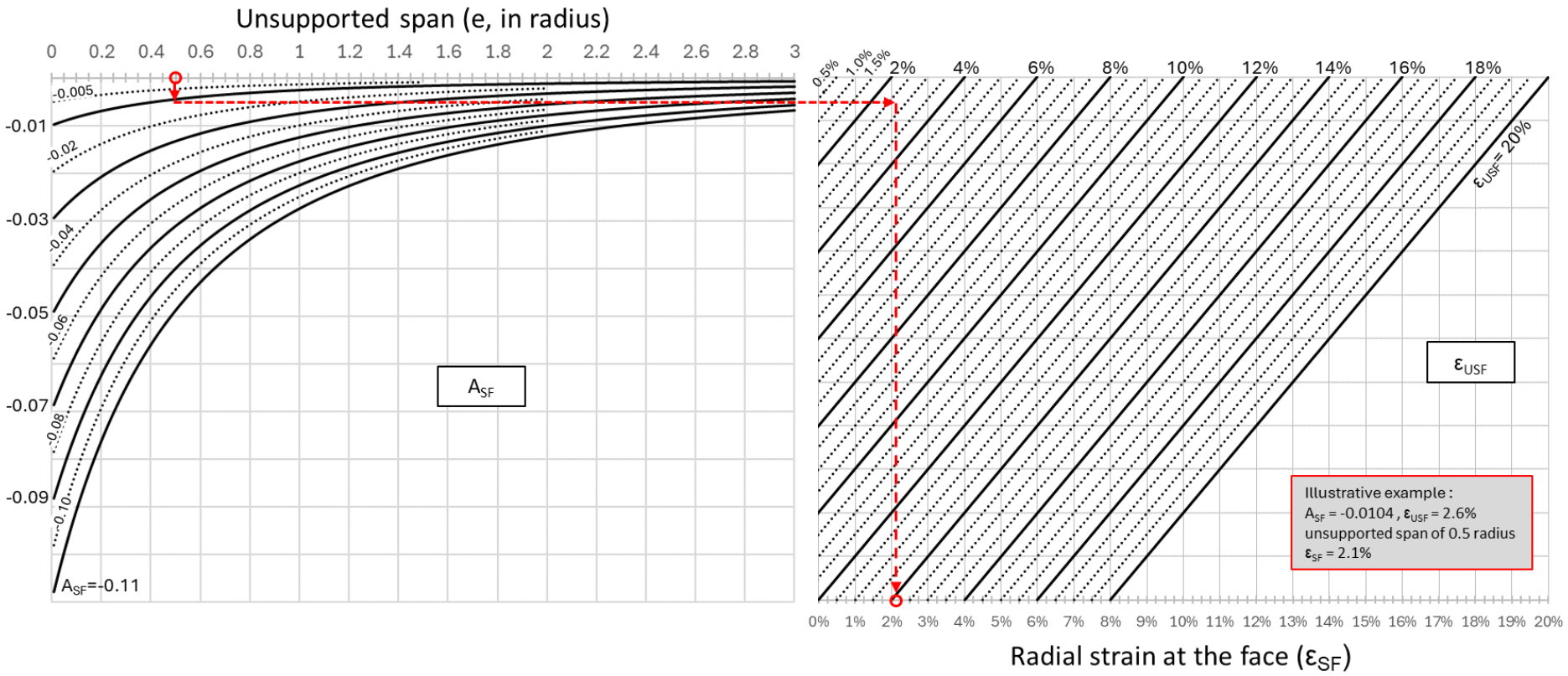
Unsupported span (e, in radius)
0 0.2 0.4 0.6 0.8 1 1.2 1.4 1.6 1.8 2 2.2 2.4 2.6 2.8 3
-0.005
-0.01
-0.02
-0.03
-0.04
-0.05
-0.06
-0.07
-0.08
-0.09
-0.10
A_SF=-0.11
A_SF
0.5% 1.0% 1.5% 2% 4% 6% 8% 10% 12% 14% 16% 18%
ε_USF= 20%
ε_USF
Illustrative example :
A_SF = -0.0104 , ε_USF = 2.6%
unsupported span of 0.5 radius
ε_SF = 2.1%
0% 1% 2% 3% 4% 5% 6% 7% 8% 9% 10% 11% 12% 13% 14% 15% 16% 17% 18% 19% 20%
Radial strain at the face (ε_SF)

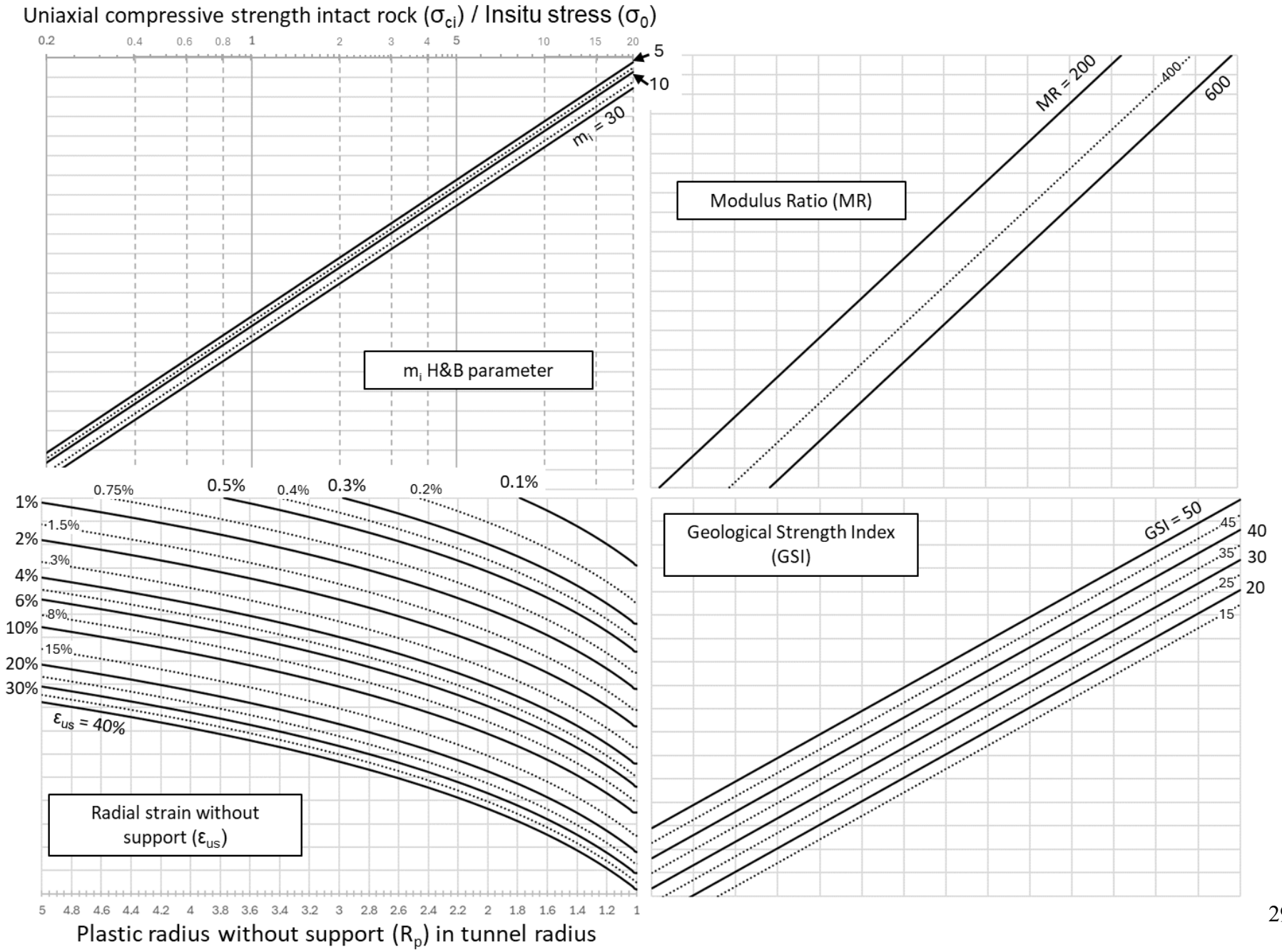
Uniaxial compressive strength intact rock (σ_{ci}) / Insitu stress (σ_0)
0.2
0.4
0.6
0.8
1
2
3
4
5
10
15
20
5
10
m_i = 30
m_i H&B parameter
MR = 200
400
600
Modulus Ratio (MR)
0.75%
0.5%
0.4%
0.3%
0.2%
0.1%
1%
1.5%
2%
3%
4%
6%
8%
10%
15%
20%
30%
ε_{us} = 40%
Radial strain without support (ε_{us})
Geological Strength Index (GSI)
GSI = 50
45
40
35
30
25
20
15
5
4.8
4.6
4.4
4.2
4
3.8
3.6
3.4
3.2
3
2.8
2.6
2.4
2.2
2
1.8
1.6
1.4
1.2
1
Plastic radius without support (R_p) in tunnel radius

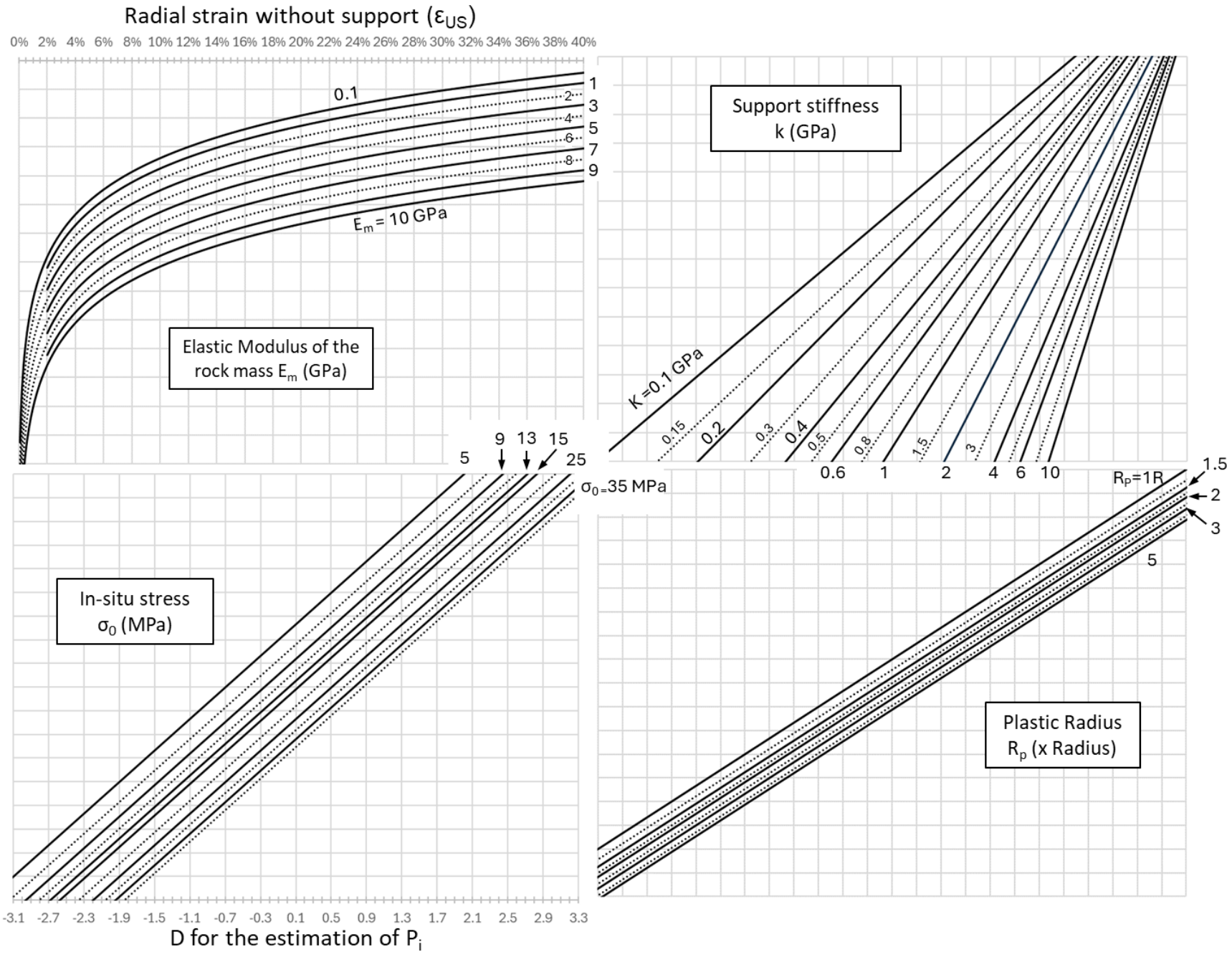
Radial strain without support (ε_{US})
0% 2% 4% 6% 8% 10% 12% 14% 16% 18% 20% 22% 24% 26% 28% 30% 32% 34% 36% 38% 40%
0.1
1
2
3
4
5
6
7
8
9
E_m = 10 GPa
Elastic Modulus of the rock mass E_m (GPa)
Support stiffness k (GPa)
K=0.1 GPa
0.15
0.2
0.3
0.4
0.5
0.6
0.8
1
1.5
2
3
4
6
10
5
9
13
15
25
σ_0=35 MPa
In-situ stress σ_0 (MPa)
R_P=1R
1.5
2
3
5
Plastic Radius R_p (x Radius)
-3.1 -2.7 -2.3 -1.9 -1.5 -1.1 -0.7 -0.3 0.1 0.5 0.9 1.3 1.7 2.1 2.5 2.9 3.3
D for the estimation of P_i

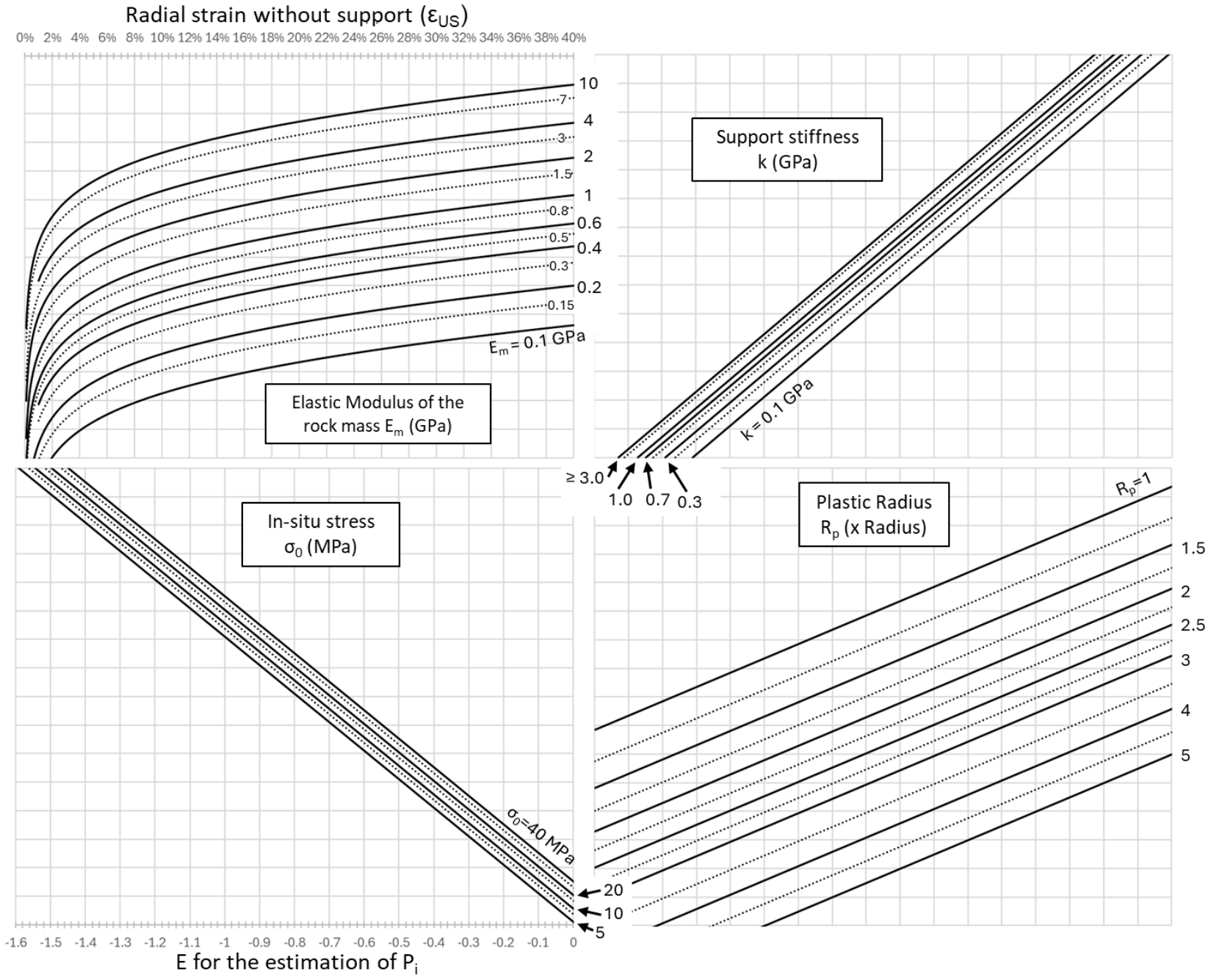
Radial strain without support (ε_{US})
0% 2% 4% 6% 8% 10% 12% 14% 16% 18% 20% 22% 24% 26% 28% 30% 32% 34% 36% 38% 40%
10
7
4
3
2
1.5
1
0.8
0.6
0.5
0.4
0.3
0.2
0.15
E_m = 0.1 GPa
Elastic Modulus of the rock mass E_m (GPa)
Support stiffness k (GPa)
k = 0.1 GPa
≥ 3.0
1.0
0.7
0.3
In-situ stress σ_0 (MPa)
σ_0=40 MPa
20
10
5
-1.6 -1.5 -1.4 -1.3 -1.2 -1.1 -1 -0.9 -0.8 -0.7 -0.6 -0.5 -0.4 -0.3 -0.2 -0.1 0
E for the estimation of P_i
Plastic Radius R_p (x Radius)
R_p=1
1.5
2
2.5
3
4
5

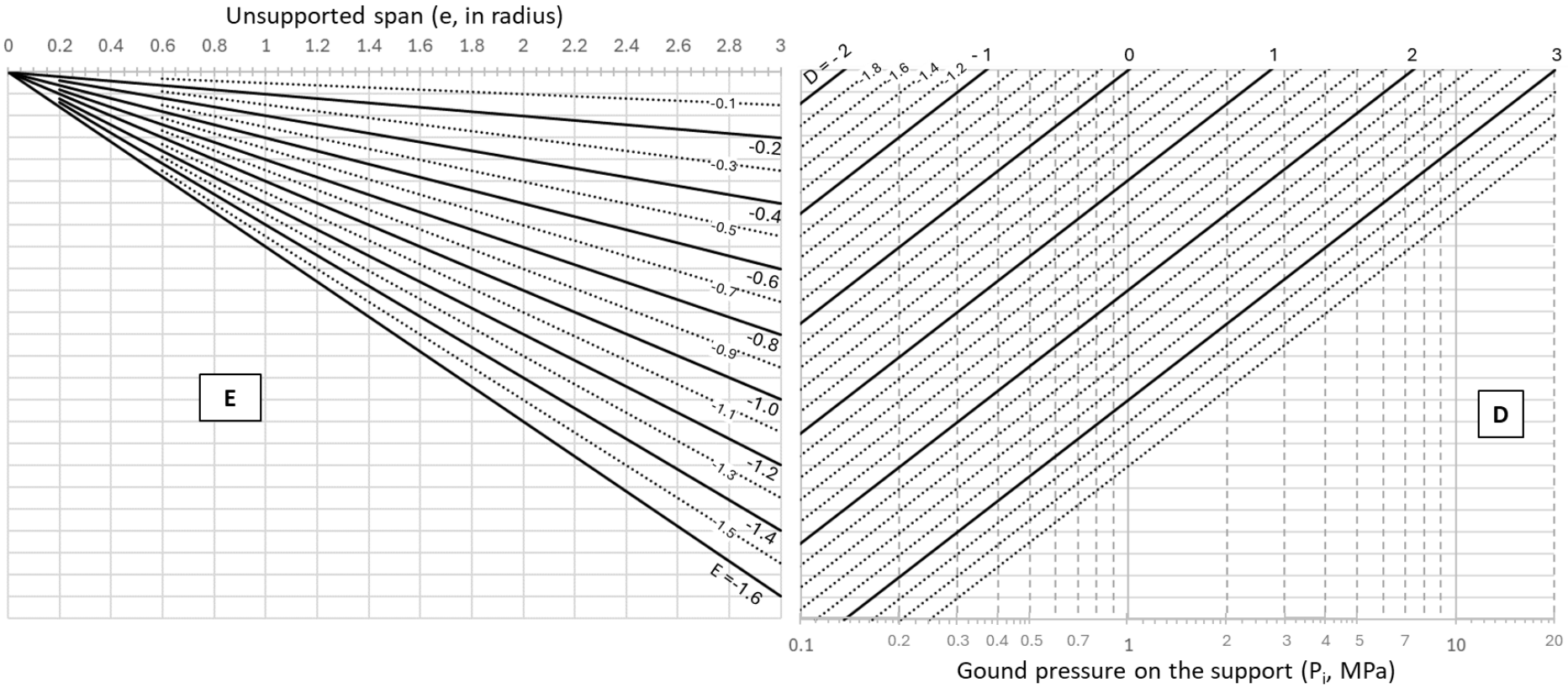
Unsupported span (e, in radius)
0 0.2 0.4 0.6 0.8 1 1.2 1.4 1.6 1.8 2 2.2 2.4 2.6 2.8 3
-0.1
-0.2
-0.3
-0.4
-0.5
-0.6
-0.7
-0.8
-0.9
-1.0
-1.1
-1.2
-1.3
-1.4
-1.5
E =-1.6
E
D = - 2
-1.8
-1.6
-1.4
-1.2
- 1
0
1
2
3
D
0.1 0.2 0.3 0.4 0.5 0.7 1 2 3 4 5 7 10 20
Gound pressure on the support (Pi, MPa)

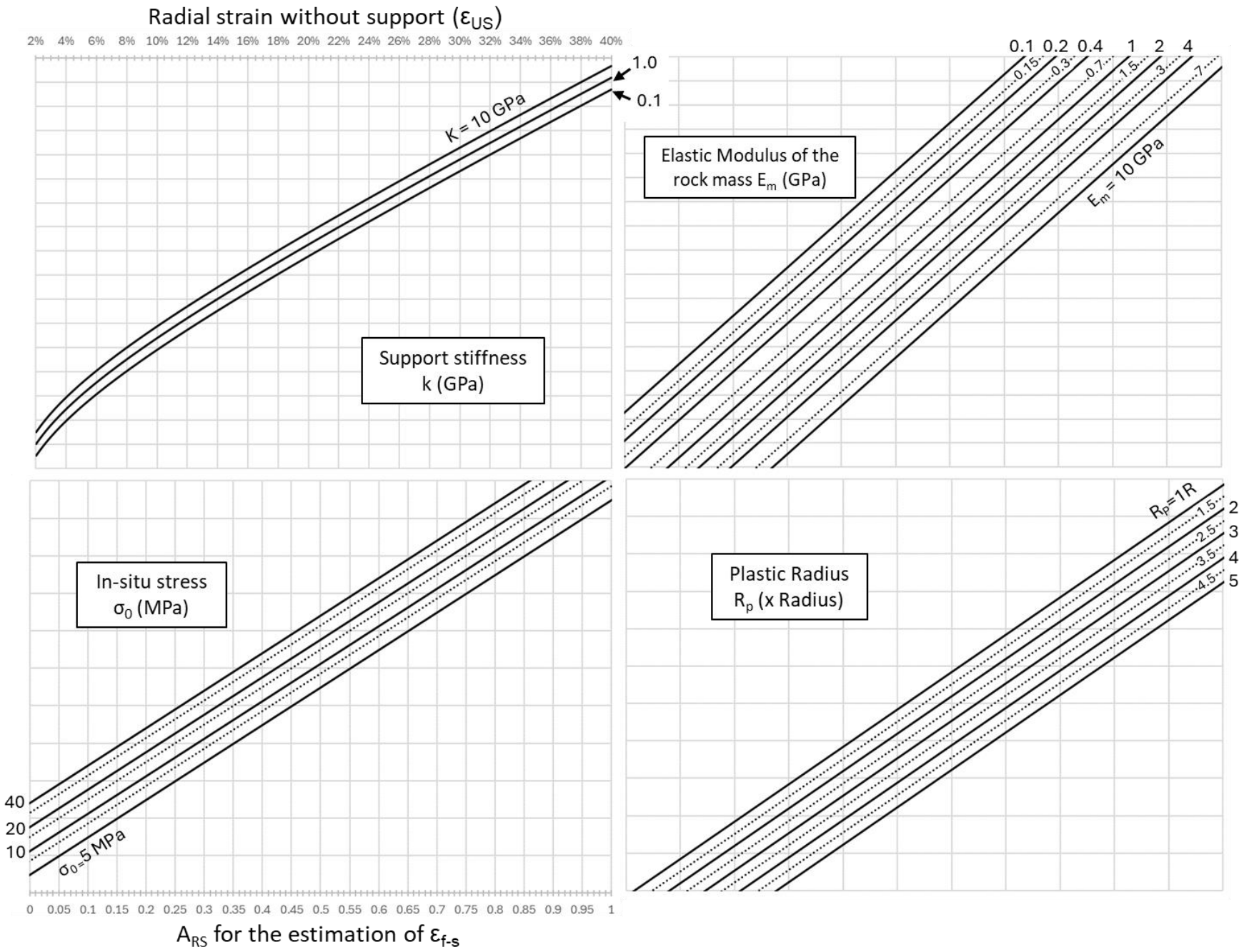
Radial strain without support (ε_{US})
2% 4% 6% 8% 10% 12% 14% 16% 18% 20% 22% 24% 26% 28% 30% 32% 34% 36% 38% 40%
1.0
0.1
K = 10 GPa
Support stiffness k (GPa)
0.1 0.2 0.4 1 2 4
0.15 0.3 0.7 1.5 3 7
Elastic Modulus of the rock mass E_m (GPa)
E_m = 10 GPa
40
20
10
In-situ stress σ_0 (MPa)
σ_0=5 MPa
0 0.05 0.1 0.15 0.2 0.25 0.3 0.35 0.4 0.45 0.5 0.55 0.6 0.65 0.7 0.75 0.8 0.85 0.9 0.95 1
A_{RS} for the estimation of $\varepsilon_{f\text{-}s}$
R_p=1R
1.5
2
2.5
3
3.5
4
4.5
5
Plastic Radius R_p (x Radius)

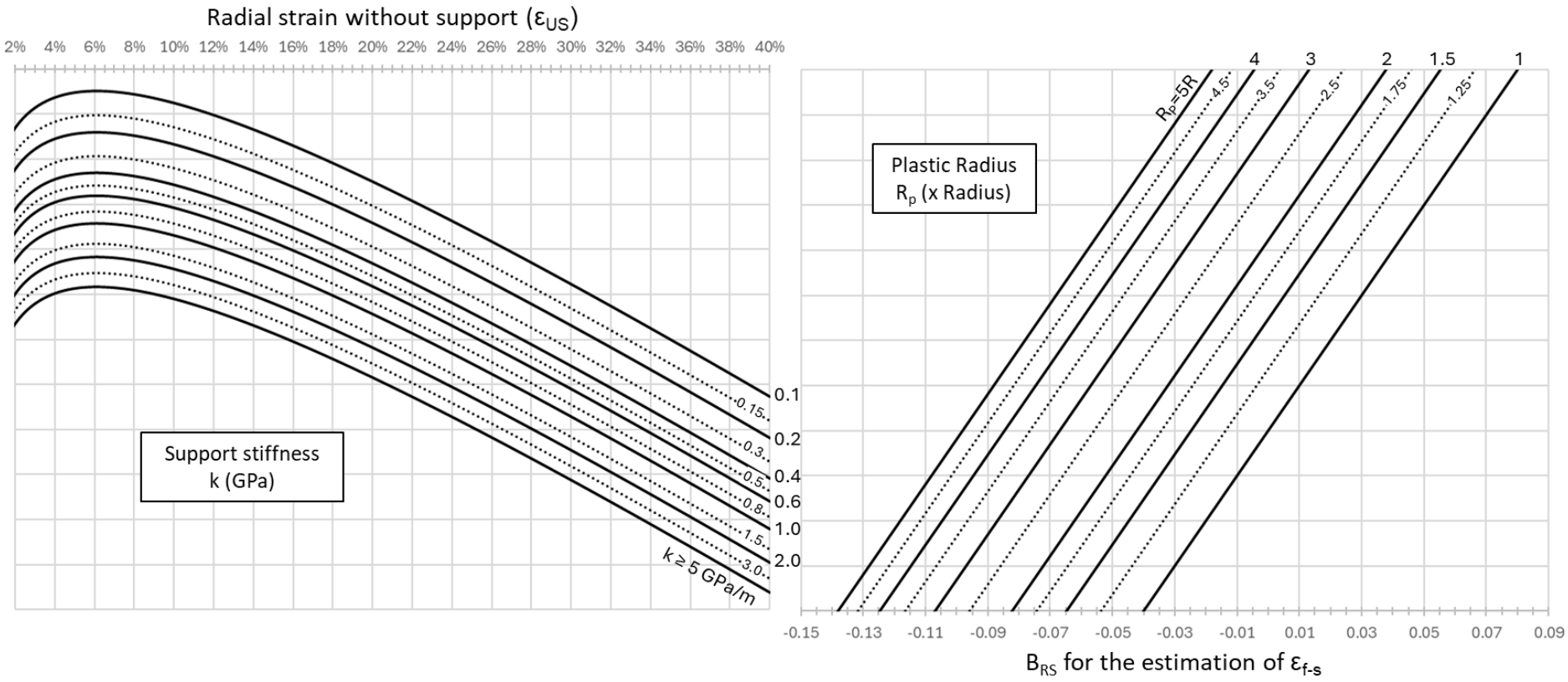
Radial strain without support (ε_{US})
2% 4% 6% 8% 10% 12% 14% 16% 18% 20% 22% 24% 26% 28% 30% 32% 34% 36% 38% 40%
Support stiffness
k (GPa)
0.1
0.2
0.4
0.6
1.0
2.0
0.15
0.3
0.5
0.8
1.5
3.0
k ≥ 5 GPa/m
Plastic Radius
R_p (x Radius)
R_p=5R
4.5
4
3.5
3
2.5
2
1.75
1.5
1.25
1
-0.15 -0.13 -0.11 -0.09 -0.07 -0.05 -0.03 -0.01 0.01 0.03 0.05 0.07 0.09
B_{RS} for the estimation of $\varepsilon_{f\text{-}s}$

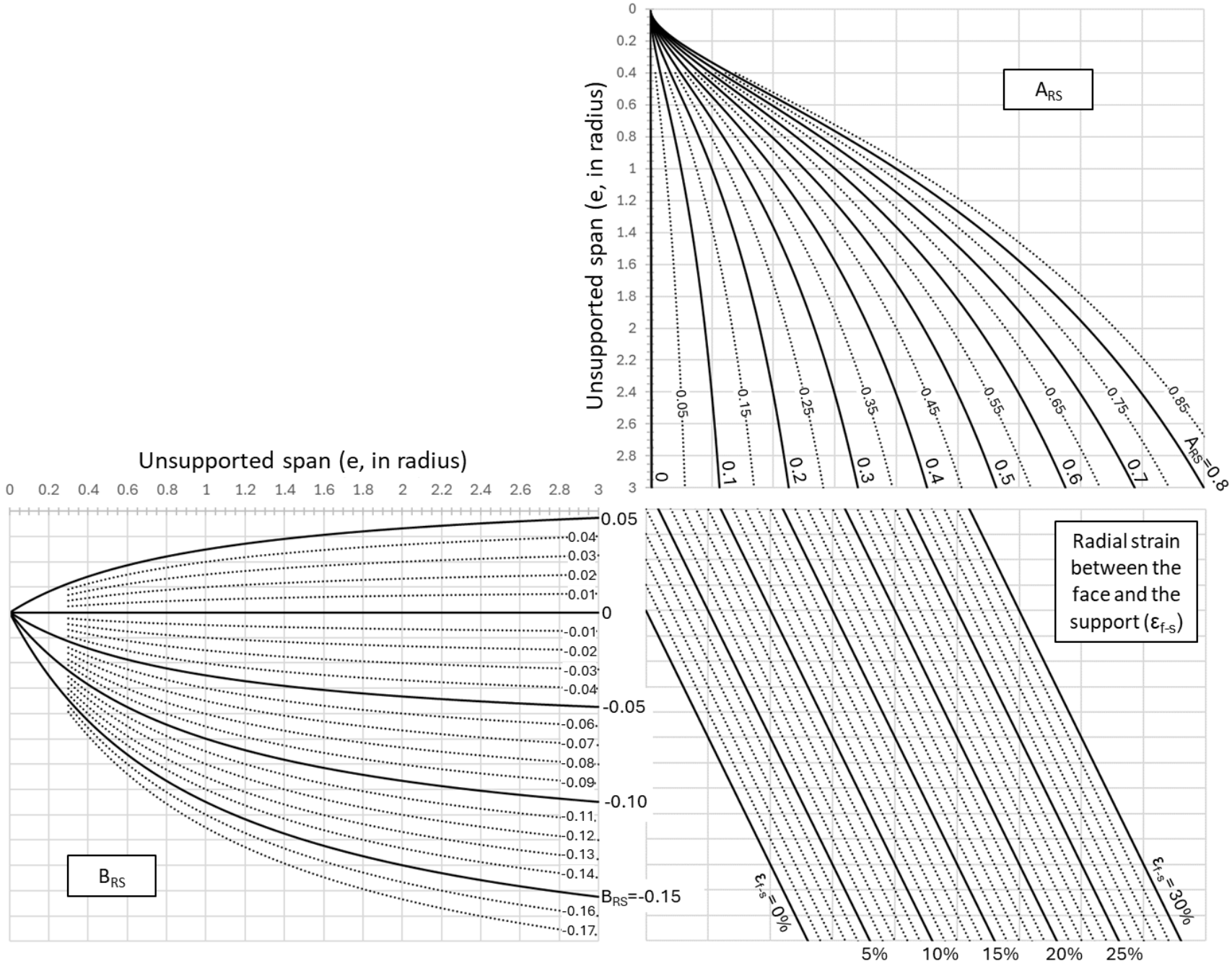
Unsupported span (e, in radius)
0 0.2 0.4 0.6 0.8 1 1.2 1.4 1.6 1.8 2 2.2 2.4 2.6 2.8 3
A_RS
0 0.05 0.1 0.15 0.2 0.25 0.3 0.35 0.4 0.45 0.5 0.55 0.6 0.65 0.7 0.75 0.85
A_RS=0.8
Unsupported span (e, in radius)
0 0.2 0.4 0.6 0.8 1 1.2 1.4 1.6 1.8 2 2.2 2.4 2.6 2.8 3
B_RS
0.05 0.04 0.03 0.02 0.01 0 -0.01 -0.02 -0.03 -0.04 -0.05 -0.06 -0.07 -0.08 -0.09 -0.10 -0.11 -0.12 -0.13 -0.14 B_RS=-0.15 -0.16 -0.17
Radial strain between the face and the support (ε_f-s)
ε_f-s = 0%
ε_f-s = 30%
5% 10% 15% 20% 25%

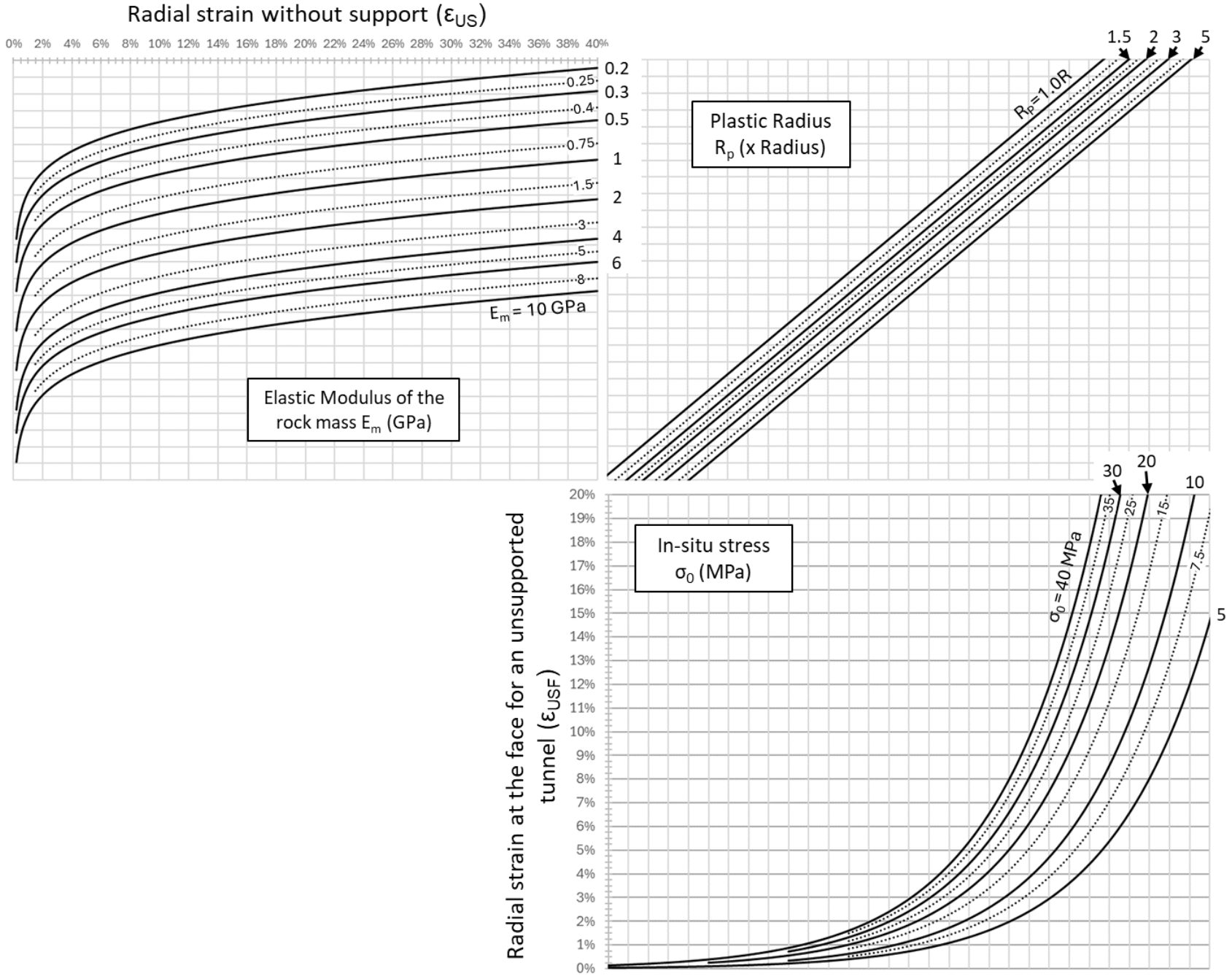
Radial strain without support (εUS)
0% 2% 4% 6% 8% 10% 12% 14% 16% 18% 20% 22% 24% 26% 28% 30% 32% 34% 36% 38% 40%
0.2
0.25
0.3
0.4
0.5
0.75
1
1.5
2
3
4
5
6
8
Em = 10 GPa
Elastic Modulus of the rock mass Em (GPa)
Plastic Radius Rp (x Radius)
Rp=1.0R
1.5 2 3 5
In-situ stress σ0 (MPa)
σ0 = 40 MPa
35
30
25
20
15
10
7.5
5
Radial strain at the face for an unsupported tunnel (εUSF)
20% 19% 18% 17% 16% 15% 14% 13% 12% 11% 10% 9% 8% 7% 6% 5% 4% 3% 2% 1% 0%

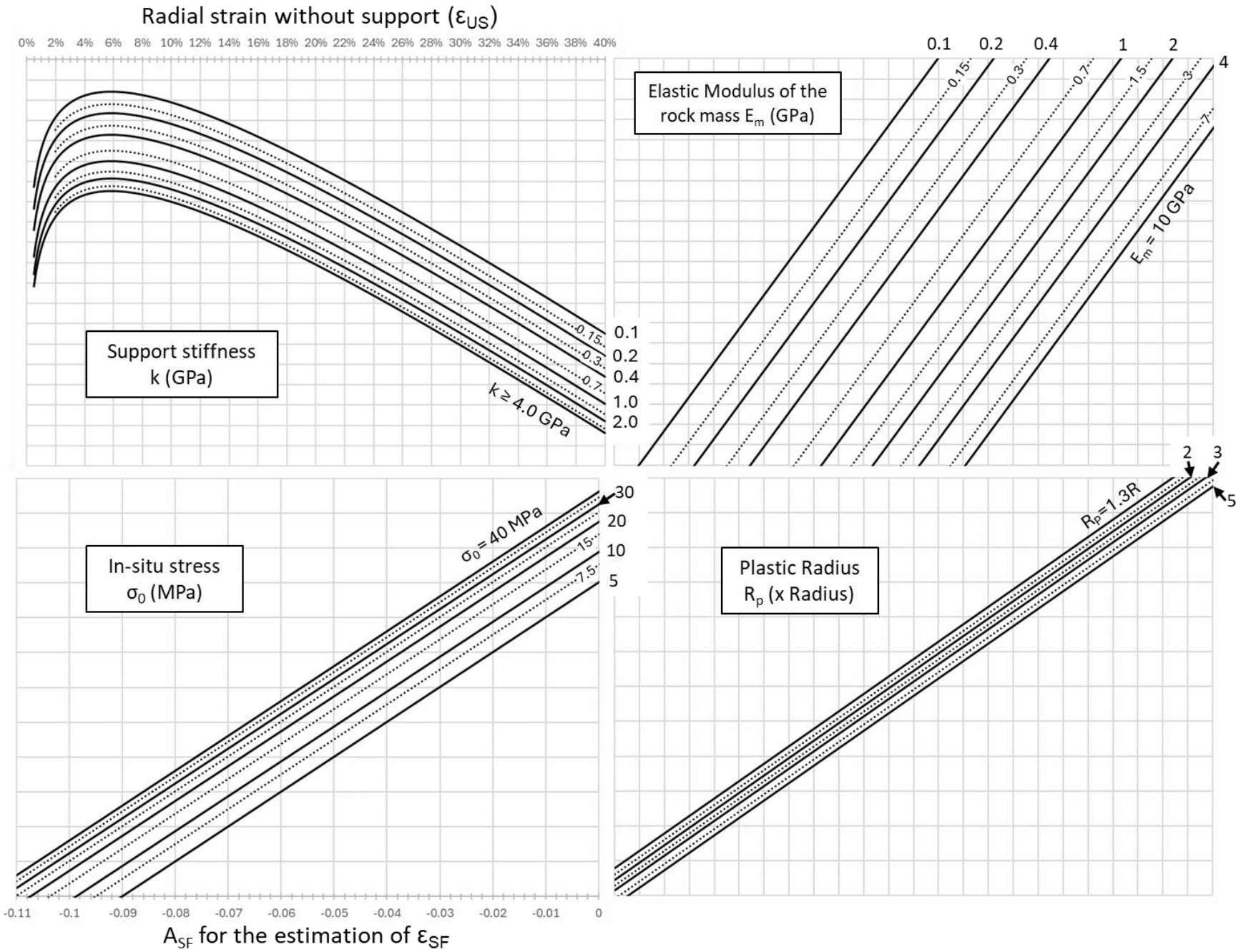
Radial strain without support (ε_{US})
0% 2% 4% 6% 8% 10% 12% 14% 16% 18% 20% 22% 24% 26% 28% 30% 32% 34% 36% 38% 40%
Support stiffness k (GPa)
0.15
0.3
0.7
k ≥ 4.0 GPa
0.1
0.2
0.4
1.0
2.0
Elastic Modulus of the rock mass E_m (GPa)
0.1 0.2 0.4 1 2 4
0.15
0.3
0.7
1.5
3
7
E_m = 10 GPa
In-situ stress σ_0 (MPa)
σ_0 = 40 MPa
15
7.5
30
20
10
5
Plastic Radius R_p (x Radius)
R_p=1.3R
2 3
5
-0.11 -0.1 -0.09 -0.08 -0.07 -0.06 -0.05 -0.04 -0.03 -0.02 -0.01 0
A_{SF} for the estimation of ε_{SF}

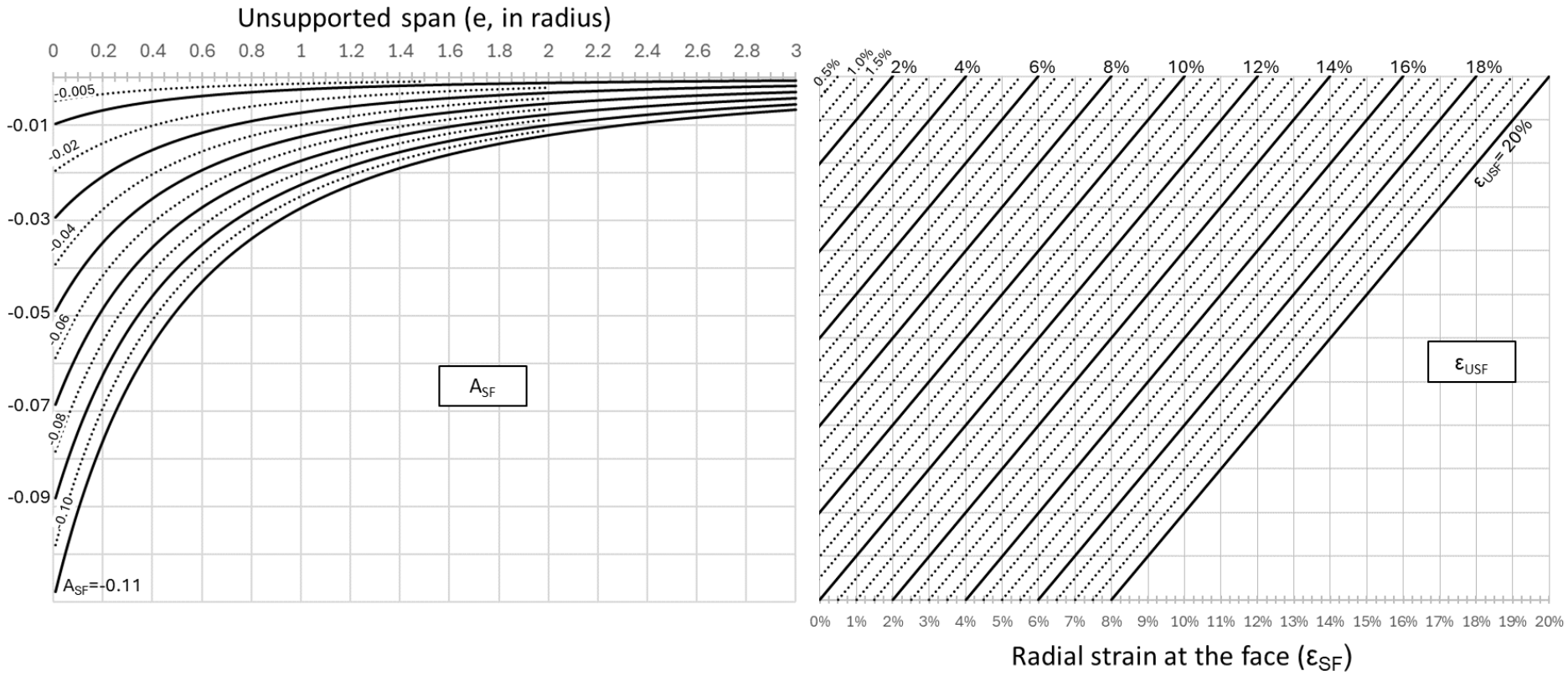
Unsupported span (e, in radius)
0 0.2 0.4 0.6 0.8 1 1.2 1.4 1.6 1.8 2 2.2 2.4 2.6 2.8 3
-0.005
-0.01
-0.02
-0.03
-0.04
-0.05
-0.06
-0.07
-0.08
-0.09
-0.10
A_SF=-0.11
A_SF
0.5%
1.0%
1.5%
2% 4% 6% 8% 10% 12% 14% 16% 18%
ε_USF= 20%
ε_USF
0% 1% 2% 3% 4% 5% 6% 7% 8% 9% 10% 11% 12% 13% 14% 15% 16% 17% 18% 19% 20%
Radial strain at the face (ε_SF)

Appendix 3 - Anisotropic stress state and equivalent isotropic stress

When speaking about anisotropic stress state and an equivalent isotropic stress to consider instead, there is one widely use formula (Russo 2014):

$$\sigma_0 = \frac{3\,\sigma_1 - \sigma_3}{2} \qquad (A3-1)$$

Where σ_1 and σ_3 are the major and minor principal stresses, and σ_0 is the equivalent isotropic stress.

This formula is obtained by considering that, for an elastic rock mass behavior, the maximal tangential stress at the tunnel boundary is equal in the anisotropic stress state and in equivalent isotropic stress. Based on Kirch's solution, the maximal tangential stress at a circular tunnel boundary in an elastic medium is $\sigma_{\theta max} = 3\,\sigma_1 - \sigma_3$. For an isotropic stress state, $\sigma_1 = \sigma_3 = \sigma_0$ leading to $\sigma_{\theta max} = 2\,\sigma_0$. The combination of these two formulas corresponds to Eq.(A3-1). In an elastic medium, Eq.(A3-1) also leads to the maximal radial strain at the tunnel boundary to be equal.

This formula is relevant for elastic medium, but it is possible to doubt its relevance in elastic-plastic medium. The development of plasticity will limit the maximal tangential stress at the tunnel boundary, while increasing the radial displacement. Considering the value proposed by Eq.(A4-1) can seem extreme as the equivalent isotropic stress is higher than the major principal stress.

2D plane strain numerical calculations are compared under anisotropic stress state and isotropic stress state to test the relevance of this hypothesis. More precisely, 8 geological situations leading to various values of plastic radius (from small plastic radius to large plastic radius) are considered and presented in Table 3-a. The calculations are performed with an anisotropic stress state, an equivalent isotropic stress state calculated with Eq.(A4-1), and an equivalent isotropic stress state equal to the major principal stress. The model considers a linear elastic perfectly plastic rock mass behavior with a generalized Hoek&Brown failure criterion. The 2D plane strain numerical model used is the one presented is Chapter 3.2.1. No support is considered. The MR is 400 and α is 0.2.

Table 3-a: Numerical calculations performed

σ_{ci}	m_i	GSI	σ_v	K_h (σ_h / σ_v)
80	20	40	10	0.7
80	20	40	10	1.3
80	20	20	10	0.7
80	20	20	10	1.3
40	10	40	20	0.7
40	10	40	20	1.3
40	10	20	20	0.7
40	10	20	20	1.3

The results are the minimal and maximal radial strain, and the minimal and maximal plastic radius for each situation (presented in Table 3-b).

Table 3-b: Results of the numerical calculations; red values are the maximal radial strain and plastic radius for the anisotropic stress state; ε_{ver}, ε_{hor} and ε_{mean} are the vertical radial strain, the horizontal radial stain and the mean radial strain

Anisotropic					**Isotropic maximal**		**Isotropic equivalent**	
ε_{ver}	**ε_{hor}**	**ε_{mean}**	**R_p ver**	**R_p hor**	**ε**	**Rp**	**ε**	**Rp**
0.32%	0.20%	0.27%	1.09	**1.19**	0.31%	1.19	0.38%	1.19
0.33%	**0.44%**	0.39%	**1.24**	1.14	0.44%	1.24	0.51%	1.24
1.48%	1.40%	1.44%	1.27	**1.57**	1.78%	1.47	2.20%	1.56
2.33%	2.21%	2.27%	**1.66**	1.41	2.67%	1.61	3.17%	1.65
2.62%	**3.92%**	3.27%	1.65	**2.47**	4.21%	2.27	5.53%	2.46
6.91%	4.73%	5.86%	**2.85**	1.98	7.08%	2.65	8.81%	2.79
20.73%	**33.87%**	27.52%	2.01	**4.19**	32.50%	3.43	39.11%	3.54
48.87%	32.52%	41.01%	**4.30**	2.42	45.14%	3.66	50.49%	3.66

Several remarks can be made:

- For an anisotropic stress state, the maximal deformation is not always in the same direction as the major principal stress. For elastic behavior, the maximal radial deformation is in the same direction because the tunnel geometry will ovalize. The maximal tangential stress is in the direction of the minimal in-situ principal stress leading to more important tangential deformation than radial deformation (influenced by Poisson's ratio). This tangential deformation creates the ovalization of the tunnel geometry (Figure 3-a). As the Poisson's ratio is always smaller than 0.5, the radial strain (ε_r) at the localization of the maximal tangential stress is always smaller than the tangential strain (ε_θ). For elastic-plastic behavior, it is more difficult to localize the position of the maximal radial strain because it will also be influenced by the amount of plasticity in the rock mass. Plasticity is generally associated with dilatancy increasing the radial strain. The larger the plastic radius is and the more radial deformation is associated with rock dilatancy, then the larger the radial strain is. As the results of the numerical calculation highlight (Table 3-b), small values of plastic radius leads to the maximal radial strain to be in the direction of the major principal strain, while for large plastic radius, the maximal radial strain is in the other direction. Dilatancy itself does not explain the change of localization of the maximal radial strain but it helps to increase the value of radial strain. The main reason for this change of direction is the amount of plasticity in the rock mass.
- Considering the equivalent isotropic stress obtained with Eq(A4-1), the maximal radial strain is higher than the maximal radial strain obtained with anisotropic calculations. For all situations except the last one, the radial strain is at least 15% higher (relative gap). The results of the last situation need to be carefully considered as it exceeds the model validity range (Chapter 3.2.1).
- Considering the equivalent isotropic stress equal to the maximal principal stress leads to a radial strain very similar to the one obtained with the anisotropic model.
- The plastic radius obtained with both isotropic models are similar to ones of the anisotropic model, except for large value, for which case they are closer to the mean plastic radius. It can be noted that the value of plastic radius is dependent on the mesh size, as the development of plasticity is the same for an entire mesh element.

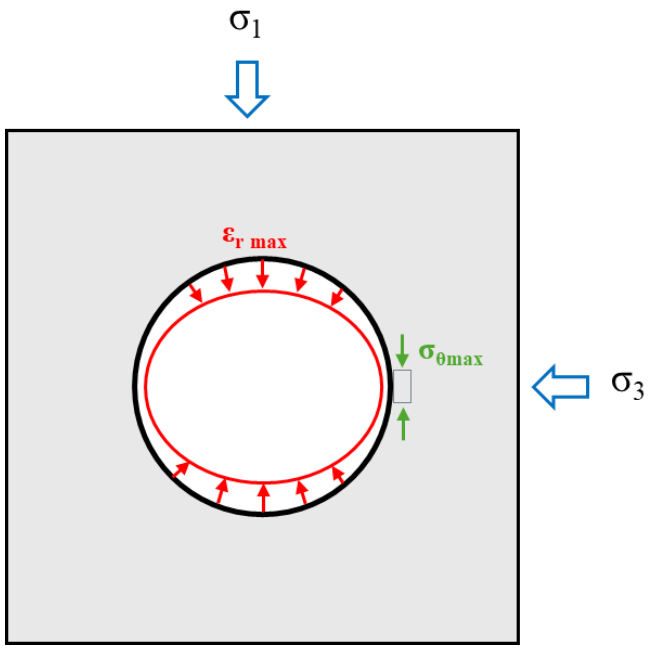

Figure 3-a: Ovalization of the tunnel geometry considering elastic behavior.

- When considering a support, the choice of the value of the equivalent isotropic stress can have some impact on the results. For example, if the following geological situation is considered: σ_{ci} = 70 MPa, m_i = 15, MR = 400, GSI = 30 and the in-situ stress state is anisotropic with a vertical stress of 15 MPa and a horizontal stress of 18 MPa. The support considered is a 20 cm thick shotcrete applied 2 m from the face and the tunnel radius is 4m. The surrogate models developed in Chapter 4.2.3.2 leads to a ground pressure on the support of 1.72 MPa (hypothesis: σ_0 = 15 MPa), 2.17 MPa (hypothesis: σ_0 = 18 MPa) and 2.39 MPa (hypothesis: σ_0 = 19.5 MPa). The choice of the equivalent isotropic stress obtained with Eq.(A4-1) results in an increase of 10% of the ground pressure on the support. If another example is considered: σ_{ci} = 50 MPa, m_i = 10, MR = 400, GSI = 25 and in-situ stress state is anisotropic with a vertical stress of 20 MPa and a horizontal stress of 15 MPa. The support is identical but installed 8 m from the face. The surrogate models developed leads to a ground pressure on the support of 1.66 MPa (hypothesis: σ_0 = 20 MPa) and 1.96 MPa (hypothesis: σ_0 = 22.5 MPa). The ground pressure on the support increases of 18%.
- It can be noted that anisotropic stress state will also create bending moments and shear forces in the support that cannot be estimated with the surrogate models proposed in Chapter 4. They are based on the hypotheses that during the preliminary design, the main design parameter will be the ground pressure and the support and the normal forces in the support.

Appendix 4 - Application of confining pressure on the unsupported span during axisymmetric numerical calculations

The surrogate models developed in Chapter 4 consider only rigid support as the objective is to provide information to the engineers on whether or not a classical support (rigid close to face) is relevant. Most of the time, when large radial deformation occurs or is expected, rigid supports cannot be used, and yielding supports need to be considered. While deforming, those yielding supports also apply some confining pressure on the rock mass. Some tools already exist allowing preliminary design of yielding support (Cantieni and Anagnostou 2009a, Chapter 4.1.2.3). The objective of this appendix is not to propose a new approach regarding yielding support design, but to allow some basic results and interpretations on the impact of yielding support installed on the unsupported span, before the installation of a rigid support, with the surrogate models already developed.

To do so, some complementary calculations are performed with the consideration of a confining pressure on the span. The confining pressure applied by a yielding support is usually between 100 kPa and 400 kPa, depending on the type of yielding supports and the tunnel radius. 100 kPa corresponds to yielding bolts with an ultimate failure load of 250 kN spaced of 1.5m (Appendix 1, Table 1-a). Steel sets with sliding gaps (TH type) with a sliding pressure of 350 kPa, spaced every 0.8m in 4m tunnel radius apply a confining pressure of 110 kPa. A 0.2 cm thick shotcrete with highly deformable elements (type HDcon, yielding pressure of 4 MPa) in a 3 m tunnel radius apply approximately 260 kPa of confinement.

To study the impact of the confining pressure on the radial deformation between the face and the rigid support installation, and on the ground pressure on the support, 576 axisymmetric calculations have been carried out with no confining pressure, 100 kPa, 200 kPa and 400 kPa. The geological situations considered are identical as the one from the study of Appendix 1, reminded below (Table 4-a). Four spans are considered (0.5R, 1R, 2R and 3R) and three stiffnesses for the rigid support (0.5 GPa, 2.5 GPa, 5 GPa).

Table 4-a: Summary of 12 geological situations used for the comparison; εus is the radial strain without support; Rp is the plastic radius without support; MR is the Modulus Ratio

Situation	σ_0	σ_{ci}	m_i	GSI	MR	ε_{us}	Rp
1	20	30	8	25	400	39.6%	3.8 R
2	20	30	8	40	400	13.4%	2.8 R
3	20	30	13	40	400	7.8%	2.1 R
4	20	30	13	25	400	24.5%	2.7 R
5	10	35	8	25	400	9.5%	2.6 R
6	10	35	8	40	400	2.3%	1.8 R
7	10	35	13	40	400	1.6%	1.5 R
8	10	35	13	25	400	5.7%	2.0 R
9	5	40	8	25	400	2.0%	1.7 R
10	5	40	8	40	400	0.5%	1.3 R
11	5	40	13	40	400	0.4%	1.1 R
12	5	40	13	25	400	1.4%	1.4 R

The axisymmetric numerical model used is similar to one presented in Chapter 4.2.1. Unlike the one used in Chapter 4, the model used here also includes the application of a confining pressure at the tunnel boundary on the span length. This pressure is applied between the "transitioning material" and the ground. The pressure is not directly applied at the face; it is applied 0.2R from face and until the rigid support is installed. After the installation of the rigid support, the confining pressure is removed. The pressure is constant. It can be noted that considering a constant confining pressure is not totally realistic. This means that the loading phase of the yielding support is neglected. In reality, the confining pressure will be applied when the support start yielding, which can be further way than 0.2 radius from the face.

Then the results with confining pressures have been compared with the results without confining pressures. Those comparisons are presented in the Figure 4-a, a), b) and c).

The first parameter in the comparison is the relative gap between the radial strain at the installation of the "stiff" support, which does not include the radial strain in front of the face, with and without confining pressure. This relative gap (δ_ε) is calculated with the following equation:

$$\delta_\varepsilon(\%) = \frac{\Delta\varepsilon_i}{\varepsilon_i(0\ kPa)} = \frac{\varepsilon_i(P_{conf}) - \varepsilon_i(0)}{\varepsilon_i(0)} \qquad (A4-1)$$

With $\varepsilon_i(P_{conf})$ the radial strain between the face and the support installation when a confining pressure P_{conf} is applied.

The second parameter in the comparison is the absolute gap between ground pressures on the "stiff" support far from the face with and without confining pressure. The use of the absolute gap has been preferred to the relative gap, because it allows a direct comparison of the ground pressure variation with the confining pressure, as it is highlighted in the following of this section. The absolute gap (ΔP_{ground}) is calculated with the following equation:

$$\Delta P_{ground}(MPa) = P_i(P_{conf}) - P_i(0) \qquad (A4-2)$$

With $P_i(P_{conf})$ the ground pressure on the "stiff" support far from the face for which a confining pressure P_{conf} is applied on the span.

Figure 4-a synthetizes the comparison for a confining pressure of 100 kPa (a), 200 kPa (b) and 400 kPa (c). The y-axis is the plastic radius estimated without support, associated with the twelve geological situations (Table 4-a). From this figure, it is possible to draw the following conclusions:

- As expected, applying a confining pressure on the span reduce the radial strain at the "rigid" support installation (all the relative gaps are negative). A bigger confining pressure leads to a bigger radial strain reduction. This can be illustrated, for example, with the red points associated with a plastic radius of 3.8R. The reduction is then around 13% for a 100kPa confining pressure, 21% for a 200kPa and 31% for a 400 kPa.
- For each geological situation, the points of each four colors are relatively close to each other (Figure 4-a). This means that the stiffness of the rigid support does not significantly impact the radial strain reduction. This is even more visible when some plasticity occurs around the tunnel (plastic radius > 1.5R).

- The span length has an impact. A longer span leads to a higher relative reduction of the radial strain. For example, a span of 0.5R (plastic radius of 2.1R) leads to a reduction of 4% with 100 kPa and span of 3R, to a reduction of 12%.
- The interpretation of the results regarding the ground pressure on the support is less obvious. When the plasticity in the rock mass is small (plastic radius without support < 1.4 Radii), applying a confining pressure leads to an increase of the ground pressure on the support. In Figure 4-a, most of the points with small plasticity are at the right of the y-axis (positive pressure gap). A higher confining pressure or a longer span leads to a higher increase of the ground pressure on the support (grey symbol on Figure 4-a a), b), c)). Those conclusions seem relevant because the rock mass behavior is close to an elastic behavior (small plastic radius), for which the ground pressure is independent of the stress path. Applying a confining pressure with an elastic behavior of the rock leads to an increase of the ground pressure on the support equal to the confining pressure.
- When the plasticity of the rock mass around the tunnel is large, the impact of a confining pressure is the opposite as for a small plasticity. Applying a confining pressure leads to a reduction of the ground pressure on the rigid support (most of the points are at the left of the y-axis). For stiffer support, the reduction of the ground pressure is more likely and higher (triangles and squares compared to circles). This result may seem counterintuitive but can be explained by the impact of the confining pressure on the development of plasticity around the tunnel. For example, in the first situation, for which the span is 3R and the radial stiffness of the support is 2.5GPa, the plastic radius without support is 3.8R, the plastic radius with a support but without confining pressure is 3.4R and the plastic radius with a support and with 400 kPa of confining pressure is 3.0R (results are not presented here). A smaller plastic radius leads to smaller ground pressure on the rigid support.
- The gap between the ground pressure with and without confining pressure are of the same order of magnitude as the confining pressure itself, whereas this gap is positive or negative. Except for stiff rigid support with large plasticity, almost all the relative gaps are included in more or less the confining pressure: $\pm$ 0.1 MPa for a), $\pm$ 0.2 MPa for b), $\pm$ 0.4 MPa for c).

From the results presented in Figure 4-a, it is possible to draw the following conclusions to be applied during preliminary design with the surrogate model:

- Considering a yielding support will not generate an overload on the rigid support, except for small value of plastic radius. Small plastic radii are generally not associated with large deformation, and so yielding support may not be necessary nor relevant.
- Table 4-b presents the relative reduction factor of radial strain that can be applied when considering a yielding support in the surrogate models presented in Chapter 4.2.3. These values are obtained by considering the minimal reduction associated with a specific confining pressure and a specific span. They are only indicative during preliminary design. For more advanced project stages, more complex studies are recommended.

Table 4-b: Radial strain relative reduction associated with the consideration of a yielding support

Pressure \ Span	0.5R	1R	2R	3R
100 kPa	4%	10%	13%	15%
200 kPa	7%	17%	21%	23%
400 kPa	12%	23%	29%	34%

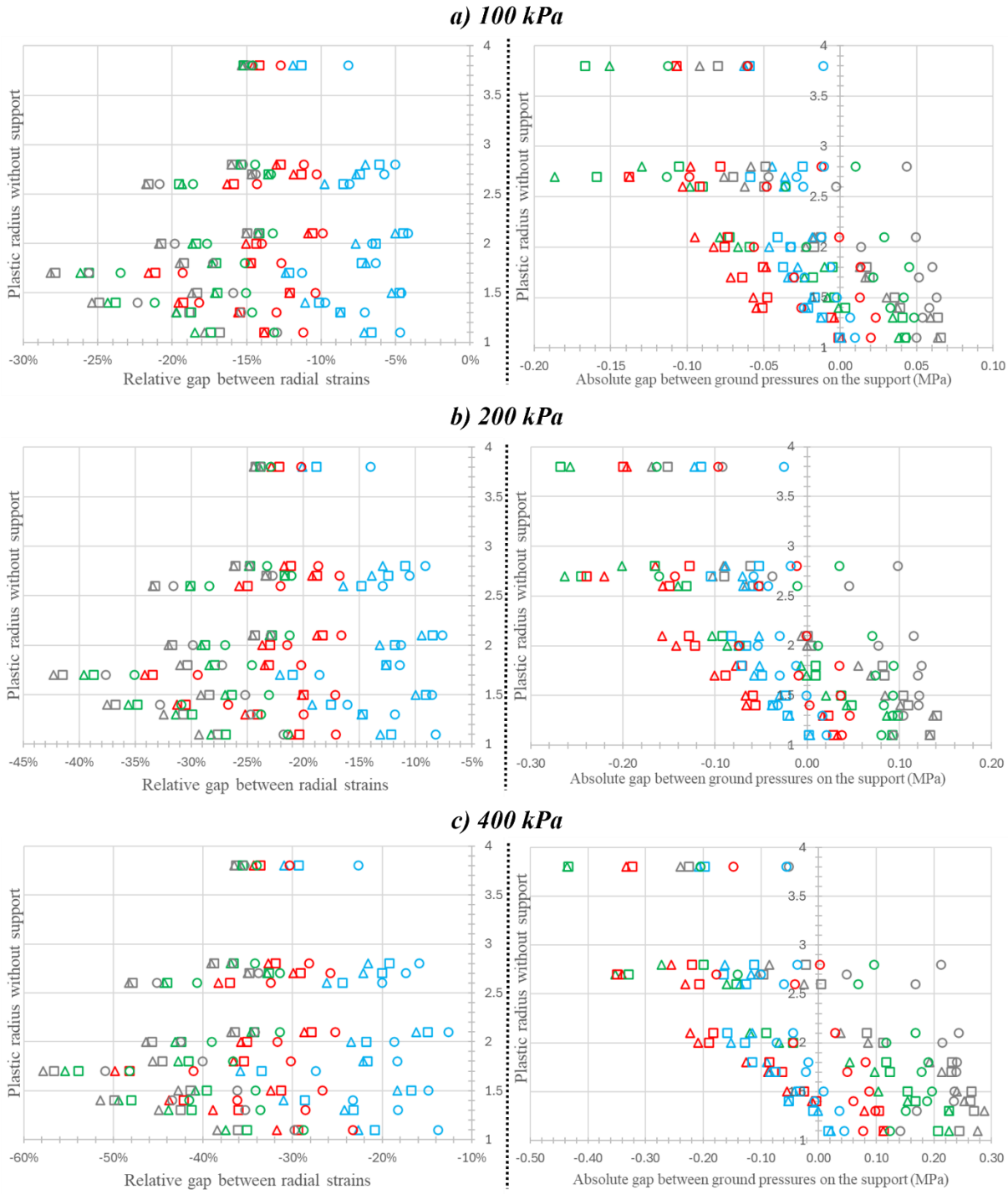

d)

Support stiffness (GPa)	Span 0.5 R	Span 1 R	Span 2 R	Span 3 R
0.5	○	○	○	○
2.5	□	□	□	□
5	△	△	△	△

Figure 4-a: Results of the comparisons between the situations for which no confining pressure is considered, and when a confining pressure is considered. The confining pressures used are: a) 100 kPa ; b) 200 kPa ; c) 400 kPa. The d) is the legend of each graphical symbol used

Appendix 5 - Consideration of the long-term behavior of the rock mass

One of the limitations of the surrogate models presented in Chapter 4 is that they can be used only for a specific rock mass condition. The rock mass condition cannot evolve, such as for example with a degradation of the rock mass properties. When tunnelling in highly fractured rock mass, it can be necessary to consider a degradation of these properties by taking into account the long-term behavior of the rock mass.

This Appendix aims to justify why it is not possible to use directly the surrogate models for the consideration of the long-term behavior of the rock mass. Nevertheless, a method based on the close-form analytical expression of Carranza-Torres and Fairhurst (1999) is proposed. This expression can be linked to the results of the surrogate models to estimate the long-term ground pressure on the support.

A 5.1. Limitation of the surrogate models for the long-term behavior of the rock mass

As presented in Chapter 2.2.1.3, the long-term behavior of the rock mass could be characterized by a modification of the rock mass properties, such as a reduction of the GSI value. The approach is similar as considering a reduction of the rock mass strength Chapter 2.2.1.3 (Figure 2-17) or increasing the radial strain without support (possibility to obtain new values of σ_{ci} and m_i by using the improved Hoek and Marinos curve). To stay relevant with the surrogate models, the degradation of the rock mass properties is considered in the entire rock mass and not just at the vicinity of the tunnel. This hypothesis is important because it is not entirely realistic and can differ from what can be done in the literature (Connor Langford and Diederichs 2013).

When speaking of long-term behavior based on the surrogate models, two approaches come initially in mind:

- Designing directly by using the long-term properties of the rock. It corresponds to the worst-case scenario, in which the degradation of the rock mass properties is happening as fast as the excavation process. In this situation, it is not possible to take advantage of the short-term properties of the rock mass (better properties). Except for relatively fast creep process, the design will potentially be overconservative and potentially incoherent compared to the short-term field observations.
- Estimating the increase of ground pressure between short-term and long-term by directly modifying the input parameters while keeping the parameters of support identical. This approach can lead to unrealistic results, as presented below.

An example of the limitations of these methods is presented below. For this theoretical example, the following properties are considered: σ_{ci} = 60 MPa, m_i = 14, σ_0 = 25 MPa, MR = 400, GSI = 35. The long-term GSI value is 25, based on the formulation of Alejano *et al.* (2012) (Chapter 2.2.1.3, Figure 2-19). Based on the various surrogate models, the radial strain without support for the short-term GSI is 4.3%, the plastic radius is 2R and the radial strain at the face 1.4%. For the long-term GSI, the radial strain without support is 10.5%, the plastic radius is 2.34R

and the radial strain at the face is 3.2%. It can be noted that considering a reduction of the GSI for the entire rock mass is unfavorable and over pessimistic. A more appropriate approach could be to reduce the GSI only in the vicinity of the tunnel (plastic radius for example). Unfortunately, it is not possible with the developed surrogate models, and only numerical calculation could be used. The reader needs to be aware of this hypothesis to propose critical judgement on the results.

The tunnel radius is considered to be 4 m. In this example, the design parameters are the thickness of the support (shotcrete, Young Modulus 10 GPa, f_{ck} = 30 MPa) and the distance from face at which it will be installed. The design is performed through a deterministic approach based on partial factors from the Eurocodes and the French Recommendation on the adaptation of the Eurocode for tunnel designs (AFTES – GT 29R2F1). A partial factor of 1.5 is considered on the strength of the shotcrete, and an increase of 1.35 on the internal forces of the support which, in the framework of the surrogate models, is similar to an increase of the ground pressure on the support (detail provided in A 1.2). Based on the specific condition of a circular tunnel in an isotropic in-situ stress state, the two partial factors are equivalent to a reduction of the maximal admissible pressure on the support of a factor 2.025 (e.g. strength of the support). The maximal pressure admissible on the support is 0.72 MPa for a thickness of 20 cm, 1.07 MPa for a thickness 30 cm, and 1.41 MPa for a thickness of 40 cm. Figure 5-a presents the evolution of the ground pressure on the support depending on the span (a) and on the radial strain between the face and the support (b) for the short-term properties (S-T) and the long-term properties (L-G). These curves have been directly obtained with the surrogate models presented in Chapter 4.

Several designs are possible based on the short-term properties. A support composed of a 20 cm thick shotcrete needs to be installed at least 10 m from the face (Figure 5-a a)), while a 40 cm can be installed closer (around 8 m). In this situation, it is more damaging to install a rigid support close to the face compared to letting the ground deform, as 20 cm more of shotcrete will reduce the radial strain of only 0.4% (1.6 cm of radial displacement). To design directly with the long-term properties will result in an increase of the span of around 3.5m, and to larger radial strain between the face and the support (more than 4%, 16 cm of radial displacement).

Considering directly the long-term behavior leads to a radial strain between the face and the support of more than 4%. It is impossible to know whether these radial strains will develop during the construction, or later. If the long-term behavior does not appear during the construction (which in generally the case), at what moment will it be chosen to install the rigid support or a lining? The answer to this question will largely impact the general tunnel design, the logistical aspects, etc. One solution could be to install the rigid support/lining later, for example, a 30 cm thick shotcrete installed 14 m from the face. The short-term properties lead to a ground pressure around 0.5 MPa (Figure 5-a a)). The installation of this rigid support will block the radial deformation at 1.2% (Figure 5-a b)). Then, the transition toward the long-term properties of the rock mass will increase progressively the ground pressure until a new equilibrium is reached. It seems that this pressure could be estimated with Figure 5-a b), by considering the intersection between the radial strain (1.2%) and the long-term curve (red dash curve): 4.0 MPa. It would mean that, the ground pressure between short-term and long-term properties is increased by more than 8 times, while the GSI is reduced of 10 only …This result seems extreme, to support the long-term pressure, the thickness of the support needs to be at least 1.3m (designed with the partial factors) …

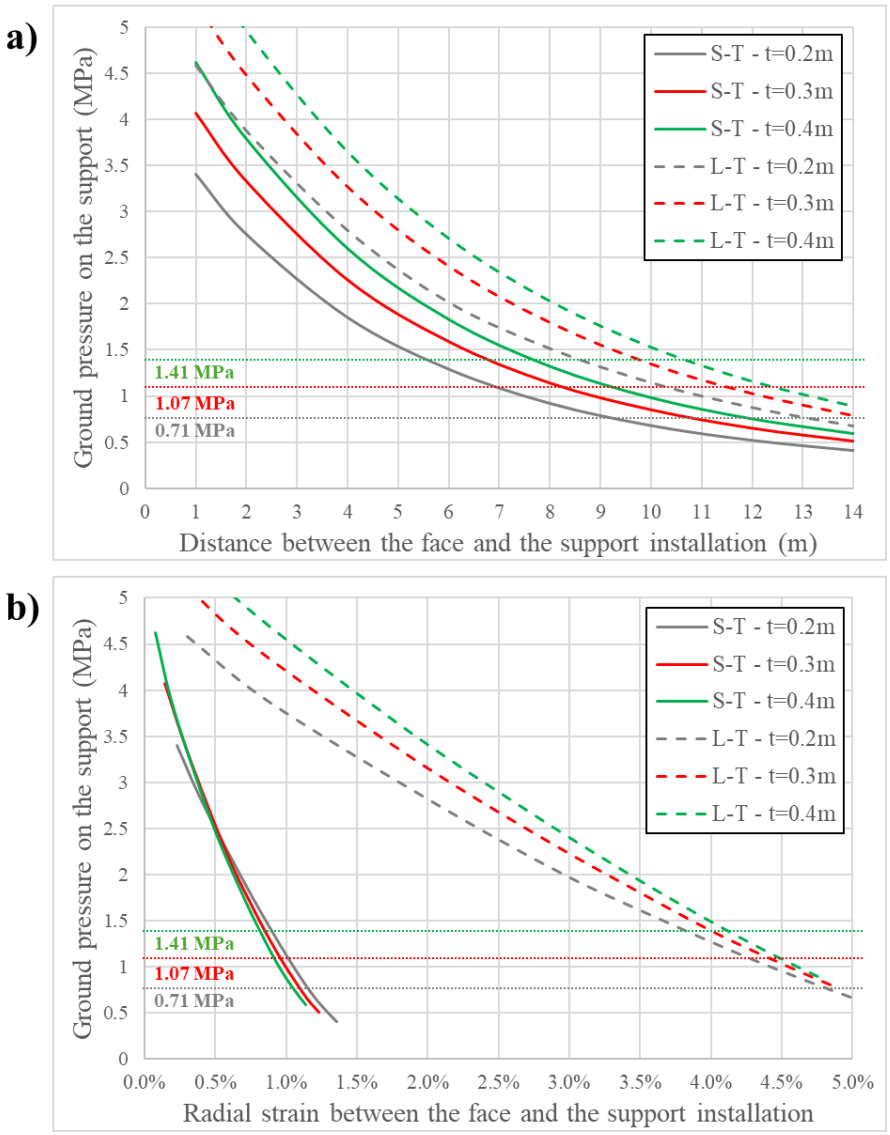

Figure 5-a: Evolution of the ground pressure on the support depending on the span (a) and on the value of radial strain between the face and the support (b)

There is at least one error in the previous reasoning. One of the objectives of the surrogate model developed is to explicitly consider the interaction between the rock mass behavior and the support behavior close to the face. When considering short-term and long-term behavior, the interaction between the face and the support needs to be considered only one time. All the curves presented in Figure 5-a explicitly consider this interaction, because they have all been obtained with the surrogate models. Using short-term properties to estimate the radial deformation, then deducing the long-term ground pressure using these curves created with the long-term properties is not a relevant approach, unlike potentially thought.

There is no real problem to perform the design directly using the long-term properties, except maybe an unfavorable interaction between the rock mass behavior and the support. Careful interpretations of the results are necessary, as field observations may not coincide with the design approach (smaller radial strain for example). In the next section, a method is proposed which tries to be more relevant to include long-term properties when the design has been performed with short-term properties.

A 5.2. Method to include the long-term behavior

Using the surrogate model with short-term properties leads to an estimation of the ground pressure on the support far from the face. The pressure will depend on the type of support (consideration of a yielding support or not, stiffness of support, etc) and the distance at which it is installed, and results of "3D approach" with an explicit consideration of the impact of the face. The final situation is "2D situation" in which the face no longer impacts the support, and only the ground parameters around the tunnel will evolve. The approach proposed in this section considers the transition between the short-term and the long-term as simple 2D plane strain problem with the increase of the radial strain and the ground pressure depending on the stiffness of the support and/or lining. This approach is similar to a convergence-confinement method.

The method can be summarized into six steps (Figure 5-b):

Step 1: Defining the short-term and long-term properties of the rock mass.

Step 2: Estimating the ground pressure $p_i(\infty)_{ST}$ on the support with the surrogate model using the short-term properties.

Step 3: Calculating the short-term and long-term ground reaction curve without support.

Step 4: Deducing from the short-term GRC the equivalent radial strain (ε_{eq} ST) associated with a 2D plane strain approach, leading to the same ground pressure on the support $p_i(\infty)_{ST}$

Step 5: If necessary, to update the support stiffness. It is possible that a lining is installed far from the face

Step 6: Computing the intersection point between the SCC and the GRC with long-term properties. This equilibrium point is the ground pressure on the support for the long-term properties $p_i(\infty)_{LT}$

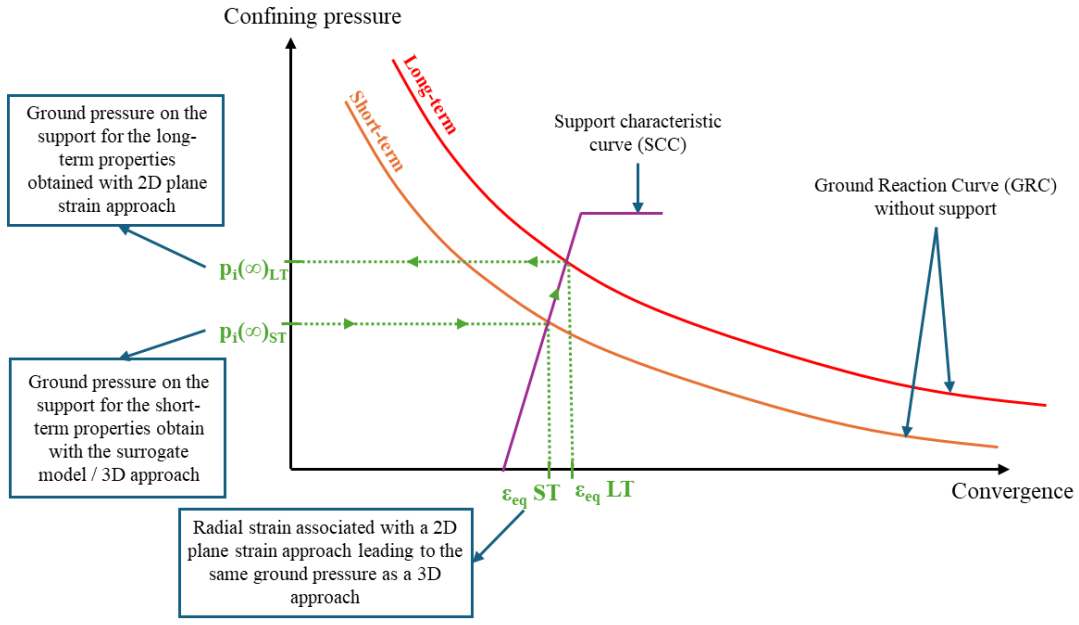

Figure 5-b: Method to estimate the long-term pressure on the support based on the surrogate model and a 2D plane strain approach

Figure 5-b summarizes the method. It can be noted that this method is very similar to one used in numerical calculations (2D plane strain or 3D). Generally, the calculations are performed for short-term properties, then the properties are modified (locally, close to the tunnel, or in the entire model) and a new equilibrium is computed (Hoek and Guevarra 2009; Langford and Diederichs 2013).

Based on the example presented in the previous section, a 20 cm thick shotcrete (E=10 GPa) is installed 10 m from the face. The short-term ground pressure on this support far from the face is $p_i(\infty)_{ST}$ = 0.7 MPa, which is the maximal pressure that can be applied on it (including partial factors, as presented above). Considering that a 50 cm lining is installed far from the face (f_{ck}=40MPa, Young modulus of 30 GPa), it is possible to use the method presented above to estimate the long-term ground pressure on the support.

The stiffness of the support is 0.53 GPa (calculated with the simplified expression presented in A 1.2.1, Table 1-a). The stiffness of the lining is 4.40 GPa. As the lining is much stiffer than the support, it is supposed that only the lining will carry the increase of ground pressure associated to the long-term properties. Figure 5-c presents the results of the method in this situation. Initially, the surrogate models are used to estimate the ground pressure on the support far from the face, when the span is 10m. $p_i(\infty)_{ST}$ is 0.7 MPa, the maximal ground pressure admissible on the support is 0.72 MPa with partial coefficients, and 1.46 without. Then, the lining is installed, and the method presented above is applied. The maximal ground pressure admissible on the lining is 2.43 MPa with partial coefficients, and 4.92 MPa without. For a long term GSI of 30, the ground pressure is around 1.6 MPa. This value is the result of the method, 2.3 MPa, minus the pressure already carried by the support, before the lining installation, 0.7 MPa (Figure 5-c). Similarly, for a long term GSI of 25, the ground pressure on the lining is 3.8 MPa. The method leads to a total ground pressure of 4.5MPa, but the support carries already 0.7 MPa (Figure 5-c), as the lining is installed very far from the face.

It can be noted that two long-term values of GSI have been considered, 30 and 25. The GRC are obtained with the analytical close form solution of Carranza-Torres and Fairhurst (1999), while the dashed curves are obtained with 2D plane strain numerical model (generalized Hoek and Brown failure criterion, large strain hypothesis).

The compatibility of the chosen lining depends on the hypothesis regarding the long-term behavior of the rock mass. For a long-term GSI of 25, the lining is not adapted when partial factors are included, as the ground pressure on the lining is around 3.8 MPa (maximal admissible pressure is 2.43 MPa with partial coefficients). Nevertheless, the maximal pressure on the support before failure (without partial factors) is 4.92 MPa, leading to global safety factor of 1.29 (4.92/3.8). For a GSI of 30, the lining is adapted as the maximal long-term ground pressure is 1.6 MPa.

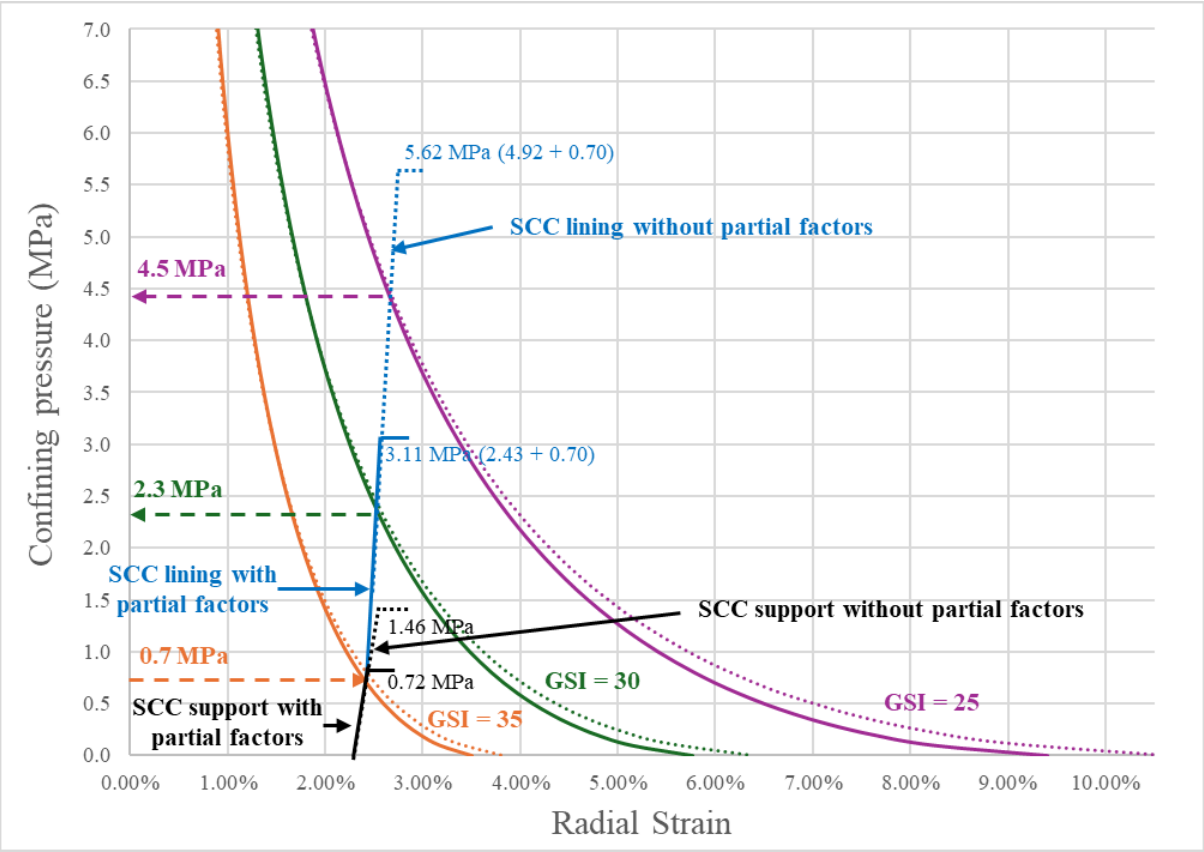

Figure 5-c: Application of the proposed method to estimate the long-term ground pressure on the support; dashed colored curves correspond to GRC obtained with numerical calculations; continuous curves are obtained with Carranza-Torres and Fairhurst (1999) close form analytical solution

Appendix 6 - Excel file used to perform reliability calculations – Practical use of the surrogate models

This Appendix presents the Excel file allowing a practical use of the various surrogate models developed and to fulfill the following objectives:

- Allowing an easy estimation of the rock mass behavior with and without support, and its impact on the support
- Introducing and propagating the uncertainties of the input parameters
- Performing the calculation of failure probabilities with the short-term properties regarding two limit states: the strength of the support and the radial strain between the face and support
- Estimating the long-term pressure on the support, and potentially the lining.
- Performing the calculation of the failure probability with the long-term properties of the support and / or the lining.

The main elements of the file and the specific characteristics are presented below to provide a good understanding of calculations performed. When calculations using the surrogate models were necessary, this file has been used, except when specific remark saying otherwise.

The "main" sheet (Figure 6-a) is the sheet where the input parameters are inserted and the results are displayed. It is composed of four main areas:

1) "Deterministic calculations" where the basic input parameter are inserted and the deterministic calculations are performed.
2) "Uncertainty introduction and propagation" where the incertitude of the input parameter (geological and geotechnical) are included. A Monte Carlo simulation can be performed and information regarding the output parameters are provided.
3) "Reliability calculation" where the information regarding support strength (including uncertainties) and potential partial factors are provided. Based on this information, and on the uncertainties of the input parameters, failure probabilities are calculated based on various hypotheses using the results of the MCS.
4) "Long-term behavior" where the long-term properties of the rock mass is considered (in this sheet, only the long term GSI), a lining can be introduced, and the deterministic and probabilistic calculations can be performed.

Each section is presented in more detail below. There are four types of cells including numbers and so four colors:

- The white cells: It is the only cell that can be modified by the user. All the input needs to be added into this type of cell
- The light green cells: It is the cells that are only providing information not necessarily used for the calculation, or with identical information than a white cell.
- The blue cells: The values of these cells are obtained through a simple calculation, and can provide relevant information to the user.
- The red cells: The results are presented in these cells.

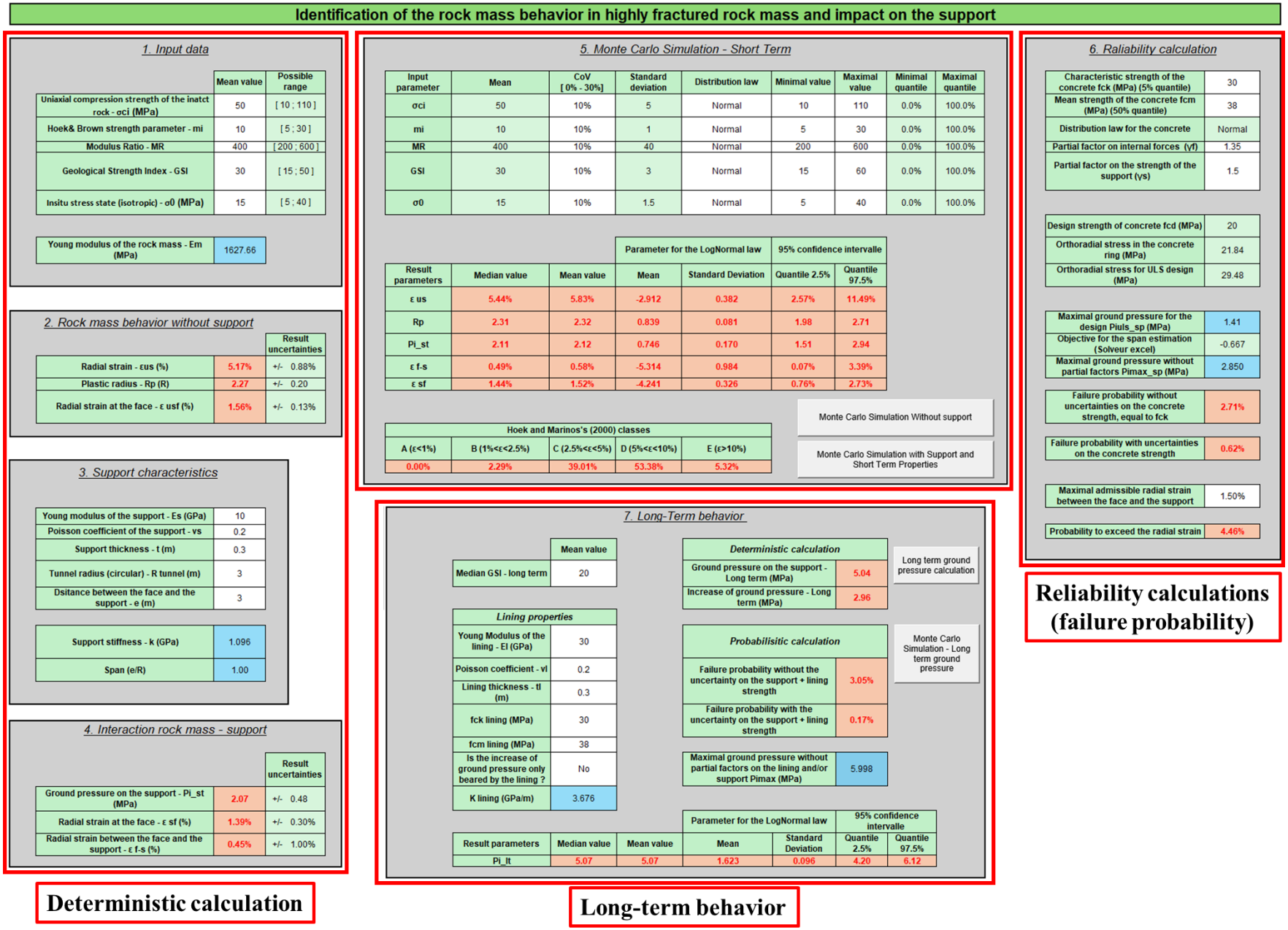

Figure 6-a: Presentation of the main Excel sheet where the input parameters are introduced and the results are displayed

A 6.1. "Deterministic calculations" area

This area allows the most basic calculations that can be performed with the surrogate models. The input parameters considered are the same as the one used in most of this thesis, and the range of possible values for each is provided to avoid using the surrogate models outside of their framework (Figure 6-b). The Young modulus of the rock mass is calculated using the equation proposed by Hoek and Diederichs (2006), linking σ_{ci}, MR and GSI (Chapter 2.1.2.2).

1. Input data

	Mean value	Possible range
Uniaxial compression strength of the inatct rock - σci (MPa)	50	[10 ; 110]
Hoek& Brown strength parameter - mi	10	[5 ; 30]
Modulus Ratio - MR	400	[200 ; 600]
Geological Strength Index - GSI	25	[15 ; 50]
Insitu stress state (isotropic) - σ0 (MPa)	10	[5 ; 40]

Young modulus of the rock mass - Em (MPa)	1197.11

Figure 6-b: Input data for deterministic calculation

These data enable the characterization of the rock mass behavior without support by using the results of the improvement the Hoek and Marinos curve (Chapter 3.3.2), the surrogate model for the calculation of the plastic radius without support (Chapter 3.3.4), and the radial strain at the face without support (Chapter 4.2.3.4.1). The uncertainties associated with the surrogate models are also provided (Figure 6-c).

2. Rock mass behavior without support

		Result uncertainties
Radial strain - εus (%)	4.19%	+/- 0.71%
Plastic radius - Rp (R)	2.15	+/- 0.19
Radial strain at the face - ε usf (%)	1.32%	+/- 0.11%

Figure 6-c: Rock mass behavior without support (deterministic calculations)

It can be noted that the improvement of the Hoek and Marinos curve developed in Chapter 3.3.2 considers specific values of GSI ({15, 20, 25, 30, 35, 40, 45, 50}) and MR ({200, 400, 600}). This Excel sheet is not restricted to these values. Intermediary values are estimated using a linear interpolation between the specific fixed values.

Then, some information about the support is introduced. The surrogate models (Chapter 4.2.3) use as input parameter the stiffness of the support and the span, both independent of the tunnel radius. To make this file easier to use in practice, the user needs to introduce the Young's modulus of the support, the Poisson's coefficient, the thickness of the support, the tunnel radius and the distance between the face and the support installation expressed in meter. The stiffness and the span are deducted (Figure 6-d)

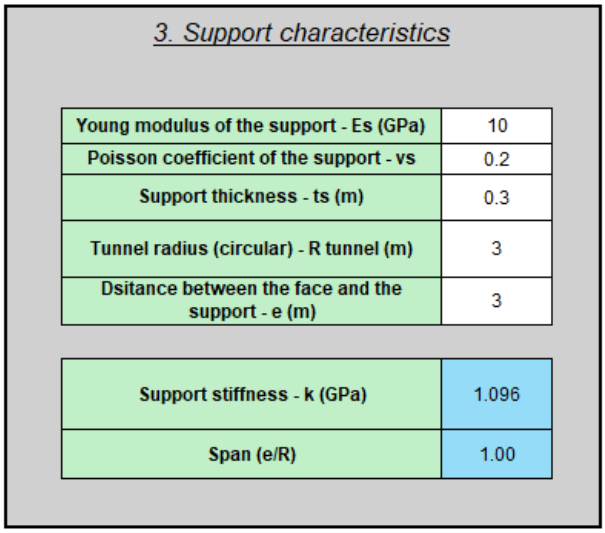

Figure 6-d: Input parameter of the support

Since the stiffness is deducted from these parameters, the formulation used for its calculation is the simplified one for a ring shape support (Barla 2001):

$$k = \frac{E_s \, t_s}{(1 - {\nu_s}^2)\left(R - \frac{t_s}{2}\right)} \qquad (A6-1)$$

For non-continuous support (steel set) or mixed support (steel set embedded) equivalent parameters should be used.

Based on these parameters (rock mass behavior without support and the support characteristics), the results of the interaction between the rock mass and the support are calculated using the surrogate models presented in Chapter 4.2.3. The result uncertainties are also presented (Figure 6-e).

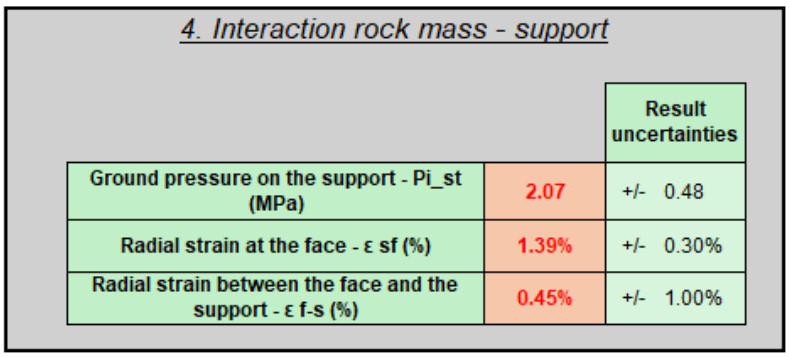

Figure 6-e: Results of the interaction between the rock mass and the support (deterministic calculation)

A 6.2. "Uncertainty introduction and propagation" area

This area aims to introduce and propagate geological and geotechnical uncertainties. It includes three tables, one to insert the uncertainties (Figure 6-f), and two returning the results of Monte Carlo simulation of 100 000 realizations.

Input parameter	Mean	CoV [0% - 30%]	Standard deviation	Distribution law	Minimal value	Maximal value	Minimal quantile	Maximal quantile
σci	50	10%	5	Normal	10	110	0.0%	100.0%
mi	10	10%	1	Normal	5	30	0.0%	100.0%
MR	400	10%	40	Normal	200	600	0.0%	100.0%
GSI	30	10%	3	Normal	15	50	0.0%	100.0%
σ0	15	10%	1.5	Normal	5	40	0.0%	100.0%

Figure 6-f: Introduction of the geological and geotechnical uncertainties

The input parameters are identical to the one presented in Figure 6-f. Their "Mean" are equals and their values cannot be modified here (light green cells).

The first information to include is the "CoV" (Coefficient of Variation), corresponding to the amount of variability of each parameter. It is defined as $CoV = \sigma/\mu$, where σ is the standard deviation and μ the mean. The standard deviation can then be deducted. It is preferred to use the CoV as an input parameter compared to the standard deviation because its practical meaning is more relevant to quantify the amount of uncertainties on a parameter and it is more general.

The second information to include is the distribution law of probability to use for each parameter. Three laws are included, the "Normal" distribution, the "LogNormal" distribution and the "Uniform" distribution. For the "Normal" distribution and the "LogNormal" distribution, it is possible to define minimal and maximal boundaries by updating the cells "Minimal value" and "Maximal value". The associated quantiles are presented in "Minimal quantile" and "Maximal quantile" cells. For the "LogNormal" distribution, the "CoV" is applied to the natural logarithm of mean. The standard deviation is the standard deviation of normal distribution associated with the natural logarithm of the random variable. For the "Uniform" distribution, the cells "Minimal value" and "Maximal value" correspond to the boundary of the distribution law. It can be noted than for "Uniform" distribution, the value of CoV does not influence the results as the distribution is entirely defined by the minimal and maximal values.

After the introduction of the uncertainties, a Monte Carlo simulation can be performed with and without considering the support (the one defined in Figure 6-d). Two macros coded using VBA language (Visual Basic) allow these Monte Carlo simulations (Figure 6-g). The first one ("Monte Carlo simulation without support") does not consider the support (estimation only of the radial strain without support and the plastic radius), and the second one takes it into account. The second one also calculates the failure probabilities, as presented in the next section. Depending on the computer performance, the Monte Carlo simulation can take between a couple tenths of a second or a couple of minutes. At the end of the simulation, a message box "End of simulation!" appears.

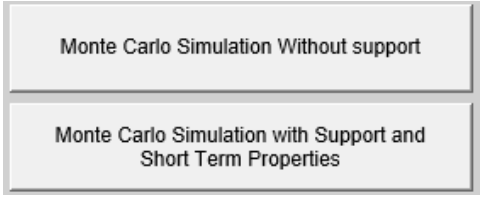

Figure 6-g: Macros allowing the Monte Carlo simulation

Two types of results are presented. The first one corresponds to the characterization of the rock mass behavior without support, returning the probability of being in each of the Hoek and Marinos classes of squeezing risk (Figure 6-h). It is obtained with the first macro (Figure 6-g).

Hoek and Marinos's (2000) classes				
A (ε<1%)	B (1%<ε<2.5%)	C (2.5%<ε<5%)	D (5%<ε<10%)	E (ε>10%)
0.00%	2.29%	39.01%	53.38%	5.32%

Figure 6-h: Results of the MCS without support to characterize the rock mass behavior depending on the existing uncertainties

The second one is the definition of the probability density of every output parameter (Figure 6-i): the radial strain without support (ε_{us}), the plastic radius without support (R_p), the ground pressure on the support (P_i), the radial strain between the face and the support ($\varepsilon_{f\text{-}s}$), and the radial strain at the face when a support is considered (ε_{sf}). ε_{us} and Rp are obtained with the first macro, while P_i, $\varepsilon_{f\text{-}s}$, and ε_{sf} are obtained with the second macro (Figure 6-g).

			Parameter for the LogNormal law		95% confidence intervalle	
Result parameters	Median value	Mean value	Mean	Standard Deviation	Quantile 2.5%	Quantile 97.5%
ε us	5.44%	5.83%	-2.912	0.382	2.57%	11.49%
Rp	2.31	2.32	0.839	0.081	1.98	2.71
Pi_st	2.11	2.12	0.746	0.170	1.51	2.94
ε f-s	0.49%	0.58%	-5.314	0.984	0.07%	3.39%
ε sf	1.44%	1.52%	-4.241	0.326	0.76%	2.73%

Figure 6-i: Results of the MCS for the various output

Based on the several tests performed with limited impact of boundary limitation ("Minimal value" and "Maximal value" correspond to small and large quantiles respectively), it was found that the results can be correctly model with a LogNormal distribution. There are some exceptions like for small value of plastic radius, as the minimal value is 1, or for small value of the radial strain between the face and the support.

The "median value" (quantile at 50%) of the results of the MCS and "mean value" are provided. The parameters of the LogNormal distribution law are also provided (e.g. the mean and the standard deviation of the normal distribution associated to the natural logarithm of the output parameter), as well as the 95% confidence interval obtained based on the parameters of LogNormal distribution.

A 6.3. "Reliability calculations" area

The third area of the Excel sheet concerns the estimation of failure probabilities. In this file and in this thesis, which focuses on preliminary design, two limit states are considered: one regarding the strength of the support, and another regarding the radial strain between the face and the support installation.

To define the limit state regarding the strength of the support, complementary information is necessary, because the ones provided in Figure 6-d correspond only to the elastic behavior of the support and does not include information about its strength (Figure 6-j). The uncertainties regarding the strength of the support can also be considered for a more relevant estimation of the failure probability.

Characteristic strength of the concrete fck (MPa) (5% quantile)	30
Mean strength of the concrete fcm (MPa) (50% quantile)	38
Distribution law for the concrete	Normal
Partial factor on internal forces (γf)	1.35
Partial factor on the strength of the support (γs)	1.5

Figure 6-j: Complementary information regarding the support strength

It can be noted that Figure 6-j referred to concrete. It can also be used for other types of continues support such as shotcrete, or for an equivalent continuous strength associated with a discontinuous support (steel set for example).

The first parameter is the characteristic strength of the concrete/shotcrete, f_{ck}, as defined by the Eurocode. It is the strength associated with a class of concrete, for example C30/37 (30 is the f_{ck} obtained on standardized cylindrical sample, while 37 is $f_{ck\ cube}$ obtained on standardized cubic sample). In reality, it corresponds to the 5% quantile of the associated class of concrete. Its means that, there is a 5% probability that the strength of the concrete is lower than f_{ck}. The mean value (f_{cm}) corresponds to f_{ck} + 8 MPa, according to the Eurocode 2 (Figure 6-k). It is considered that the distribution of the strength of the support is Normal (hypothesis).

f_{ck} (MPa)	12	16	20	25	30	35	40	45	50	55	60	70	80	90	
$f_{ck,cube}$ (MPa)	15	20	25	30	37	45	50	55	60	67	75	85	95	105	
f_{cm} (MPa)	20	24	28	33	38	43	48	53	58	63	68	78	88	98	$f_{cm} = f_{ck} + 8$ (MPa)

Figure 6-k: Extract of the strength classes of concrete, from Table 3.1 of the Eurocode 2 - NF EN 1992-1-1

Partial factors can also be added. They are not directly used for the calculation of the failure probability, but it can be necessary to perform an optimization of the design using a classical semi-probabilistic approach (e.g. based on partial factors). It can be noted that on this specific configuration: circular support under homogenic ground pressure and isotropic stress state, the design constraint is the tangential stress inside the support. Considering these partial factors is equivalent to targeting a global safety factor equal to their multiplication ($\gamma_s * \gamma_f$ of Figure 6-j).

Based on the partial factors and results of the deterministic calculations, some relevant information can be deducted, such as the design strength of the support ($f_{cd} = f_{ck} / \gamma_s$), the orthoradial/tangential compressive stress inside the circular support ring (σ_θ), and the orthoradial stress considered as the ultimate limit state (ULS) $\sigma_{\theta\ ULS} = \sigma_\theta * \gamma_f$ (Figure 6-l).

Design strength of concrete fcd (MPa)	20
Orthoradial stress in the concrete ring (MPa)	23.44
Orthoradial stress for ULS design (MPa)	31.64

Figure 6-l: Complementary results for the deterministic calculation

σ_θ is obtained with the following equation:

$$\sigma_\theta = P_i \frac{2 {R_{ext}}^2}{{R_{ext}}^2 - (R_{ext} - t_s)^2} \qquad (A6-2)$$

Where P_i is the ground pressure on the support obtained in Figure 6-e, R_{ext} is the external tunnel radius (m) and t_s is the thickness of the support (m).

It is also possible to perform an optimization of the distance (span) of the support installation based on the chosen support and partial factors (Figure 6-m). The optimization is performed using the "solver" package available in Excel. The objective to fulfill is: the ground pressure associated with a specific span (Pi(e)) equals the maximal admissible ground pressure on the support at the ultimate limit state (P_{iULS}).

Maximal ground pressure for the design Piuls (MPa)	1.41
Objective for the span estimation (Solveur excel)	-0.819
Maximal ground pressure without partial factors Pimax (MPa)	2.850

Figure 6-m: Optimization of the distance of the support installation using a semi-probabilistic approach and maximal ground pressure with and without partial factors

P_{iULS} is calculated based on the following expression:

$$P_{iULS} = \frac{f_{ck}}{\gamma_s} \frac{{R_{ext}}^2 - (R_{ext} - t_s)^2}{2 {R_{ext}}^2 \gamma_f} \qquad (A6-3)$$

It can be noted that in Eq(A6-3), P_{iULS} is divided by γ_f, the partial factor associated with the external load (or internal forces for tunnel design). Rigorously, this factor γ_f should be applied to Pi(e), the ground pressure on the support, to increase it artificially and not to decrease P_{iULS}, the maximal admissible ground pressure on the support. In the situation of this file, the results are identical for both situations, and the choice is made to apply it to P_{iULS} to allow a direct comparison between the result of the surrogate model (Pi(e)) and the maximal admissible pressure including the partial factors.

P_{imax} is the maximal admissible pressure on the support without partial factors, e.g. maximal pressure before failure. It is calculated using Eq(A6-3) with $\gamma_f = \gamma_s = 1$. This parameter is used for the estimation of the failure probability.

The last part of this area is about the calculation of the failure probabilities (Figure 6-n). The failure probability is the ratio between the number of realizations during which the results exceed a criterion, divided by the total number of realizations. Three failure probabilities are calculated:

- The failure probability without considering the uncertainties associated with the strength of the support. The maximal admissible ground pressure on the support is fixed for every realization of the MCS, and based on f_{ck} (no partial factors when performing reliability calculation), P_{imax}.
- The failure probability which considers the uncertainty associated with the strength of the support, defined in Figure 6-j. At each realization, a value of the support strength is randomly drawn, which leads to a maximal admissible ground pressure used for the comparison with Pi(e).

- The failure probability associated with the radial strain between the face and the support exceeding the maximal admissible value. The limit is fixed for every realization and is defined in Figure 6-n.

Failure probability without uncertainties on the concrete strength, equal to fck	3.09%
Failure probability with uncertainties on the concrete strength	0.67%
Maximal admissible radial strain between the face and the support	1.00%
Probability to exceed the radial strain	0.19%

Figure 6-n: Calculation of the failure probabilities

It can be noted that only the strength of the support is considered as a random variable. Rigorously, all the uncertain parameters need to be included as random variables during the reliability calculation. In this situation, it could have been the thickness of the support, the Young's modulus of the support, or the tunnel radius. For preliminary design, it was considered unnecessary to include these parameters as random variables. Nevertheless, it is totally possible to use the surrogate model when these uncertainties are considered.

A 6.4. Consideration of the long-term behavior of the rock mass

The last part of the Excel sheet is the "Long-Term Behavior". This part aims to calculate the long-term ground pressure on the support, and the associated failure probability, when considering a degradation of the rock mass properties. It is also possible to add a lining in the calculation.

In this Excel sheet, only the GSI is considered to be modified between the short-term properties and the long-term properties (Figure 6-o). This value is the mean value of the long term GSI, compared to the short-term value introduced in Figure 6-b. During probabilistic calculations, the short-term GSI value is reduced by the difference between the "GSI" (short-term GSI, Figure 6-b) and "Median GSI – long term" (Figure 6-o). For example, if the median short-term value is 30, and the long-term GSI value is 20, the difference is 10. If during the probabilistic calculation, a short-term value of 27 is drawn, the long-term value considered is 17 (27-10).

	Mean value
Median GSI - long term	20

Figure 6-o: Introduction of the long-term GSI value

It can be noted that the GSI reduction is applied to the entire rock mass and not just to the vicinity of the tunnel (as proposed by Connor Langford and Diederichs 2013), and so for the choice of the long-term GSI value, this point needs to be taken into account. It can also be noted that the uncertainty on this parameter is not directly considered in this sheet. It is totally possible to transform this parameter into a random variable, or also to modify other parameters for the long-term properties, such as the uniaxial compressive strength of the intact rock.

If needed, it is also possible to introduce the impact of a lining (Figure 6-p) which is supposed to be installed far from the face and aims to carry the increase of ground pressure at long-term. The lining is characterized by the same type of parameters than the support: its Young's modulus, its Poisson's coefficient, the thickness, its characteristic strength (f_{ck}) and its mean strength (f_{cm}).

Lining properties	
Young Modulus of the lining - El (GPa)	30
Poisson coefficient - vl	0.2
Lining thickness - tl (m)	0.3
fck lining (MPa)	30
fcm lining (MPa)	38
Is the increase of ground pressure only carried by the lining ?	No
k lining (GPa/m)	3.676

Figure 6-p: Introduction of the lining properties

The stiffness of the lining is calculated as follows (similarly as for the support):

$$k_l = \frac{E_l\, t_l}{(1-{\nu_l}^2)\left(R_{ext} - t_s - \frac{t_l}{2}\right)} \qquad (A6-4)$$

Where E_l is the Young Modulus of the lining, t_l is the thickness of the lining, ν_l is the Poisson's coefficient of the lining, t_s is the thickness of the support, and R_{ext} is the excavation radius. It can be noted that the external radius of the lining is reduced compared to the excavation radius (diminution of the support thickness).

A specific cell is added: "Is the increase of ground pressure only carried by the lining?" This cell can take whether "Yes" or "No" as input, allowing to consider or not the strength of the support in the long-term calculation:

- "Yes": The calculations are performed (the Monte Carlo simulation for the failure probabilities) without considering the strength of the support. The increase of ground pressure associated with the long-term property is carried entirely by the lining. In this case, the stiffness used in the long-term calculation is the one of the lining (A6-4). This situation is typical of a lining much stiffer than the support, in which case, it would be loaded preferably. It can be noted that it is supposed that the support still carries the short-term ground pressure.
- "No": The calculations are performed with the consideration the strength of the support. The increase of ground pressure associated with the long-term property is carried by both the support and the lining. In this case, the stiffness used in the long-term calculation is the summation of the support and lining stiffnesses, and the maximal ground pressure admissible is the summation of the one from the support and from the lining. It corresponds to a situation without lining, or when the stiffness of the support and the lining is similar.

The choice to use both options is let to the user.

The calculation of the long-term ground pressure is performed using the methodology presented in Chapter 4.3.3, based on a 2D plane strain problem, and the close form analytical expression proposed by Carranza-Torres and Fairhurst (1999).

Two types of calculations are possible: deterministic calculation (Figure 6-q) and probabilistic calculation (Figure 6-r). The deterministic calculations are performed using the macro "Long-term ground pressure calculation". The result is presented in the first cell (Figure 6-q), while the second cell presents the increase of ground pressure between the short-term and the long-term.

Deterministic calculation	
Ground pressure on the support - Long term (MPa)	5.04
Increase of ground pressure - Long term (MPa)	2.96

Long term ground pressure calculation

Figure 6-q: Results of the deterministic calculation

The results of the probabilistic calculation are dependent on the situation and are obtained thought Monte Carlo simulation (macro: "Monte Carlo Simulation – Long term ground pressure"). If "No" is selected above (Figure 6-p), the failure probabilities calculated are for the combination of the lining and the support, with and without considering the variability on their strengths. If "Yes" is selected, the failure probabilities calculated are for the lining only. The maximal admissible ground pressure on the lining is compared with the increase of ground pressure associated with the transition between the short-term and the long-term behavior. It is supposed that the support still carries the short-term ground pressure. The parameters of the distribution law for the ground pressure are also presented (Figure 6-s).

Probabilisitic calculation	
Failure probability without the uncertainty on the support and/or lining strength	3.05%
Failure probability with the uncertainty on the support and/or lining strength	0.17%
Maximal ground pressure without partial factors on the lining and/or support Pimax (MPa)	5.998

Monte Carlo Simulation - Long term ground pressure

Figure 6-r: Results of the probabilistic calculations

			Parameter for the LogNormal law		95% confidence intervalle	
Result parameters	Median value	Mean value	Mean	Standard Deviation	Quantile 2.5%	Quantile 97.5%
Pi_lt	5.07	5.07	1.623	0.096	4.20	6.12

Figure 6-s: Parameters of the distribution law of the long-term ground pressure

Appendix 7 - Results of situations 1 and 2, Mont Cenis base tunnel case study (Chapter 7)

This appendix presents the results of the situations 1 and 2 associated with the probabilistic rockburst risk assessment performed on the case study of the Mont Cenis Base Tunnel in Chapter 7.3.2.2.2.

Situation 1 corresponds to an isotropic in-situ stress state with a vertical stress equal to the lithostatic stress. The results are presented in Figure 7-a, Figure 7-b, and Figure 7-c.

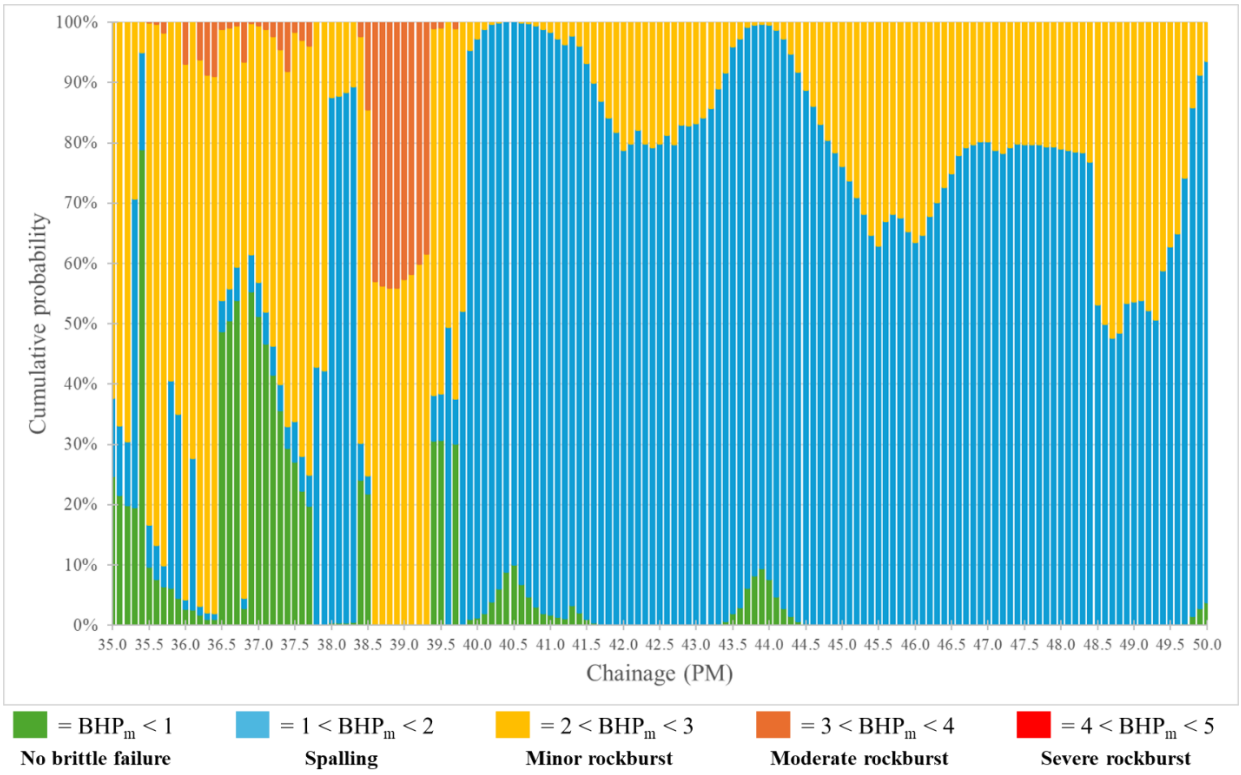

Figure 7-a: Results of the rockburst risk assessment for the Mont Cenis base tunnel (PM 35.000 - 50.000), situation 1

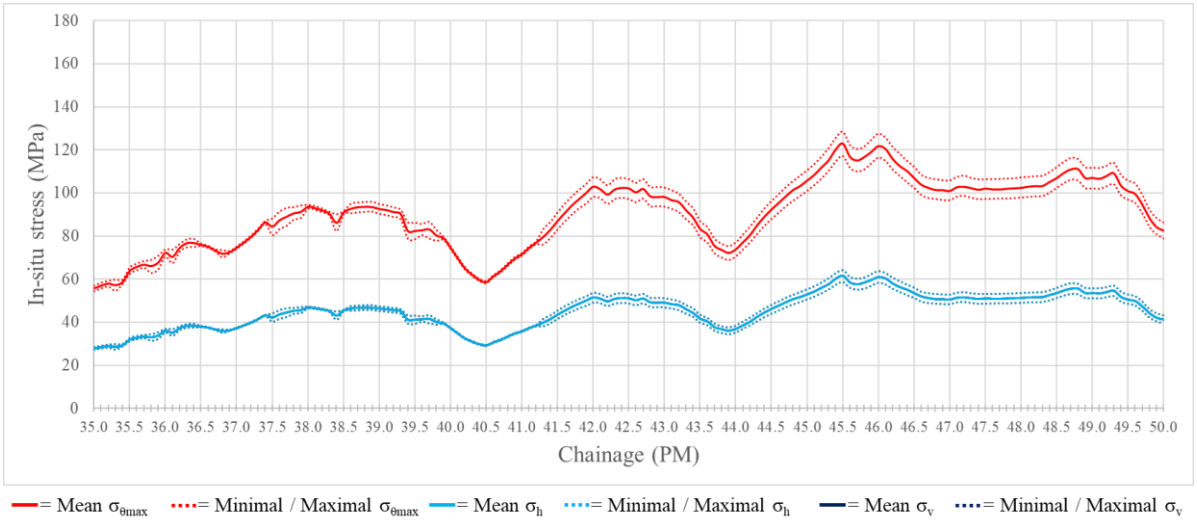

Figure 7-b: Results of the in-situ stress state associated with the Monte Carlo simulation for each section, situation 3; $\sigma_{\theta max}$ is maximal tangential stress at the tunnel boundary for an elastic behavior of the rock mass; σ_v is the vertical in-situ stress; σ_h is the horizontal stress perpendicular to the tunnel direction

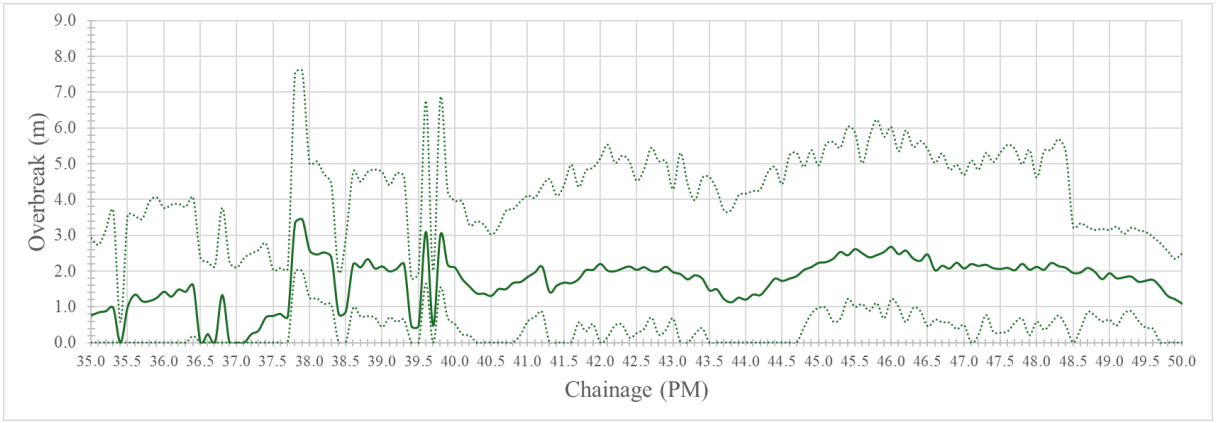

Figure 7-c: Estimation of the overbreak / depth of failure based on Eq. (6-5) of the Diederichs's (2018) method, situation 2; the solid line is the median value of the overbreak for each tunnel section; the dash lines are the minimal and maximal values of overbreak

Situation 2 corresponds to a situation where the minimal and maximal values of K_v and K_h are chosen based on the results of the in-situ tests and are used on the entire section studied. The distribution laws are uniform between 0.8 and 1.4 for K_v and 0.6 and 1.3 for K_h. The results are presented in Figure 7-d, Figure 7-e, and Figure 7-f.

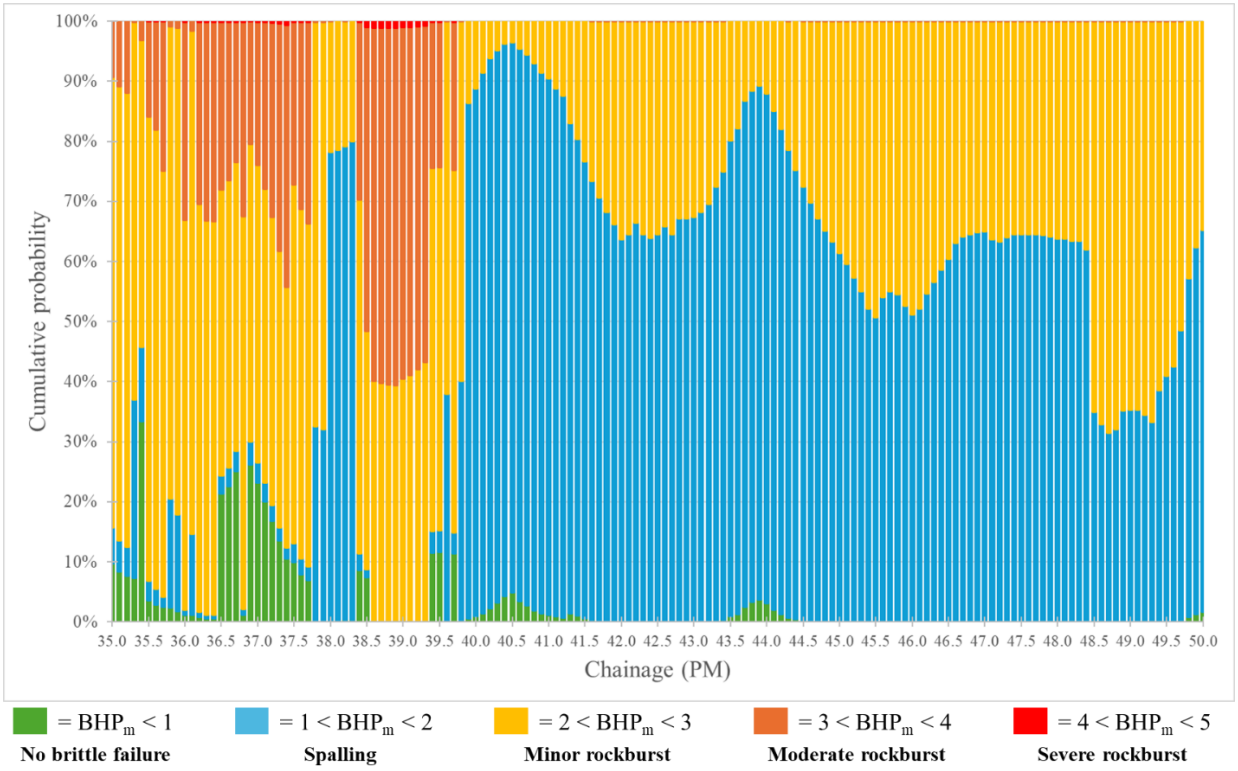

Figure 7-d: Results of the rockburst risk assessment for the Mont Cenis base tunnel (PM 35.000 - 50.000), situation 2

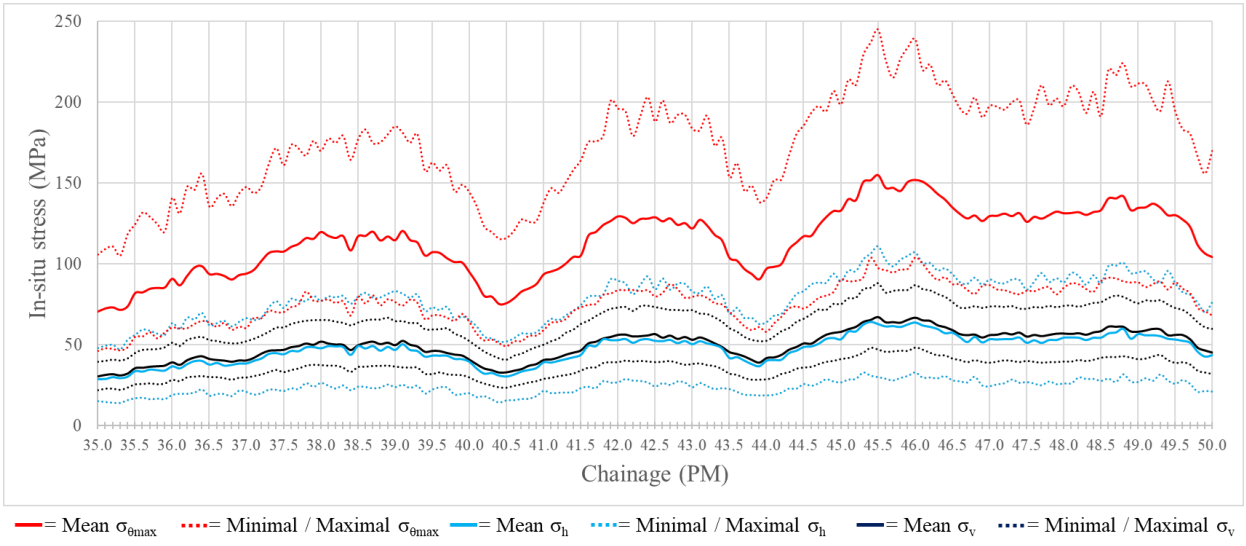

Figure 7-e: Results of the in-situ stress state associated with the Monte Carlo simulation for each section, situation 2; $\sigma_{\theta max}$ is maximal tangential stress at the tunnel boundary for an elastic behavior of the rock mass; σ_v is the vertical in-situ stress; σ_h is the horizontal stress perpendicular to the tunnel direction

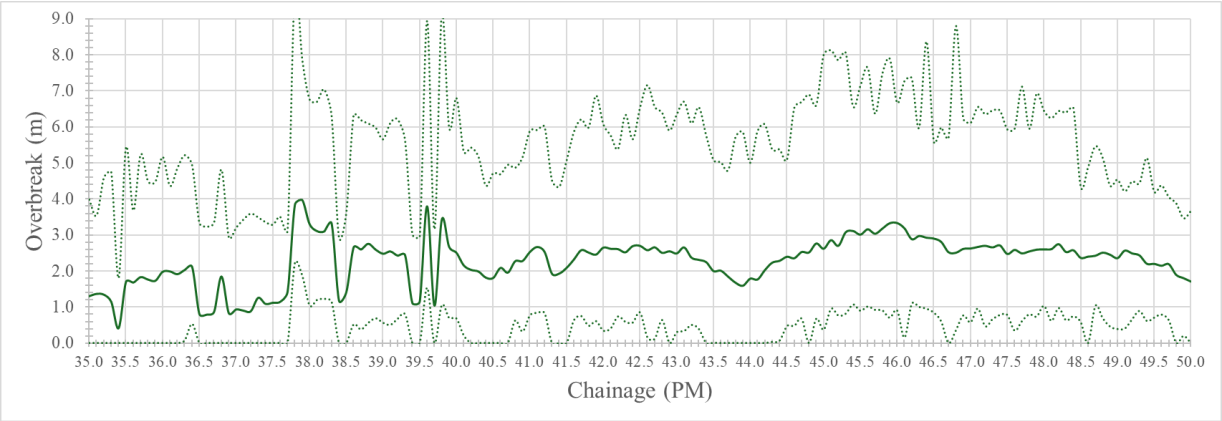

Figure 7-f: Estimation of the overbreak / depth of failure based on Eq. (6-5) of the Diederichs's (2018) method, situation 2; the solid line is the median value of the overbreak for each tunnel section; the dash lines are the minimal and maximal values of overbreak

Appendix 8 - Analytical comparison of $M_{s\text{-}s}$ and $k_{f\text{-}d}$ on nonrectangular notch (Chapter 8)

As presented in Chapter 8.2.1.1, $M_{s\text{-}s}$ and $k_{f\text{-}d}$ can be linked by the following relationship:

$$M_{s-s} = \frac{\frac{L}{2}}{t * d} k_{f-d} \qquad (A8-1)$$

The objective of this appendix is to demonstrate that the above relationship is limited to rectangular notch based on analytical calculations

A 8.1. Example 1: Notch characterized by two mesh elements (depth size) with various lengths

Let's consider the following notch geometry:

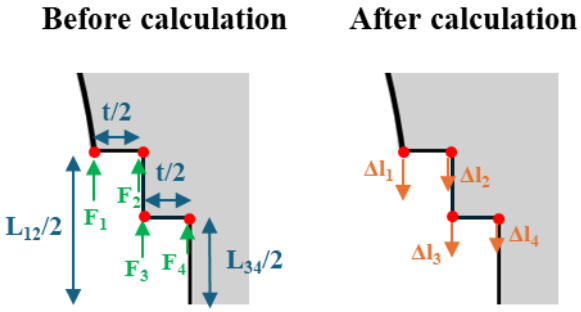

Figure 8-a: Notch geometry for example 1

Only half of the notch is represented as the forces and displacements are supposed to be symmetrical. In this situation, the mathematical expressions of $M_{s\text{-}s}$ and $k_{f\text{-}d}$ are as follows:

$$M_{s-s} = \frac{\sigma_{mean}}{\varepsilon_{mean}} = \frac{\frac{\sigma_{12} + \sigma_{34}}{2}}{\frac{\varepsilon_{12} + \varepsilon_{34}}{2}} = \frac{\frac{F_1 + F_2}{\frac{t}{2} * 1} + \frac{F_3 + F_4}{\frac{t}{2} * 1}}{\frac{\Delta l_1 + \Delta l_2}{L_{12}} + \frac{\Delta l_3 + \Delta l_4}{L_{34}}} = \frac{2}{t * 1} \frac{\sum F_i}{\frac{\Delta l_1 + \Delta l_2}{L_{12}} + \frac{\Delta l_3 + \Delta l_4}{L_{34}}} \qquad (A8-2)$$

$$k_{f-d} = \frac{F_1 + F_2 + F_3 + F_4}{\Delta l_{mean}} = \frac{F_1 + F_2 + F_3 + F_4}{\frac{\Delta l_1 + \Delta l_2 + \Delta l_3 + \Delta l_4}{4}} = \frac{4 \sum F_i}{\sum \Delta l_i} \qquad (A8-3)$$

To simplify, let's test several assumptions:

1) It is assumed that all the Δl_i are equal and that $L_{12} = 2\, L_{34}$. Eq.(A8-2) and Eq.(A8-3) can be written as follows:

$$M_{s-s} = \frac{2 * 2 * L_{34}}{t * 1 * 6} \frac{\sum F_i}{\Delta l_1} = \frac{2\, L_{34}}{3\, t * 1} \frac{\sum F_i}{\Delta l_1} \qquad (A8-4)$$

$$k_{f-d} = \frac{4 \sum F_i}{4\, \Delta l_1} = \frac{\sum F_i}{\Delta l_1} \qquad (A8-5)$$

The relationship between M_{s-s} and k_{f-d} is:

$$M_{s-s} = \frac{2\, L_{34}}{3\, t * 1} k_{f-d} = \frac{L_{12}}{3\, t * 1} k_{f-d} \qquad (A8-6)$$

2) It is assumed that all the Δl_i are equal and that $L_{12} = 11/10\, L_{34}$. Eq.(A8-2) can be written as follows, while Eq.(A8-3) is still equal to Eq.(A8-5):

$$M_{s-s} = \frac{2 * 11 * L_{34}}{t * 1 * 42} \frac{\sum F_i}{\Delta l_1} = \frac{11\, L_{34}}{21\, t * 1} \frac{\sum F_i}{\Delta l_1} \qquad (A8-7)$$

The relationship between M_{s-s} and k_{f-d} is:

$$M_{s-s} = \frac{11\, L_{34}}{21\, t * 1} k_{f-d} = \frac{10\, L_{12}}{21\, t * 1} k_{f-d} \approx \frac{L_{12}}{2\, t * 1} k_{f-d} \qquad (A8-8)$$

3) It is assumed that $\Delta l_1 = 2\Delta l_2 = 4\Delta l_3 = 8\Delta l_4$ and that $L_{12} = 2\, L_{34}$. Eq.(A8-2) and Eq.(A8-3) can be written as follows:

$$M_{s-s} = \frac{2}{t * 1} \frac{\sum F_i}{\frac{8\Delta l_4 + 4\Delta l_4}{2\, L_{34}} + \frac{2\Delta l_3 + \Delta l_4}{L_{34}}} = \frac{2 * 2 *\, L_{34}}{t * 1 * 17} \frac{\sum F_i}{\Delta l_4} = \frac{4\, L_{34}}{17\, t * 1} \frac{\sum F_i}{\Delta l_4} \qquad (A8-9)$$

$$k_{f-d} = \frac{4 \sum F_i}{15\, \Delta l_4} \qquad (A8-10)$$

The relationship between M_{s-s} and k_{f-d} is:

$$M_{s-s} = \frac{15\, L_{34}}{17\, t * 1} k_{f-d} = \frac{15\, L_{12}}{34\, t * 1} k_{f-d} \qquad (A8-11)$$

Based on Eq.(A8-6), Eq.(A8-8) and Eq.(A8-11), the smaller the gap between L_{12} and L_{34} is, the closest the relationship between M_{s-s} and k_{f-d} are from Eq.(A8-1).

A 8.2. Example 2: Notch characterized by three mesh elements (depth size) with various lengths

Now, let's consider the following notch geometry which is similar to the previous one with one more mesh element in the depth size:

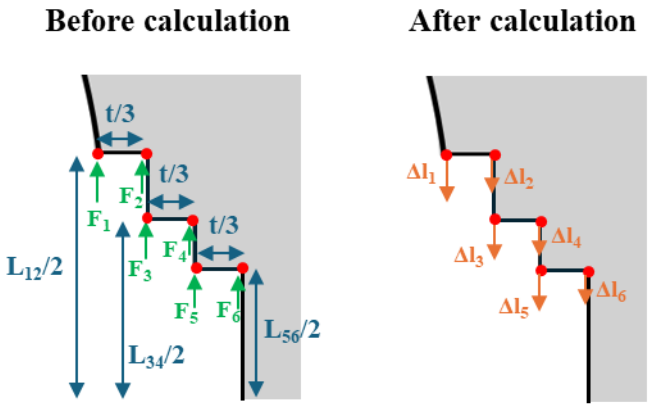

Figure 8-b: Notch geometry for example 2

Only half of the notch is represented as the forces and displacements are supposed to be symmetrical. In this situation, the mathematical expressions of M_{s-s} and k_{f-d} are as follows:

$$M_{s-s} = \frac{\sigma_{mean}}{\varepsilon_{mean}} = \frac{\frac{\sigma_{12} + \sigma_{34} + \sigma_{56}}{3}}{\frac{\varepsilon_{12} + \varepsilon_{34} + \varepsilon_{56}}{3}} \qquad (A8-12)$$

$$M_{s-s} = \frac{\frac{F_1 + F_2}{\frac{t}{3} * 1} + \frac{F_3 + F_4}{\frac{t}{3} * 1} + \frac{F_5 + F_6}{\frac{t}{3} * 1}}{\frac{\Delta l_1 + \Delta l_2}{L_{12}} + \frac{\Delta l_3 + \Delta l_4}{L_{34}} + \frac{\Delta l_5 + \Delta l_6}{L_{56}}} = \frac{3}{t * 1} \frac{\sum F_i}{\frac{\Delta l_1 + \Delta l_2}{L_{12}} + \frac{\Delta l_3 + \Delta l_4}{L_{34}} + \frac{\Delta l_5 + \Delta l_6}{L_{56}}} \qquad (A8-13)$$

$$k_{f-d} = \frac{F_1 + F_2 + F_3 + F_4 + F_5 + F_6}{\Delta l_{mean}} = \frac{\sum F_i}{\frac{\sum \Delta l_i}{6}} = \frac{6 \sum F_i}{\sum \Delta l_i} \qquad (A8-14)$$

To simplify, let's test several assumptions:

1) It is assumed that all the Δl_i are equal and that $L_{12} = 2\,L_{34} = 4\,L_{56}$. Eq.(A8-2) and Eq.(A8-3) can be written as follows:

$$M_{s-s} = \frac{3 * 4\,L_{56}}{t * 1 * 14} \frac{\sum F_i}{\Delta l_6} = \frac{3\,L_{12}}{14\,t * 1} \frac{\sum F_i}{\Delta l_6} \qquad (A8-15)$$

$$k_{f-d} = \frac{6 \sum F_i}{6\,\Delta l_6} = \frac{\sum F_i}{\Delta l_6} \qquad (A8-16)$$

The relationship between M_{s-s} and k_{f-d} is:

$$M_{s-s} = \frac{3\,L_{12}}{14\,t * 1} k_{f-d} \qquad (A8-17)$$

2) It is assumed that all the Δl_i are equal and that $L_{12} = \frac{11}{10} L_{34} = \frac{12}{10} L_{56}$. Eq.(A8-2) can be written as follows, while Eq.(A8-3) is still equal to Eq.(A8-5):

$$M_{s-s} = \frac{3 * 12\, L_{56}}{t * 1 * 66} \frac{\sum F_i}{\Delta l_6} = \frac{5\, L_{12}}{11\, t * 1} \frac{\sum F_i}{\Delta l_6} \qquad (A8-18)$$

The relationship between M_{s-s} and k_{f-d} is:

$$M_{s-s} = \frac{5\, L_{12}}{11\, t * 1} k_{f-d} \approx \frac{L_{12}}{2\, t * 1} k_{f-d} \qquad (A8-19)$$

3) It is assumed that $\Delta l_1 = 2\Delta l_2 = 4\Delta l_3 = 8\Delta l_4 = 16\Delta l_5 = 32\Delta l_6$ and that $L_{12} = 2\, L_{34} = 4\, L_{56}$. Eq.(A8-2) and Eq.(A8-3) can be written as follows:

$$M_{s-s} = \frac{3}{t * 1} \frac{\sum F_i}{\frac{32\Delta l_6 + 16\Delta l_6}{4L_{56}} + \frac{8\Delta l_6 + 4\Delta l_6}{2L_{56}} + \frac{2\Delta l_6 + \Delta l_6}{L_{56}}} = \frac{3 * L_{56}}{t * 1 * 21} \frac{\sum F_i}{\Delta l_6} \qquad (A8-20)$$

$$k_{f-d} = \frac{6 \sum F_i}{63\, \Delta l_6} = \frac{2 \sum F_i}{21\, \Delta l_6} \qquad (A8-21)$$

The relationship between M_{s-s} and k_{f-d} is:

$$M_{s-s} = \frac{3\, L_{12}}{2\, t * 1} k_{f-d} \qquad (A8-19)$$

There is no general relationship between M_{s-s} and k_{f-d}, and Eq.(A8-1) is valid only for rectangular notch.

Appendix 9 - Simplified surrogate model for ground pressure on the support

This Appendix presents briefly the surrogate model used for graphical representations. It is based on two smaller surrogate models (the one presented in Chapter 4.2.3.2 considered three).

As a reminder, the mathematical expression linking the two smaller surrogate models to the ground pressure on the support is:

$$ln(P_i) = D(\sigma_0, \varepsilon_{us}, R_p, E_m, K) + E(\sigma_0, \varepsilon_{us}, R_p, E_m, K) * e \qquad (A9-1)$$

Where D and E are constant.

A 9.1. Surrogate models of D(σ_0, ε_{us}, R_p, E_m, K)

The surrogate model of D is similar to the one of A (Chapter 4.2.3.2.1). It was obtained with nonlinear regression:

$$D = d_0 \ln(\sigma_0) + {R_p}^{d_1} + \frac{d_2 E_m + d_3 \ln(\varepsilon) + d_4}{d_6 k^{d_5} + d_6} \qquad (A9-2)$$

Where d_i are constants determined through nonlinear fitting, presented in Table 9-a.

Table 9-a: Values of the fitting parameters obtained for the surrogate model D

Contants	d_0	d_1	d_2	d_3	d_4	d_5	d_6	d_7
Value	0.75	-0.63	-3.8 x 10^{-5}	0.21	-0.24	0.34	0.089	0.202

The comparison between the estimated value of D using Eq.(A9-2) and the "real" value are presented in Figure 9-a.

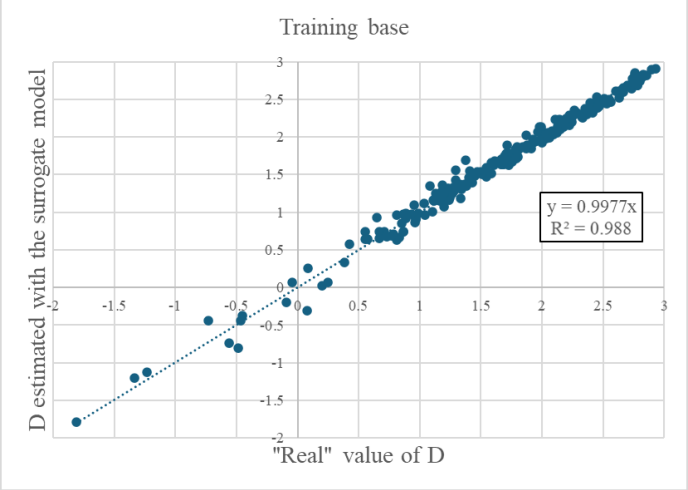

Figure 9-a: Comparison of the real values of D and the one obtained with the surrogate model

A 9.2. Surrogate models of E(σ_0, ε_{us}, R_p, E_m, K)

The surrogate model to estimate the value of B has been obtained with multilinear regression:

$$E = e_0 + e_1 \ln(\sigma_0) + e_2 E_m + e_3 \ln(E_m) + e_4 \varepsilon + e_5 \ln(\varepsilon) + e_6 R_p + e_7 \ln(R_p) + e_8 k + e_9 \ln(e_{10} k) \quad (A9-3)$$

Where e_i are constants determined through linear fitting, presented in Table 9-b.

Table 9-b: Values of the fitting parameters obtained for the surrogate model E

Constants	e_0	e_1	e_2	e_3	e_4	e_5	e_6	e_7	e_8	e_9	e_{10}
Value	-0.64	0.068	4.2 x 10^{-6}	-0.10	-0.10	-0.064	0.065	0.42	-5.9 x 10^{-3}	0.037	0.202

The comparison between the estimated value of E using Eq.(A9-3) and the "real" value are presented in Figure 9-b.

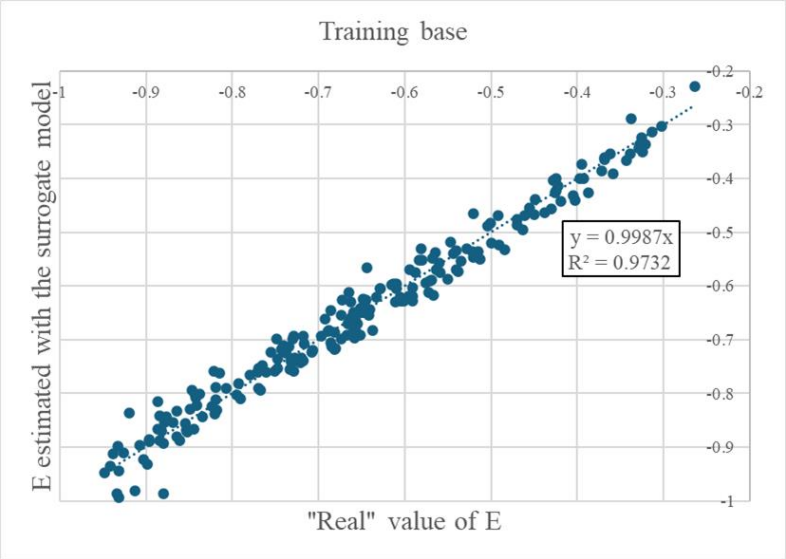

Figure 9-b: Comparison of the real values of E and the one obtained with the surrogate model

A 9.3. Prediction of the ground pressure on the support

For the graphical representation, Eqs.(A9-1) is used. Figure 9-c presents the application of this surrogate model based the model D and model E. The 95% confidence interval is [-25.7%; 24.1%] on the training base, and [-25.2%; 25.4%] on the validation base.

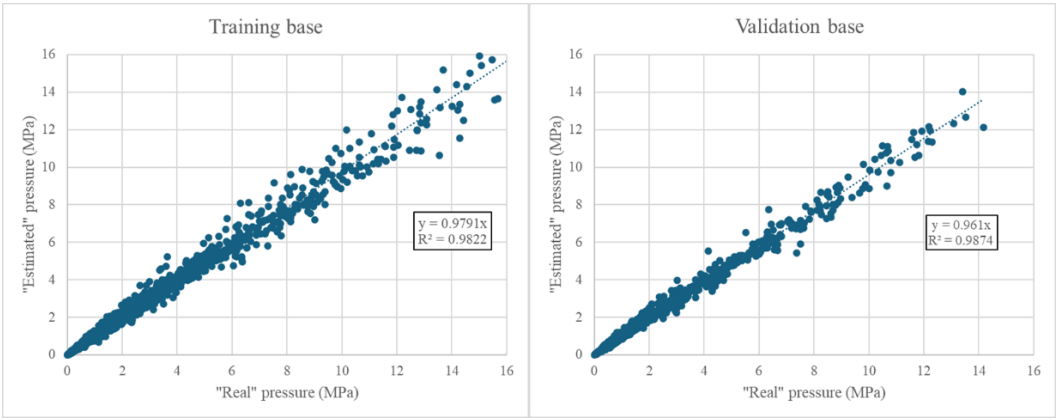

Figure 9-c: Simplified surrogate model for the prediction of the ground pressure on the support, based on the model D and E